

# **RIKEN** **Accelerator** **Progress Report**

1997

vol. **31**

理化学研究所  
*The Institute of Physical and Chemical Research (RIKEN)*

**RIKEN Accelerator Progress Report** 1997  
**January-December**

**vol. 31**

理化学研究所  
**The Institute of Physical and Chemical Research (RIKEN)**  
**Wako, Saitama, 351-0198 JAPAN**

### **Editors**

T. Abe      A. Goto  
T. Ichihara   R. Kadono  
T. Kambara   Y. Kobayashi  
A. Ozawa      I. Shimamura  
S. Yamaji     Y. Yamazaki

All rights reserved. This report or any part thereof may not be reproduced in any form (including photostatic or microfilm form) without written permission from the publisher.

All reports are written on authors' responsibility and thus the editors are not liable for the contents of the report.

# CONTENTS

	Page
<b>I. PREFACE</b> .....	1
<b>II. OPERATION OF ACCELERATORS</b>	
RILAC Operation .....	3
RRC and AVF Cyclotron Operations .....	5
The Tandem Operation .....	7
<b>III. RESEARCH ACTIVITIES</b>	
1. Nuclear Physics	
Momentum Distributions of the Core Fragment from the Nuclear Breakup Reaction within the Glauber Model .....	9
Astrophysical $S$ -Factors for ${}^7\text{Be}(p,\gamma){}^8\text{B}$ Determined by Coulomb Dissociation Measurements .....	10
Shell Model Calculation of Magnetic Moments of Light Mirror Nuclei .....	11
Spin Dipole States of Deformed Nuclei .....	12
A Giant Halo at the Neutron Drip Line .....	13
The Proton and Neutron Distributions in Na Isotopes: The Development of Halo and Shell Structure .....	14
Structure of Unstable Nuclei Studied by Monte Carlo Shell Model .....	15
Quantum Monte Carlo Diagonalization Method with Condensed-Pair Bases .....	16
The Pseudo-Spin Symmetry in Realistic Nuclei .....	17
Double Giant Quadrupole Resonance .....	18
Possible Enhancement of the $E1$ Decay Rates of Double Giant Dipole States .....	19
Possible Deviation of the Sum of Strengths for Double Giant Dipole Resonance from Harmonic Oscillator Limit .....	20
Constrained GCM Calculations Based on 3D-CHFB .....	21
Exotic State of 3D-CHFB .....	22
Signature and Angular Momentum in 3D-Cranked HFB States .....	23
Doubly Periodic Motion in Superdeformed States .....	24
Triaxial Nuclei in Relativistic Mean Field Theory .....	25
The Deformation Effect on the Pairing Gap .....	26
Thermal Damping Width of Giant Dipole Resonance in Hot Nuclei .....	27
Relation between the Damping of the Hot Giant Dipole Resonance and the Complex Admittance of an Irreversible Process .....	28
Temperature Dependence of Quantal and Thermal Dampings of Hot Giant Dipole Resonance .....	29

Stability of the Thermal HFB Equation .....	30
Variation of Transport Coefficients for Average Fission Dynamics with Temperature and Shape .....	31
Collective Motion at Finite Excitations in Terms of Cassini Ovaloids .....	32
Nucleus as a Canonical Ensemble: The Inverse Laplace Transformation .....	33
Damping Width of the Mie Plasmon .....	34
Explosion of a Neutron Star Just Below the Minimum Mass: A Possible Site for r-Process Nucleosynthesis .....	35
Relativistic Equation of State for Supernova .....	36
Can the Equation of State of Asymmetric Nuclear Matter Be Studied Using Unstable Nuclei? .....	37
Exotic Nuclear Rod Formation Induced by Superfluid Vortices in Neutron Star Crusts .....	38
Dynamics of Exotic Nuclear Rod Formation for Neutron Star Glitches .....	39
High Ratio of $^{44}\text{Ti}/^{56}\text{Ni}$ in Cas A and Axisymmetric Collapse-Driven Supernova Explosion .....	40
Low Energy Aspects of the Field Strength Approach .....	41
Nuclear Transparency in a Relativistic Harmonic Oscillator Quark Model .....	42
Quark Distributions in the Nucleon by the Semi-Inclusive Reaction on the Proton- and $^3\text{He}$ -Target .....	43
Parameterization of the Polarized Parton Distribution Functions .....	44
$Q^2$ Evolution of Polarized Parton Distributions .....	45
NLO $Q^2$ -Evolution of the Nucleon's Transversity Distribution $h_1(x, Q^2)$ .....	46
The $\psi'$ Production in Polarized $pp$ Collisions as a Test of Color-Octet Mechanism ....	47
Heavy Quark Physics with Spin .....	48
Measurement of $\alpha$ -Sticking Probability in Muon Catalyzed $dt$ Fusion by X-ray Method at RIKEN-RAL Muon Facility .....	49
Fusion Neutron Yield and Muon Cycling Rate in Muon Catalyzed $dt$ Fusion at RIKEN-RAL Muon Facility .....	50
$K_\beta/K_\alpha$ Sticking X-ray Ratio in Muon Catalyzed $dt$ Fusion at RIKEN-RAL Muon Facility .....	51
RHIC Spin Project .....	52
Results from Beam Tests of PHENIX Muon Identifier .....	53
Spin Physics with Photon Detection at PHENIX .....	54
Studies of Systematic Problems in the Spin Dependent Structure Functions of the Nucleon .....	55
High Spin Isomer Beam Experiment at RIKEN .....	56
Search for High-Spin Isomer in $^{143}\text{Nd}$ .....	57

$\gamma$ -Ray Linear Polarization Measurement by Segmented Ge .....	58
Measurements of Neutron Spallation Cross Sections of $^{59}\text{Co}$ and $^{\text{nat}}\text{Cu}$ .....	59
Polarization Observables for the $^3\vec{\text{He}}(\vec{d}, p)^4\text{He}$ Reaction .....	60
Study of Spin Flip Signatures via $^{12}\text{C}(d, d')$ Reaction .....	61
Measurement of the $^{28}\text{Si}(\vec{d}, \vec{d}')$ Reaction at $E_d = 270$ MeV .....	62
Gamow-Teller Strength Distribution in fp Shell Nuclei .....	63
Low Background Measurement of $^8\text{B}$ Coulomb Dissociation .....	64
Measurement of Cross Sections of the $^8\text{Li}(\alpha, n)^{11}\text{B}$ and $^8\text{Li}(\alpha, \alpha n)^7\text{Li}$ Reactions with a New-MUSIC Detector .....	65
Density Distribution of $^9\text{C}$ Derived from Reaction Cross Sections .....	66
Inelastic Proton Scattering on $^{12}\text{Be}$ in Inverse Kinematics .....	67
Coulomb Excitation of $^{11}\text{Be}$ .....	68
Coulomb Dissociation of $^{12}\text{N}$ .....	69
Quadrupole Moment of $^{13}\text{O}$ .....	70
Coulomb Dissociation of $^{17}\text{C}$ and $^{19}\text{C}$ .....	71
Measurements of the $^{18}\text{N}$ Magnetic Moment and Electric Quadrupole Moment .....	72
Measurements of Half Lives and Neutron Emission Probabilities of the Neutron Drip Line Nuclei $^{19}\text{B}$ , $^{22}\text{C}$ , and $^{23}\text{N}$ .....	73
Lifetime Measurement of $^{31,32}\text{Ne}$ .....	74
Coulomb Excitation of $N \sim Z \sim 28$ .....	75
Production Cross Sections of Projectile-like Fragments in the $^{40}\text{Ar} + ^{181}\text{Ta}$ Reaction at 94A MeV .....	76
Polarized $^{129}\text{Xe}$ Solid for Polarizing Unstable Nuclei .....	77
Coulomb Dissociation of $^8\text{B}$ at 254 MeV/u .....	78
Measurement of Interaction Cross Sections for Light Neutron Rich Nuclei .....	79

## 2. Atomic and Solid-State Physics

Electron Capture in Collisions of $\text{H}^+$ Ions with S Atoms and Its Reverse Process below keV-Energies .....	81
Theoretical Attempt for Double Ionization of Helium by Energetic Charged-Particle Impact .....	82
Superexcited States of the Hydrogen Molecule .....	83
Theoretical Study of Electron Scattering from $\text{CH}_2\text{F}_2$ Molecules .....	84
Fluorination Effects in Electron Scatterings from $\text{CH}_4$ , $\text{CH}_3\text{F}_1$ , $\text{CH}_2\text{F}_2$ , $\text{CH}_1\text{F}_3$ , and $\text{CF}_4$ .....	85
The Coupling of Electron Thermalization and Electron Attachment in $\text{CCl}_4/\text{Ar}$ and $\text{CCl}_4/\text{Ne}$ Mixtures .....	86
Resonances in $\text{Ps}^-$ System .....	87

Auger Transition Rates for Metastable States of the Antiprotonic Helium $\text{He}^+\bar{p}$ .....	88
Fine and Quadrupole Structures of the Weakly Bound Systems $[(d\bar{t}\mu)_{11}dee]$ and $[(dd\mu)_{11}dee]$ .....	89
State-Selective Differential Cross Sections of Electron Capture in 10 MeV $\text{Ar}^{8+}$ -He Collisions .....	90
Beam Foil Spectra of Highly Charged Neon Ions in Visible Region .....	91
Beam Foil Spectra of Highly Charged Krypton Ions in Visible Region .....	92
Lifetimes of Intercombination Lines in Highly Charged Nb .....	93
Inherent Problems with Beam-Foil Lifetime Measurements .....	94
Electron Spectra Arising from Collisions between 50 keV $\text{N}^{5+}$ and Ar .....	95
VUV Photon Emission Spectroscopy of Slow, Highly Charged Ions .....	96
Defect Production and Electronic Excitation in Ion-Irradiated High- $T_c$ Superconductors .....	97
Effect of Heavy-Ion Irradiation on the Bi-Based Superconductors .....	98
Irradiation Effects of Swift Heavy-Ion on Polycrystalline $\text{La}_{1.85}\text{Sr}_{0.15}\text{CuO}_4$ .....	99
Observation of Columnar Defects in Layered Materials Bombarded by $^{136}\text{Xe}^{+31}$ , $^{181}\text{Ta}^{+37}$ , and $^{209}\text{Bi}^{+37}$ by STM and TEM .....	100
Experimental Study of Single Event Burnout (SEB) Hardening on POWER MOSFET .....	101
Change of Site Occupancy of Hydrogen in Nb on Alloying with Undersized Mo .....	102
Annealing of the $\text{Cu}_3\text{Au}$ Irradiated with Protons, $\alpha$ -Particles and C Ions at Liquid Nitrogen Temperature .....	103
Development of Experimental Setup for Laser Spectroscopic Study of Ions in Superfluid Helium .....	104
Muon Spin Relaxation in $\text{KCuCl}_3$ .....	105
$\mu\text{SR}$ Studies on $(\text{Nd}_{1-y}\text{Sm}_y)_{0.5}\text{Sr}_{0.5}\text{MnO}_3$ .....	106
Critical Spin Dynamics in $\text{Nd}_{1-x}\text{Sr}_x\text{MnO}_3$ with $x \approx 0.5$ .....	107
$\mu^+\text{SR}$ Study of Heavy-Fermion Magnetism in $\text{Ce}(\text{Cu}_{1-x}\text{Ni}_x)_2\text{Ge}_2$ .....	108
$\mu\text{SR}$ Studies of Non-Fermi-Liquid Behaviour in $\text{Ce}_7\text{Ni}_3$ .....	109
Behavior of the Positive Muon in $2H\text{-NbSe}_2$ .....	110
$\mu\text{SR}$ Study on 2D Kagome Organic Magnet, $m\text{-MPYNNBF}_4$ .....	111
$\mu\text{SR}$ Study of Critical Behavior of $p\text{-Cl-C}_6\text{H}_4\text{-CH=N-TEMPO}$ .....	112
$\mu^+\text{SR}$ Study of Polaron Motion in Polyaniline .....	113
Muon Studies on the Weak Charge Transfer System Anthracene/Tetracyanobenzene .....	114
Electronic State of $\mu\text{Al}$ Pseudo-Acceptor Centers in Si Probed by $\mu^-\text{SR}$ .....	115
Development of an RF Resonance System for Pulsed Muon Beam Method at RIKEN-RAL .....	116

### 3. Radiochemistry and Nuclear Chemistry

The Jump Mechanism of Self-Interstitials in Pure Iron .....	119
Dynamic Behavior of $^{57}\text{Fe}$ Atoms in Solid Ar and Solid Xe .....	120
$^{57}\text{Fe}$ Mössbauer Studies Using $^{57}\text{Mn}$ Nuclei Implanted into Al and Si .....	121
Coulomb Excitation in In-beam Mössbauer Spectroscopy .....	122
Multitracer Study on the Permeation of Rare Earth Elements through a Supported Liquid Membrane .....	123
Model Study of Acid Rain Effect on Adsorption of Trace Elements on Soils (III) .....	124
Simultaneous Determination of Stability Constants of Humate Complexes with Various Metal Ions Using Multitracer Technique .....	125
Comparative Subcellular Distribution of Radioactive Mn, Fe, Zn, and Se Tracers in Brain and Liver: Why, in Brain, Do most of Their Proteins Exist in Mitochondrial and Nuclear Fraction? .....	126
Comparative Distribution of the Trace Elements Sc, Mn, Fe, Co, Zn, Se, Rb, and Zr in the Brain and Other Organs of C57BL/6N Mice .....	127
Metabolic and Biochemical Studies of Trace Elements in Hypercholesterolemic Model Mice (I) .....	128
Metabolic and Biochemical Studies of Trace Elements in Hypercholesterolemic Model Mice (II) .....	129
Metabolic Study of Trace Elements in Se-Deficient Rats (II) .....	130
Influence of pH on Release of Various Trace Elements from Transferrin .....	131
Affinity of Bio-Trace Elements to Cell Component: <i>In vitro</i> Study Using Multitracer .....	132
Multitracer Study on Binding Activity of Various Trace Elements to Metallothionein .....	133
Multitracer Study on Coordinating of the Rare-Earth Element with Metallothionein .....	134
Transfers of Trace Elements from the Placenta to the Fetus of Pregnant Rat .....	135
Uptake and Translocation of Sr, Tc, and Cs in Soybean Plants .....	136
Multitracer Study on Uptake of Elements by Turnip .....	137
Metabolism of Trace Elements in <i>Euglena gracilis</i> Using the Multitracer Technique ...	138
Possibility of the Existence of a Special Substance Involved in the Uptake of REE by <i>Dryopteris erythrosora</i> .....	139
Study on the Uptake Rate of Various Elements into <i>Dryopteris erythrosora</i> by Multitracer Technique .....	140
Multitracer Study on Biosorption of Various Trace Elements in Yeast <i>Saccharomyces cerevisiae</i> .....	141
Heavy-Ion Induced Fission in the Medium Energy Region .....	142
Development of High Intensity Polarized Slow Positron Beam Using $^{18}\text{F}$ .....	143

4. Radiation Chemistry and Radiation Biology	
Screening of Plants for Soil-Radionuclide Accumulators .....	145
Possible Role of Soil-Microbes in Plant Uptake of Radionuclides .....	146
Effects of Heavy Ions on Survival of <i>Arabidopsis thaliana</i> .....	147
Effective Plant-Mutation Method Using Heavy-Ion Beams (II) .....	148
Cell Death and Mutation Induction on Cultured Cells by Irradiation of Heavy Ions and X-rays .....	149
Cell Cycle Progression after Heavy-Ion Irradiation .....	150
DNA Analysis of HPRT Mutations Induced by High-LET Carbon- and Neon-ion Beams .....	151
A 100 ps Lived New Luminescence Component in Ion Irradiated Alumina .....	152
Luminescence Spectra and Decay Curves of Ion Irradiated Diamonds .....	153
5. Instrumentation	
Computing Environment Surrounding the Accelerator Research Facility .....	155
Optimization of Hexapole Magnet for ECR Ion Source .....	156
Development of the Slow Highly Charged Ion Beam below 100 eV/q from an ECR Ion Source for Ion-Atom Collision Experiments .....	157
Precise Determination of Neutron Beam Polarization at 16 MeV .....	158
Development and Characterization of the Self-TOF Neutron Detector .....	159
Proton Induced Activation in GSO, BGO Scintillators .....	161
In-Vacuum Plastic-Scintillator Hodoscope for Low-Background Measurements of Charged Particles .....	162
Beta-Ray Imaging Detector Using Scintillating Fibers .....	163
Development of a Fast Two-Dimensional PPAC .....	164
A Large Area PPAC/Ionization Chamber .....	165
A New Fluorescence Photon Detection System for Collinear Laser Spectroscopy .....	167
Final Calibration of Cosmic Ray Heavy Ion Telescope for First Brazilian Scientific Satellite .....	168
Performance Study of Radiation Detectors for Spacecraft .....	169
Fabrication of the Muon Magnet for the RHIC SPIN Project .....	170
Plan of Computing Facility for RHIC Spin Project .....	171
Factory Plan for PHENIX Muon Identifier .....	172
Design of Proton Polarimeter for AGS-E925 .....	173
6. Material Analysis	
RBS Study of Na Implanted Polystyrene .....	175
Chemical State Analysis of Third Period Elements in Atmospheric Air by High-Resolution PIXE .....	176

Improvement in the Detection Limits of ERDA Using a Time-of-Flight Detection . . . .	177
Determination of the Mass and Depth Resolutions of TOF-ERDA . . . . .	178
<b>IV. NUCLEAR DATA</b>	
Status Report of the Nuclear Data Group . . . . .	179
<b>V. DEVELOPMENT OF ACCELERATOR FACILITIES</b>	
Progress of RI Beam Factory Project . . . . .	181
Improvement of Sextupole Magnet for RIKEN 10 GHz ECRIS . . . . .	182
Improvements of Low RF Power System in RIKEN 10 GHz ECRIS . . . . .	183
Electron Beams Indeed Lower the Ion-Trapping Potential Barrier via Sheaths to Enhance the HCI Component in an ECRIS: Analytical Proof . . . . .	185
RIKEN Duoplasmatron Ion Source: The Operating Principles Compared with ECRIS, and the Direction for Future . . . . .	187
Warm-Electron Heating Mechanism in the Core of ECRIS Nucleus, and Relevant Diagnostic System . . . . .	189
Production of Multicharged Os Ion Beams from Organic Metal Compounds Using RIKEN 18 GHz ECRIS . . . . .	191
Recent Development of the Variable-Frequency RFQ Linac for RILAC . . . . .	192
Phase Stabilization of Injection Beam to RIKEN Ring Cyclotron . . . . .	194
Beam Orbit Simulation in the Central Region of RIKEN AVF Cyclotron . . . . .	196
Design of a Resonator for a Flat-Top Acceleration System in RIKEN AVF Cyclotron . . . . .	198
New Emittance Measurement Using Two PPACs . . . . .	200
Heavy Ion Microbeam Project in RIKEN Accelerator Research Facility . . . . .	202
Initial Design of a Charge State Multiplier System for RIKEN RI Beam Factory . . . . .	203
The Two Booster Ring Cyclotrons for RIKEN RI Beam Factory . . . . .	205
Orbit Analysis of RIKEN Superconducting Ring Cyclotron . . . . .	206
Design of Sector Magnets for RIKEN Superconducting Ring Cyclotron . . . . .	208
Design of a Prototype Sector Magnet for RIKEN Superconducting Ring Cyclotron . . . . .	210
Quench Stabilities of the Superconducting Wires for the Sector Magnets of RIKEN Superconducting Ring Cyclotron . . . . .	212
Analysis of the Injection and Extraction Trajectories in RIKEN Superconducting Ring Cyclotron . . . . .	214
Design Study of Injection System for RIKEN Superconducting Ring Cyclotron . . . . .	216
Optimization of the Superconducting Dipole Coils for Injection System of RIKEN Superconducting Ring Cyclotron . . . . .	218
Numerical Study of Single-Turn Extraction for RIKEN Superconducting Ring Cyclotron . . . . .	220
Design of the RF Resonators for RIKEN Superconducting Ring Cyclotron . . . . .	222

Estimation of Beam Chamber Pressure Required for RIKEN Superconducting Ring Cyclotron .....	224
Design of Debuncher System in the Injection Line to Accumulator Cooler Ring of MUSES .....	225
Study of Stochastic Cooling at Accumulator Cooler Ring of MUSES .....	227
Design of Booster Synchrotron for MUSES .....	229
Design of Slow Extraction System at Booster Synchrotron for MUSES .....	231
Simulation Study of Ion Beam Bunching with Electron Cooler at Double Storage Ring of MUSES .....	233
Diffusion Beam-Beam Instability in the Presence of Beam Cooling .....	235
Stationary Particle Distribution of Intense Bunched Beam in RF Accelerating Field .....	237
High Brightness Beam Transport in a Quadrupole Focusing Channel with Octupole Field Component .....	239
Design of 300 MeV Electron Linac at MUSES .....	241
Design of Apple-II Type Undulator for MUSES .....	243
Safety Design of RIKEN RI Beam Factory .....	245
Spin Depolarization Due to Beam-Beam Instability .....	246
Study of Spin and Orbital Motion in Siberian Snake Based on Calculated Three Dimensional Magnetic Field .....	248
Calculation and Measurement of Magnetic Field in Half-Length Helical Snake Magnet for RHIC .....	250
Optimization of Full-Length Helical Snake Magnet for RHIC .....	251
<b>VI. RADIATION MONITORING</b> .....	
Routine Works for Radiation Safety in the Ring Cyclotron Facility .....	253
Dose Rates Due to Residual Radioactivity in the Ring Cyclotron Facility .....	254
Residual Induced-Radioactivity at the Old 160 cm Cyclotron .....	256
<b>VII. LIST OF PUBLICATIONS</b> .....	257
<b>VIII. LIST OF PREPRINTS</b> .....	262
<b>IX. PAPERS PRESENTED AT MEETINGS</b> .....	264
<b>X. LIST OF SYMPOSIA</b> .....	272
<b>XI. LIST OF SEMINARS</b> .....	273
<b>XII. LIST OF PERSONNEL</b> .....	275
<b>AUTHOR INDEX</b>	

## I. PREFACE

This issue of RIKEN Accelerator Progress Report reports research activities of the RIKEN Accelerator Research Facility (RARF) during the calendar year of 1997. The research programs have been coordinated in the framework of the project entitled Multidisciplinary Researches on Heavy Ion Science. The project involves a variety of fields such as: nuclear physics, atomic physics, nuclear chemistry, radiation biology, condensed matter physics in terms of accelerator or radiation application, basic studies on energy production, basic studies on accelerator cancer therapy, material characterization, application to space science, accelerator physics and engineering, laser technology, and computational technology. These activities involved 12 laboratories in RIKEN and more than 400 researchers including outside users from domestic and foreign institutions.

Major research activities of the RARF are based on a heavy-ion accelerator complex consisting of the K = 540 MeV RIKEN Ring Cyclotron (RRC) and its subordinate accelerators, i.e., the energy-variable heavy-ion linear accelerator (RILAC) and the K = 70 MeV azimuthally variable field cyclotron (AVF), which have altogether provided a beam time (on the target) of more than 8000 hours through the year. Besides, the RARF carries two international collaboration programs using oversea accelerator facilities: one is the muon science project at ISIS in collaboration with the Rutherford-Appleton Laboratory (RAL), and another is the spin physics program at RHIC in collaboration with the Brookhaven National Laboratory (BNL).

The three accelerators currently available deliver heavy ion beams of a variety of elements with energies ranging from a few A MeV to 135A MeV. The two injector machines (AVF and RILAC) are equipped with ECR heavy ion sources. The AVF is additionally equipped with a polarized ion source for vector and tensor polarized deuterons. Recently, the RILAC has dramatically enhanced its capability by newly accommodating an 18 GHz ECR ion source accompanied with a frequency-variable RFQ pre-accelerator. Heavy ion intensities have increased ten to hundred times as compared to the original setup. The three accelerators injectors and RRC have been used in various configurations. The RRC was mostly used for nuclear physics study, while the RILAC and AVF were often used for other fields in their stand-alone mode of operation. Nuclear physics and all the other disciplines shared the total allocated beam time almost evenly.

The RARF is characterized by its emphasis on the scientific application of radioactive beams. Uniquely, three different types of radioactive beams, i.e., 1)

projectile-fragment (PF) radioactive beam, 2) spin-polarized radioactive beam, and 3) high-spin isomer beam, have been cultivated to facilitate a broad scope of nuclear research. The PF beams are most widely used by virtue of their versatility and prominent intensities. The spin polarized beams are particularly useful for radioactive NMR experiments. The isomer beam intensity has been significantly improved, approaching a realistic level for application. These beams are primarily used for the study of nuclear physics. Major subjects pursued are: 1) exotic nuclear structure and new dynamics of extremely neutron-rich nuclei (such as those with a neutron halo or skin), 2) nuclear astrophysics involving unstable-nucleus reactions, 3) synthesis of new unstable isotopes far from the valley of stability, 4) extensive measurement of nuclear moments, and 5) high spin physics by means of isomer beams. Characteristic features of intermediate-energy direct reactions are often exploited for such studies. Symbolizing the achievements of this year, extremely neutron-rich nuclei,  $^7\text{H}$  and  $^{31}\text{F}$ , were newly synthesized. The radioactive beams were useful for other domains of science as well. In particular, application to condensed matter science has been started to a large extent by exploiting on-line capability of Mössbauer and PAC spectroscopies which are feasible only with RI beams.

Intermediate-energy heavy ions from the RRC have found their own applicabilities. A strikingly efficient mutagenic effect has been observed when the embryo of a Tobacco plant is shot by heavy ions. High-energy heavy ions were irradiated to the plants naturally placed in the air for desirable strength of LET through sample. This has led to establishment of a new scheme of mutant production which is efficient and well-controlled. The method is so efficient that it is expected to offer new possibilities of bio-science research through comparison between normal and mutagenic samples. Several proposals along this direction are currently being prepared. Another remarkable development has been seen in the application field of radioactive tracer technique. High-energy heavy ion reactions facilitate production of a wide variety of isotopes at a time. This feature is exploited to cultivate a novel multi-tracer methodology in which a radioactive tracer source containing a variety of elements is prepared to be injected into a sample. This enables to study circulation behaviors of different elements for a common sample under a same condition, drastically improving reliability and efficiency over the single-tracer experiments. Application of the method is rapidly extending to the fields of bio-inorganic chemistry, dietetics, toxicology,

cology, pharmacology, environmental issues, and medical fields in general.

Primary beams from RILAC were often used for studies of atomic physics. In this context an extensive program of beam-foil spectroscopy for highly-charged heavy ions continues in collaboration with a group of Lund University. More generally, atomic physicists appreciate a rich capability of the entire RARF accelerator complex in producing very highly charged ions. For instance, a high precision recoil-ion momentum spectroscopy has been developed at RRC to open up a new possibility of the impact parameter dependence analysis of high-energy atomic/ionic reactions.

As for the international collaboration projects, the pulsed muon beam facility at ISIS has entered into a stage of steady operation. Success in application of  $\mu$ SR method on biological investigation was one of the research highlights. Meanwhile, the spin physics program to investigate quark-gluon spin structure func-

tions of nucleons is in progress to be ready for the commissioning of RHIC operation in 1999.

Beyond these activities of on-going programs the RARF has been undertaking continuous efforts further to strengthen scientific opportunities for future. In this regard, the year of 1997 has marked a big mile stone: A new project so-called RIKEN Radioactive Ion Beam (RIB) Factory has been approved by the Government to promote the next generation RIB science. To start with, the first construction phase for the factory was started this year, which involves a set of cyclotrons to achieve  $K = 2500$  MeV acceleration capability. The RARF has also committed to strengthen the international collaboration program. In this context, a new RIKEN branch called RIKEN BNL Research Center has been installed to promote the RHIC physics program effectively. With these new projects approved we look forward to significant enhancement of the RARF scientific activities in coming years.

M. Ishihara  
*Director*  
*RIKEN Accelerator Research Facility*

## **II. OPERATION OF ACCELERATORS**



## RILAC Operation

E. Ikezawa, M. Hemmi, T. Chiba, S. Kohara, T. Aihara,\* T. Ohki,\*  
H. Hasebe,\* H. Yamauchi,\* and Y. Miyazawa

A new pre-injector system (consisting of a variable-frequency folded-coaxial RFQ linac and a 18-GHz ECR ion source) for RILAC was installed on the beam transport line coming from the existing 450 kV Cockcroft-Walton injector with a 8-GHz ECR ion source (NEOMAFIOS) in the end of 1996. The beam acceleration tests with the new pre-injector system have been performed successfully. The detailed results of the beam acceleration tests are reported in this issue.<sup>1)</sup> The beam acceleration tests with the existing injector system were also carried out. The beam transmission efficiency of the beam transport line using the existing injector was increased from 30 to 50% by matching the first gap voltage of the acceleration column with the beam extraction voltage of the NEOMAFIOS.

The RILAC beam service for users by using the new pre-injector and existing one was reopened in January 1997. In this reporting period, RILAC has been in a steady operation and has supplied various kinds of ion beams for the experiments. Table 1 gives the statistics of the operation from January through December 1997. Table 2 summarizes the number of days allotted to individual research groups. The percentage of the beam time used by RIKEN Ring Cyclotron (RRC) was about 51% of the total. The ions of  $^4\text{He}$ ,  $^{11}\text{B}$ ,  $^{12}\text{C}$ ,  $^{16}\text{O}$ ,  $^{36}\text{Ar}$ ,  $^{40}\text{Ar}$ ,  $^{56}\text{Fe}$ ,  $^{58}\text{Ni}$ ,  $^{84}\text{Kr}$ ,  $^{128}\text{Te}$ ,  $^{129}\text{Xe}$ ,  $^{136}\text{Xe}$ ,  $^{181}\text{Ta}$ ,  $^{208}\text{Pb}$ , and  $^{209}\text{Bi}$  accelerated by RILAC were injected to RRC. Tables 3 and 4 give statistics of the RILAC ion beams injected from the existing injector with the NEOMAFIOS and from the new pre-injector with the 18-GHz ECR ion source, respectively. The ion beams of 17 kinds of element were used for the experiments and for beam acceleration tests. The percentage of the beam time to have used metallic ions amounted to about 27% of the total.

Table 1. Statistics of the RILAC operation from January 1 through December 31, 1997.

	Days	%
Beam time	182	49.9
Frequency change	12	3.3
Overhaul and improvement	49	13.4
Periodic inspection and repair	19	5.2
Machine trouble	0	0.0
Scheduled shut down	103	28.2
Total	365	100

Table 2. Beam time allocated for individual research groups.

	Days	%
Atomic physics	45	24.7
Nuclear physics	2	1.1
Material analysis and development	8	4.4
Radiation chemistry	18	9.9
Accelerator research	16	8.8
Beam transport to RRC	93	51.1
Total	182	100

Table 3. Statistics of the RILAC ion beams using the Cockcroft-Walton injector.

Ion	Mass	Charge state	Days
He	4	1,2	8
B	11	2,3	9
C	12	2,5	4
N	14	3	1
O	16	2,3	8
Ne	20	3	7
Mg	24	5	2
Ar	36	5	4
Ar	40	6,8	19
Kr	84	11,13	19
Nb	93	12	2
Xe	136	15	7
Ta	181	16	3
Pb	208	16	4
Bi	209	16	9
Total			106

Table 4. Statistics of the RILAC ion beams using the new pre-injector.

Ion	Mass	Charge state	Days
N	14	2,5	2
O	16	5	2
Ar	36	5	2
Ar	40	5,8,11,12	23
Fe	56	7	5
Ni	58	8,9	7
Kr	84	11,18	3
Te	128	18	8
Xe	129	17	4
Xe	136	15,18,19, 20,27	20
Total			76

\* Sumijyu Accelerator Service, Ltd.

Table 5. Ion beam currents ( $\mu\text{A}$ ) of all ion species that we have obtained by the NEOMAFIOS until now. The beam extraction voltage ( $V_{\text{ext}}$ ) was 10 kV for this case. The reverse white letter number represents the ions accelerated by RILAC.

Element	Charge State																						Remarks
	1+	2+	3+	4+	5+	6+	7+	8+	9+	10+	11+	12+	13+	14+	15+	16+	17+	18+	19+	20+	21+	22+	
4 He	500	210																					He
12 C	82	89		31	3.3																		CO: ( $V_{\text{ext}}=13\text{kV}$ )
14 N	90	95	63	50	30	2.8																	N:
16 O	93	118	118	15	6	0.25																	O:
19 F	120	110	40	13	3																		LiF: 4×4, rod
20 Ne	215	96	82	65		6.5	1.7																Ne
32 S				11																			SF <sub>6</sub>
40 Ar		75	55	50		30	24	26	10		0.7	0.1											Ar
84 Kr				18		16		17	12	9	6.8		3.7		1.2		1		0.5				Kr
129 Xe					11	11	13.5		10	6.6		3.8	3.1	2.5	2.2		1.3	1.1		0.4			Xe
136 Xe								5.8				3.7	3.7	3.4	3.2	2.4							<sup>136</sup> Xe (83.5%)
7 Li	106	7.2																					LiF: 4×4, rod
11 B	17.2	10.5	3	1.4																			B: $\phi$ 4, rod
24 Mg	45				30		7.5																MgO: $\phi$ 4, rod
27 Al		22	34	33		15	6	2															Al <sub>2</sub> O <sub>3</sub> : $\phi$ 4, rod
28 Si					33			1															SiO <sub>2</sub> : $\phi$ 3, rod
31 P	34	33	23	14	10	2.3	1.1	0.2															Ni <sub>3</sub> P: 5×5, rod
40 Ca		72	70	55		36	27	27	26		5.5	1											CaO: $\phi$ 5.7, rod
48 Ti		5.2			15		14			6.5	4.4		0.3										Ti: $\phi$ 2, rod
51 V		2.5		7.5	12	12	12	10	7.5	4.8	2.4	1											V: $\phi$ 1, 2rods
52 Cr		9		27	30	33	26	15	8.3	5.8	3.6	2		0.3									Cr: $\phi$ 2, rod
55 Mn				51	68	60	42	19	9	4	2.6	0.8											Mn: 4×2, rod
56 Fe					15	15				11	8.2	4.6	3	1									Fe: $\phi$ 1, 2rods
58 Ni		4	4.8	5.2	8	12	14	14	11	8		1.7	0.8	0.3									Ni: $\phi$ 3, rod
59 Co		3.6	7	16	26	26	19	11	6	2.2		2	0.7	0.2									Co: $\phi$ 1, 2rods
63 Cu			9		17	19	17	15		6.5	4												Cu <sub>2</sub> O: 4×4, rod
64 Zn			32		35	34	26		8.3	3.3	1.1												ZnO: 4×4, rod
69 Ga		6.2	7.8		14.5	13	12.7	9.5	5.8	4	1												Ga <sub>2</sub> O <sub>3</sub> : 4×4, rod
74 Ge		1.8	3		4.3	5.5	5.3	6	4.6	2.6	1.3	0.5	0.3										GeO <sub>2</sub> : 4×4, rod
89 Y			5.4	3.1		2.6	3	4.5	6.6	7.5		5.6		1.1									Y <sub>2</sub> O <sub>3</sub> : 4×4, rod
90 Zr				1		1.7	1.9	2.6	4.2	4.5	5	6.5		2.6	0.8								Zr: $\phi$ 2, rod
93 Nb			11	19	23	13	9.5	7	7	7	5	3	1.7	0.6									Nb: $\phi$ 3, rod
98 Mo		1.1	3.8	5			6	5.6	4.3		0.7			0.3									Mo: $\phi$ 2, rod
102 Ru			9.3	14		9.3	7.0	5.2	4.3	3.1	2.5		0.5	0.3									Ru: 2×2, rod
103 Rh		0.5	1.2	2.3		4.1	5.2	8.1	8.9	9.2	8.9	5.7		2.1	0.7								Rh: $\phi$ 1, rod
106 Pd		0.4	0.7	1.4	1.7		2.4	2.6	3.8	3.4	2.7	1.3	0.3										Pd: $\phi$ 2, rod
107 Ag		1.2	2.6	5.2		8.4	8.7	9	7.3	6.5	4.9	2.5	1.6	1.2	0.9	0.4							Ag: $\phi$ 3, rod
115 In		10	21	31	24	22	16	14	11	7.5	5.3	4.5	3	2	1.2	0.6	0.2						In <sub>2</sub> O <sub>3</sub> : 4×4, rod
120 Sn			3	5.2	5.7		10	7		4.2	2.7	1.8	1	0.2									SnO <sub>2</sub> : 4×4, rod
130 Te			3.7	4.8	11	11		7.9	5	3.1	1.8	1	0.4	0.2									TeO <sub>2</sub> : 4×4, rod
139 La					1.3	1.6	3.8		7.3	7.9	7.3	6.5	5.2	3.6			1.4	0.7					La <sub>2</sub> O <sub>3</sub> : 4×4, rod
140 Ce			1		1.1	1.3	1.3		2.8	4.2	3.2	2.6	1.6	1	0.4								CeO <sub>2</sub> : 4×4, rod
141 Pr			1		2.3	3.1	4.7	8.0		9.7	9.1	7.8	5.7	3.3	2	1.0	0.2						$\phi$ 4, Ta crucible
152 Sm			0.4		0.8	1.3	1.8		4.7	5.1	6	5.8	5.3	4.9	3.6	2.4							Sm: $\phi$ 4, rod
158 Gd						0.8	1			2		0.3											Gd <sub>2</sub> O <sub>3</sub> : 4×4, rod
159 Tb			6.5	10	12	13	13	12	10	7.7	8.0	8.1	8	7.4	6.1	4.7	3.1	1.8	1.0			0.2	Tb: 5×5, rod
164 Dy				4	5.1	5.9			6.7	4.9	2.9	2	1.8	1.5	1.1	0.7	0.3						Dy: $\phi$ 6.3, rod
165 Ho						0.7	1.2		2.5	5.3	6.4		6	5	3.9	2.6	1.6	0.6				0.2	Ho: $\phi$ 1, rod
166 Er						2	3	4.3		11	13.2		9.5	7.7	5.7	4.1	1.9						Er: $\phi$ 4, rod
169 Tm					3.3	5.2	6.6	8.3	9.8	10	10	9.0	7.3	4.7	2.5	1.3	0.6	0.1					Tm: 2×2, rod
174 Yb					16.0	15.0	12	8	5.7	4.2		4.9	4.7	3.6	2.1	1.3		0.4	0.2				Yb: $\phi$ 4, rod
175 Lu					18	25	26	23	19	14	10	6.1	3.3	1.5	0.5	0.1							Lu: 2×2, rod
180 Hf						2	2.5	3.7		7.6		6.6		4.3	3		1.3	1	0.5				Hf: $\phi$ 2, rod
181 Ta					8.5		18	19	19		14	12	8.2		5.5	5	4.3	3	2	1.1	0.6		Ta: $\phi$ 1, rod
184 W					0.9	1	1.4	1.7	2.4		4		3		1.5	0.9	0.5	0.2					W: $\phi$ 1, rod
187 Re					4.8	7	10.6	12	11	8.3		4.1	4.3	3.6	2.3	1.8	1	0.6	0.3				Re: $\phi$ 1, rod
193 Ir						2.9	9.2	11	8.5	6.5		5.4	4.8	3.5		1.7	0.9	0.5	0.2	0.1			Ir: 1×1, rod
195 Pt							0.7	0.8	1.2			3		3.1		2.4	1.8	1.4	1.2	0.7			Pt: $\phi$ 3, rod
197 Au							13.7	19	17	14		10	6		4.3	4	2.6	1.5	0.8	0.4	0.3		$\phi$ 4, Ta crucible
208 Pb						7.7	14	13	11	8.9			5.2		3.5		1.7	1	0.5	0.3	0.1		PbO: 4×4, rod
209 Bi						3.3	8.3	10	8.7	7.6	5.6		5.9		3.6	2.3	1.4	0.9	0.5	0.3	0.1		Bi <sub>2</sub> O <sub>3</sub> : 4×4, rod

We experienced following machine troubles in this reporting period: (1) The No. 4 resonator had a small vacuum leak on a cooling pipe cooling a shorting plate. The leaky part was soldered. (2) The No. 1 and No. 6 rf power amplifiers were splashed with water due to the cooling pipe having had a small hole. Consequently, the teflon insulators for a grid stub of the No. 6 rf power amplifier were scorched by the leak current on its wet surface. (3) An obsolete filament power supply for the final vacuum tube (No. 1) was replaced by a new one. (4) Three water pumps for the cooling tower water circuit, the ordinary water circuit, and the deionized-water circuit were overhauled because of a deterioration of the mechanical seals. (5) A part of the chamber wall (2 mm thick stainless steel) of the

switching magnet had a big vacuum leak caused by the heat of the converged ion beam hit on it. In this case the beam power on the wall was about 500 Watts.

With the NEOMAFIOS the ions of P, Ru, Pr, Tb, Tm, Yb, Lu, and Pt were newly produced by using the rod insertion method during this year. Table 5 summarizes the beam currents of all ion species that we have obtained by using the NEOMAFIOS until now. The beam extraction voltage has been raised from 10 to 13 kV. As the result, the beam intensity has increased by about 30%.

#### References

- 1) O. Kamigaito et al.: RIKEN Accel. Prog. Rep. **31**, 192 (1998).

## RRC and AVF Cyclotron Operations

M. Kase, A. Goto, T. Kageyama, I. Yokoyama, M. Nagase, S. Kohara, T. Nakagawa, N. Inabe, K. Ikegami, O. Kamigaito, M. Kidera, J. Fujita, H. Isshiki,\* H. Akagi,\* R. Abe,\* R. Ichikawa,\* N. Tsukiori,\* K. Takahashi,\* T. Maie,\* T. Homma,\* K. Kobayashi,\* A. Yoneda, M. Kobayashi, and Y. Yano

In the annual period from January to December 1997, many kinds of beams were accelerated with the RIKEN Ring Cyclotron (RRC) similarly to previous years. Figure 1 shows the distribution of these beams on an energy-mass space using open circles for the ions accelerated in 1997. Among them, beams which were tried for the first time, or whose intensities were remarkably improved during this period, are listed in Table 1, together with their acceleration data.

In the summer of 1997, several improvements were made on a preinjector of RILAC. An extraction voltage of 18 GHz ECR ion source has been increased by a factor of two, and the vane structure of FC-RFQ has been changed accordingly. As the result, we have achieved beam intensities higher than 1 pμA for the <sup>40</sup>Ar beam at 7.6 MeV/nucleon. Since the officially restricted upper limit of beam intensity is presently one pμA for all kinds of beams, we could not use the full beam for experiment. We offered to increase this restricted number by a factor of 10 for the low energy beams, and received the permission from the Government at the end of the year. In the following year on, it will become possible to make the experiment of

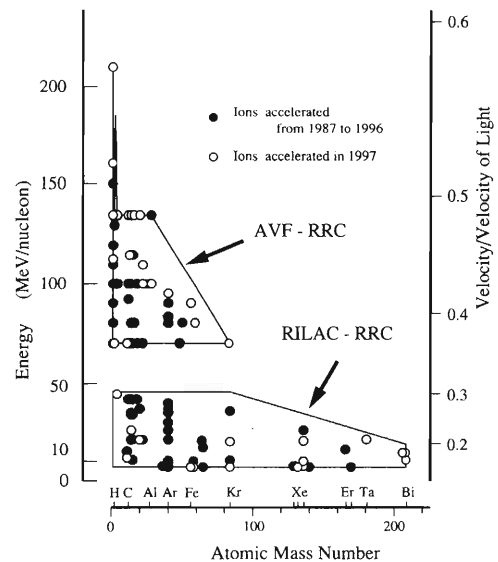


Fig. 1. The performance of RRC. The beams which were accelerated during the year 1997 are shown by open circles and those which have been accelerated since 1987 are shown by solid circles.

Table 1. List of typical beams accelerated in 1997.

Particle	Charge state		Energy (MeV/n)	Frequency (MHz)	Harmonic No. (RRC)	Injector	Beam Intensity (pμA)	
	IS	RRC						
<sup>28</sup> Si	+8	+13	100	29.0	5	10ECR+AVF	46	New beam
<sup>40</sup> Ar	+5	+5	7.6	18.8	11	18ECR+RFQ+RILAC	>1000	
<sup>40</sup> Ar	+11	+17	95	28.0	5	10ECR+AVF	70	
<sup>56</sup> Fe	+7	+7	7.6	18.8	11	18ECR+RFQ+RILAC	200	New beam
<sup>58</sup> Ni	+8	+8	7.6	18.8	11	18ECR+RFQ+RILAC	120	
<sup>84</sup> Kr	+18	+18	21	28.1	10	18ECR+RFQ+RILAC	33	
<sup>84</sup> Kr	+20	+36	70	25.0	5	10ECR+AVF	1	New beam
<sup>136</sup> Xe	+19	+19	8.5	19.9	11	18ECR+RFQ+RILAC	180	
<sup>136</sup> Xe	+19	+19	9.5	19.1	10	18ECR+RFQ+RILAC	120	
<sup>208</sup> Pb	+16	+36	15	23.9	9	N-ECR+RILAC	0.8	New beam
<sup>209</sup> Bi	+16	+37	12	21.4	9	N-ECR+RILAC	1	New beam
<sup>209</sup> Bi	+16	+37	15	23.9	9	N-ECR+RILAC	0.5	New beam

10ECR : 10GHz ECR Ion Source  
 18ECR : 18GHz ECR Ion Source  
 N-ECR : Neomafios ECR Ion Source

\* Sumijyu Accelerator Service, Ltd.

super-heavy element research more efficiently using this upgraded beam of several  $\mu\text{A}$ , while using a rotary target which was newly developed.

In this reporting period, some very heavy ions were accelerated one after another.  $^{209}\text{Bi}$ , which is the heaviest ion for the case of RILAC-RRC operation, and  $^{208}\text{Pb}$  were accelerated up to 15 MeV/nucleon to be used for nuclear physics experiments. On the other hand,  $^{84}\text{Kr}$  which is the heaviest ion acceleratable for the case of AVF-RRC operation was successfully accelerated too up to 70 MeV/nucleon to be used for biomedical experiments. As the result, the beam available regions in the energy-mass map have covered up all the area as shown in Fig. 1.

For the production of metallic-ion beams, a new method so-called MIVOC (Metal Ion from Volatile Compounds)<sup>1)</sup> was tried with the 18 GHz ECR ion source. Organic metal compounds, whose vapor pressure is high at room temperature, were used, instead of conventional metallic or metal-oxide rod, for charging metal vapor into an ECR plasma. Beams of  $\text{Fe}^{+7}$  and  $\text{Ni}^{+8}$  were accelerated by RRC using the compounds of  $\text{Fe}(\text{C}_5\text{H}_5)_2$  and  $\text{Ni}(\text{C}_5\text{H}_5)_2$ , respectively. We obtained a remarkable improvement on the intensity: ten times (e.g., for Ni) compared to conventional method.

Table 2 shows the statistics of the RRC operation during January to December 1997. A total of operation hours of the year amounted to 6500 hr, and among those, 4500 hr were spent for experiments. This value is about several percent less than that of the previous year. It is because most of nuclear physics experiments have been concentrated on the use of RIPS. This forced us to arrange all their experiments with considerable time intervals between two experiments for preparation since the same room is used: loss of the total experimental hours a year.

Table 2. Statistics of RRC Operation from Jan. to Dec. 1997.

	(in hours)	
Total (365 d)	8760	(100%)
Total Operation Time	6475	(74%)
● Beam Tuning	1877	(29%)
● Experiment	4509	(70%)
○ Nuclear Physics Experiment	3404	(75%)
○ Other field Experiment	1105	(25%)
Machine Trouble	271	(3.1%)
Guest Time	40	(0.5%)
Maintenance & Holidays	2064	(24%)

Most of the beam time (75%) was devoted to the nuclear physics experiments. The rest (25%) was devoted to the other fields such as: medical science, radio-chemistry, health physics, material science, biology, and atomic physics.

A total of beam time for the stand-alone use of AVF

cyclotron amounted to 700 hr. The beam time is limited by a periodic maintenance (once per two months) for a deflector of AVF cyclotron. Four kinds of low-energy beams (polarized-d, alpha, C, and Ar) were used for Moessbauer, nuclear physics, and for RI production.

A total of hours of unscheduled shutdown was reduced slightly compared to that in the previous years. It is because a scheduled maintenance for deflector in AVF cyclotron used up this period. The septum of deflector was cleaned once per two months.

In July, the machine was stopped for three days due to a trouble of the electric deflector channel (EDC) of RRC. At the end of 1997, one of the power supplies for injection dipole magnets of RRC had a trouble around its sensing shunt. This shunt was of the facility's oldest type: namely, a directly-water-cooled type. A part of the shunt material was electrically eroded because the silicon rubber coating on it became aged. As the result, the current stability became worse. A change of the all old type shunts into a new type will be required in the near future, as the shunts in most power supplies were already converted into new ones of indirect-water-cooled type several years ago.

A new vacuum leak has occurred in the resonator#2 of RRC, which caused from some part of the high pressure air line to actuate the contact finger of a movable box. Fortunately, this leak has become small to a tolerable level during operation, though the reason for it is not clear. Though its urgent repair is not required badly at present, it should be done during the next long-term maintenance period.

In order to increase the total efficiency through RRC in the RILAC-RRC, two improvements have been made as follows: (1) The structure of four-gap drift tube in rebuncher, which is located half-way in the beam transport line between RILAC and RRC, was changed to be matched to the harmonic number of RRC. The three sets of drift tube are now available for harmonic numbers, 9, 10, and 11. (2) Beam energy at the exit of RILAC was stabilized by a feedback loop to the rf of RILAC.<sup>2)</sup> Since the fluctuation of beam energy causes the beam phase fluctuation after drifting along the beam transport line toward RRC, the rf phase can be controlled in the final resonator of RILAC according to the beam phase measured near the rebuncher. This method was applied in the cases of 7.6 MeV/nucleon  $^{40}\text{Ar}$  and  $^{136}\text{Xe}$  accelerations. As the result, we were successful to improve the beam transmission efficiency through RRC, as well as the beam stability.

#### References

- 1) T. Nakagawa et al.: Jpn. J. Appl. Phys. **36**, 7375 (1997).
- 2) M. Kobayashi et al.: Proc. 11th Symp. on Accelerator Science and Technology, Hyogo, Oct. 1997, p. 531.

## The Tandem Operation

K. Ogiwara, E. Yagi, and T. Urai

The tandem accelerator was operated for 90 days, except for the machine inspection, beam test, and so on, during the annual reporting period from Nov. 1, 1996 to Oct. 31, 1997. A new beam line was constructed for the conventional Particle-Induced X-ray Emission (PIXE) spectroscopy.

Experimental studies on the following subjects have been performed and are in progress.

- (1) Rutherford Backscattering Spectroscopy (RBS)
  - (a) Behavior of the Xe atoms implanted into iron (Muon Science Lab).
  - (b) RBS analysis of the polystyrene surfaces modified by ion implantation (Surface Characterization Center).
  - (c) RBS study of multilayer films, welded steel, and oxides (Linear Accelerator Lab).
- (2) Nuclear Reaction Analysis (NRA)

- (a) Lattice location identification of hydrogen in niobium alloys by a channeling method (Muon Science Lab).

- (3) Particle-Induced X-ray Emission (PIXE)

- (a) Application of PIXE to the biomedical and material sciences: Trace element analysis using energy-dispersive X-ray spectrometry, and chemical state analysis using wave-dispersive X-ray spectrometry (Inorganic Chemical Physics Lab).

- (b) Development of an X-ray detector (Cyclotron Lab).

- (c) Development of an in-air high-resolution PIXE system for chemical state analysis (Inorganic Chemical Physics Lab).

- (d) Channeling analysis of dopants in II-VI compound semiconductors (Muon Science Lab).

- (e) Trace element analysis of feather (Safety Center).



### **III. RESEARCH ACTIVITIES**



# 1. Nuclear Physics



# Momentum Distributions of the Core Fragment from the Nuclear Breakup Reaction within the Glauber Model

Y. Ogawa and I. Tanihata

[Longitudinal momentum distribution, Core absorption effect, Centrifugal force]

It has been considered that the core fragment momentum distribution arising from the breakup reaction is a good probe to investigate the motion of the nucleon at the nuclear surface. This method, as well as the measurement of the interaction cross section, is applied to study the structure of the neutron and proton-rich drip-line nuclei. Since the reaction mechanism has been usually ignored, there is a serious discrepancy between the interpretations of experimental result of the nuclear size and of the momentum distribution. In order to solve this problem we have demonstrated the influence of the core absorption effect on the width of the momentum distribution for different orbitals ( $s$ ,  $p$ , and  $d$ ) of the last nucleon by calculating the longitudinal momentum distribution of core fragment within the Glauber model. The ( $^{11}\text{Be}$ ,  $^{10}\text{Be}$ ), ( $^8\text{B}$ ,  $^7\text{Be}$ ), and ( $^{19}\text{C}$ ,  $^{18}\text{C}$ ) reactions on the light target are taken as the typical examples for the  $s$ ,  $p$ , and  $d$  orbitals of the last nucleon.<sup>1)</sup>

We have obtained the following conclusions:

(1) The core absorption effect is small for the  $s$ -orbital case but is remarkably large for the  $p$  and  $d$ -orbital cases. The probability with which the last nucleon is found in the core absorption area (see Fig. 1) is larger for the  $p$  and  $d$ -orbital cases than the  $s$ -orbital case due to the centrifugal force. In this region, even if the last nucleon hits the target, since the core nucleus is simultaneously absorbed with a large probability, such a channel does not contribute to the cross section which we detect. Since this large cross section reduction occurs in not so high momentum region either, the width of distribution becomes narrow for the non-zero orbital case.<sup>1,2)</sup>

(2) We can consistently understand the narrow width of  $^7\text{Be}$  core fragment momentum distribution with the spatial extent like the normal  $p$ -shell nuclei of the  $^8\text{B}$  nucleus by taking into account the core

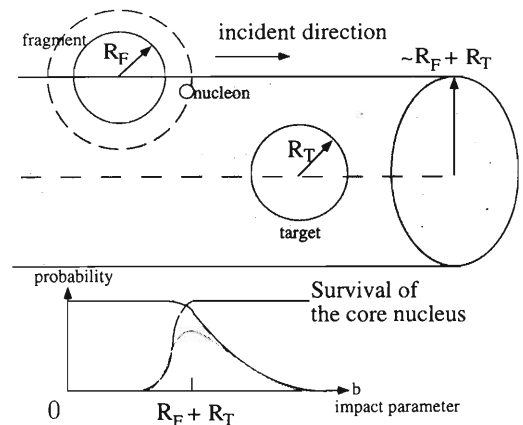


Fig. 1. The core fragment breakup with a large probability in the cylindrical region whose radius is the sum of the core and target nuclear radii.

absorption effect.<sup>1)</sup>

(3) Even if the large cross section reduction occurs for the  $d$ -orbital case, the difference in the momentum widths between the  $s$  and  $d$ -orbital cases is very large. We can distinguish the dominant component of last nucleon in the projectile according to the width of measured fragment momentum distribution and the total cross section. Our calculation indicates that the  $s$ -state is a dominant component in the ground state of  $^{19}\text{C}$  nucleus.<sup>2)</sup>

## References

- 1) Y. Ogawa and T. Tanihata: Nucl. Phys. A **616**, 239c (1997).
- 2) Y. Ogawa: Proc. 3rd Japan China Nuclear Physics Symp., July 24-29, 1997, Sendai, Ogata, Niigata, Japan.

# Astrophysical $S$ -Factors for ${}^7\text{Be}(p,\gamma){}^8\text{B}$ Determined by Coulomb Dissociation Measurements

T. Motobayashi, T. Kikuchi, N. Iwasa, Y. Ando, M. Kurokawa, S. Moriya, H. Murakami, T. Nishio, J.-Z. Ruan, S. Shirato, S. Shimoura, T. Uchibori, Y. Yanagisawa, T. Kubo, H. Sakurai, T. Teranishi, Y. Watanabe, M. Ishihara, M. Hirai, T. Nakamura, S. Kubono, M. Gai,<sup>\*1</sup> R. France III,<sup>\*1</sup> K. I. Hahn, T. Delbar,<sup>\*2</sup> P. Lipnik,<sup>\*2</sup> and C. Michotte<sup>\*2</sup>

[ ${}^{208}\text{Pb}({}^8\text{B}, {}^7\text{Be}){}^{208}\text{Pb}$ , Coulomb dissociation, Astrophysical  $S$ -factors for  ${}^7\text{Be}(p,\gamma){}^8\text{B}$ ]

We report new data of the astrophysical  $S_{17}$  factors for the  ${}^7\text{Be}(p,\gamma){}^8\text{B}$  reaction extracted from our second  ${}^8\text{B}$  dissociation experiment.<sup>1)</sup> The radiative proton capture by  ${}^7\text{Be}$  at low energies is the most uncertain nuclear input to solar models, and has direct relation to the high-energy neutrino flux relevant to the “solar neutrino puzzle”. The first experiment<sup>2)</sup> measured the  $S_{17}$  factors at the center-of-mass energies ranging from 0.7 to 1.7 MeV. The results are consistent with the direct capture cross sections measured by Vaughn et al.<sup>3)</sup> and Filippone et al.<sup>4)</sup> The second experiment was aimed at improving statistical accuracy of data as well as at measuring precise angular distribution to extract E2 mixtures in the E1-dominant Coulomb dissociation yield.<sup>1)</sup>

Radioactive  ${}^8\text{B}$  beams at 51.9 MeV/nucleon were provided by the RIPS separator, which bombarded a  $50\text{ mg/cm}^2$   ${}^{208}\text{Pb}$  target. Outgoing proton and  ${}^7\text{Be}$  were detected in coincidence by a plastic-scintillator hodoscope. The Coulomb dissociation yield was obtained as a function of the  $p$ - ${}^7\text{Be}$  relative energy and of the scattering angle  $\theta_8$ , angle of the  $p$ - ${}^7\text{Be}$  center-of-mass with respect to the beam direction. The resultant  $\theta_8$  distributions were analyzed by a distorted wave calculation. The result suggests very small  $\ell = 2$  amplitudes, which supports the analysis with pure E1 transition in extracting  $S_{17}$  factors. Details of the experimental setup and of the analysis on the  $\theta_8$  distributions were reported in Ref. 1.

The  $S_{17}$  factors extracted from the second experiment are shown in Fig. 1 together with the results from the first experiment and those from the direct  ${}^7\text{Be}(p,\gamma){}^8\text{B}$  measurements. As seen in the figure, a much better statistical accuracy is achieved in the second experiment. The Coulomb dissociation results shown in the figure were obtained by assuming E1 tran-

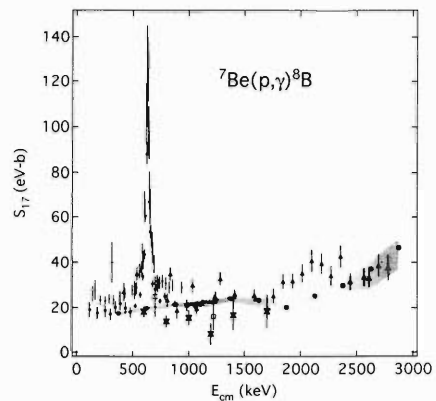


Fig. 1. Astrophysical  $S_{17}$ -factors extracted from the first (thick crosses) and second (large solid dots) experiments together with existing  $(p,\gamma)$  data.

sition with small corrections due to the  $\ell = 2$  component evaluated by the analysis of the  $\theta_8$  distribution discussed in Ref. 1. The two results are slightly different from each other, but both are consistent with the  $(p,\gamma)$  data by Vaughn et al.<sup>3)</sup> and Filippone et al.,<sup>4)</sup> who observed low values compared with the other direct-capture results.

## References

- 1) T. Kikuchi et al.: Phys. Lett. B **391**, 261 (1007); T. Motobayashi et al.: RIKEN Accel. Prog. Rep. **30**, 51 (1997).
- 2) T. Motobayashi et al.: Phys. Rev. Lett. **73**, 2680 (1994); N. Iwasa et al.: J. Phys. Soc. Jpn. **65**, 1256 (1996).
- 3) F. J. Vaughn et al.: Phys. Rev. C **2**, 1657 (1970).
- 4) B. W. Filippone et al.: Phys. Rev. Lett. **50**, 412 (1983); Phys. Rev. C **28**, 2222 (1983).

<sup>\*1</sup> Department of Physics, University of Connecticut, U.S.A.

<sup>\*2</sup> Institut de Physique Nucléaire, Université Catholique de Louvain, Belgium

# Shell Model Calculation of Magnetic Moments of Light Mirror Nuclei

H. Kitagawa, M. Tanigaki, T. Suzuki, and H. Sagawa

[Shell model, Magnetic moment]

Magnetic moment ( $\mu$ ), sum of spins ( $S$ ) and angular momenta ( $J$ ) of nucleons, gives information on their occupation numbers in each orbit, which is a good probe for the nuclear physics. Recently, an anomaly in the ( $A = 9, T = 3/2$ ) mirror pair was reported<sup>1)</sup> providing that  $A$  is the mass number and  $T$  is the total isospin.

The experimentally observed value<sup>1)</sup> of the isoscalar part of this system is significantly larger than the value calculated under the conventional shell model. The effect of the first order configuration mixing is already included in the shell model calculation. Fukunishi<sup>2)</sup> estimated the isoscalar part of the ( $A = 9, T = 3/2$ ) mirror pair, and has shown that it is impossible to reproduce the experimental value within the first order configuration mixing. The effect of the second order configuration mixing needs to be estimated. We have therefore calculated both isoscalar and isovector parts for the light nuclei whose mass numbers are from  $A = 8$  to 13. Comparing with the experimental values, large deviations are found in the isovector part of the ( $A = 8, T = 1$ ) pair, and in the isoscalar part of the ( $A = 9, T = 3/2$ ) pair.

We have then estimated the contributions of the second order configuration mixing to the isoscalar and isovector parts for the following five mirror pairs: ( $A = 8, J^\pi = 2^-, T = 1$ ), ( $A = 9, J^\pi = 3/2^-, T = 3/2$ ), ( $A = 11, J^\pi = 3/2^-, T = 1/2$ ), ( $A = 13, J^\pi = 1/2^-, T = 1/2$ ), and ( $A = 13, J^\pi = 3/2^-, T = 3/2$ ). This correction is divided into two parts: the one-body operator (core polarization Fig. 1) and the two-body operator (valence polarization Fig. 2). Two body matrix elements are calculated from the one-boson exchange potential,<sup>3)</sup> which includes the  $\pi$ -,  $\rho$ -,  $\omega$ -, and  $\sigma$  mesons from the s-shell to the phf-shell. Particle excitations are taken up to  $4\hbar\omega$ . Wave functions of the nucleon are the harmonic oscillator type.

Results of calculations of the isoscalar part are shown in Table 1. Corrections due to the second order configuration mixing (core and valence polarizations), together with the experimental and calculated values by the shell model (within the first order configuration mixing), are listed. For the  $A = 9$  mirror pair it is desired to increase the isoscalar part of magnetic moment,  $\mu^{IS}$ , in order to reproduce the experimental value. We can obviously see that the corrections of these polarizations are not enough. It may be difficult to reproduce such a large deviation in the  $A = 9$  pair with the harmonic oscillator wave functions. As for

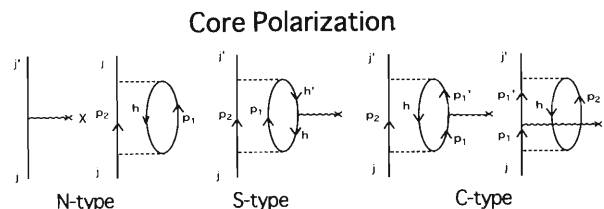


Fig. 1. Typical diagrams of the second order configuration mixing, core-polarizations.

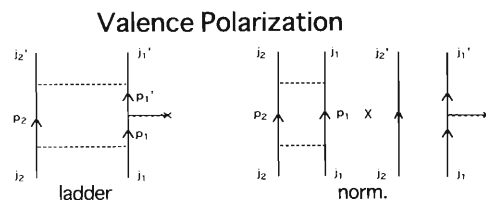


Fig. 2. Typical diagrams of the second order configuration mixing, valence-polarizations.

Table 1. Results of calculations of the isoscalar part of magnetic moment under the second order configuration mixing.

$(A, J^\pi, T)$	$\delta\mu^{IS}$			$\mu^{IS}$		
	core	val.	total	exp.	cal.	diff.
(8, $2^+$ , 1)	-0.018	-0.008	-0.026	1.344	1.332	+0.012
(9, $\frac{3}{2}^-, \frac{3}{2}$ )	-0.010	-0.005	-0.015	1.024	0.947	+0.077
(11, $\frac{3}{2}^-, \frac{1}{2}$ )	-0.006	-0.003	-0.009	0.862	0.871	-0.008
(13, $\frac{1}{2}^-, \frac{1}{2}$ )	-0.009	+0.001	-0.008	0.190	0.186	+0.004
(13, $\frac{3}{2}^-, \frac{3}{2}$ )	-0.006	-0.004	-0.010	0.894	0.887	+0.008

the isovector part, effect of the meson exchange current will change it. We should also estimate the other corrections of the Coulomb force and of the binding energy effect, by changing the wave functions of nucleon. Our formulation is possible to include these effects.<sup>4)</sup>

## References

- 1) K. Matsuta et al.: *Hyperfine Interact.* **97/98**, 519 (1996).
- 2) N. Fukunishi: *RIKEN Accel. Prog. Rep.* **29**, 9 (1996).
- 3) I. S. Towner: *Phys. Rep.* **155**, 263 (1987).
- 4) H. Horie and K. Sasaki: *Prog. Theor. Phys.* **25**, 475 (1961).

# Spin Dipole States of Deformed Nuclei

H. Kurasawa\* and T. Suzuki

[Spin dipole states, Deformed nuclei]

The spin dipole states which are excited by  $(\mathbf{r} \times \boldsymbol{\sigma})_M^J \tau$  have the total spin of either  $0^-$ ,  $1^-$  or  $2^-$ . Since they are a counterpart of the well-known giant dipole states, it is a longstanding problem how they are distributed as a function of the excitation energy.

So far, the  $(e, e')$  and  $(p, n)$  reactions for  $^{12}\text{C}$  target showed the existence of the spin dipole states in the giant dipole resonance region, and most of them were considered to be  $1^-$  states.<sup>1,2)</sup> Recently, however, Okamura et al.<sup>3)</sup> have performed the  $(d, ^2\text{He})$  experiment, and found, through the tensor analyzing power, that the spin dipole resonance is mainly due to the  $2^-$  states. We have thus studied theoretically the distribution of the spin dipole states in a deformed nuclear model.

It is well-known that giant dipole states are split into two groups in deformed nuclei. We take the oblate shape nuclei, as an example. Then, the first group with low excitation energy is composed of the  $K = 1$  states, while the second one with high excitation energy is due to the  $K = 0$  states. In the  $\gamma$ -absorption and  $(p, \gamma_0)$  reaction, the ratio of the E1-strength of the first group to that of the second one is 2 to 1, according to the  $K$ -degrees of freedom. On the contrary, in the  $(p, \gamma_1)$  reaction, the ratio is 1 to 2, according to the angular momentum coupling.<sup>1)</sup>

We can discuss the splitting of the spin dipole states as to the matrix elements of  $(\mathbf{r} \times \boldsymbol{\sigma})_M^J \tau_3$  in the same way. The  $0^-$  spin dipole states are split into two groups. The ratio of the strength of the first group to that of the second group is 2 to 1. The  $1^-$  spin dipole states are split into two groups, but in a different way from that of the dipole states. The  $1^-$  states with  $K = 0^-$  are included in the first group, while those with  $K = 1^-$  are separated into the first and the second groups with the same strength. The  $2^-$  states with  $K = 1^-$  are distributed in the same way as that of the  $1^-$  spin dipole states with  $K = 1^-$ . On the other hand, the  $2^-$  states with  $K = 2^-$  appear only in the first group. The  $2^-$  states with  $K = 0^-$  are split into the two groups with the strength ratio to be 1 to 2.

We apply the deformed nuclear model to the giant dipole and spin dipole states of  $^{12}\text{C}$ . We have

performed RPA calculations to describe the intrinsic states of  $^{12}\text{C}$  using the Nilsson potential with the separable dipole-dipole and spin-dipole-spin-dipole interactions.

The results for the  $(\gamma, n)$  cross section show that the two peaks at 22.5 and 25.5 MeV of the experimental data are well reproduced by the  $K = 1^-$  and  $0^-$  dipole states, respectively. Comparison of our results with the  $^{11}\text{B}(p, \gamma_0)^{12}\text{C}$  and  $^{11}\text{B}(p, \gamma_1)^{12}\text{C}$  cross sections also supports the present model very well.

Within the same framework, we have calculated the strength of the spin dipole states. The collective  $2^-$  state is observable experimentally at 19.4 MeV. The B(M2) value of this state is estimated to be  $200 \pm 50 \mu_N^2 \text{fm}^2$  from electron scattering data,<sup>2)</sup> while the present model yields  $228 \mu_N^2 \text{fm}^2$ . Our calculations show that the peak around 21 MeV is composed of the  $1^-$  and  $2^-$  states, and about 2/3 of the strength is due to the  $2^-$  states. We interpret this peak as the spin dipole resonance like observed at 22 MeV in various reactions.

In the present model, the collective  $2^-$  states with  $K = 1^-$  and  $K = 2^-$  are found in the resonance region. In particular the  $K = 1^-$  state almost exhausts the sum rule value.<sup>1)</sup> In contrast to the  $2^-$  states, the  $0^-$  and  $1^-$  states are not so collective, and the strength is distributed over a wide energy region.

In conclusion, the distribution of the spin dipole states of  $^{12}\text{C}$ , which is recently revealed by the tensor analyzing power of the  $(d, ^2\text{He})$  reaction, is qualitatively explainable in the deformed nuclear model. The  $(\gamma, n)$ ,  $(p, \gamma_0)$  and  $(p, \gamma_1)$  data are also reproducible consistently. The distribution of the spin dipole states in  $^{12}\text{C}$ , however, is fairly affected by the spin-orbit force and the residual forces. It will be interesting to explore how the spin dipole states are distributed in heavy nuclei.

## References

- 1) T. Suzuki and C. Hinohara: Nucl. Phys. A **204**, 289 (1973).
- 2) C. Gaarde et al.: Nucl. Phys. A **422**, 189 (1984).
- 3) H. Okamura et al.: Phys. Lett. B **345**, 1 (1995).

\* Department of Physics, Faculty of Science, Chiba University

# A Giant Halo at the Neutron Drip Line<sup>†</sup>

J. Meng and P. Ring\*

[Giant neutron halo, RHB theory]

With perpetual improvement in the techniques of producing radioactive beams, the study of exotic nuclei very far away from the line of  $\beta$ -stability has now become feasible. Experiments of this kind may cast new light on nuclear structure, and novel and entirely unexpected Features may appear: Neutron rich nuclei can have a structure very different from normal nuclei. They consist of a normal core surrounded by a skin of neutron matter. Close to the drip line, where the coupling to the continuum becomes important, a neutron halo can develop, as it has been observed in several light nuclei, the most famous of which is  $^{11}\text{Li}$ . However, in all of the halos observed so far, one halo has only a very small number of neutrons, namely one or two neutrons outside of the normal core. Even in the chain of He-isotopes, only  $^6\text{He}$  shows indications of a possible halo containing 2 neutrons, whereas  $^8\text{He}$  with its large 2-neutron separation energy of 2.24 MeV has only a skin of neutron.

In order to study the influence of correlations and many-body effects it would be very interesting to find also the nuclei with a larger number of neutrons distributed in the halo. In this letter we report on the theoretical prediction of a giant neutron halo for Zr-isotopes close to the neutron drip line. This halo is formed by up to six neutrons outside of the  $^{122}\text{Zr}$  core with the magic neutron number  $N = 82$ .

Recently, a fully self-consistent relativistic method has been developed for the description of halo nuclei. It is based on Relativistic Hartree-Bogoliubov (RHB) theory in coordinate space.<sup>1)</sup> It is a relativistic extension of conventional Hartree-Fock-Bogoliubov theory in coordinate space.<sup>2)</sup> Being relativistic, it is able to take into account at the same time the proper isospin dependence of the spin-orbit term which is very crucial for the accurate reproduction of recent measurements of the isotopic shifts in the Pb-region<sup>3)</sup> and for the reliable description of nuclei far away from the line of  $\beta$ -stability.<sup>4)</sup> In addition, this theory provides a self-consistent treatment of pairing correlations in the presence of the continuum. As it has been shown in Ref. 1 the scattering of Cooper pairs into the continuum containing low-lying resonances of small angular momentum plays an important role for the formation of a neutron halo. By using the density dependent zero range interaction, the halo in  $^{11}\text{Li}$  has been successfully reproduced in a self-consistent picture. Very good

agreement with recent experimental data has been obtained without any further adjustment of parameters. To obtain these results, a complete solution of the RHB equations in coordinate space is necessary. The expansion in a harmonic oscillator basis which is very useful only for the nuclei close to the line of  $\beta$ -stability, provides a very poor approximation in the continuum, even if a large number of oscillator shells is taken into account. The simple Bardeen-Cooper-Schrieffer (BCS)-approximation used leads to a partial occupation of unbound states in the continuum and therefore leads to a gas of evaporating neutrons. Here we report on calculations (where the same method as in Ref. 1 has been used) made to investigate halos in Zr-nuclei at the neutron drip line.

We predict neutron halos in the Zr nuclei close to the neutron drip line, which are composed not only by one or two neutrons, as is the case in the halos investigated so far in light  $p$ -shell nuclei, but which contain up to 6 neutrons. This is a new phenomenon, which has not been observed experimentally. It would allow the study of collective phenomena in neutron matter of low density. This prediction is based on RHB theory in the continuum. It combines the advantage of a proper description of the spin orbit term with that of full Hartree-Bogoliubov theory in the continuum which allows in the canonical basis the scattering of Cooper pairs into low-lying resonances in the continuum. A density dependent force of zero range has been used in the pairing channel. It contains no free-parameter, because its strength is adjusted for the isotope  $^{116}\text{Zr}$  to a similar calculation with Gogny's force D1S in the pairing channel. The halos are formed by two to six neutrons scattered as Cooper-pairs mainly to the levels  $3p_{3/2}$ ,  $2f_{7/2}$ ,  $3p_{1/2}$ , and  $2f_{5/2}$ . This is made possible by the fact that these resonances in the continuum come down very close to the Fermi level in these nuclei and due to their coupling with the loosely-bound levels just below the continuum limit.

## References

- 1) J. Meng and P. Ring: Phys. Rev. Lett. **77**, 3963 (1996).
- 2) J. Dobaczewski, H. Flocard, and J. Treiner: Nucl. Phys. A **422**, 103 (1984).
- 3) M. M. Sharma, G. A. Lalazissis, and P. Ring: Phys. Lett. B **317**, 9 (1993).
- 4) M. M. Sharma, G. A. Lalazissis, W. Hillebrandt, and P. Ring: Phys. Rev. Lett. **72**, 1431 (1994).

<sup>†</sup> Condensed from the article in Phys. Rev. Lett. **80**, 460 (1998)

\* Physik-Department der Technischen Universität München, Germany

# The Proton and Neutron Distributions in Na Isotopes: The Development of Halo and Shell Structure

J. Meng, I. Tanihata, and S. Yamaji

[Halo, Shell structure, RHB theory]

The recent developments in the accelerator technology and in the detection techniques around the world have changed the nuclear physics scenario. It is now possible to produce and study the nuclei far away from the stability line—so called “EXOTIC NUCLEI”. Experiments of this kind have cast a new light on nuclear structure, and novel and entirely unexpected features appeared: e.g. the neutron halo in  $^{11}\text{Li}$ <sup>1)</sup> and neutron skin along with a rapid increase in the measured interaction cross-sections in the neutron-rich light nuclei. The extremely low proton to neutron ratio of these nuclei and physics connected with these low density matter have attracted increasing attentions in nuclear physics as well as other fields such as astrophysics.

With an exotic matter distribution near the drip line, a lot of questions are still open: e.g., the relation between the halo and the shell effect, the difference between the proton and neutron distributions on and away from the stability line. How is the halo formed? Are there a rapid change from the normal nuclear density to the halo density, or a gradual change in the particle number? As the matter distribution is not measurable directly, series of experiments at different incident beam energies are necessary in order to determine the model-independent density distribution of both proton and neutron. Among all the experiments carried out so far, Na isotopes provide a good opportunity to study the density distributions over a wide range of neutron numbers.<sup>2)</sup> We report here a systematic study of nuclear density distributions in Na isotopes within the Relativistic Mean Field (RMF) theory, with the pairing and blocking effects for odd particle system properly described by Hartree-Bogoliubov theory in coordinate representation, and we try to answer some of the general questions in these low-density nuclear matter.

Recently, a fully self-consistent calculation within the Relativistic Hartree-Bogoliubov (RHB) theory in coordinate space for the description of the chain of lithium isotopes ranging from  $^6\text{Li}$  to  $^{11}\text{Li}$  was reported.<sup>3)</sup> It combines the advantages of a proper description of the spin-orbit term with those of full Hartree-Bogoliubov theory in the continuum, which allows in the canonical basis the scattering of Cooper pairs to low lying resonances in the continuum. Excellent agreement including binding energy, matter radius, and matter distribution with the experimental data was obtained without any modification of the neutron  $1p_{1/2}$  level like the former works. As the theory used here is fully microscopic and parameter free, it gives consistent description of the proton and neutron distributions, and the development of proton and neu-

tron halos or skins could be examined.

Summarizing our investigations, the development of a proton skin as well as a neutron skin has been systematically studied with a microscopic RHB theory, where the pairing and blocking effects have been treated self-consistently. A systematic set of calculations for the ground state properties of nuclei in Na isotopes is presented using the RHB together with standard Glauber theories. The RHB equations are solved self-consistently in the coordinate space, so that the continuum and pairing have been better treated. The calculated binding energies are in good agreement with the experimental values. A Glauber model calculation has been carried out with the density obtained from the RHB. A good agreement has been obtained with the measured cross sections for  $^{12}\text{C}$  as a target, and a rapid increase of the cross sections has been predicted for neutron rich Na isotopes beyond  $^{32}\text{Na}$ . The systematics of the proton and neutron distributions are presented. After systematic examination of the neutron, proton, and matter distributions in the Na nuclei from the proton drip-line to the neutron drip-line, the connection between the tail part of the density and the shell structure has been found. The tail of the matter distribution is not so sensitive to how many particles are filled in the major shell. Instead, it is very sensitive to whether this shell has an occupation or not. The physics behind the skin and halo has been revealed as a spatial demonstration of shell effect: simply the extra neutrons are filled in the next shell and sub-shell. This is in agreement with the mechanism observed so far in the halo system but more general. As the  $1f_{7/2}$  is very close to the continuum, the  $N = 28$  closed shell for stable nuclei fails to appear due to the coming down of the  $2p_{3/2}$  and  $2p_{1/2}$  levels. Another important conclusion here is that, contrary to the usual impression, the proton density distribution is less sensitive to the proton to neutron ratio. Instead, it is almost unchanged from the proton drip-line to the neutron drip-line. Similar conclusion has been obtained recently by charge exchange reaction experiment.<sup>4)</sup> The influence of the deformation, which is neglected in the present investigation, is also interesting to us, a further more extensive study to extend the present study in deformed cases are in progress.

## References

- 1) I. Tanihata et al.: Phys. Rev. Lett. **55**, 2676 (1985).
- 2) T. Suzuki et al.: Phys. Rev. Lett. **75**, 3241 (1995).
- 3) J. Meng and P. Ring: Phys. Rev. Lett. **77**, 3963 (1996).
- 4) O. Bochkarev et al.: submitted to Z. Phys.

## Structure of Unstable Nuclei Studied by Monte Carlo Shell Model

Y. Utsuno, T. Mizusaki, T. Otsuka, M. Honma, and N. Fukunishi

[Monte Carlo method, Shell model, Shell closure]

Recent experimental studies on the neutron-rich nuclei have indicated that the shell gap at  $N = 20$  vanishes in the  $^{32}\text{Mg}$  region.<sup>1,2)</sup> Theoretically, the shell-model approach to include lower part of the pf shell have succeeded in describing the structure of  $N = 20$  isotones.<sup>3)</sup>

In order to obtain the eigen solutions of many-body quantum systems, the Quantum Monte Carlo Diagonalization (QMCD) method has been proposed recently.<sup>4)</sup> The QMCD method is applied to the large-scale shell-model calculations, and is proved to be very efficient.<sup>5)</sup>

We apply the QMCD method to the large-scale shell model calculations for the  $N = 20$  region. The same valence shell and effective interaction as Ref. 3 are adopted. We have developed a method to remove the spurious center-of-mass motion suitable for the QMCD method. Eigenvalues of the Hamiltonian for yrast states obtained by three calculations are shown in Fig. 1. The energies obtained by the QMCD method are much lower than those of any truncated model spaces. Note that the basis dimensions of the  $M = 0$  model space become about 1 million for the 4p4h calculation. In the QMCD calculation, the expectation value of the center-of-mass Hamiltonian becomes about  $10^{-4}\hbar\omega$ , which is a very small quantity. Thus,

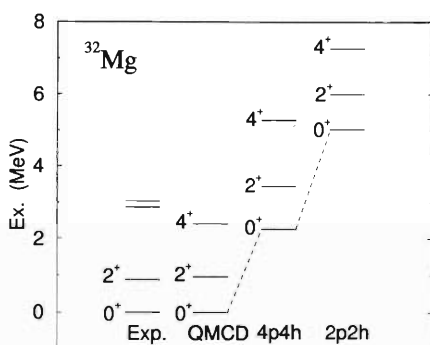


Fig. 1. Energy levels of the lowest states of  $^{32}\text{Mg}$ . The 2p2h (4p4h) means the truncated model space, where the number of neutrons excited to the pf shell is restricted to 2 (4). For the 2p2h and 4p4h, the energies relative to the ground-state energy of QMCD calculation are shown.

the feasibility of the QMCD method is confirmed.

Figure 2 shows the  $B(E2)$  values and pf-shell neutron-occupation probabilities for  $N = 20$  isotones by using the same Hamiltonian as Ref. 3. It turns out that the neutron-rich  $N = 20$  isotones are too much deformed for the Hamiltonian designed for the truncated model space. Therefore, we are looking for a Hamiltonian appropriate for the larger model space, and about to start, for nuclei around  $^{32}\text{Mg}$ , the systematic calculations which were impossible with the conventional shell model.

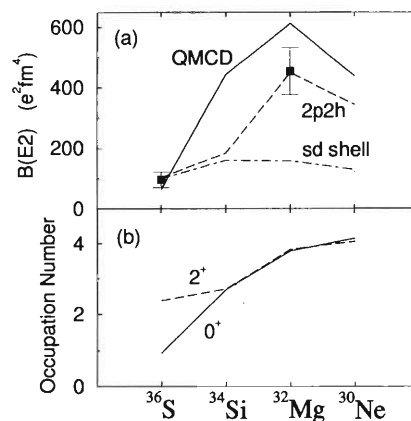


Fig. 2. (a)  $B(E2; 0_1^+ \rightarrow 2_1^+)$  values, and (b) pf-shell neutron occupation numbers, for  $N = 20$  isotones. The dashed and dot-dashed lines in (a) correspond, respectively, to the  $B(E2)$  values by the 2p2h truncation and sd-shell calculation. The  $e_p = 1.3e$  and  $e_n = 0.5e$  are adopted as the effective charges.

### References

- 1) D. Guillemaud-Mueller et al.: Nucl. Phys. A **426**, 37 (1984).
- 2) T. Motobayashi et al.: Phys. Lett. B **346**, 9 (1995).
- 3) N. Fukunishi, T. Otsuka, and T. Sebe: Phys. Lett. B **296**, 279 (1992).
- 4) M. Honma, T. Mizusaki, and T. Otsuka: Phys. Rev. Lett. **75**, 1284 (1995).
- 5) M. Honma, T. Mizusaki, and T. Otsuka: Phys. Rev. Lett. **77**, 3315 (1996).

# Quantum Monte Carlo Diagonalization Method with Condensed-Pair Bases

N. Shimizu, T. Otsuka, T. Mizusaki, and M. Honma

[Shell model, Quantum Monte Carlo method, Nuclear structure]

In order to study nuclear structure, the shell model is one of the most useful approaches. In many shell-model calculations, however, one has to diagonalize Hamiltonian matrix in the full valence-nucleon Hilbert space. The dimension of such a model space becomes too large for heavier nuclei, prohibiting the diagonalization of the matrix. In order to overcome this difficulty, the Quantum Monte Carlo Diagonalization (QMCD) method was proposed by Honma et al.<sup>1-3)</sup>

We outline first the framework of the QMCD here. The QMCD is a method of solving many-body problems by diagonalizing the Hamiltonian in a subspace consisting of a tractable number ( $\lesssim 50$ ) of bases. Each basis is generated by utilizing an auxiliary field Monte Carlo technique. The auxiliary field is controlled stochastically, while the number of the bases needed to express the eigenstates under investigation is suppressed by selecting more favorable bases.

This method mentioned above is successful in large-scale shell model calculations. We can calculate wave functions and restore various symmetries explicitly.

The basis has been a Slater determinant till now. This seems to be very efficient for the nuclei lighter than  $A \sim 100$ . However, it turns out that we need too many bases to handle larger systems with stronger pairing correlations. Therefore, we propose to use condensed-pair bases as the basis states instead of Slater determinants.

The condensed-pair basis is written as  $|\Phi\rangle = (\Lambda^\dagger)^N |-\rangle$ , where  $N$  denotes one half of the number of valence nucleons, and  $|-\rangle$  is an inert core. The  $\Lambda^\dagger$  is so-called lambda pair:  $\Lambda^\dagger \equiv \sum_{ij} \Lambda_{ij} c_i^\dagger c_j^\dagger$  with  $\Lambda_{ij}$  being the amplitude and  $c_i^\dagger$  the nucleon creation operator.<sup>4)</sup>

One of the advantages to use this type of bases is capability of using the solution of Hartree-Fock-Bogoliubov method as an initial state.

We then compare the calculation with condensed-

pair bases to the one with Slater determinant bases by taking a simple system (Fig. 1). The Hamiltonian in this system consists of a pairing interaction and single particle energies. One can see that the condensed-pair basis can express this system quite efficiently.

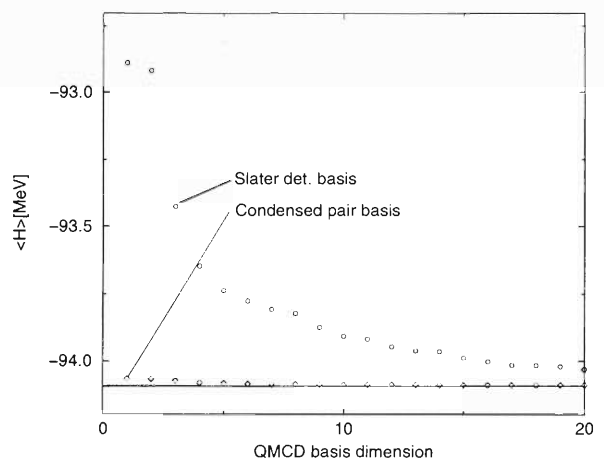


Fig. 1. Energies as a function of the QMCD basis dimension for the  $pf$ -shell.  $H = G \sum P^\dagger P$  with  $G = -0.25$  MeV. The Hartree-Fock-Bogoliubov solution is used as the first basis in the condensed-pair basis calculation.

## References

- 1) M. Honma, T. Mizusaki, and T. Otsuka: Phys. Rev. Lett. **75**, 1284 (1995).
- 2) M. Honma, T. Mizusaki, and T. Otsuka: Phys. Rev. Lett. **77**, 3315 (1996).
- 3) M. Mizusaki, M. Honma, and T. Otsuka: Phys. Rev. C **53**, 2786 (1996).
- 4) T. Otsuka and N. Yoshinaga: Phys. Lett. B **168**, 1 (1986).

# The Pseudo-Spin Symmetry in Realistic Nuclei

J. Meng, K. Sugawara-Tanabe, S. Yamaji, P. Ring,\* and A. Arima

[Pseudo-spin symmetry, Relativistic mean field]

For thirty years the pseudo-spin symmetry<sup>1,2)</sup> has been used as a convenient concept, even though its deep physical reason remains unknown. While the relativistic mean field has been proposed for more than two decades and has been used as a relativistic version of the conventional nuclear theory, it has proven to be very successful.

Starting from the Dirac equation, Ginocchio found an elegant way to connect between the pseudo-spin symmetry and the equality in the scalar and vector potentials. It was revealed that pseudo-orbital angular momentum is the “orbital angular momentum” of the lower component of the Dirac wave function.<sup>3)</sup> From the point of Relativistic Mean Field (RMF), it is very interesting to check how good the pseudo-spin symmetry is for the realistic nuclei. Here, starting from the standard RMF, instead of assuming the equality in magnitude of the scalar and vector potentials, we have treated the equation exactly and obtained a general formalism leading to the pseudo-spin symmetry. It will be shown that there are two ways to solve the Dirac equation. Concerning the energies of the solution for the large and small components, they appear to be the same. The conventional way is to reduce the Dirac equation to a Schrödinger type equation for the upper component, and the spin-orbital splitting is discussed. On the other hand, we can obtain an equation for the lower component, and then the splitting will be in pseudo-spin. For example, we have chosen <sup>88</sup>Zr and <sup>120</sup>Zr to study the energy splitting of the pseudo-spin partners and its energy dependence in realistic cases.

The standard Dirac equation of RMF is as follows:

$$[\vec{\alpha} \cdot \vec{p} + V_V(\vec{r}) + \beta(M + V_S(\vec{r}))]\psi(\vec{r}) = \epsilon\psi(\vec{r}), \quad (1)$$

which describes a Dirac spinor moving in a potential denoted by the scalar potential  $V_S(\vec{r})$  and vector potential  $V_V(\vec{r})$ . In the following we will introduce the potential  $V = V_V(\vec{r}) + V_S(\vec{r})$ , which is around  $-50$  MeV, and the effective mass  $M^* = M + V_S(\vec{r})$ . In the spherical case, the  $V$  depends only on the radius. We have chosen the phase convention of the vector spherical harmonics as:

$$(\vec{\sigma} \cdot \vec{r})Y_{jm}^{l'} = -Y_{jm}^{l''} \quad (2)$$

where

$$l' = 2j - l = \begin{cases} l+1, & j = l+1/2 \\ l-1, & j = l-1/2 \end{cases}. \quad (3)$$

Here,  $l'$  is nothing but the pseudo-orbital angular momentum. After some tedious simplification, one reaches the radial equation of the lower component:

$$\begin{aligned} & \left[ \frac{d^2}{dr^2} + \frac{1}{E-V} \frac{dV}{dr} \frac{d}{dr} \right] F_i^{lj}(r) \\ & + \left[ \frac{\kappa(1-\kappa)}{r^2} - \frac{1}{E-V} \frac{\kappa}{r} \frac{dV}{dr} \right] F_i^{lj}(r) \\ & = -(E + 2M^* - V)(E - V)F_i^{lj}(r). \end{aligned} \quad (4)$$

We can discuss the approximation of the pseudo-spin symmetry by considering the equation of the small component. For this purpose, the recently developed Relativistic Hartree-Bogoliubov (RHB) theory in coordinate space has been used.<sup>4)</sup> We find that the degree of the degeneracy improves if the corresponding levels are less bound. In <sup>88</sup>Zr, as the  $2d_{3/2}$  and  $3s_{1/2}$ ,  $2d_{5/2}$  and  $1g_{7/2}$  pairs are near the fermi surface, so that their splittings are very small. Similar cases for <sup>120</sup>Zr are also observed.

The pseudo-spin symmetry is examined for the first time in realistic nuclei in the framework of RHB.<sup>4)</sup> We have found a more general condition for the hidden pseudo-spin symmetry from the Dirac equation for the lower component: i.e.,  $dV/dr = 0$ , which includes  $V = 0$  discussed in Ref. 3 as a special case. From the simple Dirac equation, it has been shown that there are two equivalent ways to solve the coupled Dirac equation for the upper and lower components: the normal spin or pseudo-spin formalism. Solving the reduced uncoupled differential equations for the lower component is the same as that for the upper component, as the eigenvalue obtained is the same. The relation between the upper and lower components indicates that the unitary transformation from the conventional to pseudo-spin formalisms has the “p-helicity”. By studying the splitting caused by the pseudo-spin orbital potential, the quality of pseudo-spin symmetry in realistic nuclei is examined. For a given angular momentum and parity channel, the centrifugal barrier multiplied by the factor  $E - V$  becomes stronger for the less bound level, so that the pseudo-spin symmetry for the weakly bound state is better than the deeply bound state. This is in agreement with the experimental observation<sup>1,2)</sup> and with the former model study to assume a spherical square potential-well.<sup>3)</sup> The above conclusion has been well supported by the examples of <sup>88</sup>Zr and <sup>120</sup>Zr.

## References

- 1) A. Arima, M. Harvey, and K. Shimizu: Phys. Lett. B **30**, 517 (1969).
- 2) K. T. Hecht and A. Adler: Nucl. Phys. A **137**, 129 (1969).
- 3) J. Ginocchio: Phys. Rev. Lett. **78**, 436 (1997).
- 4) J. Meng and P. Ring: Phys. Rev. Lett. **77**, 3963 (1996).

\* Physik-Department der Technischen Universität München, Germany

## Double Giant Quadrupole Resonance

H. Kurasawa\* and T. Suzuki

[Giant resonance]

The double giant quadrupole resonance (DGQR) has been observed with nuclear interaction using heavy ion beams at intermediate energies.<sup>1)</sup> Recent experiments on  $(\pi^+, \pi^-)$  and relativistic heavy ion reactions have also revealed the existence of the double giant dipole states (DGDR) in various nuclei.<sup>1)</sup> The giant resonance states are characterized by their excitation energy, width, and excitation strength. Emling et al.<sup>1)</sup> have summarized the experimental data, and found the relationship of the excitation energies and widths of DGDR and DGQR to those of the single giant resonance states (GDR and GQR), as  $\omega_2 = (1.91 \pm 0.02)\omega_1$  and  $\Gamma_2 = (1.60 \pm 0.03)\Gamma_1$ . Here,  $\omega_2$  ( $\omega_1$ ) stands for the excitation energy and  $\Gamma_2$  ( $\Gamma_1$ ) the width of the double giant resonance state (single giant resonance state). They have also compared the strength of double giant resonance states with various theoretical values, and found that all the theoretical values obtained so far underestimate the data by more than a factor of 2. Contrary to DGDR, the strength of GDR is well known to be reproduced by the Thomas-Reiche-Kuhn (TRK) sum rule.

In Ref. 2, we have derived the model-independent sum rule for DGDR strength which corresponds to TRK sum rule. We have shown that the excitation energy and width of DGDR are well understood model-independently, but the sum rule value is only a half of the experimental one. As far as we know, this disagreement has not been solved yet.

We can also derive the sum rule for the DGQR strength, although some assumptions are required. Let us define the strength function of DGQR as

$$S_2(E) = \sum_f |A_f|^2 \delta(E - E_f), \quad (1)$$

where  $A_f$  is given by

$$A_f = \sum_n \langle f|Q|n\rangle \langle n|Q|0\rangle = \langle f|Q^2|0\rangle, \quad (2)$$

with  $Q = \sum_{i=1}^A (2z_i^2 - x_i^2 - y_i^2)$ . For this function the non energy-weighted and energy-weighted sum rules are given as

$$S_2^{(0)} = \sum_f |\langle f|Q^2|0\rangle|^2. \quad (3)$$

$$S_2^{(1)} = \sum_f (E_f - E_0) |\langle f|Q^2|0\rangle|^2. \quad (4)$$

The non energy-weighted sum over  $|f\rangle$  should not include the ground state  $|0\rangle$ , but the energy-weighted sum can include  $|0\rangle$  as well as  $|f\rangle$ . Because of this fact

the energy-weighted sum can be expressed in terms of the double commutator,

$$S_2^{(1)} = \frac{1}{2} \langle 0|[Q^2, [H, Q^2]]|0\rangle. \quad (5)$$

The commutator with  $Q^2$  is rewritten with  $Q$  as

$$S_2^{(1)} = \frac{1}{2} \langle 0|Q^2[Q, [H, Q]] + 2Q[Q, [H, Q]]Q + [Q, [H, Q]]Q^2|0\rangle. \quad (6)$$

When we assume  $[Q, [V, Q]] = 0$ , as in TRK sum rule, we obtain:

$$S_2^{(1)} = \sum_f (E_f - E_0) |\langle f|Q^2|0\rangle|^2 = \frac{8}{m} \{2\langle 0|Q^2 M|0\rangle + \langle 0|Q^3|0\rangle\}, \quad (7)$$

where  $M$  is defined by  $M = \sum_{i=1}^A r_i^2$ . If we assume furthermore that the nucleus is spherical and that

$$\langle 0|Q^2|n\rangle \langle n|M|0\rangle = 0 \quad (n \neq |0\rangle), \quad (8)$$

then Eq. (7) is expressed in terms of the sum rules of GQR,

$$S_2^{(1)} = 4S_1^{(0)} S_1^{(1)}, \quad (9)$$

where  $S_1^{(0)}$  and  $S_1^{(1)}$  are described as,

$$S_1^{(1)} = \sum_n (E_n - E_0) |\langle n|Q|0\rangle|^2, \quad (10)$$

$$S_1^{(0)} = \sum_n |\langle n|Q|0\rangle|^2. \quad (11)$$

Now we define the mean energies of DGQR and GQR by using the energy-weighted and non energy-weighted sum rules,

$$\omega_2 = S_2^{(1)}/S_2^{(0)}, \quad \omega_1 = S_1^{(1)}/S_1^{(0)}. \quad (12)$$

Then, the sum rule in Eq. (9) gives

$$\frac{\omega_2}{\omega_1} = 4 \frac{\{S_1^{(0)}\}^2}{S_2^{(0)}}. \quad (13)$$

Thus the ratio of DGQR strength to GQR one is related to that of their excitation energies. If we take the experimental value  $\omega_2 \approx 2\omega_1$ , Eq. (13) gives

$$S_2^{(0)} \approx 2\{S_1^{(0)}\}^2. \quad (14)$$

This result contradicts the experimental value by factor 2, as in the case of DGDR.<sup>2)</sup> It is very important to understand this disagreement in nuclear physics.

### References

- 1) H. Emling: Prog. Part. Nucl. Phys. **33**, 729 (1994); Ph. Chomaz and N. Francaria: Phys. Rep. **252**, 275 (1995).
- 2) H. Kurasawa and T. Suzuki: Nucl. Phys. A **597**, 374 (1996).

\* Department of Physics, Faculty of Science, Chiba University

## Possible Enhancement of the $E1$ Decay Rates of Double Giant Dipole States<sup>†</sup>

V. G. Soloviev,\* A. Arima, and N. Dinh Dang

[Double-giant dipole resonance,  $E1$  decay rates]

The electromagnetic excitation of the double giant dipole resonance (DGDR) in relativistic heavy-ion reactions has been studied in a wide range of nuclei. The observed excitation energy of the DGDR is about twice as much compared to the energy of the giant dipole resonance (GDR). The observed width of the DGDR is larger than the GDR width by 1.6 times.<sup>1)</sup> The most striking point is that the strength of the DGDR was found strongly enhanced as compared to any theoretical estimations available so far. Among theoretical studies, which have been devoted to the description of the DGDR states, we notice Ref. 2, where the general properties of the DGDR were treated making use of a sum rule approach. One of the major results obtained in Ref. 2 is, if the mean energy of the DGDR is twice as much compared to the GDR energy, the DGDR strength is larger than that of the GDR by a factor of  $\sqrt{2}$ . It means that there is a discrepancy between the strength of DGDR determined by the sum rules and the experimental systematics.

The aim of the present work is to study a possibility for the enhancement of the  $E1$  decay as well as excitation of DGDR in a two-step process. The present paper shows that:

(1) the  $E1$  transition rates from the DGDR states

to the GDR ones can be enhanced as compared to those between the two-dipole-phonon components in wave functions of the DGDR states and the one-dipole-phonon components in wave functions of the GDR states. This enhancement can be observed experimentally in the  $\gamma$ -decay spectra of the  $E1$  transition from the DGDR to the GDR.

(2) it is possible to expect an enhancement of the DGDR states, which are formed in a two-step process of two consequent  $E1$  transitions rather than in a Coulomb excitation.

The observation of the DGDR may also serve as a signature of order in chaos, which takes place at such high excitation energies in nuclei.

### References

- 1) T. Aumann et al.: Phys. Rev. C **47**, 1728 (1993); R. Schmidt et al.: Phys. Rev. Lett. **70**, 1767 (1993); H. Emling: Prog. Part. Nucl. Phys. **33**, 729 (1994); Ph. Chomaz and N. Francaria: Phys. Rep. **252**, 275 (1995); J. Stroth et al.: Nucl. Phys. A **599**, 307c (1996); K. Boretzky et al.: Phys. Lett. B **384**, 30 (1996).
- 2) H. Kurasawa and T. Suzuki: Nucl. Phys. A **597**, 374 (1996).

<sup>†</sup> Condensed from the article in Phys. Rev. C **56**, R603 (1997)

\* Bogolyubov Laboratory of Theoretical Physics, JINR, Russia

## Possible Deviation of the Sum of Strengths for Double Giant Dipole Resonance from Harmonic Oscillator Limit<sup>†</sup>

N. Dinh Dang, A. Arima, V. G. Soloviev,\* and S. Yamaji

[Double-giant dipole resonance, Harmonic oscillators' limit]

The recent observation of the double giant resonance dipole (DGDR) in relativistic heavy-ion reactions of a wide range of nuclei has attracted a considerable attention.<sup>1)</sup> The observed excitation energy of the DGDR is about twice as much compared to the energy of the giant dipole resonance (GDR). Its width is larger than that of GDR by 1.6 times. While these parameters of the DGDR are in a good agreement with the representation of the multiphonon giant resonance, which is formed by non-interacting harmonic oscillators, the most striking point is that its strength has been found to be strongly enhanced as compared to any theoretical estimations available so far. Recently, making use of a sum rule approach, Kurasawa and Suzuki<sup>2)</sup> have demonstrated that, if the mean energy of the DGDR is twice as much compared to the GDR energy, the DGDR strength is larger than that of the GDR by a factor of  $\sqrt{2}$ . Thus, there is a discrepancy between the strength of the DGDR determined by the sum rules and the experimental data.

In the present paper we have shown the importance of the part containing the products of the particle - particle ( $pp$ ) and hole - hole ( $hh$ ) pair operators (the so-called scattering terms) of the nuclear Hamiltonian in calculating the energy weighted sum of strengths (EWSS) for the DGDR. This part is known to have a little influence on the phonon energy within the random phase approximation (RPA) except for only the lowest levels in transitional and deformed nuclei. In the region of the GDR the contribution of this part is negligible. This is the reason why it has been neglected in all microscopic calculations of the GDR so far. The present paper shows that it is no more allowed in the study of the DGDR. Even though the  $pp$

and  $hh$  pair operators cannot be expressed exactly in term of  $ph$  phonon operators, one can use the exact commutation relations of the former and the latter. The complete EWSS for the DGDR has been derived here for the first time, and a possible deviation from the value of this EWSS in the harmonic limit has been found. The formalism has been tested within a framework of a degenerate two-level model, where the RPA has the simplest analytical solution. We found an example when this deviation is quite large and enhances strongly the EWSS for the DGDR at various particle numbers, while the EWSS for the GDR itself and the energy of GDR change only slightly.

The present study, even though by the numerical calculations within a schematic model, shows that it is decisively important to include the full nuclear Hamiltonian in the study of the DGDR because some part of the Hamiltonian, while having a small influence on the GDR, may affect strongly the DGDR characteristics. It also shows that the DGDR is not a superposition of independent harmonic oscillators, but a complex of interacting multiphonon configurations. The latter makes the DGDR properties strongly deviated from the harmonic picture.

### References

- 1) T. Aumann et al.: Phys. Rev. C **47**, 1728 (1993); R. Schmidt et al.: Phys. Rev. Lett. **70**, 1767 (1993); H. Emling: Prog. Part. Nucl. Phys. **33**, 729 (1994); Ph. Chomaz and N. Francaria: Phys. Rep. **252**, 275 (1995); J. Stroth et al.: Nucl. Phys. A **599**, 307c (1996); K. Boretzky et al.: Phys. Lett. B **384**, 30 (1996).
- 2) H. Kurasawa and T. Suzuki: Nucl. Phys. A **597**, 374 (1996).

<sup>†</sup> Condensed from the article in Phys. Rev. C **56**, 1350 (1997)

\* Bogolyubov Lab. of Theor. Physics, JINR, Dubna, Russia

# Constrained GCM Calculations Based on 3D-CHFB

T. Horibata, M. Oi, and N. Onishi

[Tilted rotation, Generator coordinate method]

We have been carrying out a systematic calculation based on a self-consistent three-dimensional Cranked Hartree-Fock-Bogoliubov (CHFB) method in  $A \sim 180$  region and have found a solution which represents a Tilted Axis Rotating (TAR) state.<sup>1,2)</sup> Then, an effect of a quantum tunneling between the two TAR wells located symmetrically with respect to an equator is expected. By taking into account the effect we tried to describe the excited bands in terms of the two-dimensional Generator Coordinate Method (GCM)<sup>3,4)</sup> in which the north-latitude along the prime meridian and the east-longitude along the equatorial line were employed as the generator coordinates. The method was a quite general and interesting approach in describing the bands as well as the yrast. However, we could not obtain the stable plateau in the GCM calculation. The reason will be attributed to the fact that we lost much information concerning the high-frequency part of wave functions which are contained in the states with small eigen values of the norm kernel. This can mostly be taken into account through angular momentum projection of HFB states.<sup>5)</sup> Calculations along this line are in progress separately from present work.

Generally, in the process of solving the GCM equation the expectation values of angular momentum and the particle number will be shifted from the values of the CHFB constraints. To maintain the correct configuration of wave functions we restrict the expectation values of the angular momentum and particle number to their correct values during the process of solving the GCM. We solve the following constrained GCM equation,

$$\sum_{k'} \left[ H_{k,k'} - \lambda_r^{(\alpha)} N_{k,k'}^r - \mu^{(\alpha)} J_{k,k'}^2 \right] g_{k'}^{(\alpha)} = E^{(\alpha)} g_k^{(\alpha)}.$$

We show the results without constraints (Fig. 1) and with constraints (Fig. 2) for the case of  $J = 18 \hbar$  of  $^{182}\text{Os}$ . In Fig. 1 we can see that two lowest solutions are almost degenerate and the next higher states lay more than 1 MeV higher positions. The solutions do not consist any stable plateau. In Fig. 2, however, we can find relatively stable plateaus. The energy splittings among the states are in the range of 10–100 KeV. These values are reasonable for the interpretation of any excited bands observed in this mass region. The angular momentum fluctuation is included in the wave function of a cranking model. As the value is  $\Delta J^2 \sim 100 \hbar$  in our calculation, we restrict the expect-

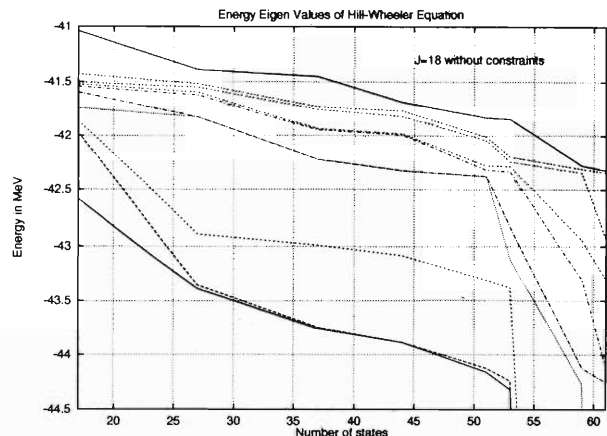


Fig. 1. GCM solutions without constraints.

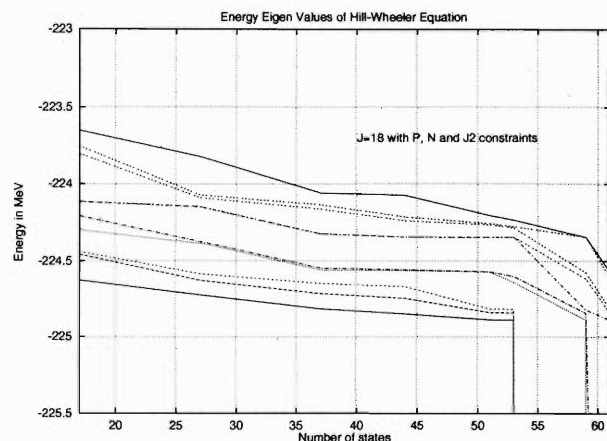


Fig. 2. GCM solutions with constraints.

tation value of  $J^2$  to  $\sim 450 \hbar$ . We found a rather stable plateau in the case where the constraints are switched on. Detail of the work will be published elsewhere.

## References

- 1) T. Horibata and N. Onishi: Phys. Lett. B **325**, 283 (1994).
- 2) T. Horibata and N. Onishi: Nucl. Phys. A **596**, 251 (1996).
- 3) T. Horibata, M. Oi, and N. Onishi: Phys. Lett. B **355**, 433 (1995).
- 4) T. Horibata, M. Oi, and N. Onishi: RIKEN Accel. Prog. Rep. **30**, 20 (1997).
- 5) M. Oi, N. Onishi, N. Tajima, and T. Horibata: Phys. Lett. B **418**, 1 (1998).

## Exotic State of 3D-CHFB

T. Horibata and N. Onishi

[Tilted rotation, Three-dimensional cranked HFB (3D-CHFB)]

A systematic calculation based on a self-consistent three-dimensional Cranked Hartree-Fock-Bogoliubov (CHFB) method revealed a possible existence of a Tilted Axis Rotating (TAR) state in  $A \sim 180$  region.<sup>1,2)</sup> In the previous calculations the force parameters were chosen so as to reproduce just the overall features of low-angular momentum states of this mass region. The observed first backbending in  $A \sim 180$  region is considered to be due to  $i13/2$  neutron states, whereas in our calculation protons were playing the role. The reason was attributed to our slightly too strong Q-Q force parameters. In the present calculation, therefore, we refine the force parameters so as to reproduce the observed characteristic features in the yrast states of nuclei in the region. Moreover, we increase the accuracy of numerical calculation by performing a backward direction as well as a forward direction along the prime meridian. As a result of the calculation we found the existence of a stable TAR state in the region of  $\theta \sim 25^\circ$  as shown in Fig. 1. Although we do not have any experimental evidences for

the existence of such states for now, this is a convincing result that the TAR indicates certain new dynamics in this mass region.

In the Fig. 1 we also find that the energy of the states near the north pole ( $\theta = 90^\circ$ ) is negative, which means that the states around the north pole are lower in energy compared with the Principal Axis Rotating (PAR) yrast state. The wave function of this state consists of the positive parity  $i13/2$  neutron states. These neutrons align their angular momenta to the symmetry axis and contribute to  $K = 8$  band state. In the experimental data we find  $K = 8^+$  bands in several nuclei in this mass region. These bands are interpreted as a candidate of the  $t$ -band.<sup>3)</sup> Therefore, the interpretation of the  $K = 8^+$  bands requires more precise analyses from both sides of experiment and theory.

Furthermore, this time we find a new state just above the PAR yrast state ( $\theta = 0^\circ$ ): at about  $E = 150$  KeV higher than the PAR. This state has been obtained in the calculation of the backward direction starting from  $\theta = 30^\circ$ . The configuration of wave function changes drastically when the north latitude takes the values at around  $\theta = 10^\circ \sim 15^\circ$ . Second phase transition occurs around  $\theta = 45^\circ$ . When the backward calculations starting from  $\theta = 60^\circ$  are performed, we found also new states in these angle regions. The curve is shown also in the Fig. 1.

Solving the Generator Coordinate Method on these states, including the new ones, will be much interesting. Detail of the results will be published in near future.

### References

- 1) T. Horibata and N. Onishi: Phys. Lett. B **325**, 283 (1994).
- 2) T. Horibata and N. Onishi: Nucl. Phys. A **596**, 251 (1996).
- 3) P. M. Walker: Proc. Int. Conf. on the Future of Nuclear Spectroscopy, Crete, p. 134 (1993).

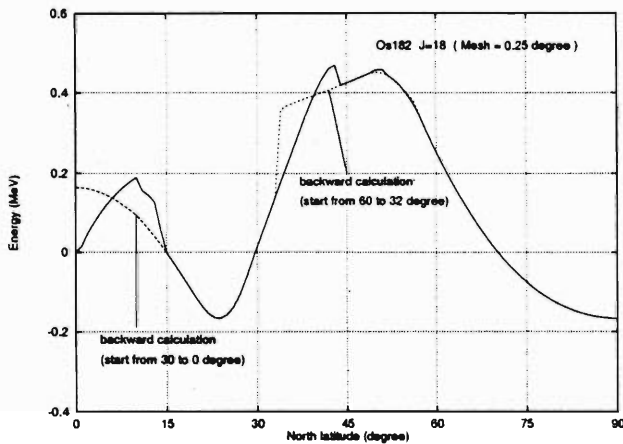


Fig. 1. Energy curves along prime meridian.

# Signature and Angular Momentum in 3D-Cranked HFB States<sup>†</sup>

M. Oi, N. Onishi, N. Tajima, and T. Horibata

[NUCLEAR STRUCTURE: Angular momentum projection, 3d-cranked HFB, Signature]

We are interested in a relation between angular momentum and “signature”, a symmetry of  $\pi$ -rotation around the intrinsic 1-axis. In the textbook by Bohr and Mottelson,<sup>2)</sup> the relation is given in the particle-rotor model as

$$r = (-1)^I \quad (\text{when } K = 0), \quad (1)$$

where  $r$ ,  $I$  and  $K$  denote the signature, total angular momentum and its projection onto the 3-axis (so-called “ $K$ -quantum number”), respectively. This implies that the even/odd members of rotational bands are classified by the  $+1/-1$  signature. This is quite favorable for the cranking model because the signature is the only quantum number in the model. However, there is a question as to whether this relation can be applied to the cranking model because this relation is derived in the context of the particle-rotor model. Usually, it is believed that the relation holds quite well even in the cranking model. It is our major aim to examine the validity of this relation in the cranking model.

In our study, cranked states are generated by the three-dimensional Hartree Fock Bogolibov (HFB) method. We solved the corresponding HFB equation in a fully self-consistent manner (the gradient method). Then, we use the exact angular momentum projection technique.

What we need is the probability  $|\langle IM | \phi \rangle|^2$ , where  $|\phi\rangle$  is a 3d-cranked HFB state. This can be calculated by the angular momentum projection as follows:<sup>2)</sup>

$$|\langle IM | \phi \rangle|^2 = \text{Tr}[N^I] \quad (2)$$

$$= \sum_{K=-I}^I N_{KK}^I \quad (3)$$

$$= \langle \phi | \hat{P}_{KK}^I | \phi \rangle. \quad (4)$$

Fig. 1 shows three pictures: (a) PAR (principal axis rotation),  $\sim$  one-dimensional cranking model; (b) TAR (tilted axis rotation),  $\sim$  3d-cranked HFB); and (c) signature projected TAR. As seen in (a), the relation (1) holds very well. The HFB state consists of only members with even angular momentum components, i.e.,  $r = +1$ . The relation breaks down a little in (b). There are two reasons for this: (1) Signature is broken down by tilting the angular momentum vector toward 3-axis from 1-axis; (2) Mixing with high- $K$  components becomes larger than the case (a) because of tilting of the angular momentum vector.

To see which is more important, we make the signature projection, which is defined as follows:

$$|r = \pm\rangle = \mathcal{N}(|+\theta\rangle \pm |-\theta\rangle). \quad (5)$$

Here,  $\mathcal{N}$  is a normalization factor and  $|\pm\theta\rangle$  is one of 3d-Cranked HFB states with positive/negative tilting

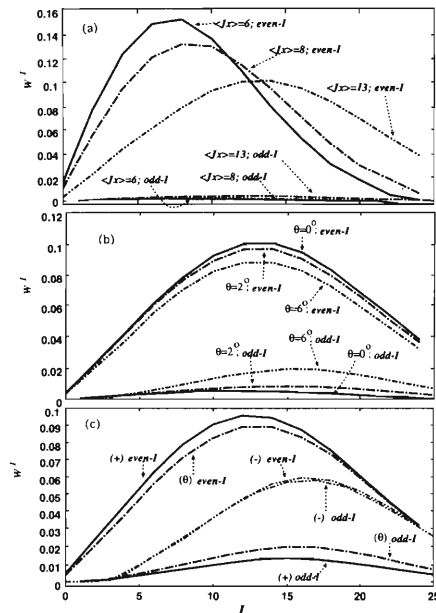


Fig. 1. Probability distributions of (a) PAR, (b) TAR and (c) Signature Projected TAR.

angle and the same angular momentum constraint. In Fig. 1(c), we see how the signature projection works. For a state with  $r = 1$ , the relation between angular momentum and signature seems to be recovered. However, for a state with  $r = -1$ , we see no relation between angular momentum and signature, i.e., even and odd angular momentum components are mixed completely.

Thus, there is no correlation between the signature and angular momentum unless the states have a dominant  $K = 0$  component. We also calculated the probability for each  $K$  components, and confirmed that the above statement should be right. PAR, TAR or Signature projected TAR with  $r = 1$  states has more than 50% of  $K = 0$  components while signature projected TAR with  $r = -1$  has less than 0.1% of  $K = 0$  components.

We conclude that the relation between angular momentum and “signature” is not a universal one, at least, in the three-dimensional cranking model. Hence, we must treat the angular momentum instead of the signature in the general case. It is quite likely that a 3d-cranked HFB plus angular momentum projection technique can describe more general nuclear dynamics, i.e., nuclear rotations beyond a mere cranking model.

## References

- 1) M. Oi et al.: Phys. Lett. B **418**, 1 (1998).
- 2) A. Bohr and B. Mottelson: *Nuclear Structure* (Benjamin, New York, 1969).

<sup>†</sup> Condensed from the article in Phys. Lett. B<sup>1)</sup>

# Doubly Periodic Motion in Superdeformed States

K. Sugawara-Tanabe and K. Tanabe\*

[ $C_{m/n}$  symmetry,  $\Delta I = 4$  bifurcation, Superdeformation]

Recently, the  $\Delta I = 4$  bifurcation in superdeformed bands has been observed,<sup>1)</sup> and has stimulated discussions on the nuclear structure. We have proposed a dynamical mechanism in the sense that the bifurcation originates from the periodicity of the intrinsic wave function.<sup>2)</sup> We start from a general microscopic Hamiltonian  $H$  defined in the laboratory frame (L). We assume a rotational motion with the rotational frequency of  $\vec{\omega}(t)$ , which is decomposed into two components; one with the constant rotational frequency  $\omega_0$  pointing to the direction of the rotational axis 1, and another with  $\Delta\vec{\omega}(t)$  which corresponds to the precessional motion caused by the small asymmetry. We transform the L-frame into the body-fixed frame (B) by employing unitary operators. Then, the corresponding Schrödinger eigenfunction at the B-frame is given by  $|\Psi^S(t)\rangle_B$ . In the interaction representation of  $|\Psi^S(t)\rangle_B = \exp(-iH_B t)|\Psi^I(t)\rangle_B$ , we obtain

$$i\frac{\partial}{\partial t}|\Psi^I(t)\rangle_B = [-\omega_0 I_1 - \Delta\vec{\omega}(t)\vec{I}]|\Psi^I(t)\rangle_B. \quad (1)$$

An important remark is that Eq. (1) has the periodicity of  $\tau_p$  and is invariant under the transformation of  $\hat{T} = \exp(i\nu\tau_p\partial/\partial t)$  with integer  $\nu$ , when the precessional angular frequency  $\Delta\vec{\omega}(t)$  has the value of  $\omega_p$  related to  $\omega_0$  through  $\omega_0/\omega_p = \tau_p/\tau_0 = \lambda$ . Thus, especially when these two periods are *commensurable* so that the ratio can be expressed as  $\lambda = m/n$  ( $< 1$ ) in terms of two irreducible positive integers  $m$  and  $n$ , the nuclear system comes back to its original position and direction after the time-lapse  $n\tau_p$ . In other words,  $\hat{T}|\Psi^I(t)\rangle_B$  obeys the same Eq.(1). Thus, the invariant solution describing the doubly periodic system can be constructed by summing up a finite series of interfering terms with different hysteresis.

Now, we solve Eq. (1) in the perturbation approximation up to the first order of  $\Delta\vec{\omega}(t)$ , and then go back from B-frame to L-frame. We identify the state  $|\Psi^H\rangle_L$  in the Heisenberg representation at L-frame ( $= \exp(iHt)|\Psi^S(t)\rangle_L$ ) with  $|IM\alpha\rangle_L$ , and  $|\Psi^I(0)\rangle_B$  with  $|IM\alpha\rangle_B$ , where  $\alpha$  corresponds to

$I_3 = K$  for the case of axially symmetric deformation (uniform rotation). Finally we obtain the wave function of the  $C_{m/n}$ -type.

$$|IM\alpha\rangle_L = \sum_{M'} D_{MM'}^I(\Omega) \left[ 1 + i\frac{C}{2} \times \sum_{\nu=0}^{n-1} (P_\nu F_\nu + F_\nu P_\nu^\dagger) \right] |IM'\alpha\rangle_B, \quad (2)$$

where  $C$  is calculated from  $\omega_0$ ,  $\omega_p$  and three kinds of moments of inertia;  $P_\nu$  as a function of  $\omega_0 I_1 \nu \tau_p$  is the normalization so that it reduces to the axially symmetric solution in the limit of  $\Delta\vec{\omega} = 0$ ; and  $F_\nu$  is given by

$$F_\nu = \sin\left(\frac{2\pi m\nu}{n}\right) I_2 + \left(1 - \cos\left(\frac{2\pi m\nu}{n}\right)\right) I_3. \quad (3)$$

The energy difference between with and without a double periodicity up to the first order of  $\Delta\vec{\omega}$  is calculated by using Eq. (2). As a simple example, we adopt the triaxial rotor Hamiltonian. We choose  $n = 4$  and  $m = 1$  ( $C_{1/4}$ -type), which reproduces the experimental data<sup>1)</sup> quite well. Similar numerical analysis was performed also for the  $C_{1/3}$ -type ( $n = 3$ ,  $m = 1$ ) symmetry, and the result predicts the  $\Delta I = 6$  trifurcation as a new possibility. From the relationship between  $\omega_0$  and  $\omega_p$ , we can show that there exists a domain of allowance for the stability of the state of  $C_{m/n}$ -type in such a way that  $|\delta(\omega_0/\omega_p)| < 1/n^2$ . The  $E2$  transition rate calculated from Eq. (2) yields the reduced transition probability value  $B(E2)$  which deviates from the ordinary result for the axially symmetric rotor only in the second order of energy shift.

## References

- 1) S. Flibotte et al.: Phys. Rev. Lett. **71**, 4299 (1993); D. S. Haslip et al.: Phys. Rev. Lett. **78**, 3997 (1997).
- 2) K. Tanabe and K. Sugawara-Tanabe: Proc. Int. Symp. on Symmetries in Science X, 1997-7, Plenum Press in press.

\* Department of Physics, Saitama University

# Triaxial Nuclei in Relativistic Mean Field Theory

S. Sugimoto, K. Sumiyoshi, D. Hirata, and H. Toki

[Relativistic mean field theory, Triaxial deformation,  $^{124}\text{Ba}$ ]

We study the properties of heavy mass nuclei including the possibility of triaxial deformation in the relativistic mean-field theory. We calculate the energy surfaces of about thirty even-even nuclei around  $^{122}\text{Xe}$  in the  $\beta\gamma$  plane on the Fujitsu VPP500/28 Supercomputer of the Computation Center in RIKEN.

The relativistic many-body theory has been extensively applied to nuclei and nuclear matter with remarkable success in recent years. Hirata et al.<sup>1)</sup> used its phenomenological version, the relativistic mean-field theory (RMF), to study the ground-state properties of the stable and unstable nuclei with axial deformation, and found the results very satisfactory. However, they found it necessary to extend the theory to include a triaxial deformation. In many nuclei the axial symmetric calculations give the energy curve as a function of the  $\beta$  deformation parameter, which has minima on both the prolate and oblate sides with energies very close to one another. For such a nucleus they cannot firmly conclude which shape it has as the ground state. Such a nucleus may have another type of deformation. Therefore, they added one more degree of freedom ( $\gamma$  deformation) to their theory, and applied it to the light mass nuclei.<sup>2)</sup> In the calculations they found the consistent results with axially symmetric deformation code, and found for the sulfur isotopes  $^{42-56}\text{S}$  a smooth transition from prolate through triaxial to oblate shapes and finally spherical shape.

Since the similar importance of the triaxial shape is expected, we calculate the energy surfaces of about thirty even-even nuclei around  $^{122}\text{Xe}$ ,  $Z = 50-58$ ,  $N = 64-72$  region to study the structure of shape transition of nuclei from prolate to oblate shapes. In the transition process, the triaxially deformed and/or gamma soft nuclei may emerge. We use the RMF theory which is extended to include the triaxial deformation.<sup>2)</sup> The RMF theory contains the meson masses, the meson-nucleon coupling constants, and the meson self-coupling constants as free parameters. We use the parameter set called TMA<sup>3)</sup> whose parameters have mass number dependence and which has been obtained to reproduce quantitatively nuclear properties in entire mass region. The wave functions of nucleons and mesons are expanded in terms of the eigenfunctions of an triaxial deformed harmonic oscillator potential. The expansion method is described in detail in the paper by Gambhir et al.,<sup>2,4)</sup> but one more degree of freedom ( $\gamma$  deformation) is included newly.<sup>2)</sup>

In the present calculation, we work with basis of the 12 major shells for fermions and 10 major shells for bosons. In order to obtain the energy surfaces, we perform the quadratic constrained calculations on the quadrupole moments of nucleon distribution,  $Q_{20}$  and  $Q_{22}$ .<sup>2,5)</sup> We note that we do not take the pairing correlations into account, although they play an important role for nuclear deformation. The investigations of how to incorporate them in the RMF theory are now in progress.

Figure 1 shows the energy surface of  $^{124}\text{Ba}$  in  $\beta\gamma$  plane. The horizontal axis ( $\gamma = 0^\circ$ ) denotes prolate shape and the tilted axis ( $\gamma = 60^\circ$ ) denotes oblate shape. The region among these axes denotes triaxially deformed shape. The larger value of  $\beta$  indicates the stronger deformation. In Fig. 1 the position of absolute minimum is denoted by the black area. From the figure we can see that  $^{124}\text{Ba}$  may have the triaxially deformed shape in the ground state. For the other nuclei we calculated, we have found many interesting structures, and we are now investigating these results.

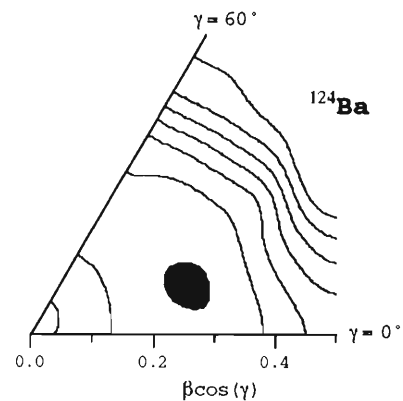


Fig. 1. The energy surface in the  $\beta\gamma$  plane of  $^{124}\text{Ba}$ . The position of the absolute minimum is denoted by the black area. This figure indicates that  $^{124}\text{Ba}$  has a triaxial shape.

## References

- 1) D. Hirata et al.: Nucl. Phys. A **616**, 438c (1997).
- 2) D. Hirata et al.: Nucl. Phys. A **609**, 131 (1996).
- 3) Y. Sugahara: Doctor thesis, Tokyo Metropolitan University (1995).
- 4) Y. K. Gambhir et al.: Ann. Phys. **198**, 132 (1990).
- 5) H. Flocard et al.: Nucl. Phys. A **203**, 433 (1973).

# The Deformation Effect on the Pairing Gap

K. Sugawara-Tanabe, N. Yoshida, and A. Arima

[Deformation, Pairing gap, HFB, BCS]

It has been discussed that the pairing gap is decreased by several effects, for example by Coriolis anti-pairing effect,<sup>1)</sup> thermal effect<sup>2)</sup> and density effect.<sup>3)</sup> Here, we propose another new effect that decreases the pairing gap, i.e., deformation effect. It is well known that the pairing interaction favors the spherical shape, while the quadrupole interaction favors the deformed shape. Comparing with the form of the mean-field in the case of Coriolis anti-pairing effect or with that in the case of thermodynamical potential, we find a similarity for the case of deformed mean-field. In the other words, the intensive variable corresponds to rotational frequency, temperature and the strength of the quadrupole field, while the extensive variable corresponds to an angular momentum, entropy and quadrupole field.

Stimulated by this analogy, we have performed the realistic calculations for <sup>152</sup>Dy using the Nilsson plus Bardeen-Cooper-Schrieffer (BCS) calculation for  $N = 3, 4, 5$  and 6 shells (148 levels), and also the constrained Hartree-Fock-Bogoliubov (HFB) calculation which is self-consistent but for smaller single-particle space (64 levels in proton and 88 levels in neutron). Both calculations give a decrease of the pairing gap ( $\Delta$ ), as a function of the deformation parameter ( $\delta$ ) or the strength of the quadrupole field ( $\chi$ ).

It is usually believed that the decrease of  $\Delta$  as a function of  $\delta$  is caused by a change in the level density. We have calculated the number of levels in the regions of  $\lambda \pm 2$  Mev and  $\lambda \pm 4$  Mev for the cases of  $\delta = 0.2, 0.4$  and 0.6. The results gave almost the same number of levels, which supports that the level density is constant in this region of the deformation. We have also calculated the level density in the schematic model which neglects the  $\ell - s$  and  $\ell^2$  interactions in the deformed Nilsson potential. For  $\delta = 0$  and  $\delta = 0.6$ , we can calculate the level density analytically, and obtains a nearly constant value independent from  $\delta$ . Thus, we can conclude that  $G\rho = C$  independent from the deformation, where  $G$  is the strength of the pairing interaction and  $\rho$  is the level density.

The HFB equation reduces to the Nilsson plus BCS equation if we set  $A_{i\mu} = \delta_{i\mu}u_\mu$  and  $B_{i\mu} = v_\mu\delta_{i\mu}$ , where

$A_{i\mu}$  and  $B_{i\mu}$  are the forward and backward amplitudes in the generalized Bogoliubov transformation from the spherical base ( $i$ ) to the deformed base ( $\mu$ ), respectively. However, there remains a difference in the self-energy term. The main difference between the Nilsson plus BCS calculation and the HFB calculation is the self-consistency. The self-energy term in the HFB becomes

$$\Gamma_{\alpha\beta}^H = -\chi(r^2Y_{20})_{\alpha\beta} \sum_{\gamma} (r^2Y_{20})_{\gamma\gamma} v_{\gamma}^2, \quad (1)$$

where  $v_{\gamma}^2$  is the the occupation probability at the level  $\gamma$ . Equation (1) indicates that the deformed field is influenced by the pairing field. On the other hand, the self-energy term in Nilsson is given by

$$\Gamma_{\alpha\beta}^N = -\delta\hbar\omega_0(r^2Y_{20})_{\alpha\beta}, \quad (2)$$

which is completely independent from the pairing field. Thus, we treat the difference between (1) and (2) as a perturbed term, i.e.,  $\Gamma_{\alpha\beta}^{(1)} = \Gamma_{\alpha\beta}^H - \Gamma_{\alpha\beta}^N$  based on the Nilsson plus BCS basis, and carry on the similar perturbation calculation as done by Mottelson and Valatin<sup>1)</sup> for the case of Coriolis anti-pairing. Contrary to Coriolis anti-pairing effect, there remains the first order perturbation term.

$$\Delta^{(1)} = -\frac{G\Delta}{4} \sum_{\alpha} \frac{\Gamma_{\alpha\alpha}^{(1)}}{E_{\alpha}^3(1 - \frac{G}{4} \sum_{\beta} \xi_{\beta}^3/E_{\beta}^3)}. \quad (3)$$

Here  $\xi_{\alpha}$  is the single-particle energy measured from the chemical potential and  $E_{\alpha}^2 = \xi_{\alpha}^2 + \Delta^2$ . Similarly, the second order perturbation term was carried out as  $\Delta^{(2)}$ . The numerical results show that both of  $\Delta^{(1)}$  and  $\Delta^{(2)}$  decrease with increasing  $\delta$ .

## References

- 1) B. R. Mottelson and J. G. Valatin: Phys. Rev. Lett. **5**, 511 (1960).
- 2) K. Tanabe and K. Sugawara-Tanabe: Nucl. Phys. A **357**, 20 (1981).
- 3) A. Bohr and B. R. Mottelson: *Nuclear Structure* (Benjamin, New York, 1969).

# Thermal Damping Width of Giant Dipole Resonance in Hot Nuclei<sup>†</sup>

N. Dinh Dang and F. Sakata\*

[Thermal damping, Hot giant dipole resonance]

A great interest has been devoted to the properties of highly excited nuclei produced in heavy-ion fusion reactions during the last decade. Analyzing the decay pattern of these hot nuclei, the giant dipole resonance (GDR) built on compound nuclear states has been observed.<sup>1)</sup> The experiments have shown that while centroid energy of the hot GDR is almost independent of excitation energy (or of temperature  $T$ ), its apparent width increases significantly as the excitation energy goes up and saturates at around 130 MeV in Sn isotopes. This attractive phenomenon has become a real puzzle to be resolved for many theoretical studies in recent years. Indeed, while most of theoretical approaches agree in reproducing the centroid energy of the GDR at  $T \neq 0$ , many of them are still in contradiction with each other in understanding the GDR width in hot nuclei.

As the temperature increases the quantal effects arising from a great number of non-collective degrees of freedom are expected to diminish, which means that they reach the thermal equilibrium much faster than a relatively smaller number of collective degrees of freedom. In the case of the hot GDR, the collective degrees of freedom are the  $ph$  phonon states, while the  $pp$  and  $hh$  configurations consist mostly of non-collective degrees of freedom. The collective degrees of freedom are experimentally relevant, while the non-collective ones are constituting a background, to which the collective degrees of freedom are coupled. If the background is very large it can be considered as a heat bath, and this coupling between collective and non-collective degrees of freedom becomes *irreversible*. It leads to the *thermal damping* of the collective  $ph$  phonon states, associated with the hot GDR, when these phonons are propagating through the heat bath.

We present an approach which allows to derive the thermal damping width of the GDR in hot nuclei in a microscopic way. We demonstrate the importance of the thermodynamical effects in the non-collective  $pp$  and  $hh$  configurations, which appear only at non-zero temperature and can play the role of a background or a heat bath. Namely, we have pointed out that the irreversible coupling of the  $ph$  GDR to this background

(or heat bath) leads to the thermal damping of GDR in hot nuclei. The application of our approach to a simple schematic model has shown that this thermal damping mechanism can be complementary to other mechanisms in understanding the behavior of the GDR width at finite temperature. Finally a semi-microscopic unification of the quantal spreading with the integrated thermal damping widths shows that the behavior of the total width found in this approach is similar to the trend in the experimental findings in hot Sn isotopes including the region of width saturation. Our analysis has been performed within an oversimplified schematic model. A drawback of this model is, while the GDR can be described by one single collective  $ph$  transition, the degeneracy of non-collective  $pp$  and  $hh$  configurations on only two levels made them too collective and therefore artificially enhanced the intensity of the low lying mode. In realistic situations we expect that a very large number of non-collective  $pp$  and  $hh$  degrees of freedom will spread out the strength distributed on them. Nonetheless, since the mechanism of the thermal damping arises from the coupling between collective and non-collective degrees of freedom, we believe that the qualitative conclusion of our formalism on the behavior of the hot GDR, including the region of width saturation, is model-independent.

## References

- 1) Proc. Gull Lake Nucl. Phys. Conf. on Giant Resonances: Nucl. Phys. A **569** (1994), (edited by M. Thoennessen); J. J. Gaardhøje et al.: Phys. Lett. B **139**, 273 (1984); J. J. Gaardhøje et al.: Phys. Rev. Lett. **53**, 148 (1984); J. J. Gaardhøje, A. M. Bruce, and B. Herskin: Nucl. Phys. A **482**, 121c (1988); C. A. Gossett et al.: Phys. Rev. Lett. **54**, 1486 (1985); D. R. Chakrabarty et al.: Phys. Rev. C **36**, 1886 (1987); D. R. Chakrabarty: Nucl. Phys. A **382**, 81c (1988); R. J. Vojtech et al.: Phys. Rev. C **40**, 2441 (1989); A. Bracco et al.: Phys. Rev. Lett. **62**, 2080 (1989); A. Bracco et al.: Nucl. Phys. A **519**, 47c (1990); G. Enders et al.: Phys. Rev. Lett. **69**, 249 (1992); H. J. Hofmann et al.: Nucl. Phys. A **571**, 301 (1994); J. H. Le Faou et al.: Phys. Rev. Lett. **72**, 3321 (1994).

<sup>†</sup> Condensed from the article in Phys. Rev. C **55**, 2872 (1997)

\* Department of Mathematical Sciences, Ibaraki University

# Relation between the Damping of the Hot Giant Dipole Resonance and the Complex Admittance of an Irreversible Process

N. Dinh Dang and F. Sakata\*

[Damping widths, Hot giant dipole resonance, Complex admittance]

At present we see two particular important issues in the theoretical study for the behavior of the giant dipole resonance as a function of temperature. The first issue is the need in a consistent description of the hot GDR width as a function of temperature, including both regions of the width's increase at low temperatures ( $0 \leq T \leq 3$  MeV) as well as of the width's saturation ( $T \geq 3$  MeV) up to the region where the GDR is thought to disappear ( $T > 4.5 \sim 5$  MeV). The second issue is the relation between the microscopic and macroscopic understandings of the damping mechanism of hot GDR. Recently we have shown in a series of works that the coupling of the phonon in the random phase approximation (RPA) to the  $pp$  and  $hh$  configurations, which appear at nonzero temperature, leads to the thermal damping of the collective vibration (phonon). In our most recent work,<sup>1)</sup> we gave our answer to the first issue. Namely, we have performed a systematic study of the damping of the GDR in  $^{90}\text{Zr}$ ,  $^{120}\text{Sn}$  and  $^{208}\text{Pb}$  as a function of temperature  $T$ . The results have shown that the coupling of collective vibration to the  $pp$  and  $hh$  excitations, which causes the thermal damping width, is responsible for the increase of the total width with increasing temperature up to  $T \approx 3$  MeV, and its saturation at higher temperatures. Our results are found in an overall agreement with the experimental data for the GDR width, obtained in the inelastic  $\alpha$  scattering and heavy-ion fusion reactions at excitation energies  $E^* \leq 450$  MeV.

In the present paper we propose an alternative method to calculate the damping width of the hot GDR via the complex admittance of an irreversible process. The relation between the microscopic theory for the damping of hot GDR and the macroscopic one for the evolution of the dynamical variable, which describes the evolution of the hot GDR, is established. The microscopic expression for the complex admittance is derived from the Green function, describing the propagation of the GDR vibration through the field of noncollective degrees of freedom (heat bath). The present formalism was then applied to a systematic study of the behavior of the GDR as a function of temperature in the nuclei  $^{120}\text{Sn}$  and  $^{208}\text{Pb}$ . The values of the calculated damping width  $\Gamma_{GDR}$  of the hot GDR, centered at  $E_{GDR}(T)$ , were compared with the recent experimental data obtained in the heavy-ion fusion reactions and inelastic  $\alpha$  scattering. An overall agreement between theory and experiment is achieved. As compared to the recent predictions by other theories,<sup>2)</sup> the present approach, which is free from the constraint on adiabaticity, seems to be able to give a better agreement with experiment, and can

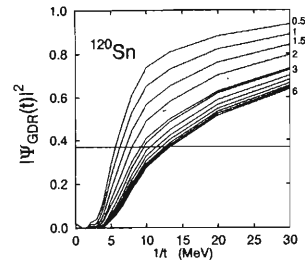


Fig. 1. The probability  $|\Psi_{GDR}(t)|^2$  for the GDR in  $^{120}\text{Sn}$  as a function of the inverted time  $1/t = \Gamma_{GDR}$  at various temperatures. The value of the temperature (in MeV), at which a curve was calculated, is given by a number near the curve. The horizontal line is  $\exp(-1)$ .

cover a much larger temperature interval, including the region of the width's saturation, where the adiabaticity is broken. The present work confirms that the thermal effects due to the coupling of the GDR collective vibration to the  $pp$  and  $hh$  configurations are the source of the increase of the GDR's width at low excitation energies (up to 130–150 MeV) and in the width's saturation at high excitation energies (see Fig. 1). These effects are fairly enough to account for the thermal fluctuations in the hot GDR in finite nuclei. The quantal width  $\Gamma_Q$  due to the coupling of the GDR to only  $ph$  configurations decreases slowly with increasing temperature  $T$ . Analyzing the calculated strength distribution of the hot GDR, we see that refined experimental methods are needed to explore the low-energy region of the GDR distribution in order to isolate a possible low-lying structure. In particular, the appearance of the low-lying structure and the difficulties of extracting it from the background are proposed in this work as one possible reason of the “disappearance” of the hot GDR in some experiments. On the other hand, a more refined study on the relationship between the excitation energy and temperature in finite nuclei at temperatures below  $T = 5$  MeV is needed in order to avoid the large uncertainties when comparing theoretical results and the data. Finally, our results seem to indicate the presence of motional narrowing in the hot GDR at  $T \geq 1\text{--}1.5$  MeV as a consequence of the quantal coupling to  $ph$  configurations.

## References

- 1) N. Dinh Dang and A. Arima: RIKEN Accel. Prog. Rep. **31**, 29 (1998).
- 2) R. A. Broglia et al.: Prog. Part. Nucl. Phys. **28**, 517 (1992); A. Bonasera et al.: Nucl. Phys. A **569**, 215c (1994); W. E. Ormand et al.: Phys. Rev. Lett. **77**, 607 (1996); W. E. Ormand et al.: Nucl. Phys. A **614**, 217 (1997).

\* Department of Mathematical Sciences, Ibaraki University

# Temperature Dependence of Quantal and Thermal Dampings of Hot Giant Dipole Resonance

N. Dinh Dang and A. Arima

[Quantal and thermal damping widths, Hot giant dipole resonance]

The study of the Giant Dipole Resonance (GDR), built on compound nuclear states (hot GDR), has been the subject of a considerable number of works during the last 15 years (See Ref. 1 for the reviews). The main feature of the hot GDR phenomenon can be summarized as follows. The energy of the hot GDR is about the same as of the one built on the ground state (g.s.) (the g.s. GDR). It can be well described within the framework of existing theories. However, its width increases rapidly as increasing the excitation energy  $E^*$  (or temperature  $T$ ) up to around 130 MeV in Sn isotopes. At higher excitation energies the width increases slowly and even saturates. Recently two new experimental methods, involving compound nuclear reactions and inelastic  $\alpha$  scattering,<sup>2)</sup> have opened a possibility to study individually the effects of thermal fluctuations and of the angular momentum on the damping of the hot GDR. The most recent theoretical evaluations in Ref. 3, which include the thermal shape fluctuations within an adiabatic model, agree nicely with the  $\alpha$ -scattering data in Ref. 3 for the GDR width in  $^{120}\text{Sn}$  and  $^{208}\text{Pb}$  at temperatures  $1 \text{ MeV} < T \leq 3 \text{ MeV}$ . The region of the width saturation ( $E^* > 130 \text{ MeV}$ ), where a considerable number of heavy-ion fusion data has been accumulated up to  $E^* \sim 450 \text{ MeV}$ , is left out in the description of Ref. 3. In the present situation, of particular importance in the theories of the hot GDR is the understanding in a consistent and microscopic way the behavior of the hot GDR as a function of temperature in a large interval. Such a theory must cover the region of the width's increase at low temperatures ( $0 \leq T \leq 3 \text{ MeV}$ ) as well as the region of the width saturation ( $T \geq 3 \text{ MeV}$ ) up to the region where the GDR is thought to disappear ( $T > 4.5 \sim 5 \text{ MeV}$ ).

In this paper we present an approach using the double-time Green function method to a systematic theoretical study of the width of the GDR as a function of temperature in the nuclei  $^{90}\text{Zr}$ ,  $^{120}\text{Sn}$ , and  $^{208}\text{Pb}$ . The results are compared with the recent experimental data of the GDR width in heavy-ion fusion reactions and inelastic  $\alpha$  scattering. An overall agreement between theory and experiment is found (see Fig. 1). This agreement is also better than those from recent theories and covers a much larger region of excitation energies up to  $E^* \sim 450 \text{ MeV}$ . For the first time the theory describes both regions of the width increase as well as the width saturation in a uniform way. The analysis in the present paper shows that: (1) Thermal effects due to the coupling of the GDR collective vi-

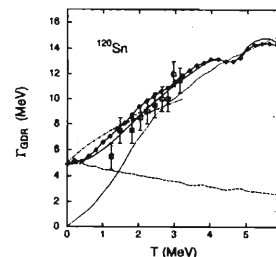


Fig. 1. Width of GDR as a function of temperature  $T$  for  $^{120}\text{Sn}$ . Experimental data of Ref. 2 are shown by open squares. The dashed curve denotes the quantal width  $\Gamma_Q$ , calculated via coupling to  $ph$  configurations; the dotted curve stands for thermal width  $\Gamma_T$ , calculated via coupling to  $pp$  and  $hh$  configurations; the solid curve with diamonds represents the total width  $\Gamma_{GDR}$ . The solid curve is  $\Gamma_{GDR}$ , calculated without the effect of single-particle damping. The dash-dotted and short dashed curves represent the widths obtained within the adiabatic model<sup>3)</sup> without and including the evaporation width, respectively.

bration to the  $pp$  and  $hh$  configurations play a decisive role in the increase of the GDR's width at low excitation energies (up to 130–150 MeV) and in the width's saturation at high excitation energies. The effects of coupling to  $pp$  and  $hh$  configurations are fairly enough to account for the thermal fluctuations in the hot GDR in finite nuclei. The quantal width  $\Gamma_Q$ , which is caused by the coupling of the GDR to only  $ph$  configurations, decreases slowly with increasing temperature  $T$ . The region where the GDR width saturates can serve as an analogue of a gradual transition from zero sound (g.s. GDR) to ordinary sound (hot GDR) in finite nuclei at nonzero temperature. (2) The effects of single-particle damping on the GDR width are small up to very high temperatures. (3) A more detail study on the relation between the excitation energy and temperature in finite nuclei at temperatures below  $T = 5 \text{ MeV}$  is called for in order to avoid the large uncertainties in confronting theoretical predictions and the data.

## References

- 1) K. Snover: Annu. Rev. Nucl. Part. Sci. **36**, 545 (1986); J. J. Gaardhøje: Ann. Rev. Nucl. Part. Sci. **42**, 483 (1992).
- 2) E. Ramakrishnan et al.: Phys. Rev. Lett. **76**, 2025 (1996).
- 3) W. E. Ormand, P. F. Bortignon, and R. A. Broglia: Phys. Rev. Lett. **77**, 607 (1996); W. E. Ormand et al.: Nucl. Phys. A **614**, 217 (1997).

# Stability of the Thermal HFB Equation

K. Sugawara-Tanabe and K. Tanabe\*

[THFB, TRPA, Stability]

We have constructed the general formalism for the thermal Hartree-Fock-Bogoliubov (THFB) equation and for the stability equation of THFB many years ago.<sup>1)</sup> Then, the thermal giant dipole resonance (TGDR) has been observed experimentally, and many papers have tried to solve the thermal RPA (TRPA) equation in order to explain the width and energy of the THFB as a function of temperature.<sup>2)</sup> Now it becomes on the topic to discuss the stability of the thermal field, because TRPA equation depends on the THFB solutions.

Thermal HFB equation is derived by minimizing the thermodynamical potential  $F$  with respect to the  $A$ ,  $B$  and  $f$ . Here,  $A_{k\mu}$  and  $B_{k\mu}$  are the forward and backward amplitudes, respectively, in the Bogoliubov transformation from the spherical base  $c_k$  to the deformed base  $\alpha_\mu$ , while  $f_\mu$  is the quasiparticle occupation number defined by

$$f_\mu = \text{Tr} \alpha_\mu^\dagger \alpha_\mu \frac{\exp(-\beta H)}{\text{Tr} \exp(-\beta H)}. \quad (1)$$

Because of an additional freedom of the temperature  $T$  in the thermal mean-field, additional variational parameter  $f_\mu$  should be included. Consequently, the stability equation is derived through  $\delta^2 F$  by the second order variation of  $\delta A$ ,  $\delta B$  and  $\delta f$ .

Since no one has ever made a success in solving the thermal stability equation self-consistently, we assume following approximations as a first step.

(1) At first, the temperature is treated as an external parameter, although it should be determined self-consistently.

(2) Secondly, we start from the axi-symmetrically deformed Nilsson levels, instead of the spherical base  $c_k$ . In this case,  $A_{k\mu}$  equals  $\delta_{k\mu} u_\mu$  and  $B_{k\mu}$  equals  $\delta_{k\mu} v_\mu$ . These two assumptions mean that we have neglected the self-consistency in solving thermal mean-field.

(3) Thirdly, we assume that the quadrupole-quadrupole interaction is already included in the deformed Nilsson potential, and we treat only the pairing

interaction as a remaining potential.

With these approximations, we obtain the stability matrix as

$$\begin{pmatrix} X & Y & 0 \\ Y & X & 0 \\ 0 & 0 & Z \end{pmatrix}, \quad (2)$$

where

$$\begin{aligned} X &= S - WZ^{-1}W^T \\ Y &= R - WZ^{-1}W^T. \end{aligned} \quad (3)$$

Here,  $S$  and  $R$  are given as a function of  $f_\mu$ ,  $u_\mu$ ,  $v_\mu$ , quasi-particle energy  $E_\mu$  and the pairing strength  $G$ . The matrix element of  $Z$  is given by

$$\begin{aligned} Z_{\mu\nu} &= \delta_{\mu\nu} \frac{kT}{f_\mu(1-f_\mu)} - G\delta_{\mu\nu}(uv)_\mu^2 \\ &\quad - \frac{G}{4}\delta_{\mu\tilde{\nu}}(u_\mu^4 + v_\mu^4), \end{aligned} \quad (4)$$

where tilded  $\nu$  denotes the time-reversed state of  $\nu$ . If the eigenvalues of Eq. (2) is negative, the solution of THFB equation becomes unstable. The submatrices of Eq. (2), i.e.,  $X$  and  $Y$  parts in Eq. (2), are proved to become a TRPA equation.<sup>3)</sup> Thus, the stability equation of THFB is the product of TRPA-term with additional  $Z$ -term. This additional term gives a constraint on the temperature with which the thermal mean-field can have the physical meaning.

Now, as a next step, we are extending our calculation to the more realistic case, without assumptions of (2) and (3). Our final goal is to eliminate assumption, i.e., the full self-consistent calculation.

## References

- 1) K. Tanabe, K. Sugawara-Tanabe, and H. J. Mang: Nucl. Phys. A **357**, 20 (1981).
- 2) K. Sugawara-Tanabe and K. Tanabe: Prog. Theor. Phys. **76**, 1272 (1986).
- 3) K. Tanabe and K. Sugawara-Tanabe: Phys. Lett. B **172**, 129 (1986).

---

\* Department of Physics, Saitama University

## Variation of Transport Coefficients for Average Fission Dynamics with Temperature and Shape<sup>†</sup>

S. Yamaji, F. A. Ivanyuk,<sup>\*1</sup> and H. Hofmann<sup>\*2</sup>

[Collective motion, Nuclear dissipation, Quasi-static thermodynamics]

We study a slow collective motion at finite thermal excitations on the basis of linear response theory applied to the locally harmonic approximation. The transport coefficients for average motion, such as, friction  $\gamma$ , inertia  $M$ , the local stiffness  $C$ , the inverse relaxation time  $\beta = \gamma/M$  and the effective damping rate  $\eta = \gamma/(2\sqrt{M|C|})$ , are computed along a fission path of <sup>224</sup>Th within a quasi-static picture. The response functions have been calculated within a realistic two-center shell model. Effects of collisions have been accounted for by using self-energies having both real and imaginary parts. The latter are allowed to depend not only on temperature but on frequency as well, in which way memory effects of the collision term are simulated. Locally collective motion is treated self-consistently, in the sense that the structure of the associated response resembles the one known from the RPA of undamped motion.

Various procedures have been described to deduce transport coefficients from the microscopically computed response, which generalize previous descriptions. They have been evaluated as a function both of temperature as well as of variation of the shape along the fission path. Considering all the effects taken into account, such a study has never been reported before. The results found invite us to draw the following conclusions.

- (1) Perhaps one of the most striking features is the weak dependence of both  $\beta$  as well as of  $\eta$  on the shape parameter, as encountered here along the fission path.
- (2) The temperature dependence of these two quantities is similar to the one reported previously<sup>1)</sup> for vibrations of <sup>208</sup>Pb: they increase with  $T$ , to eventually reach a saturation around  $T \approx 4$  MeV.
- (3) This behavior is in agreement with findings reported,<sup>2)</sup> at least qualitatively. Our damping rate is somewhat smaller, and its variation with the shape is weaker than needed in the analysis of the  $\gamma$ -ray multiplicity encountered for fission of <sup>224</sup>Th.<sup>2)</sup>
- (4) However, it must be said that we have not yet striven for quantitative agreements. For instance, there is room for a more appropriate choice of the two parameters of collisional damping. In the present paper only their "standard choice" has been used, but these values are open for changes within a certain

margin,<sup>3)</sup> and such modifications will not only change the values of the transport coefficients but also their variation with  $T$ .<sup>1)</sup> Furthermore, one should mention the influence of pairing, which still might be important at a value of  $T$  smaller than 1 MeV, but which we have left out for the sake of simplicity. Moreover, the influence of angular momentum ought to be taken into account (see below).

It should be said, of course, that the numbers extracted from the comparisons with experiment are model dependent. Moreover, in simplified studies Kramers' picture is often applied, even in the cases where the barrier is too low to guarantee that the flux across the barrier can be described by Kramers' solution of the Fokker-Planck equation. This problem can only be cured by performing genuinely dynamical studies along the lines reported<sup>4-8)</sup> but where all ingredients into macroscopic descriptions with Fokker-Planck or Langevin equations come from the same theory.

(5) Finally, we would like to come back to the angular momentum, once more, which influences fission dynamics in a manifold way. First of all, it changes the quasi-static energy through the centrifugal potential. Generally, this reduces the height of the barrier and thus restricts further the range of temperatures for which Kramers' formula of the fission decay rate is applicable. The centrifugal force will also modify the local stiffness, which in turn affects the local response in various ways. However, even in zero frequency limit rotations will have a sizable impact on the transport coefficients. This has been demonstrated in the case of friction.<sup>9)</sup> The reason for such a behavior is found in the fact that in the rotating frame the level structure may become very different from the one without rotations.

### References

- 1) H. Hofmann et al.: Nucl. Phys. A **598**, 187 (1996).
- 2) P. Paul and M. Thoennessen: Ann. Rev. Part. Nucl. Sci. **44**, 65 (1994).
- 3) H. Hofmann: Phys. Rep. **284**, 137 (1997).
- 4) E. Strumberger et al.: Nucl. Phys. A **529**, 522 (1991).
- 5) P. Fröbrich and I. I. Gontchar: Nucl. Phys. A **563**, 326 (1993).
- 6) T. Wada et al.: Phys. Rev. Lett. **70**, 3538 (1993).
- 7) T. Wada et al.: 2nd RIKEN-INFN Joint Int. Conf. on Heavy Ion Collisions, Wako, World Scientific, Singapore (1995).
- 8) K. Pomorski et al.: Nucl. Phys. A **605**, 87 (1996).
- 9) K. Pomorski and H. Hofmann: Phys. Lett. B **263**, 164 (1991).

<sup>†</sup> Condensed from the article in Nucl. Phys. A **616**, 1 (1997)

<sup>\*1</sup> Institute for Nuclear Research of the Ukrainian Academy of Sciences, Russia

<sup>\*2</sup> Physik-Department der Technischen Universität München, Germany

## Collective Motion at Finite Excitations in Terms of Cassini Ovaloids<sup>†</sup>

F. A. Ivanyuk,<sup>\*1</sup> H. Hofmann,<sup>\*2</sup> V. V. Pashkevich,<sup>\*3</sup> and S. Yamaji

[Collective motion, Nuclear dissipation, Quasi-static thermodynamics]

Previous computations of the potential landscape with the shapes parameterized in terms of Cassini ovaloids<sup>1,2)</sup> are extended to collective dynamics at finite excitations. Taking fission as the most demanding example of large scale collective motion, transport coefficients are evaluated along a fission path. We concentrate on those for average motion, namely stiffness  $C$ , friction  $\gamma$  and inertia  $M$ . Their expressions are formulated within a locally harmonic approximation on the basis of the linear response theory. Different approximations are examined and comparisons are made both with a previous study,<sup>3)</sup> which involved different descriptions of single particle dynamics, as well as with macroscopic models. Special attention is paid to an appropriate definition of the deformation of the nuclear density and its relation to that of the single particle potential. For the temperatures above 3 MeV the

inertia agrees with that of the irrotational flow to less than a factor of two, but shows larger deviations below 3 MeV, in particular in its dependence on the shape. Also, friction exhibits large fluctuations along the fission path for small excitations. They are smoothed out above 3–4 MeV where  $\gamma$  attains values in the range of the wall formula. For  $T \geq 2$  MeV the inverse relaxation time  $\beta = \gamma/M$  turns out to be rather insensitive to the shape and increases with  $T$ .

### References

- 1) V. S. Stavinsky, N. S. Rabotnov, and A. A. Seregin: *Yad. Fiz.* **7**, 1051 (1968).
- 2) V. V. Pashkevich: *Nucl. Phys. A* **169**, 275 (1971).
- 3) S. Yamaji, F. A. Ivanyuk, and H. Hofmann: *Nucl. Phys. A* **616**, 1 (1997).

---

<sup>†</sup> Condensed from the article in *Phys. Rev. C* **55**, 1730 (1997)  
<sup>\*1</sup> Institute for Nuclear Research of the Ukrainian Academy of Sciences, Russia  
<sup>\*2</sup> Physik-Department der Technischen Universität München, Germany  
<sup>\*3</sup> Joint Institute for Nuclear Research, Russia

## Nucleus as a Canonical Ensemble: The Inverse Laplace Transformation

H. Sato

[NUCLEAR STRUCTURE  $w$ ,  $E$ , and thermal properties of nuclei]

The nuclear level density is an important quantity to extract nuclear thermodynamical quantities of highly excited nuclear states formed by the nucleus-nucleus collision. A conventional formula for the nuclear level density is obtainable employing the saddle-point approximation in the inverse Laplace transformation of microcanonical treatment of the free Fermi gas. If we employ this approximation, we obtain an  $\exp(\sqrt{2aE})$  type dependence of level density for the excitation energy  $E$ .<sup>1)</sup> However, if the saddle-point method is not an adequate approximation for the inverse Laplace transformation of the nuclear system, the  $\exp(\sqrt{2aE})$  type energy dependence may not work. In previous works, we have studied the nuclear system at both low and high excitation energies in terms of the canonical ensemble, employing the temperature dependent antisymmetrized many particle density matrix in a harmonic oscillator (HO) potential with its trace:<sup>2)</sup>

$$Z_N(\beta) = \frac{1}{N} \sum_{n=1}^N (-1)^{n+1} H_{n\beta} Z_{N-n}(\beta) \quad \text{with } Z_0 = 1.$$

Here,  $H_{n\beta}$  is the trace of one particle density matrix having a temperature of  $n\beta$ . We found that this ensemble is equivalent to the ground state of the HO

shell model in the low temperature limit, and that the various phenomena observed in the intermediate and high energy nuclear collisions are nicely explainable as the property of this ensemble at high temperatures. In this work, we perform an exact calculation of the inverse Laplace transformation:

$$\rho(N, E) = \frac{1}{2\pi i} \int_{-i\infty}^{i\infty} Z_N(\beta) \exp(+\beta E) d\beta,$$

employing a computational program of the multi-precision arithmetics extended so as to include the complex functions needed in the calculation. The multi-precision arithmetic calculation is based on the method described elsewhere,<sup>3)</sup> and the calculation becomes feasible under the accessibility of 64 bit integers in the computer. Then, we can study the validity of the conventional formula for the nuclear level density given by a saddle-point approximation.

### References

- 1) A. Bohr and B. R. Mottelson: *Nuclear Structure*, Vol. 1 (Benjamin, New York, 1969), p. 281.
- 2) H. Sato: *Phys. Rev. C* **36**, 785 (1987).
- 3) H. Sato: *RIKEN Accel. Prog. Rep.* **26**, 31 (1993).

# Damping Width of the Mie Plasmon

H. Kurasawa,\*<sup>1</sup> K. Yabana,\*<sup>2</sup> and T. Suzuki

[Giant resonance states]

Giant resonance state is a fundamental collective state of nuclei. It is characterized by the excitation strength, mean excitation energy and width. The strength is understood in terms of the classical energy-weighted sum rules, while the mean energy is described with the random phase approximation. As a result, the mass number dependence of the strength and mean energy is well understood theoretically. The width, on the other hand, is estimated with various models, but not studied in a systematic way so far. In order to find a way to investigate the systematics of the width, we have applied Tomonaga theory<sup>1)</sup> to Mie Plasmon of the metal clusters.<sup>2)</sup> Before discussing nuclear giant resonances, we have studied Mie plasmon, because Hamiltonian of the atomic clusters is rather well known.

The Hamiltonian of the electrons in an atomic cluster is given by

$$H = \sum_{i=1}^{N_e} \frac{p_i^2}{2m} - \sum_{i=1}^{N_e} \sum_{\alpha=1}^{N_i} \frac{Ze^2}{|\mathbf{r}_i - \mathbf{R}_\alpha|} + \frac{1}{2} \sum_{i,j}^{N_e} \frac{e^2}{|\mathbf{r}_i - \mathbf{r}_j|},$$

where  $N_i$  and  $N_e$  denote the number of ions with charge  $Ze$  and that of electrons, respectively. The Mie plasmon is a dipole oscillation of electrons against ions, which is similar to nuclear dipole states. Hence, we introduce the collective variables for the Mie plasmon,

$$\xi = \frac{1}{\sqrt{N_e}} \sum_{i=1}^{N_e} z_i, \quad \pi = \frac{1}{\sqrt{N_e}} \sum_{i=1}^{N_e} p_{zi}, \quad (1)$$

which satisfies the canonical relationship,  $[\xi, \pi] = i$ . Then we can expand the Hamiltonian in terms of the canonical variables according to Tomonaga theory,

$$H = H_0 + H_1^\xi \xi + \frac{1}{2m} \pi^2 + \frac{1}{2} H_2^\xi \xi^2, \quad (2)$$

where  $H_i$ 's do not include  $\xi$  and  $\pi$  by the definition, and  $H_1^\xi$  and  $H_2^\xi$  are given by

$$H_1^\xi = i[\pi, H] + \xi[\pi, [\pi, H]] - \pi[\xi, [\pi, H]], \quad (3)$$

$$H_2^\xi = -[\pi, [\pi, H]]. \quad (4)$$

Assuming the ion distribution,

$$\rho_i(r) = \frac{3N_i}{4\pi R^3} \theta(R-r), \quad (5)$$

with the radius  $R$ , we calculate  $H_1^\xi$  and  $H_2^\xi$  explicitly. Then we obtain the frequency of the Mie plasmon,<sup>2)</sup>

$$\omega = \sqrt{\frac{e^2 N_{\text{eff}}}{mR^3}}, \quad (6)$$

where  $N_{\text{eff}}$  is given by

$$N_{\text{eff}} = 4\pi \int_0^R \rho_e(r) r^2 dr \leq N_e \quad (7)$$

for the spherical electron density distribution,  $\rho_e(r)$ . If there is no spill-out of the electron density from the surface of the ion distribution, the above equation is reduced to the well-known Mie frequency of the classical electrodynamics.<sup>3)</sup>

The width of the Mie plasmon is discussed with variance which is given by<sup>2)</sup>

$$\sigma = \sum_m |\langle m | H_1^\xi \xi | \omega \rangle|^2 = \frac{1}{2m\omega} \sum_m |\langle m | H_1^\xi | 0 \rangle|^2, \quad (8)$$

where  $|m\rangle$  represents the state orthogonal to the collective state,  $|\omega\rangle$ . Since  $H_1^\xi$  does not excite the collective state,  $|\omega\rangle$ , the sum over  $|m\rangle$  in  $\sigma$  can be replaced by that over the complete set,  $|n\rangle$ , which includes  $|\omega\rangle$ . Finally we obtain<sup>2)</sup>

$$\sigma \approx \frac{N_e e^4}{2m\omega} \int f^2 \rho_e(r) dr, \quad (9)$$

where we have defined  $f = z(r^{-3} - R^{-3})\theta(r-R)$ . The above equation shows that the width comes from the spill-out of the electron density from the surface of the ion distribution. If there is no quantum effect, then we have  $\sigma = 0$ . The ground state density of large clusters is well described by the Fermi-type function<sup>4)</sup> as the nuclear density,

$$\rho_e(r) = \frac{n_0}{1 + \exp((r-R-\delta R)/a)}, \quad (10)$$

where  $\delta R$  expresses the difference between the electron and ion distributions. Since both  $a$  and  $\delta R$  are known to be small compared with  $R$ , we expand Eq. (9) in terms of  $a/R$  and  $\delta R/R$ . Finally we have

$$\sigma(R \rightarrow \infty) = \frac{9}{2} m \omega_M^3 \frac{a^3}{R} \phi(\delta R/a), \quad (11)$$

where  $\phi(\delta R/a)$  is a function which is independent of  $R$ . The above equation shows that the width given by the square root of  $\sigma$  is proportional to  $1/\sqrt{R}$ . Since  $R$  is known to be  $\sim N_e^{1/3}$ , we can obtain the  $N_e$ -dependence of the width.

In conclusion, Tomonaga theory is useful to explore the systematics of the width. Its application to discussions on the width of nuclear giant resonance states is in progress.

## References

- 1) S. I. Tomonaga: Prog. Theor. Phys. **13**, 467 (1955); T. Suzuki: J. de Phys. **45**, C4-251 (1984).
- 2) H. Kurasawa et al.: Phys. Rev. B **56**, R10063 (1997).
- 3) G. F. Bertsch and R. A. Broglia: *Oscillations in Finite Quantum System* (Cambridge Univ. Press, 1994).
- 4) N. D. Lang and W. Kohn: Phys. Rev. B **1**, 4555 (1970).

\*<sup>1</sup> Department of Physics, Faculty of Science, Chiba University

\*<sup>2</sup> Department of Physics, Niigata University

# Explosion of a Neutron Star Just Below the Minimum Mass: A Possible Site for r-Process Nucleosynthesis

K. Sumiyoshi, S. Yamada, H. Suzuki, and W. Hillebrandt\*

[r-process, neutron star,  $\beta$ -decay]

Neutron star explosion is extremely interesting since it is connected with the origin of elements. Dense matter in neutron stars contains a plenty of free neutrons and seed elements, which can supply the conditions for r-process nucleosynthesis. Therefore, the expansion of the neutron star matter may lead to a rapid-neutron capture with  $\beta$ -decay, and may produce heavy elements through r-process. However, prediction of the abundance of heavy elements in neutron star explosions has a large uncertainty, depending on the dynamics of expansion of the neutron star matter, since the mechanism of the explosion is not known very well yet.

We study the evolution of a neutron star with a mass slightly below the minimum stable mass as a possible scenario for the explosion of neutron star and for r-process nucleosynthesis. Possibilities of the formation of a neutron star with the minimum mass have been discussed in various contexts such as neutron star - neutron star (or - black hole) binaries or fragmentation of a rotating core of massive stars.

It is known that the neutron star with the minimum mass is unstable against perturbation if the neutron star matter is in chemical equilibrium having enough fast nuclear reaction rates. However, nuclear reactions like  $\beta$ -decays of neutron-rich nuclei have a wide range of time scale, which depends on hydrodynamics and can be much longer than the hydrodynamical time scale. Therefore, one has to treat both hydrodynamics and nuclear reactions simultaneously in order to find out whether the star becomes unstable and explodes.

We have performed numerical simulations using a new implicit hydrodynamic code<sup>1)</sup> with nuclear reactions to investigate: the dynamical instability of a neutron star just below the minimum mass, the thermal history of the matter, and its consequence on nucleosynthesis.<sup>2)</sup> General relativistic hydrodynamics is solved with the nuclear processes treating  $\beta$ -decay, neutron capture and fission of nuclei, which change the equation of state of the neutron star matter and provide the sources of heating and cooling.

We have followed the evolution of a neutron star with the minimum mass after a small portion of the mass is removed from the surface as an initial perturbation. We have found that such a neutron star first undergoes a phase of quasi-static expansion, caused by slow  $\beta$ -decays, lasting for about 20 seconds, but then explodes violently within 0.1 seconds. (See Fig. 1) The

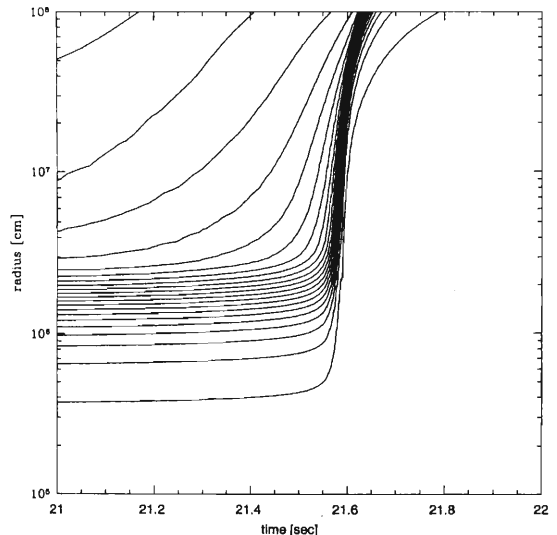


Fig. 1. The trajectories of selected mass-zones of the neutron star are plotted as a function of time.

phenomena look like a “mini-supernova” event having the kinetic energy of the order of  $10^{49}$  erg and the peak luminosity in electron anti-neutrinos of the order of  $10^{52}$  erg/s.

The thermodynamic conditions of the expanding matter are found favorable for the r-process nucleosynthesis with the peak temperature close to  $5 \times 10^9$  K due to  $\beta$ -decays and fissions. This temperature is high enough to proceed the nucleosynthesis having charged particle nuclear reactions, but not high enough to reach a nuclear statistical equilibrium. The path of nucleosynthesis goes through neutron-rich side of the nuclear chart having a rapid neutron capture with  $\beta$ -decays and fissions. Therefore, the nucleosynthesis proceeds as a kind of r-process, and produces heavy elements reflecting the initial composition in the neutron star matter.<sup>2)</sup>

We are extending the investigation by adopting more realistic equation of state of dense matter and  $\beta$ -decay and fission of unstable nuclei, so that we can predict the outcome of r-process nucleosynthesis more quantitatively and can compare with observational abundances.

## References

- 1) S. Yamada: *Astrophys. J.* **475**, 720 (1997).
- 2) K. Sumiyoshi, S. Yamada, H. Suzuki, and W. Hillebrandt: submitted to *Astron. & Astrophys.*, astro-ph/9707230.

\* Max-Planck-Institut für Astrophysik, Germany

## Relativistic Equation of State for Supernova

H. Shen, K. Sumiyoshi, K. Oyamatsu, and H. Toki

[Equation of state, Relativistic mean field theory, Thomas-Fermi calculation]

The equation of state (EOS) is one of the most important inputs in the study of the supernova explosion and some other astrophysical processes. Therefore, great efforts have been made by several groups to derive the EOS covering a wide variety of conditions. Lattimer and Swesty made the EOS for stellar collapse calculations using the compressible liquid-drop model for nuclei.<sup>1)</sup> They used the parameterized form for the bulk energy of nuclear matter, and extrapolated it to high densities. Another approach to the EOS table for supernova was done by Hillebrandt and Wolff.<sup>2)</sup> They applied the nonrelativistic Hartree-Fock theory with the Skyrme interaction to extract the EOS covering a wide range of the density, proton fraction, and temperature.

Recently, on the other hand, the relativistic many-body approach is gaining popularity. The relativistic mean field (RMF) theory was demonstrated to be successful in describing the properties of both stable nuclei and unstable ones.<sup>3)</sup> Hence, it is very important to study the properties of the EOS for supernova in the RMF theory which is best supported by both the theoretical and experimental information currently available.

It is the primary aim of this paper to provide a relativistic EOS for simulation studies of the supernova explosion, which is covering a wide range of the density ( $n_B = 10^5 \sim 10^{15.5} \text{ g/cm}^3$ ), proton fraction ( $Y_p = 0 \sim 0.5$ ), and temperature ( $T = 0 \sim 50 \text{ MeV}$ ). The relativistic mean field theory with non-linear terms is used in this calculation. We use the parameter set called TM1,<sup>4)</sup> which was extracted from the properties of finite nuclei in the wide mass range in the periodic table including neutron-rich nuclei. For the densities from  $10^5 \text{ g/cm}^3$  to  $10^{14} \text{ g/cm}^3$ , the matter is inhomogeneous as modeled by a mixture of electrons, muons, free neutrons, free protons, and a single species of heavy nuclei. In this case, we perform the Thomas-Fermi calculations following the work done by Oyamatsu.<sup>5)</sup> At the density around  $10^{14} \text{ g/cm}^3$  the phase transition between non-uniform matter and uniform matter may occur. We follow the work done by Sumiyoshi et al.<sup>6)</sup> in the uniform matter case. We are treating the uniform matter and non-uniform matter consistently. So, all the thermodynamic quantities, like energy per particle, pressure, chemical potential, and so on, are very smooth in the whole region. It is amazing to see that the density of phase transition between non-

uniform matter and uniform matter depends on  $Y_p$  only weakly, while the density of neutrons dripping out from nuclei depends on  $Y_p$  very strongly at zero temperature (see Fig. 1). It will be very interesting to see this kind of phase transition at finite temperature. This EOS has been applied to the studies of the neutron star property and neutron star profiles. We are currently working out relativistic EOS at finite temperature.

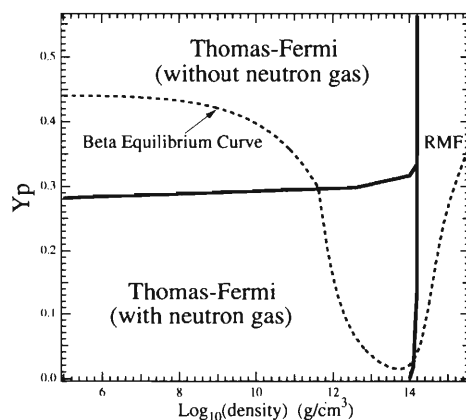


Fig. 1. The configurations of nuclear matter at zero temperature. The region denoted by RMF corresponds to the uniform matter described by RMF theory. The regions denoted by Thomas-Fermi (without and with neutron gas) correspond to the non-uniform matter without and with neutron gas, calculated with the Thomas-Fermi model using the EOS of RMF.  $\beta$  equilibrium curve is also provided, which indicates  $Y_p$  at various densities with  $\beta$  equilibrium condition.

### References

- 1) J. M. Lattimer and F. D. Swesty: Nucl. Phys. A **535**, 331 (1991).
- 2) W. Hillebrandt and R. G. Wolff: in *Nucleosynthesis-Challenges and New Developments*, edited by W. D. Arnett and J. M. Truran (Univ. Chicago Press, Chicago, 1985), p. 131.
- 3) D. Hirata et al.: Nucl. Phys. A **616**, 438c (1997).
- 4) Y. Sugahara and H. Toki: Nucl. Phys. A **579**, 557 (1994).
- 5) K. Oyamatsu: Nucl. Phys. A **561**, 431 (1993).
- 6) K. Sumiyoshi, H. Kuwabara, and H. Toki: Nucl. Phys. A **581**, 725 (1995).

# Can the Equation of State of Asymmetric Nuclear Matter Be Studied Using Unstable Nuclei?

K. Oyamatsu, I. Tanihata, Y. Sugahara, K. Sumiyoshi, and H. Toki

[Unstable nuclei, Equation of state, Atomic masses, Nuclear radii]

This paper shows that nuclear radii and neutron skins do directly reflect the saturation density of asymmetric nuclear matter (Fig. 1). The proton distributions in a nucleus have been found to be remarkably independent of the equation of state (EOS) of the asymmetric matter. It is the neutron distributions that are dependent on the EOS (Fig. 2).

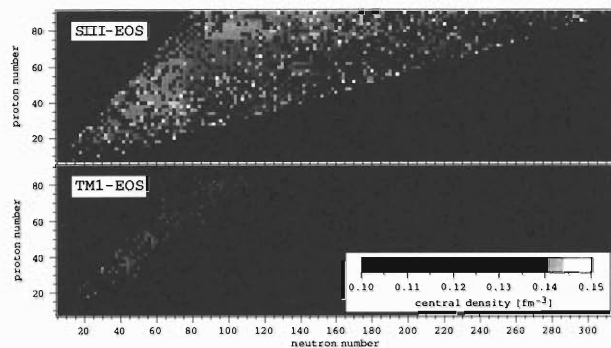


Fig. 1. Central densities of nuclei obtained from macroscopic calculations in SIII-EOS (upper figure) and TM1-EOS (lower figure).

Macroscopic model calculations have been performed over the entire range of the nuclear chart based on two popular phenomenological, but distinctively different, EOS: the SIII parameter set for the non-relativistic Skyrme Hartree-Fock theory and the TM1 parameter set in the relativistic mean field theory. The saturation density for a small proton fraction remains almost the same as the normal nuclear matter density for the SIII EOS, but it becomes significantly small for the TM1 EOS.

The key EOS parameters used to describe the saturation density are the density derivative of the symmetry energy and the incompressibility of symmetric

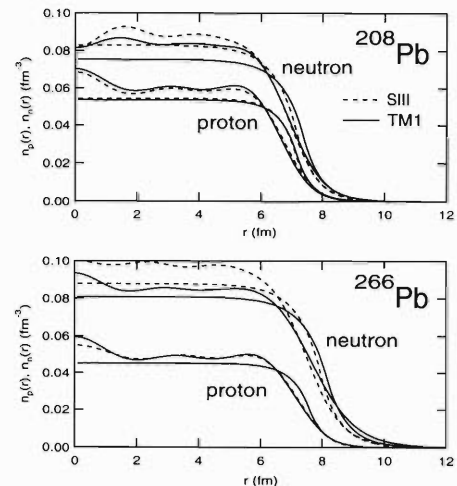


Fig. 2. Proton and neutron distributions in  $^{208}\text{Pb}$  and  $^{266}\text{Pb}$  calculated with SIII-EOS (dashed lines) and TM1-EOS (solid lines). The winding curves depict the results of microscopic calculations. Macroscopic calculations for the proton distributions in  $^{266}\text{Pb}$  are indistinguishable.

nuclear matter, while the saturation energy is written using the symmetry energy alone as a good approximation.

We conclude that a systematic experimental study of heavy unstable nuclei would enable us to determine the EOS of asymmetric nuclear matter at around the normal nuclear matter density with a fixed proton fraction down to approximately 0.3. Therefore, the answer to the title is yes.

## References

- 1) K. Oyamatsu, I. Tanihata, Y. Sugahara, K. Sumiyoshi, and H. Toki: to be published in Nucl. Phys. A.

## Exotic Nuclear Rod Formation Induced by Superfluid Vortices in Neutron Star Crusts<sup>†</sup>

Y. S. Mochizuki, K. Oyamatsu, and T. Izuyama

[Neutron stars, Pulsars, Dense nuclear matter, Screened Coulomb potential, Glitches]

The inner crust of a neutron star consists of a lattice of nuclei, relativistic degenerate electrons, and a neutron superfluid. Since the star is rotating, there are a number of quantized vortices in the superfluid. Mochizuki & Izuyama (1995) pointed out that such vortex lines may induce nuclear matter rods along the vortex cores. The exotic nuclear structure is possible in a very limited region of the inner crust. However, the short nuclear rod can completely pin the vortex line and can be an origin of vortex accumulation. The accumulation goes on until the local Magnus force among the accumulated vortices reaches a critical magnitude for unpinning of the trapped vortices. The unpinning at this stage, which must be collective, leads to pulsar glitches (sudden increases in rotation rates).

In this paper, we first reconsider energetics of this vortex-induced nuclear matter rod given by Mochizuki and Izuyama.<sup>1)</sup> We present a view that the nuclear rod is constructed by successive captures of certain neighboring nuclei into the vortex core and subsequent fusion reactions of the captured nuclei with those inside the vortex core. We found that the marginal region, where the induced nuclear rods are stable, is not

trivial.

As the next step, the possibility of nuclear rod formation should be warranted by dynamical analysis. The crucial part of the dynamics is the Coulomb potential barrier, which seems at first sight to prohibit fusion if one neglects the screening due to electrons. Then we report also our theoretical estimate of this Coulomb barrier, *i.e.*, the energy increase when a nucleus deviates from its equilibrium site to the onset position of nuclear fusion. The screening of nuclear charge by the background electrons is accurately taken into consideration. We found that the Coulomb barrier against the rod formation is of the order of 1 MeV throughout the marginal region. The obtained barrier is only several times as large as the zero-point energy of nuclei forming crystalline lattice. This result suggests that pycnonuclear reactions are feasible for the rod formation.

### References

- 1) Y. Mochizuki and T. Izuyama: *Astrophys. J.* **440**, 263 (1995).

---

<sup>†</sup> Condensed from the article in *Astrophys. J.* **489**, 848 (1997)

## Dynamics of Exotic Nuclear Rod Formation for Neutron Star Glitches<sup>†</sup>

Y. S. Mochizuki, T. Izuyama, and I. Tanihata

[Neutron stars, Pulsars, Dense nuclear matter, Pycnonuclear fusion reaction, Glitches]

The inner crust of a neutron star comprises lattices of neutron rich nuclei and a neutron superfluid, in which many quantized vortex lines exist. The vortex lines are pinned by nuclei but can jump from a pinning site to another. In the previous papers by Mochizuki & Izuyama (1995)<sup>1)</sup> and by Mochizuki, Oyamatsu & Izuyama (1997),<sup>2)</sup> it was pointed out that such vortex lines may induce nuclear matter rods along the vortex cores. This exotic nuclear rod along a vortex line is formed by captures of nuclei from outside the vortex core and by subsequent fusion reactions of the captured nuclei with the nuclei inside the core.

The nuclear rod was shown to have a lower energy than the original nuclear lattice. As the next step, dynamics for the rod formation is required. Namely, to conclude that the nuclear rods are actually formed in the neutron star, we need to confirm that the formation time of the nuclear rod is shorter than the time

of the vortex sojourn at a pinning site. It is the purpose of this paper to confirm this. We find that, under certain plausible conditions appropriate to the Vela pulsar, the rod formation time is indeed much shorter than the vortex sojourn time in *the frontier region* (the region where a vortex line is tangent to the central core of the star). The rod formation is attained by pycnonuclear reactions rather than by thermonuclear ones. The resulting exotic nuclear rod formation in the frontier region is crucial to understand the physical origin of pulsar glitches (sudden increases in rotation rates) as proposed by Mochizuki and Izuyama.<sup>1)</sup>

### References

- 1) Y. Mochizuki and T. Izuyama: *Astrophys. J.* **440**, 263 (1995).
- 2) Y. S. Mochizuki, K. Oyamatsu, and T. Izuyama: *Astrophys. J.* **489**, 848 (1997).

---

<sup>†</sup> Condensed from the article submitted for the publication in *Astrophys. J.* (1997); RIKEN-AF-NP-266(preprint)

## High Ratio of $^{44}\text{Ti}/^{56}\text{Ni}$ in Cas A and Axisymmetric Collapse-Driven Supernova Explosion<sup>†</sup>

S. Nagataki,<sup>\*1</sup> M. Hashimoto,<sup>\*2</sup> K. Sato,<sup>\*1</sup> S. Yamada,<sup>\*1,3</sup> and Y. S. Mochizuki

[ $^{44}\text{Ti}$  half-life, Supernova, Cas A, SN 1987A, Nucleosynthesis]

Cassiopeia A (Cas A) is a young supernova remnant which is located relatively close to us ( $2.9 \pm 0.1$  kpc). There is an old record that John Flamsteed observed this supernova phenomenon (ca.1680 AD) and the new star had an apparent brightness of the 6th magnitude. The mass of the progenitor is estimated to be (15–30) times the mass of the sun  $M_{\odot}$ , which implies that Cas A is the remnant of a collapse-driven supernova explosion.

Recently, Cas A was observed by the COMPTEL telescope aboard the Compton Gamma-Ray Observatory, and the gamma-ray line (1.157 MeV) from  $^{44}\text{Ti}$  decay was detected at the significance level of  $\sim 4\sigma$ . The measured line flux was  $(4.8 \pm 0.9) \times 10^{-5}$  photons/cm<sup>2</sup>/sec. The inferred amount of  $^{44}\text{Ti}$  is larger than  $1 \times 10^{-4}M_{\odot}$ , although this estimate depends on the distance and the age of Cas A, and especially, on the half-life of  $^{44}\text{Ti}$  which is still very uncertain. The half-life of  $^{44}\text{Ti}$  has been reported to fall in the range from  $39 \pm 4$  yr to  $66.6 \pm 1.6$  yr. This range corresponds to (50–98) yr in terms of the lifetime.

The inferred initial mass of  $^{44}\text{Ti}$ ,  $1 \times 10^{-4}M_{\odot}$ , is larger than the theoretical prediction<sup>1)</sup> even if we adopt the lower limit of the COMPTEL observation. Moreover, this amount of  $^{44}\text{Ti}$  should be accompanied by the ejection of at least  $0.05 M_{\odot}$  of  $^{56}\text{Ni}$ , if we assume that the theoretical prediction<sup>2)</sup> for the ratio of mass fractions,  $X(^{44}\text{Ti})/X(^{56}\text{Ni}) \leq 1.89 \times 10^{-3}$ , is correct. However, this much  $^{56}\text{Ni}$  would have led to the peak absolute brightness of magnitude  $\sim -4$ , and would have been much brighter than the recorded 6th mag-

nitude of the apparent brightness. This is the puzzling abundance problem of Cas A.

It is noted here that the above constraint on  $X(^{44}\text{Ti})/X(^{56}\text{Ni})$  is obtained on the assumption that the explosion is spherically symmetric, whereas Cas A is famous for the axisymmetric form of the remnant. Recently, Nagataki et al. (1997)<sup>3)</sup> calculated the explosive nucleosynthesis of an axisymmetrically deformed collapse-driven supernova. They reported that the ratio of  $^{44}\text{Ti}/^{56}\text{Ni}$  was enhanced by the stronger alpha-rich freezeout in the polar region.

In present paper, we apply these results to Cas A and examine whether this effect can explain the large amount of  $^{44}\text{Ti}$  and the large ratio of  $^{44}\text{Ti}/^{56}\text{Ni}$ . We demonstrate that the conventional spherically symmetric explosion model cannot explain the  $^{44}\text{Ti}$  mass produced in Cas A if its lifetime is shorter than  $\sim 80$  years. On the other hand, we show that the axisymmetric explosion models can solve the problem. We expect the same effect from a three-dimensionally asymmetric explosion, since the stronger alpha-rich freezeout will also occur in that case in the region where the larger energy is deposited.

### References

- 1) F. X. Timmes et al.: *Astrophys. J.* **464**, 332 (1996).
- 2) S. E. Woosley and R. D. Hoffman: *Astrophys. J. Lett.* **368**, L31 (1991).
- 3) S. Nagataki, M. Hashimoto, K. Sato, and S. Yamada: *Astrophys. J.* **486**, 1026 (1997).

<sup>†</sup> Condensed from the article in *Astrophys. J.* **492**, L45 (1998): RIKEN-AF-NP-277 (preprint)

<sup>\*1</sup> Department of Physics, School of Science, the University of Tokyo

<sup>\*2</sup> Department of Physics, Faculty of Science, Kyusyu University

<sup>\*3</sup> Max-Planck-Institut für Physik und Astrophysik

# Low Energy Aspects of the Field Strength Approach

T. Matsuki

[Quantum chromodynamics, 1+1 dim, Field strength formalism, Confinement]

The field strength formalism<sup>1)</sup> (FSF) of gauge theory has recently attracted attention. The non-Abelian case was shown to exhibit gluon condensation, even at the classical level.<sup>2)</sup> Clearly, it would be favorable if cases were found where the FSF could be solved at the full quantum level. Here, we analyze QCD<sub>1+1</sub> on a spatial circle (space-time cylinder), where the solution is known to give a non-trivial spectrum.

The FSF consists in introducing the auxiliary field  $\chi$  which is conjugate to the field strength  $F_{\mu\nu}^a$ . Naturally,  $\chi$  is an anti-symmetric tensor which transforms adjointly under local color rotations. Integrating over the gauge field  $A_\mu^a$  in the path integral gives  $Z = \int [D\chi] e^{-\langle L \rangle}$  in which

$$L = \frac{1}{2}\chi^2 - \frac{1}{2}\delta^4(0) \text{Tr}(\ln \hat{\chi}) - \frac{1}{g}\partial_\rho \chi_{\mu\rho}^a [\hat{\chi}^{-1}]_{\mu\nu}^{ab} \partial_\eta \chi_{\nu\eta}^b,$$

where  $\hat{\chi}_{\mu\nu}^{bc} \equiv \chi_{\mu\nu}^a f^{abc}$  and  $\langle \dots \rangle$  denotes the integration over space time ( $\int d^D x$ ).

Since there is only one Lorentz component  $\chi_{01}$  for the case  $D = 2$ , the inverse of  $\chi^a f^{abc}$  is ill defined. Thus, people have refrained from using FSF in 1+1 dimensions. Nevertheless, one has only to integrate over the non-singular directions of  $\chi$ , which means that diagonalization of  $\chi$  is necessary. As a result, we find

$$L = -\frac{1}{2}\rho^2 - i\rho(\partial_0 C_3 - \partial_1 C_3) - \delta^2(0) \ln \rho^2 + \frac{f^{abc}}{\rho g} \chi^a \partial_0 \chi^b \partial_1 \chi^c.$$

Obvious notations are  $\chi^a \equiv \chi_{01}^a$ ,  $\rho \equiv \sqrt{\chi^a \chi^a}$  and  $C^a \equiv P^{\dagger ab} A^b$ , where  $P$  is the unitary matrix required for diagonalization.

One observes a complicated kinetic term and a singular  $\ln \rho$  term in the Lagrangian. Importance of the singular term has been emphasized in,<sup>2)</sup> since it renders gluon condensation at the classical level. It requires a non-perturbative treatment, since it cannot be expanded in polynomial form.

In the case of QCD<sub>1+1</sub> we can take care of both difficulties by considering a point transformation whose Jacobian explicitly cancels the singular term. This is seen by writing for the SU(2) case

$$D\chi \approx D\rho D\theta D\varphi \prod_x \rho^2 \sin \theta(x),$$

where  $\{\chi^1, \chi^2, \chi^3\} = \{\rho \sin \theta \cos \varphi, \rho \sin \theta \sin \varphi, \rho \cos \theta\}$ . The  $\rho^2$  term arising from the Jacobian is exactly what is required to cancel the singular term.

The kinetic term is a topological invariant which is an integer defined by the degree of mapping from the

torus to  $S^2$ . The integer is invariant against continuous deformations of the field  $\theta(x)$ . Thus, we have a manifestly gauge invariant form of Lagrangian for pure SU(2) on a cylinder.

We may equivalently start from the gauge fixed Lagrangian, and the F-P ghost term plays the role of the Jacobian. The gauge which meets our requirements is evidently the Diagonal gauge<sup>3)</sup> in terms of  $\chi$ , since our method consists in diagonalizing the matrix  $\hat{\chi}^{bc} = \chi^a \varepsilon^{abc}$ . The calculation is performed to give

$$Z = \int [D\chi DC_3] \prod_x \frac{1}{\rho^2} \delta(\chi^a)_{a=1,2} \Delta_{FP}(\chi) e^{-S[\chi, C_3]},$$

with  $\Delta_{FP}(\chi) = \|\varepsilon_{ab3} \chi^3\| = (\chi^3)^2$ . This gives

$$Z = \int [D\chi^3 DA_0^3 DA_1^3] e^{\left\langle -\frac{1}{2}\chi_3^2 - i\chi_3(\partial_0 A_1^3 - \partial_1 A_0^3) \right\rangle},$$

which is just QED for the U(1) subgroup of SU(2).

In order to obtain the spectrum, one has only to calculate the partition function for time-periodic gauge fields, but with gauge equivalent fields identified. The configurations that are equivalent modulo large gauge transformations have nontrivial consequences on the spectrum. Careful evaluation of the boundary condition gives

$$Z = \sum_n e^{-E_n T} = \sum_n \int [D\chi] \delta(\partial_\mu \chi) e^{-\int \frac{1}{2}\chi^2 + \frac{4\pi}{g} n \chi},$$

which renders  $E_n = \frac{1}{8}g^2 L n^2$  in agreement with previous analysis.<sup>4)</sup> The result can be extended straightforwardly to SU( $N$ ) for an arbitrary  $N$ .

We have also calculated the ground state energy in the presence of static sources in a separate work. Half integer charges showed confinement, whereas integer charges were screened at the distance where the total loop around the torus became lower in energy than the static potential between the charges. This confirms the charge screening scenario of adjoint charges.<sup>5)</sup>

Thus we have presented an example where QCD is solved non-perturbatively, using the FSF. We have elucidated the problems which arise when one tries to solve the problem quantum mechanically.

## References

- 1) M. B. Halpern: Phys. Rev. D **16**, 1798 (1977).
- 2) M. Schaden et al.: Nucl. Phys. B **339**, 595 (1990).
- 3) G. 'tHooft: Nucl. Phys. B **190**, 455 (1981).
- 4) J. E. Hetrick et al.: Phys. Lett. B **230**, 88 (1989).
- 5) A. M. Polyakov: *Gauge Fields and Strings* (Harwood Academic, 1987).

# Nuclear Transparency in a Relativistic Harmonic Oscillator Quark Model<sup>†</sup>

T. Iwama, A. Kohama, and K. Yazaki

[Color transparency, Relativistic quark model]

We examine the nuclear transparency in the quasi-elastic ( $e, e'p$ ) process at large momentum transfer in a relativistic harmonic oscillator model<sup>1)</sup> to take the internal dynamics of the struck proton into account. A proton in a nuclear target is struck by the incident electron and then propagates through the residual nucleus suffering from soft interactions with other nucleons. We call the proton “dynamical” when we take into account of internal excitations, and “inert” when we freeze it to the ground state.

When the dynamical proton is struck with a hard (large-momentum transfer) interaction, it shrinks, *i.e.*, small-sized configuration dominates the process. It then travels through nuclear medium as a time-dependent mixture of intrinsic excited states, and thus travels changing its size,<sup>2)</sup> suffering from the absorption due to the soft interactions with nuclear medium which depends on the transverse-size of the proton. Since the nuclear transparency is a measure of the absorption strength, we calculate it in our model for the dynamical case. The results are compared with those for the inert case.

We compare our results also with the experimental data to examine the target-mass-number ( $A$ ) dependence (Fig. 1). The effect of the internal dynamics is observed, *i.e.*, the transparencies of the dynamical proton are enhanced from that of the inert proton if a correlation parameter,  $\nu$ , has a finite value, which is in accord with the idea of the color transparency. This phenomena, the color transparency, was predicted by Brodsky and Mueller in the early 80's as a candidate of observing the effects of internal dynamics of proton in high-energy nuclear reactions.<sup>3)</sup>

We also find that the  $A$ -dependence will reveal the color-transparency effect more clearly. Based on a *model-independent* discussion the transparency of the inert proton approaches to  $A^{-1/3}$  line for large  $A$ . Therefore, deviations from the  $A^{-1/3}$ -lines in the large- $A$  regime could be a signature of the color transparency.

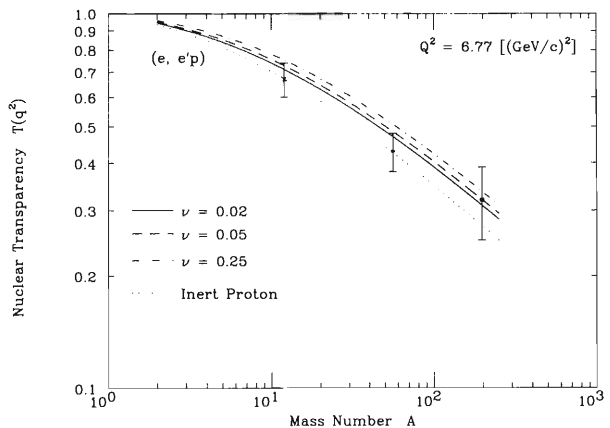


Fig. 1. Comparison of the nuclear transparency with experimental data of  $^{12}\text{C}$ ,  $^{56}\text{Fe}$ , and  $^{197}\text{Au}$ <sup>4)</sup> as a function of the mass number of the target,  $A$ .  $Q^2 (= -q^2) = 6.77$   $[(\text{GeV}/c)^2]$ , where  $q$  is the 4-momentum transfer. The dotted curve is the case of the inert proton. The solid, dashed, and dot-dashed curves are the cases of the dynamical proton with  $\nu = 0.02$ ,  $0.05$ , and  $0.25$ , respectively. Here,  $\nu$  is a parameter to specify the longitudinal-transverse dynamical correlation between quarks in the struck proton. This correlation excites the transverse mode of the struck proton. The larger the value of  $\nu$  becomes, the stronger the correlation becomes.

The hadronic process, such as ( $p, 2p$ ), will show us other aspects of the color transparency. We will leave it for our future work.

## References

- 1) K. Fujimura, T. Kobayashi, and M. Namiki: Prog. Theor. Phys. **43**, 73 (1970).
- 2) K. Yazaki, T. Iwama, and A. Kohama: J. Korean Phys. Soc., Suppl. **29**, S388 (1996).
- 3) S. J. Brodsky and A. H. Mueller: Phys. Lett. B **206**, 685 (1988).
- 4) T. G. O'Neill et al.: Phys. Lett. B **351**, 87 (1995).

<sup>†</sup> Condensed from the article in Nucl. Phys. A **627**, 620 (1997)

# Quark Distributions in the Nucleon by the Semi-Inclusive Reaction on the Proton- and $^3\text{He}$ -Target

H. Kitagawa and Y. Sakemi\*

[Semi-inclusive reaction, Quark distribution]

Semi-inclusive reaction, in which the scattered lepton and produced hadron are detected simultaneously, provides many kinds of information on the target depending on the tagged hadron, and is expected to give a unified view on the distributions of gluons and of sea quarks. By this reaction the quark and gluon distributions are being investigated with polarized positron beam and polarized gas targets (helium-3 ( $^3\text{He}$ ) and hydrogen) tagging pion and neutral kaon at Deutsches Elektronen-Synchrotron (DESY).

The semi-inclusive cross section for production of a hadron,  $h$ , is given by

$$\frac{1}{\sigma_{\text{total}}} \frac{d\sigma^h(z, x, Q^2)}{dz} = \frac{\sum_f e_f^2 q_f(x, Q^2) D_f^h(z)}{\sum_f e_f^2 q_f(x, Q^2)}.$$

We relate the spin asymmetry,  $A_{\text{target}}^h$ , with the quark spin distributions in the nucleon by using the quark parton model for the  $^3\text{He}$ -target. The  $^3\text{He}$  can be regarded as a state of purely  $(1s_{1/2})^3$  configuration: i.e.,  $^3\text{He}_{\uparrow} = p_{\uparrow} + p_{\downarrow} + n_{\uparrow}$ . We also assume the isospin symmetry between the proton and the neutron. We predict the spin asymmetries,  $A_p^h$  and  $A_{^3\text{He}}^h$ , using the existing parametrizations for the quark distributions: CTEQ3L<sup>1)</sup> for the unpolarized quarks  $q(x)$ , and Gehrman-Stirling A(LO)<sup>2)</sup> for the polarized quarks  $\Delta q(x)$ . For the fragmentation functions  $D(z)$ , we use the recent parametrization<sup>3)</sup> for the charged pions and Kaons. Due to the experimental layout, the range of the kinematical variable,  $z$ , is limited. We integrate the fragmentation function from  $z_{\text{min}}$  to 1, where  $z_{\text{min}}$  is 0.1. When both pions and kaons are tagged, expected events are

$$N_{\uparrow\downarrow, \uparrow\uparrow}^{\pi^+K} = \sum_{f, \text{nucleon}} e_f^2 q_f^{\pm}(x) (D_f^{\pi}(z) + D_f^K(z)).$$

Results of calculations are shown in Fig. 1 for the cases of the proton and  $^3\text{He}$  targets tagging positively charged hadrons ( $\pi^+ + K^+$ ), negatively charged hadrons ( $\pi^- + K^-$ ), the sum of them ( $\pi^+ + \pi^- + K^+ + K^-$ ) and the difference of them ( $\pi^+ - \pi^- + K^+ - K^-$ ). Absolute values of the spin asymmetries of the case of  $^3\text{He}$  target are smaller than those of the proton-target case. Asymmetries including kaons are not so different from those of only pions. This may be because the fragmentation functions for kaons are not so different from those of pions. These asymmetries are sensitive to the value of the lower limit of  $z$ .

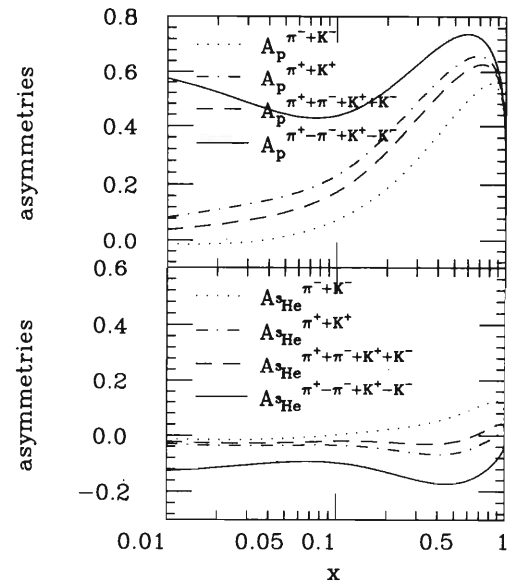


Fig. 1. Spin asymmetries in which target is proton (upper) and  $^3\text{He}$  (lower) tagging pions and kaons are shown. Lower limit of the kinematical variable  $z$  is 0.1.

For the precise prediction, we must know more about the fragmentation function, to which the above asymmetries are sensitive. In the experimental side, it is desired to have data at each  $z$ -bin, and the data of the other nuclear targets are desired. In the theoretical side, quantitative estimations of the fragmentation functions especially of pions are necessary. The lowest moment  $\int_0^1 D(z) dz$  is not sufficient for the quantitative estimation, since the  $D(z)$  is singular at  $z = 0$ . We also should discuss a relation of the fragmentation functions with the Lund model. It will be desirable to consider the case of tagging short-lived neutral kaons in order to investigate the unpolarized and polarized strange quark distributions.<sup>4)</sup>

## References

- 1) H. L. Lai et al.: Phys. Rev. D **51**, 4763 (1995).
- 2) T. Gehrmann and W. J. Stirling: Phys. Rev. D **53**, 6100 (1996).
- 3) J. Binnewies, B. A. Kniehl, and G. Kramer: Z. Phys. C **65**, 471 (1995).
- 4) H. Kitagawa and Y. Sakemi: RIKEN Accel. Prog. Rep. **30**, 31 (1997).

\* Faculty of Science, Tokyo Institute of Technology

# Parameterization of the Polarized Parton Distribution Functions

Y. Goto, N. Hayashi, M. Hirai,<sup>\*1</sup> H. Horikawa,<sup>\*2</sup> S. Kumano, M. Miyama,<sup>\*1</sup>  
T. Morii, N. Saito, T.-A. Shibata, E. Taniguchi, and T. Yamanishi

[Polarization, Structure functions, Spin structure, Nucleon]

Polarized structure functions,  $g_1(x)$ , are now available for protons, neutrons and deuterons over a wide range of the Bjorken  $x$  and squared momentum transfer  $Q^2$  from lepton to nucleon with a high precision, due to the experiments of polarized lepton scatterings off polarized nucleon targets. Data of the first moment of structure functions have indicated that the spin of a nucleon is little carried by the quarks, and moreover the sea-quarks have negative polarization. In order to obtain a good knowledge of the nucleon spin structure, it is necessary to decompose the polarized structure functions into each flavor. So far, several kinds of parametrizations on the polarized parton distribution functions (pPDFs)<sup>1-3)</sup> have been proposed. Recently, however, it has been reported that the value of SMC data at the lowest  $x$  dramatically decreased.<sup>4)</sup> This prompted us to re-analyze the pPDFs.

Our purpose here is to make a new parametrization of the pPDFs for quarks and gluons having a high reliability at the leading order of QCD. We start with the following parametrization of the pPDF at the initial  $Q_0^2 = 1 \text{ GeV}^2$ :

$$\Delta f_i(x, Q_0^2) = \eta_i A_i x^{\alpha_i} (1-x)^{\beta_i} f_i(x, Q_0^2), \quad (1)$$

where  $i$  represents the valence quarks  $u_v$  and  $d_v$ , sea-quark  $\bar{q}$  and gluon  $g$ , and  $f_i(x, Q_0^2)$  is the unpolarized parton distribution function. The value of  $\eta_i$  means the amount of the parton  $i$  carrying the nucleon spin with the normalization factor  $A_i$ . In Eq. (1), we assume a power-law behavior for the  $x$  dependence,  $x^{\alpha_i}$ , for small- $x$  regions, and a counting rule,  $(1-x)^{\beta_i}$ , for large- $x$  regions. Since the deep inelastic scattering (DIS) alone provides no sufficient information on the behavior of the sea flavor, we simply assume the SU(3) flavor symmetry  $\Delta\bar{u}(x) = \Delta\bar{d}(x) = \Delta\bar{s}(x)$  at the initial  $Q_0^2$ .

By using the observed values of the neutron and hy-

peron  $\beta$ -decay as follows,

$$\eta_{u_v} - \eta_{d_v} = F + D = 1.2573 \pm 0.0028, \quad (2)$$

$$\eta_{u_v} + \eta_{d_v} = 3F - D = 0.579 \pm 0.025, \quad (3)$$

we can obtain  $\eta_{u_v} = 0.918$  and  $\eta_{d_v} = -0.339$ . Both  $\eta_g$  and  $\eta_{\bar{q}}$  remain as a free parameter because DIS cannot probe the gluon and cannot separate the contributions of the quark and anti-quark. The remaining ten parameters are determined by fitting the experimental data on polarized DISs of the proton, neutron and deuteron for  $Q^2 \geq 1 \text{ GeV}^2$ . For the purpose to obtain a good parametrization, we follow the two step analysis. First step: by using the reliable equation,

$$g_1^p(x) - g_1^n(x) = \frac{1}{6} \{ \Delta u_v(x) - \Delta d_v(x) \}, \quad (4)$$

we roughly constrain the range of  $\alpha_{u_v}$ ,  $\alpha_{d_v}$ ,  $\beta_{u_v}$  and  $\beta_{d_v}$ . Then, we use the combined data on  $g_1^p$ ,  $g_1^n$  and  $g_1^d$ . Second step: we determine the values of all parameters from the best fitting to all existing data. In practice, we take the GRV95 parametrization as a typical unpolarized PDF.<sup>5)</sup>

The analysis is currently in progress.

We are indebted to Prof. T. Hatsuda, Dr. H. Kitagawa, and Dr. Y. Watanabe for useful discussions.

## References

- 1) S. J. Brodsky, M. Burkardt, and I. Schmidt: Nucl. Phys. B **441**, 197 (1995).
- 2) M. Glück, E. Reya, M. Stratmann, and W. Vogelsang: Phys. Rev. D **53**, 4775 (1996).
- 3) T. Gehrmann and W. J. Stirling: Phys. Rev. D **53**, 6100 (1996).
- 4) B. Adeva et al., Spin Muon Collaboration: preprint CERN-PPE/97-118.
- 5) M. Glück, E. Reya, and A. Vogt: Z. Phys. C **67**, 433 (1995).

<sup>\*1</sup> Department of Physics, Saga University

<sup>\*2</sup> Faculty of Human Development, Kobe University

## $Q^2$ Evolution of Polarized Parton Distributions

M. Hirai, S. Kumano, and M. Miyama\*

[ $Q^2$  evolution, Structure function]

We have been working for obtaining the optimum polarized parton distributions by analyzing existing experimental data.<sup>1)</sup> This collaboration consists of three subgroups: data analysis, parametrization, and  $Q^2$  evolution. We belong to the third group, which contributes to the  $Q^2$  evolution program. The evolution equations are coupled integrodifferential equations with complex splitting functions in the next-to-leading order (NLO). This subgroup tries to develop an efficient program for numerical solution of the evolution equations. Here, we report on its  $Q^2$  evolution studies.<sup>2)</sup>

In solving the integrodifferential equations, we divide the variables  $x$  and  $Q^2$  into small steps and calculate the differentiation and integration by a brute-force method. The same Gehrman-Stirling (GS) set-A polarized parton distributions<sup>3)</sup> are used as the input distributions at  $Q^2 = 4 \text{ GeV}^2$  in both LO and NLO cases. Our evolution results are compared with spin-asymmetry data. The asymmetry  $A_1$  is given by the structure functions  $g_1$  and  $F_1$  as

$$A_1 \cong \frac{g_1(x, Q^2)}{F_1(x, Q^2)} = g_1(x, Q^2) \frac{2x(1+R)}{F_2(x, Q^2)}, \quad (1)$$

where the function  $R$  is given by  $R = (F_2 - 2xF_1)/(2xF_1)$ . In Fig. 1, our evolution curves at  $x = 0.25$  are shown with the  $A_1$  data by the SLAC-E130, SLAC-E143, EMC, and SMC. The unpolarized MRS-G distributions are used for calculating the  $F_2$  structure function. The dashed and solid curves indicate the LO and NLO evolution results, respectively. In the large  $Q^2$  region, both results are almost the same; however, they differ significantly at small  $Q^2$  particularly in the region  $Q^2 < 1 \text{ GeV}^2$ . It indicates that perturbative QCD could not be applied in the small  $x$  region. From the figure, we find that the asymmetry has  $Q^2$  dependence although it is not large. People used to assume that the asymmetry is independent of  $Q^2$  by neglecting the  $Q^2$  evolution difference between  $g_1$  and  $F_1$  in analyzing the experimental data. We found clearly that it is not the case. For a precise

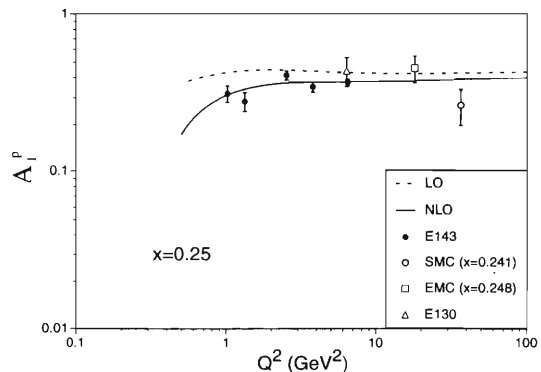


Fig. 1.  $Q^2$  dependence of the spin asymmetry  $A_1$  is calculated for the proton in the LO and NLO cases. Calculated results at  $x = 0.25$  are compared with the SLAC-E130, SLAC-143, EMC, and SMC experimental data.

analysis, the  $Q^2$  dependence of the asymmetry has to be taken into account.

We have investigated the numerical solution of the DGLAP  $Q^2$  evolution equations for longitudinally polarized structure functions. A FORTRAN program is provided for the  $Q^2$  evolution and devolution of polarized nonsinglet-quark, singlet-quark,  $\Delta q_i + \Delta \bar{q}_i$ , and gluon distributions (and corresponding structure functions). It will be used for obtaining the optimum polarized parton distributions in the parametrization studies.<sup>1)</sup>

### References

- 1) RHIC-SPIN-J parametrization group: Y. Goto, N. Hayashi, M. Hirai, H. Horikawa S. Kumano, M. Miyama, T. Morii, N. Saito, T.-A. Shibata, E. Taniguchi, and T. Yamanishi, research in progress.
- 2) M. Hirai, S. Kumano, and M. Miyama: *Comput. Phys. Commun.* **108**, 38 (1998). Study of an efficient program for the parametrization is still in progress.
- 3) T. Gehrmann and W. J. Stirling: *Phys. Rev. D* **53**, 6100 (1996).

\* <http://www.cc.saga-u.ac.jp/saga-u/riko/physics/quantum1/structure.html>.

# NLO $Q^2$ -Evolution of the Nucleon's Transversity Distribution $h_1(x, Q^2)$

A. Hayashigaki, Y. Kanazawa, and Y. Koike

[Transversity, Twist-2, Anomalous dimension]

We present a calculation of the two-loop anomalous dimension for the transversity distribution  $h_1(x, Q^2)$  where  $x$  is the parton's momentum fraction and  $Q^2$  is the scale at which  $h_1$  is measured. It turns out that the next-to-leading order (NLO)  $Q^2$ -evolution of  $h_1$  is very different from that of the other twist-2 distributions,  $f_1$  and  $g_1$ , in particular in the small  $x$ -region.

$h_1(x, Q^2)$  is the third and final twist-2 quark distribution function of nucleon. Because of its chiral-odd nature,  $h_1$  can not be measured in the totally inclusive deep inelastic scattering (DIS), but it appears as a leading contribution in the transversely polarized nucleon-nucleon Drell-Yan process, and the semi-inclusive DIS which detects pions,  $\Lambda$ 's, or correlated two pions in the final states.<sup>1,2)</sup>

Since  $h_1$  is twist-2, its  $Q^2$  evolution is described by the Dokshitzer-Gribov-Lipatov-Altarelli-Parisi (DGLAP) equation. The leading order splitting function for  $h_1$  has been known for a quite some time.<sup>2)</sup> In the recent literature, three papers<sup>3-5)</sup> discussed the NLO  $Q^2$  evolution of  $h_1$ : Vogelsang<sup>3)</sup> carried out a light-cone gauge calculation of the two-loop splitting function for  $h_1$  and converted it into the anomalous dimension. We have carried out a Feynman gauge calculation of the two-loop anomalous dimension.<sup>4)</sup> The final results of these two calculations based on different formalisms have agreed with each other. The result

was subsequently confirmed by Ref. 5 in the same formalism as Ref. 4.

It turns out that  $\gamma_n^{h(1)}$  (coefficient of the two loop anomalous dimension for  $h_1$ ) is significantly larger than  $\gamma_n^{f,g(1)}$  (coefficient of the nonsinglet anomalous dimension for  $f_1$  and  $g_1$ ) at small  $n$ , but approaches very quickly to  $\gamma_n^{f,g(1)}$  at large  $n$ , keeping the condition  $\gamma_n^{h(1)} > \gamma_n^{f,g(1)}$ . This NLO effect in the anomalous dimension leads to a drastic difference in the  $Q^2$ -evolution between  $h_1$  and  $g_1$  in the small  $x$  region. To confront with future experiments, we have to combine the NLO parton distribution function with a relevant NLO short distance cross section in the same factorization scheme.

## References

- 1) J. P. Ralston and D. E. Soper: Nucl. Phys. B **152**; R. L. Jaffe and X. Ji: Phys. Rev. Lett. **67**, 552 (1991); R. L. Jaffe and X. Ji: Phys. Rev. Lett. **71**, 2547 (1993); R. L. Jaffe, X. Jin, and J. Tang: hep-ph/9709322.
- 2) X. Artru and M. Mekhfi: Z. Phys. C **45**, 669 (1990); Nucl. Phys. A **532**, 351c (1991).
- 3) W. Vogelsang: Phys. Rev. D **57**, 1886 (1998).
- 4) A. Hayashigaki, Y. Kanazawa, and Y. Koike: Phys. Rev. D **56**, 7350 (1997).
- 5) S. Kumano and M. Miyama: Phys. Rev. D **56**, R2504 (1997).

# The $\psi'$ Production in Polarized $pp$ Collisions as a Test of Color–Octet Mechanism

T. Yamanishi, T. Morii, D. Roy,<sup>\*1</sup> K. Sudoh,<sup>\*2</sup> Z. Sun, and S. Tanaka<sup>\*3</sup>

[Charmonium,  $\psi'$  anomaly, Color–octet model, Spin structure]

Recently the CDF collaboration<sup>1)</sup> has reported that the cross sections of prompt  $J/\psi$  and  $\psi'$  productions in unpolarized  $p\bar{p}$  collisions are largely inconsistent with the calculation by the quantum chromodynamics (QCD) lowest order process with the color-singlet mechanism (CSM), and aroused renewed interest in heavy quarkonium productions. The long-studied CSM is essentially a nonrelativistic model,<sup>2)</sup> in which one cannot quantitatively estimate various uncertainties such as: the higher order QCD corrections; the quarkonium binding effects; and the corrections due to relativistic effects of the quarkonium, which are sometimes treated as the “K-factor”. The CDF result suggests the necessity of other mechanisms in addition to the CSM.

In these years, a new model called color–octet mechanism (COM), has been advocated by several people<sup>3)</sup> as one of the most promising candidates that could remove such a big discrepancy between the experimental data and the prediction of CSM. The model is quite successful in explaining the CDF data for large- $p_T$  heavy quarkonium productions. However, the prediction of the COM on  $\gamma + p \rightarrow J/\psi + X$  is inconsistent with recent data at HERA,<sup>4)</sup> and thus the discussion seems still controversial. To go beyond the present theoretical understandings, it is necessary to study other processes.

In this report, as another test of the COM, we propose a different process, the  $\psi'$ -hadroproduction at small- $p_T$  regions in longitudinally polarized  $pp$  collisions, which will be observed in the forthcoming RHIC experiment. The process is of great advantage to clearly test the COM as described in the following. Since the process is dominated by the s-channel gluon-gluon fusion, there is no direct productions of the color-singlet  $\psi'$  because of the charge conjugation. Only two mechanisms contribute this process: the COM and the  $2^3P_2$  production. Using the three typical polarized gluon distributions: (a) set A (LO) of GS parametrization,<sup>5)</sup> (b) the BBS parametrization,<sup>6)</sup> and (c) “standard” scenario GRSV parametrization,<sup>7)</sup> we have calculated the double spin asymmetry  $A_{LL}$  which is positive for the COM and negative for the  $2^3P_2$  production. As shown in Fig. 1, we have found that the

sum of both contributions becomes inevitably positive if the COM really contributes to this process. Furthermore, since the cross section of this process is directly proportional to the product of  $\Delta g(x)$  in both protons, the process is very useful to test the behavior of  $\Delta g(x)$ .

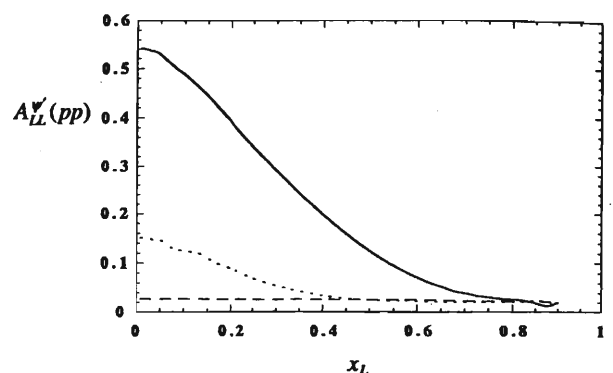


Fig. 1. The two-spin asymmetry  $A_{LL}^{\psi'}(pp)$  at  $\sqrt{s} = 50$  GeV (lowest  $\sqrt{s}$  for RHIC), calculated with various types of  $\Delta g(x)$ , as a function of the longitudinal momentum fraction  $x_L$  of  $\psi'$ . The solid, dashed and dotted lines denote the set A of Ref. 5, 6, and 7, respectively.

## References

- 1) G. A. Schuler: “Quarkonium production and decays”, CERN–TH–7170–94.
- 2) F. Abe et al.: Phys. Rev. Lett. **69**, 3704 (1993); Phys. Rev. Lett. **71**, 2537 (1993).
- 3) E. Braaten and T. C. Yuan: Phys. Rev. Lett. **71**, 1673 (1993); G. T. Bodwin, E. Braaten, and G. P. Lepage: Phys. Rev. D **51**, 1125 (1995); P. Cho and A. K. Leibovich: Phys. Rev. D **53**, 150 (1996); W.-K. Tang and M. Vanttinen: Phys. Rev. D **53**, 4851 (1996).
- 4) M. Cacciari and M. Krämer: Phys. Rev. Lett. **76**, 4128 (1996).
- 5) T. Gehrmann and W. J. Stirling: Phys. Rev. D **53**, 6100 (1996).
- 6) S. J. Brodsky, M. Burkardt, and I. Schmidt: Nucl. Phys. B **441**, 197 (1995).
- 7) M. Glück, E. Reya, M. Stratmann, and W. Vogelsang: Phys. Rev. D **53**, 4775 (1996).

<sup>\*1</sup> Faculty of Human Development, Kobe University

<sup>\*2</sup> Department of Education, Kobe University

<sup>\*3</sup> Department of Physics, Hyogo University of Education

## Heavy Quark Physics with Spin

T. Morii

[Charmonium, Spin structure, Color-octet model]

Physics of the heavy quarks like charm and bottom quarks is an important laboratory of testing both perturbative and nonperturbative Quantum Chromodynamics (QCD). Although the QCD, which is an underlying field theory of strong interactions of quarks and gluons, is very successful in describing physics for perturbative regions, it is not served well for nonperturbative regions. It cannot be directly applied for the light quark hadrons at low energy where the system is essentially nonperturbative. To deal with such a system, people have to rely on some effective theories such as: the chiral perturbation theory, the Skyrminion model, the Bag model, and so on. On the other hand, we do not need to worry about the nonperturbative effect on the top quark system since the top quark is extremely heavy and hence immediately decays into a bottom quark emitting a  $W$  boson as a real process, and there is no chance to make a top hadron or toponium. However, the charm and bottom quarks which we call hereafter heavy flavored quarks are in between these two limit of quark masses, and knowledge of both perturbative and nonperturbative QCD is necessary. The potential model is still effective in these systems together with the heavy quark effective theory (HQET).<sup>1)</sup>

Recently, there have been new interests in physics of the heavy flavored quarks: how they work effectively in extracting the information on the spin structure of nucleons, and how they are produced in high energy collisions. In the present report, we concentrate on the following two topics which we have studied recently and are related to these subjects above.

The first topic is on the extraction of the polarized gluon distribution,  $\Delta g(x)$ , in the nucleon. Study of the gluon polarization in the nucleon which is still poorly known is very important in order to solve the so-called spin puzzle.<sup>2)</sup> So far many processes are proposed to examine various models of  $\Delta g(x)$ . Here we propose a different process,  $\ell + \vec{p} \rightarrow \vec{\Lambda}_c^+ + X$ , which might be observed in the forthcoming COMPASS experiment.<sup>3)</sup> This process is expected to be effective for testing  $\Delta g(x)$  since its cross section is directly proportional to  $\Delta g(x)$ . In addition, the spin of  $\Lambda_c^+$  is carried by the charm quark and thus measurement of polarization of  $\Lambda_c^+$  in the target fragmentation region could determine the gluon polarization,  $\Delta g(x)$ . We have calculated the two-spin asymmetry for this process and found that the process would be promising

to test various models of polarized gluons.

The second topic is on a test of the color-octet model of heavy quarkonium productions. Recently, the CDF collaboration has observed prompt productions of charmonium at Tevatron which were too large compared to the conventional QCD calculations.<sup>4)</sup> This dramatic discrepancy might make a new step toward the deep understandings of the heavy quarkonium production mechanism. One interesting and promising model is the color-octet model.<sup>5)</sup> To test this model, we propose here an interesting process,  $\vec{p} + \vec{p} \rightarrow \psi' + X$ , at small  $p_T$  regions.<sup>6)</sup> Since this process is dominated by the gluon-gluon fusion, there is no direct production of color-singlet  $\psi'$ . There are only two states which are expected to contribute to the  $\psi'$  production in the final states: the color-octet state decaying to  $\psi' + g$  and the  $2^3P_2$  state decaying to  $\psi' + \gamma$ . By using various models of  $\Delta g(x)$ , we have calculated the two-spin asymmetry,  $A_{LL}$ , for these processes, and found that it is positive for the color-octet state and negative for the  $2^3P_2$  state. Furthermore, the sum of both contributions becomes positive for the present parameter regions, in particular, at  $\sqrt{s} = 50$  GeV. Hence, if we observe a positive  $A_{LL}$  in the future RHIC experiment, we can definitely tell that the color-octet model really contribute to this process. The process is therefore very effective to test the color-octet model.

While much of experimental and theoretical progress has been done thus far for the spin physics and heavy quark productions together with the spectroscopy of heavy flavored hadrons, the heavy quark physics is a still challenging subject which needs further investigation.

### References

- 1) T. Matsuki and T. Morii: Phys. Rev. D **56**, 5646 (1997).
- 2) H.-Y. Cheng: hep-ph/9607254 (1996).
- 3) N. I. Kochelev, T. Morii, and T. Yamanishi: Phys. Lett. B **405**, 168 (1997).
- 4) F. Abe et al.: Phys. Rev. Lett. **69**, 3704 (1992); Phys. Rev. Lett. **71**, 2537 (1993).
- 5) E. Braaten and T. C. Yuan: Phys. Rev. Lett. **71**, 1673 (1993); G. T. Bodwin, E. Braaten, and G. P. Lepage: Phys. Rev. D **51**, 1125 (1995); P. Cho and A. K. Leibovich: Phys. Rev. D **53**, 150 (1996); W.-K. Tang and M. Vanttinen: Phys. Rev. D **53**, 4851 (1996).
- 6) T. Morii, D. Roy, A. Sudoh, Z. -X. Sun, S. Tanaka, and T. Yamanishi: hep-ph/9708415 (1997).

## Measurement of $\alpha$ -Sticking Probability in Muon Catalyzed $dt$ Fusion by X-ray Method at RIKEN-RAL Muon Facility

K. Ishida, K. Nagamine, T. Matsuzaki, S. N. Nakamura, N. Kawamura, S. Sakamoto, M. Tanase, M. Kato, K. Kurosawa, M. Hashimoto, K. Kudo,\*<sup>1</sup> N. Takeda,\*<sup>1</sup> and G. H. Eaton\*<sup>2</sup>

[Muon catalyzed fusion, Muonic X-ray]

The muon to alpha sticking probability  $\omega_s$  is one of the most important observables in muon catalyzed  $dt$  fusion, since it gives the upper limit on the number of fusions that one muon can catalyze. The  $\omega_s$  has been usually determined from the muon loss probability  $W$  per cycle measured by the time distribution of fusion neutrons, and has always shown smaller values than theoretical calculations. The measurement of muonic  $K_\alpha$  X-rays from the recoiling  $(\mu\alpha)^+$  ions provides an independent method,<sup>1)</sup> which more directly measures the product that is related to the  $(\mu\alpha)^+$  ion itself. At the RIKEN-RAL Muon Facility,<sup>2)</sup> muons were stopped in the target of solid or liquid D-T mixture of various tritium concentrations,  $C_t$ . For each target condition, a clear  $K_\alpha$  peak was observed at 8.2 keV with the help of the strong pulsed muon beam above the bremsstrahlung background coming from tritium decay.<sup>3,4)</sup>

The muon loss per cycle  $W$  can be determined by combining the neutron yield  $Y_n$  (per muon) and the neutron disappearance rate  $\lambda_n$  as  $W = (1 - \lambda_0/\lambda_n)Y_n^{-1}$ , where  $\lambda_0$  is the free muon decay rate. In Fig. 1 shown is the muon loss  $W$  obtained in our neutron measurement<sup>5)</sup> for solid D-T mixture. Similar  $C_t$  dependence was observed for liquid data also. It is considered that the main component of  $W$  is the muon to alpha sticking in  $dt$  fusion while the increase of  $W$  at low  $C_t$  is from muon sticking to  $^3\text{He}$  through  $dd$  fusion, and that at high  $C_t$  is from muon to alpha sticking through  $tt$  fusion. The muon transfer to  $^3\text{He}$ , which accumulates as tritium decays, was controlled with the use of the advanced tritium gas handling system with *in situ*  $^3\text{He}$  removal capability,<sup>6)</sup> and the data in Fig. 1 are already extrapolated to  $^3\text{He}$  free limit. By subtracting contributions of  $dd$  and  $tt$  processes the  $\omega_s$  in  $dt$  fusion was obtained to be around 0.45%, and seems to be consistent with the previous measurements for liquid at PSI and LAMPF.

The number of  $K_\alpha$  X-ray yield per fusion ( $Y(K_\alpha)$ ) was obtained as a function of tritium concentration as in Fig. 1. There has been several calculations on the number of X-rays emitted from  $(\mu\alpha)^+$  recoil ions, and the obtained  $Y(K_\alpha)$  can be converted to the sticking probability by using the result of those calculations.

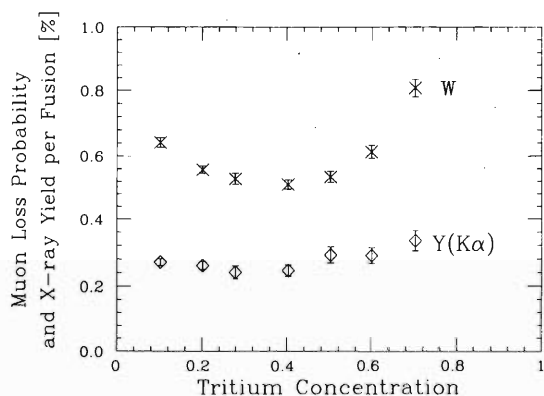


Fig. 1. Muon loss probability  $W$  obtained from neutron measurement, and  $K_\alpha$  X-ray yield per fusion  $Y(K_\alpha)$ , for muon catalyzed fusion in solid D-T mixture.

Although there is one ambiguity coming from the size of the contribution from  $tt$  fusion, for which a measurement is under planning,  $Y(K_\alpha)$  from  $dt$  fusion is obtained to be around 0.24% after minor correction of  $dd$  fusion. This value, when converted to the effective muon sticking probability, gives  $\omega_s$  of between 0.45% and 0.56% depending on the calculation selected.

Although the above mentioned analysis is not yet final, it can be concluded that both neutron and X-ray measurements show  $\omega_s$  values below or around 0.50%, which are still significantly smaller than theoretical values of around 0.60%.

### References

- 1) K. Nagamine, T. Matsuzaki, K. Ishida et al.: Muon Catalyzed Fusion **5**, 1239 (1990); Hyperfine Interact. **82**, 343 (1993).
- 2) K. Nagamine, T. Matsuzaki, K. Ishida, I. Watanabe et al.: Hyper Interact. **85**, 1091 (1994).
- 3) K. Ishida et al.: RIKEN Accel. Prog. Rep. **30**, 39 (1997).
- 4) S. N. Nakamura et al.: RIKEN Accel. Prog. Rep. **31**, 51 (1998).
- 5) N. Kawamura et al.: RIKEN Accel. Prog. Rep. **31**, 50 (1998).
- 6) T. Matsuzaki et al.: RIKEN Accel. Prog. Rep. **30**, 151 (1997).

\*<sup>1</sup> Electrotechnical Laboratory, Japan

\*<sup>2</sup> Rutherford Appleton Laboratory, UK

# Fusion Neutron Yield and Muon Cycling Rate in Muon Catalyzed $dt$ Fusion at RIKEN-RAL Muon Facility

N. Kawamura, S. N. Nakamura, K. Nagamine, T. Matsuzaki, K. Ishida, S. Sakamoto, M. Tanase, M. Kato, K. Kurosawa, M. Hashimoto, K. Kudo,\*<sup>1</sup> N. Takeda,\*<sup>1</sup> and G. H. Eaton\*<sup>2</sup>

[Muon catalyzed fusion, Fusion produced neutron]

This article reports the analysis method and preliminary result of the muon catalyzed fusion ( $\mu$ CF) experiments in deuterium and tritium mixture, which were carried out at Port 1 of RIKEN-RAL Muon Facility. Details of the setup and the adopted detectors are discussed in the other articles in Ref. 1.

The most essential  $\mu$ CF parameters, the muon cycling rate ( $\lambda_c$ ) and the muon loss rate ( $W$ ) can be deduced from fusion neutron information such as the neutron disappearance rate ( $\lambda_n$ ) and the neutron yield ( $Y_n$ ).

Figure 1 shows a typical neutron energy spectrum with a clear 14 MeV edge which characterizes  $dt$  fusion. The  $\gamma$ -ray background was removed by the pulse shape discrimination technique.

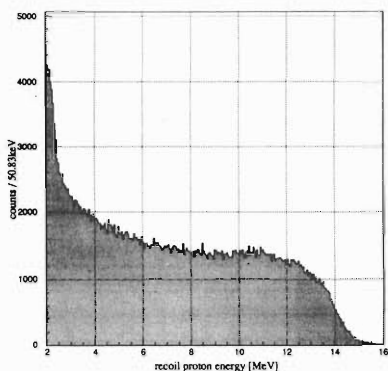


Fig. 1. A typical neutron energy spectrum. Background from  $\gamma$ -ray were removed with a  $n$ - $\gamma$  discrimination technique. The edge of a fusion neutron (14 MeV) can be seen clearly.

The number of the measured neutrons with more than the energy of 4 MeV was corrected for pileup and multi-hit effects (0.3 and 3%, respectively) and normalized by a solid angle of detectors ( $2.4 \times 10^{-3}$ ) and neutron detection efficiency ( $10.3 \pm 0.1\%$ ) to get total neutron yield ( $Y_n$ ).

The neutron disappearance rate ( $\lambda_n$ ) can be obtained from a time spectrum (Fig. 2). The muon cycling rate ( $\lambda_c$ ) can be deduced from  $Y_n$  and  $\lambda_n$  as:

$$Y_n = \int \phi \lambda_c \exp(-\lambda_n t) dt = \frac{\phi \lambda_c}{\lambda_n},$$

\*<sup>1</sup> Electrotechnical Laboratory (ETL), Japan

\*<sup>2</sup> Rutherford-Appleton Laboratory (RAL), U.K.

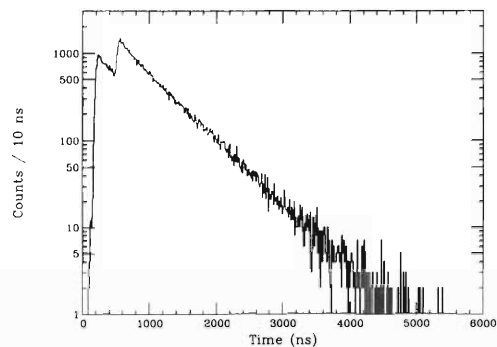


Fig. 2. A typical neutron time spectrum. Two prompt peaks can be seen due to double pulse structure of ISIS beam.

where  $\phi$  denotes the normalized  $dt$ -target density.

The experiments were carried out as a series of the tritium concentration in liquid and solid phase, and the obtained data were analyzed. Analysis is still preliminary, but no large difference has been observed between the liquid and solid phase data, except for the neutron disappearance rate at a high tritium concentration. This discrepancy might be explained with the difference in the target volume. Total amount of tritium in our system is limited, and some of  $dt$  gas should be remained in the buffer volume for the safety reason. In addition to this, the vapor pressure of liquid is much larger than solid. Therefore a target volume of liquid was much smaller than that for solid. Small volume of the liquid target enhances the "wall effect": the muons, captured by a heavier nucleus in the target container wall, could not take a part in  $\mu$ CF cycle, and thus the muon disappearance rate becomes larger.

The tritium concentration ( $C_t$ ) dependence of the cycling rate ( $\lambda_c$ ) is more similar to the LAMPF result<sup>2)</sup> than to the PSI result<sup>3)</sup> especially at high tritium concentration. Our preliminary analysis indicates that the muon cycling rate reaches its maximum value ( $\sim 150 \mu s^{-1}$ ) at  $C_t \sim 40\%$  in the both cases of liquid and solid phase. Further analyses are now in progress.

## References

- 1) RIKEN-KEK-JAERI-ETL-RAL- $\mu$ CF collaboration: RIKEN-RAL Muon Facility Report 1, p. 11 (1997).
- 2) S. E. Jones et al.: Phys. Rev. Lett. **56**, 588 (1986).
- 3) W. H. Breunlich et al.: Phys. Rev. Lett. **58**, 329 (1987).

## $K_\beta/K_\alpha$ Sticking X-ray Ratio in Muon Catalyzed $dt$ Fusion at RIKEN-RAL Muon Facility

S. N. Nakamura, K. Nagamine, T. Matsuzaki, K. Ishida, N. Kawamura, S. Sakamoto, M. Tanase, M. Kato, K. Kurosawa, M. Hashimoto, K. Kudo,\*<sup>1</sup> N. Takeda,\*<sup>1</sup> and G. H. Eaton\*<sup>2</sup>

[ $\mu$ CF]

The  $\mu^- \alpha$  sticking probability is the most crucial to the application of  $\mu$ CF and thus, plenty of theoretical studies have been performed. However, calculations on a single molecule give only initial sticking probability ( $\omega_s^0$ ) which cannot directly be compared with the experimentally observable, effective sticking probability ( $\omega_s$ ). They are associated with each other with a help of model calculation on collisional relaxation, stripping, and so on. These calculations require detailed information about  $\mu\alpha$  kinetics as well as initial populations of the  $\mu^- \alpha$  atom. The observation of  $\mu^- \alpha$  sticking X rays provides such information.  $K_\alpha$  yield provides normalization of the calculation and  $K_\beta$  yield enables us to discriminate the correct calculation from others. For example, Cohen, Markushin, and Stodden theoretically calculated  $K_\beta/K_\alpha$  yield ratio as 0.115,<sup>1)</sup> 0.127,<sup>2)</sup> and 0.087,<sup>3)</sup> respectively. However, observation of  $K_\beta$  X ray was impossible due to large bremsstrahlung background. The world strongest pulsed muon beam enables us to measure  $K_\beta$  X ray for the first time.

Figure 1 shows a X-ray energy spectrum for the tritium concentration,  $C_t = 10\%$ , solid  $dt$  target with a time gate of  $625 < t < 2625$  ns after the muon beam arrival, which enhances  $\mu\alpha$  X rays because bremsstrahlung background has no time structure and prompt X rays has shorter decay time. The energy spectrum of bremsstrahlung was obtained with a time gate of  $8000 < t < 10000$  ns where the beam effects had totally disappeared. After subtracting bremsstrahlung spectrum, the background shape can be described by a parabolic function.

The line shape of  $\mu^- \alpha$  X ray is broadened by Doppler effects. The shape of  $K_\alpha$  may be described by a Gaussian function, but  $K_\beta$  cannot (Fig. 2). We fitted the  $K_\beta$  peak with a box function whose edges were skewed by a Fermi function to describe the  $K_\beta$  shape predicted by Cohen.<sup>1)</sup>

The same analysis was performed for different tritium concentration data. Obtained ratio between  $K_\beta$  and  $K_\alpha$  peak areas was corrected by a difference of X-ray attenuation.

The  $K_\beta/K_\alpha$  ratio is very sensitive to the way of background subtraction and its systematic error has not been studied enough; however, we can see some tendencies. The preliminary experimental result shows

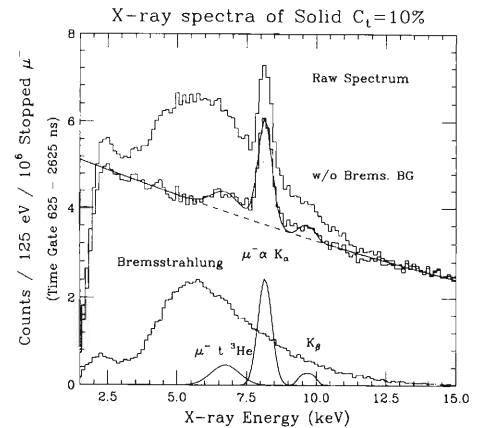


Fig. 1. Solid 10% X-ray energy spectrum with a time gate of  $625 < t < 2625$  ns. Bremsstrahlung background,  $\mu^- \alpha$   $K_\alpha$ ,  $K_\beta$  X rays, and  $\mu^- t^3\text{He}$  X-ray candidate were separated.

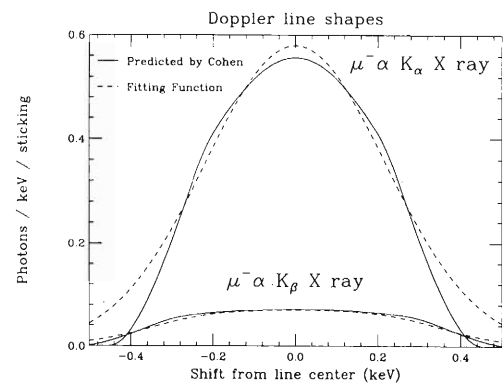


Fig. 2. The solid lines are Doppler broadened  $K_\alpha$  and  $K_\beta$  X-ray line shapes predicted by Cohen.<sup>1)</sup> They were convoluted by our Si(Li) detector resolution ( $K_\alpha$  :  $\sigma = 116$  eV,  $K_\beta$  : 120 eV). The dashed lines are our fitting functions to describe X-ray data.

smaller  $K_\beta/K_\alpha$  ratio than the theoretical values in low  $C_t$  region, while  $K_\beta/K_\alpha$  is larger in high  $C_t$  region.

### References

- 1) J. S. Cohen: Muon Catal. Fusion **3**, 421 (1988).
- 2) V. E. Markushin: Muon Catal. Fusion **3**, 395 (1988).
- 3) C. D. Stodden: Phys. Rev. A **41**, 1281 (1990).

\*<sup>1</sup> Electrotechnical Laboratory, Japan

\*<sup>2</sup> Rutherford Appleton Laboratory, UK

## RHIC Spin Project

H. Akikawa, Y. Batygin, H. En'yo, E. Fujisawa, Y. Goto, K. Hatanaka, N. Hayashi, T. Ichihara, K. Imai, M. Ishihara, T. Katayama, T. Kawaguchi, K. Kurita, Y. Mao, A. Masaike, Y. Nakada, H. Okamura, M. Okamura, N. Saito, H. Sakai, Y. Sakemi, T. Sakuma, H. Sato, H. Sato, T.-A. Shibata, Z. Sun, A. Taketani, E. Taniguchi, T. Tominaka, H. Torii, T. Wakasa, Y. Watanabe, H. Wu, M. Xiao, S. Yoneyama, and M. Yosoi

[*pp* interaction, Structure function, Spin, Asymmetry, Polarized beam]

RHIC Spin project is the integrated efforts of accelerator physics, experimental physics and theoretical physics to study the polarization phenomena in high energy hadron reactions using polarized proton beams at RHIC. This is a report of the third year of this project.

For the accelerator part, a major progress was the completion of the prototype of the helical dipole superconducting magnet, which is going to be used as Siberian Snakes and Spin Rotators. The performance of the prototypes has been compared in detail in Refs. 1 and 2. Effects of beam tune shift on the polarized proton beam has been studied and the result is reported in Ref. 3. The status of simulation of spin dynamics in the RHIC main rings is reported in Ref. 4.

The polarization of the accelerated proton beams will be measured with RHIC polarimeter. To verify the current design, we have proposed an experiment at BNL-AGS. It is approved as E925, and we received a test beam for commissioning of the detector system in May '97 at AGS B1-line. We have designed a polarimeter for the extracted beam down to B1-line. The design concept and its performance is described in Ref. 5.

The experimental part focused on the construction of PHENIX Muon Arms. The magnet system for the muon detector has been completed in Japan and shipped to BNL in April '97. Figure 1 shows an assembled magnet system at MELCO factory in Kobe for excitation test. The results of factory test is described in Ref. 6. The magnet is going to be reassembled at PHENIX experimental hall soon and excited to the full current to measure the field in detail for precision momentum reconstruction.

Another major area of our efforts on the Muon Arm



Fig. 1. Muon magnet system assembled at factory.

is the beam test of the muon identifier system. The test have proven the required performance of the muon identification and pion rejection for PHENIX.<sup>7)</sup> Now the design has been fixed, and factory setup for the construction is in progress at BNL and at KEK.<sup>8)</sup> We are going to finish the construction and installation of muon identifier by the end of September '98.

For the timely publication of the physics output from RHIC spin project, we are preparing both hardware and software for offline analysis. The hardware configuration has been studied under the name of PHENIX-CC-J, which means regional analysis center for the PHENIX. The current plan is described in Ref. 9. One of the software development has been focused on the extraction of polarized gluon density, since it is one of the urgent questions to be answered by RHIC Spin project. Results of simulation studies on prompt photon analysis for extraction of gluon polarization are described in Ref. 10.

We have formed a working group with theorists on polarized parton distributions last year.<sup>11)</sup> A global fit of existing data on the formula in the leading order of perturbative QCD is in progress<sup>12)</sup> using the computer code for  $Q^2$ -evolution.<sup>13)</sup> The effects of structure function  $R(x, Q^2)$  on the fit results have been studied in Ref. 14.

### References

- 1) M. Okamura et al.: RIKEN Accel. Prog. Rep. **31**, 250 (1998).
- 2) M. Okamura et al.: RIKEN Accel. Prog. Rep. **31**, 251 (1998).
- 3) Y. Batygin et al.: RIKEN Accel. Prog. Rep. **31**, 246 (1998).
- 4) M. Xiao et al.: RIKEN Accel. Prog. Rep. **31**, 248 (1998).
- 5) N. Hayashi et al.: RIKEN Accel. Prog. Rep. **31**, 173 (1998).
- 6) T. Ichihara et al.: RIKEN Accel. Prog. Rep. **31**, 170 (1998).
- 7) Y. Mao et al.: RIKEN Accel. Prog. Rep. **31**, 53 (1998).
- 8) A. Taketani et al.: RIKEN Accel. Prog. Rep. **31**, 172 (1998).
- 9) Y. Watanabe et al.: RIKEN Accel. Prog. Rep. **31**, 171 (1998).
- 10) Y. Goto et al.: RIKEN Accel. Prog. Rep. **31**, 54 (1998).
- 11) Y. Goto et al.: RIKEN Accel. Prog. Rep. **30**, 35 (1997).
- 12) T. Yamanishi et al.: RIKEN Accel. Prog. Rep. **31**, 44 (1998).
- 13) M. Hirai et al.: RIKEN Accel. Prog. Rep. **31**, 45 (1998).
- 14) Y. Goto et al.: RIKEN Accel. Prog. Rep. **31**, 55 (1998).

## Results from Beam Tests of PHENIX Muon Identifier

Y. Mao, N. Saito, Y. Watanabe, N. Hayashi, Y. Goto, H. En'yo, Y. Nakada, H. Sato, K. Imai, H. Torii,\* H. Akikawa,\* T.-A. Shibata, E. Fujisawa, S. Yoneyama, and M. Ishihara

[Muon identifier, Muon detection efficiency, Pion/muon rejection rate]

PHENIX is one of the two large experiments which are going to be carried out in near future by using the underconstructing Relativistic Heavy Ion Collider (RHIC) in Brookhaven National Laboratory (BNL). The detection of muon, both single muon and di-muon, plays a key role to probe Quark-Gluon-Plasma with  $\sqrt{s} = 200A$  GeV Au + Au collision<sup>1)</sup> and to probe the spin structure of proton with 50 GeV  $< \sqrt{s} < 500$  GeV polarized p + p collision.<sup>2)</sup> On the other hand, due to the high energy involved in the collision, the pion/muon yield ratio will be as high as  $10^2$ – $10^3$  in the interested momentum region. Therefore, a high efficiency of pion/muon rejection is highly required to PHENIX muon identifier.

Based on the conceptual design, we have constructed a prototype of the muon identifier with 2.5 m long Iarroc tubes,<sup>3)</sup> which are the same type of tubes for PHENIX muon identifier, to investigate the muon detection efficiency and pion/muon rejection rate. The prototype consisted of five detector layers, one horizontal panel and one vertical panel in a layer, sandwiched by iron slabs (180 cm  $\times$  200 cm) with thickness of 10, 10, 10, 20, 20 cm, respectively. In front of the first iron slab, we put additional iron blocks with thickness of 10 cm to simulate the south muon arm and 20 cm to simulate the north muon arm. The number of tubes in each panel has been optimized to  $3\sigma$  of perpendicular expansion of 2 GeV muons with PISA (PHENIX Integrated Simulation Application) v2.4 and total 54 tubes were used to construct the prototype.

The test experiment was carried out in KEK using PI2 beam line where pion beam is obtained by bombarding an inner target with 12 GeV proton beam. The momentum of beam, 1–4 GeV/c is predefined by the magnetic system acting as a momentum selector, was used in the experiment. Figure 1 shows the experimental setup which may be described as beam ID part and muon ID part. Four Scintillation counters, ST1  $\sim$  4, were set to define the beam ( $beam = ST1 \otimes ST2 \otimes ST3 \otimes ST4$ ) and 3 gaseous Cerenkov detectors, GC1  $\sim$  GC3, were set to define the muon beam in beam ID part. GC1 and GC2 were pressured at a threshold to separate pion and muon while GC3 was pressured at a threshold to separate muon and electron, namely,  $muon = beam \otimes GC1 \otimes GC2 \otimes GC3$  and  $pion = beam \otimes GC1 \otimes GC2 \otimes GC3$ . Experimentally, we obtained that muon beam purity was better than

99% and pion beam purity was better than 99.9% if we don't consider the muon from  $\pi$  decay after GC2. This ensured us a precise measurement of muon detection efficiency and pion/muon rejection rate of the muon identifier.

All 54 Iarroc tubes were operated with "standard" gas mixture Ar:i-C<sub>4</sub>H<sub>10</sub> = 25%:75%, at a high voltage of 4.8 kV. The average muon detection efficiency of a muon ID layer is listed in Table 1. For the final construction of PHENIX muon identifier, we will use two tubes displaced by a half cell in each panel. Therefore, the result in Table 1 implies that a muon detection efficiency of  $>96\%$  can be expected to each muon ID layer. The pion/muon rejection rate has been obtained by applying a discriminant analysis (DA) to the experimental data and to the PISA simulation data with a quadratic discriminant function. A comparison of experimental result with the simulation is shown in Fig. 2. With the simulation result, we may identify the misidentified pion (dot-dashed line) from muon from  $\pi$  decay after GC2 (dash line). It is obtained that a pion/muon rejection rate of 1–2% could be expected for the north muon arm and 1–3% for the south muon arm in 1–4 GeV/c momentum region. If we consider the center magnetic yoke as an inner absorber of hadrons, this pion/muon rejection rate could be improved 1–2 orders of magnitude.

Table 1. The average muon detection efficiency.

Momentum	South Arm	North Arm
1.8 GeV/c	$0.854 \pm 0.046$	$0.837 \pm 0.049$
2.0 GeV/c	$0.860 \pm 0.045$	$0.851 \pm 0.048$
2.5 GeV/c	$0.862 \pm 0.047$	$0.866 \pm 0.049$

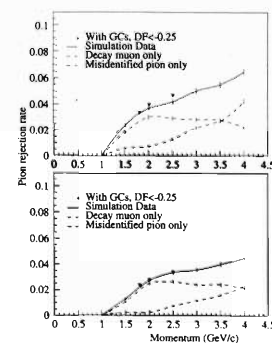


Fig. 2. Pion/muon rejection rate (solid line = dashed line + dot-dashed line).

### References

- 1) PHENIX Conceptual Design Report, BNL-48922, 1993.
- 2) N. Saito: Spin Physics with PHENIX Detector System at RHIC, RIKEN-AF-Np-226, 1996.
- 3) E. Iarocci: Nucl. Instrum Methods Phys. Res. A **217**, 30 (1983).



Fig. 1. The experimental setup.

\* Faculty of Science, Kyoto University

## Spin Physics with Photon Detection at PHENIX

Y. Goto, N. Hayashi, K. Kurita, and N. Saito

[ $pp$  interaction, Structure function, Spin, Asymmetry, Polarized beam]

Prompt photon production in hadronic collision is an appealing probe to investigate the structure of the nucleon because theoretical interpretation for the process is clear-cut. The main contribution comes from the gluon Compton process,  $gq \rightarrow \gamma q$  (and some from the annihilation process,  $q\bar{q} \rightarrow \gamma g$ ). This provides an important opportunity to measure the gluon content inside nucleon.

We can investigate polarized structure of the proton using polarized  $pp$  collision at RHIC.<sup>1)</sup> For the collision of the longitudinally polarized proton, the asymmetry  $A_{LL} = (d\sigma^{++} - d\sigma^{+-})/(d\sigma^{++} + d\sigma^{+-})$  is obtained by using the differential cross section for parallel spin direction ( $d\sigma^{++}$ ) and that for anti-parallel direction ( $d\sigma^{+-}$ ). The asymmetry of the prompt photon production is denoted by  $A_{LL} = \frac{\Delta G}{G} \cdot A_1^p \cdot \hat{a}_{LL}(gq \rightarrow \gamma q)$ , where  $A_1^p$  means a ratio of the polarized to unpolarized distributions of quark and this  $A_1^p$  can be measured by deep inelastic scattering experiments. The asymmetry for elementary process of  $gq \rightarrow \gamma q$ ,  $\hat{a}_{LL}(gq \rightarrow \gamma q)$  is calculable. As a result, we can obtain a ratio of the polarized to unpolarized distributions functions of gluon,  $\Delta G/G$ .

Experimentally, however, it is challenging to identify the prompt photon. First issue is extraction of the prompt photon from many backgrounds. The major background against the measurement of prompt photon originates from the two-photon decay of  $\pi^0$ 's. We will detect photons with an electromagnetic calorimeter (EMCal) at PHENIX. The PHENIX EMCal has a fine granularity which works powerfully to distinguish background particles. Size of one channel is 0.01 in both the rapidity bin and azimuthal angle bin. We have studied the isolation method<sup>2)</sup> to distinguish them and found that we can identify prompt photon in the region of transverse momentum ( $p_T$ ):  $10 \text{ GeV}/c < p_T < 30 \text{ GeV}/c$  for center-of-mass energy,  $\sqrt{s} = 200 \text{ GeV}$ , and  $10 \text{ GeV}/c < p_T < 40 \text{ GeV}/c$  for  $\sqrt{s} = 500 \text{ GeV}$ . Table 1 shows the result of the present estimations of yield and statistical error. Figure 1 presents the sensitivity of our measurement for the  $\Delta G/G$  distribution overplotted on some model calculations.<sup>3)</sup>

Another issue is calibration of the EMCal. We will accomplish it as small systematic uncertainties as possible in the measurement of cross section by implementing good enough calibration systems to use cosmic muon, and laser.

Although  $\pi^0$  is a background for the prompt photon measurement, it is also a good probe for the parton re-

Table 1. Result of the present estimations of yield and statistical error. Luminosity for the  $\sqrt{s} = 200 \text{ GeV}$  run is  $374 \text{ pb}^{-1}$ , which corresponds to the sum of the first and second year runs in the RHIC polarized proton operation. That for  $\sqrt{s} = 500 \text{ GeV}$  run is  $800 \text{ pb}^{-1}$ , which corresponds to 1-year run.

$\sqrt{s} = 200 \text{ GeV}$		Errors on	
Photon $p_T$	Yield	$A_{LL}$	$\Delta G/G$
10 - 15 GeV/c	$1.2 \times 10^5$	0.0062	0.046
15 - 20 GeV/c	$1.6 \times 10^4$	0.0168	0.089
20 - 25 GeV/c	$3.1 \times 10^3$	0.0376	0.171
25 - 30 GeV/c	$6.9 \times 10^2$	0.0799	0.309
$\sqrt{s} = 500 \text{ GeV}$		Errors on	
Photon $p_T$	Yield	$A_{LL}$	$\Delta G/G$
10 - 15 GeV/c	$9.0 \times 10^5$	0.0022	0.045
15 - 20 GeV/c	$1.8 \times 10^5$	0.0059	0.059
20 - 25 GeV/c	$5.3 \times 10^4$	0.0081	0.081
25 - 30 GeV/c	$1.9 \times 10^4$	0.0115	0.115
30 - 35 GeV/c	$7.7 \times 10^3$	0.0141	0.141
35 - 40 GeV/c	$3.3 \times 10^3$	0.0198	0.198

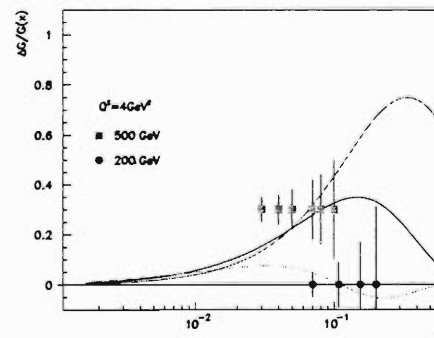


Fig. 1. The sensitivity of our measurement for the  $\Delta G/G$  distribution overplotted on some model calculations, where  $x$  denotes the momentum fraction carried by the gluon.

action. QCD (quantum chromodynamics) jet production is measured by detecting the leading  $\pi^0$ , which represents jet will provide more information on both polarized and unpolarized structures of the nucleon.

### References

- 1) H. En'yo et al.: RIKEN Accel. Prog. Rep. **30**, 33 (1997); RIKEN Accel. Prog. Rep. **30**, 34 (1997).
- 2) For example, description in G. Sterman et al.: Rev. Mod. Phys. **67**, 157 (1995).
- 3) T. Gehrmann and W. J. Stirling: Phys. Rev. D **53**, 6100 (1996).

## Studies of Systematic Problems in the Spin Dependent Structure Functions of the Nucleon

Y. Goto, N. Hayashi, N. Saito, T.-A. Shibata, and E. Taniguchi

[Deep inelastic scattering, Structure functions, Spin]

Since the “spin puzzle” was discovered in 1987, various polarized deep inelastic scattering (pol-DIS) experiments have been carried out at CERN, SLAC, and DESY. A large amount of data have been obtained. We accumulate the data from those experiments, investigate them systematically and reevaluate them.

The structure function  $g_1 (= \frac{1}{2} \sum_i e_i^2 \Delta q_i)$ , which represents spin dependent structure function from pol-DIS, is not a direct observable in the experiments. The experimentally observable quantity is the asymmetries  $A_{\parallel}$  and  $A_{\perp}$ , where the target polarization is parallel (transverse) to the beam direction. Those asymmetries are related to the fundamental cross section asymmetries,  $A_1$  and  $A_2$  by

$$A_{\parallel} = \mathcal{D}(A_1 + \eta A_2). \quad (1)$$

Here,  $\mathcal{D}$  represents the photon depolarization which involves  $R$  parameter:

$$\mathcal{D} = \frac{y(2-y)}{2(1-y)(1+R)} + y^2 \quad (\gamma \rightarrow 0); \quad (2)$$

$\eta$  represents the kinematical factor:

$$\eta = \gamma \frac{1-y}{1-y/2}; \quad (3)$$

$y$  represents the energy function transferred to target or  $y = \nu/E$ ; and  $\gamma$  represents the kinematical factor or  $\gamma = \sqrt{Q^2}/\nu$ .

Using the cross section asymmetries, the spin dependent structure function  $g_1$  can be derived:

$$\frac{g_1}{F_2} = \frac{1}{2x(1+R)}(A_1 + \gamma A_2), \quad (4)$$

where  $F_2$  the represents the non-polarized structure function and  $x$  represents the Bjorken  $x$ .

We have investigated the systematic problems in determining  $g_1$ , which arise from the choice of  $R$  parameter and  $F_2$ . The fitted value by EMC or a constant value was used for  $R$  in early times. Since 1990, the  $R_{fit}^{1990}$  fitted by SLAC experiment<sup>1)</sup> is mainly used. As for  $F_2$ , the parameterization and a set of parameters of  $F_2$  by NMC has been used by most experimental

groups. In 1995, NMC published a new set of  $F_2$  parameters.<sup>2)</sup> The latter parameter set fits well to the new data.

In 1996, NMC published 10 points of  $R^{NMC}$  in the range of  $0.0045 \leq x \leq 0.110$  and  $1.38 \leq \langle Q^2 \rangle \leq 20.6$ .<sup>3)</sup> We investigate the influence of  $g_1$  when  $R$  is changed from  $R_{fit}^{1990}$  to  $R^{NMC}$ . When  $g_1$  is obtained from  $A_{\parallel}$  and  $A_{\perp}$ ,  $g_1$  is influenced by  $\mathcal{D}$  as well as by  $R$ . Therefore,

$$\frac{g_1^{1990}}{g_1^{NMC}} \propto \frac{x \mathcal{D}^{NMC} (1 + R^{NMC})}{x \mathcal{D}^{1990} (1 + R^{1990})}, \quad (5)$$

where,  $g_1^{1990}$  and  $\mathcal{D}^{1990}$  represent the quantities using  $R_{fit}^{1990}$ , while  $g_1^{NMC}$  and  $\mathcal{D}^{NMC}$  represent those using  $R^{NMC}$ . The average of the ratio is 1.0028. The maximum of the ratio is 1.028.

On the contrary, when  $g_1$  is obtained from  $A_1$ ,  $g_1$  is influenced only by  $(1+R)^{-1}$ :

$$\frac{g_1^{1990}}{g_1^{NMC}} \propto \frac{x(1+R^{NMC})}{x(1+R^{1990})}. \quad (6)$$

In this case, the average of the ratio is 1.046, and the maximum is as large as 1.13.

To summarize, when we obtain  $g_1$  from experimental data of  $A_{\parallel}$  and  $A_{\perp}$ ,  $R$  used in  $\mathcal{D}$  cancels the  $R$  used in getting  $g_1$  from  $A_1$ . As a result,  $g_1$  is rather independent of the choice of  $R$ . However, when we obtain  $g_1$  from  $A_1$ , we need to pay attention because  $g_1$  is affected up to about 10% by the choice of  $R$ .

We reevaluated the data on the spin dependent structure function of EMC and of E130 experiment because  $R$  has been much improved since their publications.  $R_{fit}^{EMC}$ , not  $R_{fit}^{1990}$  was used in  $\mathcal{D}$  in their original publications. We thus obtained an appropriate asymmetry  $A_{\parallel}$  by this reevaluation. As a results of this reevaluation,  $A_1$  and  $\mathcal{D}$  are modified by about 10%.

### References

- 1) L. W. Whitlow et al.: Phys. Lett. B **250**, 193 (1990).
- 2) NMC, M. Arneodo et al.: Phys. Lett. B **364**, 107 (1995).
- 3) NMC, M. Arneodo et al.: Nucl. Phys. B **483**, 3 (1997).

## High Spin Isomer Beam Experiment at RIKEN

E. Ideguchi, Y. Gono, T. Kishida, X. H. Zhou, S. Mitarai, T. Morikawa, A. Odahara, H. Tsuchida, M. Shibata, H. Watanabe, M. Miyake, S. Motomura, T. Tsutsumi, B. Cederwall, T. Murakami, and M. Ishihara

$$\left[ \begin{array}{l} \text{NUCLEAR REACTIONS } ^{24}\text{Mg}(^{136}\text{Xe},\alpha 9n)^{147m}\text{Gd}, \\ ^{12}\text{C}(^{147m}\text{Gd},xn)^{159-x}\text{Yb}, \text{ High spin isomer beam} \end{array} \right]$$

Recently, large Ge arrays such as EUROBALL and Gammasphere have made it possible to investigate very high spin states.<sup>1)</sup> Search for the hyperdeformed states collected much attention after they were predicted in the extremely high spin states.<sup>2)</sup> However, unambiguous experimental evidence for existence of the hyperdeformed states was not found yet. The most important experimental difficulty seems to be how to make such an extremely high spin state.

Secondary fusion reaction by using High Spin Isomer Beam (HSIB) will give a solution to this problem, since the HSIB itself has a high angular momentum and the secondary fusion will make much higher spin states. In order to make very high spin states, a development of HSIB and a secondary fusion experiment are planned in RIKEN Accelerator Research Facility.

The most important development in the secondary fusion experiment is getting a high yield of HSIB at the secondary target position. Recent development of the ion source in RIKEN made it possible to use high intensity  $^{136}\text{Xe}$  beam, i.e. of more than 100 pnA, which is 10 times larger beam intensity than previously used. It was anticipated that a usual metal foil target may be melted by such a high intensity primary beam. In order to avoid such a problem we have developed a rotating target system.

In the secondary reaction by using HSIB, correction of Doppler effect is also important since velocity of the secondary beam is expected at about 10% of light velocity, which will cause a serious Doppler broadening. A Ge telescope system was developed to decrease the Doppler broadening and to acquire a high detection efficiency.<sup>3)</sup>

In order to check the yield of HSIB at the final focal plane and to test the rotating target system as well as the Ge telescope system, we have conducted an experiment by using  $^{24}\text{Mg}(^{136}\text{Xe},\alpha 9n)^{147m}\text{Gd}$  and  $^{12}\text{C}(^{147m}\text{Gd},xn)^{159-x}\text{Yb}$  for the primary and secondary fusion reactions, respectively.

The  $^{136}\text{Xe}$  beam was accelerated to 8.5 MeV/u by RIKEN Ring Cyclotron. The maximum intensity of the  $^{136}\text{Xe}$  beam was 260 pnA. HSIB was separated from the primary beam and transported to the final focal plane by RIPS. The rotating target system was operated under the 160 pnA and 260 pnA intensities. The yield of HSIB was almost constant during the operation: around  $6.5 \times 10^3$  in the 160 pnA intensity and 1.5 times larger yield of HSIB was obtained in the

260 pnA run. This result implies that the rotating target system was operated stably although the yield of HSIB was 10 times less than the estimate based on CASCADE calculations. This might be caused by the lower cross section in  $\alpha 9n$  channel than calculated. Actually, many gamma ray peaks are originated from xn channel, and pxn channel was observed at the same time; whose intensities were more than 10 times larger than that of  $\alpha 9n$  channel. The  $\alpha 9n$  channel also caused the increase of momentum spread which decreased the transmission efficiency between primary target and final focal plane.

The efficiency calibration of Ge telescope system was made by using  $^{152}\text{Eu}$  standard source. The telescope system was located 114.5 mm apart from the gamma source. Fig. 1 shows the result of the measurement. The efficiency of the Ge telescope system was almost constant ( $\sim 2.5 \times 10^{-4}$ ) in the high energy region, i.e. higher than 500 keV.

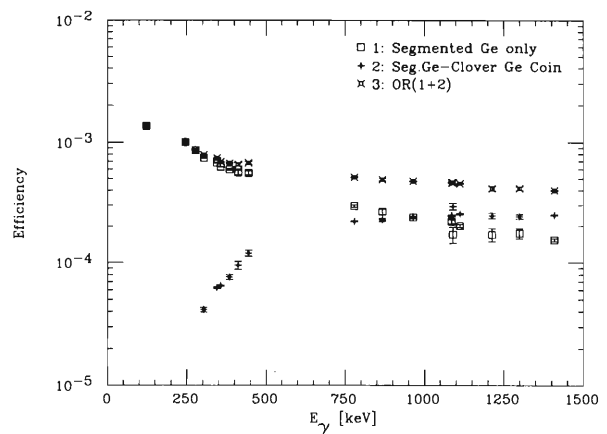


Fig. 1. Efficiency curve of Ge telescope system. 1: Hit only one of segment in Segmented Ge. 2: Hit both Segmented Ge and Clover Ge. 3: OR of 1 and 2 cases.

Data analysis of the secondary reaction experiment is still in progress.

### References

- 1) C. W. Beausang and J. Simpson: J. Phys. G **22**, 527 (1996).
- 2) S. Aberg: Nucl. Phys. A **557**, 17c (1993).
- 3) E. Ideguchi et al.: RIKEN Accel. Prog. Rep. **27**, 121 (1993).

## Search for High-Spin Isomer in $^{143}\text{Nd}$

X. H. Zhou, E. Ideguchi, Y. Gono, T. Kishida, S. Mitarai, T. Morikawa, H. Tsuchida, M. Shibata, H. Watanabe, M. Miyake, T. Tsutsumi, S. Motomura, and M. Ishihara

[NUCLEAR REACTION:  $^{18}\text{O} + ^{130}\text{Te}$  at  $E_{lab} = 80$  MeV; Time measurement; Half life]

The search for high-spin isomeric states has attracted much interest, because the occurrence of isomer at a high spin state would indicate a change in nuclear properties such as nuclear shape. High-spin isomers were observed systematically in the  $N = 83$  isotones with proton number  $Z$  from 68 to 61,<sup>1-9)</sup> the characteristics of these high-spin isomers can be well interpreted in the framework of a deformed independent particle model (DIPM).<sup>10)</sup> In this model, the sum of single-particle angular momenta of valence nucleons along the symmetry axis was taken as the total angular momentum of the nucleus, and the excitation energies for different configurations were calculated by the Strutinsky method. The DIPM calculations assigned the isomers to be of the stretched configurations  $[\nu(f_{7/2}h_{9/2}i_{13/2})\pi(h_{11/2}^2)]_{49/2}^+$  and  $[\nu(f_{7/2}h_{9/2}i_{13/2})\pi(d_{5/2}^{-1}h_{11/2}^2)]_{27}^+$  for the odd and odd-odd  $N = 83$  isotones, respectively,<sup>6)</sup> which may induce an oblate deformation, while the low-spin states have a near spherical shape. Therefore, these isomers were interpreted caused by sudden changes in nuclear shape, which was confirmed by the deformation parameters of the yrast isomers in  $^{147}\text{Gd}$  deduced from the experimental quadrupole moments.<sup>11)</sup> It is worth while pointing out that the excitation energies of these isomers in the  $N = 83$  isotones with  $61 \leq Z \leq 65$  are almost constant and around 8.5 MeV, it implies, taking the shell gap energy of  $Z = 64$  as a parameter in the DIPM calculations, that the shell gap energies change from 2.4 to 2.0 MeV as the proton number decreases from 65 to 61.<sup>6)</sup> In order to extend the systematic study of the high-spin isomers in  $N = 83$  isotones, we have performed an experiment to search for the corresponding high-spin isomer in  $^{143}\text{Nd}$  with a proton number of 60, whose level scheme was constructed up to 10 MeV, although no high-spin isomer was reported so far.<sup>12)</sup>

The  $^{143}\text{Nd}$  nucleus was produced by using the  $^{130}\text{Te}(^{18}\text{O}, 5n)^{143}\text{Nd}$  reaction at the 80 MeV beam energy. The  $^{18}\text{O}$  beam was provided by the cyclotron at KEK-Tanashi/CNS. The target consisted of 1.8 mg/cm<sup>2</sup> of enriched  $^{130}\text{Te}$  evaporated onto a 2.8 mg/cm<sup>2</sup> aluminium backing. A delayed  $\gamma$ - $\gamma$  coincidence measurement between a NaI scintillator and a group of HPGe detectors was performed. The NaI scintillator having a very large detection efficiency was used to detect the prompt  $\gamma$  rays corresponding to the beam burst. Also to determine the excitation energy of the isomer, a  $\gamma$ - $\gamma$  coincidence measurement was car-

ried out with five HPGe detectors with anti-Compton shields.

For the strong  $\gamma$  rays of  $^{143}\text{Nd}$  which were observed with the HPGe detectors, their time distributions were obtained relative to the time signal given by the NaI scintillator. All the time distributions show a delayed component, indicating the existence of a high-lying isomer. Fig. 1 presents the summation of time distributions of the 379, 421 and 791 keV  $\gamma$  rays in  $^{143}\text{Nd}$ . Unfortunately, the pulsed beam with 51 ns interval between bursts has severely contaminated the delayed part in Fig. 1, so a half-life value for this isomer could not be extracted reliably from an exponential fit. At present, only an estimated half-life of about 50 ns can be assigned to this isomer. The data analysis to fix the position of the isomer in terms of the excitation energy is in progress.

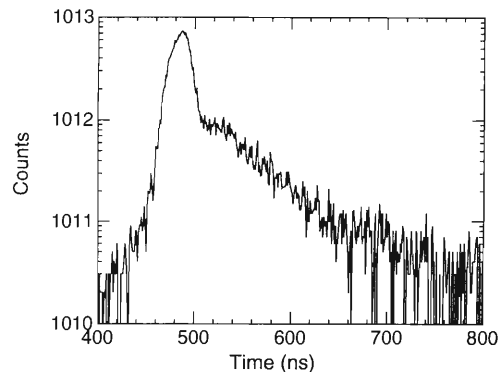


Fig. 1. The summation of the time distributions for the 379, 421 and 791 keV  $\gamma$  rays of  $^{143}\text{Nd}$ , indicating the existence of a high-lying isomer.

### References

- 1) S. Andre et al.: *Z. Phys. A* **337**, 349 (1990).
- 2) J. Mcneill et al.: *Z. Phys. A* **325**, 27 (1986).
- 3) J. Pedersen et al.: *Phys. Rev. Lett.* **39**, 990 (1977).
- 4) D. Hageman et al.: *Phys. Lett. B* **84**, 301 (1979).
- 5) J. Borggreen et al.: *Z. Phys. A* **294**, 113 (1980).
- 6) A. Odahara et al.: *Nucl. Phys. A* **620**, 363 (1997).
- 7) E. Ideguchi et al.: *Phys. Soc. Jpn.* **108** (1993).
- 8) A. Odahara et al.: *Z. Phys. A* **350**, 185 (1994).
- 9) Y. Zhang et al.: *RIKEN Accel. Prog. Rep.* **27**, 32 (1993).
- 10) T. Dossing et al.: *Phys. Scripta* **24**, 258 (1981).
- 11) O. Hausser et al.: *Nucl. Phys. A* **443**, 135 (1985).
- 12) O. J. Tekyi-Mensah et al.: *Phys. Rev. C* **50**, R1759 (1994).

## $\gamma$ -Ray Linear Polarization Measurement by Segmented Ge

H. Tsuchida, Y. Gono, S. Mitarai, T. Morikawa, A. Odahara, M. Shibata, H. Watanabe, M. Miyake, S. Motomura, T. Tsutsumi, T. Kishida, E. Ideguchi, X. H. Zhou, and M. Ishihara

[NUCLEAR REACTION  $^{139}\text{La} + ^{10}\text{B}$ ,  $E(^{10}\text{B}) = 50$  MeV,  $^{130}\text{Te} + ^{18}\text{O}$ ,  $E(^{18}\text{O}) = 80$  MeV]

$\gamma$ -ray linear polarization is a valuable information in a nuclear spectroscopic study. In the case of an in-beam  $\gamma$ -ray measurement to use fusion reactions, the angular momentum vectors of compound nuclei are aligned in a perpendicular plane with respect to the beam axis.  $\gamma$ -rays emitted from these reaction products are then scattered by a scatterer in different directions depending on their electric or magnetic characters. A scatterer is usually placed at  $90^\circ$  with respect to the beam. Analyzer detectors are placed in parallel(X) and perpendicular(Y) directions with respect to the beam axis in a plane which is perpendicular to the axis(Z) connecting the scatterer and a  $\gamma$ -ray source. In this XYZ-coordinate, an X-axis is parallel to the beam axis. Germanium detectors are used, in these days as a scatterer and as analyzers. Typical examples of detector set-ups to measure a  $\gamma$ -ray linear polarization are described in Ref. 1.

Recently, a segmented Ge detector was prepared for a position sensitive  $\gamma$ -ray detection.<sup>2)</sup> This detector is a planar type and has a square shape of  $50 \times 50 \times 20$  tmm<sup>3</sup>. The  $\gamma$ -ray measurement using this detector can provide information of  $\gamma$ -ray linear polarization by placing this at  $90^\circ$  with respect to the beam axis in the in-beam  $\gamma$ -ray spectroscopy mentioned above. When one makes spectra by adding coincident signals of two segments aligned in X or Y direction, the linear polarization information can be obtained by a ratio of the counts of concerned peaks in these spectra. The notations of  $N_X$  and  $N_Y$  will be used below for the peak areas of spectra made by summing the signals from segments aligned in X and Y directions, respectively.

Linear polarization measurements of  $\gamma$ -rays in  $^{143}\text{Nd}$  and  $^{145}\text{Sm}$  were performed by using  $^{139}\text{La}(^{10}\text{B},4n)-^{145}\text{Sm}$  and  $^{130}\text{Te}(^{18}\text{O},5n)^{143}\text{Nd}$  reactions. The  $^{10}\text{B}$  and  $^{18}\text{O}$  beams of 50 and 80 MeV, were provided by the Kyushu University tandem accelerator and the SF cyclotron of KEK-Tanashi, respectively. The segmented Ge was placed at 70 mm from a target in the above mentioned set-up.

The ratios  $N_Y/N_X$  obtained in the experiments are plotted in Figs. 1, 2, and 3. Since a linear polarization information can be obtained in  $\gamma$ -ray measurements discussed in this report, only when  $\gamma$ -rays are emitted from the nuclear states with aligned angular momenta, the ratios  $N_Y/N_X$  of  $\gamma$ -rays emitted through long-lived isomers do not show deviations from 1. Fig. 1 shows the  $N_Y/N_X$  ratios of the 133, 150, 381, and 531 keV  $\gamma$ -rays in  $^{144}\text{Sm}$  emitted through a 880 ns isomer as well as those of known 253 (M1) and 801(E1) keV

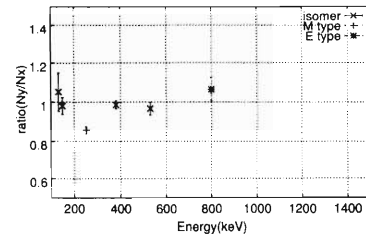


Fig. 1.  $\gamma$ -rays of  $^{144}\text{Sm}$  below(x) and above(+,\*) long-lived ( $T_{1/2} = 880$  ns) isomer.

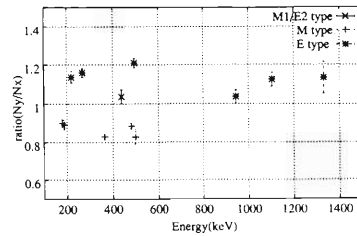


Fig. 2.  $N_Y/N_X$  ratios of previously known<sup>3)</sup>  $\gamma$ -rays of  $^{145}\text{Sm}$ .

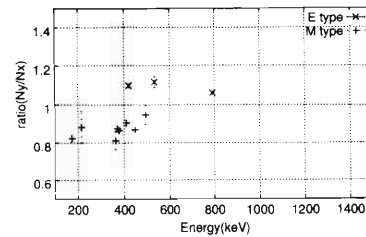


Fig. 3.  $N_Y/N_X$  ratios of previously known<sup>4)</sup>  $\gamma$ -rays of  $^{143}\text{Nd}$ .

$\gamma$ -rays which are transitions above the isomer. The nucleus  $^{144}\text{Sm}$  produced in the reaction was used to study  $^{145}\text{Sm}$  simultaneously. The experimental results on  $\gamma$ -rays of  $^{143}\text{Nd}$  and  $^{145}\text{Sm}$  are shown in Figs. 2 and 3, respectively. Electric and magnetic characters were known<sup>3,4)</sup> previously for those  $\gamma$ -rays shown in the figures, and they were reproduced in the present experiments. Further analysis is in progress.

### References

- 1) A. von der Werth et al.: Nucl. Instrum. Methods Phys. Res. A **357**, 458 (1995).
- 2) Y. Gono et al.: RIKEN. Accel. Prog. Rep. **30**, 137 (1996).
- 3) M. Piiparinen et al.: Z. Phys. A **338**, 417 (1991).
- 4) E. Ott et al.: Z. Phys. A **348**, 248 (1994).

# Measurements of Neutron Spallation Cross Sections of $^{59}\text{Co}$ and $^{\text{nat}}\text{Cu}$

E. Kim,<sup>\*1</sup> T. Nakamura, Y. Uwamino, M. Imamura, N. Nakao, S. Shibata, and S. Tanaka<sup>\*2</sup>

[Neutron spallation cross section]

Neutron reaction data in the energy range above 20 MeV are quite scarce and no evaluated data file exists at present. In this study, we have measured the neutron spallation cross section using quasi-monoenergetic p-Li neutrons in the energy range above 20 MeV. The experiments were performed at three cyclotron facilities of (1) Institute for Nuclear Study (INS), University of Tokyo, (2) Takasaki Research Establishments, Japan Atomic Energy Research Institute (TIARA), and (3) Institute of Physical and Chemical Research (RIKEN).

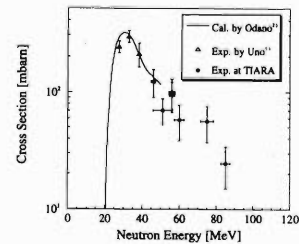
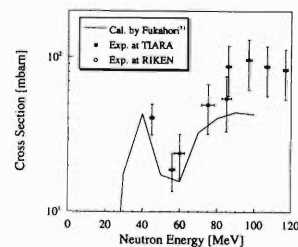
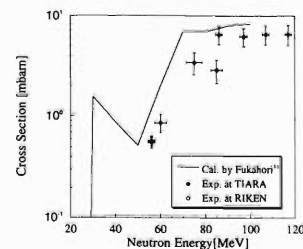
Irradiation experiments utilized quasi-monoenergetic neutrons which were produced by  $^7\text{Li}(p,n)^7\text{Be}$  reaction. The Li-targets of 2 to 10 mm thicknesses were bombarded by proton beams of 20 to 120 MeV energies from AVF cyclotron. The neutron produced in the forward direction from the target were transported through a collimator to irradiation samples, and the proton beams passed through the target were swept out by a magnet and led to a beam dump. The neutron spectra were measured with the TOF method using an organic liquid scintillator. The absolute neutron fluence was determined with the PRT (Proton Recoil counter Telescope) at TIARA and further with the Li activation method to detect the  $^7\text{Be}$  activity from the  $^7\text{Li}(p,n)^7\text{Be}$  reaction at RIKEN.

The irradiation samples were  $^{\text{nat}}\text{Cu}$  and  $^{59}\text{Co}$ . The samples were located at 400 cm and 837 cm behind the Li-target at TIARA and RIKEN, respectively. Irradiation consisted of a short period (1 to 2 hrs) and a long period (about 20 hrs) by considering the half-life of produced nuclei. The gamma rays emitted from produced nuclei were measured with a high purity Ge detector.

The cross sections were obtained by dividing the reaction rate with the peak neutron fluence which is given by PRT or Li activation method, after correcting the contribution of low-energy neutron components. The errors of cross section data were evaluated from the error propagation law by combining the errors of reaction rate (about 0.4–30%), peak neutron fluence (about 12–15%), FWHM of peak neutron spectrum (2.8–5.0 MeV), and of contribution from the reference cross section used to estimate the low energy neutron component (about 5–92%).

We have obtained values of the cross sec-

tion of the  $^{59}\text{Co}(n,xn)^{58,57,56,55}\text{Co}$ ,  $^{59}\text{Co}(n,\text{sp})^{59}\text{Fe}$ ,  $^{59}\text{Co}(n,\text{sp})^{56,54,52}\text{Mn}$ ,  $^{\text{nat}}\text{Cu}(n,\text{sp})^{56,54,52}\text{Mn}$ ,  $^{\text{nat}}\text{Cu}(n,\text{sp})^{61,60,58,56,55}\text{Co}$ ,  $^{\text{nat}}\text{Cu}(n,xn)^{64,61,60}\text{Cu}$ , and  $^{\text{nat}}\text{Cu}(n,\text{sp})^{65}\text{Ni}$  reactions. As examples, Figs. 1–3 give cross sections of the  $^{59}\text{Co}(n,3n)^{57}\text{Co}$ ,  $^{\text{nat}}\text{Cu}(n,\text{sp})^{58}\text{Co}$  and  $^{\text{nat}}\text{Cu}(n,\text{sp})^{56}\text{Mn}$  reactions, respectively. The results are compared with the calculated results by Odano<sup>2)</sup> and Fukahori.<sup>3,4)</sup> Our experimental results in the energy range above 40 MeV are the first experimental data, and are generally in good agreement with the calculated data.

Fig. 1.  $^{59}\text{Co}(n,3n)^{57}\text{Co}$  reaction cross section.Fig. 2.  $^{\text{nat}}\text{Cu}(n,\text{sp})^{58}\text{Co}$  reaction cross section.Fig. 3.  $^{\text{nat}}\text{Cu}(n,\text{sp})^{56}\text{Mn}$  reaction cross section.

## References

- 1) Y. Uno et al.: Nucl. Sci. Eng. **122**, 247 (1996).
- 2) N. Odano and S. Iwasaki: JAERI-M 94-019, p. 310; Proc. 1993 Symp. on Nuclear Data (1994).
- 3) T. Fukahori et al.: JAERI-M 92-039, p. 114 (1992).
- 4) M. Blann: CODE ALICE/89, private communication (1989).

<sup>\*1</sup> Cyclotron and Radioisotope Center, Tohoku University

<sup>\*2</sup> Takasaki Research Establishment, Japan Atomic Energy Research Institute

# Polarization Observables for the ${}^3\text{He}(\vec{d}, p){}^4\text{He}$ Reaction

T. Uesaka, H. Okamura, T. Ohnishi, Y. Satou, S. Ishida, N. Sakamoto, H. Otsu, T. Wakasa, T. Nonaka, G. Yokoyama, K. Itoh, K. Sekiguchi, T. Wakui, and H. Sakai

[  ${}^3\text{He}(d,p){}^4\text{He}$ ,  $E_d = 270$  MeV, Measured analyzing powers, ]  
 Measured polarization correlation coefficients ]

We have proposed a new experimental approach to study the high momentum component of the deuteron D-state wave function by measuring the polarization correlation coefficient,  $C_{//}$ , for the  ${}^3\text{He}(\vec{d}, p){}^4\text{He}$  reaction. The first experiment was carried out at RIKEN Accelerator Research Facility in 1996.<sup>1)</sup> In this report, the experimental results and its comparison with the related experimental data are presented.

Experimental result of  $C_{//}$ , which is expected to be proportional to the D-state density, is plotted together with Plane-Wave Born Approximation (PWBA) calculations in Fig. 1. The experimental data is significantly smaller than what are predicted by the plane wave calculations. If we interpret this result as it is, the D-state density is reduced to be almost one third. However, it is hardly acceptable. That is, the reduced  $C_{//}$  should be due to the complexity of reaction mechanism. A multiple scattering effect or a quark exchange effect might be examples of such candidates. Indeed, these effects are considered to be quite important to describe the observed discrepancies in the polarization observables for the  $d+p$  backward scattering (DPBS) and for the deuteron inclusive breakup (DIB) reaction<sup>2,3)</sup> The large discrepancy between experiment and theory in Fig. 1 leads to the conclusion that the  $C_{//}$  is sensitive to these reaction-mechanism effects, and therefore we can use  $C_{//}$  to test the given reaction models.

We compare the individual components of  $C_{//}$ ,  $A_{yy}$ ,  $C_{y,y}$ , and  $C_{x,x}$ , with polarization observables for DPBS and DIB. The expressions of  $T_{20}$  and  $\kappa_0$  for DPBS and DIB have similar forms as those of  $A_{yy}$  and  $C_{y,y}$  ( $C_{x,x}$ ) for the  ${}^3\text{He}(\vec{d}, p){}^4\text{He}$  reaction, respectively.<sup>5)</sup> This similarity can be understood from the common nature of

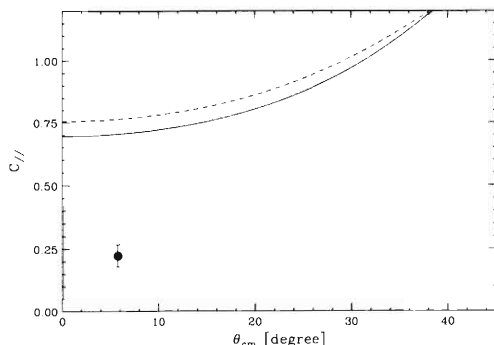


Fig. 1. The experimental result (filled star) and plane-wave calculations of  $C_{//}$ . The solid and broken curves are calculations with the Paris and Bonn potentials, respectively.

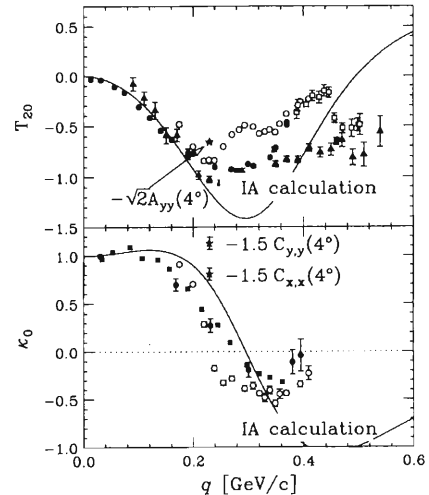


Fig. 2. Comparison of the present data (filled stars) with polarization observables for the  $d+p$  and deuteron breakup. As for the present experimental data,  $-\sqrt{2}A_{yy}$  and  $-1.5C_{y,y}$  ( $-1.5C_{x,x}$ ) are plotted instead of  $T_{20}$  and  $\kappa_0$ , respectively. Open symbols denote the data for the  $d+p$  backward scattering, and filled symbols indicate the data for the deuteron inclusive breakup on hydrogen target.<sup>4)</sup> Solid curves denoted by IA are plane-wave calculations.

these reactions: one nucleon exchange. In Fig. 2, the comparisons among these three reactions are shown. For comparison, the present results are multiplied by factors  $-\sqrt{2}$  and  $-1.5$  for  $A_{yy}$  and  $C_{y,y}$  ( $C_{x,x}$ ), respectively. A similarity can be seen in the cases of both  $T_{20}$  and  $\kappa_0$ :  $-\sqrt{2}A_{yy}$  has a large negative value and is less negative than the plane-wave calculation as  $T_{20}$  for DPBS and DIB is.  $-1.5C_{y,y}$  ( $-1.5C_{x,x}$ ) has a positive value as  $\kappa_0$  does. These facts suggest that the polarization observables for the  ${}^3\text{He}(\vec{d}, p){}^4\text{He}$  reaction are expected to give us significant information on the unsolved problems encountered in the DPBS and DIB experiments.

## References

- 1) T. Uesaka et al.: RIKEN Accel. Prog. Rep. **30**, 46 (1997).
- 2) A. P. Kobushkin, A. I. Syamtomov, and L. Ya. Glozman: Preprint ITP-95-9E 1995 (LANL hep-ph 9503435).
- 3) M. G. Dolidze and G. I. Lykasov: Z. Phys. A **336**, 339 (1990).
- 4) L. S. Azhgirey et al.: Phys. Lett. B **391**, 22 (1997), and references therein.
- 5) T. Uesaka et al.: Doctor Thesis (Univ. of Tokyo), 1997.

## Study of Spin Flip Signatures via $^{12}\text{C}(d, d')$ Reaction

S. Ishida, Y. Satou, H. Sakai, H. Okamura, H. Otsu, N. Sakamoto, T. Uesaka,  
T. Wakasa, T. Ohnishi, T. Nonaka, G. Yokoyama, T. Niizeki,  
T. Ichihara, K. Hatanaka, and N. Nishimori\*

[NUCLEAR REACTION  $^{12}\text{C}(\vec{d}, \vec{d}')$ ,  $E_d=270$  MeV, Measured  $S_1$ ,  $S_2$  and other signatures]

Inelastic deuteron scattering should be the most efficient probe to study the isoscalar spin excitations, because it excites exclusively the isoscalar states.<sup>1-3)</sup> Moreover, the measurement of the deuteron spin flip is needed to separate the spin strength from the non-spin strength. The first polarization transfer measurement by using the newly developed focal plane Deuteron Polarimeter DPOL<sup>4)</sup> has been carried out on  $^{12}\text{C}$ . A part of the result was previously reported.<sup>5)</sup> Further measurements on this reaction have been carried out to improve poor statistics of the double scattering measurement. The analysis including new measurements is now in the final stage.

DPOL is designed to measure all the vector and tensor polarization components within the single counter configuration of the polarimeter, so that one can determine all the eight polarization observables with respect to  $y$  axis in one measurement: i.e.,  $P^{y'}$ ,  $A_y$ ,  $P^{y'y'}$ ,  $A_{yy}$ ,  $K_y^{y'}$ ,  $K_{yy}^{y'y'}$ ,  $K_y^{y'y'}$  and  $K_{yy}^{y'y'}$ , where  $y$  and  $yy$  denote the vector and tensor polarization, respectively. The probabilities of non-spin-flip ( $S_0$ ), spin-flip ( $S_1$ ), and double-spin-flip ( $S_2$ ) are extracted from these polarization observables as

$$S_0 = \frac{1}{6}(2 + 3K_y^{y'} + K_{yy}^{y'y'}) ,$$

$$S_1 = \frac{1}{9}(4 - P^{y'y'} - A_{yy} - 2K_{yy}^{y'y'}) ,$$

$$S_2 = \frac{1}{18}(4 + 2P^{y'y'} + 2A_{yy} - 9K_y^{y'} + K_{yy}^{y'y'}) ,$$

where the subscript  $\Delta m$  of the spin transfer probability  $S_{\Delta m}$  is the change in  $S_y$ . The spin flip probability  $S_1$  in the  $(d, d')$  reaction will be a good signature of the spin excitations as  $S_{nn}$  is in the  $(p, p')$  reaction.

The experiment was performed with a 270 MeV deuteron beam for the excitation energy range of about  $3 < E_x < 25$  MeV. DPOL was installed in the second focal plane of the spectrograph SMART. The beam swinger magnet was set at  $5^\circ$ , which covers the angular range of  $2.5^\circ < \theta_{lab} < 7.5^\circ$ . The target nucleus

$^{12}\text{C}$  has the unnatural parity states  $1^+$  at 12.71 MeV and  $2^-$  at 18.3 MeV in the measured  $E_x$  region, which are known as isoscalar spin states, and also the natural parity states such as  $2^+$  at 4.44 MeV,  $0^+$  at 7.65 MeV and  $3^-$  at 9.64 MeV.

The preliminary result of the measurement is shown in Fig. 1. The spin flip probability  $S_1$  has large values for the unnatural parity  $1^+$  and  $2^-$  states, and the  $S_2$  values are around 0 for all excitation energy region. Further analysis is now in progress.

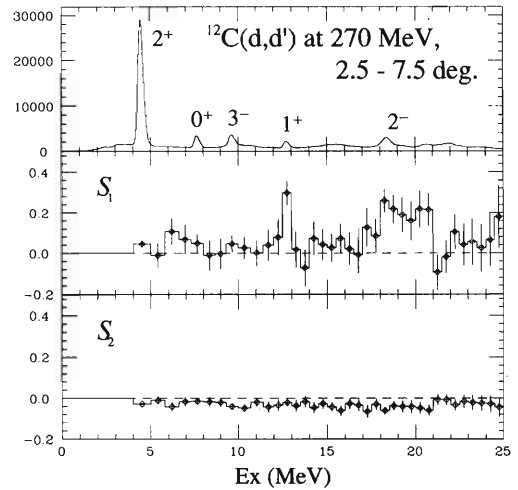


Fig. 1. Excitation energy spectrum, the spin flip probability  $S_1$  and the double spin flip probability  $S_2$ , for the scattering angle  $2.5^\circ$ - $7.5^\circ$ .

### References

- 1) S. Ishida et al.: Phys. Lett. B **314**, 279 (1993).
- 2) M. Morlet et al.: Phys. Lett. B **247** 228 (1990); M. Morlet et al.: Phys. Rev. C **46** 1008 (1992); B. N. Johnson et al.: Phys. Rev. C **51** 1726 (1995).
- 3) C. Furget et al.: Phys. Rev. C **51** 1562 (1995).
- 4) S. Ishida et al.: AIP Conf. Proc. **343**, 182 (1995).
- 5) Y. Satou et al.: RIKEN Accel. Prog. Rep. **29**, 57 (1996).

\* Japan Atomic Energy Research Institute

# Measurement of the $^{28}\text{Si}(\vec{d}, \vec{d}')^{\prime}$ Reaction at $E_d = 270$ MeV

Y. Satou, S. Ishida, H. Sakai, H. Okamura, N. Sakamoto, H. Otsu, T. Uesaka, T. Wakasa, T. Nonaka, T. Ohnishi, G. Yokoyama, K. Sekiguchi, K. Yakou, S. Fukusaka, K. Itoh, T. Ichihara, T. Niizeki, and K. Hatanaka

[NUCLEAR REACTION,  $^{28}\text{Si}(\vec{d}, \vec{d}')^{\prime}$ ,  $E_d = 270$  MeV]

In the past three decades much of magnetic transitions and spin giant resonances has been investigated by using various nuclear reactions such as  $(e, e')$ ,  $(p, p')$  and  $(p, n)$ . These reactions preferentially excite isovector ( $\Delta T = 1$ ) transitions. Therefore, the understanding of the isoscalar spin excitations ( $\Delta T = 0$ ,  $\Delta S = 1$ ) is still limited. The  $(\vec{d}, \vec{d}')^{\prime}$  reaction at intermediate energies is considered to be a promising tool for the study of  $\Delta T = 0$ ,  $\Delta S = 1$  transitions, because (a) it exclusively excites the isoscalar states, (b) the reaction mechanism becomes selective in spin-flip transitions at energies above 100 MeV/nucleon, and (c) the spin-flip probability  $S_1$ , obtained by measuring the polarization transfer observables, is useful in separating the spin-flip ( $\Delta S = 1$ ) and non-spin-flip ( $\Delta S = 0$ ) strengths. The feature (c) has been established by the previous experimental study of the  $^{12}\text{C}(\vec{d}, \vec{d}')^{\prime}$  reaction.<sup>1)</sup>

In this report we describe our experimental study of the isoscalar M1 ( $1^+$ ) states via the  $^{28}\text{Si}(\vec{d}, \vec{d}')^{\prime}$  reaction. The nucleus,  $^{28}\text{Si}$ , is known to have at least one isoscalar spin-flip state ( $J^\pi = 1^+$ , 9.5 MeV) which is strongly excited in the  $(p, p')$  reaction.<sup>2)</sup> The differential cross sections ( $\frac{d\sigma}{d\Omega}$ ) and eight spin observables ( $A_y$ ,  $A_{yy}$ ,  $P^{y'}$ ,  $P^{y'y'}$ ,  $K_y^{y'}$ ,  $K_y^{y'y'}$ ,  $K_{yy}^{y'}$  and  $K_{yy}^{y'y'}$ ) were measured over an angular range from  $2.5^\circ$  to  $7.5^\circ$  and an excitation energy range from 4 to 24 MeV. A 270 MeV polarized deuteron beam from the RIKEN Ring Cyclotron was used to bombard a 58.1 mg/cm<sup>2</sup>-thick  $^{nat}\text{Si}$  target ( $^{28}\text{Si}$ : 92.2%,  $^{29}\text{Si}$ : 4.7%,  $^{30}\text{Si}$ : 3.1%). Typical beam intensity was 10 nA. The scattered deuterons were momentum analyzed by a magnetic spectrometer, SMART, and their polarization components were determined by the asymmetry measurement using a polarimeter, DPOL,<sup>3)</sup> which was placed in the second focal plane (FP-2) of SMART. The elastically scattered deuterons and the deuterons that excite the target nucleus to the first  $2^+$  state at 1.78 MeV were removed by a 5-cm thick lead slit located at the intermediate focusing point of SMART.

Figure 1(a) shows the excitation energy spectrum of  $^{nat}\text{Si}$  target. The isovector  $1^+$  states, which usually dominate in the forward angle  $(p, p')$  spectra, are entirely suppressed based on the isospin selection rule. All the levels observed are, therefore, isoscalar ( $\Delta T = 0$ ) states. A prominent peak was observed at the excitation energy of 18.8 MeV. To the best of our knowledge, no  $J^\pi$  assignment has ever been done for this peak structure. Since this peak had already

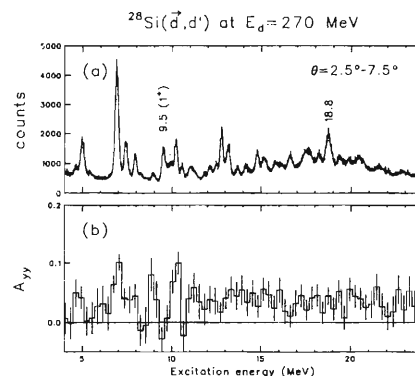


Fig. 1. Experimental results of the deuteron inelastic scattering from  $^{28}\text{Si}$ . (a) Measured excitation energy spectrum. (b) Spectrum of the tensor analyzing power,  $A_{yy}$ .

been observed in the  $(\alpha, \alpha')$  experiment,<sup>4)</sup> it may be ascribed to a non-spin-flip state (or a resonance). The previously known isoscalar  $1^+$  state at 9.5 MeV is clearly excited. Figure 1(b) shows the excitation energy spectrum of a tensor analyzing power,  $A_{yy}$ . The  $A_{yy}$  takes negative values for the  $1^+$  state at 9.5 MeV, indicating the spin-flip nature of this state. As one sees,  $A_{yy}$  also becomes negative at  $\text{Ex} \approx 8.3$  MeV and 10.6 MeV. At the former excitation energy region, an isoscalar ( $T = 0$ )  $1^+$  state has been known on the basis of  $\gamma$ -decay systematics.<sup>5)</sup> At the latter region, two isovector ( $T = 1$ )  $1^+$  states have been known at 10.60 and 10.73 MeV. These levels were regarded as a mixed analogue of the  $^{28}\text{Al}$  1.37 MeV state, and it has been expected that they have appreciable  $T = 0$  components.<sup>5)</sup>

Further analysis is under progress to deduce the other spin observables. The spin-flip probability  $S_1$ , obtained through the relationship,

$$S_1 = \frac{1}{9}(4 - A_{yy} - P^{y'y'} - 2K_{yy}^{y'y'}),$$

is expected to play an important role in identifying the isoscalar spin-flip strengths in a more definitive manner.

## References

- 1) Y. Satou et al.: RIKEN Accel. Prog. Rep. **30**, 45 (1997).
- 2) G. M. Crawley et al.: Phys. Rev. C **39**, 311, (1989).
- 3) S. Ishida et al.: RIKEN Accel. Prog. Rep. **29**, 179 (1996).
- 4) H. Riedesel et al.: Nucl. Phys. A **454**, 85 (1986).
- 5) P. M. Endt: Nucl. Phys. A **521**, 1 (1990).

## Gamow-Teller Strength Distribution in fp Shell Nuclei

T. Niizeki, S. Fukusaka, T. Ichihara, S. Ishida, K. Itoh, T. Ohnishi, H. Ohnuma,  
H. Okamura, H. Orihara, H. Sakai, N. Sakamoto, Y. Satou, K. Sekiguchi,  
Y. Tajima, T. Uesaka, K. Yakou, and G. Yokoyama

[NUCLEAR REACTION ( $d, {}^2\text{He}$ ), GT  $\beta$  decay]

The ( $d, {}^2\text{He}$ ) reaction at intermediate energy is very useful to measure the  $\beta^+$  Gamow-Teller transition strength,  $B(\text{GT}_+)$ . This reaction excites spin-isospin states selectively. This reaction has advantages in efficiency and energy resolution<sup>1)</sup> over other reactions such as ( $n, p$ ). Because of these advantages, we can measure  $\text{GT}_+$  transitions to the discrete states in intermediate-mass nuclei.

We have carried out the ( $d, {}^2\text{He}$ ) reaction experiment at  $E_d = 270$  MeV to obtain  $B(\text{GT}_+)$  on  $N = 29$  isotones. Obtained energy spectra at  $0^\circ$  are shown in Fig. 1 as a function of  $\beta$  decay Q-value,  $Q_\beta$ .  ${}^{54}\text{Mn}$ ,  ${}^{52}\text{V}$ ,  ${}^{51}\text{Ti}$  and  ${}^{50}\text{Sc}$  spectra are shown to be compared each other. We used a sheet of  ${}^{50}\text{Ti}$  enriched thin foil of  $1.7$  mg/cm<sup>2</sup> thickness to obtain the  ${}^{50}\text{Sc}$  spectrum. We can use such a thin target of  ${}^{50}\text{Ti}$  because of the enough efficiency of our ( $d, {}^2\text{He}$ ) experiment.

These spectra are preliminaries. Therefore, we see only the outline of these spectra. The shaded peaks show the  $\text{GT}_+$  state candidates which are excited strongly at  $\theta = 0^\circ$ . From the angular distributions of the cross sections, these peaks can be identified as  $\text{GT}_+$  states. On  ${}^{52}\text{V}$  spectra, three peaks of similar strength can be seen and these are distributed rather widely than other nuclei. On  ${}^{54}\text{Mn}$ ,  ${}^{51}\text{Ti}$  and  ${}^{50}\text{Sc}$  spectra, substantial strong peaks can be seen. On  ${}^{50}\text{Sc}$  spectrum, a significant peak stands and there is no other substantial peak.

Energies of the low-lying peaks decrease with proton number. Strength of that peak increases with proton number. This feature has been suggested for the case of  $N = 15$  isotone.<sup>2)</sup> Further analysis and the comparison with shell model and with other reactions should be carried out.

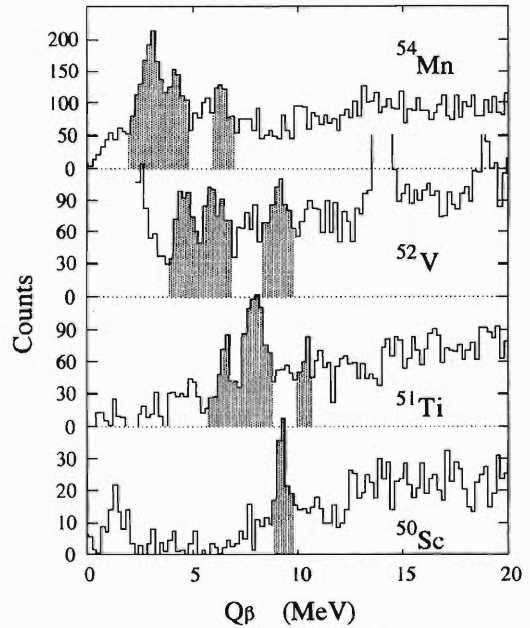


Fig. 1. The energy spectra of  $N = 29$  isotones obtained by the ( $d, {}^2\text{He}$ ) reaction. Horizontal axis is the excitation energy converted to the  $\beta$ -decay Q-value. Vertical axis is the counts per channel. The top spectrum is obtained by the  ${}^{54}\text{Fe}(d, {}^2\text{He}){}^{54}\text{Mn}$  reaction. The lower panels are  ${}^{52}\text{V}$ ,  ${}^{51}\text{Ti}$  and  ${}^{50}\text{Sc}$  spectra, respectively. The shaded peaks are candidates of  $\text{GT}_+$  states.

### References

- 1) H. Okamura et al.: Phys. Lett. B **345**, 1 (1995);  
H. Ohnuma et al.: Phys. Rev. C **47**, 648 (1993).
- 2) T. Niizeki et al.: Nucl. Phys. A **577**, 37c (1994).

## Low Background Measurement of $^8\text{B}$ Coulomb Dissociation

M. Hirai, T. Kikuchi, T. Motobayashi, T. Minemura, S. Shimoura, H. Murakami, Y. Ando, K. Ieki, T. Nishio, Y. Yanagisawa, M. Suzuki, H. Fujiwara, T. Uchibori, Y. Iwata, H. Sakurai, Y. Watanabe, K. I. Hahn, H. Utsunomiya, K. Miki, S. Kubono, T. Teranishi, N. Aoi, T. Nakamura, M. Ishihara, M. Gai, and E. L. Wilds\*

[NUCLEAR REACTIONS:  $^{208}\text{Pb}(^8\text{B}, p^7\text{Be})^{208}\text{Pb}$ , Coulomb dissociation]

Directly relating to the solar neutrino problem, studies of the reaction  $^7\text{Be}(p,\gamma)^8\text{B}$  in sub-MeV energy region are very important. The Coulomb dissociation reaction  $^{208}\text{Pb}(^8\text{B}, p^7\text{Be})^{208}\text{Pb}$ , in the intermediate energy region is a powerful tool for that study. We have already performed two experiments of  $^8\text{B}$  dissociation at RIKEN in '91 and '94, and extracted the  $S$ -factors within the range of  $0.5 < E_{rel} < 2.0$  MeV.<sup>1,2)</sup>

Here we report the third experiment performed in '96, which aimed at measuring the  $S$ -factors in the lower energy region by improving the setup to achieve a lower background measurement. The present experiment is expected also to measure the angular correlation between the fragments, which may be affected possible E1-E2 interference.<sup>3)</sup>

Figure 1 shows the experimental setup.

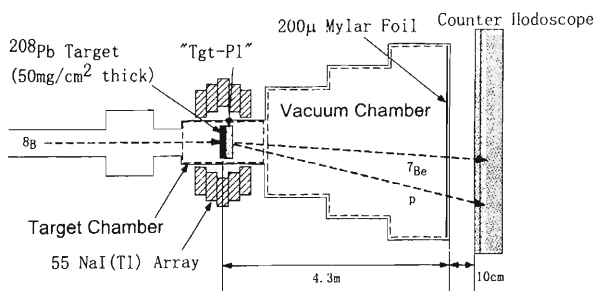


Fig. 1. Schematic view of the experimental setup.

The secondary beams, which contain  $^8\text{B}$  as a dominant component (2/3), were provided by the RIPS fragment separator. The energy of  $^8\text{B}$  was 52.5 MeV/nucleon, and the intensity was  $2 \times 10^5$  cps on average.

The secondary beams bombarded a 50 mg/cm<sup>2</sup>  $^{208}\text{Pb}$  target which placed at the third focal point at RIPS. A 0.5 mm thick plastic scintillator (Tgt-PL) was also placed in the target chamber, adjacent to the target itself. Fifty-five NaI(Tl) scintillators<sup>4)</sup> have surrounded the target to detect the  $\gamma$  rays emitting from the excited fragment  $^7\text{Be}^*$  in the  $1/2^-$  states at 429 keV with a branching ratio of approximately 5%.<sup>2)</sup>

About 4.4 m downstream of the lead target, we placed a counter hodoscope which consisted of 13( $\Delta E$ ) and 18( $E$ ) plastic scintillators, and detected p and  $^7\text{Be}$  in coincidence. The effective area of the hodoscope is

$0.96 \times 1 \text{ m}^2$ . The complete kinematics of the p- $^7\text{Be}$  system were reconstructed by using the detected positions on the hodoscope and the time-of-flight from Tgt-PL to the hodoscope.

In the two former experiments, a helium gas bag was inserted between the target and the hodoscope, but we have found it to be created many background events. In the present experiment, we installed a vacuum chamber, and the space between the target chamber and the hodoscope was evacuated. A mylar foil (200  $\mu\text{m}$ ) was placed at the end of the chamber, leaving 10–15 cm of the air gap between the mylar foil and the hodoscope.

Figure 2 shows spectra of the relative energy  $E_{rel}$  of the p- $^7\text{Be}$  system. The data obtained with the lead target and the background data obtained without the lead target are shown in Fig. 2(a). Figure 2(b) shows the background-subtracted spectrum. Solid line represents the result of a Monte-Carlo simulation, done with a constant  $S$ -factor of 20 eV-b.

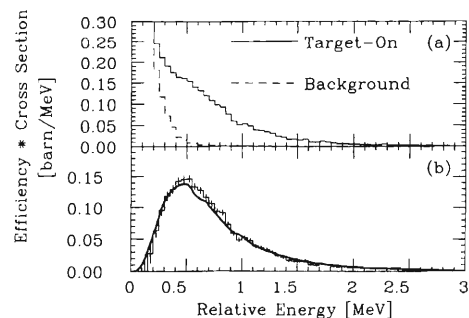


Fig. 2. (a) Relative energy spectra taken with and without the target. (b) Background-subtracted spectrum and the Monte-Carlo estimation with a constant  $S$ -factor of 20 eV-b (solid curve).

Preliminary results of the angular correlation exhibit some asymmetries, which will be analyzed in terms of the interference discussed above.

### References

- 1) T. Motobayashi et al.: Phys. Rev. Lett. **73**, 2680 (1994); N. Iwasa et al.: J. Phys. Soc. Jpn. **65**, 1256 (1996).
- 2) T. Kikuchi et al.: Phys. Lett. B **391**, 2680 (1997).
- 3) H. Esbensen and G. F. Bertsch: Phys. Lett. B **359**, 13 (1995); Nucl. Phys. A **600**, 37 (1996).
- 4) T. Nishio et al.: RIKEN Accel. Prog. Rep. **29**, 184 (1996).

\* Department of Physics, Yale University, U.S.A.

# Measurement of Cross Sections of the ${}^8\text{Li}(\alpha, n){}^{11}\text{B}$ and ${}^8\text{Li}(\alpha, \alpha n){}^7\text{Li}$ Reactions with a New-MUSIC Detector

Y. Mizoi, T. Fukuda, Y. Matsuyama, T. Miyachi, H. Miyatake, N. Aoi, N. Fukuda, M. Notani, Y. X. Watanabe, K. Yoneda, H. Sakurai, Y. Watanabe, A. Yoshida, and M. Ishihara

[Nuclear Reactions  ${}^8\text{Li}(\alpha, n){}^{11}\text{B}$ ,  ${}^8\text{Li}(\alpha, \alpha n){}^{11}\text{B}$ ;  $E_{lab}=2-7$  MeV; Measured  $\sigma(E)$ ]

We have measured the cross section of the  ${}^8\text{Li}(\alpha, n){}^{11}\text{B}$  as well as  ${}^8\text{Li}(\alpha, \alpha n){}^7\text{Li}$  reactions with a New-MUSIC<sup>1)</sup> detector system in coincidence with the neutron in order to identify the final states of  ${}^8\text{Li}(\alpha, n)$  reactions. We report the present status of the analysis.

The  ${}^8\text{Li}(\alpha, n){}^{11}\text{B}$  reaction is one of the key processes in the primordial nucleosynthesis which is described by inhomogeneous big-bang models. Historically, this reaction was studied by using the inverse reaction,  ${}^{11}\text{B}(n, \alpha){}^8\text{Li}$ .<sup>2)</sup> In addition, a direct measurement of the  ${}^8\text{Li}(\alpha, n){}^{11}\text{B}$  reaction<sup>3,4)</sup> was performed by a MUSIC<sup>5)</sup> detector. The cross section of the former measurement is smaller than the latter measurement by a factor of 5. This difference is explained by the fact that the former includes only a ground state of  ${}^{11}\text{B}$ , while the latter includes all states of  ${}^{11}\text{B}$ .

In addition to the  ${}^8\text{Li}(\alpha, n){}^{11}\text{B}$  reaction, the  ${}^8\text{Li}(\alpha, \alpha n){}^7\text{Li}$ -breakup reaction can occur above 2.0 MeV at the center of mass system. To estimate the contributions of each  ${}^{11}\text{B}$  state and of breakup channel to the cross section, we have performed for the first time the exclusive direct measurement of the  ${}^8\text{Li}(\alpha, n){}^{11}\text{B}$  and  ${}^8\text{Li}(\alpha, \alpha n){}^7\text{Li}$  reactions with the New-MUSIC detector.

The New-MUSIC detector is a MUSIC (Multi-Sampling Ionization Chamber)-type detector, which can measure the energy loss along the particle track. The main advantage of the New-MUSIC is its capability to work as a time-projection chamber employing flash-ADC's (Analogue to Digital Converter) to identify multi-track events. This advantage is effective to reject the background events and also to identify the final channels like the  ${}^8\text{Li}(\alpha, \alpha n){}^7\text{Li}$  reaction.

The experiment was performed with RIPS at RIKEN Ring Cyclotron Facility. The  ${}^8\text{Li}$  beams were produced by a fragmentation reaction of the  ${}^{12}\text{C}$  beams at an energy of 70 MeV/nucleon. The energies of  ${}^8\text{Li}$  beams were degraded by Al-plate degraders to 10–30 MeV. The energies of  ${}^8\text{Li}$  were determined event by event through a time of flight measurement. The  ${}^8\text{Li}$  beams were irradiated into the New-MUSIC detector filled by the gases of  ${}^4\text{He}$  admixed with 5%(10%) of iso-butane at 400 torr pressure. The  ${}^4\text{He}$  gas works as a detector gas as well as a target. Neutron counters surrounded the New-MUSIC detector from 0 to 90 degree.

Figure 1 shows the cross sections of the  ${}^8\text{Li}(\alpha, n){}^{11}\text{B}$ (all states) and  ${}^8\text{Li}(\alpha, \alpha n){}^7\text{Li}$  reactions. The threshold energy of the analysis is set to be 2.0 MeV at the center of mass system, because we have difficulties to identify the reactions at the present stage of the analysis. It is found that the escape channel,  ${}^8\text{Li}(\alpha, \alpha n){}^7\text{Li}$  has a comparable cross section to the  ${}^8\text{Li}(\alpha, n){}^{11}\text{B}$  channel. In order to determine the absolute cross sections, we need yet to estimate the efficiencies by computer simulations.

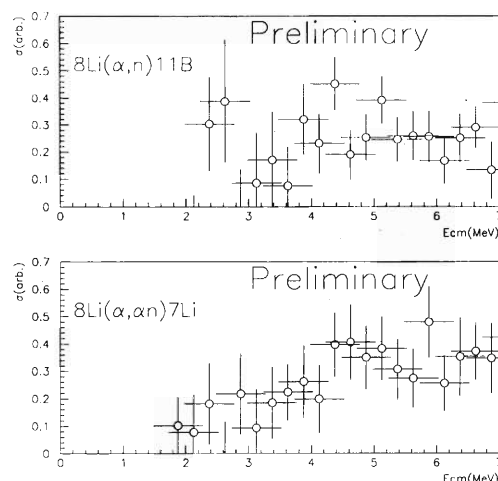


Fig. 1. The upper spectrum shows the total cross section ( $\sigma$ ) of the  ${}^8\text{Li}(\alpha, n){}^{11}\text{B}$  reaction. The lower spectrum shows the  $\sigma$  of  ${}^8\text{Li}(\alpha, \alpha n){}^7\text{Li}$ . The x-axis represents  $E_{c.m.}$ (MeV) The y-axes of the both spectra are relatively normalized.

At the present stage of the analysis, a half of the total events were analyzed. The further analyses are now in progress. We will determine the absolute cross section of these reactions and branching ratios.

## References

- 1) Y. Mizoi et al.: RIKEN Accel. Prog. Rep. **30**, 143 (1997).
- 2) T. Paradellis et al.: Z. Phys. A **337**, 211 (1990).
- 3) R. N. Boyd et al.: Phys. Rev. Lett. **68**, 1283 (1992).
- 4) X. Gu et al.: Phys. Lett. B **343**, 31 (1995).
- 5) K. Kimura et al.: Nucl. Instrum. Methods Phys. Res. A **297**, 190 (1990).

## Density Distribution of ${}^9\text{C}$ Derived from Reaction Cross Sections

M. Fukuda, M. Mihara, T. Fukao, M. Tanigaki, T. Onishi, K. Matsuta, Y. Nojiri, T. Minamisono, T. Ohtsubo, S. Fukuda, S. Ito, T. Kobayashi, S. Momota, A. Ozawa, T. Suzuki, I. Tanihata, K. Yoshida, M. Ishihara, and T. Nakamura

[ NUCLEAR REACTION:  $\text{Be}({}^{12}\text{C}, {}^9\text{C})$ ,  $E = 135$  MeV/nucleon, Measured ]  
 ${}^9\text{C}$  reaction cross sections, Deduced  ${}^9\text{C}$  density distribution ]

The nuclear structure of the proton drip-line nucleus  ${}^9\text{C}$  has attracted much interest ever since its magnetic moment was found to be anomalous.<sup>1)</sup> It is important to determine the density distribution of  ${}^9\text{C}$  for studies of its nuclear structure. In order to investigate the density distribution of  ${}^9\text{C}$ , we have measured the reaction cross sections ( $\sigma_R$ 's) for  ${}^9\text{C}$  on the Be, C, and Al targets at the beam energies of 40 and 70 MeV/nucleon using the transmission method. The methods of the experiment and analysis were essentially the same as the ones in Ref. 2 in which  ${}^8\text{B}$  was studied.

The unstable nuclear beam of  ${}^9\text{C}$  was produced by the projectile fragmentation of the 135 MeV/nucleon  ${}^{12}\text{C}$  primary beam provided from the RIKEN Ring Cyclotron. The nuclide selection was made through the RIPS (RIKEN Projectile fragment Separator). The beam energy of 40 MeV/nucleon was chosen to gain large nucleon-nucleon total cross sections that are about three times of those at the LBL energies which were around 700 MeV/nucleon.<sup>3)</sup> At 70 MeV/nucleon the cross sections take approximately the middle values in between these two energies.

The particle counting and identification before the reaction target were done by a thin Si counter for  $\Delta E$  measurement and three parallel plate avalanche counters (PPACs) that provided the time and position information. Downstream of the reaction target, the identification was made from  $\Delta E$  taken by Si counters and from the time-of-flight (TOF) taken in between the PPACs and plastic counters which were placed 2 m downstream from the reaction target. The energy loss in the reaction target was about 20 MeV/nucleon for both energies.

In order to connect the experimental reaction cross sections  $\sigma_R$  to the density distribution of  ${}^9\text{C}$ , we employed the Glauber-type calculation.<sup>2)</sup> An enhancement factor was introduced for the calculations at the intermediate energy range. This factor was the same as the one<sup>2)</sup> used in the study of  ${}^8\text{B}$  and deduced from the  $\sigma_R$  data for other stabler nuclides such as  ${}^6\text{Li}$ ,  ${}^7\text{Be}$ , and  ${}^{12}\text{C}$ , whose densities can well reproduce the interaction cross sections at high energies.<sup>3)</sup>

We assumed a shape of the density distribution of  ${}^9\text{C}$  and fitted it to the  $\sigma_R$  data including the high-energy data through the Glauber-type calculation. The assumed shape for the proton density in  ${}^9\text{C}$  was a Gaussian at the core and a Yukawa-square tail at the outer region, while that the neutron density was only a Gaus-

sian with the same width as the proton core. The preliminary result is shown by the shaded region in Fig. 1, where the best-fit density is shown by the dashed curve and the error is indicated as the height of the shade.

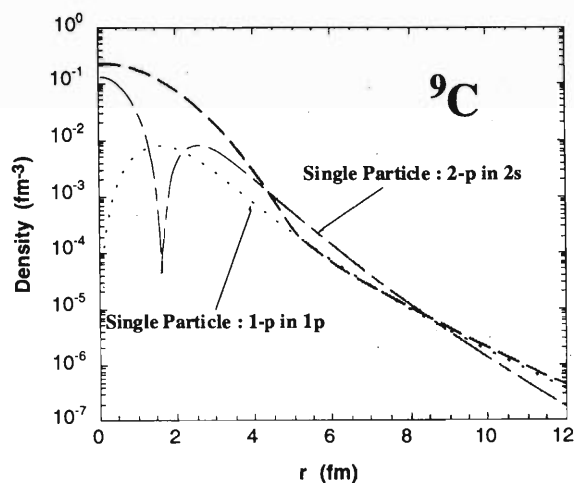


Fig. 1. Density distribution of  ${}^9\text{C}$  derived by a fitting to the experimental  $\sigma_R$  data (dashed curve) and single-particle calculated densities (dotted and dash-dotted curves). The shaded region indicates the experimental error.

The dotted curve in Fig. 1 shows a single particle density for one proton in 1p orbit in the Woods-Saxon potential, the depth of which was adjusted to reproduce the experimental one-proton binding energy of 1.296 MeV for  ${}^9\text{C}$ . The dash-dotted curve shows a similar single particle calculation for two protons in 2s orbit with the binding energy of 1.433 MeV, in which the two protons are assumed to form a single cluster. Though the present density has a large error, these simple calculations with the realistic proton binding energies are compared to show a good agreement with the best-fit density as shown in Fig. 1. These densities have 5–10 times smaller amplitude at the tail region compared to the case of  ${}^8\text{B}$ .

### References

- 1) K. Matsuta et al.: Nucl. Phys. A **588**, 153c (1995).
- 2) M. Fukuda et al.: RIKEN Accel. Prog. Rep. **30**, 54 (1996).
- 3) A. Ozawa et al.: Nucl. Phys. A **608**, 63 (1996).

## Inelastic Proton Scattering on $^{12}\text{Be}$ in Inverse Kinematics

H. Iwasaki, T. Motobayashi, H. Akiyoshi, Y. Ando, N. Fukuda, H. Fujiwara, Zs. Fülöp, K. I. Hahn, Y. Higurashi, M. Hirai, I. Hisanaga, N. Iwasa, T. Kijima, T. Minemura, T. Nakamura, M. Notani, S. Ozawa, H. Sakurai, S. Shimoura, S. Takeuchi, T. Teranishi, Y. Yanagisawa, and M. Ishihara

$$\left[ \begin{array}{l} \text{NUCLEAR REACTIONS: } ^1\text{H}, ^{208}\text{Pb}(^{12}\text{Be}, ^{12}\text{Be}\gamma) ^1\text{H}, ^{208}\text{Pb}, \\ E(^{12}\text{Be}) = 54 \text{ A MeV; Deduced deformation parameter } \beta_2 \end{array} \right]$$

Collective behavior of the even-even nuclei has been studied through measurements of the reduced transition probability  $B(E2; 0^+_{gs} \rightarrow 2^+)$ . As well as electromagnetic processes such as Coulomb excitation and  $\gamma$ -decay lifetime, the inelastic proton scattering has been studied for estimating the  $B(E2)$ , where the interaction between the proton and the nucleus of interest is dominated by the nuclear force.<sup>1)</sup> Differences between the results obtained from the inelastic proton scattering and the electromagnetic probes were discussed in terms of the ratio of neutron- to proton- transition matrix elements  $M_n/M_p$ .<sup>2,3)</sup> We have investigated the inelastic proton scattering in the inverse kinematics exciting the neutron-magic nucleus  $^{12}\text{Be}$  to its first bound excited  $2^+$  state, where the  $B(E2)$  is unknown. Here we report the experimental arrangement and preliminary results.

A  $^{12}\text{Be}$  beam was produced by using the projectile fragmentation of a 100 A MeV  $^{18}\text{O}$  beam incident on a 1.11 g/cm<sup>2</sup> Be target. By the RIKEN Projectile-fragment Separator (RIPS), the  $^{12}\text{Be}$  beam was separated with a high purity of around 96%. The secondary beam intensity was typically a few tens of thousands counts per second with the momentum spread  $\pm 1\%$ . Two 1.0 mm thick plastic scintillators (PL) were located at the first achromatic focal plane of the RIPS (F2) and at the final focal plane (F3). Two parallel plate avalanche counters (PPAC's) were placed at F3 to determine the incident angle of the beam. The particle-identification of the incident beam was carried out event-by-event with the time-of-flight (TOF) measurement. The TOF was determined between F2-PL and F3-PL timings. The secondary  $^{12}\text{Be}$  beam bombarded a 90.2 mg/cm<sup>2</sup> thick  $(\text{CH}_2)_n$  target at F3, with its average energy on the target 53.8 A MeV. The background originating from the  $^{12}\text{Be} + ^{12}\text{C}$  scattering was measured using a 89.8 mg/cm<sup>2</sup> thick  $^{12}\text{C}$  target and subtracted from the  $(\text{CH}_2)_n$  yields. In order to study a possible contribution of the Coulomb force, measurements with a 351 mg/cm<sup>2</sup> thick  $^{208}\text{Pb}$  target were also performed.

The scattered  $^{12}\text{Be}$  was detected by a hodoscope consisted of 13  $\Delta E$ - and 16  $E$ - plastic scintillators, located 4.9 m downstream of the target. This hodoscope was mounted on a vacuum chamber, details of which are described elsewhere,<sup>4)</sup> for reduction of background. The particle identification was performed in the stan-

dard  $\Delta E$ - $E$  method. The scattering angle was determined by the hit positions at the two PPAC's and the hodoscope. The de-excitation  $\gamma$  rays were detected with 55 pieces of NaI(Tl) crystal scintillators surrounding the target from 60 to 163 degree. Each scintillator crystal has a rectangular shape with the size  $6 \times 6 \times 12 \text{ cm}^3$  coupled with a 5.1 cm  $\phi$  photomultiplier tube. The energy resolution was typically 7.0% FWHM for 1275 keV  $\gamma$  ray as calibrated from the  $^{22}\text{Na}$  standard source.

To test of the validity of the method, we performed the same measurements with 59 A MeV  $^{10}\text{Be}$ , where the  $B(E2)$  is known.

Figure 1 shows the  $\gamma$ -ray spectrum obtained in coincidence with inelastically scattered  $^{12}\text{Be}$ , for which Doppler shift is corrected. A full-energy peak corresponding to the  $2^+ \rightarrow 0^+$  transition is clearly seen at 2.1 MeV. Another peak at around 3.4 MeV is possibly the  $\gamma$  rays associated with the breakup reaction,  $^{12}\text{Be} \rightarrow ^{10}\text{Be}^*(2^+ : 3.368 \text{ MeV}) + 2n$ . Further analyses of the data are now in progress.

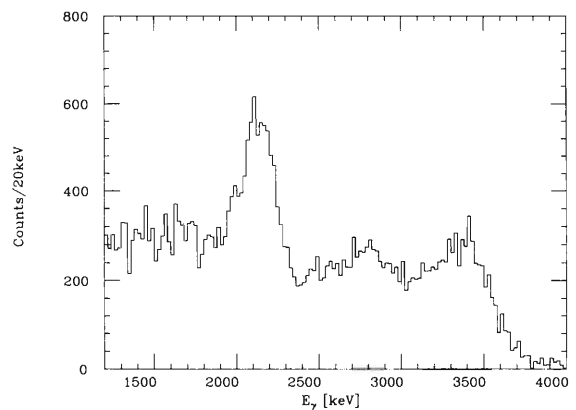


Fig. 1. De-excitation  $\gamma$ -ray energy spectrum observed in the  $^1\text{H} + ^{12}\text{Be}$  inelastic scattering. Doppler shift is corrected for (see text).

### References

- 1) G. Kraus et al.: Phys. Rev. Lett. **73**, 1773 (1994).
- 2) J. H. Kelley et al.: Phys. Rev. C **56**, R1206 (1997).
- 3) M. A. Kennedy et al.: Phys. Rev. C **46**, 1811 (1992).
- 4) I. Hisanaga et al.: RIKEN Accel. Prog. Rep. **31**, 162 (1998).

## Coulomb Excitation of $^{11}\text{Be}^\dagger$

T. Nakamura, T. Motobayashi, Y. Ando, T. Nishio, H. Sakurai, S. Shimoura,  
T. Teranishi, Y. Yanagisawa, and M. Ishihara

[NUCLEAR REACTION  $^{11}\text{Be} + \text{Pb}$ , Coulomb excitation, Neutron halo]

The Coulomb excitation of a halo nucleus  $^{11}\text{Be}$  to its first bound excited state (E1:  $1/2^+ \rightarrow 1/2^-$ ) has been studied using a 64 MeV/u  $^{11}\text{Be}$  radioactive beam incident on a  $^{208}\text{Pb}$  target. The electric dipole strength

deduced by a first-order perturbation analysis is in good agreement with the result of previous life-time measurements of the  $^{11}\text{Be}$   $1/2^-$  state.

---

<sup>†</sup> Condensed from the article in Phys. Lett. B **394**, 11 (1997)

## Coulomb Dissociation of $^{12}\text{N}$

T. Minemura, T. Motobayashi, S. Shimoura, H. Murakami, Y. Ando, T. Nishio, Y. Yanagisawa, M. Suzuki, H. Fujiwara, T. Kikuchi, T. Uchibori, Y. Iwata, H. Sakurai, Y. Watanabe, K. I. Hahn, T. Teranishi, M. Hirai, N. Aoi, T. Nakamura, M. Ishihara, H. Utsunomiya, and K. Miki

[ $^{208}\text{Pb}(^{12}\text{N}, ^{11}\text{C p})^{208}\text{Pb}$ , Coulomb dissociation, Relative energy spectra]

The Coulomb breakup technique was employed to determine the radiative width of excited levels in  $^{12}\text{N}$  and the direct proton-capture contribution in the  $^{11}\text{C}(p,\gamma)^{12}\text{N}$  reaction. This reaction is important in the hot pp chain nuclear burning<sup>1)</sup> in hydrogen-rich massive objects. At a high-temperature and high-density condition, this capture reaction becomes faster than the  $\beta^+$  decay of  $^{11}\text{C}$ . However, this  $^{11}\text{C}(p,\gamma)^{12}\text{N}$  reaction is difficult to study experimentally because the life-time of  $^{11}\text{C}$  is too short ( $T_{1/2} = 20.4$  min) to prepare it as target.

In the energy region of astrophysical interest, there are two resonant states in  $^{12}\text{N}$ . The first one at the p- $^{11}\text{C}$  center-of-mass energy  $E_{\text{cm}} = 0.359$  MeV corresponds to the  $J^\pi = 2^+$  excited state at  $E_{\text{ex}} = 0.960$  MeV. The second one at  $E_{\text{cm}} = 0.589$  MeV can be formed by s-wave proton capture, and corresponds to the  $J^\pi = 2^-$  state at  $E_{\text{ex}} = 1.19$  MeV which decays to the ground state by an E1 transition. For the radiative width  $\Gamma_\gamma$  of the 1.19 MeV state, Wiescher et al.<sup>2)</sup> suggest  $\Gamma_\gamma = 2$  meV using the mean value of the  $\gamma$ -transition strength distribution in mass region around  $A = 12$ . With a model based on the generator coordinate method, Descouvemont and Baraffe<sup>3)</sup> predict a much larger value  $\Gamma_\gamma = 140$  meV for the same level.

The related experiments have been performed at RIKEN using the secondary beam line, RIPS. A 72.2 MeV/nucleon  $^{12}\text{N}$  radioactive beam was produced through fragmentation reactions of a primary 135 MeV/nucleon  $^{14}\text{N}$  beam. A 50 mg/cm<sup>2</sup>  $^{208}\text{Pb}$  target was bombarded by the secondary  $^{12}\text{N}$  beam, and the breakup fragments,  $^{11}\text{C}$  and proton, were detected in coincidence after traveling through 4.4 m flight-path.

The energies and scattering angles of proton and  $^{11}\text{C}$  were measured. From these quantities, we can reconstruct the p- $^{11}\text{C}$  relative energy and scattering angle of the p- $^{11}\text{C}$  center-of-mass. The experimental relative-energy spectra are shown in Fig. 1. The histogram (a) shows the yield measured with the  $^{208}\text{Pb}$  target, and (b) shows the yield without the target which is consid-

ered as the background. The background-subtracted net spectrum is shown in (c), where a broad bump is seen at around 0.5 MeV. This bump might contain the two peaks corresponding to the  $2^+$  state ( $\Gamma < 20$  keV) and the  $2^-$  state ( $\Gamma = 118$  keV), which overlap with in the experimental energy resolution estimated to be about 150 keV presently. A more complete analysis of the data including the evaluation of the  $^{12}\text{N} \rightarrow \text{p} + ^{11}\text{C}^*$  process is under way.

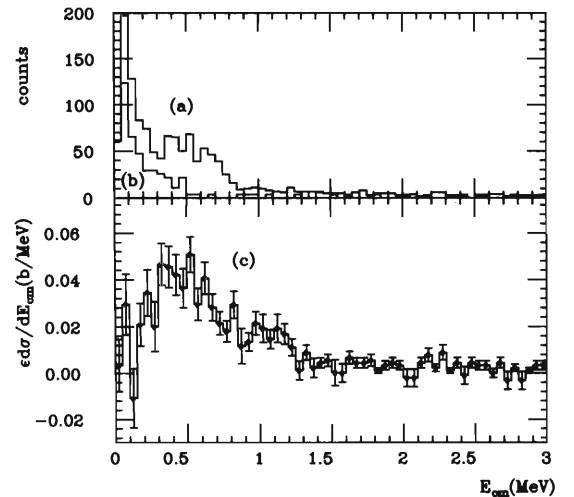


Fig. 1. Relative energy spectra obtained for the  $^{208}\text{Pb}(^{12}\text{N}, ^{11}\text{C p})^{208}\text{Pb}$  reaction. The three histograms correspond to the yields with (a) and without (b) the  $^{208}\text{Pb}$  target, and the background subtracted net yield (c).

### References

- 1) A. Jorissen and M. Arnould: *Astron. Astrophys.* **221**, 116 (1989).
- 2) M. Wiescher, J. Görres, S. Graff, L. Buchmann, and F. K. Thielemann: *Astrophys. J.* **343**, 352 (1989).
- 3) P. Descouvemont and I. Baraffe: *Nucl. Phys. A* **514**, 66 (1990).

## Quadrupole Moment of $^{13}\text{O}$

K. Matsuta, M. Tanigaki, K. Sato, T. Minamisono, M. Fukuda, Y. Nojiri, M. Mihara, S. Takeda,\*<sup>1</sup>  
 T. Miyake, K. Minamisono, A. Morishita, T. Fukao, Y. Matsumoto, T. Ohtsubo,  
 S. Fukuda, S. Momota, K. Yoshida, A. Ozawa, T. Kobayashi, I. Tanihata,  
 G. F. Krebs,\*<sup>2</sup> J. R. Alonso,\*<sup>2</sup> and T. J. M. Symons\*<sup>2</sup>

[ NUCLEAR STRUCTURE, Nuclear magnetic resonance,  
 Measured quadrupole moment of  $^{13}\text{O}$  ground state ]

The electric quadrupole ( $Q$ ) moment of  $^{13}\text{O}$  ( $I^\pi = 3/2^-$ ,  $T_{1/2} = 8.6$  ms) has been determined reliably from the  $\beta$ -Nuclear Quadrupole Resonance ( $\beta$ -NQR) on  $^{13,19}\text{O}$  and Fourier Transformed NMR (FT-NMR) on  $^{17}\text{O}$  in  $\text{TiO}_2$ . The preliminary value of the  $Q$  moment reported previously<sup>1)</sup> was revised based on the present precise field gradient.

The electric quadrupole coupling constant  $eqQ/h$  of the  $^{13}\text{O}$  implanted in  $\text{TiO}_2$  was determined from the  $\beta$ -NQR on the polarized  $^{13}\text{O}$  provided by RIKEN Ring Cyclotron and RIPS fragment separator, as was reported previously.<sup>1)</sup> The  $c$  axis of the (tetragonal)  $\text{TiO}_2$  catcher was set parallel to the external magnetic field,  $H_0 = 8$  kOe. From the observed NQR spectrum shown in Fig. 1 (essentially the same as Fig. 2 in Ref. 1), the coupling constant was obtained as  $(1-\eta')|eq'Q|/2h$  ( $^{13}\text{O}$  in  $\text{TiO}_2$ ) = 128(6) kHz by fitting a theoretical function to the peak at the higher frequency (peak 2). The peak at the lower frequency (peak 1) can not be analyzed due to the lack of resolution.

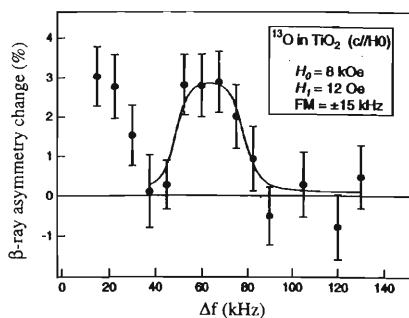


Fig. 1. NQR spectrum for  $^{13}\text{O}$  in  $\text{TiO}_2$ .

The  $eqQ/h$  and the asymmetry parameter  $\eta$  for  $^{17}\text{O}$  in enriched  $\text{Ti}^{17}\text{O}_2$  were re-measured using the pulsed FT-NMR method without any dopant since the old value was not reliable enough due to the Cr impurities used for the signal amplification. From the resonance frequencies as a function of the rotation angle,  $|eqQ|/h$  ( $^{17}\text{O}$  in  $\text{TiO}_2$ ) = 1512(4) kHz and  $\eta = 0.831(7)$  were determined for substitutional  $^{17}\text{O}$ .

We have studied the  $\beta$ -NQR on  $^{19}\text{O}$  in  $\text{TiO}_2$  using the 5-MV Van de Graaff accelerator at Osaka

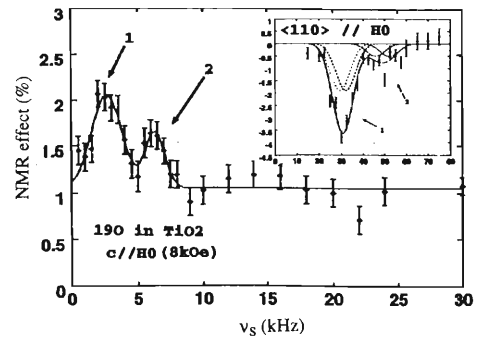


Fig. 2. NQR spectrum for  $^{19}\text{O}$  in  $\text{TiO}_2$ .

Univ. As shown in NQR spectrum for  $c//H_0$  (Fig. 2), we found two different implantation sites. Combined with another spectrum for  $\langle 110 \rangle // H_0$  shown in the inset,  $eqQ/h$  and  $\eta$  were determined. From this  $\eta$ , the peak in Fig. 2 with small coupling frequency was found to be the one from the substitutional site, and  $|eqQ|/h$  ( $^{19}\text{O}$  in  $\text{TiO}_2$ ) = 208(17) kHz was obtained. Therefore, the ratio of the  $Q$  moments for  $^{17,19}\text{O}$  was determined from the ratio of their coupling constants to be  $|Q(^{19}\text{O})/Q(^{17}\text{O})| = 0.138(11)$ . The coupling constant of the other implantation site was determined to be  $(1-\eta')|eq'Q|/2h$  ( $^{19}\text{O}$  in  $\text{TiO}_2$ ) = 42.1(0.8) kHz. The clear peak for  $^{13}\text{O}$  in Fig. 1 corresponds to this second site, not the substitutional site which we previously thought. Thus, the ratio of the  $Q$  moments is determined to be  $|Q(^{13}\text{O})/Q(^{19}\text{O})| = 3.04(16)$ . Here, we have,

$$\begin{aligned} |Q(^{17}\text{O})| : |Q(^{19}\text{O})| : |Q(^{13}\text{O})| \\ = 1 : 0.138(11) : 0.42(4), \end{aligned}$$

Using the known  $Q(^{17}\text{O}) = 26(3)$  mb,  $Q$  moments are determined as

$$|Q(^{19}\text{O})| = 3.6(5) \text{ mb, and } |Q(^{13}\text{O})| = 11.0(1.6) \text{ mb.}$$

The shell model value  $Q(^{13}\text{O}) = +16$  mb calculated by the OXBASH code using a harmonic oscillator radial wave function is significantly larger than the present value. Advanced theoretical investigation on a proton-halo effect, for example, is needed.

### References

- 1) K. Matsuta et al.: RIKEN Accel. Prog. Rep. 29, 60 (1995).

\*<sup>1</sup> Faculty of Engineering, Gunma University

\*<sup>2</sup> LBL, Berkeley, U.S.A.

## Coulomb Dissociation of $^{17}\text{C}$ and $^{19}\text{C}$

T. Nakamura, N. Fukuda, T. Kobayashi, N. Aoi, M. Ishihara, H. Iwasaki, T. Kubo,  
A. Mengoni, M. Notani, H. Otsu, H. Sakurai, S. Shimoura,  
T. Teranishi, K. Yoneda, and Y. X. Watanabe

[ $^{17,19}\text{C} + \text{Pb}$ , Coulomb dissociation, Neutron halo]

Neutron halo structure has been one of highlights in the recent nuclear physics research. A neutron halo structure has so far been established for  $^{11}\text{Li}$ ,  $^{11,14}\text{Be}$ , and  $^{17}\text{B}$ . All of these nuclei possess the characteristic nature of loosely-bound valence neutron(s). Recently, the neutron rich carbon isotopes  $^{17,19}\text{C}$  draw attentions as neutron-halo candidates since their separation energies are small ( $S_n(^{17}\text{C}) = 729 \pm 18$  keV,  $S_n(^{19}\text{C}) = 170 \pm 110$  keV). Recent measurements on longitudinal momentum distribution for the core fragment have in fact suggested a halo structure for  $^{19}\text{C}$  and an ordinary structure for  $^{17}\text{C}$ .<sup>1)</sup> However, the experimental difficulties have strongly limited their structure information available for these nuclei. In particular, the ground-state total angular momentum and parity have not yet been determined for these two nuclei. The determination of their ground-state spin is important since the centrifugal barrier related to the nuclear spin may prevent the formation of the neutron halo. A Coulomb dissociation reaction is suitable for probing the halo structure since it is sensitive to the halo wave function and thus can be used to determine the matter distribution and spin of the valence neutron.<sup>2)</sup>

We have measured the Coulomb dissociation of  $^{17,19}\text{C}$  using the radioactive beam line RIPS at RIKEN Ring Cyclotron Facility. The momentum vectors of

the two outgoing particles,  $^{16}\text{C} + \text{neutron}$  and  $^{18}\text{C} + \text{neutron}$ , have been measured in coincidence, respectively, for the reactions  $^{17}\text{C} + \text{Pb}$  and  $^{19}\text{C} + \text{Pb}$  at 67 MeV/nucleon to determine the Coulomb excitation energy spectrum. The  $^{17}\text{C}$  and  $^{19}\text{C}$  ion beams have been produced from the  $^{22}\text{Ne}$  primary beam at 110 MeV. The typical secondary beam intensities were about 30 kcps and 300 cps, respectively, for  $^{17}\text{C}$  and  $^{19}\text{C}$ . The time of flight for the beam ion was measured with the two thin plastic scintillators that were placed 5.15 m apart. The position and direction of the beam ion were measured with four sets of Multi-Wire Proportional Counters (MWPC). The outgoing fragment was measured by the magnetic spectrometer with two sets of tracking drift chambers and by the plastic scintillator hodoscopes. The outgoing neutron was measured with the plastic scintillator hodoscopes placed at 0 degree. The experimental setup is essentially same as that once used for the  $^{11}\text{Be}$  Coulomb dissociation experiment.<sup>2)</sup> The analysis of the experimental data is now in progress.

### References

- 1) D. Bazin et al.: Phys. Rev. Lett. **74**, 3569 (1995).
- 2) T. Nakamura et al.: Phys. Lett. B **331**, 296 (1994).

# Measurements of the $^{18}\text{N}$ Magnetic Moment and Electric Quadrupole Moment

H. Ogawa, K. Asahi, K. Sakai, A. Yoshimi, M. Tsuda, Y. Uchiyama, T. Suzuki, K. Suzuki, N. Kurokawa,<sup>\*1</sup>  
 M. Adachi, H. Izumi, H. Ueno, T. Shimoda, S. Tanimoto, N. Takahashi, W.-D. Schmidt-Ott,  
 M. Schäfer, S. Fukuda,<sup>\*2</sup> A. Yoshida, T. Kubo, H. Okuno, H. Sato, M. Notani,  
 N. Aoi, K. Yoneda, H. Iwasaki, N. Fukuda, M. Ishihara, and H. Miyatake

[ $^{18}\text{N}_{\text{g.s.}}$ ;  $\beta$ -NMR; measured magnetic moment, electric quadrupole moment]

We report on the measurement of the magnetic moment and electric quadrupole moment of the  $^{18}\text{N}$  ground state ( $J^\pi = 1^-, T_{1/2} = 624 \text{ ms}$ )<sup>1)</sup> by means of the  $\beta$ -ray detected nuclear magnetic resonance ( $\beta$ -NMR). The standard shell-model calculations lead to a predicted ground-state spin and parity<sup>2)</sup> of  $J^\pi = 2^-$ , while the experimental assignment is  $J^\pi = 1^-$ .

The experiment was carried out using the RIKEN Projectile-fragment Separator, RIPS. A spin-polarized beam of  $^{18}\text{N}$  was obtained from the fragmentation of  $^{22}\text{Ne}$  projectiles at 110 A MeV on a carbon target, by selecting the emission angle and momentum. To facilitate the measurement for such an isotope of low production yield, we developed a new scheme, based on an adiabatic rotation of the holding field, to determine the degree of polarization before the NMR was observed. The experimental setup used is shown in Fig. 1.

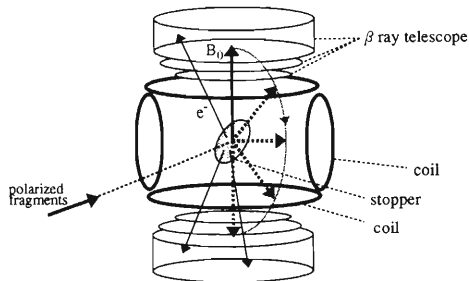


Fig. 1. Experimental setup for the measurement of the fragment polarization by the method of magnetic field rotation. The setup includes two pairs of air-core coils, respectively producing the vertical and horizontal components of a holding field  $B_0$ . The combined  $B_0$  field is rotated by slowly varying the currents in these two pair coils, thus rotating the nuclear spin adiabatically by  $180^\circ$ .

With this scheme, the optimization of the emission angle and momentum for the maximum polarization was made, eventually yielding a  $^{18}\text{N}$  polarization of  $2.2 \pm 0.7\%$  (here the  $\beta$ -asymmetry factor  $A_\beta = -0.37$  was assumed). Then, the  $\beta$ -NMR measurement was

<sup>\*1</sup> Research Laboratory for Nuclear Reactors, Tokyo Institute of Technology

<sup>\*2</sup> The Energy Research Center, Wakasa Bay

successfully performed to determine the electromagnetic moments, as shown in Figs. 2 and 3. The magnetic moment of the  $^{18}\text{N}$  ground state was determined to be  $|\mu| = 0.3279 \pm 0.0017 \mu_N$  and the quadrupole coupling constant in Mg to be  $\left| \frac{eqQ}{h} \right| = 73.2 \pm 1.8 \text{ kHz}$ . From the latter, the electric quadrupole moment of  $^{18}\text{N}$  was deduced as  $|Q| = 12.1 \pm 1.2 \text{ mb}$ , by taking an electric field gradient  $q$  for the N impurity in Mg from Ref. 3. The comparisons of the above obtained  $\mu$  and  $Q$  values with theories will be presented elsewhere.

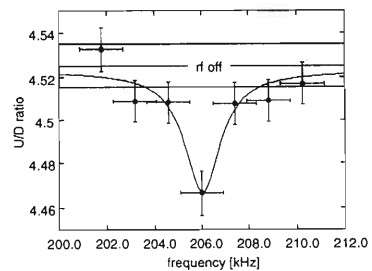


Fig. 2. NMR Spectra obtained for the  $^{18}\text{N}$  implanted in Pt at  $T = 30 \text{ K}$ .

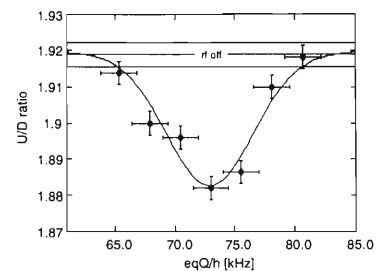


Fig. 3. Result of the measurement of the electric quadrupole coupling constant for the  $^{18}\text{N}$  implanted in a Mg cry stal. The up/down ratio of  $\beta$ -ray intensities is plotted as a function of  $eqQ/h$ .

## References

- 1) W. Olness et al.: Nucl. Phys. A **373**, 13 (1982).
- 2) F. C. Barker et al.: Aust. J. Phys. **37**, 17 (1984).
- 3) T. Minamisono et al.: to be published in Phys. Lett. B.

# Measurements of Half Lives and Neutron Emission Probabilities of the Neutron Drip Line Nuclei $^{19}\text{B}$ , $^{22}\text{C}$ , and $^{23}\text{N}$

K. Yoneda, N. Aoi, H. Iwasaki, H. Sakurai, H. Ogawa, T. Nakamura, W.-D. Schmidt-Ott, M. Schäfer, M. Notani, N. Fukuda, E. Ideguchi, T. Kishida, S. S. Yamamoto, and M. Ishihara

[RADIOACTIVITY  $^{19}\text{B}$ ,  $^{22}\text{C}$ ,  $^{23}\text{N}$ ; Measured  $T_{1/2}$ , Delayed n emission probabilities]

For the past few decades, extensive experimental studies of neutron-rich light nuclei have been performed. However, in the extremely neutron-rich region, some nuclei are still difficult to study experimentally, even concerning the measurement of their half lives, because of their small production rate. Here, the first measurement of half lives and  $\beta$ -delayed neutron emission probabilities of the neutron drip line nuclei  $^{19}\text{B}$ ,  $^{22}\text{C}$ , and  $^{23}\text{N}$  is reported.

The experiment was carried out at RIPS. The nuclei  $^{19}\text{B}$ ,  $^{22}\text{C}$ , and  $^{23}\text{N}$  were produced by projectile fragmentation, using a 95 MeV/nucleon  $^{40}\text{Ar}$  primary beam with an average intensity of 60 pA impinging on a 666 mg/cm<sup>2</sup> Ta target. Each fragment was identified on-line by measuring its time of flight and its energy loss inside of a 0.5 mm thick silicon detector. The typical intensities of  $^{19}\text{B}$ ,  $^{22}\text{C}$ , and  $^{23}\text{N}$  were 0.04, 0.003, and 0.09 cps, respectively. The unstable nuclei were separately implanted into an active stopper, a 12 mm thick plastic scintillator. After the implantation of a nucleus with  $Z \geq 5$ , the primary beam was turned off for 100 ms, a much larger period than the expected half lives, during which the decay of nuclei was measured. The stopper plastic scintillator was used for the detection of  $\beta$  rays emitted from the implanted unstable nuclei. A neutron detector array was placed around the stopper to measure  $\beta$ -delayed neutrons in coincidence with  $\beta$  rays.<sup>1)</sup> The neutron detector consisted of 14 liquid scintillation counters (BC501A) covering a solid angle of about 80% of  $4\pi$ . Neutrons and  $\gamma$  rays were separated by a pulse shape analysis (Fig. 1).

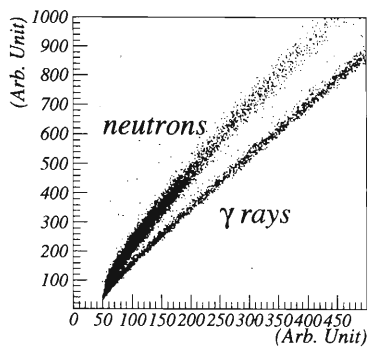


Fig. 1. Separation of the neutrons from  $\gamma$  rays achieved by using  $^{15}\text{B}$ . The vertical axis is the total light output and the horizontal axis is the amount of light being integrated in the first 60 ns.

The energy threshold for the neutrons was set to be 50 keV in electron equivalent energy, which corresponds to about 400 keV in neutron energy. The efficiency obtained was 30%, determined by measuring  $\beta$ -delayed neutrons from the  $^{15}\text{B}$  which has a known neutron emission probability of 100%.<sup>2)</sup>

The decay curves obtained for the nuclei are shown in Fig. 2. The horizontal axis is the time interval between the implantation of one fragment and the detection of the  $\beta$  decay. The values of half lives were deduced from the least-squares fits to the data, assuming a functional form given by an exponential plus a constant background. The preliminary results of the half lives are  $3.3 \pm 0.2$  ms for  $^{19}\text{B}$ ,  $9 \pm 3$  ms for  $^{22}\text{C}$ , and  $14.5 \pm 1.4$  ms for  $^{23}\text{N}$ , with the quoted errors being of statistical origin only.

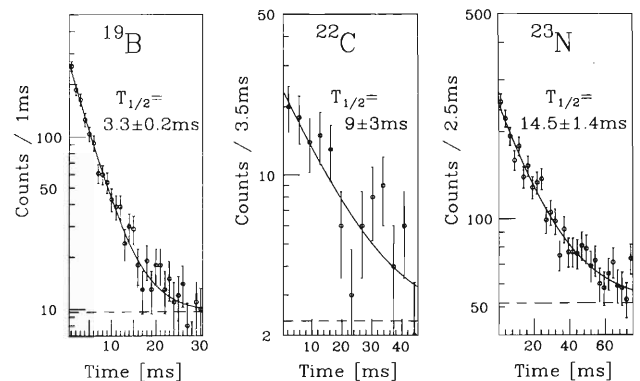


Fig. 2. Preliminary decay curves of  $^{19}\text{B}$ ,  $^{22}\text{C}$ , and  $^{23}\text{N}$ . Solid lines represent best-fit curves and dashed lines do the adopted constant backgrounds.

The values of the neutron emission probabilities were determined from the ratio of the number of detected neutrons to that of  $\beta$  rays, considering the efficiency of the neutron detector array. Tentatively deduced neutron emission probabilities of  $^{19}\text{B}$ ,  $^{22}\text{C}$ , and  $^{23}\text{N}$  are  $125 \pm 32\%$ ,  $99 \pm 39\%$ , and  $80 \pm 21\%$ , respectively. Here, both statistical and systematic errors of the n- $\gamma$  separation are taken into account.

## References

- 1) V. Kunze et al.: Nucl. Instrum. Methods Phys. Res. A **361**, 263 (1995).
- 2) R. Harkewicz et al.: Phys. Rev. C **44**, 2365 (1991).

Lifetime Measurement of  $^{31,32}\text{Ne}$ 

M. Notani, N. Aoi, N. Fukuda, E. Ideguchi, M. Ishihara, H. Iwasaki, H. Ogawa,  
T. Kubo, S. M. Lukyanov, T. Nakamura, Yu. E. Penionzhkevich, H. Sakurai,  
T. Teranishi, Y. X. Watanabe, K. Yoneda, and A. Yoshida

[ NUCLEAR REACTIONS:  $^{181}\text{Ta}(^{40}\text{Ar},\text{X})$ ;  $E(^{40}\text{Ar}) = 95A$  MeV, ]  
[ Half-life measurement of  $^{31,32}\text{Ne}$  ]

Beta-decay half-lives of two very neutron-rich nuclei  $^{31,32}\text{Ne}$  have been measured for the first time. The two nuclei are the heaviest stable neon isotopes observed so far.<sup>1,2)</sup>

The secondary beams of neutron-rich nuclei were produced by the projectile-like fragmentation of a 95A MeV  $^{40}\text{Ar}^{17+}$  beam with a mean intensity of 40.3 pnA. From the preliminary investigation on target dependence of fragment yields,<sup>3,4)</sup> we used a 607 mg/cm<sup>2</sup> thick  $^{181}\text{Ta}$  target. Very neutron-rich nuclei in  $9 \leq Z \leq 11$  were separated by means of the RIKEN Projectile Fragment Separator (RIPS)<sup>5)</sup> with a 221 mg/cm<sup>2</sup> aluminium energy-degrader at the momentum dispersive focal plane, F1.

The identification of the fragments was carried out by means of measurement of time-of-flight (TOF) and energy deposit ( $\Delta E$ ). At the final focal point F3, all the detectors were mounted: a 1 mm thick plastic scintillation counter (PL), two 0.5 mm surface barrier type silicon detectors, and three lithium drift type silicon detectors with thickness of 1, 3 and 1 mm, respectively; plus a 2 mm thick plastic scintillation veto counter. The TOF of fragments between the production target and F3 was obtained from the PL timing and RF signal of the cyclotron. The  $\Delta E$  of heavy ion was obtained from the first two silicon detectors.

This system of detectors was served as both the fragment identification and  $\beta$ -decay measurement. We measured the time interval from the PL timing to the  $\beta$ -ray timing. The last three Li-drift type silicon detectors allowed us to perform the  $\beta$ -ray detection. When the fragments of interest reached the detectors, we suspended the primary beam for 100 ms in order to measure the time intervals and avoid the pile-up of fragments in the meantime. In order to stop the neutron-rich nuclei,  $^{32}\text{Ne}$  and  $^{31}\text{Ne}$ , at the 4th Si detector, the secondary beam energy was reduced with a 3.2 mm aluminium degrader located between 2nd and 3rd silicon detectors.

Figure 1 shows the  $\beta$ -decay curve of  $^{31,32}\text{Ne}$  and their daughter nuclei. We have achieved the  $\beta$ -ray detection efficiency 75% from the sum of time-interval histograms divided by the net number of identified ions. At this experiment, the half-lives of other neutron-rich isotopes  $^{27,29}\text{F}$ ,  $^{29,30}\text{Ne}$  and  $^{31,32,33}\text{Na}$  were reexamined. The measured results of these half-lives are shown in Table 1.

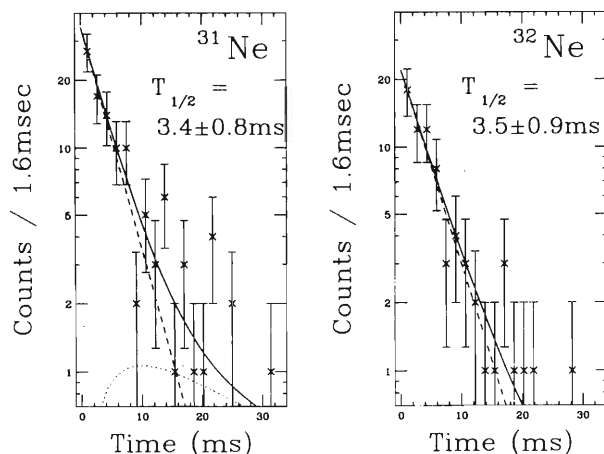


Fig. 1. Time-interval histogram for  $^{31,32}\text{Ne}$ . The solid line is a likelihood fit with sum of two exponential functions. The dashed and dotted lines are drawn as parent and daughter components, respectively.

Table 1. Experimental half-lives in milliseconds.

Nuclei (A,Z)	$T_{1/2}$ [ms]		
	This work	Tarasov <sup>6)</sup>	Table'97 <sup>7)</sup>
$^{27}\text{F}$	$4.9 \pm 0.2$	$5.3 \pm 0.9$	—
$^{29}\text{F}$	$2.6 \pm 0.4$	$2.4 \pm 0.8$	—
$^{29}\text{Ne}$	$15.6 \pm 0.5$	$15 \pm 3$	$200 \pm 100$
$^{30}\text{Ne}$	$5.8 \pm 0.2$	$7 \pm 2$	—
$^{31}\text{Ne}$	$3.4 \pm 0.8$	—	—
$^{32}\text{Ne}$	$3.5 \pm 0.9$	—	—
$^{31}\text{Na}$	$19 \pm 4$	$18 \pm 2$	$17.0 \pm 0.4$
$^{32}\text{Na}$	$11.5 \pm 0.8$	—	$13.2 \pm 0.4$
$^{33}\text{Na}$	$8.5 \pm 0.4$	—	$8.2 \pm 0.4$

## References

- 1) D. Guillemaud-Mueller et al.: Phys. Rev. C **41**, 937 (1990).
- 2) H. Sakurai et al.: Phys. Lett. C **54**, R2802 (1996).
- 3) Y. Doki: JAERI-M 94-028, p. 70; Master thesis, Tokyo University (1994).
- 4) H. Iwasaki et al.: RIKEN Accel. Prog. Rep. **31**, 76 (1998).
- 5) T. Kubo et al.: Nucl. Instrum. Methods Phys. Res. B **70**, 309 (1992).
- 6) O. Tarasov et al.: Phys. Lett. B **409**, 64 (1997).
- 7) G. Audi et al.: Nucl. Phys. A **624**, 1 (1997).

## Coulomb Excitation of $N \sim Z \sim 28$

Y. Yanagisawa, T. Motobayashi, S. Shimoura, Y. Ando, H. Fujiwara, I. Hisanaga, H. Iwasaki, Y. Iwata, H. Murakami, T. Minemura, T. Nakamura, T. Nishio, M. Notani, H. Sakurai, S. Takeuchi, T. Teranishi, Y. X. Watanabe, and M. Ishihara

[ $^{208}\text{Pb}(^{56}\text{Ni}, ^{56}\text{Ni})\gamma^{208}\text{Pb}$ , Coulomb excitation, Deduced  $B(E2)$ ]

Recently, Coulomb excitation at several tens MeV/u has been studied using unstable beam.<sup>1,2)</sup> From the spectroscopic point of view, the electromagnetic excitations are properties useful in studying basic structures of the nuclei. We studied Coulomb excitation of the  $N \sim Z \sim 28$  nucleus such as  $^{56}\text{Ni}$  and  $^{56}\text{Fe}$ , using an unstable beam provided by the RIPS at Riken Ring Cyclotron Facility.

A  $^{208}\text{Pb}$  target of  $285 \text{ mg/cm}^2$  thickness was set in the vacuum at the focal point of the RIPS, and was bombarded by a  $^{56}\text{Ni}$  beam with  $800 \text{ particles s}^{-1}$  intensity. Scattered  $^{56}\text{Ni}$  nuclei were detected by a  $\Delta E$ -E silicon detector telescope placed at 35 cm from the target after passing through a  $50 \mu\text{m}$  thick mylar window. The detected charged particle was identified by the  $\Delta E$ -E method. The excitation to the  $2^+$  state of  $^{56}\text{Ni}$  was identified by measuring the  $\gamma$ -ray deexcitation of the  $2^+$  state in coincidence with the scattered  $^{56}\text{Ni}$  particles.

Fifty-six NaI(Tl) scintillators were placed around the target to detect the  $\gamma$  rays. Each scintillator crystal is of 6 cm square rod with 12 cm in length, coupled with a 5.1 cm  $\phi$  photomultiplier tube. Their energy resolution was typically 7.5% for the 662 keV  $\gamma$  ray. A 0.5 mm thick plastic scintillator was placed in front of the silicon detector telescope to obtain a timing signal providing the coincidence condition with the  $\gamma$ -ray detector. Lead blocks with 20 cm thickness shielded the NaI(Tl) detectors from the spurious  $\gamma$  rays due to nuclear reaction in silicon detector.

Figure 1 shows the  $\gamma$ -ray spectrum for the  $^{56}\text{Ni} + ^{208}\text{Pb}$  inelastic scattering after the doppler shift correction. As clearly seen in the spectrum, a single photopeak at the 2.7 MeV corresponding to the  $2^+ \rightarrow 0^+$  transition has been observed. The total full-energy efficiency was calculated by a simulation code GEANT.

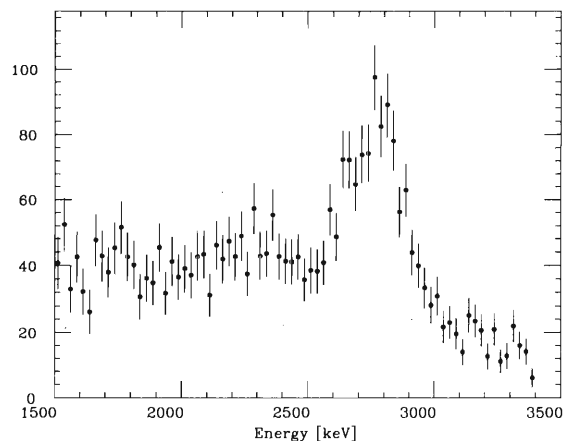


Fig. 1. Doppler-corrected spectrum for  $\gamma$ -ray energy emitted from the inelastic scattering  $^{56}\text{Ni} + ^{208}\text{Pb}$  measured by NaI(Tl) counters.

The excitation cross section was obtained to be  $212 \pm 13 \text{ mb}$ . An experimental deformation parameter  $\beta_C$  was extracted by comparing the predicted cross section, which was calculated by a coupled channel code ECIS88, with the experimental one. Since this parameter  $\beta_C$  is directly related to  $B(E2)$ , The parameter  $\beta_C$  is related to  $B(E2)$  by  $\beta_C = 4\pi\sqrt{B(E2)}/3ZR^2e$ , a  $B(E2)$  value for the  $^{56}\text{Ni}$   $2^+$  excitation was obtainable. The result,  $B(E2 : 0^+ \rightarrow 2^+) = 580 \pm 70 \text{ e}^2\text{fm}^4$ , agrees with the value deduced from an analysis of the  $^{56}\text{Ni} + p$  inelastic scattering<sup>3)</sup> within experimental errors.

### References

- 1) T. Motobayashi et al.: Phys. Lett. B **346**, 9 (1995).
- 2) T. Nakamura et al.: Phys. Lett. B **394**, 11 (1997).
- 3) G. Kraus et al.: Phys. Rev. Lett. B **264**, 1773 (1994).

## Production Cross Sections of Projectile-like Fragments in the $^{40}\text{Ar} + ^{181}\text{Ta}$ Reaction at 94A MeV

H. Iwasaki, N. Aoi, N. Fukuda, E. Ideguchi, M. Ishihara, T. Kubo, T. Nakamura, M. Notani, H. Ogawa, H. Sakurai, T. Teranishi, Y. Watanabe, Y. X. Watanabe, and K. Yoneda

[ NUCLEAR REACTIONS:  $^{181}\text{Ta}(^{40}\text{Ar},X)$ ,  $E(^{40}\text{Ar}) = 94A$  MeV; Measured yields of the isotopes of B, C, N, O, F, Ne, Na, Mg, Al and Si ]

The projectile fragmentation has been one of the main methods for the production of radioactive beams. It was reported that the yields of the neutron-rich isotopes by a 44A MeV  $^{48}\text{Ca}$  beam have a strong dependence on the  $N/Z$  ratio of the target; the  $^{181}\text{Ta}$  target provides larger yields than  $^9\text{Be}$  and  $^{64}\text{Ni}$  targets in the extremely neutron-rich region, if one uses the energy-loss-equivalent production targets.<sup>1)</sup> However, the prediction of the fragment yields by INTENSITY code,<sup>2)</sup> which is based on production cross sections given by an empirical formula EPAX,<sup>3)</sup> does not include such target dependence and overestimates yields.<sup>4)</sup> Therefore we have investigated the fragment yields in the  $^{40}\text{Ar} + ^{181}\text{Ta}$  reaction, and we found the best-fit parameter ( $U$ ) for this specific reaction under the EPAX formalism.

A 94A MeV  $^{40}\text{Ar}$  beam accelerated by the RIKEN ring cyclotron was incident upon a 623 mg/cm<sup>2</sup>  $^{181}\text{Ta}$  target. The reaction products were analyzed by the RIPS spectrometer.<sup>5)</sup> The magnetic rigidity of RIPS was varied in steps in the range 3.02 ~ 4.52 Tm to cover  $2.8 \leq A/Z \leq 4.2$  nuclei. A 2.0 mm thick plastic scintillation counter (PL) and three 0.5 mm thick surface-barrier silicon detectors were set at the first achromatic focus of the RIPS (F2). Particles were identified event-by-event by measuring the time-of-flight (TOF) and the energy loss ( $\Delta E$ ). The TOF of each fragment over 21.3 m flight path between the target position and F2 was determined from the difference of timing signals between RF signal of the cyclotron and the PL. The  $\Delta E$  was independently determined using three silicon detectors. The measured values of TOF and  $\Delta E$ 's were combined to identify the proton number ( $Z$ ) and the mass number ( $A$ ). By using the transmission calculated by the INTENSITY, we deduced the production cross sections from measured yields for the isotopes:  $^{19}\text{B}$ ,  $^{17-20}\text{C}$ ,  $^{20-23}\text{N}$ ,  $^{19-24}\text{O}$ ,  $^{21-29}\text{F}$ ,  $^{24-32}\text{Ne}$ ,  $^{27-33}\text{Na}$ ,  $^{30-35}\text{Mg}$ ,  $^{33-36}\text{Al}$ , and  $^{36}\text{Si}$ , as shown in Fig. 1. In analysis, we chose the  $B\rho$  setting for each nucleus to have the best transmission.

To describes the yield distribution as the functions of  $A$  and  $Z$  of the fragments, the following empirical formula was used in the EPAX,

$$\sigma(A, Z) = Y(A) N \exp(-R |Z_p - Z|^U).$$

The first term  $Y(A)$  gives the mass yield and the second term describes the  $Z$  distribution of the cross sections around the most probable charge ( $Z_p$ ) in each isobar. The parameter  $U$ , which specifies the width

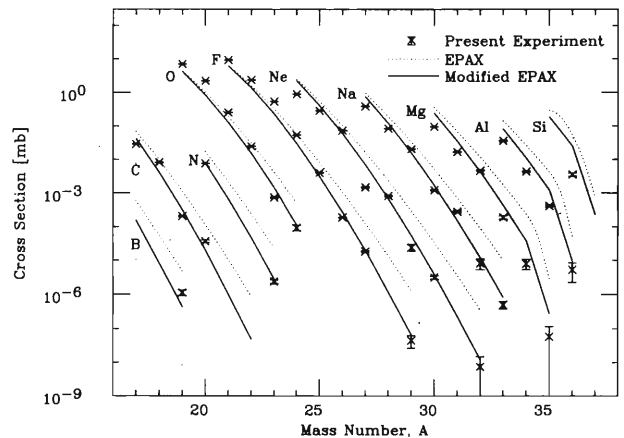


Fig. 1. Production cross sections in the  $^{40}\text{Ar} + ^{181}\text{Ta}$  reaction. The dotted line and solid line are calculated by using EPAX<sup>3)</sup> ( $U = 1.5$ ) and modified EPAX ( $U = 1.6$ ), respectively.

and shape of the  $Z$  distribution of cross sections, is fixed by 1.5 for the neutron-rich side in the EPAX.<sup>3)</sup> However, it was reported in the  $^{40}\text{Ar} + ^9\text{Be}$  reaction at 93.6A MeV that the parameter  $U = 1.7$  gives a better description of the fragment yields.<sup>6)</sup> In the present experiment, we have found that the parameter  $U = 1.6$  describes the yields in the  $^{40}\text{Ar} + ^{181}\text{Ta}$  reaction best, as shown in Fig. 1. The present result as well as the result from Ref. 6 shows that the parameters in EPAX depends on the beam and target combination. It may also indicate the beam energy dependence of  $\sigma(A, Z)$ . Further accumulation of production cross sections under the various projectile-target combinations at various beam energies is necessary.

### References

- 1) D. Guillemaud-Mueller et al.: Phys. Rev. C **41**, 937 (1990).
- 2) J. A. Winger, B. M. Sherrill, and D. J. Morrissey: Nucl. Instrum. Methods Phys. Res. B **70**, 380 (1992).
- 3) K. Sümmer et al.: Phys. Rev. C **42**, 2546 (1990).
- 4) M. Notani et al.: RIKEN Accel. Prog. Rep. **30**, 48 (1997).
- 5) T. Kubo et al.: Nucl. Instrum. Methods Phys. Res. B **70**, 309 (1992).
- 6) Y. Doki: JAERI-M 94-028, p. 70; Master Thesis, Tokyo University (1994).

## Polarized $^{129}\text{Xe}$ Solid for Polarizing Unstable Nuclei

K. Sakai, Y. Mizumura, Y. Uchiyama, T. Suzuki, K. Suzuki, M. Tsuda, A. Yoshimi, H. Ogawa, M. Adachi, K. Asahi, H. Sato, H. Okuno, T. Kubo, A. Yoshida, M. Ishihara, K. Yoneda, M. Notani, S. Fukuda,\* and H. Izumi

[Nuclear magnetic moment,  $^{129}\text{Xe}$  solid stopper]

Measurements of nuclear moments provide useful information in the study of microscopic structure of nuclei far from stability.<sup>1-4)</sup> In such experiments, spin polarization of the objective nuclei plays a key role. We have proposed a new method to produce the spin polarization, which comprises an implantation of unstable nuclei into a highly polarized stopper and subsequent transfer of the host nuclear polarization to unstable nuclei through dipole-dipole interaction. As a polarized stopper, we are developing a polarized  $^{129}\text{Xe}$  solid for which a large spin polarization as well as a long relaxation time can be attained.<sup>5)</sup>

The  $^{129}\text{Xe}$  nuclear spin can be polarized by spin exchange with an optically polarized Rb atom. A cylindrical glass cell, 4 cm long and 2 cm in diameter, is filled with an enriched (79.2%)  $^{129}\text{Xe}$  gas of a partial pressure  $p_{\text{Xe}}$ , a  $\text{N}_2$  gas of 100 Torr, and a small amount of Rb vapor. The cell has a rectangular part ( $8 \times 20 \times 2 \text{ mm}^3$ ) at the bottom, which thermally contacts with the surface of a liquid nitrogen vessel. The inner surface of the cell is coated with SurfaSil<sup>6)</sup> in order to reduce the spin relaxation rate  $\Gamma_w (= 1/T_w)$  due to the collision of a Xe atom with the cell wall. The cell is illuminated by a circularly polarized light from two 15-W AlGaAs diode lasers. We made several cells with the surface coating, among which some exhibited relaxation times as long as  $T_w \approx 24$  min. The maximum  $^{129}\text{Xe}$  gas polarizations ( $P_{\text{gas}}$ ) thus obtained were  $P_{\text{gas}} = 11\%$  at 800 Torr and  $P_{\text{gas}} = 5.6\%$  at 2400 Torr.<sup>7)</sup> They were then cooled down to about 80 K in a liquid nitrogen.

Within 10 min after the cooling was started, about 1/3 (80 mg) of the  $^{129}\text{Xe}$  gas condensed into a solid. Typical polarization measured for such a solid was

$P_{\text{solid}} = 1\%$ , amounting to about 1/4 of the gas-phase polarization, measured before freezing. A possible explanation of this relatively large loss of polarization during the freezing process is the relaxation in gas phase because of the relatively long condensing time. The relaxation time  $T_1$  of the polarized solid was measured under 10 to 60 mT. The longest value  $T_1 \sim 25$  min was observed at the highest field strength 60 mT. According to literature,<sup>5-8)</sup>  $T_1 \sim 25$  min implies that the solid was at around 120 K.  $T_1 \sim 160$  min would be achieved by lowering the temperature of the solid to about 77 K.

Our experimental result for a polarized solid  $^{129}\text{Xe}$  suggested that the problems of large polarization loss during freezing and of short  $T_1$  in solid would be solved by cooling to a lower temperature and in a shorter time. In order to realize these, we made a slight change in the setup improving the heat contact between the cell and the liquid nitrogen vessel. As a result, almost the entire part of 2400 Torr ( $\sim 240$  mg) of  $^{129}\text{Xe}$  gas condensed within 5 min after liquid nitrogen was poured into the vessel. We expect that the polarization loss and  $T_1$  will be much improved in this condition. The measurements are in progress.

### References

- 1) H. Okuno et al.: Phys. Lett. B **354**, 41 (1995).
- 2) H. Izumi et al.: Phys. Lett. B **336**, 51 (1995).
- 3) H. Ueno et al.: Phys. Rev. C **53**, 2142 (1996).
- 4) K. Asahi et al.: Nucl. Phys. A **588**, 135c (1995).
- 5) M. Gatzke et al.: Phys. Rev. Lett. **70**, 690 (1993).
- 6) X. Zeng et al.: Phys. Lett. **96A**, 191 (1983).
- 7) H. Sato et al.: RIKEN Accel. Prog. Rep. **30**, 64 (1997).
- 8) C. D. Cates et al.: Phys. Rev. Lett. **65**, 2591 (1990).

\* The Energy Research Center, Wakasa Bay

## Coulomb Dissociation of $^8\text{B}$ at 254 MeV/u

N. Iwasa, K. Sümmerer,<sup>\*1</sup> F. Boué,<sup>\*1</sup> G. Surowka,<sup>\*1</sup> P. Senger,<sup>\*1</sup> P. Koczon,<sup>\*1</sup> E. Schwab,<sup>\*1</sup> H. Geissel,<sup>\*1</sup>  
 M. Hellström,<sup>\*1</sup> F. Laue,<sup>\*1</sup> A. Surowiec,<sup>\*1</sup> T. Baumann,<sup>\*1</sup> W. Schwab,<sup>\*1</sup> A. Ozawa, E. Grosse,<sup>\*1</sup>  
 A. Förster,<sup>\*2</sup> H. Oeschler,<sup>\*2</sup> C. Sturm,<sup>\*2</sup> F. Uhlig,<sup>\*2</sup> A. Wagner,<sup>\*2</sup> B. Kohlmeyer,<sup>\*3</sup>  
 J. Speer,<sup>\*3</sup> B. Blank,<sup>\*4</sup> C. Marchand,<sup>\*4</sup> M. S. Pravikoff,<sup>\*4</sup> S. Czajkowski,<sup>\*4</sup>  
 R. Kulesa,<sup>\*5</sup> W. Walus,<sup>\*5</sup> T. Motobayashi, T. Teranishi, and M. Gai<sup>\*6</sup>

[ $^{208}\text{Pb}(^8\text{B},\text{p } ^7\text{Be})^{208}\text{Pb}$ , Coulomb dissociation]

The  $^7\text{Be}(p,\gamma)^8\text{B}$  reaction at low energy is of crucial importance for predicting the high-energy solar-neutrino flux relevant to the “solar neutrino problem”, defined as a serious discrepancy between the measured and predicted neutrino fluxes.<sup>1)</sup>

Recently, Motobayashi et al. succeeded to measure the  $^7\text{Be}(p,\gamma)^8\text{B}$  cross section at  $E_{\text{C.M.}} = 600\text{--}1700$  keV from the Coulomb dissociation of  $^8\text{B}$  into  $^7\text{Be}$  and proton at  $E(^8\text{B}) = 46.5$  MeV/u.<sup>2)</sup> The result demonstrated that the Coulomb dissociation process is an alternative method for studying the  $^7\text{Be}(p,\gamma)^8\text{B}$  reaction. However, for more precise measurement of the  $^7\text{Be}(p,\gamma)^8\text{B}$  cross section, experimental information on E2 and M1 admixtures to the dominant E1 amplitude is desired.

We have studied the Coulomb dissociation process at  $E(^8\text{B}) = 254$  MeV/u to extract information on the M1 admixture experimentally, and to obtain the  $(p,\gamma)$  cross section at low center-of-mass energies down to the 100 keV region with a higher statistical accuracy. A radioactive  $^8\text{B}$  beam provided by the fragment separator at GSI impinged on an enriched  $^{208}\text{Pb}$  target with a thickness of 200 mg/cm<sup>2</sup>. The reaction products,  $^7\text{Be}$  and proton, were analyzed by the KaoS Spectrometer (KaoS)<sup>3)</sup> which has a large momentum acceptance ( $\Delta p/p \approx 200\%$ ). For track reconstruction of the two charged particles,  $^7\text{Be}$  and proton, before entering the KaoS magnet, two sets of two-dimensional position-sensitive device were installed at approximately 14 and 31 cm downstream of the target. Each device consisted of x- and y-projection silicon micro-strip detectors. Each micro-strip detector had a thickness of 300  $\mu\text{m}$ , an active area of  $56 \times 56$  mm<sup>2</sup>, and a strip pitch of 0.1 mm. This configuration enabled us to measure emission angles with an accuracy of 0.9 mrad, as well as vertex points of the two charged particles. By using the vertex information, a large amount of background events produced in the matters other than the target was eliminated. The particle’s momenta were analyzed by trajectory reconstruction in the KaoS by using position information from the strip detectors and

two multi-wire proportional chambers (MWPC; one for proton and the other for  $^7\text{Be}$ ) placed at approximately the focal plane of the KaoS. Thirty plastic scintillators were placed just behind the MWPC’s for producing trigger conditions to the data acquisition system.

The p- $^7\text{Be}$  coincidence yields are plotted in Fig. 1 as a function of p- $^7\text{Be}$  relative energy. The solid (dashed) histogram represents the E1+M1 (pure E1) yield estimated by Monte Carlo simulations. The continuum-E1 and resonant-M1 direct-capture cross sections measured by Filippone et al.<sup>4)</sup> and Vaughn et al.<sup>5)</sup> were used in the simulations. The cross sections are renormalized with the resonant  $^7\text{Li}(d,p)^8\text{Li}$  cross section,  $157 \pm 10$  mb. The shape and magnitude of the experimental energy dependence are fairly well-described by the simulated results. Because of low background condition, the  $^7\text{Be}(p,\gamma)^8\text{B}$  cross sections at 150–2950 keV are expected to be determinable from this experiment. Further analysis is in progress.

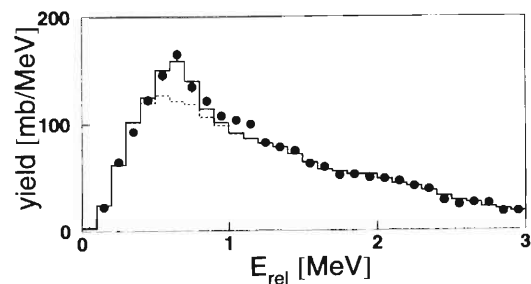


Fig. 1. The p- $^7\text{Be}$  coincidence events plotted as a function of relative energy shown by filled circles. The solid (dashed) histogram represents the E1+M1 (E1) amplitudes predicted by Monte Carlo simulations.

### References

- 1) J. N. Bahcall and M. H. Pinsonneault: *Rev. Mod. Phys.* **64**, 885 (1992).
- 2) T. Motobayashi et al.: *Phys. Rev. Lett.* **70**, 2680 (1994); N. Iwasa et al.: *J. Phys. Soc. Jpn.* **65**, 1256 (1996).
- 3) P. Senger et al.: *Nucl. Instrum. Methods Phys. Res. A* **327**, 393 (1993).
- 4) B. W. Filippone et al.: *Phys. Rev. C* **28**, 2222 (1983).
- 5) F. J. Vaughn et al.: *Phys. Rev. C* **2**, 1657 (1970).

<sup>\*1</sup> GSI, Germany

<sup>\*2</sup> Technische Hochschule Darmstadt, Germany

<sup>\*3</sup> Universität Marburg, Germany

<sup>\*4</sup> CEN Bordeaux, France

<sup>\*5</sup> Jagellonian University, Poland

<sup>\*6</sup> University of Connecticut, U.S.A.

## Measurement of Interaction Cross Sections for Light Neutron Rich Nuclei

A. Ozawa, K. Suemmerer,<sup>\*1</sup> O. Bochkarev,<sup>\*2</sup> L. Chulkov,<sup>\*2</sup> D. Cortina,<sup>\*1</sup> H. Geissel,<sup>\*1</sup> M. Hellsröm,<sup>\*1</sup>  
M. Ivanov,<sup>\*3</sup> R. Janik,<sup>\*3</sup> K. Kimura, T. Kobayashi, A. Korshennikov, G. Muenzenberg,<sup>\*1</sup> F. Nickel,<sup>\*1</sup>  
A. Ogloblin,<sup>\*2</sup> M. Pfutzner,<sup>\*1</sup> V. Pribora,<sup>\*2</sup> C. Scheidenberger,<sup>\*1</sup> H. Simon,<sup>\*1</sup> B. Sitar,<sup>\*3</sup>  
T. Suzuki, P. Strmen,<sup>\*3</sup> I. Tanihata, M. Winkler,<sup>\*1</sup> and K. Yoshida

[ NUCLEAR REACTIONS;  $^{40}\text{Ar}+\text{Be}$ ,  $E \sim 1 A \text{ GeV}$ ; Secondary beams;  
 $\sigma_I$  ( $^{17,19}\text{B}$ ,  $^{12-20}\text{C}$ ,  $^{14-23}\text{N}$ ,  $^{16-24}\text{O} + \text{C}$ ) ]

The recent development of radioactive nuclear beams provides new measurements of the radii of unstable nuclei at the relativistic energy.<sup>1,2</sup> It is important to extend the measurement of interaction cross sections ( $\sigma_I$ 's) and the determination of radii, so that we can view the isotope, isospin, and energy dependences of the radii over a wide region in the nuclear chart. The above systematics over a wide region makes it possible to search for the new nuclei having an anomalous structure, such as a halo and/or skin.

We have measured the  $\sigma_I$ 's for light neutron rich nuclei, so called  $p$ - $sd$  shell region, by using FRagment Separator (FRS) facility at GSI. Figure 1 shows the schematic view of the FRS and our experimental setup. The setup was almost identical to the previous experiment,<sup>2</sup> except for using Time Projection Chambers (TPC's) developed at Comenius University in Slovak Republic,<sup>3</sup> instead of the conventional MultiWire Proportional Chambers (MWPC's).

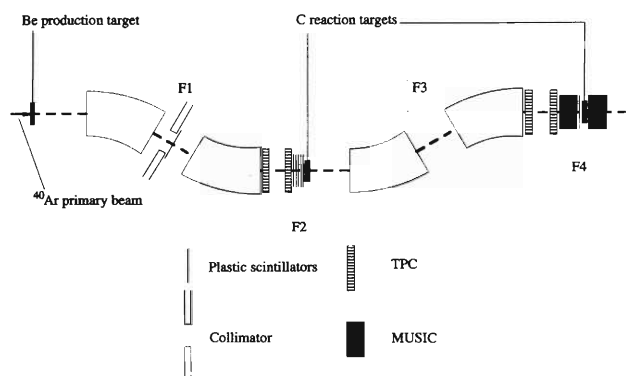


Fig. 1. Experimental setup at FRS in GSI.

The secondary beams of radioactive isotopes  $^{17,19}\text{B}$ ,  $^{12-20}\text{C}$ ,  $^{14-23}\text{N}$ , and  $^{16-24}\text{O}$  were produced through

the projectile fragmentation of an  $^{40}\text{Ar}$  primary beam (approximately  $1 A \text{ GeV}$ ) accelerated by the heavy-ion synchrotron (SIS) at GSI. The secondary beams produced in a Be target located at the entrance of FRS were separated by their rigidities at F1, then guided to reaction targets located at F2. Individual nucleus was identified by its Time Of Flight (TOF) (between F1 and F2) and  $dE/dx$ . The  $\sigma_I$ 's were measured by means of a transmission method with carbon (C) reaction targets at a mean energy of around  $950 A \text{ MeV}$ . Two kinds of reaction targets different in thickness (one  $\sim 5.5 \text{ g/cm}^2$  and another  $\sim 11 \text{ g/cm}^2$ ) were used in order to estimate systematical errors for the measurements.

Downstream of the reaction targets, non-interacted nuclei were guided through F3 to F4. These nuclei were identified again by their TOF (between F2 and F4) and  $dE/dx$ . Now that we measured the non-interacted nuclei at F4, we need to know the transmission of the non-interacted nuclei from F2 to F4. The transmission depends on the position and direction of the nuclei at F2. Thus, in order to measure them at F2 event-by-event, we put two TPC's upstream of the reaction targets, that served X and Y positions and the directions for the nuclei. We also put an additional reaction target (a  $\sim 2.3 \text{ g/cm}^2$  thick C) at F4 and measured  $dE/dx$  after the target. By this setup we have simultaneously measured the charge changing cross sections at F4, which can give the maximum size of the charge matter radii.<sup>4</sup>

Analysis is now in progress.

### References

- 1) I. Tanihata et al.: Phys. Rev. Lett. **55**, 2676 (1985).
- 2) T. Suzuki et al.: Phys. Rev. Lett. **75**, 3241 (1995).
- 3) T. Baumann et al.: Acta Physica Universitatis Comenianae **37**, 3 (1996).
- 4) O. Bochkarev et al.: Z. Rhys. A, in press.

\*1 GSI, Darmstadt, Germany

\*2 Kurchatov Institute, Moscow, Russia

\*3 Comenius Univ., Bratislava, Slovak Republic



## 2. Atomic and Solid-State Physics

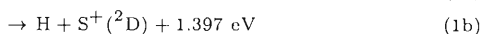
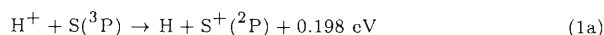


## Electron Capture in Collisions of $H^+$ Ions with S Atoms and Its Reverse Process below keV-Energies

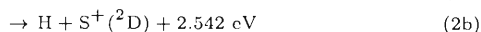
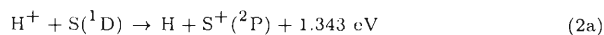
M. Kimura, T. Watanabe, H. Sato, I. Shimamura, J.-P. Gu,\* G. Hirsch,\* and R. J. Buenker\*

The distribution of ionic states of atomic elements provides important information for diagnoses of the ionic structure in the interstellar gas, solar corona, and planetary nebulae.<sup>1)</sup> Also, it is essential in designing and operating controlled thermonuclear fusion devices based on the confined hot plasma.<sup>2)</sup> Standard models which describe forbidden lines of neutral carbon and sulfur underestimate the intensities of the observed [C I] and [S I] lines, and it has been proposed that inclusion in the models of charge transfer reactions with atomic hydrogen may account some parts of the discrepancies,<sup>3)</sup> i.e.,

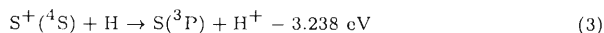
(i) ground atom:



(ii) excited atom:



(iii) capture by  $S^+$  ions:



Butler and Dalgarno<sup>4)</sup> estimated the capture rate coefficient at a temperature of  $1 \times 10^4$  K and found that the process is slow with a rate coefficient of the order of less than  $10^{-15}$   $\text{cm}^3/\text{s}$ . To the best of our knowledge, there is no rigorous experimental attempt to study the capture process of this system at low to intermediate energies, and capture cross sections are needed urgently.

In present, the *ab initio* potential curves and nonadiabatic coupling matrix elements for the  $HS^+$  system are obtained from multireference single- and double-excitation configuration interaction (MRD-CI) calculations employing a relatively large basis set. A semi-classical molecular orbital expansion method with a straight-line trajectory of the incident ion was employed to study the collision dynamics below 10 keV. A set of first-order coupled equations was solved numerically to obtain scattering amplitudes for transitions. The molecular states included in the dynamical calculations are the three sets of states as shown in Fig. 1: (i) triplets;  $[H + S^+(^2P)]$  ( $1^3\Sigma^+$ ,  $2^3\Pi$ ) and  $[H + S^+(^2D)]$  ( $2^3\Sigma^-$ ,  $1^3\Pi$ ) states for electron capture from the initial ground states  $[H^+ + S(^3P)]$  ( $3^3\Sigma^+$ ,  $3^3\Pi$ ), (ii) singlets;  $[H + S^+(^2P)]$  ( $1^1\Sigma^+$ ,  $2^1\Pi$ ) and  $[H + S^+(^2D)]$  ( $1^1\Pi$ ) states for electron capture from the initial excited  $[H^+ + S(^1D)]$  ( $2^1\Sigma^+$ ,  $3^1\Pi$ ) states, and (iii) the molecular states included for the  $[H + S^+(^4S)]$  collision system are:  $[H + S^+(^4S)]$  ( $1^3\Sigma^-$ ) for the initial, and  $[H^+ + S(^3P)]$  ( $3^3\Sigma^-$ ) state for charge transfer, and  $[H + S^+(^2D)]$  ( $2^3\Sigma^-$ ) state for excitation.

\* Theoretische Chemie, Universitaet Wuppertal, Wuppertal, Germany

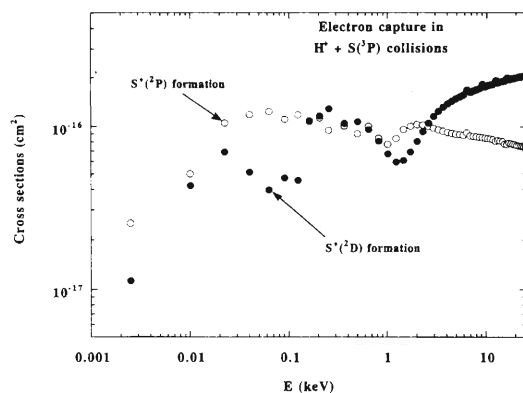


Fig. 1. Electron capture cross sections for the  $H^+ + S(^3P)$  collisions. Solid circles represent the  $S^+(^2D)$  formation and open circles are for the  $S^+(^2P)$  formation.

The spin-averaged electron capture cross section from the ground state  $S(^3P)$  atoms by  $H^+$  impact is illustrated in Fig. 1, as an example. A few interesting features are seen, and they include: (i) both electron capture cross sections to the  $[H + S^+(^2P)]$  and  $[H + S^+(^2D)]$  states increase rapidly as the collision energy increases from 10 eV, with a slightly larger magnitude for the  $[H + S^+(^2P)]$  formation, (ii) the cross sections to these two states show slight out-of-phase oscillatory structures at intermediate energies from 30 eV to 2 keV region, indicating rather strong interference between these two channels, (iii) above 3 keV, the electron capture to  $[H + S^+(^2D)]$  becomes dominant in magnitude over that of  $[H + S^+(^2P)]$ , even though the asymptotic energy defect is larger. This is because the  $\Sigma - \Sigma$  radial coupling between the initial and  $2^3\Sigma^-$  state becomes more effective in this energy domain, resulting in a larger flux population in the  $\Sigma$  state, and (iv) the  $[H + S^+(^2P)]$  state formation begins to show a slight decrease beyond  $E = 2$  keV because of the less effective  $\Pi - \Pi$  radial coupling being the sole driving force in this energy region. Between 0.2 and 1.0 keV, both cross sections are similar in magnitude and in energy dependence, causing a strong mixing between the two channels, and their magnitudes are found to exceed the value of  $10^{-16}$   $\text{cm}^2$ .

### References

- 1) J. B. Kingdon and G. J. Ferland: *Astrophys. J. Suppl. Ser.* **106**, 205 (1996).
- 2) J. W. Gallagher, B. H. Bransden, and R. K. Janev: *J. Phys. Chem. Ref. Data* **12**, 873 (1983).
- 3) D. Pequignot, S. M. V. Aldrovani, and G. Stasinska: *Astron. Astrophys.* **58**, 411 (1978).
- 4) S. E. Butler and A. Dalgarno: *Astron. Astrophys.* **85**, 144 (1980).

## Theoretical Attempt for Double Ionization of Helium by Energetic Charged-Particle Impact

Y. Kawabata,\* K. Hino, N. Miyashita,\* S. Watanabe, and M. Matsuzawa

[Double ionization of helium]

We report the present status of the investigation underway in our group on the double ionization process of a helium atom due to impact of energetic charged-particles such as proton, anti-proton and other various multiply-charged ions. A great deal of attention was paid about a decade ago on the experimental evidences for significant roles of the electron correlation effect of helium during the dynamic processes, resulting marked differences between cross sections by proton impact and those by anti-proton impact. While there were a number of follow-up studies from both theoretical and experimental sides, the deeper understandings are still required. Most of theoretical works rely just on perturbation approximations based on the independent-particle models for double-continuum states of helium and are thus incapable of providing quantitative understandings of the processes. (Although only the so-called forced impulse approximation well reproduces the relative values of the observed quantities, its predictions for the absolute values considerably underestimate the experimental results and its theoretical structure seems vague and complicated.) Aside from a theoretical framework of how to deal with the collision dynamics, the way of incorporating the substantial electron correlation interactions with the target wavefunctions of double continuum dominates the qualities of theory for the problem.

Our basic strategy is the full employment of the hyperspherical coordinate method for incorporating the things mentioned above effectively into theory. It has resulted a great success in reproducing the measured cross sections of the electron-emission spectra due to autoionization from lower-lying doubly-excited states of helium caused by proton impact.<sup>1)</sup> Here, the continuum basis functions introduced in the close-coupling (CC) equations for the time-propagation of collision dynamics were the accurate eigenfunctions of the helium autoionizing states, and they are discretized suitably based on the wave-packet description. For the double ionization processes, however, such frameworks encounter numerical difficulties that the enormous number of basis functions would be needed to express the double continuum states accurately, which are composed of infinite numbers of open channels, up to the relatively higher-energy region of emitted

electrons. Thus the resulting CC equations seem intractable.

In order to remedy these problems, the following manipulations will be adopted. First of all, instead of using as basis functions the exact wave functions of helium for continuum states, as done in the above-mentioned autoionization spectra, an advantage is made of a more tractable set of discrete eigenfunctions of a model Hamiltonian, which provides the hyperspherical adiabatic potentials with the infinite barriers artificially placed at a relatively large distance. The discrete variable representation<sup>2)</sup> is suitable for constructing the wave functions of the model Hamiltonian. These wavefunctions remain well-correlated. It is also expected that they serve to reduce, to some extent, the number of basis functions to be incorporated into the CC equations, since only a single wave function is assigned to each grid of energy spectra, differing much from the real wave functions adopted before.

However, neither the basis functions fabricated here nor the obtained coefficient vectors of the CC equations satisfy the correct scattering boundary conditions for ionizing states. This is a price for the present manipulation. In order to satisfy the conditions properly, we enforce the operation of projecting on the coefficient vectors a complete set consisting of wave functions of a real helium rather than a model helium, which already satisfies the suitable boundary conditions. This procedure is equivalent to transform the coefficient vectors by the overlap matrices between wavefunctions of real Hamiltonian and those of the model one, although the matrices are not always unitary. The *ab initio* calculations of double ionization cross sections of helium induced by the impact of charged-particles are in progress along this direction.

One of the authors (K. H.) acknowledges the financial support by Matsuo Foundation to the present work.

### References

- 1) T. Morishita et al.: Phys. Rev. A **53**, 2345 (1996), and other references therein.
- 2) A. S. Dickinson and P. R. Certain: J. Chem. Phys. **49**, 4209 (1968).

\* Department of Applied Physics and Chemistry, University of Electro-Communications

# Superexcited States of the Hydrogen Molecule

S. Uramoto, H. Sato, and I. Shimamura

Doubly excited states of molecules play an important role in various phenomena such as photoionization, photodissociation, and dissociative attachment and vibrational excitation in electron collisions with molecular ions. In other words, these processes can occur through doubly excited states, which often leads to fine structures in the cross sections as a function of energy. Many calculations and experiments have been performed for doubly excited Rydberg series of superexcited states of the hydrogen molecule  $H_2$ . These states lie above the ionization threshold, and the Rydberg series converging to the  $2p\sigma_u$  ( $2p\pi_u$ ) state of  $H_2^+$ , which is the second (third) ionization threshold of  $H_2$ , are called  $Q_1$  ( $Q_2$ ) series. Unfortunately, the calculations of the higher members of the  $Q_1$  and  $Q_2$  series are scarce because of the computational complexity. The present work is devoted to such calculations in the Born-Oppenheimer approximation based on the Feshbach projection operator.

As for the molecular orbitals for these calculations of doubly excited  $H_2$ , we need both low-lying and high-lying states of  $H_2^+$ . Bound-state calculations are normally performed by using the Slater-type or Gaussian-type orbitals centered on each of the two nuclei as basis functions. For accurate calculations of high-lying states, however, these basis functions are physically inappropriate and computationally inconvenient, causing a linear dependence if many of them are to be included in the basis set. To remedy this difficulty we have used a set of orthogonal functions involving Sonine polynomials and centered not only on the nuclear positions but also on the center of mass of the nuclei. In other words, we have used three-center functions.

The calculated potential energy curves  $1s\sigma_g$  and  $6d\sigma_g$  of  $H_2^+$  are compared quite favorably with the exact numerical results in Fig. 1. Figure 2 shows some doubly excited  $Q_2$  states  $^1\Sigma_g^+(i)$  ( $i = 1 - 5$ ) of  $H_2$  calculated by using  $n\sigma_g$ ,  $n\sigma_u$ ,  $n\pi_g^\pm$ ,  $n\pi_u^\pm$ ,  $n\delta_g^\pm$ ,  $n\delta_u^\pm$  ( $n = 1 - 10$ ) orbitals. The lowest of these states was calculated by Guberman<sup>1)</sup> by using a less elaborate trial function than the present work, but the agreement with the present result is reasonable. Calculations of higher states are not found in the literature.

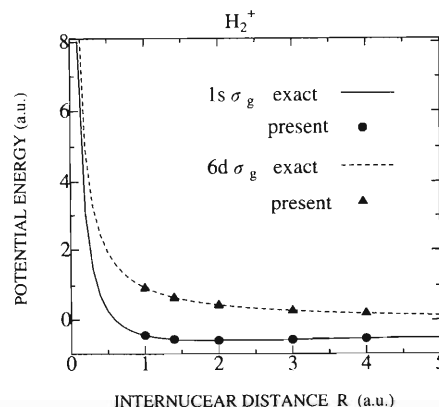


Fig. 1. Potential energy curves, including the nuclear repulsion term, of the  $1s\sigma_g$  and  $6d\sigma_g$  states of  $H_2^+$ .

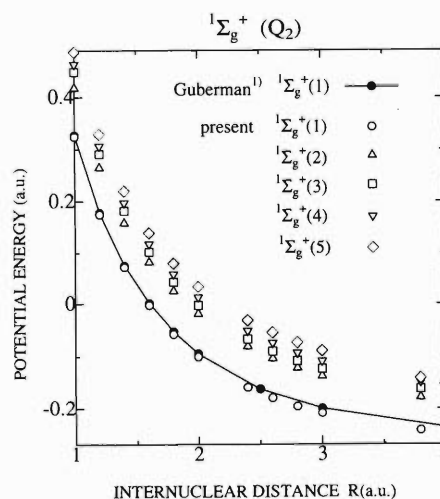


Fig. 2. Calculated potential energy curves of the five lowest members of the doubly excited superexcited  $Q_2$  states  $^1\Sigma_g^+(i)$  ( $i = 1 - 5$ ) of  $H_2$ . The result for the lowest state is compared with Guberman's results.<sup>1)</sup>

## References

- 1) S. L. Guberman: J. Chem. Phys. **78**, 1404 (1983).

# Theoretical Study of Electron Scattering from CH<sub>2</sub>F<sub>2</sub> Molecules

T. Nishimura

Here we report our theoretical work on the vibrationally elastic scattering of electrons from CH<sub>2</sub>F<sub>2</sub> molecules (C<sub>2v</sub> point group). This is an extension of our previous work on the electron-molecule collision system.<sup>1)</sup> No elaborate study for this system has been published so far. In a practical point of view, the data of the e+CH<sub>2</sub>F<sub>2</sub> system are in great demand because of the application to the plasma processing in the semiconductor industry.

The present calculation is based on the fixed-nuclei approximation. In order to properly consider the molecular symmetry, the wavefunction of scattered electron  $F$  is expanded in terms of the symmetry-adapted angular basis functions  $X_{l\nu}^\nu$  as follows:

$$F(\mathbf{r}) = \frac{1}{r} \sum_{l\nu} f_{l\nu}(r) X_{l\nu}^\nu(\hat{\mathbf{r}}), \quad (1)$$

where  $\mathbf{r}$  denotes the position vector of the incident electron. The index  $\nu$  stands for indices collectively specifying an irreducible representation (IR) and those distinguishing the degenerated members of the same  $l$  and IR. The interaction between an electron and a target molecule is represented by a local potential, which is constituted of the electrostatic, electron exchange and correlation-polarization terms. All of the terms depend only on the electron density of the target molecule. In a manner similar to Eq. (1), the interaction potential  $V$  is expanded as

$$V(\mathbf{r}) = \sum_{\lambda\mu} V_{\lambda\mu}(r) X_{\lambda\mu}^\mu(\hat{\mathbf{r}}). \quad (2)$$

Then, the radial part  $f(r)$  in Eq. (1) satisfies a set of coupled differential equations:

$$\left\{ \frac{d^2}{dr^2} - \frac{l(l+1)}{r^2} + k^2 \right\} f_{l\nu}(r) = 2 \sum_{l'\nu'} \langle l\nu | V | l'\nu' \rangle f_{l'\nu'}(r), \quad (3)$$

where

$$\langle l\nu | V | l'\nu' \rangle = \int d\hat{\mathbf{r}} X_{l\nu}^{\nu*}(\hat{\mathbf{r}}) V X_{l'\nu'}^{\nu'}(\hat{\mathbf{r}}). \quad (4)$$

By solving Eq. (3) with an appropriate boundary condition, we obtain the scattering matrix. Since differential cross section (DCS) represented by the partial-wave expansion converges very slowly for a polar molecule, the Born-closure formula<sup>1)</sup> is employed to sum over the higher partial waves. The contribution from these partial waves to the resulting DCS is dominated by the electron-dipole interaction. The dipole interaction can be calculated by means of the first Born

formula which involves in the rotational state of the target molecule.

The present calculation of the target wavefunction was made at an equilibrium geometry. In order to obtain the electron density of molecule, we used the molecular orbital code *GAMESS*<sup>2)</sup> in the self-consistent-field approximation. In the expansion of Eq. (2), we retained the terms up to  $\lambda = 40$ . The coupled equations (3) were solved with inclusion of partial waves up to  $l = 20$ . The DCS was calculated in the region of the collision energies from 5 to 30 eV.

Figure 1 shows the DCS at 20 eV as a representative result. The agreement between the theory and the experiment<sup>3)</sup> is generally good. It should be noted that the DCS has a very sharp peak in the forward direction, which makes it difficult to extrapolate the measured DCSs toward the forward direction. The present DCS would be helpful in compensating the uncertainty of the experimental data. In order to obtain the relevant integral cross sections (ICSs) theoretically, however, the rotational-state population should be taken into account, especially in the case of a polar molecule due to the strong dependence of the forward scattering caused by the dipole interaction on the ICS. The calculation of the ICSs is under way.

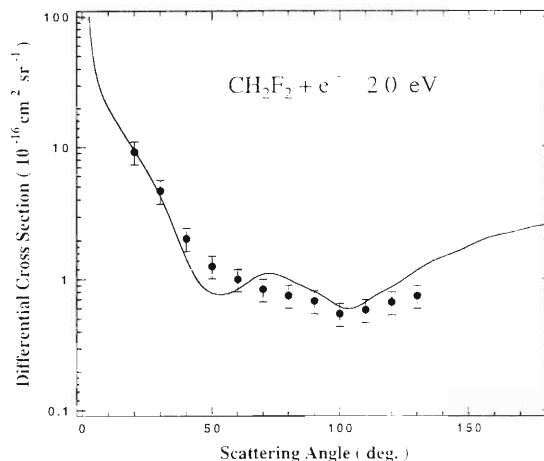


Fig. 1. Differential cross section (in  $10^{-16} \text{ cm}^2 \text{ sr}^{-1}$ ) for the elastic scattering of electrons from CH<sub>2</sub>F<sub>2</sub> at the collision energy of 20 eV. The present calculation (full curve) is compared with the experiment by Masai (filled circles with error bars).<sup>3)</sup>

## References

- 1) Y. Okamoto et al.: J. Phys. B **26**, 745 (1993).
- 2) M. W. Schmidt et al.: J. Comp. Chem. **14**, 1347 (1993).
- 3) T. Masai: Master thesis (Sophia Univ. 1997), p. 44.

## Fluorination Effects in Electron Scatterings from $\text{CH}_4$ , $\text{CH}_3\text{F}_1$ , $\text{CH}_2\text{F}_2$ , $\text{CH}_1\text{F}_3$ , and $\text{CF}_4$

H. Tanaka,\* T. Masai,\* M. Kimura, T. Nishimura, and I. Shimamura

Due to basic interests of their own fundamental natures of molecular electronic structure and scattering process as well as vast applications in plasma chemistry and material sciences, a study on the elastic and inelastic processes of electron scattering from methane and fluoromethanes ( $\text{CH}_4$ ,  $\text{CH}_3\text{F}_1$ ,  $\text{CH}_2\text{F}_2$ ,  $\text{CH}_1\text{F}_3$ , and  $\text{CF}_4$ ) has become increasingly important in recent years, and thus has attracted a great deal of interests.<sup>1)</sup> Comparative studies of electronic structure and scattering process from  $\text{CH}_4$  to  $\text{CF}_4$  by replacing a H atom in a methane molecule with a F atom would provide much deeper insight for basics of atomic and molecular physics in hydrocarbons and their dynamical interaction mechanisms. Furthermore, a set of cross section data for electron scattering from partially fluorinated-methane gases are urgently needed in plasma processing, material sciences and earth sciences since these molecules, which have a shorter-life time than that of the  $\text{CF}_4$  in the atmosphere, are considered to be "environmental acceptable, next generation plasma processing gases".<sup>2)</sup> Although there have been earlier studies for these systems by using the electron energy-loss techniques to identify electronic states<sup>3)</sup> as well as by theoretical approaches for  $\text{CH}_4$  and  $\text{CF}_4$ .<sup>4)</sup> However, no complete study based on electron scattering elastic differential cross sections (DCS's), important objective for a detailed and high-precision study, has been carried out to date to the best of our knowledge. Therefore, as a series of studies, we have initiated the present joint experimental and theoretical investigation for any signature of the fluorination effect in these molecules on DCS's in the energy range from 0.7 to 100 eV, which may possess wider potentials for further understanding of interactions and for possible application for molecular structure analysis.

Figure 1 presents an example of elastic DCS's observed for all molecules at 30 eV. We tentatively classify the molecules treated here into two groups for the later discussion, (i) one for ( $\text{CH}_4$  and  $\text{CF}_4$ ); non-polar molecules, and (ii) another for ( $\text{CH}_3\text{F}_1$ ,  $\text{CH}_2\text{F}_2$ , and  $\text{CH}_1\text{F}_3$ ); polar molecules.

Salient features in the present results are summarized here: (a) At 1.5 eV, DCS's for the class (i) show an increasing trend at small angles below  $70^\circ$ , while those for the class (ii), i.e., all partially F-substituted (polar) methanes, rapidly grow to result in strong forward peaks: typical characteristics of the long-range interaction, (b) At larger angles above  $100^\circ$ , these two classes of molecules show again a deviation in DCS's causing less strong backward scattering for the class (i), (c) At 30 eV, the sharp forward peaking in DCS's at small angle scattering below  $50^\circ$  is very similar to all molecules, indicating less effective dipole-effect at this energy, (d) Within each class of molecules, DCS's

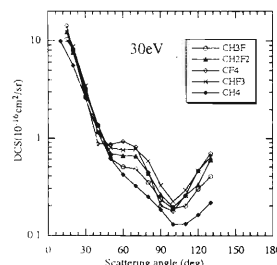


Fig. 1. Experimental DCS's from  $\text{CH}_4$ ,  $\text{CH}_3\text{F}_1$ ,  $\text{CH}_2\text{F}_2$ ,  $\text{CH}_1\text{F}_3$ , and  $\text{CF}_4$  molecules at the electron impact energy of 30 eV.

are similar with respect to scattering angles at all energies, and all DCS's become more resembled (except for a structure near at  $60^\circ$ , as seen below) at higher energies above 20 eV, (e) The conspicuous shoulder begins to appear around  $60^\circ$ – $65^\circ$  as each hydrogen is replaced by a fluorine atom, and the magnitude of the DCS at this angle is proportional to the number of F atom in a molecule: *the fluorination effect*, (f) At higher energies above a few 10 eV, the strength of the DCS show more complicated features and do not appear to depend strongly on molecular natures. Particularly, it shows much complicated trend for small-scattering ( $< 50^\circ$ ) and large-scattering ( $> 100^\circ$ ) angles except for much higher energies where the magnitude of the DCS is in the order of the number of F atom, and (g) At above 30 eV, more undulations can be seen at small angles, especially for those molecules which contain more F atoms, suggesting the atomic (fluoride) effect due to the multiple scattering.

In summary, we have carried out a joint experimental and theoretical study of electron scattering from  $\text{CH}_4$ ,  $\text{CH}_3\text{F}_1$ ,  $\text{CH}_2\text{F}_2$ ,  $\text{CH}_1\text{F}_3$ , and  $\text{CF}_4$  molecules. We have found a prominent structure around  $60^\circ$  at intermediate scattering energies, and this structure grows as the number of F atom in a molecule increases. The origin of this structure is a combination of a mixing of many partial waves and of a resonance due to unoccupied molecular orbitals.

### References

- 1) L. G. Christophorou, J. K. Olthoff, and M. V. V. S. Rao: *J. Phys. Chem. Ref. Data.* **25**, 1341 (1996).
- 2) L. G. Christophorou, J. K. Olthoff, and M. V. V. S. Rao: *J. Phys. Chem. Ref. Data.* **26**, 1 (1997).
- 3) M. B. Robin: in *Higher Excited States of Polyatomic Molecules* (Academic Press, New York and London, 1974), p. 178.
- 4) W. M. Huo: *Phys. Rev. A* **38**, 3303 (1988); *J. Phys. B* **22**, 1225 (1989).

\* Department of Physics, Sophia University

# The Coupling of Electron Thermalization and Electron Attachment in $\text{CCl}_4/\text{Ar}$ and $\text{CCl}_4/\text{Ne}$ Mixtures<sup>†</sup>

K. Kowari, K. Leung,\* and B. D. Shizgal\*

We study the time evolution of the electron nonequilibrium distribution function from some initial distribution under the influence of elastic and inelastic collisions of electrons with the ambient gases, and electron attachment to some electronegative gas. We consider a mixture of either Ar or Ne and  $\text{CCl}_4$  so that the collision processes to be considered are elastic electron-inert gas and electron- $\text{CCl}_4$  collisions, vibrationally inelastic electron- $\text{CCl}_4$  collisions, and electron attachment to  $\text{CCl}_4$ . The inert gas moderators are chosen so as to have an example of a gas (Ar) with a Ramsauer-Townsend minimum and a second moderator (Ne) for which the momentum transfer cross section is nearly constant with energy.

The time dependent electron energy distribution function is obtained from the Boltzmann equation, and the energy relaxation times are determined. The steady average energy of the electrons can be above the ambient temperature of the moderators because of the effect of attachment heating. This effect was discussed by Shizgal<sup>1)</sup> except that inelastic collisions were neglected in that study.

Kowari and Shizgal<sup>2)</sup> extended this previous work to include vibrationally inelastic collisions as well. However, the portion of the attachment cross section below 0.1 eV used in Ref. 2 does not coincide with the actual cross section for the system studied. The calculations are repeated in the present paper for the correct cross section,<sup>3)</sup> and the results are reinterpreted. Both cross sections are shown in Fig. 1. We use the attachment cross section above 0.1 eV given by Hayashi.<sup>4)</sup> The time dependence of the average electron energy for the two attachment cross sections is shown in Fig. 2.

Warman and Sauer<sup>5)</sup> reported an experimental technique to determine the energy relaxation rate coefficients and the relaxation times in pure inert gases and other moderators by following the reaction kinetics of electron attachment to  $\text{CCl}_4$ . In this paper, we study the validity of the analysis used by Warman and Sauer to extract relaxation times from the electron kinetics associated with attachment. We compare the relaxation times extracted from the electron kinetics with those determined directly from the relaxation of the average energy. We also compare with the very recent measurements by Shimamori and Sunagawa.<sup>6)</sup>

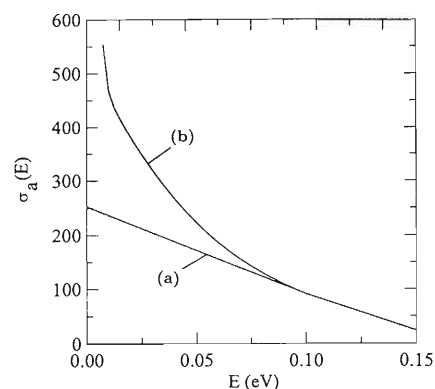


Fig. 1. Electron attachment cross section,  $e\text{-CCl}_4$ : (a) cross section used by Kowari and Shizgal, (b) cross section used in the present work.

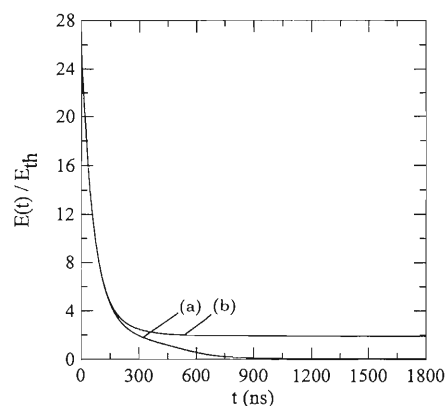


Fig. 2. Time variation of the average energy,  $\text{CCl}_4$  in Argon with all collision processes included,  $X_{\text{CCl}_4} = 5 \times 10^{-6}$ . (a) Results for the attachment cross section used by Kowari and Shizgal, Fig. 1(a). (b) Results for the attachment cross section used in the present work, Fig. 1(b).

## References

- 1) B. Shizgal: *J. Phys. B* **24**, 2909 (1991).
- 2) K. Kowari and B. Shizgal: *Chem. Phys. Lett.* **260**, 365 (1996).
- 3) A. Chutjian and S. H. Alajajian: *Phys. Rev. A* **31**, 2885 (1985).
- 4) M. Hayashi: in *Swarm Studies and Inelastic Electron Molecule Collisions*, edited by L. C. Pitchford, B. V. Mckoy, A. Chutjian, and S. Trajmar (Springer-Verlag, New York, 1987), p. 167; (private communication).
- 5) J. M. Warman and M. C. Sauer, Jr.: *J. Chem. Phys.* **62**, 1971 (1975).
- 6) H. Shimamori and T. Sunagawa: *Chem. Phys. Lett.* **267**, 334 (1997).

<sup>†</sup> Condensed from the article in *J. Chem. Phys.* **108**, 1587 (1998)

\* Department of Chemistry, University of British Columbia, Vancouver, Canada

## Resonances in $\text{Ps}^-$ System

A. Igarashi and I. Shimamura

The positronium negative ion  $\text{Ps}^-(e^-e^-e^+)$  is a special system where three particles with the same mass are interacting via Coulomb forces. It is also an intermediate three body system between the atomic limit  $\text{H}^-$  and the molecular limit  $\text{H}_2^+$ . Even in  $\text{H}^-$ , some of the resonance states, where two electrons are excited simultaneously, exhibit a spectrum similar to the rotational-vibrational spectra of molecules. Therefore, it would be quite interesting to see the resonance structures in  $\text{Ps}^-$ . However, many resonances are still to be calculated for the higher partial waves.

For the resonances in the  $\text{Ps}^-$  system, continuous efforts have been made by Ho and Bhatia<sup>1)</sup> with the complex rotation method for high-lying resonances associated with the  $\text{Ps}(N \leq 6)$  thresholds for the total angular momentum  $L \leq 2$ . References to the published results on the resonances in  $\text{Ps}^-$  can be found in the recent review by Ho.<sup>2)</sup>

We have calculated the resonance parameters of  $\text{Ps}^-$  associated with the  $\text{Ps}(N = 2, 3)$  thresholds for partial waves  $L \leq 5$ . We have employed the hyperspherical close-coupling method for the scattering calculation of  $e^- + \text{Ps}$ .

To specify the channels by which resonances are supported, we label them  $N(K, T)^A 2^{S+1}L^\Pi$  after Ref. 3. Here we show in Table 1 just the resonance parameter for the lowest  $N = 3$ ,  $(K, T)^A$  resonances in each symmetry to compare them with the results in the complex rotation method; the agreement is generally good. Some of the resonances are found new in the present work. From Table 1, we see that resonance energies with the same  $(K, T)^A$  become shallower for larger  $L$  and that those of the same  $(K, T \neq 0)^A$  and  $L$  but different parities are almost degenerate.

In the  $3(2, 0)^+$  rotor series, there is a resonance of the  ${}^3H^o$  symmetry, which is absent from  $\text{H}^-$  reflecting the shell structure of the atom. This additional rotor state manifest itself because  $\text{Ps}^-$  is an intermediate system between  $\text{H}^-$  and  $\text{H}_2^+$ . The  ${}^1D^e$   $3(0, 0)^+$  shape resonance calculated by the complex rotation method was not reproduced in the present calculation. The existence of this resonance seems to be subtle as is expected from the hyperspherical adiabatic potential curve, since its width is quite large and since it

Table 1. Energy  $E$  and widths  $\Gamma$  (in a.u.) of resonances associated with the  $\text{Ps}(N = 3)$  threshold in  $\text{Ps}^-$ . The shape resonances are distinguished from the Feshbach resonances by inspecting the adiabatic hyperspherical potential curves, and underlined in the table.  $a[b] = a \times 10^b$ .

Label	$2^{S+1}L^\Pi$	Present		Complex rotation	
		$E$	$\Gamma$	$E$	$\Gamma$
$(2, 0)^+$	${}^1S^e$	-3.5338[-2]	7.6[-5]	-3.5341[-2]	7.5[-5]
	${}^3P^o$	-3.4868[-2]	6.1[-5]	-3.4871[-2]	6.06[-5]
	${}^1D^e$	-3.3911[-2]	2.4[-5]	-3.3914[-2]	2.36[-5]
	${}^3F^o$	-3.2473[-2]	8.5[-5]		
	${}^1G^e$	-3.0673[-2]	8.2[-5]		
	${}^3H^o$	-2.8527[-2]	5.6[-6]		
$(2, 0)^-$	${}^3S^e$	-2.9368[-2]	2.1[-7]	-2.9365[-2]	1.[-5]
	${}^1P^o$	-2.9212[-2]	1.5[-6]	-2.9215[-2]	1.5[-6]
	${}^3D^e$	-2.8906[-2]	2.9[-6]	-2.8907[-2]	4.2[-6]
	${}^1F^o$	-2.8380[-2]	2.7[-5]		
	${}^3G^e$	-2.8046[-2]	4.4[-7]		
$(1, 1)^+$	${}^1P^o$	-3.1621[-2]	2.2[-4]	-3.1622[-2]	2.21[-4]
	${}^3P^e$	-3.1626[-2]	1.8[-4]	-3.1631[-2]	1.79[-4]
	${}^3D^e$	-3.0410[-2]	1.3[-4]	-3.0411[-2]	1.32[-4]
	${}^1D^o$	-3.0434[-2]	7.3[-5]	-3.0441[-2]	7.2[-5]
	${}^1F^o$	-2.8696[-2]	4.0[-5]		
	${}^3F^e$	-2.8599[-2]	1.1[-5]		
$(1, 1)^-$	${}^3P^o$	-2.8182[-2]	4.5[-6]		
	${}^1P^e$	-2.8201[-2]	8.2[-9]		
	${}^1D^e$	-2.7951[-2]	9.4[-7]		
	${}^3D^o$	-2.7947[-2]	7.1[-7]	-2.7949[-2]	<1.50[-6]
$(0, 2)^+$	${}^1D^e$	-2.7394[-2]	3.5[-4]	-2.7400[-2]	3.2[-4]
	${}^3D^o$	-2.7452[-2]	3.2[-4]	-2.7485[-2]	3.10[-4]
$(0, 0)^+$	${}^1S^e$	-2.7741[-2]	7.0[-6]	-2.7725[-2]	4.2[-5]
	${}^3P^o$	-2.720[-2]	5.4[-4]	-2.725[-2]	4.60[-4]
	${}^1D^e$			-2.618[-2]	2.04[-3]

is located rather above the potential maximum.

### References

- 1) Y. K. Ho and A. K. Bhatia: Phys. Rev. A **50**, 2155 (1994).
- 2) Y. K. Ho: Chin. J. Phys. (Taipei) **35**, 97 (1997).
- 3) C. D. Lin: Adv. At. Mol. Phys. **22**, 77 (1986).

## Auger Transition Rates for Metastable States of the Antiprotonic Helium $\text{He}^+\bar{p}$

V. I. Korobov and I. Shimamura

The recently measured time spectra of decay products after stopping of the antiprotons ( $\bar{p}$ ) in helium have clearly shown delayed components, and have revealed the existence of extremely long-lived  $\bar{p}$ ; about 3% of the stopped  $\bar{p}$  lived as long as a few microseconds, to be compared with a lifetime of some picoseconds for the most of  $\bar{p}$ .<sup>1)</sup> These long-lived  $\bar{p}$  states have been observed both in  $^4\text{He}$  and in  $^3\text{He}$ ,<sup>2)</sup> but not in any other materials hitherto studied, and are considered to be due to a mechanism<sup>3)</sup> similar to that for long-lived kaons and pions in helium already known from bubble-chamber experiments in the sixties.<sup>4)</sup>

The scenario in the independent-particle picture is the following. Most of the  $\bar{p}$  that stopped in helium in the process  $\text{He} + \bar{p} \rightarrow \text{He}^+\bar{p} + e^-$  occupy highly excited orbitals in  $\text{He}^+\bar{p}$  with the principal quantum numbers  $n$  around 40. These  $\bar{p}$  cascade down to the lower and lower orbitals by emission of an Auger electron, by radiative transitions, and by energy and angular-momentum transfer in collisions of  $\text{He}^+\bar{p}$  with ambient He atoms, thus eventually decaying into the intra-atomic encounter with the helium nucleus either in a low- $n$  state or in a high- $n$ ,  $s$ -state.

The long-lived  $\bar{p}$  are considered to be those that are captured into high  $n$ , nearly circular states, for which both radiative and Auger transitions are slow. Accurate radiative rates were calculated previously,<sup>5)</sup> and were found to be of the order of microseconds for  $25 < n < 50$ . Thus, the Auger rates are crucial in distinguishing between long-lived and short-lived  $\bar{p}$  and in determining the fraction of the former among all the stopped  $\bar{p}$ . The Auger rates are also indispensable for the study of the whole cascade process.

In the present work the rates of Auger transitions of antiprotonic helium  $^4\text{He}^+\bar{p}$  and  $^3\text{He}^+\bar{p}$  were calculated

by using a variational scattering method with an elaborate three-body trial function. The shift of the energy levels of these systems due to the coupling with Auger-decay channels was also obtained from this calculation. Thus, an improvement was made over the previously calculated nonrelativistic energies. Together with the relativistic corrections calculated elsewhere,<sup>6)</sup> the theoretical transition wavelength between the states  $(n, l) = (37, 34)$  and  $(38, 33)$  of  $^4\text{He}^+\bar{p}$  (where  $l$  is the azimuthal quantum number), for example, was significantly improved to be 713.593 nm, which agrees well with the experimental value  $713.578 \pm 0.006$  nm. The calculated Auger lifetime of the level  $(38, 33)$  turned out to be 3.2 ps, which should be compared with the value  $4.1 \pm 0.2$  ps deduced from the measured line broadening. Auger rates were calculated also using Fermi's golden-rule formula with a regular Coulomb function having no phase shift for the Auger electron. The results agree fairly well with the accurate variational results.

Further details are reported elsewhere.<sup>7)</sup>

### References

- 1) M. Iwasaki et al.: Phys. Rev. Lett. **67**, 1246 (1991).
- 2) T. Yamazaki et al.: Nature **361**, 238 (1993).
- 3) G. T. Condo: Phys. Lett. **9**, 65 (1964).
- 4) J. G. Fetkovich and E. G. Pewitt: Phys. Rev. Lett. **11**, 290 (1963); M. M. Block et al.: Phys. Rev. Lett. **11**, 301 (1963); M. M. Block et al.: Phys. Rev. **140**, B 143 (1965); J. G. Fetkovich et al.: Phys. Rev. D **2**, 1803 (1970).
- 5) I. Shimamura: Phys. Rev. A **46**, 3776 (1992).
- 6) V. I. Korobov and D. Bakalov: Phys. Rev. Lett. **79**, 3379 (1997).
- 7) V. I. Korobov and I. Shimamura: Phys. Rev. A **56**, 4587 (1997).

## Fine and Quadrupole Structures of the Weakly Bound Systems $[(dt\mu)_{11}dee]$ and $[(dd\mu)_{11}dee]$

D. Bakalov,<sup>\*1</sup> K. Bakalova,<sup>\*2</sup> V. Korobov,<sup>\*3</sup> H. J. Monkhorst,<sup>\*4</sup> and I. Shimamura

The study of the muonic molecules  $dt\mu$  and  $dd\mu$  is not only a central problem for the physics of muon catalyzed fusion but also a challenge to the theory of few-body problems, since it allows a very precise experimental verification for the theoretical predictions.<sup>1,2)</sup> A point of particular interest is the anomalously weakly excited bound states of  $dt\mu$  and  $dd\mu$  with orbital angular momentum  $J_\mu = 1$  and vibrational excitation quantum number  $v_\mu = 1$ . These systems are formed inside of larger six-body bound systems in the resonant reactions  $d\mu + D_2 \rightarrow [(dd\mu)_{11}dee]^*$  and  $t\mu + D_2 \rightarrow [(dt\mu)_{11}dee]^*$ , in which the energy released is transferred to a rotational-vibrational excitation of the six-body systems.

The six-body system  $[(dd\mu)_{11}dee]^*$  can be considered as an excited state of the diatomic molecule  $DM$ , similar to the  $DT$ , in which a hypothetic point-like heavy nucleus  $M$  of the mass equal to the total mass of  $dd\mu$  is replaced by an ion  $(dd\mu)_{11}^+$ . Accordingly, the energy levels  $E_{[(dd\mu)_{11}dee]^*}$  of the six-body system can be represented in the form:

$$E_{[(dd\mu)_{11}dee]^*} = E_{(dd\mu)_{11}} + E_{(DM)_{J_r, v_r}} + \Delta E. \quad (1)$$

Here,  $E_{(dd\mu)_{11}}$  is the energy level of the isolated 3-body system  $(dd\mu)_{11}$ ,  $E_{(DM)_{J_r, v_r}}$  is the energy of the corresponding excited state of the hydrogenlike molecule  $DM$ , and  $\Delta E$  is a "finite size" correction term due to the interaction of the constituents of  $dd\mu$  with the particles in  $DM$  other than  $M$ . The argument henceforth may be easily carried over to  $[(dt\mu)_{11}dee]^*$ .

The complicated structure of the energy levels of  $E_{[(dd\mu)_{11}dee]^*}$  is due to the fine and hyperfine splittings of the Coulomb level  $E_{(dd\mu)_{11}}$ ,<sup>3)</sup> to the rotational-vibrational excitation spectrum of  $DM$ , and to the quadrupole splitting of the third term in Eq. (1), i.e., the finite size correction  $\Delta E$ .<sup>4-6)</sup>

In the present work we have considered these three contributions simultaneously for the first time, coupling all relevant angular momenta in a proper way. We are basically following the approach developed ear-

lier in Ref. 4, but we also take advantage of the precise numerical results of Refs. 5 and 6 for the matrix elements of the perturbation Hamiltonian. We have found that the "quadrupole splitting" of the energy levels of the six-body complexes  $E_{[(dd\mu)_{11}dee]_{J_r, v_r}}$  and  $E_{[(dt\mu)_{11}dee]_{J_r, v_r}}$  has the same order of magnitude as the fine splitting of  $E_{(dd\mu)_{11}}$  and  $E_{(dt\mu)_{11}}$ , as was found previously,<sup>4-6)</sup> and should certainly be taken into account in an appropriate way, when interpreting the experimental data on the resonant formation of muonic molecules.

The quadrupole corrections preserve the general form of the hyperfine structures of  $(dt\mu)_{11}$  and  $(dd\mu)_{11}$ , but disperse its components quite significantly. For instance, the three hyperfine states of  $(dt\mu)_{11}$  with the total spin  $F$  of  $t\mu$  equal to 0, the total spin  $S$  of  $dt\mu$  equal to 1, and the total angular momentum  $J_a$  of  $dt\mu$  equal to 0, 1, and 2 lie within less than 0.2 meV, while the quadrupole interactions disperse them to nearly 3.5 meV; similar dispersions occur for the other hyperfine levels too. As a result, formation rates shall be much smoother functions of temperature with much less pronounced resonant peaks than originally predicted.

Further details will be reported elsewhere.<sup>7)</sup>

### References

- 1) L. I. Ponomarev: *Contemp. Phys.* **31**, 219 (1991).
- 2) A. Scrinzi, P. Kammel, J. Zmeskal, W. H. Breunlich, J. Marton, M. P. Faifman, L. I. Ponomarev, and T. A. Strizh: *Phys. Rev. A* **47**, 4691 (1993).
- 3) G. Aissing, D. Bakalov, and H. J. Monkhorst: *Phys. Rev. A* **42**, 116 (1990).
- 4) D. Bakalov and V. S. Melezhik: JINR Communication, P4-81-835, Dubna, 1981 (unpublished).
- 5) M. R. Harston, I. Shimamura, and M. Kamimura: *Phys. Rev. A* **45**, 94 (1992).
- 6) M. R. Harston, S. Hara, Y. Kino, I. Shimamura, H. Sato, and M. Kamimura: *Phys. Rev. A* **56**, 2685 (1997).
- 7) D. Bakalov, K. Bakalova, V. Korobov, H. J. Monkhorst, and I. Shimamura: *Phys. Rev. A* **57**, No. 4 (1998), in press.

<sup>\*1</sup> Institute for Nuclear Research and Nuclear Energy, Sofia, Bulgaria

<sup>\*2</sup> Solar-Terrestrial Influences Laboratory, Sofia, Bulgaria

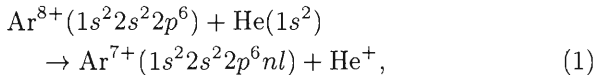
<sup>\*3</sup> Joint Institute for Nuclear Research, Dubna, Russia

<sup>\*4</sup> QTP, University of Florida, Gainesville, U.S.A.

# State-Selective Differential Cross Sections of Electron Capture in 10 MeV Ar<sup>8+</sup>-He Collisions

T. Kambara, Y. Nakai, T. M. Kojima, V. Mergel, H. Schmidt-Böcking, and M. Kimura

Dynamical processes have been studied for the single-electron capture in collisions of 10 MeV Ar<sup>8+</sup> ions with He atoms:



through a state-selective measurement of differential cross sections. The projectile Ar<sup>8+</sup> energy corresponds to a velocity of 3.17 atomic unit (au). An Ar<sup>8+</sup> ion has a neon-like electronic configuration where K and L shells are filled, and hence the electron can be captured to  $n = 3$  or a higher orbital. The final-state selective differential cross section is related to the transition amplitude, and its measurement is useful for detailed discussion of the collision process. However, only few measurements have been reported for the collisions between highly-charged heavy ions at energies higher than hundreds of keV/u because the projectile scattering angles in these collisions are so small that their measurements are extremely difficult. In the present experiment, we have measured, instead of the projectile scattering angle, all the momentum components of the recoil He<sup>+</sup> ions applying the COLd Target Recoil Ion Momentum Spectroscopy (COLTRIMS)<sup>1,2)</sup> in coincidence with the projectile which captures one electron. From the momentum analyses we have obtained (1) the kinetic energy gain which corresponds to the final state of the captured electron, and (2) differential cross sections for these final states as a function of the transverse recoil-ion momentum which corresponds to the scattering angle.

The experimental setup of the COLTRIMS at the RILAC was described previously.<sup>3)</sup>

The resolution of the recoil-ion momentum was about 0.2 au in all the directions, which corresponds to a resolution of 17 eV in the binding energy of the captured electron, and of 0.9 microradian in the scattering angle.

The final states of the captured electron in Ar<sup>7+</sup>( $nl$ ) were clearly separated to the  $n = 3$  state and the higher excited states from the longitudinal momentum of the recoil ions. The capture to the  $n = 4$  state was observed as a shoulder on the  $n = 5$  state which was separated with Gaussian fittings. The electron capture predominantly occurs into the  $n = 5$  excited state.

Figure 1 shows the differential cross section of single-electron capture to the  $n = 3 - 5$  states. The experimental results of the differential cross sections are compared with calculations of the close-coupling approximation based on a molecular representation.<sup>4)</sup> The experimental results are normalized with a common multiplication factor, so that the total yield summed over  $n = 3 - 5$  states and integrated over the transverse momentum up to 4 au is equal to the corresponding theoretical value. The theoretical calculations agree reasonably well with the experimental results.

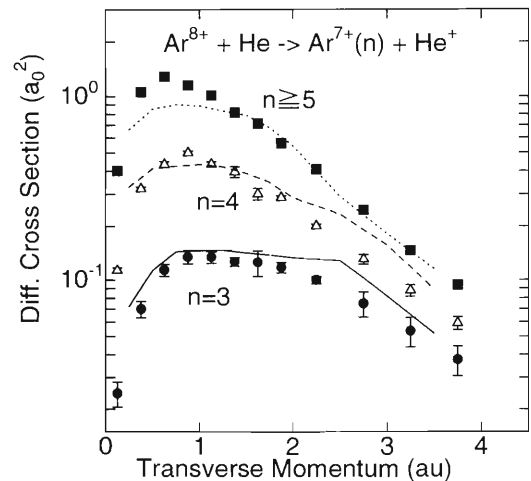


Fig. 1. Differential cross section of one-electron capture by 10 MeV Ar<sup>8+</sup> ions into different final states with the principal quantum numbers  $n = 3 - 5$ . Symbols denote the experimental results and lines are the calculation results.

## References

- 1) T. Kambara: *Butsuri* **52**, 18 (1997). (in Japanese)
- 2) J. Ullrich, R. Moshhammer, R. Dörner, O. Jagutzki, V. Mergel, H. Schmidt-Böcking, and L. Spielberger: *J. Phys. B: At. Mol. Opt. Phys.* **30**, 2917 (1997).
- 3) T. Kambara, Y. Awaya, Y. Kanai, T. M. Kojima, Y. Nakai, R. Dörner, V. Mergel, H. W. Schmidt-Böcking, M. Jäger, and B. D. DePaola: *RIKEN Accel. Prog. Rep.* **30**, 75 (1997).
- 4) M. Kimura and R. E. Olson: *Phys. Rev. A* **31**, 489 (1985).

## Beam Foil Spectra of Highly Charged Neon Ions in Visible Region

K. Ishii, S. Kawae, T. Nakano, K. Ando, H. Ōyama, and T. Kambara

Beam-foil spectra of highly charged Ne ions at the energy of 0.4–1.0 MeV/amu were recorded in the region between 200 and 700 nm. Photons emitted from the Ne ion after its passage through a thin carbon foil were dispersed by a monochromator and detected by a liquid-nitrogen cooled CCD detector covering the wavelength range of about 80 nm. The comparison of the spectra recorded at two different energies has provided the charge state identification of the individual lines.

Most of the intense lines are classified as transitions of high  $n, \ell$  levels in Ne V to Ne X, based on the calculation of the hydrogenic term energies, the wavelengths and the transition probabilities for the Rydberg transitions.<sup>1,2)</sup>

The lines between 370 and 390 nm were classified as  $1s^2 2s 7\ell - 1s^2 2s 8\ell$  transitions in Be-like Ne VII. It was found that the transitions were split into  $\ell$ -components by the perturbation of the nearby lying doubly excited  $2pn\ell$  configuration to the  $2s8\ell$ .<sup>3,4)</sup>

In the present work of spectral line intensity decay measurement, we take a full advantage of the multi-channel capability of the CCD detector. The decay data for all the lines in the region between 210 and 290 nm were simultaneously recorded at forty-five different positions along the beam from the foil. The first ten positions were increased by 0.10 mm step size and the second ten by 0.20 mm. Thereafter, the step size was increased on a semi-logarithmic scale over a total distance of 324 mm. The majority of the lines show a multi-exponential decay characteristic of heavy cascading effects that result from the yrast transitions.

In Fig. 1, typical decay curves are displayed, where the intensity is normalized to unity at its maximum. The lines numbered “a” through “f” reach to the maximum just after the foil position and decay in multi-exponential nature. On the other hand, the lines numbered “g1”, “g2” and “h” show somewhat different decay mode. They reach slowly to their maximum and decay in a single exponential feature. The designations attached with the label “a–h” are all for Be-like Ne VII, except the Ne VIII 8–10. Plausible assign-

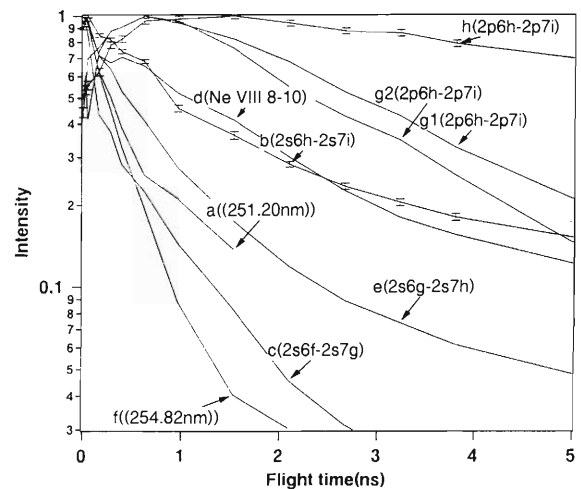


Fig. 1. Intensity decay curves of the lines around 250 nm plotted on a semi-logarithmic scale. The distance from the foil position is converted to the flight time of the ion from the foil. The intensity for each line is normalized to unity at its maximum. All the lines except that denoted by Ne VIII are Be-like Ne VII.

ments were given based on the atomic structure calculation by including the perturbing configurations as many as possible.<sup>5)</sup> It is worthwhile to note that the lines which show single exponential decay feature are due to the transitions of multiply excited states, and their upper states lie slightly above the first ionization limit.

### References

- 1) H. A. Bethe and E. E. Salpeter: in *Quantum Theory of One- and Two-Electron Atoms* (Springer-Verlag, Berlin, 1957).
- 2) B. Edlén: in *Handbuch der Physik*, edited by S. Flügge (Springer-Verlag, Berlin, 1964) Vol. XXVII, p. 80.
- 3) K. Ishii et al.: RIKEN Accel. Prog. Rep. **30**, 78 (1997).
- 4) K. Ishii et al.: Phys. Scr. T **73**, 73 (1997).
- 5) R. D. Cowan: in *The Theory of Atomic Structure and Spectra* (University of California Press, Berkeley, 1981).

# Beam Foil Spectra of Highly Charged Krypton Ions in Visible Region

K. Ishii, T. Nakano, S. Kawae, K. Ando, H. Ōyama, and T. Kambara

Beam-foil spectra of highly charged Kr ion at the energy of 1.0 and 2.5 MeV/amu were recorded in the region between 200 and 700 nm. Photons emitted from the Kr ion after its passage through a thin carbon foil were dispersed by a Czerny-Turner spectrometer and detected by a liquid-nitrogen cooled CCD detector. The detector placed at the exit focal plane covered the wavelength range of about 80 nm. In order to reduce the Doppler width, the spectrometer was refocused.<sup>1)</sup> The line width of 0.3–0.4 nm was thus achieved. Comparison of the relative intensity change in the spectra recorded at two different beam energies has provided the charge state identification of the observed lines. A portion of the spectra in the range 227–316 nm at the beam energy of 1.0 MeV/amu is shown in Fig. 1.

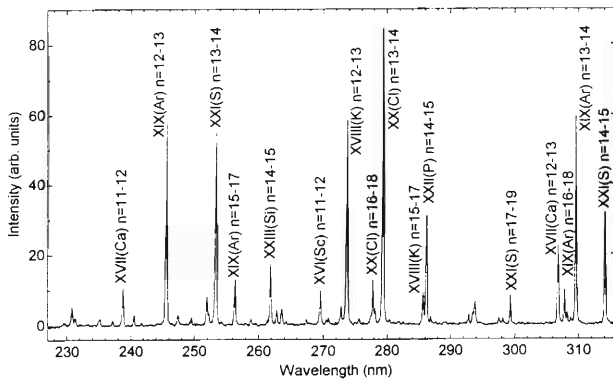


Fig. 1. A portion of Kr ion spectra of 1.5 MeV/amu energy at immediate down stream of the foil.

Using the hydrogenic term energies, the wavelengths and the transition probabilities for the Rydberg transitions were calculated.<sup>2,3)</sup> All the lines are thus classified as transitions of high  $n, \ell$  levels in Kr XIX to Kr XXVI, among which the relatively strong lines are listed in Table 1. Weak lines not included in the table are  $\Delta n > 3$  transitions. In the fourth column, the

Table 1. Observed and calculated transitions of Kr ions.

Obs.	Wavelength		Classification
	Calc.	diff.	
2387.95	2387.88	0.07	XVII (Ca) n=11-12
2456.37	2456.34	0.03	XIX (Ar) n=12-13
2533.94	2534.14	-0.20	XXI (S) n=13-14
2564.00	2563.90	0.10	XIX (Ar) n=15-17
2618.59	2618.63	-0.04	XXIII(Si) n=14-17
2695.56	2695.73	-0.17	XVI (Sc) n=11-12
2736.88	2736.91	-0.03	XVIII(K) n=12-13
2778.08	2777.96	0.12	XX (Cl) n=16-18
2793.94	2793.92	0.02	XX (Cl) n=13-14
2856.75	2856.72	0.03	XVIII(K) n=15-17
2862.13	2862.13	0.00	XXII (P) n=14-15
2993.35	2993.27	0.08	XXI (S) n=17-19
3068.32	3068.40	-0.08	XVII (Ca) n=12-13
3078.12	3078.10	0.02	XIX (Ar) n=16-18
3095.75	3095.79	-0.04	XIX (Ar) n=13-14
3141.23	3141.23	0.00	XXI (S) n=14-15
Std. dev.=		0.09	

element symbol of the isoelectronic sequence to which the line belongs is shown in parenthesis. Almost all the lines except those which are very weak/broad were identified over the spectra from 195 to 700 nm in this way.

The further study on  $n$ -dependence of the level population in a charge state is now in progress. This may be practiced by calibrating the sensitivity of the spectrometer system against the standard light source.

## References

- 1) J. O. Stoner, Jr. and J. A. Leavitt: *Appl. Phys. Lett.* **18**, 477 (1971).
- 2) H. A. Bethe and E. E. Salpeter: in *Quantum Theory of One- and Two-Electron Atoms* (Springer-Verlag, Berlin, 1957).
- 3) B. Edlén: in *Handbuch der Physik*, edited by S. Flügge (Springer-Verlag, Berlin, 1964) Vol. XXVII, p. 80.

## Lifetimes of Intercombination Lines in Highly Charged Nb

R. Hutton, Y. Zou, S. Hultdt, I. Martinson, K. Ando, B. Nyström,  
H. Oyama, and T. Kambara

In an earlier report<sup>1)</sup> we discussed beam-foil spectroscopy (BFS) of highly charged Nb ions. The work reported in Ref. 1 was done using the BFS set up described by Ando et al.<sup>2)</sup> Recently, we have upgraded the BFS spectrometer with a CCD detection system. This upgrade was described in the last year progress report.<sup>3)</sup> We have now repeated some of the Nb work using the CCD detector. In Fig. 1, we compare delayed

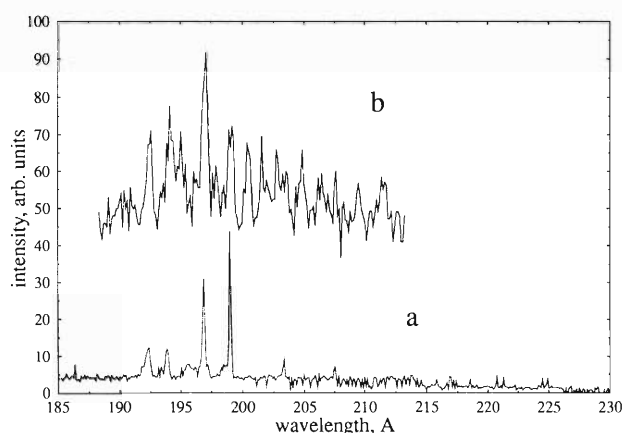


Fig. 1. Beam foil spectra of 183 MeV Nb taken using two different detector systems. Figure 1.a shows the spectrum recorded with a CCD detector system. Figure 1.b shows the same spectrum recorded using a single channel (ceratron) detector. The peaks are temporarily identified as (1): Al-like  $3s^2 3p^2 P_{1/2} - 3s 3p^2 P_{1/2}$ , (2): Si-like  $3s^2 3p^2 P_1 - 3s 3p^3 S_2$ , (3): Mg-like  $3s^2 S_0 - 3s 3p^3 P_1$  and (4): Al-like  $3s^2 3p^2 P_{3/2} - 3s 3p^2 P_{5/2}$  transitions.

spectra, i.e. spectra taken with a 10 mm separation between the exciter foil and the spectrometer entrance slit, for 183 MeV Nb taken with the CCD (Fig. 1a) and with the old detection system (Fig. 1b). Figure 1a shows clearly the improved signal/noise ratio obtained with the CCD system. By measuring intensity as a function of foil position we could measure the decay time of all lines focused on the CCD chip. As the results of Refs. 4 and 5, that the measured lifetime of the Mg-like  $3s^2 S_0 - 3s 3p^3 P_1$  line is shorter than theory by a significant amount (around 30 percent) was confirmed. The same was found for the Al-like  $3s^2 3p^2 P_{3/2} - 3s 3p^2 P_{5/2}$  line. A number of other intercombination lines appear in the spectrum shown in Fig. 1a (e.g. the Si-like  $3s^2 3p^2 P_{1,2} - 3s 3p^3 S_2$  lines) and these decay times are under investigation. Using the CCD the decay of the line profile can be measured. By generating decay curves for different parts of the line profile we found a non-unique lifetime. This interesting finding is discussed more in Ref. 6.

### References

- 1) R. Hutton et al.: RIKEN Accel. Prog. Rep. **28**, 69 (1995).
- 2) K. Ando et al.: J. Spectr. Soc. Jpn. **41**, 370 (1992).
- 3) R. Hutton et al.: RIKEN Accel. Prog. Rep. **30**, 146 (1997).
- 4) R. Hutton et al.: RIKEN Accel. Prog. Rep. **30**, 79 (1997).
- 5) R. Hutton: Proc. 8th Int. Conf. on the Physics of Highly Charged Ions, Omiya, 1996, Invited contribution, Phys. Scr. T **73**, 25 (1997).
- 6) R. Hutton et al.: RIKEN Accel. Prog. Rep. **31**, 94 (1998).

## Inherent Problems with Beam-Foil Lifetime Measurements

R. Hutton, Y. Zou, S. Huldt, I. Martinson, K. Ando, B. Nyström,  
T. Kambara, and Y. Awaya

We have attempted to measure the lifetimes of the  $1s^2 2p^2 \ ^2P_{1/2,3/2}$  levels of Li-like argon using the techniques of beam-foil spectroscopy (BFS). This measurement was done to help understand a series of measurements for the lifetime of the  $3s^2 \ ^1S_0 - 3s3p \ ^3P_1$  intercombination line in Mg-like ions.<sup>1)</sup> There can be no shortcomings in the theoretical treatment of Li-like ions whereas such is not so obvious in the case of Mg-like ions. In the experiment here the signal (total spectral line plus background) was recorded using a CCD detector system installed on a 2.2 meter grazing incidence spectrometer.<sup>2)</sup> Figure 1 shows a full CCD image taken using a 1200 lines/mm grating installed on the spectrometer. The  $^2S_{1/2} - ^2P_{3/2}$  line is seen to be isolated in the spectrum taken at a time delay of 50

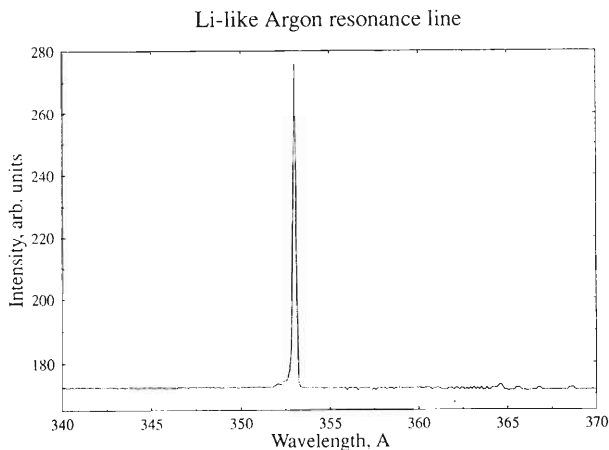


Fig. 1. Spectral recording in the region of the Li-like Argon  $2s \ ^2S_{1/2} - 2p \ ^2P_{3/2}$  line. The line is seen to be asymmetric, but clear of any spectral blends.

ps. Figure 2 shows this line in more detail, recorded at a number of foil positions. This shows that the line is asymmetric and that the shape changes as a function of foil position which corresponds to the time of flight after the excitation. Thus, no unique value for the decay time of this line can be found, instead a range of values were obtained depending of how the data was

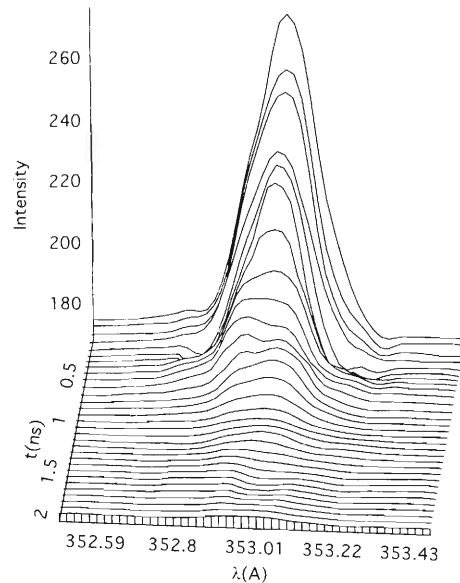


Fig. 2. The intensity of the line shown in Fig. 1 as a function of the time of flight ( $t$ ) corresponding to the exciter foil position. It is clear that the decay of this line cannot be described by a single exponential decay.

analysed. In a recent experiment a similar behavior was seen for the decay of the Mg-like Nb intercombination line.<sup>3)</sup> These phenomena may be caused by satellite lines contaminating the decay of the line of interest. These problems need to be understood, especially as to why in some cases measurements give a good agreement with theory, as BFS is still the most general method for measuring lifetimes of atomic energy levels of highly charged ions.

### References

- 1) R. Hutton: Proc. 8th Int. Conf. on the Physics of Highly Charged Ions, Omiya, 1996, Invited contribution, Physica Scripta T **73**, 25 (1997).
- 2) R. Hutton et al.: RIKEN Accel. Prog. Rep. **30**, 146 (1997).
- 3) R. Hutton et al.: RIKEN Accel. Prog. Rep. **31**, 93 (1998).

## Electron Spectra Arising from Collisions between 50 keV $N^{5+}$ and Ar

D. Chiba, T. Kamei, T. Takayanagi, K. Wakiya, Y. Kanai, and Y. Nakai

Multiple-electron capture in slow ion-atom collisions produces multiply excited ionic states, which may reveal their quantum properties through analyses of the subsequent photon or Auger electron emissions. The angular distribution of Auger electron emission, measured with respect to the projectile beam direction, carries a complete information on the  $M_L$  (magnetic substate) alignment determined in the capture process.

For measurement of the angular distribution of Auger electron emission arising from the collisions between highly charged ions and neutral atoms, we have constructed a toroidal-type electron energy analyzer.<sup>1)</sup>

Since March 1996, we have installed the above analyzer at the beam line of the RIKEN 14.5 GHz ECR ion source (Caprice), and have tried to measure the Auger electrons from  $N^{3+**}(1s^23l3l')$  produced by the collisions of 50 keV  $N^{5+}$  on Ar as a test of our apparatus.<sup>2)</sup> The angular distributions of Auger electrons emitting from  $N^{3+**}(1s^23l3l')$  were measured with a channel electron multiplier (CEM). Typical spectrum measured at 0-degree with respect to the projectile beam axis is shown in Fig. 1. The upper states of Auger decay are indicated in Fig. 1. Our 0-degree spectrum agrees with that by Kitazawa et al.<sup>3)</sup> in both the energy and relative intensity. As for the other angles, we have obtained spectra but with a larger background compared with that of 0-degree because of the kinematics effects. We will make an effort to suppress the

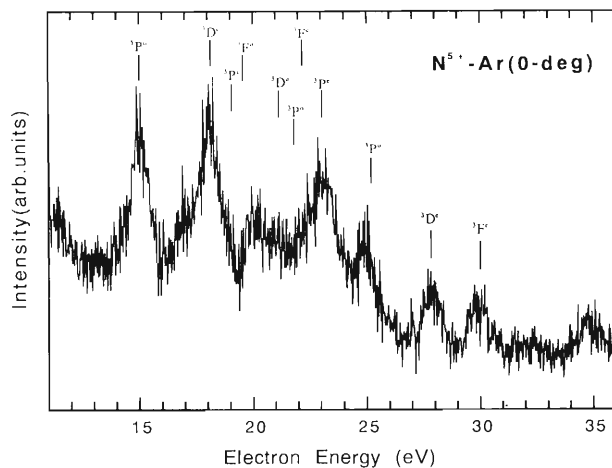


Fig. 1. The 0-degree Auger spectrum from  $N^{3+**}(1s^23l3l')$  states produced by double-electron capture in the collisions of 50 keV-beam  $N^{5+}$  ions against Ar atoms.

background.

### References

- 1) H. A. Engelhardt, W. Back, and D. Menzel: *Rev. Sci. Instrum.* **52**, 835 (1981).
- 2) Y. Tamagawa et al.: *RIKEN Accel. Prog. Rep.* **30**, 145 (1997).
- 3) S. Kitazawa et al.: *Physica Scripta T* **73**, 207 (1997).

## VUV Photon Emission Spectroscopy of Slow, Highly Charged Ions

B. Nyström, Y. Nakai, T. Kambara, and Y. Kanai

To enable studies of the low energy, highly-charged ion-atom collision processes using Photon Emission Spectroscopy (PES), we installed a 1 m grazing incidence spectrometer, Minutemann 310 G, at the 14.5 GHz Caprice<sup>1)</sup> ion source. The purposes are (1) to study the collision processes when highly charged ions collide with neutral atoms, and (2) to study the electronic structure of highly charged ions, using the ion-atom collision as a way to create excited ions. Ions from the ion-source is momentum-analyzed and focused on an effusive gas-target. The target-region is observed with the spectrometer at an angle of 54.7 degrees forward with respect to the beam-direction. This observation-angle is selected because at this angle, the light of different polarizations contribute equal to the amount of emitted photons. At this observation-angle, the light emitted from the projectiles will have a small Doppler-shift, information that might be useful in the symmetric collision-systems where both projectile-ion and target-atom might end up in equal excited states, e.g.,  $\text{He}^{2+} + \text{He}$ .<sup>2)</sup> The spectrometer is working in the grazing incidence: the angle of incidence is 86 degrees. The entrance slit can be selected to be 100, 50 or 20  $\mu\text{m}$ . The instrument can be used with four different gratings with 133.3, 600, 1200 or 2400  $\text{mm}^{-1}$  ruling. The wavelength-range that can be covered and the resolution that can be obtained are then defined by the combination of slit and grating that is used with the spectrometer. Figure 1 shows a spectra recorded when a beam of  $\text{N}^{5+}$  collides with air as the target-gas. This spectra was measured with 100  $\mu\text{m}$  slits and the 133  $\text{mm}^{-1}$  grating giving a wavelength range 100–3000 Å at a theoretical resolution of  $\text{FWHM} = 7.5$  Å. This spectra is the first successful test-measurement per-

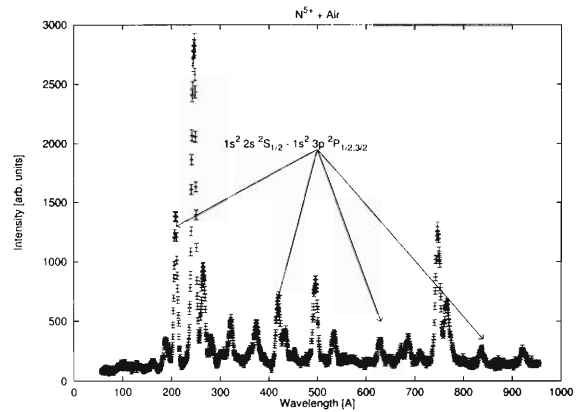


Fig. 1. Spectra recorded when 70 keV  $\text{N}^{5+}$  collides with air. The position of the  $1s^2 2s \ ^2S_{1/2} - 1s^2 3p \ ^2P_{1/2,3/2}$  transitions in N V (the spectra of  $\text{N}^{4+}$ ) are marked in the figure. Note that this is two unresolved transitions, that are marked in 1st, 2nd, 3rd and 4th order respectively.

formed, where the resolution is close to the theoretical and the spectra is calibrated with known transitions.<sup>3)</sup> Note that most of the transitions in this spectra can be identified, but since this measurement is made at rather low resolution it is not possible make any further conclusions.

### References

- 1) Y. Kanai et al.: RIKEN Accel. Prog. Rep. **30**, 168 (1997).
- 2) B. Nyström et al.: Physica Scripta T **73**, 212 (1997).
- 3) R. L. Kelly: J. Phys. Chem. Ref. Data **16** Supl. 1 (1987).

## Defect Production and Electronic Excitation in Ion-Irradiated High- $T_c$ Superconductors<sup>†</sup>

N. Ishikawa, Y. Chimi, A. Iwase, K. Tsuru,<sup>\*1</sup> O. Michikami,<sup>\*2</sup> and T. Kambara

We have measured the irradiation fluence dependence of  $c$ -axis lattice parameter for the  $\text{EuBa}_2\text{Cu}_3\text{O}_y$  high- $T_c$  superconductor irradiated with various ions from Cl to Au over the wide energy range from 80 MeV to 3.80 GeV. The irradiating ions were as follows: 120 MeV  $^{35}\text{Cl}$ , 90 MeV and 200 MeV  $^{58}\text{Ni}$ , 125 MeV  $^{79}\text{Br}$ , 80 MeV and 200 MeV  $^{127}\text{I}$ , and 120 MeV  $^{197}\text{Au}$  available from the tandem accelerator at JAERI-Tokai; and 3.54 GeV  $^{136}\text{Xe}$  and 3.80 GeV  $^{181}\text{Ta}$  available from RIKEN Ring Cyclotron. In this range of energy and ions, defects were uniformly introduced along the sample thickness, and we could exclude the effect from ion implantation. We have measured the X-ray ( $\text{Cu } K\alpha$ ) diffraction pattern both before and after the irradiation in order to estimate the change in  $c$ -axis lattice parameters. We have observed a linear increase of the  $c$ -axis lattice parameter with the fluence,<sup>1)</sup>  $\Phi$ , as can be seen in Fig. 1. For a low energy ( $\leq 2$  MeV) ion irradiation, the  $(\Delta c/c_0)/\Phi$  which corresponds to the defect production rate is proportional to the nuclear stopping power  $S_n$ :<sup>1)</sup> i.e.,  $(\Delta c/c_0)/\Phi = aS_n$ , where  $a = 3 \times 10^{-16}$  mg/MeV. The contribution of electronic excitation to the  $(\Delta c/c_0)/\Phi$

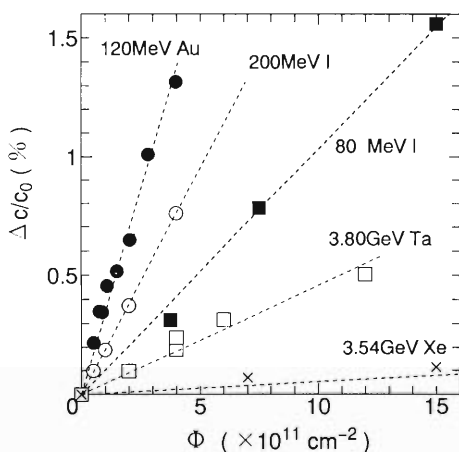


Fig. 1. The  $\Delta c/c_0$  value as a function of  $\Phi$  for  $\text{EuBa}_2\text{Cu}_3\text{O}_y$  irradiated with high energy ions, where  $\Delta c/c_0$  is the increment in  $c$ -axis lattice parameter normalized by the  $c$ -axis lattice parameter before irradiation, and  $\Phi$  is the fluence of irradiation.

value is precisely estimated by assuming that the observed  $(\Delta c/c_0)/\Phi$  value is the sum of the contributions of elastic displacement and of electronic excitation. The former contribution is expressed as a linear function of  $S_n$  as stated above. The latter contribution is designated as  $[(\Delta c/c_0)/\Phi]_{\text{electronic}}$  and was plotted as a function of  $dJ/dx$  in Fig. 2, where  $dJ/dx$  is the number of atoms ionized per unit path length. The value of  $dJ/dx$  was calculated based on the Bethe formula.<sup>2-4)</sup> The figure shows that  $[(\Delta c/c_0)/\Phi]_{\text{electronic}}$  is scaled by  $(dJ/dx)^4$ . Since  $dJ/dx$  is the number of atoms ionized per unit path length of projectile and is not the energy deposited to the target, this suggests that the line density of induced space charge is responsible for the defect production in high- $T_c$  superconductors.<sup>4)</sup>

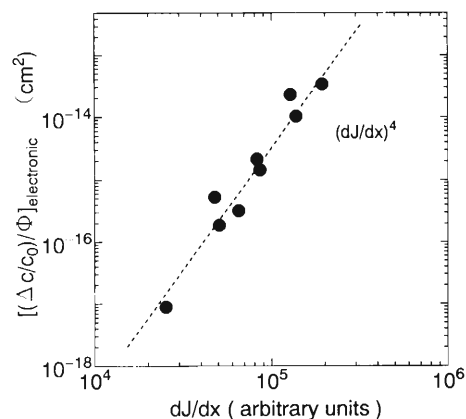


Fig. 2.  $[(\Delta c/c_0)/\Phi]_{\text{electronic}}$  as a function of  $dJ/dx$ . The dotted line shows the line proportional to  $(dJ/dx)^4$ .

### References

- 1) N. Ishikawa, A. Iwase, Y. Chimi, H. Maeta, K. Tsuru, and O. Michikami: *Physica C* **259**, 54 (1996).
- 2) R. L. Fleischer, P. B. Price, R. M. Walker, and E. L. Hubbard: *Phys. Rev.* **156**, 353 (1967).
- 3) H. A. Bethe: *Ann. Physik* **5**, 325 (1930).
- 4) N. Ishikawa, Y. Chimi, A. Iwase, H. Maeta, K. Tsuru, O. Michikami, T. Kambara, T. Mitamura, Y. Awaya, M. Terasawa: *Nucl. Instrum. Methods Phys. Res. B.* (to be published).

<sup>†</sup> Condensed from the article in *Nucl. Instrum. Methods Phys. Res. B.* (to be published)

<sup>\*1</sup> NTT Integrated Information & Energy Systems Laboratories, Information Hardware Systems Laboratory

<sup>\*2</sup> Faculty of Engineering, Iwate University

## Effect of Heavy-Ion Irradiation on the Bi-Based Superconductors

N. Kuroda, N. Ishikawa, S. Okayasu, A. Iwase, H. Ikeda,\* R. Yoshizaki,\*  
and T. Kambara

Columnar defects produced by the irradiation with high-energy ( $\sim 1$  GeV) heavy ions can pin magnetic vortices much more effectively than the other kinds of defects such as point defects. The Bi-based oxide superconductors can be classified into three types depending on the number of  $\text{CuO}_2$  stackings:  $\text{Bi}_2\text{Sr}_2\text{Ca}_{n-1}\text{Cu}_n\text{O}_y$ , in which  $n = 1, 2, 3$ . We have investigated the pinning properties of the three types of Bi-based superconductors with columnar defects.

$\text{Bi}_{2+x}\text{Sr}_{2-(x+y)}\text{La}_y\text{CuO}_{6+\delta}$  (Bi-2201) ( $T_c \approx 20$  K) and  $\text{Bi}_2\text{Sr}_2\text{CaCu}_2\text{O}_y$  (Bi-2212) ( $T_c \approx 90$  K) single crystals were grown by the traveling-solvent floating zone (TSFZ) method. Highly  $c$ -axis-oriented  $\text{Bi}_{1.8}\text{Pb}_{0.4}\text{Sr}_{1.8}\text{Ba}_{0.2}\text{Ca}_{2.2}\text{Cu}_{3.0}\text{O}_y$  (Bi-2223) ceramics with  $T_c \approx 108$  K were synthesized by means of a hot-press technique.<sup>1)</sup> These materials were irradiated by the 3.5 GeV  $^{136}\text{Xe}^{31+}$  beam at RIKEN Ring Cyclotron Facility to produce columnar defects along  $c$ -axis. In all cases, the pin density ( $n_{\text{pin}}$ ) was  $1.2 \times 10^{11}/\text{cm}^2$ , which corresponds to a dose-equivalent matching field  $B_\Phi = n_{\text{pin}} \Phi_0 = 2.4$  T, where  $\Phi_0$  is the flux quantum. The irradiation reduced  $T_c$  by 5, 3, and 1 K for Bi-2201, Bi-2212 and Bi-2223, respectively.

We have investigated the irreversibility line which marks the onset of reversible flux motion in the magnetic field ( $B_{\text{ex}}$ ) versus temperature ( $T$ ) phase diagram, using the AC loss peaks ( $T_p$ ) in the temperature dependence of the imaginary part of susceptibility ( $\chi''$ ). When the amplitude of AC field is low, 0.5 Oe, the AC response was linear. For the linear response the irreversibility line determined by the AC loss peaks corresponds to the constant resistivity line with  $\rho_{\text{ab}} = 0.225\pi wd\mu_0 f$  in  $B_{\text{ex}}-T$  plane,<sup>2)</sup> where  $w$  is the width of the sample,  $d$  the thickness, and  $f$  the frequency of the AC field. Figure 1 shows the irreversibility lines determined by the criterion of  $\rho_{\text{ab}} \approx 0.1\mu\Omega\text{cm}$  (at frequency of 5 kHz and AC field of 0.5 Oe) for Bi-2201, Bi-2212 and Bi-2223 before and after the Xe

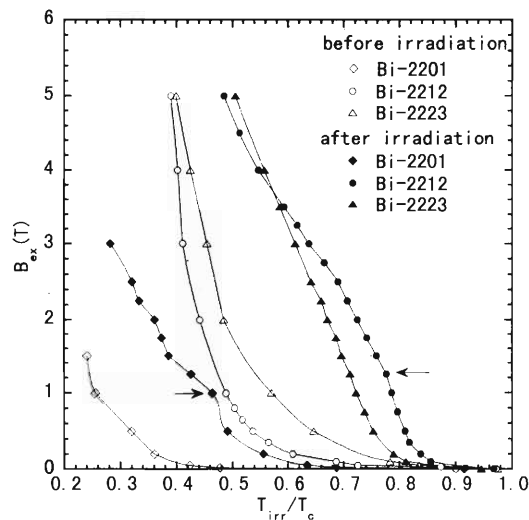


Fig. 1. Irreversibility lines for Bi-2201, Bi-2212 and Bi-2223 before and after the Xe irradiation.

irradiation. After the irradiation all the irreversibility lines show strong shifts to the higher reduced temperature. Xe irradiation has improved the pinning properties strongly for Bi-2201, Bi-2212 and Bi-2223. Another interesting feature was observed for the Bi-2201 and Bi-2212 single crystals after irradiation. That is, a kink appeared in the irreversibility line at about  $0.5B_\Phi$  ( $\approx 1$  T), above which the motion of the vortices lying in the interstitial spaces between columns is believed to be relevant to the irreversibility line,<sup>3)</sup> as shown by the arrows in Fig. 1.

### References

- 1) H. Ikeda et al.: Jpn. J. Appl. Phys. **29**, L430 (1990).
- 2) E. H. Brants: Phys. Rev. Lett. **71**, 2821 (1993).
- 3) L. Krusin-Elbaum et al.: Phys. Rev. Lett. **72**, 1914 (1994).

\* Cryogenics Center, University of Tsukuba

# Irradiation Effects of Swift Heavy-Ion on Polycrystalline $\text{La}_{1.85}\text{Sr}_{0.15}\text{CuO}_4$

T. Mitamura, M. Terasawa, X.-J. Fan, T. Kohara, K. Ueda, and T. Kambara

For practical application of the high-temperature superconductor, the achievement of high critical current density under high magnetic fields is very important, because the critical current density tends to decrease rapidly by easy motion of vortices when the temperature approaches the critical temperature. Enhancement of the pinning strength in high- $T_c$  cuprates due to introduction of parallel or multi-direction columnar defects by ion irradiation has been reported.<sup>1-5)</sup> In the present study, a high-temperature superconducting material, polycrystalline  $\text{La}_{1.85}\text{Sr}_{0.15}\text{CuO}_4$ , (henceforth LSCO), was irradiated by swift heavy ions in order to introduce columnar defects as vortex pinning centers, and the characteristics of superconductivity were investigated.

The polycrystalline LSCO bulk specimens with the surface of about  $2 \text{ mm} \times 10 \text{ mm}$  and thickness of  $0.1 \text{ mm}$  were irradiated at room temperature in a high vacuum by the  $3.5 \text{ GeV } ^{136}\text{Xe}^{31+}$  ions which were accelerated by RIKEN Ring Cyclotron. Ion irradiation was carried out by two ways; single direction irradiation perpendicularly to the surface of specimen (parallel irradiation), and multi-direction irradiation (splay irradiation). In the present case, the splay irradiation was performed by combining two irradiation directions: the direction normal to the specimen surface and the direction tilted at an angle of  $\theta$  from the normal line ( $\theta$  degree splay-irradiated specimen). In the splay irradiation, total irradiation doses were set to be the same amount for each direction. The measurements of magnetization hysteresis and vortex creep were carried out by a Quantum Design SQUID magnetometer by applying an external magnetic field normal to the surface of specimen.

Figure 1 shows examples of the magnetization hysteresis loops obtained at temperature  $5 \text{ K}$  for a  $\theta = 0$  (parallel) as well as irradiated specimen, and  $\theta = 5$  and  $\theta = 45$  degree splay-irradiated specimens with the

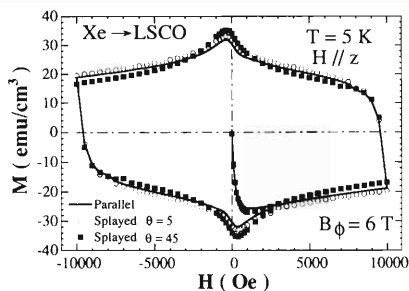


Fig. 1. Comparison of magnetic hysteresis loops of the  $3.5 \text{ GeV } ^{136}\text{Xe}^{31+}$  ion between splay-irradiated ( $\theta = 5$  and  $45$  degree) and parallel-irradiated polycrystalline LSCO specimens. The total irradiation dose corresponds to  $B_\phi = 6.0 \text{ T}$ .

same total irradiation dose of  $B_\phi = 6.0 \text{ T}$ . ( $B_\phi$  is the field-equivalent irradiation dose, and the vortex density at  $B_\phi = 1.0 \text{ T}$  corresponds to the irradiation dose of  $0.5 \times 10^{11} \text{ Xe/cm}^2$ ) From the figure, it is suggested that total strength of vortex flux pinning depends on the spray-irradiation angle  $\theta$ . It was observed that the columnar defects introduced by low angle (below about  $10$  degree) splay-irradiation can more strongly pin the vortices. In the other experiments, the irreversibility line, which corresponds to the boundary dividing the pinning region of magnetic flux lines (vortices) from the complete depinning region in the temperature-vs.-magnetization plane, is most effectively enhanced also at  $\theta = 10$  degree splay-irradiation. Optimum splay-irradiation angle for the most effective vortex pinning is tentatively obtained to be about  $10$  degree.

The examples of normalized changes of magnetic relaxation (vortex flux creep) are illustrated in Fig. 2 for three different irradiation modes. In the figure, the splay-irradiation angle was  $10$  degree. The magnetic relaxation proceeds slowest in the splay-irradiated specimen, which is considered an evidence that the configuration of columnar defects produced by the splay-irradiation is more effective for vortex pinning than that by the parallel irradiation. Many theoretical explanations have been proposed so far.<sup>6)</sup> We are now making the comparison of our data with those theoretical predictions.

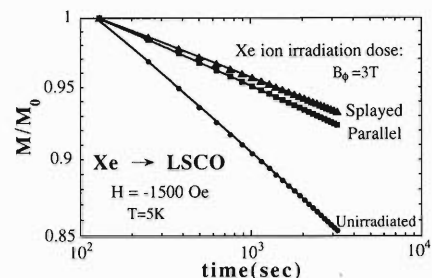


Fig. 2. Comparison of the normalized magnetic relaxation curve of the unirradiated specimen with those of the parallel and  $\theta = 10$  degree splay-irradiated polycrystalline LSCO specimens.

## References

- 1) V. Hardy et al.: Nucl. Instrum. Methods Phys. Res. B **54**, 472 (1991).
- 2) Th. Becker et al.: Physica C **245**, 273 (1995).
- 3) M. Terasawa et al.: Physica C **235**, 2805 (1994).
- 4) T. Hwa et al.: Phys. Rev. Lett. **71**, 3545 (1993).
- 5) Th. Schuster et al.: Phys. Rev. B **51**, 16358 (1995).
- 6) Y. Yeshurun et al.: Rev. Mod. Phys. **68**, 991 (1996).

## Observation of Columnar Defects in Layered Materials Bombarded by $^{136}\text{Xe}^{+31}$ , $^{181}\text{Ta}^{+37}$ , and $^{209}\text{Bi}^{+37}$ by STM and TEM

N. Nishida, H. Sakata, S. Kaneko, Y. Ono, Y. Taguchi, and T. Kambara

In some materials the high-energy heavy ions generate columnar defects which are linear damage tracks of  $\sim 10$  nm diameter along the tracks of heavy ions. Recently, the columnar defects in copper-oxide high temperature superconductors have attracted attentions, because they are effective to pin vortices in high magnetic fields. The formation mechanism of columnar defects has not been well understood: Heavy ions may locally melt the crystal and generate amorphous columns along their tracks, or the recovery time of electrons to ionized atoms are so long that ionized atoms change their position before they become neutral and thus the crystal is destroyed locally. We have reported<sup>1)</sup> that the 3.4 GeV  $^{136}\text{Xe}^{+31}$  ions generate columnar defects in mica or high- $T_c$  oxide-superconductors with diameter of about 10 nm, but not in 2H-NbSe<sub>2</sub> and 1T-TaS<sub>2</sub> at all. In this report we mention the experimental results of the  $^{181}\text{Ta}^{+37}$  and  $^{209}\text{Bi}^{+37}$  bombardments on the 2H-NbSe<sub>2</sub> and 1T-TaS<sub>2</sub> single crystals at room temperature at the E5a beam line of RIKEN Ring Cyclotron Facility. The columnar defects were observed to have been generated by  $^{181}\text{Ta}^{+37}$  and  $^{209}\text{Bi}^{+37}$  both in 2H-NbSe<sub>2</sub> and 1T-TaS<sub>2</sub>. In Fig. 1 shown is a scanning tunneling microscope (STM) image of a columnar defect generated by  $^{181}\text{Ta}^{+37}$  in 2H-NbSe<sub>2</sub>; a triangular-shaped

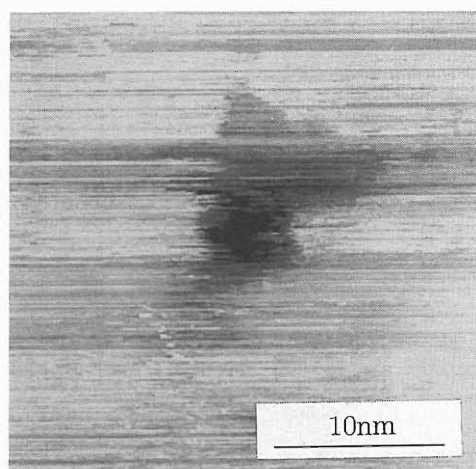


Fig. 1. Columnar defects observed by STM in 2H-NbSe<sub>2</sub>. The black region is a columnar defect of amorphous structure. A triangular shape region around the columnar defect has a crystal structure.

contrast can be seen around a columnar defect. This has also been observed by transmission electron microscope (TEM). It is not known what is the meaning of the triangular region; a structural change or a change of electronic states around a columnar defect. In Fig. 2 shown is a TEM photograph of tracks of  $^{181}\text{Ta}^{+37}$  in 1T-TaS<sub>2</sub>. Ta ion beam was injected into 1T-TaS<sub>2</sub> crystal slightly canted against the *c*-axis and TEM photograph was taken with the electron beam parallel to the *c*-axis. Discontinuous tracks can be seen. This means that an amorphous columnar region is generated discontinuously along the track. This amorphous structure has been confirmed by the TEM and STM observations. Thus, in 2H-NbSe<sub>2</sub> and 1T-TaS<sub>2</sub>, columnar defects have been generated by using heavy ions of Ta and Bi, but columnar defects are found not to be continuous in 1T-TaS<sub>2</sub> or the border region is vague in 2H-NbSe<sub>2</sub>; these features are different from those in Bi<sub>2</sub>Sr<sub>2</sub>CaCu<sub>2</sub>O<sub>x</sub>. These observations will be related with a formation mechanism of the columnar defects induced by high energy heavy ions and will help to understand the physics. Consideration is under way.

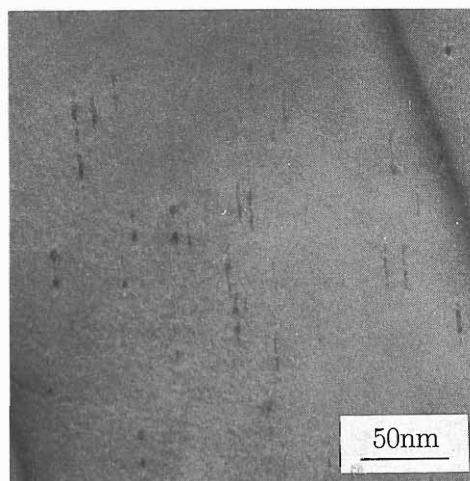


Fig. 2. TEM photograph of the  $^{181}\text{Ta}^{+37}$  beam bombarded 1T-TaS<sub>2</sub>. Amorphous columnar region is seen to be generated discontinuously.

### References

- 1) N. Nishida et al.: RIKEN Accel. Prog. Rep. 29, 123 (1996).

# Experimental Study of Single Event Burnout (SEB) Hardening on POWER MOSFET

S. Matsuda, S. Kuboyama, S. Shugyo, T. Suzuki, K. Sugimoto,  
T. Hirose, H. Ohira, T. Kohno, and M. Kase

Semiconductor devices, which are essential in artificial satellites and spacecrafts, are degraded by radiation in space. The radiation environment around the earth includes the electrons and protons trapped by the Earth's magnetosphere, and the solar protons and heavy ions in galactic cosmic rays. It is well known that the impingement of high energy heavy ions on semiconductor devices causes single event phenomenon (SEP) like single event upset (SEU) on memory device, single event latch up (SEL) on CMOS, LSI etc., and single event burnout (SEB) caused by the heavy ion passing through the active area of POWER MOSFET. NASDA (National Space Development Agency of Japan) has studied SEB and single event gate rupture (SEGR) on POWER MOSFET with heavy ions available from the RIKEN Ring Cyclotron.<sup>1)</sup>

We are developing 250V POWER MOSFET to be used for the future artificial satellites which will be launched in 2002. To fix the design parameters of the POWER MOSFET, we have performed irradiation test on several types of samples with a beam of Ni<sup>25+</sup> at 7.6 MeV/u (440.8 MeV) and studied the breakdown

voltage data concerning with SEB and SEGR. After an energy degrader the energy of beam on the samples was about 260 MeV/u where the linear energy transfer (LET) of the ions in the material (Si) was about 27 MeV/(mg/cm<sup>2</sup>) and the range was about 36  $\mu$ m (Si).

It is obvious from the former experimental data that the single event effect (SEE) tolerance of POWER MOSFET depends on the BV<sub>DS</sub> (Drain-Source Breakdown Voltage) of POWER MOSFET.<sup>2)</sup> When the BV<sub>DS</sub> is higher, the tolerance is higher; but the high BV<sub>DS</sub> leads to a high R<sub>on</sub> value (R<sub>on</sub>: a resistance value when the transistor goes "ON" state). To keep a low R<sub>on</sub> value on the same BV<sub>DS</sub>, it is necessary to enlarge the chip size, then the capacitance increases and the switching speed slows down. Therefore, we prepared several types of samples that were fabricated with various parameters for space applications. The design parameters on each samples together with the irradiation test results are shown in Table 1. Other irradiation test data (underlined data) mainly performed on SEGR at Brookhaven National Laboratory in USA are shown, too.

Table 1. The design parameters on each samples and irradiation test data.

description	process condition			chip design		result of SEB test	result of SEGR test	remark
	BV <sub>ds</sub>	n <sup>+</sup> layer(As) dose	gate thickness	cell geometry	p-pitch	SEB threshold(V <sub>ds</sub> )	SEGR threshold(V <sub>gs</sub> )	
6F	250V	4.00E+15	800 Å	stripe	9 $\mu$ m	190, 200, 200, 210	250V<	T <sub>c</sub> =100°C
6C	250V	4.00E+15	800 Å	square	3 $\mu$ m	130, 135	140V	T <sub>c</sub> =T <sub>a</sub>
6H	250V	4.00E+15	800 Å	stripe	3 $\mu$ m	165, 173, 175, 185	175V<(SEB threshold)	T <sub>c</sub> =100°C
2C	300V	4.00E+15	800 Å	square	3 $\mu$ m	160, 170	190V	T <sub>c</sub> =100°C
6I	250V	4.00E+15	800 Å	square	5 $\mu$ m	125, 127	200V<	T <sub>c</sub> =100°C
7F	250V	4.00E+15	1000 Å	stripe	9 $\mu$ m	190, 190, 195, 200	200V<	T <sub>c</sub> =100°C
10F	300V	3.50E+15	800 Å	stripe	9 $\mu$ m	240, 240	250V<	T <sub>c</sub> =100°C

remark : temperature condition on SEGR test

T<sub>c</sub> : case temp., T<sub>a</sub> : ambient temp.

The underlined data was acquired at Brookhaven National Laboratory.

First, we compared the effect of cell geometry. From the former study, the uniformity of electronic fields in the chip contributes to improve the SEB tolerance. Table 1 shows that the stripe pattern cell has better SEB tolerance than the square one has. The reason is that the square pattern cell leads to 2 and 3 dimensional localized charge at the corner of cell. (On the other hand, however it is also said that the cell geometry does not influence the failure threshold of SEGR.<sup>3)</sup>) As a result, the cell geometry was determined to be stripe pattern.

Second, we compared the effect of p-pitch size. In ordinary, if p-pitch is smaller, the SEB tolerance increases; but the R<sub>on</sub> characteristic worsens, at the same time. Therefore, p-pitch size had to reduce under 10  $\mu$ m on our samples. From the data of former irradi-

ation test, the SEB threshold was 120 V on 16  $\mu$ m p-pitch samples. In this test, we irradiated 9  $\mu$ m p-pitch samples, and as the Table 1 shows the result was better than 16  $\mu$ m p-pitch, and better than 3  $\mu$ m p-pitch, too. We expect there is an optimum p-pitch size of POWER MOSFET, and continue to analyze the data.

## References

- 1) S. Kuboyama et al.: IEEE Trans. Nucl. Sci. **NS-39**, 1698 (1992).
- 2) K. F. Galloway et al.: Proc. 2nd Int. Workshop on Radiation Effects of Semiconductor Devices for Space Application, p. 88 (1996).
- 3) J. L. Titus et al.: IEEE Trans. Nucl. Sci. **NS-42**, 1928 (1995).

## Change of Site Occupancy of Hydrogen in Nb on Alloying with Undersized Mo<sup>†</sup>

E. Yagi and S. Koike\*

Regarding the effect of alloying on the terminal solubility of hydrogen (TSH) in group V<sub>a</sub> metals (V, Nb and Ta), it has been reported that for undersized metal solutes, e.g., Nb in Ta and Mo in Nb, the TSH increases rapidly with solute concentration.<sup>1,2)</sup> To understand this effect the lattice location of hydrogen in Nb-Mo alloys has been investigated by the channeling method utilizing a nuclear reaction  ${}^1\text{H}({}^{11}\text{B},\alpha)\alpha$  with an  ${}^{11}\text{B}$  beam of an energy of approximately 2 MeV.<sup>3)</sup> In this method the hydrogen can be detected by measuring the emitted  $\alpha$ -particles. Previous studies on H in Nb-3at%Mo and Nb-10at%Mo alloys demonstrated that a portion of H atoms are trapped at room temperature by Mo atoms to be located at the sites displaced from the tetrahedral (*T*) sites by about 0.6 Å towards the Mo atoms substituting Nb atoms (trapped sites) and the remaining H atoms are located at *T* sites. They also demonstrated that the number of H atoms located at the trapped sites per one Mo atom (the trapping efficiency  $\gamma$ ) decreases from 0.7–1.0 in the Nb-3at%Mo alloy to 0.2–0.3 in the Nb-10at%Mo alloy.<sup>4–6)</sup> In the present study the lattice location of hydrogen in a more concentrated Nb-20at%Mo alloy is investigated as in a previous study.<sup>3)</sup>

The lattice parameter of this alloy was measured to be about 0.8% smaller than that of Nb. Hydrogen was doped from the gas phase up to the three different concentrations ( $C_{\text{H}}$ ) 2.6, 4.2 and 8.0 at%.

The results are shown in Fig. 1. For  $C_{\text{H}} = 2.6$  and 4.2 at% the angular profiles of the  $\alpha$ -particle yields ( $\alpha$ -angular profiles) are very similar. Being superposed on a shallow dip, they exhibit subpeaks at the angular positions expected for the *T*-site occupancy which are indicated by arrows.<sup>7)</sup> The subpeaks characteristic of the trapped-site occupancy<sup>4)</sup> are not observed. These results suggest that a large portion of H atoms are located at *T* sites, and some portion of them are located at the sites which give the shallow dip in the  $\langle 100 \rangle$  and  $\langle 110 \rangle$   $\alpha$ -angular profiles. Namely, those sites are shadowed by  $\langle 100 \rangle$  and  $\langle 110 \rangle$  atomic rows. These shadowed sites are considered to be octahedral (*O*) sites. For  $C_{\text{H}} = 8.0$  at%, similar subpeaks are still observable, but the shallow dips for the  $\langle 100 \rangle$  and  $\langle 110 \rangle$  channels become much shallower or they disappear.

The lattice locations of hydrogen and its distribution were determined by fitting the calculated  $\alpha$ -angular profiles to the observed ones. It is concluded as follows: In Nb-20at%Mo alloys, H atoms are located at both *T* and *O* sites, but not at the trapped sites, i.e.,  $\gamma = 0$ . For  $C_{\text{H}} = 2.6$  and 4.2 at%, the fraction of the *O*-site occupancy is 20–30%, while, for  $C_{\text{H}} = 8.0$  at%, it remarkably decreases to 0–10%.

<sup>†</sup> Condensed from the article in J. Phys. Soc. Jpn. **67**, 340 (1998)

\* Dept. Phys. II, Fac. Sci., Science Univ. of Tokyo

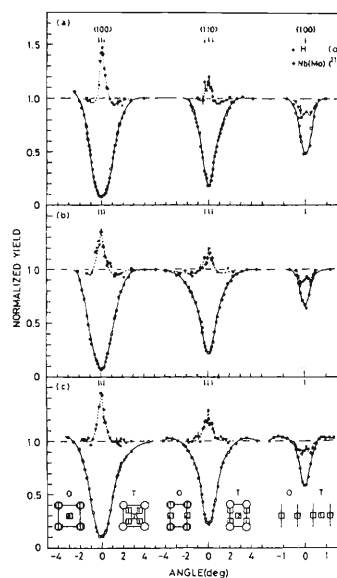


Fig. 1 Channeling angular profiles of  $\alpha$ -particle yield (●) and the yield of  ${}^{11}\text{B}$  ions backscattered by host metal atoms (○), obtained at room temperature for Nb-20 at%Mo alloys containing H by (a) 2.6, (b) 4.2, and (c) 8.0 at%. The full and dashed curves have been drawn to guide the eye. In the insets the projections of *T* and *O* sites onto the plane perpendicular to the channel in question are shown by open squares with relative weights. The open circles and lines represent the projections of atomic rows and planes, respectively.

The appearance of the *O*-site occupancy in Nb-20at%Mo alloys can be understood as a result of the reduction of the energy difference between *T* and *O* sites due to the decrease of the lattice parameter on alloying with undersized Mo atoms. The trapping model<sup>1)</sup> proposed as a mechanism for the enhancement of the TSH in Nb on alloying with Mo atoms is considered to be effective in the region of the Mo concentration lower than about 5 at%. The reduced fraction of the *O*-site occupancy at  $C_{\text{H}} = 8$  at% is considered to be due to the interaction between H atoms.

More detailed description is given in Ref. 8.

### References

- 1) T. Matsumoto et al.: J. Phys. Chem. Solids **36**, 215 (1975).
- 2) J. F. Miller and D. G. Westlake: Trans. Jpn. Int. Met. **21**, Suppl., 153 (1980).
- 3) E. Yagi et al.: Phys. Rev. B **31**, 1640 (1985).
- 4) E. Yagi et al.: Phys. Rev. B **39**, 57 (1989).
- 5) E. Yagi et al.: Proc. Jpn. Academy **65B**, 38 (1989).
- 6) E. Yagi: Radiat. Eff. and Defects Solids **124**, 21 (1992).
- 7) E. Yagi et al.: J. Phys. Soc. Jpn. **54**, 1855 (1985).
- 8) E. Yagi and S. Koike: J. Phys. Soc. Jpn. **67**, 340 (1998).

# Annealing of the $\text{Cu}_3\text{Au}$ Irradiated with Protons, $\alpha$ -Particles and C Ions at Liquid Nitrogen Temperature

H. Sakairi,\* E. Yagi, and A. Koyama

Ordered alloys are most promising type of systems to study the replacement collision in damage production processes and the migration of vacancies, because their effects are observable as a large change in the ordered state. Succeeding to the studies on the damage production rate and the isochronal annealing up to 90 K on the  $\text{Cu}_3\text{Au}$  irradiated below 30 K with high energy ions,<sup>1,2)</sup> in the present study the isochronal annealing experiments were extended up to 460 K. The irradiation was performed for both initially ordered and disordered  $\text{Cu}_3\text{Au}$  specimens at a temperature below 85 K with protons,  $\alpha$ -particles or C ions of various energies from 6 to 90 MeV provided from the Cyclotron under the condition for incident ions to penetrate the specimens. Heat treatment for preparing the ordered specimens followed the previous work.<sup>2)</sup> However, the perfect ordering could not be achieved. After each annealing period of 10 min, the electrical resistivity was measured at the liquid  $\text{N}_2$  temperature. The results are shown in Fig. 1. Irradiation-introduced defects increase the electrical resistivity. The resistivity increment  $\Delta\rho$  is normalized to the initial resistivity increment  $\Delta\rho_0$  in the as-irradiated state.

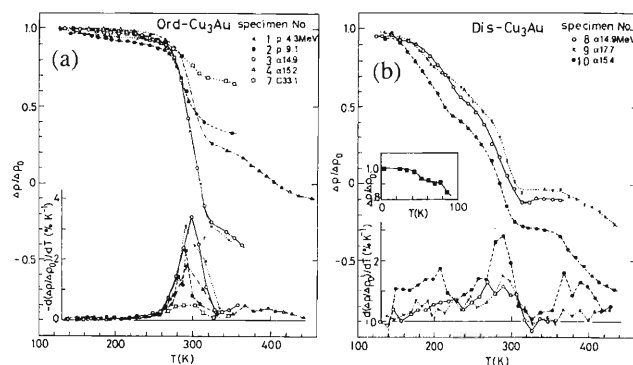


Fig. 1. Isochronal annealing curves of the electrical resistivity for 10 min annealing periods and their temperature derivatives for (a) the initially ordered and (b) initially disordered  $\text{Cu}_3\text{Au}$  specimens. The inset shows the previous result obtained for a disordered specimen after the irradiation with 20.5 MeV  $\alpha$ -particles at 13.5 K.

In the ordered specimens two large stages are evident in the temperature regions 240–340 K and 340–460 K. Hereafter, these stages are called 290K-stage and the 380K-stage, respectively.

In the disordered specimens three large recovery stages are observed in the temperature regions 100–220 K (190K-stage), 220–320 K (280K-stage) and 340–440 K (380K-stage), respectively. The latter two regions

are approximately same as those in the ordered specimens. In addition to these three stages, the recovery curves have an inflection around 150 K, indicating the presence of a recovery stage (150K-stage). However, with increasing  $\Delta\rho_0$ , this stage gradually joins the 190K-stage. Combined with the previous result shown in the inset of Fig. 1(b), it can be said that there exists a recovery stage in the temperature region between 80 and 110 K (85K-stage).

At the 280K- or 290K-stages and the 380K-stage, in both ordered and disordered alloys, the resistivity becomes lower than the value before irradiation in some case, indicating an enhancement of the long-range ordering. (The initially ordered specimens were not perfectly ordered.) Such defect-enhanced ordering has been observed in the experiments of quenching of the initially disordered or partially ordered  $\text{Cu}_3\text{Au}$  from temperatures not only above but also below  $T_C$  (the critical temperature for ordering) followed with annealing at temperatures below 473 K.<sup>3-5)</sup> Therefore, the recovery in the two stages in question is considered to be related to the irradiation-introduced vacancies. Considering the results of the positron annihilation experiments,<sup>6)</sup> the two recovery stages can be interpreted to be the recovery due to migration of free vacancies to sinks or for the formation of clusters and the recovery of long-range order associated with it, and due to migration of the vacancies supplied as a result of evaporation of vacancy clusters and the associated ordering, respectively.

As for recovery stages above 80 K in the initially disordered  $\text{Cu}_3\text{Au}$ , five stages were observed in the isochronal annealing after the electron irradiation.<sup>7)</sup> Taking account of the incident electron-energy dependence of their five stages,<sup>7)</sup> the 85K-, 150K- and 190K-stages observed in the present experiments are interpreted to be due to the close-pair recovery of Cu-Frenkel defects, the migration of Cu interstitials, and that of Au interstitials, respectively.

## References

- 1) H. Sakairi, E. Yagi, A. Koyama, and R. R. Hasiguti: *J. Phys. Soc. Jpn.* **43**, 999 (1977).
- 2) E. Yagi, H. Sakairi, A. Koyama, and R. R. Hasiguti: *Phys. Rev.* **38**, 3189 (1988).
- 3) R. A. Dugdale: *Phil. Mag.* **11**, 537 (1956).
- 4) P. Wright and J. C. Goodchild: *Proc. Phys. Soc.* **79**, 196 (1962).
- 5) S. Benci, G. Gasparrini, E. Germagnoli, and G. Schianchi: *J. Phys. Chem. Solids* **26**, 2059 (1965).
- 6) M. Doyama, P. Moser, D. Huguenin, A. Alamo, and C. Corbel: *Positron Annihilation*, ed. P. C. Jain, R. M. Singru, and K. P. Gopinathan (World Scientific, Singapore, 1985), p. 903.
- 7) J. Gilbert, H. Herman, and A. C. Damask: *Rad. Eff.* **20**, 37 (1973).

\* Present address: Sping-8 Service Co. Ltd.

## Development of Experimental Setup for Laser Spectroscopic Study of Ions in Superfluid Helium

Q. Hui and M. Takami

We are preparing a new experiment to implant atomic ions into superfluid helium (He II) and to measure the laser induced fluorescence (LIF) spectra of these ions. Of particular interests are the alkaline earth ions, *i.e.*  $\text{Be}^+$ ,  $\text{Mg}^+$ ,  $\text{Ca}^+$ ,  $\text{Sr}^+$ , and  $\text{Ba}^+$ . In the ground state, each of these ions has only one *s*-electron outside its closed ion core. Recent studies in our and other groups have shown that the neutral atoms with single *s*-valence electron (group IA and IB atoms in the periodic table) form metal- $\text{He}_n$  exciplexes in the first excited *P*-states in liquid helium.<sup>1,2)</sup> Because the alkaline earth ions have similar electronic structure as the group IA and IB atoms, the same phenomenon is expected to be observed for these ions. The LIF emissions of the alkaline earth ion- $\text{He}_n$  exciplexes are expected to be in the visible and UV regions, more convenient to study than that of alkali atom- $\text{He}_n$  exciplexes. Therefore, the alkaline earth ions are an ideal system to study the dynamics of the exciplex formation process. Furthermore, two light members of these ions, *i.e.*  $\text{Be}^+$  and  $\text{Mg}^+$ , may form solid helium shells surrounding them (“snowballs”),<sup>3)</sup> due to strong attractions between these two ions and helium atoms. If “snowballs” are formed, the LIF excitation spectra of these two ions should show blue-shifts much larger than the other ions do.

So far, many methods have been used to implant ions into liquid helium. We adopt the laser ablation method which has been proved to be a simple but very efficient way.<sup>4)</sup> The experimental setup is illustrated in Fig. 1. A metal Dewar (Oxford) equipped with quartz windows contains He II. A quartz cell is placed above the liquid and the cell itself is filled also with He II. Two or three He II pumps, utilizing the “fountain effect” of He II, are used to transfer the liquid into the cell. The surface of the He II in the cell is determined by the height of the cell. A piece of metal sample is hung about 1 cm above the quartz cell. An ablation laser beam ( $1.06 \mu\text{m}$ , a few mJ/pulse) is focused onto the sample through one of the windows. A pair of electrodes are immersed into the liquid in such a way that the upper one stays just a few millimeters below the liquid surface. The upper electrode (extractor) is typically at +100 V and the lower one (collector) is grounded. The sample is at about +200 V. The distance between the extractor and collector is about 1–2 cm. The positively charged ions produced via the laser ablation are extracted into He II by the electric field. A

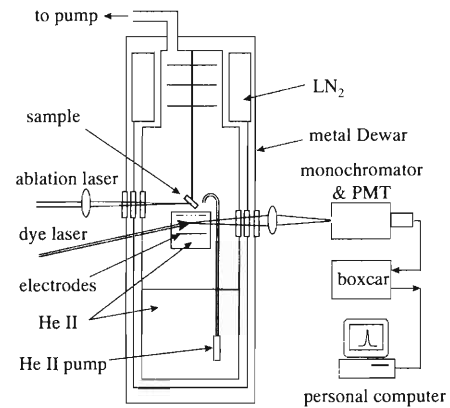


Fig. 1. Illustration of the experimental setup.

pulsed dye laser beam intersects the ion beam between the extractor and collector and excites the ions. The LIF emitted by the ions is detected at a right angle by a photomultiplier (PMT) through a monochromator. The electric signal is averaged by a boxcar integrator and sent to a computer.

In a preliminary test of the setup, we have observed  $\text{Ba}^+$  emission from the plasma produced by the laser ablation near the sample surface. We find that this emission becomes weaker a few minutes after the ablation is started due to a change of the surface condition. This problem can be solved by scanning the ablation laser beam over the sample surface. Another problem is the heating of the liquid by the He II pumps which have heaters inside. The helium gas pressure in the Dewar is typically 6 Torr when the pumps are off, and about 20 Torr when they are on. These pressures correspond to He II temperatures of about 1.6 K and 2 K respectively. Because the mobilities of ions in He II decrease rapidly with increasing temperature, it is necessary to keep the temperature as low as possible. We plan to use two-stage “fountain” pumps with lower power consumption to solve this problem.

### References

- 1) J. L. Persson et al.: Phys. Rev. Lett. **76**, 1501 (1996).
- 2) J. Dupont-Roc: Z. Phys. B **98**, 383 (1995).
- 3) K. R. Atkins: Phys. Rev. **116**, 1339 (1959).
- 4) G. zu Putlitz and M. R. Beau: in *Topics in Applied Physics* **70**, *Dye Lasers: 25 Years*, edited by M. Stuke (Springer-Verlag, Berlin, Heidelberg, 1992), p. 237.

# Muon Spin Relaxation in $\text{KCuCl}_3$

W. Higemoto, H. Tanaka,\* I. Watanabe, and K. Nagamine

[ $\mu^+$ SR,  $\text{KCuCl}_3$ , Low Dimensional Magnetism]

Low dimensional magnetism is one of the subjects of the recent study. In particular, quasi one dimensional systems have attracted much interests.

We report the results of a positive muon spin relaxation ( $\mu^+$ SR) experiment on the  $S = 1/2$  double chain system of  $\text{KCuCl}_3$ . Figure 1 illustrates the exchange interaction paths in the double chain. The present system can be described as a  $S = 1/2$  Heisenberg spin ladder system consisting of the  $J_1$  and  $J_2$  (or  $J_3$ ) interactions with an additional diagonal interaction  $J_3$  (or  $J_2$ ). Previous magnetic susceptibility measurement<sup>1)</sup> suggests that the ground state of  $\text{KCuCl}_3$  is a spin singlet state with a finite spin gap of  $\Delta/k_B \sim 35$  K. This spin gap has also been observed in the other measurements.

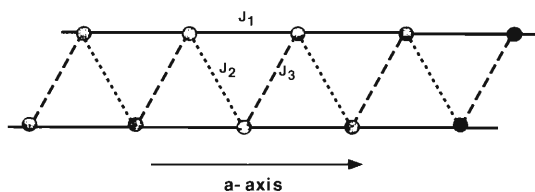


Fig. 1. The arrangement of the Cu atoms of the double chain and the interactions  $J_1$ ,  $J_2$ , and  $J_3$ .

$\mu^+$ SR experiments were carried out at Port-2 of the RIKEN-RAL Muon Facility. Although, the ground state of  $\text{KCuCl}_3$  is suggested as a spin liquid state, we observed the fast relaxation below 20 K. Figure 2(a) shows the temperature dependence of the  $\mu^+$ SR spectra under a longitudinal magnetic field (LF) of 100 G. Above 20 K, we saw no significant muon spin relaxation, but below 20 K, the muon spin showed fast relaxation. We fit the data with a power-law-type relaxation function,  $G_z = \exp(-(\lambda t)^\beta)$ , and the solid lines in Fig. 2(a) are the results of the fitting. The temperature dependences of the relaxation rate  $\lambda$  and of the power  $\beta$  are shown in Fig. 2(b). Below 20 K,  $\lambda$  increases with decreasing temperature. In LF of 3800 G, however, we found a cusp in the temperature dependence of the relaxation rate around 5 K.

Our results show the existence of a local magnetic field of the order of kG at the muon site below 20 K, while other macroscopic and microscopic experiments

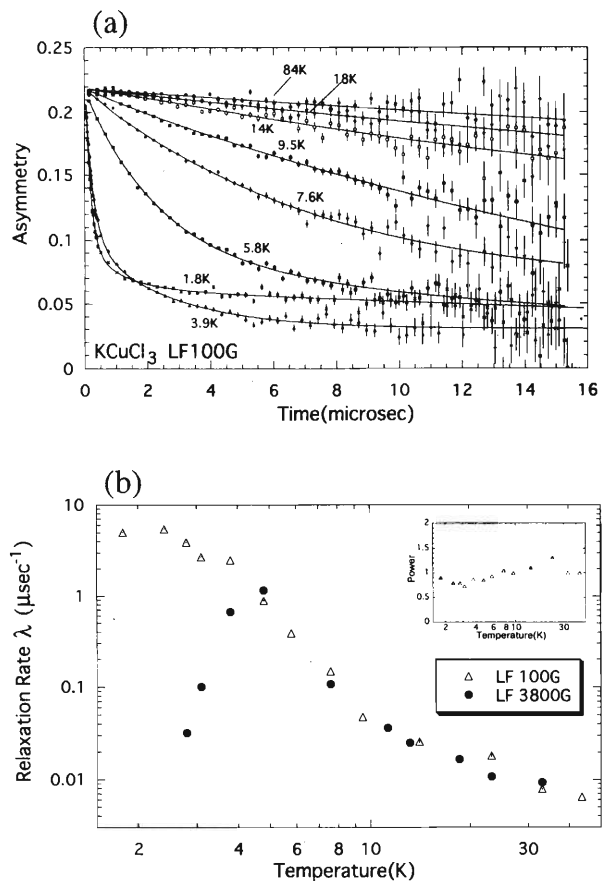


Fig. 2. (a): Temperature dependence of the muon spin relaxation spectra. Solid curves represent the fitting results. (b): Temperature dependence of the muon spin relaxation rate  $\lambda$  in LF of 100 G and 3800 G. The inset figure shows the power  $\beta$ .

suggest a non-magnetic ground state with a finite spin gap. Our sample contains very little concentration of paramagnetic impurities, and thus it is unlikely that our observed relaxation occurs only due to such an extrinsic component.

For the investigation of the microscopic muon states, a muon spin resonance experiment is going on.

## References

- 1) H. Tanaka et al: J. Phys. Soc. Jpn. **65**, 1945 (1996).

\* Department of Physics, Tokyo Institute of Technology

## $\mu$ SR Studies on $(\text{Nd}_{1-y}\text{Sm}_y)_{0.5}\text{Sr}_{0.5}\text{MnO}_3$

W. Higemoto, K. Nishiyama, I. Watanabe, K. Nagamine,  
A. Asamitsu,\* H. Kuwahara,\* and Y. Tokura\*

[ $\mu^+$ SR, Manganese Oxide, CMR]

Recent systematic studies on the perovskite type manganese oxide  $(\text{Nd}_{1-y}\text{Sm}_y)_{0.5}\text{Sr}_{0.5}\text{MnO}_3$ <sup>1,2)</sup> have revealed a competitive nature existing between the ferromagnetic double-exchange interaction and the antiferromagnetic charge ordering instability which gives rise to a temperature, magnetic field, and pressure induced transition from the ferromagnetic metal (FM) to antiferromagnetic insulator (AFI). This transition is accompanied with change of the resistance by several orders of magnitude, and the phenomenon is known as the colossal magneto resistance (CMR). The competition between the FM state and AFI state is rather sensitive to the Mn-O-Mn bond angle or Sm ratio  $y$ . In particular, a metastable FM phase appears in the  $0.85 < y < 1$  region below 100 K. We have performed the muon spin rotation/relaxation ( $\mu$ SR) measurements in  $(\text{Nd}_{1-y}\text{Sm}_y)_{0.5}\text{Sr}_{0.5}\text{MnO}_3$  ( $y = 0.875$ ) for the investigation of competition between FM state and AFI state.

$\mu^+$ SR experiments were carried out at Port-2 of RIKEN-RAL Muon Facility (pulsed beam) at the ISIS Facility of Rutherford Appleton Laboratory in the U.K. and at M9B decay muon channel of TRIUMF (continuous beam) in Vancouver, Canada. These two muon beam channels provide us two different types of muon beam. By using these two beam channels, we can carry out the experiments covering entire time resolution as well as time range.

Above 132 K or in the paramagnetic phase, slow muon spin relaxations were observed under a zero magnetic field (ZF). Figure 1 shows a time evolution of the muon spin asymmetry at 293 K under ZF. The data can be represented by using an exponential relaxation function,  $P_z(t) = A \exp(-\lambda t)$ , and the solid line in Fig. 1 shows the fitted result. In the previous measurement of temperature dependence of the magnetization  $M$  in  $(\text{Nd}_{1-y}\text{Sm}_y)_{0.5}\text{Sr}_{0.5}\text{MnO}_3$ , Kuwahara *et al.*<sup>2,3)</sup> have observed Curie Weiss-like behavior above 300 K, but clear deviation is evident with a slight upturn from around 200 K to  $T_c$  in the  $H/M$  versus  $T$  curve. Such a deviation was also observed in our  $\mu^+$ SR experiment. Above 250 K, linear temperature dependence of the muon spin relaxation time was observed, and below 250 K, a clear deviation from such linearity was seen.

Figure 2 shows the  $\mu^+$ SR data at 39 K under ZF, and the solid line in Fig. 2 shows the fitting result obtained by using the relaxation function  $G_z =$

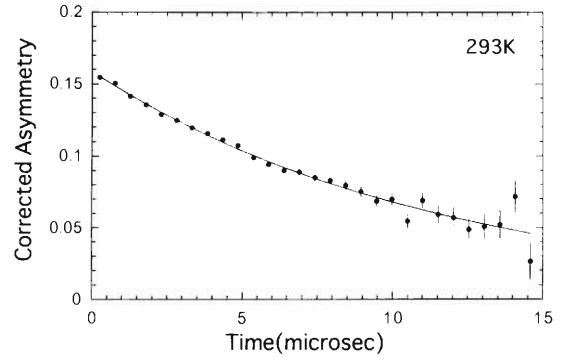


Fig. 1. ZF- $\mu$ SR spectrum at 293 K (paramagnetic phase), taken at RIKEN-RAL Muon Facility.

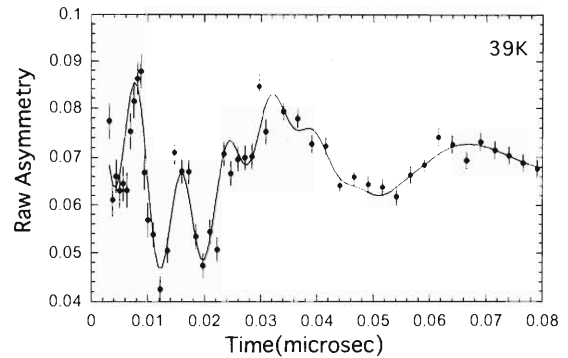


Fig. 2. ZF- $\mu$ SR spectrum at 39 K (ferromagnetic phase), taken at TRIUMF.

$\sum_{i=1,2} (A_{p,i} \exp(-\lambda_i t) \cos(\omega_i t + \phi) + A_{r,i} \exp(-\Lambda_i t))$ . Below 127 K or in the ferromagnetic phase, we have observed two frequencies of the zero field muon spin precession with temperature independent hyperfine fields. This means that implanted muon stopped at magnetically inequivalent two sites: probably apical and planer oxygen sites. Between 132 and 127 K, the signal showed a sudden change from paramagnetic phase to ferromagnetic phase, and these results clearly show the first order phase transition.

### References

- 1) Y. Tokura *et al.*: Phys. Rev. Lett. **76**, 3184 (1996).
- 2) H. Kuwahara *et al.*: Phys. Rev. B **56**, 9386 (1997).
- 3) H. Kuwahara *et al.*: Science **272**, 80 (1996).

\* JRCAT

## Critical Spin Dynamics in $\text{Nd}_{1-x}\text{Sr}_x\text{MnO}_3$ with $x \approx 0.5$

V. V. Krishnamurthy, I. Watanabe, K. Nagamine, H. Kuwahara,\* and Y. Tokura\*

[CMR, Manganites, Relaxation, Critical phenomena]

Recently, Kuwahara et al. have discovered colossal magnetoresistance (CMR) at a magnetic field induced first-order insulator-to-metal phase transition in hole-doped perovskite  $\text{Nd}_{0.5}\text{Sr}_{0.5}\text{MnO}_3$  single crystals.<sup>1)</sup> The electronic properties and the magnetic ground state of doped manganites are correlated with the one-electron bandwidth  $W$  which is determined by the radii of constituent ions.  $\text{Nd}_{0.5}\text{Sr}_{0.5}\text{MnO}_3$  single crystals show a paramagnetic-to-ferromagnetic transition at  $T_C \approx 251$  K and a ferromagnetic-to-antiferromagnetic transition at  $T_N = 158$  K.  $\text{Nd}_{0.45}\text{Sr}_{0.55}\text{MnO}_3$  is a layered A-type antiferromagnet ( $T_N \sim 220$  K) which exhibits metallic behaviour in the ferromagnetically coupled  $ab$ -plane ( $[110]$ ) and exhibits insulating behaviour along the antiferromagnetically coupled  $c$ -axis. Further studies on these magnetic transitions are desirable for a better understanding of the interplay between the magnetism and magneto-transport in CMR materials. In this study, we have applied muon spin relaxation ( $\mu^+$ SR) spectroscopy as a microscopic magnetic probe to investigate the spin dynamics of Mn ions near magnetic phase transitions by measuring the muon spin-lattice relaxation rates  $\lambda$  in the perovskite manganite  $\text{Nd}_{1-x}\text{Sr}_x\text{MnO}_3$  with  $x = 0.5$  and  $0.55$ .

The  $\mu^+$ SR spectra of  $\text{Nd}_{1-x}\text{Sr}_x\text{MnO}_3$  with  $x = 0.5$  and  $0.55$  measured in zero applied field at different temperatures between  $0.3$  and  $290$  K (see Fig. 1) were fitted by an exponential power law:  $P_Z(t) = A_0 \exp[-(\lambda t)^\beta]$ , where  $A_0$  is the muon decay asymmetry at time  $t = 0$ ,  $\lambda$  is the muon spin longitudinal relaxation rate, and  $\beta$  is the exponent coefficient. The relaxation rate  $\lambda$  gives a measure of the fluctuating local magnetic fields due to the neighbouring magnetic ions through dipolar coupling.  $\lambda$  is plotted against temperature for the  $x = 0.5$  and  $0.55$  crystals in Fig. 2. The  $A_0$  measured in  $\text{Nd}_{1-x}\text{Sr}_x\text{MnO}_3$  ( $x = 0.5$  and  $0.55$ ) drops with the decrease of temperature across the second order phase transitions from paramagnetic to magnetically-ordered state. The measured  $\lambda$  in  $\text{Nd}_{1-x}\text{Sr}_x\text{MnO}_3$  ( $x = 0.5$  and  $0.55$ ) crystals sensitively probe the spin dynamics at the second order magnetic phase transitions. The absolute values of muon spin relaxation rates in  $\text{Nd}_{1-x}\text{Sr}_x\text{MnO}_3$  ( $x = 0.5$  and  $0.55$ ) ( $0.12 \mu\text{s}^{-1}$  at  $T_C$ ) are smaller compared to those in  $\text{La}_{0.7}\text{Ca}_{0.3}\text{MnO}_3$  ( $\sim 0.4 \mu\text{s}^{-1}$  at  $T_C$ )<sup>2)</sup> at least by a factor of  $\sim 4$ , and indicate that the relaxation rates decrease with the decrease of the one-electron bandwidth  $W$ .

The temperature dependence of  $\lambda$  above  $T_C$  for  $251 \text{ K} \leq T \leq 290 \text{ K}$  is associated with the critical slowing down of spin fluctuations of Mn moments. In the inset of Fig. 2 the  $\lambda$  is parameterized by a power law:  $\lambda(T) \propto t^w$ , where  $t \equiv [(T-T_C)/T_C]$ , to extract the dynamic critical exponent  $w$ . Surpris-

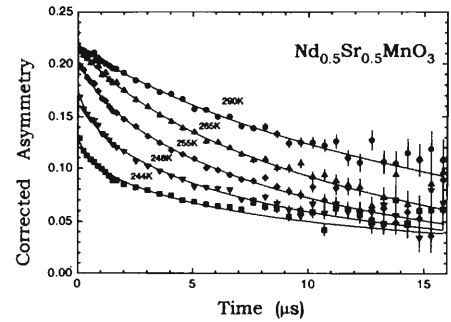


Fig. 1. Zero-field  $\mu^+$ SR time-spectra of  $\text{Nd}_{0.5}\text{Sr}_{0.5}\text{MnO}_3$  showing the critical slowing down of local field fluctuations at the paramagnetic-to-ferromagnetic transition with  $T_C = 251$  K.

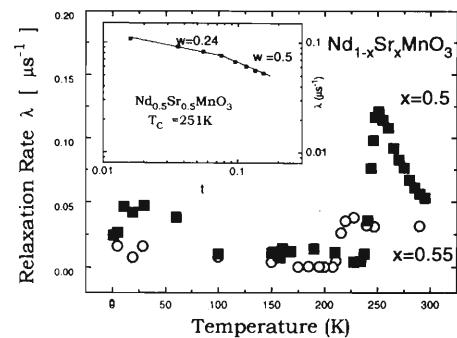


Fig. 2. Temperature dependence of  $\lambda$  measured in  $\text{Nd}_{1-x}\text{Sr}_x\text{MnO}_3$ .

ingly, the critical exponent shows a crossover behaviour with  $w = 0.5$  for  $0.08 \leq t \leq 0.15$  and  $w = 0.24$  for  $0.015 \leq t \leq 0.08$ . Such a change in the dynamic critical exponent, which has also been observed in Ni, EuO and EuS, is associated with a crossover from the exchange critical regime away from  $T_C$  to the dipolar critical regime closer to the  $T_C$ . However, the absolute values of  $w$  are much smaller compared to the theoretical values of  $1.0$  and  $0.7$  of a Heisenberg ferromagnet at the crossover region.  $\beta$  is close to  $1$  in paramagnetic phases. In magnetically ordered phases,  $\beta$  drops to  $0.5$  in both  $x = 0.5$  and  $0.55$  crystals suggesting a stretched exponential relaxation. We believe that the spin disorder due to hole (Sr) doping may introduce a spread in the correlations among the localized Mn spins and may manifest a stretched exponential relaxation.

### References

- 1) H. Kuwahara et al.: Science **270**, 961 (1995).
- 2) R. H. Heffner et al.: Phys. Rev. Lett. **77**, 1869 (1996).

\* JRCAT, Tsukuba

# $\mu^+$ SR Study of Heavy-Fermion Magnetism in $\text{Ce}(\text{Cu}_{1-x}\text{Ni}_x)_2\text{Ge}_2$

V. V. Krishnamurthy, I. Watanabe, K. Nagamine, C. Geibel,\* G. Sparn,\* and F. Steglich\*

[Heavy-fermions, Kondo Lattice, non-Fermi liquid behaviour]

The magnetic behaviour of heavy-fermion (HF) systems at the crossover from the RKKY-interaction dominated magnetic regime to the pure Kondo region is a topic of current interest. Recently, the quasiternary HF system  $\text{Ce}(\text{Cu}_{1-x}\text{Ni}_x)_2\text{Ge}_2$  is reported to exhibit an interesting magnetic phase diagram, determined by the DC susceptibility ( $\chi_{DC}$ ) and specific heat measurements, consisting of local moment antiferromagnetism ( $T_N = 4.1$  K) for  $0 \leq x \leq 0.1$  and HF band magnetism for  $0.2 \leq x < 0.75$ .<sup>1)</sup> Neutron diffraction (ND) studies showed a static spin wave for  $x = 0.285$ , but magnetic reflections could not be observed for  $x \geq 0.5$ . Further, non-Fermi liquid behaviour (NFL) may appear for  $x \geq 0.8$  due to the suppression of  $T_N$  to 0 K. Buettgen *et al.* have observed a logarithmic scaling of spin-lattice relaxation rate  $1/T_1$  measured by NMR at  $^{63}\text{Cu}$  in  $\text{Ce}(\text{Cu}_{0.2}\text{Ni}_{0.8})_2\text{Ge}_2$ .<sup>2)</sup> In the present study, we have applied the muon spin relaxation ( $\mu^+$ SR) spectroscopy to the  $\text{Ce}(\text{Cu}_{1-x}\text{Ni}_x)_2\text{Ge}_2$  system to investigate the occurrence of long range magnetic ordering, the size of the ordered moment at  $x = 0.5$ , and the NFL behaviour at  $x = 0.8$ .

The zero-field (ZF)  $\mu^+$ SR spectra of polycrystalline  $\text{Ce}(\text{Cu}_{0.5}\text{Ni}_{0.5})_2\text{Ge}_2$  for  $T \geq 4$  K are fitted by a stretched exponential relaxation function, of the form:

$$G_z(t) = A_0 \exp[-(\lambda t)^\beta] + A_{bg} \quad (1)$$

where  $A_0$  is the initial asymmetry,  $\lambda$  is the muon spin relaxation rate and  $A_{bg}$  is a constant background.  $\lambda$  remains constant at  $0.032 \mu\text{s}^{-1}$ , and the exponent  $\beta$  also remains constant at 1.50(25) for temperatures above 4.0 K. The ZF spectra, which show a fast relaxing component in addition to the slowly relaxing one between 3.4 and 4 K, could be described by the functional form:

$$G_z(t) = A_0 e^{-(\lambda_{slo} t)^{\beta_s}} + A_1 e^{-(\lambda_{fst} t)^{\beta_f}} + A_{bg}. \quad (2)$$

The first and second terms describe the slow relaxation component and the fast relaxation one observed in the first 1  $\mu\text{s}$ , respectively. The asymmetry of the slowly relaxing component  $A_0$  starts to decrease sharply at 3.97 K (see Fig. 1). A constant fraction of 2/5 is lost for  $T \lesssim 3.4$  K. These features are consistent with the magnetic transition inferred from  $\chi_{DC}$  measurements. From the temperature dependence of asymmetry  $A_0$ , we could extract the Neel temperature  $T_N$  as 4.0 K, which is consistent with the appearance of cusp in  $\chi_{DC}$ .

Temperature dependences of  $\lambda_{fst}$ ,  $\lambda_{slo}$  and  $\lambda$  are displayed in Fig. 2. Best fits to Eq. (2) yielded  $\beta_s = 1$  and  $\beta_f = 2$ .  $\beta_s = 1$  is consistent with the  $4f$  spin fluctuations which are longitudinal to initial muon spin polarization. Gaussian ( $\beta_f = 2$ ) relaxation of the fast

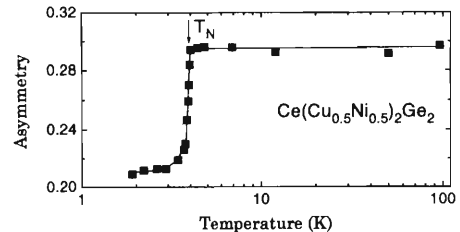


Fig. 1. Temperature dependence of the initial asymmetry  $A_0$  measured in  $\text{Ce}(\text{Cu}_{0.5}\text{Ni}_{0.5})_2\text{Ge}_2$ .

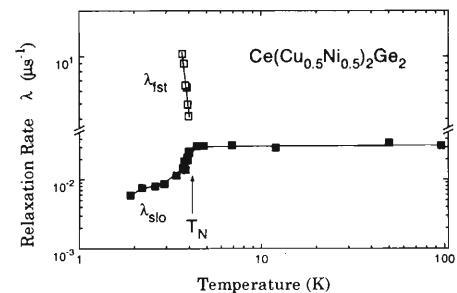


Fig. 2. Temperature dependence of the muon spin relaxation rate  $\lambda$  in  $\text{Ce}(\text{Cu}_{0.5}\text{Ni}_{0.5})_2\text{Ge}_2$  in zero applied field.

component suggests the distribution of static internal fields at the muon site. The decoupling of the asymmetry lost in magnetically ordered state at 2 K could be described by assuming a single muon site yielding the static internal field at the muon site,  $B_\mu = 0.49(6)$  kG.

We have also searched for the possible non-Fermi liquid behaviour in  $\text{Ce}(\text{Cu}_{0.2}\text{Ni}_{0.8})_2\text{Ge}_2$ . The zero field  $\mu^+$ SR spectra measured at temperatures between 2 K and 200 K are also represented by Eq. (1) with a temperature independent relaxation rate of  $0.05 \mu\text{s}^{-1}$  and a temperature dependent exponent  $\beta$  which gradually increases from 1.25 at 200 K to 1.75 at 2 K. Therefore, we do not observe the logarithmic scaling of muon spin relaxation rates  $\lambda$  with temperature, in contrast to  $^{63}\text{Cu}$  NMR results. A likely reason for the discrepancy between  $\mu^+$ SR and  $^{63}\text{Cu}$  NMR measurements could be that  $4f$  spin fluctuations of Ce in the paramagnetic phase are too slow, as indicated by the values of  $^{63}\text{Cu}$  NMR relaxation rates  $1/T_1$  ( $\sim \text{s}^{-1}$ ), to be observable in the  $\mu\text{sec}$  time scale of  $\mu^+$ SR. Long range magnetic ordering is not observed either down to 2 K.

## References

- 1) Loidl *et al.*: *Ann. Physik* **1**, 78 (1992).
- 2) Buettgen *et al.*: *Phys. Rev. B* **53**, 5557 (1996).

\* IFKP, Technische Hochschule Darmstadt, Germany

## $\mu$ SR Studies of Non-Fermi-Liquid Behaviour in $Ce_7Ni_3$

T. Takabatake,\*<sup>1</sup> K. Umeo,\*<sup>1</sup> R. Kadono, I. Watanabe, G. M. Kalvius,\*<sup>2</sup> and A. Kratzer\*<sup>2</sup>

A heavy fermion compound,  $Ce_7Ni_3$ , shows non-Fermi-liquid behaviour when an antiferromagnetic ordering is destroyed under the pressure of 4 kbar.<sup>1)</sup> However, nature of the magnetic transition even at the ambient pressure is complicated due to the presence of three nonequivalent Ce sites in the crystal. The crystal structure of  $Ce_7Ni_3$  is the hexagonal  $Th_7Fe_3$ -type structure as shown in Fig. 1, where the three sites are named as CeI, CeII, and CeIII. The ratio of each Ce site in these sub-lattices is 1:3:3. Recent neutron diffraction study by Motoya et al.<sup>2)</sup> has shown that only CeI and CeII have formed the spin-density-wave (SDW) state below  $T_N = 1.8$  K.

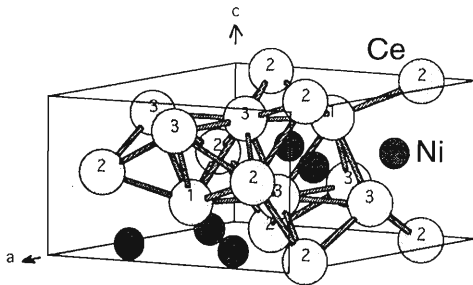


Fig. 1. Crystal structure of  $Ce_7Ni_3$ . The atoms 1–4 are CeI, CeII, CeIII, and Ni, respectively.

In order to study the magnetic state in  $Ce_7Ni_3$  from a microscopic point of view, we have performed  $\mu^+$ SR experiments on a single-crystal sample at RIKEN-RAL Muon Facility in the UK. A pulsed positive muon beam was injected parallel to the hexagonal  $c$  axis. The sample was cooled down to 0.3 K by using a  $^3He$ -cryostat. The single crystal was prepared by the RF-heated Czochralski method at Hiroshima University.

In a zero field (ZF), the  $\mu$ SR time spectra at 10 K showed depolarization behaviour. This suggests that dynamical magnetic correlations develop from far above  $T_N$ . Below  $T_N$ , about 30% of the asymmetry of a muon spin decreases as shown in Fig. 2. This change in the asymmetry means the existence of a fast depolarization component which can not be resolved within a time resolution of the present  $\mu^+$ SR experiment. Such a fast depolarization can be caused by a broad field distribution due to static moments in an incommensurate SDW state. Remaining part of the asymmetry includes two components. One was decoupled in a longitudinal field of about 100 G, whereas

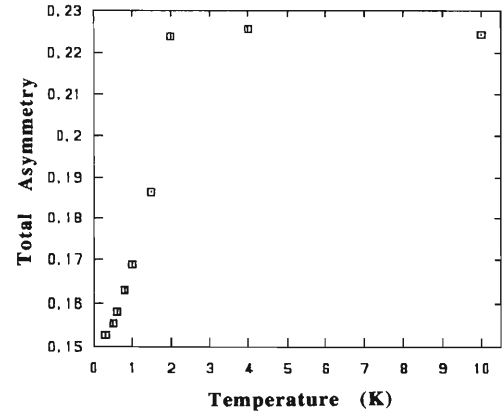


Fig. 2. Temperature dependence of ZF- $\mu$ SR asymmetry parameter. The base line was determined from transverse field experiments.

the other was not affected even by 3800 G. The latter must be of a dynamical origin, since its depolarization rate of  $2.5 \mu s^{-1}$  would correspond to a static width of only 30 G which should be decoupled by about 200 G if the origin is static.

In order to understand these findings, we have to know the muon sites in  $Ce_7Ni_3$ . At present, there is no experimental result on the muon site. But results of the electrostatic potential calculations are available.<sup>3)</sup> According to these calculations, there are two possible muon sites, site-A and site-B. Site-A is surrounded by six CeII atoms, and site B by one CeI atom and three CeIII atoms. Possible interpretation of our data is as follows. The 30% loss of the asymmetry below  $T_N$  originates from the muons at site-A. This is due to the SDW order of CeII moments. Remaining signal comes from the muons at site-B. The depolarization has both the fast relaxation and slow relaxation components. The former is the dynamic part due to the paramagnetic CeIII moments, while the latter is the static part due to the ordered CeI moments. In order to confirm this interpretation, we will perform experiments in different beam orientations with respect to the crystal axis in near future.

### References

- 1) K. Umeo, H. Kadomatsu, and T. Takabatake: *J. Phys.: Cond. Matt.* **8**, 9743 (1996).
- 2) K. Motoya: private communication.
- 3) D. Noakes: private communication.

\*<sup>1</sup> Department of Materials Science, Hiroshima University

\*<sup>2</sup> Physics Department, TU Munich

## Behavior of the Positive Muon in $2H\text{-NbSe}_2$

W. Higemoto, K. Nagamine, S. Kuroda,\* and K. Takita\*

[ $\mu^+$ SR, CDW, Superconductivity]

Behavior of the positive muon in the transition metal dicalcogenide  $2H\text{-NbSe}_2$  was studied by a zero field muon spin relaxation (ZF- $\mu^+$ SR) technique.  $2H\text{-NbSe}_2$  is known to exhibit two phase transitions. One is the Charge Density Wave (CDW) transition at 32 K and another is the superconducting transition at 7 K in which CDW state coexists.<sup>1)</sup> Both transitions are related to the change of the electronic states near the Fermi surface. It is known that the hopping motion or quantum tunneling of muons in metal is related to the conduction electrons<sup>2)</sup> through the electron-drag effect, and muon diffusion phenomenon is one of the important subjects. We are investigating the relation between the muon behavior and CDW state or superconducting state in  $2H\text{-NbSe}_2$ . At the same time, the transition metal dicalcogenide compound is known to be able to intercalate the molecules or atoms into the interlayer. In  $2H\text{-NbSe}_2$ , muon is expected to behave as one kind of the intercalants, and its behavior is also interesting from the view of the intercalation phenomena.

ZF- $\mu^+$ SR experiment was carried out at Port 2 of the RIKEN-RAL Muon Facility. We found that the muon spin relaxation phenomena under ZF can be divided into four temperature regions from the characteristic features of the  $\mu$ SR spectra. Figure 1 shows the typical ZF- $\mu^+$ SR spectra in  $2H\text{-NbSe}_2$  in each temperature region. At 293 K, about half of the implanted muons (called fast component) showed a Kubo-Toyabe-type spin relaxation, and the rest of the muons (called slow component) took a very slow spin relaxation. At 110 K (not shown here), we found that the ratio of fraction of these two components and its hopping rates change, as seen for 63.8 K data in Fig. 1. Such changes of the muon states are also observed at 32 K (CDW transition temperature) and 7 K (superconducting transition temperature). These facts clearly show that muon

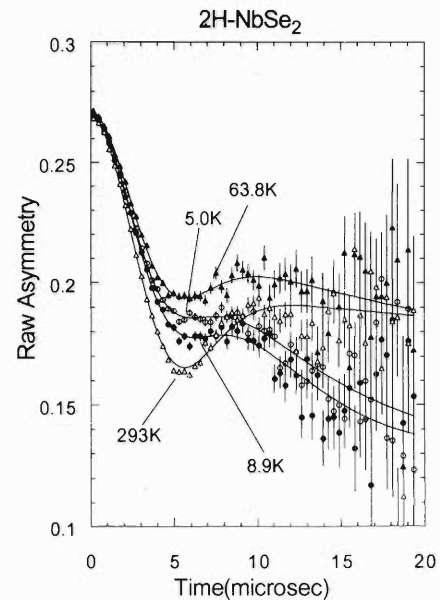


Fig. 1. ZF- $\mu$ SR spectra at 293, 63.8, 8.9 (CDW phase) and 5.0 K (CDW and superconducting phases).

states are affected by the CDW and superconducting states. The change of the  $\mu$ SR spectra found at 110 K might be showing a new phase transition.

Microscopic muon state is very important for the  $\mu^+$ SR study of matter. Our result is considered as a new feature of the muon behavior, and further investigation is in progress.

### References

- 1) R. Sooryakumar and M. V. Klein: Phys. Rev. Lett. **45**, 660 (1980).
- 2) For example, R. Kadono et al.: Phys. Rev. B **39**, 23 (1989).

\* Institute of Materials Science, University of Tsukuba

## $\mu$ SR Study on 2D Kagome Organic Magnet, $m$ -MPYNNBF<sub>4</sub>

I. Watanabe, N. Wada,\* H. Yano,\* A. Yamaguchi,\* K. Awaga,\*  
S. Ohira, K. Nishiyama, and K. Nagamine

Ground state of 2D Kagome magnet, in which magnetic moments on Kagome lattices are coupled through an antiferromagnetic (AF) interaction, is of interest from a view point of a frustrated system. The organic antiferromagnet (AFM),  $m$ -MPYNNBF<sub>4</sub>, comprises magnetic layers of an  $\alpha$ -nitronyl nitroxide cation allylradical with  $S = 1/2$ .<sup>1)</sup> The radical makes a dimer state with  $S = 1$  through a strong intermolecular ferromagnetic interaction, and the dimer couples antiferromagnetically each other through the inter-dimer AF interaction as shown in Fig. 1.<sup>2)</sup> The system has been suggested from a susceptibility measurement to show a spin gap state below 240 mK with a non-magnetic ground state.<sup>2)</sup> If the spin gap state is confirmed in this system, it could be the first example in 2D systems.

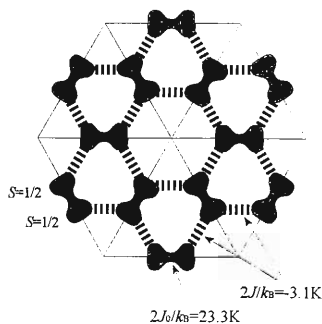


Fig. 1. Model of a crystal structure of  $m$ -MPYNNBF<sub>4</sub>.

Zero-field (ZF) and longitudinal-field (LF) muon spin relaxation ( $\mu$ SR) measurements have been carried out on a single crystal of  $m$ -MPYMMNF<sub>4</sub> down to 30 mK to study the ground state of the system.<sup>3)</sup> The measurements were performed at KEK-MSL by using a top-loading dilution refrigerator and an ordinary gas flow cryostat.

Figure 2 shows the ZF- $\mu$ SR time spectra obtained at 265, 100, 2.9 K and 30 mK. The spectrum at each temperature was normalized at  $t = 0$  to compare the difference among various time spectra. Any strong enhancement of the critical slow down of the dimer spin was not observed. Dynamical and static properties of the dimer spin is expected to be almost temperature independent. The motional narrowing effect due to the diffusion of the muon can be observed at the temperature higher than about 200 K.

Figure 3 shows the LF dependence of the time spectrum at 30 mK. The decoupling behavior by the LF was observed. The spectra were analyzed by using the dynamical Kubo-Toyabe function. A half width of the statically distributed component of the internal field was about 10 G. The muon spin is depolarized also by the dynamical fluctuating component of the internal

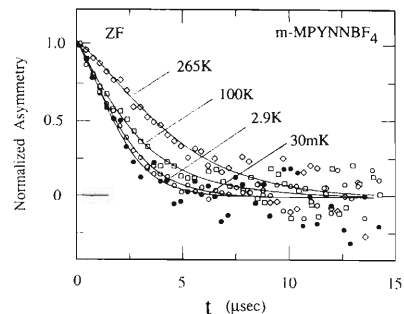


Fig. 2. ZF- $\mu$ SR time spectra.

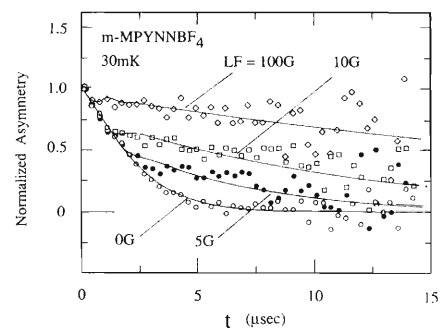


Fig. 3. Longitudinal-field (LF) dependence of the  $\mu$ SR time spectrum at 30 mK.

field with the depolarization rate of about  $0.5 \mu\text{sec}^{-1}$ .

It is known that the implanted muon in a crystal which contains F<sup>-</sup> ion forms a strong  $F\mu F$  state through a hydrogen bonding.<sup>4)</sup> In this case, the distance between the F<sup>-</sup> ion and the muon is about a nominal radius 1.16 Å of the F<sup>-</sup> ion. If the muon which was implanted in  $m$ -MPYNNBF<sub>4</sub> makes such a hydrogen bonding with the F<sup>-</sup> ion, the nuclear dipole field of the nearest <sup>19</sup>F is estimated to be about 8.5 G at the muon site. This value is comparable to the internal static field distribution at muon sites that was obtained from the present  $\mu$ SR study. No other additional field which is expected to be accompanied with a magnetic ordering of the dimer spins was observed.

Therefore, it can be concluded that no clear magnetic ordering of the dimer spins can not be expected for the dimer spins, and that the ground state of  $m$ -MPYNNBF<sub>4</sub> is non-magnetic. This result supports the spin gap feature of this system which has been suggested by the susceptibility measurement.<sup>2)</sup>

### References

- 1) K. Awaga et al.: Phys. Rev. B **49**, 3975 (1993).
- 2) N. Wada et al.: J. Soc. Phys. Jpn. **66**, 961 (1997).
- 3) I. Watanabe et al.: in preparation.
- 4) J. H. Brewer et al.: Phys. Rev. B **33**, 7813 (1986).

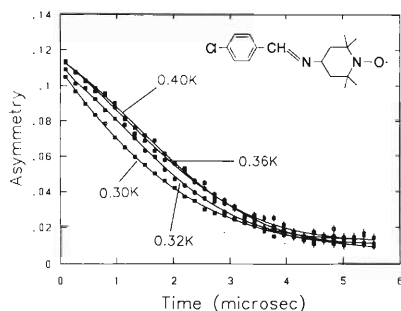
\* Graduate School of Arts and Science, Univ. of Tokyo

## $\mu$ SR Study of Critical Behavior of *p*-Cl-C<sub>6</sub>H<sub>4</sub>-CH=N-TEMPO

S. Ohira, I. Watanabe, T. Ishida,\* T. Nogami,\* and K. Nagamine

Organic radical ferromagnets having 2, 2, 6, 6-tetramethylpiperidin-1-yloxy (TEMPO) group form 2D zig-zag networks of N-O radicals in the crystal. The stable radicals contribute to their magnetism which is considered to reflect their zig-zag sheet structure.<sup>1)</sup> One of them, *p*-Cl-C<sub>6</sub>H<sub>4</sub>-CH=N-TEMPO, has been suggested from an ac susceptibility to show a ferromagnetic transition.<sup>2)</sup> Our previous muon spin relaxation ( $\mu$ SR) measurement revealed clear oscillations of muon spins below 0.28 K, where the susceptibility showed a peak in its temperature dependence; indicating the existence of a *bulk* ferromagnetic ordered state.<sup>3)</sup> From these results, some magnetic ordering seems to start below 0.4 K, where a divergence of the ac susceptibility starts. In order to clarify the magnetic state in the temperature range of 0.28–0.4 K, we have carried out the zero field (ZF) and longitudinal field (LF)  $\mu$ SR measurements on a single crystal of *p*-Cl-C<sub>6</sub>H<sub>4</sub>-CH=N-TEMPO down to 0.30 K.

The measurements were carried out at RIKEN-RAL Muon Facility by using a <sup>3</sup>He cryostat. Figure 1 shows the ZF- $\mu$ SR time spectra. The enhancement of relaxation rate due to a critical slow down effect is observable at  $\sim$ 0.3 K. Furthermore, an internal field at the muon site also increases rapidly as temperature approaches to 0.3 K (Fig. 2); indicating that a random static internal field due to radical spins appears at the muon site above the transition temperature observed in the previous  $\mu$ SR study.

Fig. 1. Temperature dependence of ZF- $\mu$ SR spectra.

The existence of the random static field due to radical spins was also confirmed by the LF experiment. Figure 3 shows the LF- $\mu$ SR spectra at 0.30 K. The time spectra below LF = 200 G can be analyzed by the LF Kubo-Toyabe function. Muon spin depolarization due to the random dipole field of the radical spins was decoupled under LF of about 300 G. This value corresponds to the internal field of about 30 G,<sup>4)</sup> which is obviously larger than the nuclear dipole field. This

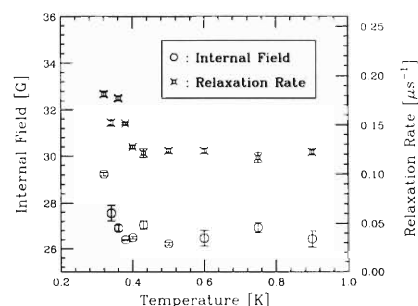


Fig. 2. Temperature dependences of fitting parameters. Increases of the relaxation rate and field distribution, with decreasing temperature, correspond to a critical slow down effect and to an appearance of a random field due to radical spins, respectively.

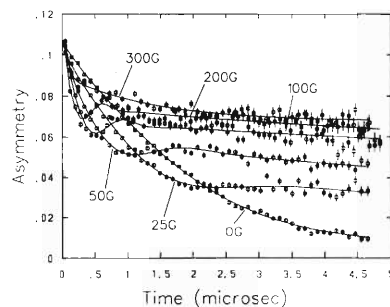


Fig. 3. Longitudinal field (LF) decoupling at 0.30 K. The time spectra under the LF less than  $\sim$ 200 G are well fitted by the LF Kubo-Toyabe function.

component appeared below 0.40 K, at which temperature divergence of the ac susceptibility starts.<sup>2)</sup> On the other hand, only the dynamical relaxations caused by a muonium formation were observed above 0.40 K.

Because this system has a strong two-dimensionality in the magnetic interaction, the magnetic ordering is expected to start in the sheet of the N-O radicals. Therefore, our  $\mu$ SR result shows that not only the spin fluctuation is suppressed, but also the random static field due to the radical spins appears, in the sheet below 0.40 K. The static field observed above 0.30 K originates from a magnetic ordering state quite different from that observed below 0.28 K; it may be caused by a fractionally occurred short-range ordering due to an intra-sheet ferromagnetic interaction. From the ac susceptibility and  $\mu$ SR measurements, a crossover from 2D to 3D ordering is suggested.

### References

- 1) T. Nogami et al.: Synth. Met. **71**, 1813 (1995).
- 2) T. Nogami et al.: Chem. Lett. **1995**, 635.
- 3) R. Imachi et al.: Chem. Lett. **1997**, 233.
- 4) Y. J. Uemura et al.: Phys. Rev. B **31**, 546 (1985).

\* University of Electro-Communications

$\mu^+$ SR Study of Polaron Motion in Polyaniline<sup>†</sup>F. L. Pratt, K. Ishida, K. Nagamine, S. J. Blundell,<sup>\*1</sup> W. Hayes,<sup>\*1</sup> and A. P. Monkman<sup>\*2</sup>

Polyaniline (PANI) is one of a number of conducting polymers that have been attracting considerable attention recently due to the high conductivities achievable by doping and due to their potential as highly tailorable semiconducting materials for use in electronics and optoelectronics. Understanding the mechanisms of polaron motion in such materials is of great importance, both for fundamental and technological reasons. However, the transport mechanisms and their relation to the underlying polymer structure and the modifications produced by doping are still poorly understood. One reason for this is that macroscopic electronic transport measurements such as conductivity are dominated by the slowest component of the transport process, which is strongly dependent on the degree of order in the sample morphology. On the other hand, microscopic dynamical probes such as ESR, NMR and  $\mu$ SR are much better placed to focus at the local level on the intrinsic transport processes governing the mobility of an electronic excitation travelling along a polymer chain. ESR and NMR work best for the doped case, since the motional linewidth contributions are proportional to the carrier density. In contrast, the positive muon is a uniquely sensitive microscopic probe of polaron excitations in the undoped state of a conducting polymer, as the muon implantation process itself generates an excitation which is initially close to the muon site (See Fig. 1). The dynamical properties of this muon-generated excitation can then be studied via the muon relaxation.

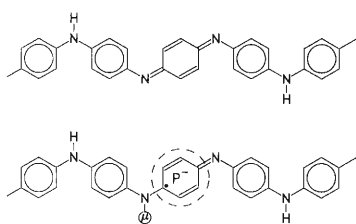


Fig. 1. Polyaniline chemical structure and the mobile negative polaron created by addition of muonium to the polymer.

As in other unsaturated organic systems, the muon picks up an electron to form muonium as it slows down in the polymer. This muonium then reacts with the polymer, resulting in the muon analogue of a hydrogenation reaction (Fig. 1), which corresponds to adding a single electron to the lowest unoccupied molecular orbital (LUMO) of the polymer. Following rapid electronic and structural relaxation of the surrounding polymer, a negative polaron is formed,

which is centred on a quinoid ring (Fig. 1). After creation, the polaron can easily move away from its initial site and diffuse up and down the polymer chain at the intrachain diffusion rate  $D_{\parallel}$ , with occasional hops to adjacent chains controlled by the inter-chain diffusion rate  $D_{\perp}$ . The measured muon relaxation data were fitted using a theory for a muon interacting with a rapidly diffusing electronic spin defect. In the regime of fast 1D diffusion, the relaxation parameter  $\Gamma$  has an inverse magnetic field dependence, which allows estimation of  $D_{\parallel}$ . As the field is reduced there will be a cut-off to the inverse field dependence of  $\Gamma$  due to a crossover to a 3D diffusion regime, which occurs when the polaron Larmor frequency becomes smaller than  $D_{\perp}$ . This crossover can be used to estimate  $D_{\perp}$ .

The temperature dependences of the diffusion rates  $D_{\parallel}$  and  $D_{\perp}$  are shown in Fig. 2.  $D_{\parallel}$  shows a weak metallic temperature coefficient at low temperatures that becomes rather stronger above 150 K. Between 150 and 200 K the diffusion rate is inversely proportional to temperature, which is suggestive of phonon limited transport. A fall in  $D_{\parallel}$  (increase in  $\Gamma$ ) occurs above 150 K. We associate this with polaron scattering by phenyl ring librations, which couple strongly to the electronic excitations. In contrast to  $D_{\parallel}$ , it can be seen that the interchain diffusion  $D_{\perp}$  shows an activated semiconducting behaviour and it increases sharply in the region above 150 K where  $D_{\parallel}$  is decreasing with temperature. This strongly suggests that the ring rotation is assisting the interchain transport, whereas it hinders the metal-like intrachain motion.

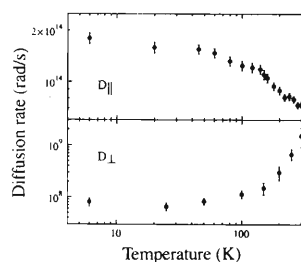


Fig. 2. Intra-chain ( $D_{\parallel}$ ) and inter-chain ( $D_{\perp}$ ) polaron diffusion rates deduced from the muon relaxation in PANI.

One important difference between PANI and the simplest conducting polymer polyacetylene is the lack of charge conjugation symmetry in the former. This produces a dramatic difference between the mobilities of positive and negative polarons. The negative polaron is relatively mobile, whereas movement of a positive polaron requires large ring rotations, making it much more massive and immobile. Protonation produces positive polarons and previous diffusion studies of these positive polarons using ESR have shown an activated  $D_{\parallel}$  below 150 K, in stark contrast to the metal-like behaviour seen here.

<sup>†</sup> Condensed from the article in Phys. Rev. Lett. 79, 2855 (1997).

<sup>\*1</sup> Department of Physics, University of Oxford

<sup>\*2</sup> Department of Physics, University of Durham

# Muon Studies on the Weak Charge Transfer System Anthracene/Tetracyanobenzene

R. M. Macrae, R. Kadono, K. Nagamine, and J. U. von Schütz\*

Binary complexes produced by co-crystallisation of two planar aromatic compounds with moderately different electron affinities have a charge-neutral ground state but display a degree of charge transfer behaviour in their electronically excited states.<sup>1)</sup> Donor-acceptor alternation in the lattice leads to increased librational freedom, resulting in molecular reorientational dynamics and order-disorder phase transitions. Additionally, triplet excitons produced by  $S_1 \leftarrow S_0$  excitation in these systems have a high degree of mobility in the lattice, with hop dimensionality partially controlled by the degree of charge transfer in the  $T_1$  state. Muon spin rotation offers the possibility of simultaneous study of these two phenomena, using the free radicals generated by muonium addition to probe the behaviour microscopically through orientational averaging and electronic relaxation processes affecting the muon-electron hyperfine interaction.<sup>2,3)</sup>

The first studies were carried out on anthracene/tetracyanobenzene, which shows a phase transition at 207 K related to averaging of the anthracene molecules between two symmetrically-related local minima and has largely in-stack exciton transport.<sup>1)</sup> The possible muonium adducts to A and TCNB are shown in Fig. 1. ALC- $\mu$ SR studies at PSI revealed the presence of at least four radicals, with  $\Delta M = 1$  resonances at 7436, 8442, 11509, and 13800 G respectively, corresponding to  $A_\mu = 203, 230, 316,$  and  $368$  MHz. In order to assign these signals, *ab initio* calculations were carried out at RIKEN using Gaussian 94.<sup>4)</sup> The isotropic (Fermi contact) parameter was computed using the UHF and UB-PW91 approximations, using the basis sets 6-31G and 6-31G(d,p) respectively. The results are displayed in Table 1. The disagreement between techniques is a result of spin contamination in the UHF wavefunction: the UB-PW91 values are likely to be more reliable. The strong signals at 7436 and 11509 G are tentatively assigned to A3 and A1. The smaller signal at 8442 G may be from a minority crystallographic A3 site or may point to a misassignment of A1, while the weak

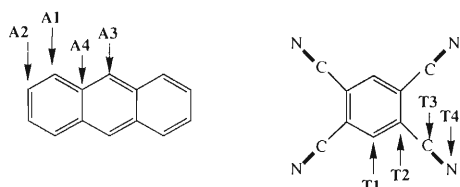


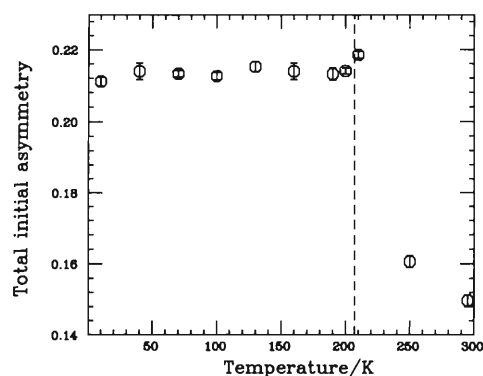
Fig. 1. Possible Mu addition sites to A and TCNB.

Table 1. Calculated isotropic hyperfine parameters for Mu adducts to A and TCNB.

Radical	$A_\mu$ /MHz		Radical	$A_\mu$ /MHz	
	UHF	UBPW		UHF	UBPW
A1	427	242	T1	513	396
A2	465	291	T2	468	319
A3	369	167	T3	691	351
A4	930	697	T4	–	654

line at 13800 G may be due to T3, the most stable TCNB adduct.

Preliminary studies were carried out at RIKEN-RAL towards the observation of reorientational dynamics by *time-dependent* LF $\mu$ SR spectroscopy. A temperature scan at 250 G revealed a discontinuity in the total time-zero asymmetry at 210 K, with about 20% of the full asymmetry missing above this temperature (see Fig. 2). This is consistent with a relaxation process affecting the muonium precursor state, possibly a result of a longer Mu lifetime in the vibrationally-averaged lattice. Future work will involve direct  $S_1 \leftarrow S_0$  laser irradiation synchronous with the  $\mu^+$  implantation in order to study interactions between the mobile  $T_1$  state and the probe radicals.

Fig. 2. ARGUS results for A/TCNB: total initial asymmetry against temperature at  $B = 250$  G.

## References

- 1) J. Krzystek and J. U. von Schütz: Adv. Chem. Phys. **LXXVI**, 167 (1993), and refs. within.
- 2) See for example E. Roduner et al.: Chem. Phys. **192**, 231 (1995).
- 3) S. F. J. Cox and D. S. Sivia: Appl. Magn. Reson. **12**, 213 (1997).
- 4) *Gaussian 94 (revision A.1)*, M. J. Frisch et al.: Gaussian Inc., Pittsburgh PA, 1995.

\* 3. Physikalisches Institut, Universität Stuttgart, Germany

## Electronic State of $\mu\text{Al}$ Pseudo-Acceptor Centers in Si Probed by $\mu^-$ SR

R. Kadono, F. L. Pratt, I. Watanabe, and K. Nagamine

It is known that the electron paramagnetic resonance (EPR) signal associated with acceptor centers is hardly observed in elemental semiconductors due to fast electron spin relaxation,<sup>1)</sup> which has been a serious obstacle to the study of electronic structure of active centers. The implanted negative muon forms a spin-polarized acceptor center and thereby the negative muon spin rotation ( $\mu^-$ SR) may serve as a complementary technique to provide microscopic information. Recently, a couple of  $\mu^-$ SR results in crystalline silicon were reported,<sup>2,3)</sup> although there remains some disagreement with each other. In this short note we report our preliminary results of  $\mu^-$ SR study in crystalline silicon.

The experiment was conducted at the port-2 channel of the RIKEN-RAL Muon Facility. A negative muon beam with a momentum of 50 MeV/c was implanted into the sample consisting of 10 intrinsic c-Si wafers in stack ([111], resistivity  $\simeq 2.2$  k $\Omega$ cm, total  $\sim 3$  mm thick) and time-differential TF- $\mu$ SR spectra were obtained by the ARGUS spectrometer.<sup>4)</sup> The applied magnetic field was 4.0 mT, which is considerably lower than those reported in Refs. 2, 3 (see below). The long-lived background rate was such that the electrons from  $\mu^-$ Si muonic atoms (lifetime  $\sim 0.8$   $\mu$ s) were clearly observed over 6  $\mu$ s range.

Figure 1 shows the observed electron decay asymmetry of  $\mu^-$ Si ( $\equiv \mu\text{Al}$ , which is diamagnetic as inferred by the frequency) versus temperature. The asymmetry decreases as temperature is lowered below 40 K, disappearing almost completely at 10 K. This result is qualitatively in good agreement with Ref. 2 and strongly suggests the paramagnetic precursor state undergoing fast relaxation. The change of asymmetry observed at 4.0 (this work) and 40 mT<sup>2)</sup> is absent at 80 mT,<sup>3)</sup> thereby suggesting that the hyperfine field for the pre-

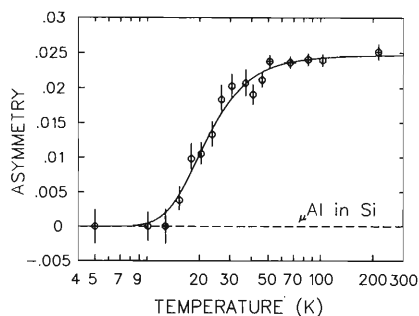


Fig. 1. TF- $\mu$ SR asymmetry of the  $\mu\text{Al}$  acceptor centers in c-Si. Solid curve is a fit with the model described in the text.

cursor state may be  $10^{1.5}$  mT.

The hyperfine parameter is more precisely determined by measuring the field-dependent recovery of the asymmetry under a longitudinal field  $B$  (i.e., LF-repolarization). The data at 10 K are shown in Fig. 2, where the solid curve is a fit assuming the isotropic hyperfine parameter  $\omega_0$  between  $\mu\text{Al}$  spin and the outermost shell electrons so that the polarization is given by

$$P_z(x) = \frac{1/2 + x^2}{1 + \nu/\kappa + x^2}, \quad (1)$$

where  $x = \gamma_\mu B/\omega_0$ ,  $\nu$  is the spin/charge exchange interaction rate for the paramagnetic precursor state, and  $\kappa$  is the rate of transition to the final diamagnetic state.<sup>5)</sup> The same model also applies to the TF data in Fig. 1 with an appropriate temperature dependence for  $\kappa$ :

$$P_{xy}(t \gg \omega_0^{-1}) = \frac{2 + 4(\kappa/\omega_0)^2(1 + 2\nu/\kappa)^2}{3 + 2\nu/\kappa + 4(\kappa/\omega_0)^2(1 + 2\nu/\kappa)^2}, \quad (2)$$

$$\kappa = \kappa_0 \exp(-E_a/k_B T). \quad (3)$$

The fitting analysis yields the hyperfine parameter  $\omega_0/2\pi = 2.80(61)$  GHz. The value is considerably smaller than that for the interstitial center (i.e., 16.13 GHz scaled from EPR result) and suggesting the substitutional center ( $\mu\text{Al}^0$ ).<sup>6)</sup> Detailed theoretical calculation is now in progress.

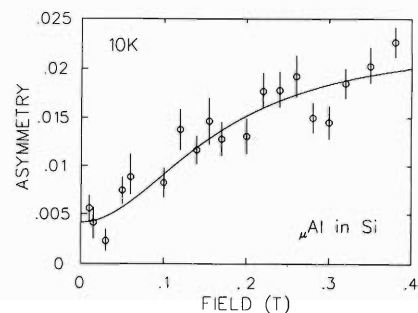


Fig. 2. LF-repolarization of the  $\mu$ -e decay asymmetry in c-Si at 10 K.

### References

- 1) See, for example, G. W. Ludwig and H. H. Woodbury: *Electron Spin Resonance in Semiconductors* (Academic Press Inc., New York, 1962).
- 2) M. Koch et al.: *Hyperfine Interact.* **65**, 1039 (1990).
- 3) T. N. Mamedov et al.: *Hyperfine Interactions* **86**, 717 (1994).
- 4) R. Kadono et al.: *RIKEN Accel. Prog. Rep.* **29**, 196 (1995).
- 5) I. G. Ivanter and V. P. Smilga: *Zh. Eksp. Teor. Fiz.* **55**, 1521 (1968) [*Sov. Phys. JETP* **28**, 796 (1969)].
- 6) T.M. Briere: private communication.

## Development of an RF Resonance System for Pulsed Muon Beam Method at RIKEN-RAL

I. Watanabe and K. Nagamine

Muon spin resonance ( $\mu$ SR) method using a radio frequency (RF) field in a strong longitudinal field (LF) is a good microscopic method to investigate hyperfine interactions, static distributions, and dynamics of a local field at a muon site in magnetic materials.<sup>1,2)</sup> One of strong advantages of the RF- $\mu$ SR is that the hyperfine field at the muon site can be obtained in a decoupled condition. Therefore, a final muon state after some chemical reaction processes in which a muon spin polarization is lost by dephasing can be measured, because the time dependence of the muon state can be obtained by changing the times of RF triggering. The other advantage is that the spin susceptibility of magnetic moments at the muon site can be obtained.

In order to generate the RF field of a couple of ten Gauss perpendicular to the LF, the peak RF power close to 100 kW has to be applied; so that a muon spin can complete its transition within the lifetime of muon. Such a strong RF field can only be achieved with a low duty factor. In the case of a pulsed muon beam, the RF field can be synchronized with a burst of the muon beam pulse and is applied for at most 30  $\mu$ sec of the  $\mu$ SR time range compared to the lifetime of muon (2.2  $\mu$ sec). Since a short RF pulse results in a low duty factor, a high peak power of the RF field can be realized.

RF resonance techniques with pulsed muon beam have been established at KEK/MSL.<sup>2)</sup> Because a lot of data points are needed to determine one resonance frequency at a fixed temperature, an intense muon beam is essential for the accuracy of data and for the efficiency of data acquisition. Therefore, an intense pulsed muon beam at RIKEN-RAL Muon Facility too is very favorable for the RF- $\mu$ SR experiments. We report here the development works of an RF resonance system at RIKEN-RAL Muon Facility.

Figure 1 shows an electric circuit diagram of the present RF resonance system. We chose a high-impedance matching system in which two variable capacitors are used to achieve a good transmission of the RF power. Advantages of this system are that a reflection of the RF power can be minimized while a high-Q value of the system can be achieved due to a small L-C tank circuit.

Figure 2 shows a test probe of the RF system. The designed frequency range is from 30 to 60 MHz. The coil with a target specimen can be cooled down to 1.5 K by using an existing gas-flow type cryostat. Two variable capacitors were made by ceramics. An electrode made of Cu-foil was wound around on a surface of the ceramic tube. An inner electrode can be

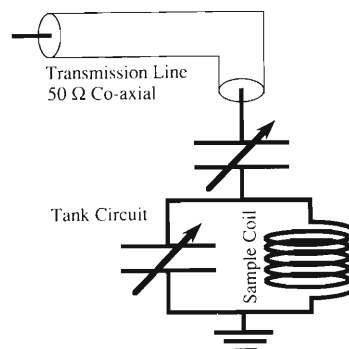


Fig. 1. Electric circuit diagram of the developed RF-resonance system.

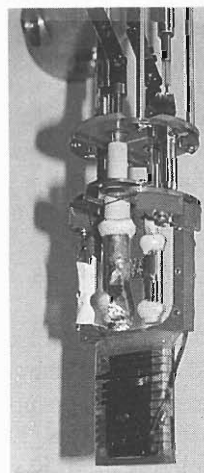


Fig. 2. The RF system testing probe made by the author.

moved mechanically up and down to vary the capacitance. A maximum capacitance was about 100 pF for the matching capacitor and about 50 pF for the tank-circuit capacitor. A sample coil was fabricated from the Cu foil with thickness of 10  $\mu$ m and was wound around on an insulating coil holder. The coil width was 2 mm. A thin coil is important for the surface muon to pass through the coil. The coil aperture was 30 mm  $\times$  6 mm with length of 40 mm, which was large enough to put  $\mu$ SR samples in it. The measured Q-value of the system ranged from 30 to 40.

Figure 3 shows a wide-band pulsed RF amplifier (AMT, Model-3445). The maximum output power is 2 kW and gain 66 dB. For easy maintenance, we chose an air-cooled solid-state amplifier which uses transistors to amplify the pulsed RF. Because the high-Q system was chosen, we did not need a high power RF source to

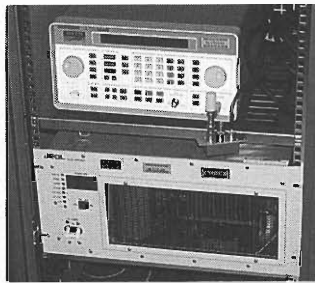


Fig. 3. Wide-band pulsed RF power amplifier AMT Model-3445, whose maximum output is 2 kW.

achieve the strong RF field. The RF power is transmitted to the tank circuit through a  $50 \Omega$  co-axial cable.

By using this test probe, we applied the RF resonance technique to investigate magnetic properties of an insulating oxide,  $\text{LaCoO}_3$ , as a demonstration of the developed RF resonance system performance. Background physics of this oxide are already reported in a separate contribution.<sup>3)</sup> The adopted RF frequency was 40.000 MHz. The pulse width was about 30  $\mu\text{sec}$  with a repetition rate of 50 Hz, so that the duty factor was 0.15%. The rising time of the RF field was about 250 nsec, which was fast enough for the RF- $\mu\text{SR}$ . The output power was 150 W.

Figure 4 shows obtained typical RF- $\mu\text{SR}$  time spectra. At the time of resonance, the precession frequency around the RF field is minimized, but the precession

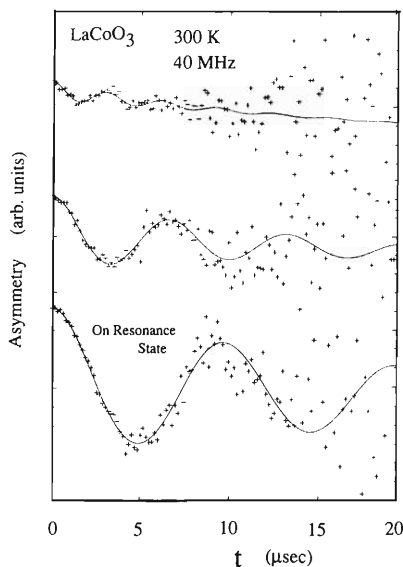


Fig. 4. RF- $\mu\text{SR}$  time spectra obtained at 300 K. The spectrum at the bottom shows the muon spin rotation around the RF field under a just-resonance condition. The other two spectra show the muon spin rotation under off-resonance conditions.

amplitude is maximized. The applied RF field was found from the precession frequency to be about 8 G.

Figure 5 shows the resonance curves obtained at 300 K and 100 K. Dashed lines show the reference resonance curves obtained from the same measurement but on carbon powder. These references show a zero-shift. The shift of the resonance frequency was 2 and 6 G at 300 and 100 K, respectively. The shift is corresponding to the paramagnetic shift caused by the hyperfine field at the muon site. This tendency of the temperature dependence of the hyperfine field at the muon site is consistent with that of the Co-spin susceptibility obtained by a  $^{59}\text{CO-NMR}$  measurement.<sup>4)</sup> Therefore, this fact shows that the obtained hyperfine field at the muon site is originated from the spin susceptibility of the Co-spin. These results indicate that we can study, under the decoupled longitudinal field, the hyperfine interactions between the muon spin and the magnetic moments by using this RF- $\mu\text{SR}$  system with the experimental tolerance of 0.1%.

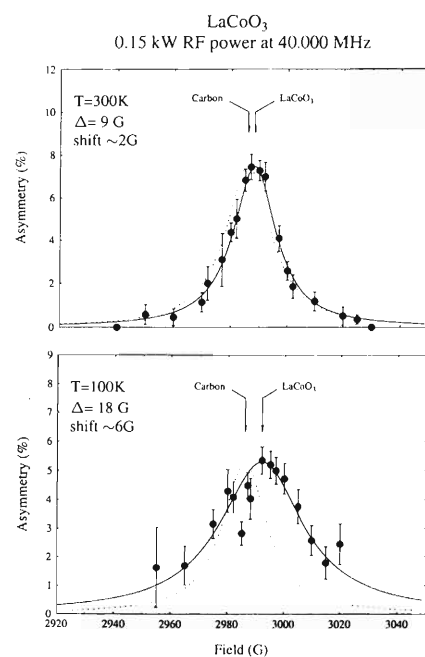


Fig. 5. Resonance curves at 300 K and 100 K. The dashed lines show the resonance curves of carbon powder as a reference of zero-shift resonances.  $\Delta$  is a halfwidth of the resonance curve.

#### References

- 1) K. Nishiyama: in *Perspective of Muon Science* (North-Holland, Amsterdam 1992), p. 199.
- 2) Y. Kitaoka et al.: *Hyperfine Interactions* **12**, 51 (1982).
- 3) I. Watanabe et al.: *RIKEN Accel. Prog. Rep.* **31**, 111 (1998).
- 4) M. Itoh et al.: *J. Phys. Soc. Jpn.* **64**, 970 (1995).



### 3. Radiochemistry and Nuclear Chemistry



# The Jump Mechanism of Self-Interstitials in Pure Iron

Y. Yoshida, Y. Kobayashi, F. Ambe, E. Yagi, R. Sielemann,\*<sup>1</sup>  
A. Feinauer,\*<sup>2</sup> and A. Seeger

The jump mechanism of self-interstitials is still not well understood in pure Fe and appears to be one of the most important problems in the field of point defects in metals. However, no direct observation of the jump processes of the self-interstitials in pure Fe has been achieved yet. The in-beam Mössbauer spectroscopy using the  $^{56}\text{Fe}(d,p)^{57}\text{Fe}$  reaction by a deuteron beam from the RIKEN AVF-Cyclotron is now opening a possibility to study the elementary jump process of self-interstitials in a pure single crystal iron.<sup>1)</sup> The excited probes of  $^{57}\text{Fe}$  were produced in a natural-Fe single crystal by the  $^{56}\text{Fe}(d,p)^{57}\text{Fe}$  reaction, followed by its ejection from the normal lattice sites due to the highly energetic deuteron, which may produce the self-interstitials of Fe. In order to determine the jump vectors of the interstitial  $^{57}\text{Fe}$  atoms, the angular dependence of Mössbauer spectrum was measured at different crystal orientations.

There was, however, a difficult problem due to the thickness (1 mm) of the sample used in the experiments<sup>1)</sup> till recently, which caused an additional complexity to the experimental results. The problem was an accumulation of the deuterons stopped about 100  $\mu\text{m}$  of depth, close to the surface, which gave a strong effect on the spectrum, so that it was rather difficult to extract information on the jump processes of the self-interstitials from the spectra. In the present investigation, however, we have succeeded to make a thinner sample as thin as 100  $\mu\text{m}$ , which made us possible to measure Mössbauer spectra without any deuteron accumulation.

The angular dependent Mössbauer spectra at 400 and 150 K are shown in Figs. 1 and 2, respectively, which correspond to the temperatures above and below the stage I, which is a recovery stage of the self-interstitials in pure iron. This means that the self-interstitials will start migrating within a time scale of the practical measuring time, i.e., 100 ns in the  $^{57}\text{Fe}$  Mössbauer spectroscopy. The spectra of Figs. 1 and 2 were fitted using two six-lines: one component with a larger magnetic splitting corresponds to the substitutional Fe, and the other with a smaller magnetic splitting to Fe atoms on a defect site. It may be possible now to compare the area intensities of defect components as a function of the angle with those predicted from different jump models.<sup>2)</sup> The result will be published elsewhere.

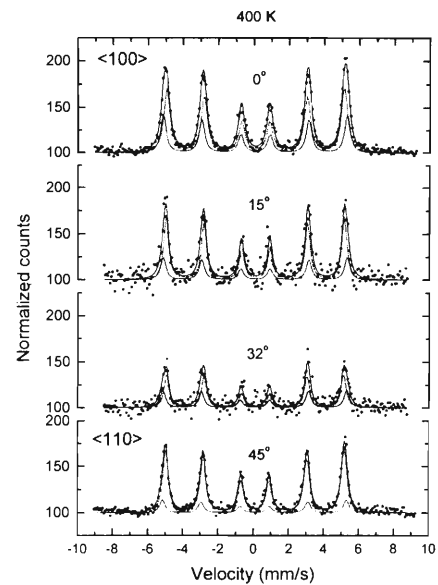


Fig. 1. The angular dependence of the Mössbauer spectra at 400 K for the detection direction between  $\langle 100 \rangle$  and  $\langle 110 \rangle$ .

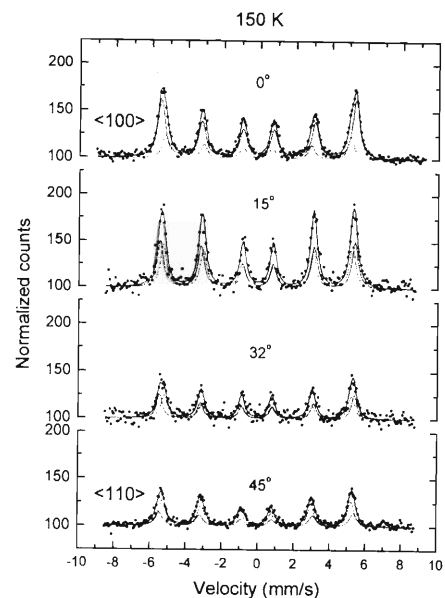


Fig. 2. The angular dependence of the Mössbauer spectra at 150 K for the same detection as Fig. 1.

## References

- 1) Y. Yoshida et al.: RIKEN Accel. Prog. Rep. **29**, 111 (1996); RIKEN Accel. Prog. Rep. **30**, 103 (1997).
- 2) A. Feinauer et al.: HMI-Berlin Ann. Rep. B **540**, 11 (1995).

\*<sup>1</sup> Hahn-Meitner Institute Berlin, Germany  
\*<sup>2</sup> Max-Planck-Institute Stuttgart, Germany

# Dynamic Behavior of $^{57}\text{Fe}$ Atoms in Solid Ar and Solid Xe

Y. Yoshida, Y. Kobayashi, K. Hayakawa,\* K. Yukihiro,\*  
S. Nasu, and F. Ambe

After Coulomb-excitation and recoil-implantation of  $^{57}\text{Fe}$  into solid Ar and solid Xe, we observed<sup>1)</sup> the Mössbauer spectrum consisting of two broad single-lines at 5 K, which further showed a motional averaging at 20 K in the solid Ar and at 50 K in the solid Xe, respectively. This suggests that the Fe atoms start jumping already at 5 K between different lattice sites in the solid-state face-centered-cubic (FCC) inert gases. During the course of the experiments, however, it was noticed that the magnitude of the line broadenings of both components changed considerably from one specimen to another, even if the spectra were measured at the same temperature by implanting the same number of  $^{57}\text{Fe}$  atoms into the inert-gas solids. In order to solve this problem, we have performed a systematic data taking as functions of the temperature, the Fe dose, and the thickness of specimen.

The thickness of the samples was varied roughly between 0.2 and 1 mm by changing the total amount of the Ar-gas condensed on a copper substrate. After the condensation at 70 K, the specimen was cooled down to the experimental temperatures between 5 and 30 K following the coexisting curve of the Ar solid-gas phases. The cooling rate was 1 K/min. Finally, we obtained a transparent crystal with a typical mosaic size of 5 mm. The Ar beam intensity was 15 pA, which allowed us to evaluate a Mössbauer spectrum every three hours to follow a development of the spectral shape. The total number of  $^{57}\text{Fe}$  atoms implanted into the solid Ar was estimated to be  $1 \times 10^{10} / \text{cm}^2$  after a typical measurement time for  $8.6 \times 10^4$  s.

Figure 1 shows the  $^{57}\text{Fe}$  Mössbauer spectra in the solid Ar at different temperatures for the specimens with different thicknesses; each column, from the left to the right, corresponds to the estimated thickness of 0.2, 0.8, and 1 mm, respectively. It is clearly seen that the line width of the singlet at the left-hand side increases not only with increasing temperature, but also with increasing the thickness of specimen. In addition, the spectra became broader with increasing the measuring time, which are not shown in this report though.

In the former works<sup>2)</sup> on  $^{57}\text{Co}/^{57}\text{Fe}$  into solid Ar, a  $3d^7$  state and a  $3d^64s^1$  state were observed, but in the present experiment, both components are not seen in these spectra. The isomer shift for the component at the right hand side in Fig. 1 is very close to that of the " $\text{Fe}^0$  monomer state (configuration  $3d^64s^2$ )", which was reported in an experiment after

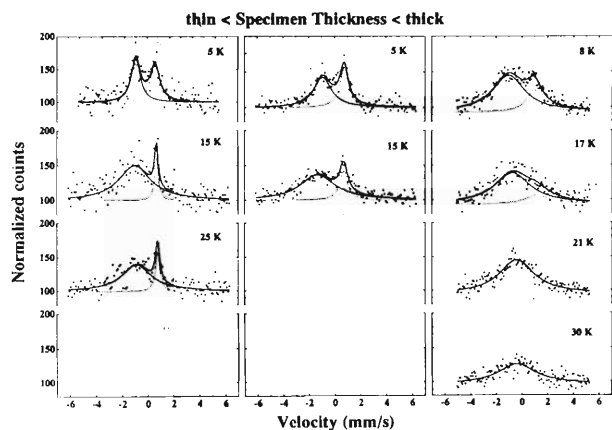


Fig. 1.  $^{57}\text{Fe}$  Mössbauer spectra in the solid Ar at different temperatures for the specimens with different thicknesses: Each column, from the left to the right, corresponds to the thickness of 0.2, 0.8, and 1 mm, respectively.

the coevaporation<sup>2)</sup> of  $^{57}\text{Fe}$  together with Xe gas. Accordingly, this component may be assigned to the  $\text{Fe}^0$  state. On the other hand, the broader component at the left-hand side appears to be the first observation in the inert-gas solids, and may correspond to either the  $\text{Fe}^0$  state on a different lattice site, or a different ionic state such as  $\text{Fe}^{2+}$  or  $\text{Fe}^{3+}$ .

In the present experiments, the implantation depth and the dose of  $^{57}\text{Fe}$  atoms and even the quality of the crystals are supposed to be quite identical for all the spectra corresponding to the different thickness. Therefore, the observed line broadenings can not be attributed to the defects produced during the Fe slowing-down process, but rather to a charge-up effect introduced by the highly ionic  $^{57}\text{Fe}$ . The accumulated charges may cause an electric field to the  $^{57}\text{Fe}$  ions, leading to an enhancement of the atomic jumps. In order to understand the fast dynamic behavior of the Fe atoms in the solid Ar, however, both the charge distributions induced by the  $^{57}\text{Fe}$  ions and its relaxation process must be further quantitatively investigated. The details will be published elsewhere.

## References

- 1) Y. Yoshida, Y. Kobayashi et al.: RIKEN Rev. No. 16, p. 19 (1997).
- 2) M. Van der Hyden et al.: Phys. Rev. B **36**, 38 (1987).

\* Shizuoka Institute of Science and Technology

## $^{57}\text{Fe}$ Mössbauer Studies Using $^{57}\text{Mn}$ Nuclei Implanted into Al and Si

Y. Kobayashi, Y. Yoshida, K. Hayakawa,\* K. Yukihiro,\* A. Yoshida,  
Y. Watanabe, N. Aoi, S. Nasu, and F. Ambe

Energetic radioisotope beams (RI-beams) which are produced as secondary beams have become very attractive in the fields of materials science. Since the implantation energy into materials can be in the order of GeV, the beams would enable to modify the microstructures and to synthesize novel species in materials on a scale of several hundred  $\mu\text{m}$  in depth. We can make use the most of RI-beams not only as nuclear probes to obtain atomic information of the materials immediately after implantation, but also as tools to change the physical and chemical properties of materials. We report here the results obtained from the in-beam Mössbauer studies on  $^{57}\text{Fe}/^{57}\text{Mn}$  in Al and Si.

Energetic  $^{57}\text{Mn}$  nuclei ( $T_{1/2} = 1.45$  min) were produced by the projectile fragmentation process of an 80 A MeV  $^{59}\text{Co}$  beam. The  $^{59}\text{Co}$  beam reacted against a production target of 185 mg/cm<sup>2</sup> Be. The reaction fragments were collected and analyzed by in-flight isotope separation using the RIPS (RIKEN Projectile-fragment Separator). To stop the  $^{57}\text{Mn}$  nuclei in the specimen for implantation, we suppressed the beam energy using a degrader of a 500- $\mu\text{m}$ -thick Al plate. The implantation intensity of  $^{57}\text{Mn}$  atoms were estimated to be typically  $2 \times 10^5$  particles/s. We used two specimens: an Al foil and a single crystal of Si wafer with thickness of 135 mg/cm<sup>2</sup> and 117 mg/cm<sup>2</sup>, respectively. The experimental set-up and details were described in Ref. 1.

The Mössbauer spectrum of  $^{57}\text{Fe}$  having decayed from  $^{57}\text{Mn}$  in the Al foil was measured at 30 K, as shown in Fig. 1. A single component was observed in the Mössbauer spectrum, and this broad line was fitted with the isomer shift, I.S. =  $-0.53$  (5) mm/s and  $\Gamma = 0.64$  (8) mm/s. The obtained value for I.S. coincides with that for substitutional  $^{57}\text{Fe}$  atoms in Al observed in the in-beam experiment after the Coulomb excitation and recoil-implantation.<sup>2)</sup> However, no lines

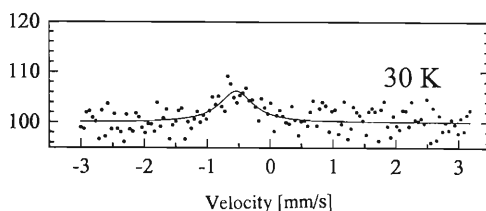


Fig. 1. Mössbauer spectra of  $^{57}\text{Fe}/^{57}\text{Mn}$  in Al at 30 K. (The total measuring time was 10 h.)

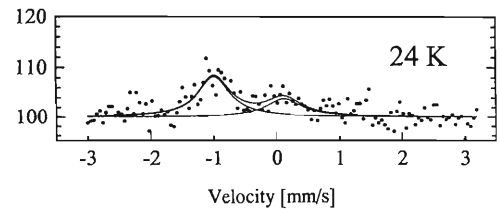


Fig. 2. Mössbauer spectra of  $^{57}\text{Fe}/^{57}\text{Mn}$  in Si at 24 K. (The total measuring time was 12 h.)

corresponding to  $^{57}\text{Fe}$  in interstitial sites, as observed remarkably at the low temperature less than 30 K in the Coulomb excitation experiment, were observed in the present experiment.

The implantation of  $^{57}\text{Mn}$  beam into the Si wafer was performed at 24 K. The spectra consists of two component, as shown in Fig. 2. In the case when it was analyzed with two Lorentzian curves, it was fitted with a relatively sharp line at around  $-1$  mm/s and a very broadened line at around  $0.1$  mm/s, respectively. The line at lower velocity appears to correspond to the interstitial  $^{57}\text{Fe}$  in Si, which was observed in the in-beam experiment after the Coulomb excitation and recoil-implantation.<sup>3)</sup>

It is quite interesting that there are differences in the results between the projectile fragmentation reaction and Coulomb excitation/recoil-implantation experiments. This is considered due to the entirely different range of time involved for measurement after the implantation in both experiments:  $^{57}\text{Mn}$  possesses a much longer half-life of 1.45 min in contrast to  $^{57}\text{Fe}$  half-life in the excited level ( $T_{1/2} = 98$  ns). Alternatively, the observed difference is ascribed to the final chemical state of implanted  $^{57}\text{Mn}$  nuclei different from that of  $^{57}\text{Fe}$  nuclei.

In conclusion, we have successfully observed, for the first time, Mössbauer spectra of the  $^{57}\text{Fe}/^{57}\text{Mn}$  nuclei implanted into specimens as an energetic RI-beam. Implantation of the projectile fragments separated by using the RIPS can open a new possibility to use as many kinds of short-lived nuclear probes for solid-state and materials science.

### References

- 1) Y. Kobayashi et al.: *Hyperfine Interact.*, in press.
- 2) M. Menningen et al.: *Europhys. Lett.* **3**, 927 (1987).
- 3) P. Schwalbach et al.: *Phys. Rev. Lett.* **64**, 1274 (1990).

\* Shizuoka Institute of Science and Technology

# Coulomb Excitation in In-beam Mössbauer Spectroscopy

Y. Hsia,\* Y. Kobayashi, and F. Ambe

The differential excitation cross-section for the electric excitation  $E\lambda$  of nuclei is<sup>1)</sup>

$$d\sigma_{E\lambda} = \left(\frac{Z_1 e}{\hbar V}\right)^2 a^{-2\lambda+2} B(E\lambda) df_{E\lambda}(\theta, \xi) \quad (1)$$

where

$$df_{E\lambda} = \frac{4\pi^2}{(2\lambda+1)^3} \sum_{\mu} \left| Y_{\lambda\mu}\left(\frac{\pi}{2}, 0\right) \right|^2 |I_{\lambda\mu}(\theta, \xi)|^2 \sin^{-4}\left(\frac{\theta}{2}\right) d\Omega \quad (2)$$

Here,  $V$  is the velocity of the projectile,  $a$  ( $= \frac{Z_1 Z_2 e^2}{m_0 V^2}$ ) the half distance of closest approach in a head-on collision,  $Z_1$  and  $Z_2$  the charge numbers of the projectile and target nuclei, and  $m_0$  ( $= \frac{A_1 A_2}{A_1 + A_2} u$ ) their reduced mass.  $B(E\lambda, I_i \rightarrow I_f)$  is the reduced transition probability associated with the multipole order  $E\lambda$ . The orbital integrals  $I_{\lambda\mu}(\theta, \xi)$  for  $E2$  Coulomb excitation has been calculated by numerical methods as a function of the scattering angle  $\theta$  in the center-of-mass system with a parameter  $\xi$  ( $= \frac{a\Delta E}{\hbar V}$ ).

The motion of projectile in the Coulomb field of nucleus is characterized by Sommerfeld parameter  $\eta$ :  $\eta = Z_1 Z_2 e^2 / \hbar V$  which is the effective strength of the interaction.

The Mössbauer state of  $^{57}\text{Fe}$  is excited via  $E2$ -transitions to the  $5^-/2$  and  $3^-/2$  states at 136 and 366 keV. About 90% of their population decays into the Mössbauer state at 14.4 keV. The  $^{57}\text{Fe}$  Coulomb excitation processes in in-beam Mössbauer study are mainly  $E2$  processes (see Fig. 1). The Mössbauer state 14.4 keV is hardly excited directly due to its small  $B(E2)$  value ( $9.7e^2 \text{ fm}^4$ ). The collision parameters were evaluated under the experimental conditions of the AVF Cyclotron at RIKEN.<sup>2)</sup> The related parameters are: (1) the initial projectile velocity  $V_i = \sqrt{\frac{2E}{m_i}} = 0.073c$  and the final relative velocity  $V_f = \sqrt{\frac{2(E-\Delta E)}{m_f}} = 0.073c$ . Here,  $\Delta E' = \left(1 + \frac{A_1}{A_2}\right) \Delta E$  is the excitation energy. For the process I,  $\Delta E'_I = 231 \text{ keV}$ , and  $\Delta E'_{II} = 622.8 \text{ keV}$  for the process II. (2) the relative excitation energy parameter  $\zeta$  is defined by:  $\zeta = \frac{\Delta E'}{E}$ . Therefore,  $\zeta_I = 3.97 \times 10^{-3} \ll 1$ ,  $\zeta_{II} = 1.07 \times 10^{-2} \ll 1$ . (3) Sommerfeld parameters. Both initial value  $\eta_i$  and final value  $\eta_f$  are close to 46.8. They are much larger than 1. This implies that the process can be described semiclassically. (4) Symmetrized parameter of orbital. Generally, the orbit is not a perfect hyperbola, because the projectile loses its energy during the excitation process. However, in our case,  $V_i \approx V_f$  and  $a = \frac{Z_1 Z_2 e^2}{m_0 V_i V_f} = 5.73 \text{ fm}$ . Therefore, we have a symmetrical orbital. (5) A parameter  $\xi$  for excitation cross-section function,  $f_{E\lambda}(\xi)$ , defined by

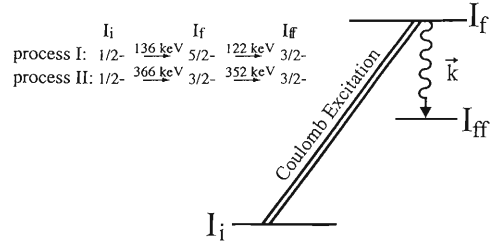


Fig. 1. The main  $^{57}\text{Fe}$  excitation process in the  $^{57}\text{Fe}$  in-beam Mössbauer study.

$$\xi = \frac{a\Delta E}{\hbar V} = \frac{Z_1 Z_2 e^2}{\hbar V} \frac{\Delta E}{2E}$$

For  $^{57}\text{Fe}$  Coulomb excitation,  $\xi_I = 0.055$  and  $\xi_{II} = 0.147$ .

As mentioned above, the excitation cross-section function can be calculated by the semiclassical approximation. According to  $f_{E2}(\eta_i = \infty, \xi)$  tabulation in Ref. 3,  $f_{E2}^I = 0.88$  and  $f_{E2}^{II} = 0.80$  for  $\xi_I = 0.055$  and  $\xi_{II} = 0.147$ . Using the experimental value of  $B(E, \lambda)$ ,  $B_{E2}^I = 410e^2 \text{ fm}^4$  and  $B_{E2}^{II} = 320e^2 \text{ fm}^4$ , we obtain the excitation cross-section from Eq. (1) as  $\sigma_{E2}^I = 822 \text{ mb}$  and  $\sigma_{E2}^{II} = 583 \text{ mb}$ .

The  $\gamma$ -emission from the Coulomb excited nucleus is not isotropic. The differential excitation cross-section for  $E2$  excitation can be calculated according to Eqs. (1) and (2) with  $\lambda = 2$  and  $\theta = \theta_c$  which is the scattering angle in the center-of-mass system.

Pure Coulomb excitation is only realized under the condition that the kinetic energy of the heavy-ion projectile is lower than the Coulomb barrier. Coulomb barrier is given by  $E_B = Z_1 Z_2 e^2 / R$  with the effective radius  $R$  of interaction

$$R = r_0 (A_1^{1/3} + A_2^{1/3}),$$

where  $r_0 = 1.5 \text{ fm}$ . The experimental condition at RIKEN is  $E_B = 61.8 \text{ MeV}$ . On the other hand, the kinetic energy  $E$  of the projectile should be high enough, otherwise the collision becomes adiabatic and the excitation cross-section becomes small. From Ref. 2, the lower limitation should be written as

$$E > 0.2 Z_1 \left(\frac{A_1}{Z_1}\right)^{1/3} (Z_2 \Delta E)^{2/3}$$

where both  $\Delta E$  and  $E$  are in the unit of MeV. Therefore, the best bombarding energy of the projectile under the experimental condition at RIKEN should be in the region of  $21.0 \text{ MeV} < E < 61.8 \text{ MeV}$ .

## References

- 1) K. Alder et al.: Rev. Mod. Phys. **28**, 422 (1956).
- 2) Y. Yoshida and Y. Kobayashi et al.: RIKEN Accel. Prog. Rep. **28**, 102 (1995).
- 3) K. Alder and A. Winther: CERN Report T/KA-AW-1, 1954.

\* On leave from Department of Physics, Nanjing University, Nanjing, China as an Eminent Scientist of RIKEN.

## Multitracer Study on the Permeation of Rare Earth Elements through a Supported Liquid Membrane

S. Ambe, T. Ozaki, S. Enomoto, and F. Ambe

Separation by means of supported liquid membranes is a useful method for the preparation and preconcentration of radioactive nuclides. The permeation of rare earth elements through a bis(2-ethylhexyl) hydrogen phosphate-decalin membrane supported on a microporous polytetrafluoroethylene sheet was studied using a multitracer containing the radioactive nuclides of Sc, Zr, Nb, Hf, Ce, Pm, Gd, Yb, and Lu.

Disks of Au were irradiated by a 135 MeV/nucleon  $^{12}\text{C}$ ,  $^{14}\text{N}$ , or  $^{16}\text{O}$  beam accelerated by the RIKEN Ring Cyclotron. The Au was removed from a multitracer by chemical separation procedures. The multitracer in the aqueous solution was separated into three groups by a cation exchange resin. The rare earth element group which also contained Zr, Nb, and Hf was stored in 3 mol  $\text{dm}^{-3}$  HCl. One hundred  $\mu\text{l}$  of the group tracer solution was added to the feed solutions, and the acidity of the solutions was adjusted to be 0.4, 0.3, 0.2 mol  $\text{dm}^{-3}$  HCl, pH 1.4, 2.4, and 3.4. As for receiving solutions, 0.5, 0.75, 1.1, 2.3, and 4.0 mol  $\text{dm}^{-3}$  HCl solutions were used.

The permeation of rare earth elements from the feed solutions of 0.4, 0.3, 0.2 mol  $\text{dm}^{-3}$  HCl, pH 1.4, 2.4, and 3.4 into the 0.5 mol  $\text{dm}^{-3}$  HCl receiving solution was carried out. Among the various feed solutions, the solution at pH 1.4 gave the highest permeation rate for Ce, Pm, and Gd, amounting to about 95% of permeation for Ce and Pm, 80% for Gd, and 10% for Yb in 21 h. Scandium, Zr, Nb, Hf, and Lu were not transported at all from the feed solution.

The permeation of rare earth elements from the feed solution at pH 1.4 into the 0.75, 1.1, 2.3, and 4.0 mol  $\text{dm}^{-3}$  HCl solutions was carried out. Figure 1 shows the transport rate of the rare earth elements from the feed solution at pH 1.4 into the 4.0 mol  $\text{dm}^{-3}$  HCl receiving solution. The percentage of permeation of the elements from the receiving solutions of different HCl concentration at 21 h is shown in Fig. 2. An increase in the HCl concentration of the receiving solutions enhanced the permeation of Gd, Yb, and Lu markedly.

The enhanced permeation of Gd, Yb, and Lu into the 4.0 mol  $\text{dm}^{-3}$  HCl receiving solution indicates that the back-extraction is a rate-determining step in the

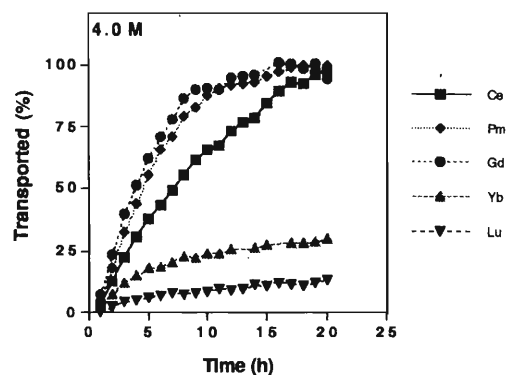


Fig. 1. The transport rates of lanthanide ions from the feed solution at pH 1.4 to the 4.0 mol  $\text{dm}^{-3}$  HCl receiving solution through a membrane with bis(2-ethylhexyl) hydrogen phosphate-decalin in the ratio of 1.

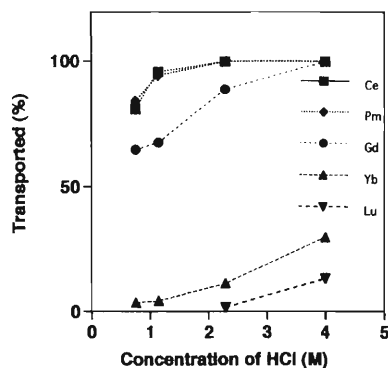


Fig. 2. Percentage transport of lanthanide ions from the feed solution at pH 1.4 to the 0.75, 1.1, 2.3, and 4.0 mol  $\text{dm}^{-3}$  HCl receiving solutions through a membrane with bis(2-ethylhexyl) hydrogen phosphate-decalin in the ratio of 1 after 21 h-permeation.

permeation of heavy rare earth elements, because they form stable complexes with bis(2-ethylhexyl) hydrogen phosphate in the membrane. Scandium, Zr, Nb, and Hf were not detected even in the 4.0 mol  $\text{dm}^{-3}$  HCl receiving solution.

## Model Study of Acid Rain Effect on Adsorption of Trace Elements on Soils (III)

H. Wang, S. Ambe, N. Takematsu, and F. Ambe

Acid rain has bad effects not only on vegetation but also on soils. It changes the adsorption or retention of many elements in the soil-pore water system, which in turn exerts a significant influence on the availability of nutrient elements for plants.

In our previous papers, adsorption of many trace elements on kaolin, forest soil, and Kureha Soil from a model acid rain (pH 1.8–5.6) has been studied using the multitracer technique.<sup>1,2)</sup> In this report, black soil (original and without organic matter) was used as an adsorbent to investigate the effect of organic matter on the adsorption of trace elements, because soil is principally composed of aluminosilicates (clay minerals), organic matter (humic substances), and Fe-Mn oxides.

The black soil is from the Mt. Nasu system (Fukushima prefecture) and its content of organic carbon is 12.5% (about 25% as organic matter). The organic matter was removed by heating with 30% H<sub>2</sub>O<sub>2</sub> at 80 °C for 2 hours. Three hundred (300) mg of soil was suspended in 10 ml of the model acid rain containing the multitracer (Be, Sc, Mn, Fe, Co, Zn, As, Se, Rb, Sr, Y, Zr, Tc, Ru, Rh and Re). The suspension pH value was adjusted to a desired value (1.8–5.6) with HCl or NaOH solution. After equilibrium (shaking for several days), the suspension was centrifuged. The pH value and the  $\gamma$ -ray spectrum of the supernatant were measured. The adsorption percentage of each element was calculated by comparing the  $\gamma$ -ray intensities at a given energy before and after adsorption.

In general, the pH dependent adsorption of elements on the black soil (Fig. 1) is similar to that on all the soils examined so far, although absolute adsorption percentages are varied. The adsorption of cationic elements increases with the increase of pH, whereas that of anionic elements (As, Se, Tc and Re) is *vice versa*. The adsorption of Sc, Fe and Zr is higher than that of other cationic elements. These trends can be explained by the complex formation between surface functional groups and cations or anions.

The adsorption of Zr, Ru, Rh, As, and Se on the black soil is not appreciably affected by the removal of organic matter, although that of Zr, As, and Se is too high to discriminate between the soils with and without organic matter. On the other hand, the removal of organic matter causes a distinct adsorption decrease of Be, Sc, Mn, Fe, Co, Zn, Rb, Sr, Y, Tc, and Re, especially of Tc and Re.

The organic matter in soil (humic substances) have high contents of carboxyl and phenolic hydroxyl groups

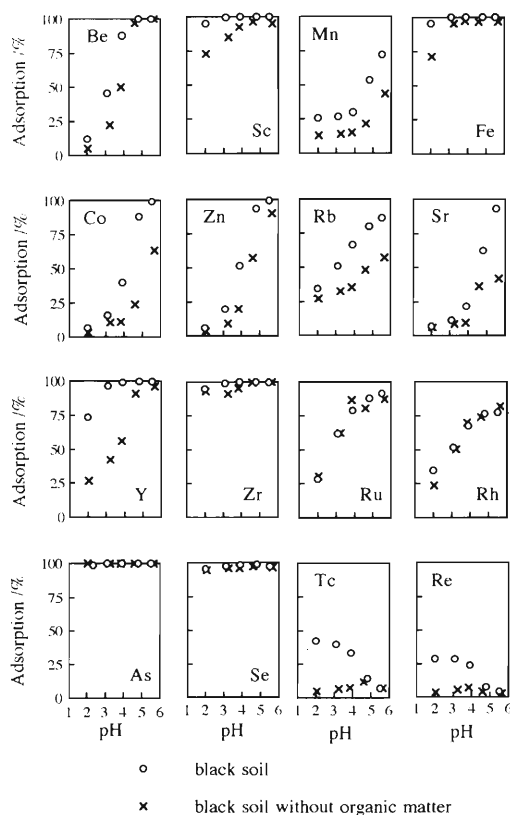


Fig. 1. The pH effect of model acid rain on the trace element adsorption on black soil and on soil without organic matter.

as ligands, with which a broad range of elements can make complexes. This is the main reason why the adsorption of many elements decreases after removal of organic matter.

In brief, the experimental results of this study predict that acid rain will reduce the retention of cationic elements in soil and that it will enhance the retention of anionic elements. The contents of organic matter and oxides in soil affect the extent of adsorption, and their pH dependence of adsorption is similar to that of aluminosilicates.

### References

- 1) H. Wang et al.: RIKEN Accel. Prog. Rep. **30**, 122 (1997).
- 2) H. Wang et al.: RIKEN Accel. Prog. Rep. **30**, 123 (1997).

# Simultaneous Determination of Stability Constants of Humate Complexes with Various Metal Ions Using Multitracer Technique†

Y. Takahashi, Y. Minai, S. Ambe, Y. Makide,\*<sup>1</sup> F. Ambe, and T. Tominaga\*<sup>2</sup>

Complexation with humic acid, naturally occurring organic polyacid, has been recognized as an important factor controlling the behavior of various elements in the natural aquifer.<sup>1)</sup> The stability constant of humate complex is an important and fundamental datum to evaluate the humate formation on the speciation of each element. In the present study, the multitracer technique was applied to obtaining the stability constants of humates of 19 elements (Be, Ca, Sc, V, Cr, Mn, Fe, Co, Zn, Ga, Sr, Y, Ba, Ce, Eu, Gd, Tm, Yb, and Lu). The stability constant ( $\beta$ ) was determined by a solvent extraction method using di(2-ethylhexyl)phosphoric acid (DEHP) as the extractant.<sup>2)</sup>

The  $\log\beta$  determined are plotted against degree of ionization of humic acid ( $\alpha$ ) and against pH in Fig. 1. As a whole, the stabilities of humate complexes apparently increase with the increase in either pH or  $\alpha$ . Similarly, the apparent  $pK_a$  of humic acid obtained by pH titration increases with either pH or  $\alpha$ . The stability constants of humates for trivalent ions are generally larger than those for divalent ions. For alkaline earth metal ions, the stability constants of humate complexes were in the order of Be-humate > Ca-humate > Sr-, Ba-humate. This shows that the humate of alkaline earth metal ion with smaller ionic radius is more stable, which suggests that the humic acid is a "hard" ligand. The increase of  $\log\beta$  and  $pK_a$  with the increase in pH or  $\alpha$  can be explained by the increase of electrostatic potential of humic acid regarded as polyelectrolyte.<sup>3)</sup> The slopes of  $\log\beta$  for divalent ions measured against either pH or  $\alpha$  were smaller than those for trivalent ions, while they were larger than those for  $VO_2^+$  and proton ( $= pK_a$ ).

A simple electrostatic model based on the coulombic interaction between a metal ion and a polyelectrolyte was employed to explain the dependence of humate stability constants of various elements on pH and  $\alpha$ .<sup>3)</sup> The intrinsic stability constant,  $\beta_{int}$ , defined in the model represents the stability of the humate complex with an ion when the electrostatic effect of humic acid is negligible. The deviation of apparent stability constant from the intrinsic one with increasing  $\alpha$  or pH reflects the increased electric field in the vicinity of the polyelectrolyte. The relationship between  $\log\beta$  and  $\log\beta_{int}$  is expressed as:<sup>3)</sup>

$$\log\beta = \log\beta_{int} + k z_i \alpha, \quad (1)$$

where  $k$  is a constant and  $z_i$  is the charge of the metal ion. The second term in the right hand side of Eq. (1)

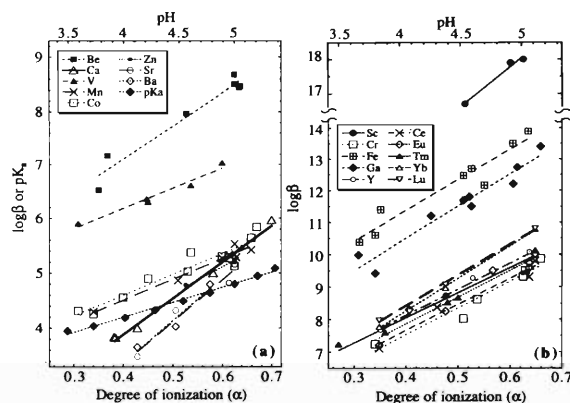


Fig. 1. The  $\alpha$  (degree of ionization of humic acid) and pH dependences of  $pK_a$  of humic acid and stability constants of humate complexes ( $\beta$ ) with (a)  $VO_2^+$ , and divalent ions of Be, Ca, Mn, Co, Zn, Sr, and Ba, and (b) trivalent ions of Sc, Cr, Fe, Y, Ce, Eu, Gd, Tm, Yb, and Lu at  $C_s = 0.020$  M.

is introduced to take account of the electrostatic interaction between humic acid molecule and the metal ion which increases with gradient of the  $\log\beta$  vs.  $\alpha$ . Based on the linear relationship observed between  $\log\beta$  and  $\alpha$  (Fig. 1),  $\log\beta_{int}$  was obtainable for various metal ions by extrapolation to  $\alpha = 0$ . The  $\log\beta_{int}$  was plotted against the stability constants of the corresponding oxalate complexes (metal ion : oxalate molecule = 1:1). It was found that each  $\log\beta_{int}$  value is identical to the stability constant of the corresponding oxalate. This suggests that a bidentate carboxylate site may act as the complexing site in the humate formation with trace elements.

Based on the stability constants obtained here and the humic acid concentration in natural water, the ratio of humate complex species to free metal ion in the natural environment was estimated; similar estimation was also conducted for carbonate and hydroxide complexes for each element. As the result, it was found that humates may be the dominant species for Be, Cr(III), Fe(III), and rare earth elements (REEs). In particular, the humate formation appears to be substantially important for REEs, in accordance with our previous study on the adsorption behavior of the trace elements including REEs.<sup>4)</sup>

## References

- 1) W. Stumm and J. J. Morgan: *Aquatic Chemistry* (Wiley, New York, 1995).
- 2) R. A. Torres et al.: *Radiochim. Acta* **35**, 143 (1984).
- 3) E. Wilson and P. Kinney: *Wat. Res.* **22**, 281 (1977).
- 4) Y. Takahashi et al.: *J. Radioanal. Nucl. Chem.* **205**, 269 (1996).

† Condensed from the article in *Sci. Total Environ.* **198**, 61 (1997).

\*<sup>1</sup> Radioisotope Center, University of Tokyo

\*<sup>2</sup> Department of Chemistry, School of Science, University of Tokyo

## Comparative Subcellular Distribution of Radioactive Mn, Fe, Zn, and Se Tracers in Brain and Liver: Why, in Brain, Do most of Their Proteins Exist in Mitochondrial and Nuclear Fraction?

R. Amano, S. Oishi, M. Ishie,\* M. Kimura,\* S. Enomoto, and F. Ambe

As expected by the low required concentrations, the micro essential elements, Mn, Fe, Zn and Se, serve primarily catalytic functions in cells and organisms.<sup>1)</sup> Iron deficiency causes anemia, providing clear evidence of Fe essentiality. It is also a component of numerous proteins that exert critical roles in energy metabolism, notably the cytochromes and the enzymes in the electron transport system. Manganese deficiency results in a distinct pathology, including reproductive failure, skeletal defects, and ataxia; the Mn ion is also a component of several enzymes, including mitochondrial superoxide dismutase, pyruvate carboxylase, and arginase, although these enzymes may not be related directly to the observed pathology of Mn deficiency. A similar situation exists in the case of Zn, whose deficiency pathology includes stunted growth, skin lesions, and reproductive difficulties. Zn is a component of enzymes that catalyzes more than 50 different biochemical reactions as well as a component of proteins involved in gene expression. However, none of these proteins or enzymes has been identified with specific Zn deficiency pathology. Besides its catalytic role in some enzymes, Zn exerts a structural role in proteins, particularly in the Zn finger proteins involved in gene transcription. Se deficiency result in severe pathology, including cardiomyopathy and skeletal muscle defects. Se is a component of some proteins, the glutathione peroxidases and the iodothyronine-5'-deiodinases.

Using a multitracer solution prepared by RIKEN Ring Cyclotron, we have studied the subcellular distribution of several trace elements in the liver and kidney, and obtained the preliminary results to speculate their biochemical or physiological functions.<sup>2,3)</sup> The present work aimed to examine the subcellular distribution of <sup>54</sup>Mn, <sup>59</sup>Fe, <sup>65</sup>Zn and <sup>75</sup>Se in the brain of normal mice, and to compare the brain distributions with the liver ones. A multitracer solution was prepared from four commercially available tracers. Four male C57BL/6N mice weighing 19–20 g (6 weeks old) were used. Physiological saline solutions (0.001N HCl, pH 2–3) containing the radioactive multitracer were intraperitoneally injected (0.2 ml/mouse). At 48 hr after injection, the mice were sacrificed under ether anesthesia, and the blood was collected. After this, the brain was excised. The excised brain was homogenized in a cold (5 °C) 0.25 M sucrose solution containing 0.01 M Tris-HCl buffer at pH 7.6 (10% weight per volume). Subcellular fractionation was carried out at 4 °C accord-

ing to a modification of the method of Hogeboom and Schneider.<sup>4)</sup> Subcellular distributions are expressed as fractionation percentages (the radioactivity percentage of nuclear, mitochondrial, microsomal or supernatant fraction in %).

Figure 1 shows the subcellular distribution of radioactive Mn, Fe, Zn and Se tracers in the brain of C57BL/6N mice at 48 hr after injection together with that of the liver of ddY mice reported in the previous paper.<sup>2,3)</sup> Surprisingly, the mitochondrial and nuclear fraction percentages of the brain were found definitely higher than those of the liver. This fact is surely due to the difference of soft tissue, not to the difference of mouse strain. We plan to examine the subcellular distributions in several soft tissues including brain of same mouse strain.

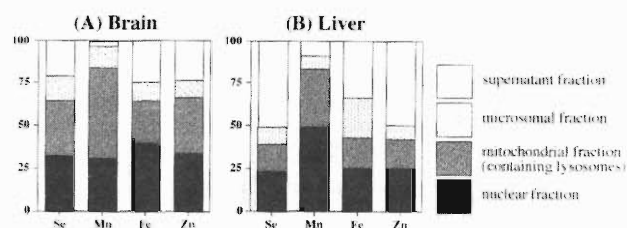


Fig. 1. Subcellular distributions of radioactive Mn, Fe, Zn and Se tracers in the brain(A) and liver(B) of mice at 48 hrs after injection.

Undoubtedly, the radioactive Mn, Fe, Zn and Se tracers in all fraction become a component of numerous proteins at 48 hr after i.p. injection. In the brain, large parts of these metal proteins probably exist in mitochondrial and nuclear fraction. In future, we will confirm and discuss these phenomena.

### References

- 1) B. L. O'Dell and R. A. Sunde: in *Handbook of Nutritionally Essential Mineral Elements*, edited by B. L. O'Dell and R. A. Sunde (Marcel Dekker, New York, 1997), p. 4.
- 2) R. Amano, S. Oishi, S. Enomoto, and F. Ambe: RIKEN Rev. No. 13, p. 31 (1996).
- 3) R. Amano, S. Oishi, S. Enomoto, and F. Ambe: Ann. Cli. Lab. Sci. **26**, 531 (1996).
- 4) G. H. Hogeboom: in *Methods in Enzymology Vol. 1*, edited by S. P. Colowick and N. O. Koplman Vol. 1 (Academic Press, New York, 1955), p. 16.

\* School of Health Sciences, Faculty of Medicine, Kanazawa University

## Comparative Distribution of the Trace Elements Sc, Mn, Fe, Co, Zn, Se, Rb, and Zr in the Brain and Other Organs of C57BL/6N Mice

S. Oishi, R. Amano, M. Nishida,\* T. Yonebayashi,\* A. Ando,\* S. Enomoto, and F. Ambe

Multitracer enables simultaneous tracing of various elements in the identical system, and makes a strict and accurate comparison of their behavior, minimizing the undesirable effects of both peculiarities of samples and variation in experimental conditions.<sup>1-5)</sup> In the present work, we have applied it to the study of biobehavior of Sc, Mn, Fe, Co, Zn, Se, Rb and Zr trace elements in normal C57BL/6N mice. The tissue distribution of the 8 elements was examined among 11 organs (brain, cardiac muscle, lung, liver, spleen, pancreas, kidney, bone, thighbone muscle, eyeballs and testes) and blood, and evaluated in terms of "tissue uptake rate (the percentage of injected dose per gram of tissue: %dose/g)".

Male C57BL/6N mice were purchased from Charles River Japan Inc., and fed with a standard laboratory diet and had a free access of drinking water in steel cages during 1 week prior to administration. A no-carrier-added radioactive multitracer solution was obtained from the Ag (purity: more than 99.99%) target irradiated by 135 MeV/nucleon N-14 beam accelerated by RIKEN Ring Cyclotron. Preparation for of the multitracer solution from Ag target was carried out in the Radioisotope Center, Kanazawa University. After evaporation of the no-carrier-added multitracer solution containing hydrochloric acid, a physiological saline solution was added to obtain the radioactive multitracer solution for injection. The 8 elements (Sc, Mn, Fe, Co, Zn, Se, Rb and Zr) were evaluated in this experiments. At 6, 12, 24 and 48 hr after intraperitoneal injection (0.2 ml) into 20 mice, the mice were sacrificed under ether anesthesia, and about 0.2 ml of blood was collected, and then the above 11 organs were excised. These tissues were weighed immediately and freeze-dried. The dried samples were subjected to the gamma-ray spectrometry with pure Ge detectors against an appropriate standard sample in order to obtain the tissue uptake rate. (See, Table 1.)

All the 8 radioactive tracers were observed in the cardiac muscle, lung, liver, spleen, pancreas and kidneys. However, in the brain, muscle and testes, the uptake rates of Fe were found negligibly low. On the other hand, in the kidneys, liver, pancreas and spleen, the uptake of Fe was significantly high. This biobehavior of the trace Fe permits us to assume the following consideration. Iron is essential and exists in all organs including brain, muscle, testes, liver, kidneys, pancreas and spleen. Our results lead to the estimation that the transportation rates of Fe tracer to brain, muscle and testes are considerably slower than those to kidneys, liver, pancreas and spleen. The transport mechanism of Fe for the former group is presumably different from

Table 1. Tissue uptake rates of the brain at 6, 12, 24, and 48 h after injection of a multitracer solution.

Brain	6 h	12 h	24 h	48 h
<sup>46</sup> Sc	0.21 ± 0.06	0.42 ± 0.08	0.36 ± 0.08	0.52 ± 0.26
<sup>54</sup> Mn	0.31 ± 0.07	0.35 ± 0.07	0.34 ± 0.02	0.58 ± 0.06
<sup>59</sup> Co	0.18 ± 0.03	0.18 ± 0.03	0.14 ± 0.05	0.12 ± 0.02
<sup>59</sup> Fe	n.d.	n.d.	n.d.	n.d.
<sup>65</sup> Zn	0.58 ± 0.12	0.89 ± 0.05	1.16 ± 0.17	1.54 ± 0.16
<sup>75</sup> Se	0.40 ± 0.06	0.41 ± 0.03	0.40 ± 0.04	0.46 ± 0.08
<sup>83</sup> Rb	1.07 ± 0.15	1.69 ± 0.14	2.36 ± 0.30	2.59 ± 0.27
<sup>88</sup> Zr	0.20 ± 0.10	0.13 ± 0.02	0.09 ± 0.03	0.04 ± 0.01

Tissue uptake rate (%dose/g) means the radioactivity percentage of injected dose per one gram of tissue.

that for the latter group. Figure 1 compares the brain uptake rates of Sc, Mn, Co, Zn, Se, Rb and Zr tracers in normal C57BL/6N mice at 6, 12, 24 and 48 h after intraperitoneal injection. The uptake rate of the Se tracer showed no significant time-dependent changes. However, the uptake rates of the Sc, Mn, Zn and Rb tracers increased with time, while those of the Co and Zr tracers decreased. According to these results, it is evident that the metal ions examined in this work are easily transported into the brain, and in addition the high retention of Se, Rb, Mn and Zn in the brain during a fairly long time suggests an active involvement of the elements in the brain function.

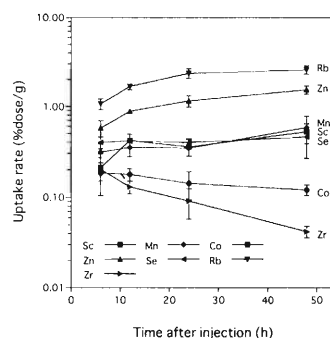


Fig. 1. The uptake behavior of Sc, Mn, Co, Zn, Se, Rb, and Zr by the brain at 6, 12, 24, and 48 h after intraperitoneal injection of a multitracer solution.

### References

- 1) S. Ambe et al.: Chem. Lett. **1991**, 149.
- 2) S. Ambe et al.: Anal. Sci. **7**, Suppl., 317 (1991).
- 3) S. Ambe et al.: J. Radioanal. Nucl. Chem. **195**, 297 (1995).
- 4) R. Amano et al.: J. Trace Elements Med. Biol. **10**, 145 (1996).
- 5) R. Amano et al.: Ambe, Ann. Cli. Lab. Sci. **27**, 358 (1997).

\* School of Health Sciences, Faculty of Medicine, Kanazawa University

## Metabolic and Biochemical Studies of Trace Elements in Hypercholesterolemic Model Mice (I)

R. G. Weginwar, S. Enomoto, R. Hirunuma, S. Ambe, and F. Ambe

Unregulated cholesterol production can lead to serious disease. Atherosclerosis (heart failure) is linked to high levels of cholesterol in the blood, and particularly high levels of Low Density Lipoprotein (LDL) bound cholesterol is a leading cause of death in industrialized societies. All steroid hormones in humans are derived from cholesterol. Two classes of steroid hormones are synthesized in the cortex of the adrenal gland: mineralocorticoids, which control the reabsorption of inorganic ions by the kidney, and glucocorticoids, which help regulate gluconeogenesis and also reduce the inflammatory response.<sup>1)</sup> The sex hormones are produced in male and female gonads and the placenta. They include androgens and estrogens, which influence the development of secondary sexual characteristics in males and females, respectively, and include progesterone, which regulates the reproductive cycle in females. In the present investigation we have studied on the metabolic abnormality of trace elements such as Be, Sc, V, Mn, Fe, Co, Zn, As, Se, Rb, Sr, Y, and Zr in the different organs of normal and hypercholesterolemic (feeding cholesterol 5% diet to male ddY mice for 2, 4 and 6 weeks) model mice.

Blood was collected in tubes from 4 to 5 animals in each group after 12 hours fasting, and plasma was separated out by centrifugation for enzymatic assessments. Total cholesterol (T-CH), High Density Lipoprotein (HDL-CH) and triglycerides (TG) in plasma were determined with enzymatic reagents, and Low Density Lipoprotein cholesterol (LDL-CH) was calculated using the formula as described below.

$$\text{LDL-CH} = [(\text{T-CH}) - (\text{HDL-CH}) - (\text{TG} \times 0.2)]$$

T-CH, TG and LDL-CH were found to be significantly increasing in plasma of hypercholesterolemic group in feeding period, while HDL-CH increased only by 10% with respect to control group. We have observed a positive relationship between T-CH and LDL-CH in plasma and hepatic uptake of Fe, Mn, Co, As, Cr, V, Sc, Be, Zr, Y, Nb, and Ru for hypercholesterolemic mice.

The analyses showed that the T-CH and LDL-CH in plasma were positively correlated with Zn in kidney (Fig. 1). On the other hand, Zn uptake in liver were negatively correlated (Fig. 2), but no correlation was found with HDL-CH and TG. Similar results were also observed for Se and Sr in liver as well as in kidney. It has been reported that glutathione peroxidase activity decreased with induced hypercholesterolemia in rabbits but it is not yet known whether the decrease

in hepatic Zn, Se and Sr uptake rate by cholesterol intake is due to altered absorptive process or alterations in other aspects of their metabolisms. In the case of kidney, almost all the elements were found to be increased with plasma cholesterol. However, it is already known that the mineralocorticoid hormones, derived from cholesterol, regulate reabsorption of inorganic ions by the kidney.<sup>1)</sup>

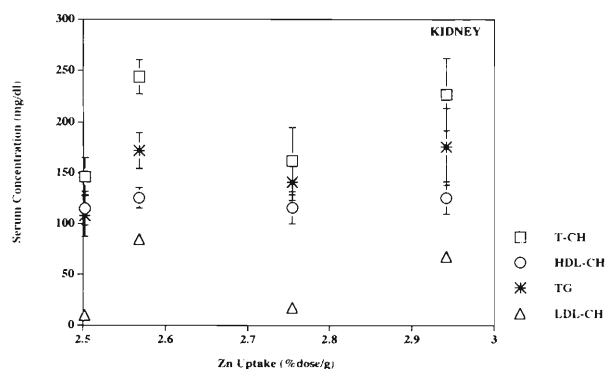


Fig. 1. Correlation between serum cholesterol and kidney Zn level in hypercholesterolemic model mice.

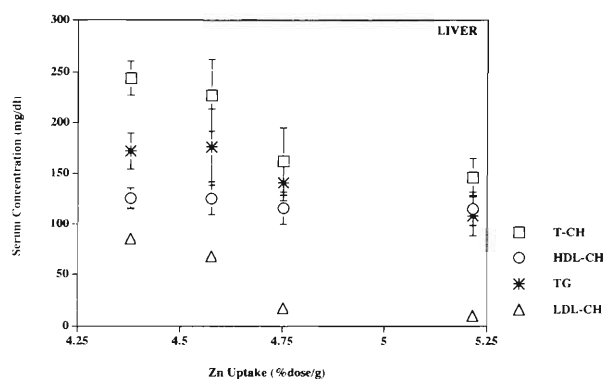


Fig. 2. Correlation between serum cholesterol and hepatic Zn level in hypercholesterolemic model mice.

Thus, our results provide a definite evidence that cholesterol and lipid concentration in the body can significantly involve in the metabolism of trace elements.

### References

- 1) A. L. Lehninger, D. L. Nelson, and M. M. Cox: in *Principles of Biochemistry*, Worth Publishers, second edition, New York, (1993), p. 680.

## Metabolic and Biochemical Studies of Trace Elements in Hypercholesterolemic Model Mice (II)

R. G. Weginwar, S. Enomoto, R. Hirunuma, S. Ambe, and F. Ambe

The radioactive multitracer technique was applied for simultaneous evaluation of bio-behavior of trace elements in different organs of the normal and hypercholesterolemic model mice. The distribution of trace elements (Be, Na, Sc, V, Cr, Mn, Fe, Co, Zn, As, Se, Rb, Sr, Y, Zr, Nb and Ru) in 8 organs (liver, kidney, brain, muscle, lung, spleen, bone and testis) and in blood was examined by using the multitracer solution prepared from the Ag target irradiated by heavy ions. The tissue distribution was evaluated by  $\gamma$ -ray spectrometry in terms of the radioactivity percentage of injected dose per gram of tissue. In this paper, only results of blood and liver are reported and discussed as typical examples.

Figure 1 shows the uptake rate of various trace elements by blood after 24 hrs of multitracer injection in the normal as well as 2 to 6 week-fed cholesterolemic mice. A positive correlation was found between the uptake rate of Sr and As in to blood with cholesterol feeding. On the other hand, a negative correlation occurred between the uptake rate of Zn, Co, Na, Be, V, Cr, Rb, Zr and Ru in to blood with cholesterol feeding. The uptake rate of Fe, Sc and Nb increased in the 2 and 4 week-fed mice compared to the normal ones, but decreased in the 6 week-fed mice. In case of Se, uptake rate was higher in cholesterolemic mice, compared to normal ones, but cholesterol dose dependence was not observed. It has already been reported<sup>1)</sup> that, plasma superoxide dismutase activity increased by feeding cholesterol to rabbits, while glutathione peroxidase activity decreased. This may

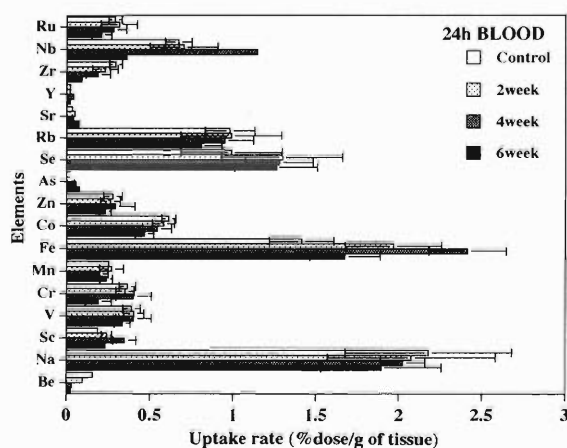


Fig. 1. Uptake rates of various elements in blood at 24 hrs after injection in the normal and hypercholesterolemic mice.

be the possible reason for different metabolism of Se.

In the liver of hypercholesterolemic mice at 24 hrs after the multitracer administration (Fig. 2), the uptake rate of Be, Sc, Zr, Y, V, Rb, Fe and Nb was observed to be much higher compared to normal mice, and increased with cholesterol feeding period. Conversely, biologically important elements such as Zn, Se and Sr uptake rate was found to be decreasing with feeding period of cholesterol.

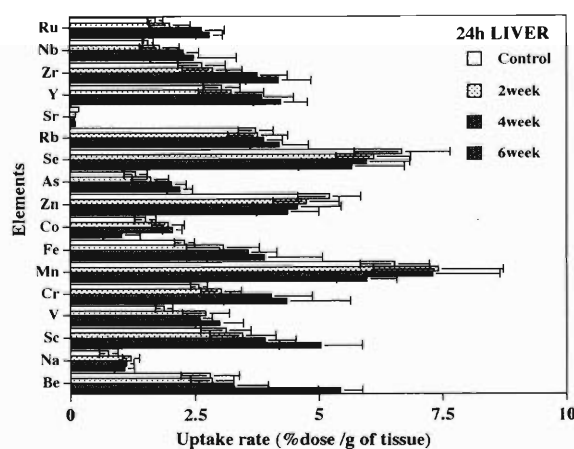


Fig. 2. Uptake rates of various elements in liver at 24 hrs after injection in the normal and hypercholesterolemic mice.

We observed many fat granulations and fiberization in liver of hypercholesterolemic mice, and it has been already reported that the bone seeking elements like Be, Sc, V, Zr, Y, Nb and so forth are stored in the part of fiberization. Such a change was assumed to be generated by hepatopathy in the cholesterolemic mice, and the uptake rate of these bone seeking elements is suggested to increase by this reason. Also, cholesterolemia seems to have some specific effects on the metabolism of some elements with high valency or some enzymes requiring inorganic elements as cofactors.

In literature, certain influence of cholesterol on the metabolism of copper, selenium, iron, zinc and magnesium is described, but the nutritional influence of cholesterol metabolism on various trace elements under similar experimental conditions is not yet studied.

### References

- 1) E. D. Silva, P. Moriel, Y. Chang, and D. S. P. Abdalla: *Biochem. Mol. Bio. Int.* **36**, 679 (1995).

## Metabolic Study of Trace Elements in Se-Deficient Rats (II)

R. Hirunuma, N. Sotogaku, K. Endo, S. Enomoto, S. Ambe, and F. Ambe

A number of studies on the role of Se in biochemistry are found in literature. It is very interesting and important to clarify the distribution of trace elements in various organs of Se-deficient rats. In the present study, the uptake and distribution of trace elements in Se-deficient rats were examined by the multitracer technique which can evaluate the behavior of many elements under the same experimental condition.

Multitracer solutions containing various radioisotopes were prepared from a Ag target which was irradiated with  $^{14}\text{N}$  or  $^{16}\text{O}$  beam of 135 MeV/nucleon extracted from RIKEN Ring Cyclotron. After chemical separation, this multitracer was dissolved in a physiological saline solution. Mother (Wistar) rats had been

fed with Se-deficient diet (produced by Oriental Yeast Co., LTD.) since their 14th day of pregnancy until the weanling period of their baby rats. The weanling male rats were separated from their mothers, and were fed with Se-deficient diet until the age of 12 weeks. A tenth ml of saline contained the multitracer was injected in to the tail vein of each rat. The Se-deficient and normal rats were sacrificed at four different times after injection, and the radioactivities in their organs and blood were determined by  $\gamma$ -ray spectrometry.

The characteristic results obtained on some of the elements (As, Fe, and Sc) in the liver are shown in Fig. 1. In the liver, the uptake of As, Fe, and Sc of Se-deficient rats was larger than that of normal ones

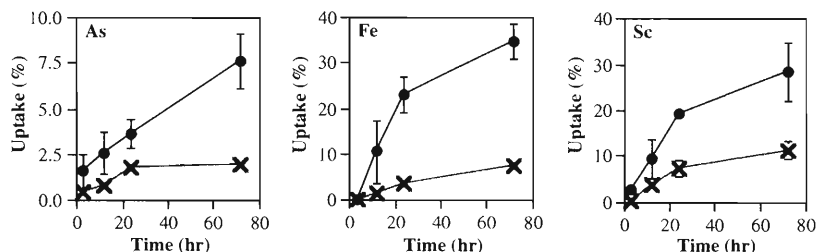


Fig. 1. Time dependence of the uptake of As, Fe, and Sc in the liver of normal (x) and Se-deficient rats (●).

at 72 hrs after injection.

The following two reasons are suggested for the accumulation of As in the liver of Se-deficient rats. The first reason is the hypofunction of As methylation in the liver of Se-deficient rats, As is in a competitive relationship with Se, and Se intoxication is preventable by As.<sup>1,2)</sup> Inorganic As, which is especially toxic to animals in this form, is detoxicated by methylation in the liver, and this methylated As is excreted through urine. Because the chemical form of As is  $\text{AsO}_3^-$  in our multitracer, the accumulation of As in the liver of Se-deficient rats can be interpreted as a result of the depression in effectiveness of the As methylation. The second reason is the decrease of As excretion to bile on account of Se-deficiency. Arsenic enhances Se excretion to bile, while Se also enhances As excretion to bile.<sup>3,4)</sup>

The accumulation of Sc and Fe in the liver increased with time in the normal and Se-deficient rats. Interestingly, the uptake behavior of Sc and Fe in the liver of normal rats was similar to that in the liver of Se-deficient rats. Iron is, of course, one of the essential elements in living organisms, whereas for Sc no beneficial role has been reported. The reason for the similar uptake behavior between Sc and Fe is considered due to the similarity of their ionic radii ( $0.73\text{\AA}$  for  $\text{Sc}^{3+}$  and

$0.64\text{\AA}$  for  $\text{Fe}^{3+}$ ) and their same ionic valence ( $\text{Sc}^{3+}$  and  $\text{Fe}^{3+}$ ).

No difference was observed in the uptake behavior of most of bone seeking elements such as Ca, Sr, and Y between normal and Se-deficient rats. On the contrary, bone uptake of Zr was clearly different between Se-deficient and normal rats. Although Zr is classified into the bone seeking elements, there are only few reports on behavior of Zr in animals. The present experiment showed that Zr behaves in a characteristic way different from other bone seeking elements. This might be due to its unique chemical form of  $\text{ZrO}^{2+}$  in the aqueous medium.

Selenium is known to be in a competitive or synergistic relationship with several metals. From the present result on Sc and Zr, it was newly elucidated that there is some interaction between these elements and Se.

### References

- 1) A. L. Moxon: *Science* **88**, 81 (1938).
- 2) A. L. Moxon and K. P. DuBois: *J. Nutr.* **18**, 447 (1939).
- 3) O. A. Levander and C. A. Baumann: *Toxicol. Appl. Pharmacol.* **9**, 98 (1966).
- 4) O. A. Levander and C. A. Baumann: *Toxicol. Appl. Pharmacol.* **9**, 106 (1966).

## Influence of pH on Release of Various Trace Elements from Transferrin

N. Sotogaku, K. Matsumoto, K. Endo, R. Hirunuma, S. Enomoto, S. Ambe, and F. Ambe

Transferrin, iron-binding protein, is composed of a single 80 kDa polypeptide chain with two domains. Each domain has a site capable of binding various metal ions other than  $\text{Fe}^{3+}$  ions. Transferrin functions to transport iron in mammalian, i.e., it transfers  $\text{Fe}^{3+}$  ions from the absorption site to the storage and/or utilization sites through body fluids. At extracellular pH 7.4, iron-loaded transferrin binds strongly to its receptor on plasma membrane. Then,  $\text{Fe}^{3+}$  ions released at intercellular endosomes at low pH (approximately 5.5).<sup>1)</sup> The detailed chemical mechanism by which iron is removed from the protein is unknown, although the biological process involved in iron release at low pH in an endosome by endocytosis has been characterized. In addition, it is known that transferrin is involved in the metabolism of other metal ions, such as Al, Cr, Mn, Co, Cu, Zn, Ga, and rare earth elements (REEs) which are either trace or toxic elements.<sup>2)</sup> Although binding and release of iron (Fe) ions have been studied, those of other metal ions have not been studied in detail till today. In the present study, we report the pH dependence on the release of metal ions (Fe, Sc, Y, Zr, Hf, Ce, Eu, and Gd) from transferrin by means of the multitracer technique.

A multitracer was prepared from a piece of gold or silver target. The preparation of the multitracer solution was followed by the established procedure.<sup>3)</sup> Apotransferrin was purchased from Wako Pure Chem. Ind., Ltd. and was used without a further purification. A solution of the metal-ion (multitracer) bound transferrin was prepared by adding the buffer solution (0.01M Tris/HCl; pH 8.0) (Tris; 2-amino-2-hydroxymethyl-1,3-propanediol) containing a multitracer (50  $\mu\text{l}$ ) to the apotransferrin solution. The solution was mildly incubated at 37 °C for 24 hr. For experiment on pH-mediated release of various metal ions from transferrin, the solution was dialyzed for 48 hr against the buffer solutions in the pH range of 7.4 to 3.0. The buffer used for various pH ranges were: pH 7.4 to 6.0, 0.01M HEPES/NaOH (HEPES; N-[2-hydroxyethyl] piperadine-N'-[2-ethanesulfonic acid]); pH 5.5 to 3.0, sodium acetate/acetic acid. All buffers contained 0.2M of NaCl. After dialysis, the mixture was ultrafiltered using Molcut II (fractional M.W. 10,000; Millipore Corporation). The  $\gamma$ -ray spectra of the filters were measured by a pure Ge detector, and were compared with that of the standard multitracer solution.

Figure 1 shows the percentage of radioactivities of Fe, Sc, Y, and Ce, bound to transferrin after dialysis, assuming those at pH 8.0 as 100%. Stability of the metal ions and transferrin has been reported in terms of the  $\text{pH}_{50}$  value, that is the pH at which 50% of metal ions release from the protein.<sup>4)</sup> The  $\text{pH}_{50}$  values were found to be 4.6 for Sc, 7.4 for Y, 5.5 for Fe, and 6.9 for Ce in the present study.

Correlation between the  $\text{pH}_{50}$  and ionic radius is ten-

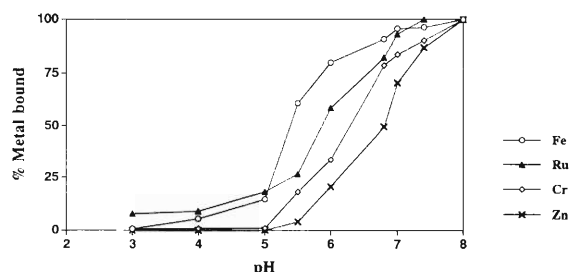


Fig. 1. The pH-dependent release of metals.

tatively shown in Fig. 2. together with the values for Hf, Zr, Gd, and Eu. The chemical forms of the tracers were assumed to be  $\text{Sc}^{3+}$ ,  $\text{Y}^{3+}$ ,  $\text{Ce}^{4+}$ ,  $\text{Eu}^{3+}$ ,  $\text{Gd}^{3+}$ ,  $\text{Zr}^{4+}$ , and  $\text{Hf}^{4+}$ . The ionic radius of the metal ions is:  $\text{Sc}^{3+}$ , 0.68 Å;  $\text{Y}^{3+}$ , 0.88 Å;  $\text{Ce}^{4+}$ , 0.92 Å;  $\text{Eu}^{3+}$ , 0.95 Å;  $\text{Gd}^{3+}$ , 0.94 Å;  $\text{Hf}^{4+}$ , 0.71 Å; and  $\text{Zr}^{4+}$ , 0.72 Å.<sup>5)</sup> The stability of transferrin metal complex depends markedly on synergistic anions, and bicarbonate (or carbonate) anions serve this function in a biological system.<sup>6)</sup> As mentioned at the beginning, transferrin has two chemically active domains. It has been reported that the C-terminal has three more cystine bridges and is more acid-stable than the N-terminal site.<sup>7)</sup> Studies on the effects of pH for the release of various metal ions from each terminal site are in progress.

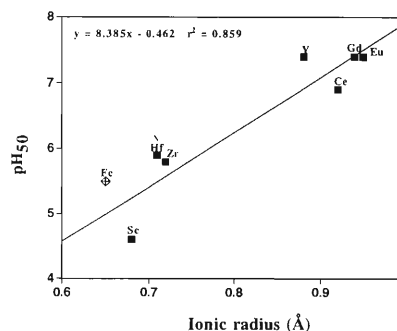


Fig. 2. Correlation between  $\text{pH}_{50}$  value and ionic radius.

### References

- 1) H. Li et al.: *Eur. J. Biochem.* **242**, 387 (1996).
- 2) L. Messori et al.: *Metal-Based Drugs*, **1**, 161 (1994).
- 3) S. Ambe et al.: *J. Radioanal. Nucl. Chem.* **195**, 297 (1995).
- 4) C. L. Day et al.: *J. Biol. Chem.* **267**, 13857 (1992).
- 5) N. T. Topp et al.: *Chemistry of the Rare-Earth Elements* (in Japanese) (Kagakudouzin, Tokyo, 1995).
- 6) M. S. Shongwe et al.: *Biochemistry*, **31**, 4451 (1992).
- 7) S. A. Kretchmar et al.: *J. Am. Chem. Soc.* **108**, 6212 (1986).

## Affinity of Bio-Trace Elements to Cell Component: *In vitro* Study Using Multitracer

K. Matsumoto, N. Sotogaku, K. Endo, S. Enomoto, S. Ambe, and F. Ambe

The metabolism of manganese (Mn), cobalt (Co), zinc (Zn), copper (Cu), and selenium (Se) in a biological system has been studied in relation to the enzyme activity by a number of workers.

Recently, the multitracer technique has been developed and applied to the studies on distribution of the bio-trace elements in rat organs. We found that iron (Fe) uptake enhanced in the liver of Se-deficient Wistar rats.<sup>1)</sup> The result suggested that alternative interaction of Se and Fe is operating in a living body. Since Se is the central ion in glutathione peroxidase (GSH-Px) and works as a reductant of hydrogen peroxide, it could be expected that Fe took the place of activity of anti-oxidative stress by Se. However, the mechanism of the interaction and distribution of the trace elements in a cell level have not yet been clarified. To examine the possibility of the interaction, it is necessary to obtain the distribution of the elements in cell components such as nucleic acid, proteins, lipid, and sugars.

DNA is an essential element that supervises the genetic information for living cells. Therefore, DNA modification or fragmentation by the reactive oxygen or other free radical species and by ligation of the metal ions might cause cell death, mutagenesis, or carcinogenesis. In order to examine possibility of distribution of metal ions in nucleic acid and in order to study interaction of metal ions within *in vivo* redox system, we studied the affinity of bio-trace metal ions to the normal and Se-deficient rat's DNA from liver, lung, and colon.

The Se-deficient Wistar rats and normal Wistar rats were sacrificed by decapitation. Subsequently, the major organs were excised. Tissues were immediately frozen and kept at  $-80^{\circ}\text{C}$  until DNA isolation. Liver, lung, and colon DNA was isolated by Kirby's method<sup>2)</sup> and prepared with concentration of 1 mg/ml by Tris-HCl (pH 8.0) buffer.

The 10  $\mu\text{l}$  of multitracer solution were added in to DNA solution. Then, the mixed solution was mildly incubated at  $37^{\circ}\text{C}$  for 60 min. After the incubation, the mixed solution were ultra-filtrated. The  $\gamma$ -rays from the multitracer remained with DNA on the filter were measured with a pure Ge  $\gamma$ -ray detector. The affinity relative to the standard multitracer solution was computed from  $\gamma$ -ray energy spectra. Although the multitracer solution used in this study included Fe, Zn, Co, Mn, Se, Cr, As, Sr, Na, Ca, Rh, Zr, Be, Ru, Rb, Sc, and Y, we analyzed Fe, Zn, Co, Mn, and Se which are related with bio-redox regulation systems in order to

clarify our purpose.

Figure 1 shows the affinity of metal ions to DNA. In normal rats, the affinity of Se was relatively low in the liver, lung, and colon. Affinity of metal ions to the liver and lung DNA were almost same. However, in the liver and colon DNA, affinities of Mn, Co, and Zn to liver DNA were significantly low, while in the lung and colon DNA, affinities of Mn and Zn to lung DNA were significantly low. In Se-deficient rats, affinity of Fe was relatively high in DNA of these three organs. No significant difference within organs was found. Collectively, the affinities of the metal ions ( $\text{Mn}^{2+}$ ,  $\text{Co}^{2+}$ , and  $\text{Zn}^{2+}$ ) to Se-deficient rats DNA were relatively low compared with normal rats.

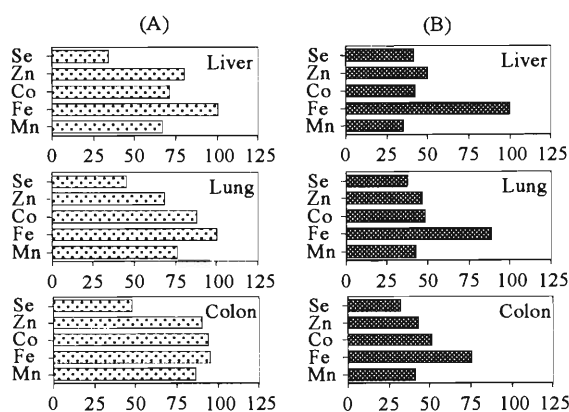


Fig. 1. Relative affinity of bio-trace elements to the normal (A) and Se-deficient (B) rat's DNA.

As a result, we suggested that affinity of metal ions decreased with DNA modification by reactive oxygen species in Se-deficient rat's DNA. A possible reason will be that the binding site of metal ions on DNA was blocked with modification by the reactive oxygen species itself or by the products of lipid peroxidation such as malondialdehyde and 4-hydroxynonenal. Relatively low affinity of the liver and lung DNA can be explained by this hypothesis: i.e., liver and lung are usually subjected to oxidative stress because liver is the place of metabolisms and because lung is usually exposed by air.

### References

- 1) R. Hirunuma, N. Sotogaku, K. Endo, S. Enomoto, S. Ambe, and F. Ambe: RIKEN Accel. Prog. Rep. **30**, 110 (1997).
- 2) K. S. Kirby: Biochem. J. **66**, 495 (1957).

## Multitracer Study on Binding Activity of Various Trace Elements to Metallothionein

J. Chou, S. Enomoto, S. Ambe, and F. Ambe

The metallothionein is a small intracellular protein.<sup>1)</sup> It is characterized by the following features: a low molecular weight, high metal content, and absence of aromatic amino acids. Metallothionein is involved in the normal metabolism of Zn and Cu. Its outstanding function has been described as detoxifying heavy metals. Cadmium, Zn and Cu are usually associated with metallothionein *in vivo*, but a wide range of other metals such as Ag, Co, and Ni can not bind to the proteins *in vivo* but can bind to the proteins *in vitro*.<sup>2)</sup> In the present work, we have studied the binding activity of a large number of trace elements to metallothionein *in vitro* and pH-dependence on the binding activity using a multitracer technique. It is reported for the first time that metallothionein can bind simultaneously with additional metals.

The interaction between metallothionein and multitracer *in vitro* at neutral solution were simultaneously determined using the multitracer technique. After element assignment based on the  $\gamma$ -ray energy and half-life, the binding percentage of 14 kinds of trace elements was obtained. The results are shown in Fig. 1. We found that for metallothionein, more additional metals could also be accommodated. The elements bound to metallothionein can be divided into the fol-

lowing four groups based on the classification of the periodic table:

(1) For alkaline metals, such as Na and Rb, the binding percentage is zero. The results indicate that alkaline metals can not bind with metallothionein.

(2) For alkaline earth metal, the data suggest that Be can bind with metallothionein more than Sr, illustrating that the binding activity of Be to metallothionein is stronger than that of Sr. Thus, for alkaline metals, the binding activity to metallothionein decreases with increasing ionic radius.

(3) For transition metal elements, such as, Sc, V, Mn, Co, Zn, Zr, Nb, Hf and Ru, it was observed that all these transition metal elements had different binding percentages to metallothionein. The results illustrate that transition metal elements can bind to metallothionein. Zinc has the highest binding percentage, while Zr, Nb and Hf have higher binding percentage. Scandium, V, Mn, Co and Ru have small binding percentage.

(4) For group VI-A, such as Se, the binding percentage to metallothionein was also obtained. Se has high binding percentage, thus it can bind to metallothionein strongly. Because the binding percentage of Se is near to the value of Zn, it was concluded that the binding activity of Se was similar to that of Zn at neutral solution.

It was also found that the binding activity of these elements to metallothionein was affected by the pH in the solution. Except Sc, Nb, Zr and Hf, the binding activity of other elements increased with increasing pH solution. For Sc, Nb, Zr and Hf, the binding activity increased with increasing pH solution at the pH lower than 5.3, then decreased at the pH lower than 7.4 and increased again at the pH higher than 7.4.

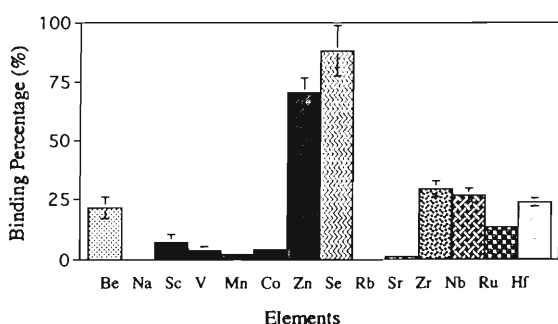


Fig. 1. The binding percentage of 14 kinds of elements binding to metallothionein at pH of 7.4. Each datum in the figure represents the mean values  $\pm$  standard deviation calculated from at least three samples.

### References

- 1) J. F. Riordan and B. L. Vallee: in *Methods in Enzymology* Vol. 205, Metallobiochemistry, part B. (Academic Press, 1991), p. 11.
- 2) H. Li and J. D. Otvos: *Biochemistry* **35**, 13929 (1996).

## Multitracer Study on Coordinating of the Rare-Earth Element with Metallothionein

J. Chou, S. Enomoto, S. Ambe, and F. Ambe

The rare-earth element (REE) has been shown to be involved in many important biological function and is considered to be harmful, interrupting physiological functions. REE can bind with some proteins, but so far, there is no report about the binding between REE and metallothionein which is able to bind a number of metal ions. In present report, multitracer was used to study the binding or coordinating between REE and metallothionein.

The binding between REE and metallothionein *in vitro* at the neutral solution was determined using multitracer technique. The coordinating coefficients (Kd) between REE and metallothionein with ionic radius are shown in Fig. 1. The results indicated that metallothionein can coordinate with some REE. Among the tested REE, Eu has the highest binding percentage and Lu has the lowest one. The metallothionein usually contains 61 or 62 amino acids, 20 of which are conserved cysteine residues. It has a unique distribution of cysteinyl residues in the amino acids sequence to accommodate the formation of metal-thiolate clusters, by which the metal ions are bound to metallothionein. But in general, Lanthanides coordinate with the unprotonated carboxyl group of amino acids in the protein. The major ligand for REE ions on proteins is the carboxyl group. Thus, for REE, they are not similar to the transition metals which bind to cysteines in the metallothionein<sup>1)</sup> and are considered to bind to unprotonated carboxyl group of amino acids. It was reported that the coordinating of the peptide, Cys-Tyr-Ile-Glu-Asn-Cys-Pro-Leu-Gly-NH<sub>2</sub>, was studied by <sup>1</sup>H-NMR spectroscopy with Yb<sup>3+</sup>, and that lanthanides were shown to coordinate with the carboxyl group of Glu and with the carbonyl side chain of Asn.<sup>2)</sup>

The pH dependence of binding percentage of REE to metallothionein was determined. The binding percentage is dependent on the pH solution. The coordinating coefficients of REE to metallothionein with pH are shown in Fig. 2. The coordinating coefficients decreased with decreasing pH. At pH of 3, for all the tested REE, the binding percentage decreased to

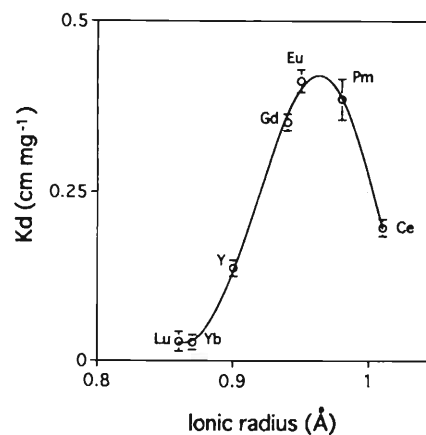


Fig. 1. The coordinating coefficients (Kd) with radius of rare-earth ions at pH of 7.4. Each datum in the figure represents the mean values  $\pm$  standard deviation calculated from at least three samples.

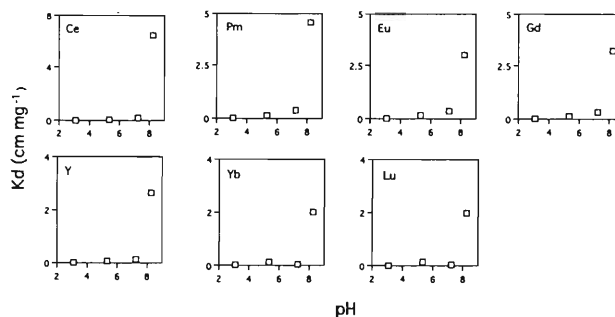


Fig. 2. The coordinating coefficients (Kd) versus solution pH.

zero. At low pH, the carboxyl group will bind with hydrogen ion.

### References

- 1) H. Li and J. D. Otvos: *Biochemistry* **35**, 13929 (1996).
- 2) R. Walter, C. W. Smith, and K. P. Sarathy et al.: *Int. J. Pept. Protein Res.* **17**, 56 (1981).

## Transfers of Trace Elements from the Placenta to the Fetus of Pregnant Rat

J. Chou, S. Enomoto, R. Hirunuma, S. Ambe, and F. Ambe

Trace elements are essential for human body for their normal growth and development, especially for a pregnant mother, and the same is true for a fetus. The placenta functions as the barrier between fetus and mother: providing regulation of heat exchange, respiration, nutrition, and excretion for the fetus. Before birth, fetuses will accumulate enough trace elements from their mother.<sup>1)</sup> Limited information is available on the transfers of trace elements from their mothers to the fetuses.<sup>2)</sup> In this study, the multitracer technique was applied to study the transfers of trace elements via placenta to the fetus.

17 day pregnant Wistar rats were used for the experiment. The pregnant rats were injected with multitracer solution and sacrificed at 24 hours after injection. The chemical forms of the tracers are  $\text{Be}^{2+}$ ,  $\text{Na}^+$ ,  $\text{VO}_2^+$ ,  $\text{Mn}^{2+}$ ,  $\text{Fe}^{3+}$ ,  $\text{Co}^{2+}$ ,  $\text{Zn}^{2+}$ ,  $\text{AsO}_4^{3-}$ ,  $\text{SeO}_3^{2-}$ ,  $\text{Rb}^+$ ,  $\text{Sr}^{2+}$  and  $\text{Ru}^{2+}$  in the solution to mice. Figure 1 shows the uptakes of 13 kinds of trace elements in the placenta and fetus. In the placenta, the V has the highest uptake among all the trace elements. Then Se, Na, Fe, Ru, Zn, Zr and Rb have higher uptakes in the placenta. Manganese, Co and As have relatively lower uptakes than the elements mentioned above. Strontium has the lowest uptake in the placenta. No radioactivity of Be appeared in the placenta, and there is no uptake of Be in the placenta.

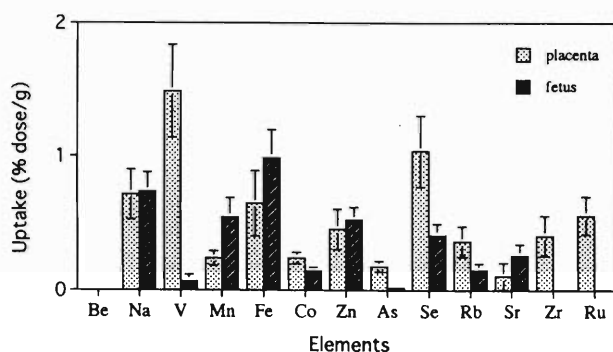


Fig. 1. The uptakes of trace elements in fetuses and placentas. The uptakes are shown in terms of percentage of the injected dose to the weight of tissues.

For fetus, the uptakes of trace elements were different from those in placenta. Iron has the largest uptake in the fetus, then Na, Zn, Mn and Se. The Sr, Co, Rb and V have relatively small uptakes in the fetus.

Arsenic, Zr and Ru have the lowest uptakes, especially for Zr and Ru the uptakes were near to zero.

Compared to the uptakes in the placenta and fetus, the uptakes of Zn and Na are similar each other. For other elements, the uptakes in placental tissue were found to be different from those in fetus. The uptakes of V, As, Se, Zr and Ru in the placenta were far higher than those in the fetus. The uptakes of Co and Rb in the placenta were a little higher than those in the fetus. However, the uptakes of Mn, Fe and Sr in the placenta were less than those in the fetus.

Because the trace elements for fetus must be obtained from their mother across placenta, the uptakes of trace elements in fetus and placenta should reflect the transfers of trace elements from placenta to fetus. The uptakes of Fe, Mn and Sr in the fetus were larger than those in the placenta, illustrating that more than half of these elements in the placenta were transferred to fetus. For Mn, two third (2/3) of Mn was transferred to the fetus. This suggests that the transfers of Fe, Mn and Sr from placenta to fetus were very rapid. The transfer of Fe from mother to fetus across the placenta maybe relating to the transferrin and the fetal iron is derived from maternal transferrin.

The uptakes of Na and Zn in the placenta were similar to those in the fetus, reflecting that half of them in the placenta were transferred to the fetus. The transfers of Na and Zn were also fast. The uptakes of Co, Se and Rb in the placenta were larger than those in the fetus, indicating that less than half of them in the placenta were transferred to the fetus. For Se, one third (1/3) of Se was transferred to the fetus. However, although the uptake of V in the placenta was the largest, the uptake in the fetus was very small. Only one twentieth (1/20) of V was transferred to the fetus across the placenta. This data indicates that the transfer of V was very slow, but V was able to penetrate the placenta and enter the fetal body. The same phenomena was observed in the uptakes of As, Zr and Ru. Very few uptakes of As, Zr and Ru were observed in the fetus, and the transfer of them from the placenta to the fetus was very slow.

### References

- 1) N. I. Ward, T. D. Macmahon, and J. A. Mason: *J. Radioanal. Nucl. Chem.* **113**, 501 (1987).
- 2) S. Honey, G. I. Dhall, and R. Nath: *J. Trace Elem. Exp. Med.* **5**, 165 (1992).

## Uptake and Translocation of Sr, Tc, and Cs in Soybean Plants

T. Shinonaga, S. Ambe, and I. Yamaguchi

The uptake and translocation of radionuclides of Sr, Tc, and Cs in the soybean plants were studied over 360 h after the administration of a multitracer to soil. Leaves, stems, and fruits were collected at every node at appropriate intervals as samples for  $\gamma$ -ray measurements. The uptake amount (%/g) in most of the leaves and stems collected from the nodes increased up to around 200 h after the administration of the multitracer, and then decreased with time. In the case of fruits, such tendency was observed for the uptake of Cs as shown in Fig. 1.

The total amount (%/plant) of Sr, Tc, and Cs in the pods increased with the cultivating time, while that of Sr and Tc in the seeds increased only slightly. The uptake amount of Tc in the pods was large, but translocation of Tc from the pods to the seeds was only a little. The uptake amounts of Tc by the leaves, stems, and pods were larger than those of Sr and Cs but the ratio of the uptake amount of Tc in the seeds to that in the pods was smaller than that of Sr and Cs. The fact that the translocation of Tc from the pods into the seeds is less than that of Sr and Cs shows a different selectivity for these elements.

The behavior of elements in the leaves, stems, and fruits of each node was mathematically analyzed with the second order function,  $A_e = c + k_1t + k_2t^2$ ,  $0 < t \leq 360$ ; where  $A_e$  is the uptake amount of the element,  $c$  the constant,  $t$  the cultivating time after the multitracer was administered, and  $k_1$  and  $k_2$  the coefficients of  $t$  and  $t^2$ , respectively.<sup>1)</sup> The fitting curves are shown in Fig. 1. This equation enables us to predict the time when the element uptake

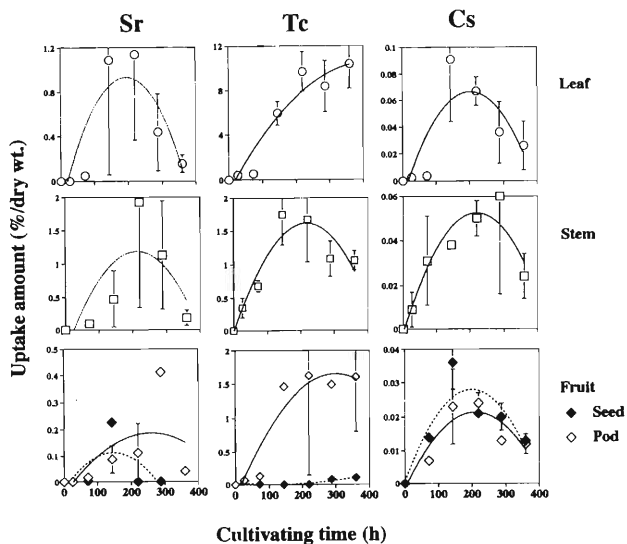


Fig. 1. Change of the uptake amount of Sr, Tc, and Cs in leaves, stems, and fruits at the sixth node as a function of the cultivating time with the multitracer. The error bars indicate the difference between two raw data. If the error bar is not shown, the datum is single. In the case of Tc-leaf and Tc-stem, the error is within the symbol, if error bar is not shown.

reaches the maximum.

### References

- 1) T. Shinonaga, S. Ambe, and I. Yamaguchi: J. Radioanal. Nucl. Chem. in press.

## Multitracer Study on Uptake of Elements by Turnip

S. Ambe, T. Shinonaga,\*<sup>1</sup> T. Ozaki, S. Enomoto, H. Yasuda,\*<sup>2</sup> and S. Uchida\*<sup>2</sup>

The absorption selectivity, a parameter of an uptake model<sup>1)</sup> for radionuclides by plants, was determined by a multitracer technique.<sup>2)</sup> The selectivity  $S$  is defined as follows:

$$A = STC_0$$

where  $A$  is the total amount of a radionuclide absorbed by a plant during the experimental period,  $T$  the amount of transpiration, and  $C_0$  the initial concentration of the nuclide.  $S$  of various elements from Be to Re was determined by changing  $C_0$  of nutrient solutions.

The nutrient solution of every 1 dm<sup>3</sup> contained 2.0 mmol of MgSO<sub>4</sub> · 7H<sub>2</sub>O, 4.0 mmol of Ca(NO<sub>3</sub>)<sub>2</sub> · 4H<sub>2</sub>O, 8.0 mmol of KNO<sub>3</sub>, 1.4 mmol of NH<sub>4</sub>H<sub>2</sub>PO<sub>4</sub>, 0.059 mmol of Fe-EDTA, 4.8 μmol of H<sub>3</sub>BO<sub>3</sub>, 76 nmol of ZnSO<sub>4</sub> · 7H<sub>2</sub>O, 910 nmol of MnCl<sub>2</sub> · 4H<sub>2</sub>O, 20 nmol of CuSO<sub>4</sub> · 5H<sub>2</sub>O, and 1.4 nmol of (NH<sub>4</sub>)<sub>6</sub>Mo<sub>7</sub>O<sub>24</sub> · 4H<sub>2</sub>O. A multitracer solution was added to the nutrient solution, and pH of the solution was adjusted to 5.5–6.0 with a 1 mol dm<sup>-3</sup> KOH solution. The solution and the ones diluted to 1/2, 1/5, 1/10, and 1/20 with distilled water were used for culturing of the plant, and their concentrations were expressed by the electric conductivity which is linearly related to the ion concentration in a solution. The electric conductivity of the original nutrient solution was 2.3–2.5 mS/cm.

Turnip (*Brassica campestris* L. var. Komatsuna) seedlings were hydroponically cultured on the nutrient solution in a plant-growth chamber at 23 °C. The plants which were cultivated for 20–30 days were transplanted into a nutrient solution containing the multitracer. After the one-day cultivation, the plants were harvested and then they were separated into leaves and roots. The dried samples were subjected to the γ-ray measurement with Ge detectors.

The selectivity of elements studied was, in general, found to decrease with an increase in the concentration of the nutrient solutions. As for alkali elements, the selectivity for the leaves was higher than those for the roots in the entire concentration range of the nutrient solution. The selectivity decreased in the order as K ≥ Rb > Cs > Na in the leaves and Rb ≥ K > Na ≥ Cs in the roots.

The selectivity of alkaline earth elements also decreased along with the concentration in a similar fashion to that of alkali elements as shown in Fig. 1. The selectivity decreased in the order as Ca ≈ Ba ≈ Sr > Be in the leaves and Be > Ba > Sr ≈ Ca in the

roots. The selectivity of Ca and Sr for the leaves was higher than that for the roots. On the contrary, Be showed low values of the selectivity for the leaves, though large values were observed for the roots.

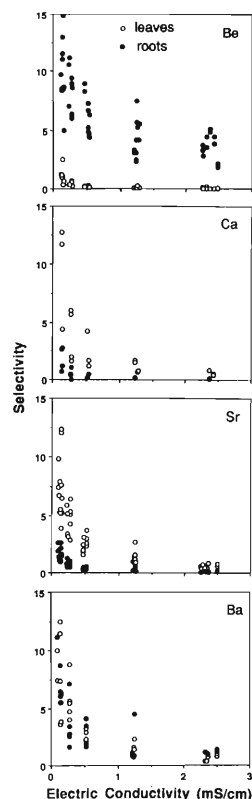


Fig. 1. Relation between the selectivity of alkaline earth elements and the concentration of nutrient solution in turnip.

The radioactivities of V, Cr, Fe, As, Rh, Ag, Sc, Y, Pm, Eu, Gd, Ir, and Pt in the leaves were below the detection limits, while their significant amounts were found in the roots. Many elements which are not regarded as useful elements for the plant growth were retained on the roots, not giving rise to their translocation to the leaves. However, Re has exhibited a contrasting result. That is, much more Re was accumulated in the leaves than in the roots.

By using the selectivity obtained in this work, a transfer factor of radionuclides can be estimated for the plants.

### References

- 1) H. Yasuda and Y. Inoue: *Hokenbutsuri* **29**, 295 (1992).
- 2) S. Ambe et al.: *J. Radioanal. Nucl. Chem.* **195**, 297 (1995).

\*<sup>1</sup> GSF-National Research Center of Environment and Health Institute of Radiation Protection

\*<sup>2</sup> National Institute of Radiological Sciences

## Metabolism of Trace Elements in *Euglena gracilis* Using the Multitracer Technique

R. G. Weginwar, M. Katayama, S. Ambe, S. Enomoto, T. Ozaki, and F. Ambe

Incorporation and excretion of multitracers in the *Euglena gracilis* cultured in two kinds of conditions were examined as follows.

Green *Euglena* was treated with streptomycin to obtain yellow *Euglena*, deficient of chlorophylls. Both green and yellow *Euglena* cultures were grown in a Koren-Hutner medium<sup>1)</sup> at 27–30 °C. The cells were centrifugally separated, washed thoroughly in a medium without trace nutrients, and suspended in an incorporation medium consisted of: ammonium sulfate, ammonium bicarbonate, potassium phosphate, magnesium carbonate, calcium carbonate, and vitamin B1 and B12.

After addition of the carrier-free multitracer mixture, the incorporation experiment was initiated at 30 °C. At such time intervals as indicated in Figs. 1 and 2, a small aliquot of the samples was extracted, cooled down in ice, and centrifuged. The cell fraction was washed with ice-cold medium thoroughly. The radioactivities in the washed cells were measured by the high purity Ge gamma detector, and were expressed by percentage as compared to the total amount in the medium at the zero time. The remaining portion of the cell suspensions was centrifuged and the cell fraction was washed thoroughly with an ice-cold complete medium and used for excretion experiments. The excretion experiment started by suspending the cells in a complete medium at 30 °C. The extracted samples were cooled down rapidly, and the cells were centrifugally separated from the medium. After the washing of the cells thoroughly, their radioactivities were determined by the Ge gamma detector.

The measured incorporation rate of the ions of zinc, selenium, manganese and cobalt into the green *Eu-*

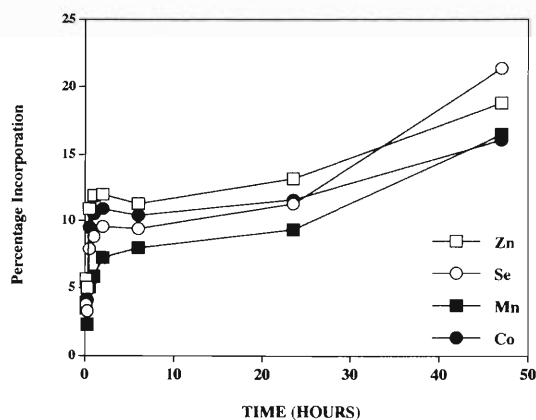


Fig. 1. Percentage incorporation of Zn, Se, Mn and Co in green *Euglena* at different time intervals.

*glena* is shown as a function of time in Fig. 1. It is noticeable that the incorporation rate was remarkable during the first few hrs, and then slowed down. Similar phenomena were observed in the case of the arsenate incorporation into marine diatoms,<sup>2)</sup> and interpreted that arsenate was metabolized to organic forms into the cells.

In the yellow *Euglena*, on the other hand, the incorporation rates were different from those in green cells Fig. 2. After the initial rapid incorporation, zinc kept a plateau until 25 hrs, although the other three elements increased a very little till 25 hrs. The different pattern of Fig. 2 increased a little till 25 hrs may suggest a unique different behavior of these four elements in the incorporation mechanism or in the metabolism into the cells. The rapid decrease of the incorporation after 25 hrs may suggest a change in the physiological conditions of the *Euglena* cells.

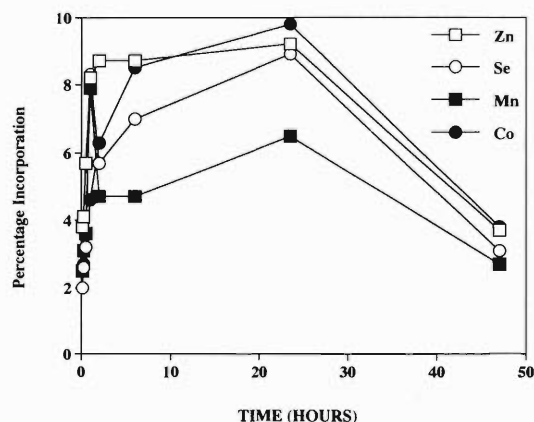


Fig. 2. Percentage incorporation of Zn, Se, Mn and Co in yellow *Euglena* at different time intervals.

The excretion rates of zinc, selenium, manganese, and cobalt were similar with each other in the green cells. They were mostly retained in the cells for longer than 50 hrs. On the other hand, manganese in the yellow cells was excreted rapidly in spite that the other three elements were retained as the case of green cells. Their chemical forms in the cells are interesting to be elucidated.

### References

- 1) L. E. Koren and S. H. Hutner: *J. Protozool.* **14**, suppl., 17 (1967).
- 2) M. Katayama, Y. Sugawa-Katayama, and A. A. Benson: *Appl. Organomet. Chem.* **4**, 213 (1990).

## Possibility of the Existence of a Special Substance Involved in the Uptake of REE by *Dryopteris erythrosora*

T. Ozaki, S. Enomoto, Y. Minai, S. Ambe, F. Ambe, and Y. Makide\*

*Dryopteris erythrosora* (a fern) is known to accumulate the rare earth elements (REEs) under natural conditions.<sup>1)</sup> Considering the difficulty in the uptake of REEs because of the strong tendency of REEs to hydrolyze under the natural conditions, some special mechanism to absorb REEs is expected to exist in the fern species. In present paper, we report a possibility of the existence of an unknown substance which might be involved in the uptake of REEs by *Dryopteris erythrosora*.

*Dryopteris erythrosora* was grown in distilled water for collection of an unknown substance, which is expected to be released from the roots. After filtered by a glass filter, followed by a membrane filter (pore size, 0.20  $\mu\text{m}$ ), the solution was concentrated at 70 °C with a small amount of thymol which was added for the purpose of sterilization of the solution. The concentrated solution was applied to cation exchange column to remove the inorganic ions chelated to the substance.

Plates of Au and Ag (300  $\mu\text{m} \times 23 \text{ mm}\phi$ ) were irradiated with a 135 MeV/nucleon  $^{12}\text{C}$  ion beam accelerated by the RIKEN Ring Cyclotron. The Au target was dissolved in aqua regia, and the solution was evaporated to dryness. After the residue was dissolved in 3.0 mol dm<sup>-3</sup> HCl, a multitracer solution was obtained by removing the Au by extraction with ethyl acetate. On the other hand, the Ag target was dissolved in HNO<sub>3</sub> and then the Ag was precipitated with HCl as AgCl, leaving another multitracer solution. Mixing the two solutions produced the final multitracer solution used in this study, which contained the radionuclides of Be, Na, Mn, Co, Zn, Y, Rb, Sr, Ce, Gd, Yb, and Lu. The solution was evaporated to dryness, and dissolved in ultrapurified water for the experiments. Additional details on the procedures have been reported previously.<sup>2-4)</sup>

In Figs. 1 and 2 were shown the uptakes of Gd and Na into the samples A: without and B: with root washing solution in the uptake solution. Each datum point in the figures was given as the mean  $\pm$  standard deviation of five replications. The uptake rates of the elements into mesophylls were represented as follows;

Uptake rate of an element  $i$   
 $= (i \text{ in a mesophyll} / i \text{ added to the uptake solution}) / (\text{Rb in a mesophyll}) / (\text{Rb added to the uptake solution})$

The uptake of Rb was applied to normalization for the purpose of estimating the individual variation of the samples as proper as possible, because the flow of

Rb is closest to that of water among the multitracer elements and as ascent of each element is highly dependent on that of water.<sup>5)</sup> As seen in Figs. 1 and 2, the uptake of Gd was enhanced, while no enhancement was observed in the uptake of Na. From this, it is suggested that the root washing solution contained some unknown substance involved in the uptake of REEs.

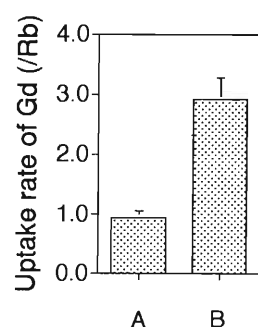


Fig. 1. Uptake rate of Gd, A: without and B: with root washing solution in the uptake solution.

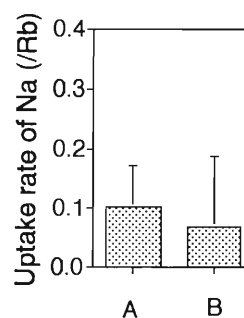


Fig. 2. Uptake rate of Na, A: without and B: with root washing solution in the uptake solution.

### References

- 1) T. Ozaki, S. Enomoto, Y. Minai, S. Ambe, F. Ambe, and T. Tominaga: *J. Radioanal. Chem.* **217**, 117 (1997).
- 2) S. Ambe, S. W. Chen, Y. Ohkubo, Y. Kobayashi, M. Iwamoto, M. Yanokura, and F. Ambe: *Chem. Lett.* **1991**, 149.
- 3) S. Ambe, S. Y. Chen, Y. Ohkubo, Y. Kobayashi, H. Maeda, and M. Yanokura: *J. Radioanal. Nucl. Chem. Articles* **195**, 305 (1995).
- 4) F. Ambe ed.: *RIKEN Rev. No.* 13 (1996).
- 5) J. J. M. Hooymans: *Planta (Berlin)* **88**, 369 (1969).

\* Radioisotope Center, Tokyo University

## Study on the Uptake Rate of Various Elements into *Dryopteris erythrosora* by Multitracer Technique

T. Ozaki, S. Enomoto, Y. Minai, S. Ambe, F. Ambe, and Y. Makide\*

Plants absorb elements in soil via the groundwater, and not directly from the surface of soil particles. Rare earth elements (REEs) have a great tendency to hydrolyze under the natural conditions, leading to their low availability to plants. Although REEs are dissolved into interstitial water, those elements are reported to stop at the surface of roots and hardly get into the upper parts.<sup>1,2)</sup> However, there are some plant species, such as *Dryopteris erythrosora*, which accumulate REEs to a high concentration. Therefore, it is expected that those species absorb REEs aggressively from the environment for some use in specific ways of their own.

Multitracer technique was recently developed at the Institute of Physical and Chemical Research (RIKEN).<sup>3)</sup> A multitracer solution contains many kinds of radioactive nuclides produced by high-energy heavy-ion irradiation of a metal target. Utilization of a multitracer solution makes it possible to efficiently acquire information on the behavior of various elements (nuclides) in the same plant. This is a great advantage, especially for the biological samples which are always accompanied with a problem arising from individual differences. We have carried out radioactive tracer experiments to examine the uptake rates of various elements using the multitracer technique.

Fern samples (*Dryopteris erythrosora*) were approximately 7 cm in length at the beginning of feeding of radioactive tracers. Uptake of each element was time dependently examined; 7, 14, and 21 days after the addition of tracers. Each time, the mesophylls were sampled, and the radioactivity was measured with a HPGe detector. The uptake rate of an element *j* into a mesophyll was represented as follows:

Uptake rate of an element *j*  

$$= (j \text{ in a mesophyll} / j \text{ added to the medium}) / (Rb \text{ in a mesophyll} / Rb \text{ added to the medium}) \times 100.$$

The uptake of Rb was used for normalization for the purpose of lowering the influence of the individual variation, because the flow of Rb is closest to that of water among the multitracer elements and because the ascent of elements is highly dependent on that of water.<sup>4)</sup>

Uptake experiments by the multitracer technique enabled us to acquire a set of data concerning 16 elements: namely Be, Mn, Co, Zn, Se, Rb, Sr, Y, Zr, Te, Ba, Ce, Eu, Gd, Yb, and Re (Figs. 1(a)–(d)). The absorptions of Zn and Mn, which are essential to the growth of plants, occurred remarkably different comparing with other elements (Fig. 1(a)). The absorption of Mn on the 14th day exceeded 100%, which means

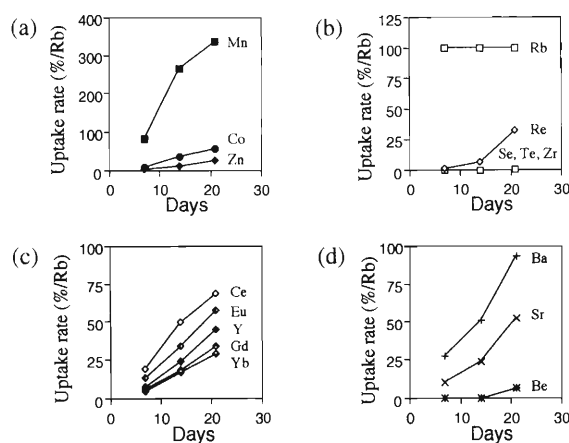


Fig. 1. (a) Uptake rates of Mn, Co, and Zn. (b) Uptake rates of Rb, Re, Se, Te, and Zr. (c) Uptake rates of REEs. (d) Uptake rates of Ba, Sr, and Be.

that some portion of Rb had diffused into the agar, and not that the need of Mn became greater than that of Rb by the day. No or almost no uptake was observed for Be, Zr, Te and Se, non of which elements have been demonstrated to bear any essentiality for plants (Fig. 1(b)). Rare earth elements were absorbed to a higher degree in comparison with those non-essential nutrient elements, and the percentage was almost equivalent to those of Sr and Ba, both of which are considered to be able to perform the same function of Ca to a certain extent (Figs. 1(c) and 1(d)). As stated already, the affinity of REEs for agar is strong, and therefore their availability to plants is much less than Sr and Ba. The smooth uptake suggests that the fern species absorbed REEs aggressively for some use to help them grow and, that some special mechanism was involved in the uptake of REEs. Further, an ionic radius dependency was observed in the uptake rate of REEs; largest one (Ce) was absorbed most and the uptake rates were decreased with the decrease in ionic radius. This is mostly because the affinity of Ce for agar is weakest among them: i.e., Ce is easiest to be released from the agar and absorbed.

### References

- 1) S. Ambe, Y. Ohkubo, Y. Kobayashi, M. Iwamoto, H. Maeda, and M. Yanokura: *J. Radioanal. Chem.* **195**, 305 (1995).
- 2) A. Wytttenbach, P. Schleppe, J. Bucher, V. Furrer, and L. Tobler: *Biol. Trace Element Res.* **41**, 13 (1994).
- 3) S. Ambe, S. Y. Chen, Y. Ohkubo, Y. Kobayashi, M. Iwamoto, and F. Ambe: *Chem. Lett.* **1991**, 149.
- 4) J. J. M. Hooymans: *Planta (Berlin)* **88**, 369 (1969).

\* Radioisotope Center, Tokyo University

## Multitracer Study on Biosorption of Various Trace Elements in Yeast *Saccharomyces cerevisiae*

Y. Nose, S. Enomoto, S. Ambe, and F. Ambe

Recently, metal uptake by microorganisms has been attracting many investigators' attention, because of its potential application for removal of toxic radionuclides and of heavy metals from the environment. Yeast is known to take up and/or adsorb several metals<sup>1)</sup> and is thought to be appropriate for research on the mechanisms of biosorption of metals. In the present study, the uptake of 16 elements (Be, Na, V, Cr, Mn, Fe, Co, Zn, As, Se, Rb, Sr, Y, Zr, Ru and Rh) by the yeast *Saccharomyces cerevisiae* was investigated using a multitracer technique. This technique enables us to examine the uptake of various elements under an identical condition.

A multitracer solution was prepared from a silver target which was irradiated with a 135 MeV/nucleon <sup>14</sup>N beam accelerated by RIKEN Ring Cyclotron. Additional details on the procedures have been previously reported.<sup>2)</sup> After the evaporation of the multitracer solution, ultrapurified water was added on it and the solution was administered to yeast.

The yeast *S. cerevisiae* (JCM No. 7255) was purchased from the Japan Collection of Microorganisms, RIKEN. Cultures were grown in the Difco Yeast Nitrogen Base (Difco) with 0.5% (w/v) glucose (growth medium) at 25 °C in a shaker. Cell growth was monitored by measuring the absorbance at 660 nm (OD<sub>660</sub>). Each five milliliter (5 ml) of cultures of OD<sub>660</sub> = 1.0 was taken into a tube and centrifuged at 700 × g for 10 min at 25 °C to obtain a yeast cell pellet. The yeast cell pellets were suspended in a 5 mM 2-(N-morpholino)ethanesulfonic acid (MES)-NaOH (pH 5.4) uptake medium, and centrifuged at 700 × g for 10 min at 25 °C for 3 times to wash the cells. The washed cells were re-suspended in 5 ml of the uptake medium, and incubated for 30 min at 25 °C in a shaker. An aliquot of multitracer solution was added to the yeast suspension, which was then incubated for 30 min at 25 °C in a shaker. After the incubation, the samples were washed for 3 times with the cold uptake medium, and filtered by suction through a cellulose acetate membrane filter (Advantec, 0.8 μm). The filters were allowed to air dry and then subjected to γ-ray mea-

surement with high-purity Ge detectors.

Figure 1 shows the uptakes of 16 elements by the yeast. The uptakes of Be, Cr, Co and Zn were very high, approximately 100%. The high uptake of Be is interesting, because Be is thought not to be essential and has toxicity for living organisms; in contrast, Cr, Co and Zn are essential. In the case of V, Mn, Fe, As, Se, Sr, Y, Zr, Ru and Rh, the uptakes were from 20 to 60%. The uptakes of Na and Rb were below detectable level. The very low uptake of Na was reported in the literature.<sup>1)</sup> There are no or few report on the biosorption of Be, V, Rb, Y, Zr, Ru and Rh by the yeast. Therefore, this report must be a base of further investigations.

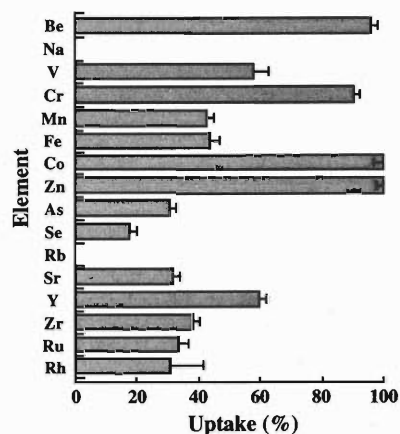


Fig. 1. Uptakes of various elements in the yeast *S. cerevisiae* from a 5 mM 2-(N-morpholino)ethanesulfonic acid-NaOH (pH 5.4) uptake medium containing the multitracer. Each data represents the average of five trials ± standard deviation.

### References

- 1) K. J. Blackwell et al.: Appl. Microbiol. Biotechnol. **43**, 579 (1995).
- 2) S. Ambe et al.: Anal. Sci. **7**, Suppl., 317 (1991).

## Heavy-Ion Induced Fission in the Medium Energy Region

H. Araki, J. Sanada, S. Morimoto, A. Yokoyama, T. Saito,  
H. Baba, Y. Ohkubo, and Y. Kobayashi

The heavy-ion induced reaction is characterized by the angular momentum brought in by projectiles. As for the fission mechanism, the larger the momentum, the smaller the fission barrier, and eventually the fission barrier vanishes at a critical angular momentum ( $L_{cr}$ ). The fission with no barrier is referred to as fast fission (FaF). In order to investigate a change in the fission phenomena affected by the onset of FaF, we observed the difference in the mass distributions when the incident energy ( $E_i$ ) is below and above the critical energy corresponding to  $L_{cr}$ .

We bombarded a gold target (5.70 mg/cm<sup>2</sup> thick) with <sup>16</sup>O ions at a so-called falling ball system installed in the E3B course at RIKEN Ring Cyclotron. The critical energy for the fast fission is calculated to be about 140 MeV under the rotating finite range model.<sup>1)</sup> The incident energies were adjusted by using an aluminum foil of appropriate thickness as degrader. The irradiated samples were analyzed by means of non-destructive  $\gamma$ -ray spectrometry with Ge detectors.

Mass distributions were deduced from the obtained formation cross sections on assuming the two assumptions that, in the fission dominant region, the width of charge distribution is constant, and that the most probable charge linearly depends on the mass number  $A$ . The resulting mass distribution for the case  $E_i = 156$  MeV and 127 MeV are shown in the center and top panels of Fig. 1, respectively.

The fusion fission mass distribution at  $E_i = 156$  MeV should be well approximated by the mass distribution at  $E_i = 127$  MeV under the assumptions that the FaF does not exist below the critical energy or below the fission excitation energy.<sup>2)</sup> Then, the fusion-fission cross sections (dashed curve in Fig. 1) were deduced on the basis of the distribution obtained at 127 MeV but by evaluating the peak position from emission of pre-fission neutron and by adjusting the peak height. They were then subtracted from the total fission cross sections. The resulting residues are plotted in the lowest panel of Fig. 1.

Since the barrier of the incomplete fusion fission (ICF) is expected to be higher<sup>3)</sup> than the complete

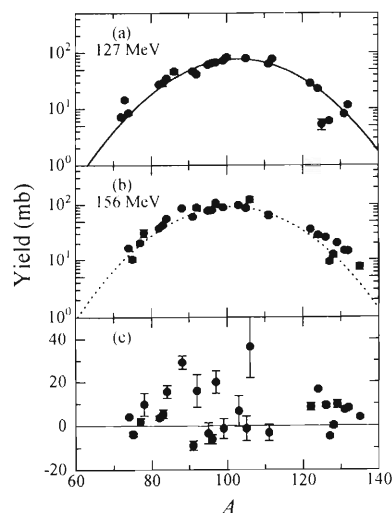


Fig. 1. The mass distributions for the reactions of <sup>197</sup>Au with <sup>16</sup>O ions at (a) 127 MeV, (b) 156 MeV. The solid curve is a Gaussian fitted to the experimental data, while the dashed curve in (b) represents the corrected fusion-fission mass distribution based on the mass distribution at 127 MeV. (c) Residual values of the 156-MeV mass distribution after subtraction of the fusion-fission mass distribution.

fusion excitation energy, the contribution of ICF is negligibly small. Therefore, the presently observed residues in Fig. 1 should be due to the FaF as in the case of Ref. 2. However, present results are only preliminary. We expect that a more clear-cut feature of fast fission may be observed by the future experiment to be performed at the higher incident energies.

### References

- 1) J. Sierk: Phys. Rev. C **33**, 2039 (1986).
- 2) H. Baba et al.: Abstracts of Asia-Pacific Symp. on Radiochemistry '97, Kumamoto, A06 (1997); H. Baba et al.: KEK-Proc.-10, Workshop on Sci. with Short-lived Nuclear Beams, in press (1997).
- 3) H. Cohen and W. J. Swiatecki: Ann. Phys. (N.Y.), **22**, 406 (1963).

## Development of High Intensity Polarized Slow Positron Beam Using $^{18}\text{F}$

Y. Itoh, T. Nozaki, N. Nakanishi, A. Goto, Y. Ito, and H. Yoshida\*

[Positron source, Polarized slow positron beam,  $^{18}\text{F}$ , Liquid target]

Short-lived positron emitters produced in liquid targets by bombardment with ion beams from a cyclotron have proven to be useful for the generation of polarized slow positron beams. We tested various solid and gas targets, BN, C, Al,  $\text{SiO}_2$ , Ni, Cu,  $\text{N}_2$  etc., as already reported.<sup>1-3)</sup> We have tried the utilization of  $^{18}\text{F}$  produced in  $^{18}\text{O}$ -enriched water by the  $^{18}\text{O}(p, n)^{18}\text{F}$  reaction. Of all the nuclear reactions induced by a small accelerator, the  $^{18}\text{O}(p, n)^{18}\text{F}$  reaction gives the highest thick-target saturation activity. The chemical property and 110 min half-life of  $^{18}\text{F}$  are also suitable for the off-line source preparation and utilization. The positron emitters were transported to the site of positron moderator, collected on a small spot, and placed close to a tungsten moderator foil. Figure 1 shows the  $^{18}\text{F}$  collection assembly. Two methods, adsorption and evaporation, have been tried for the collection and fixation of the  $^{18}\text{F}$  from the  $^{18}\text{O}$ -water, which should be recovered.

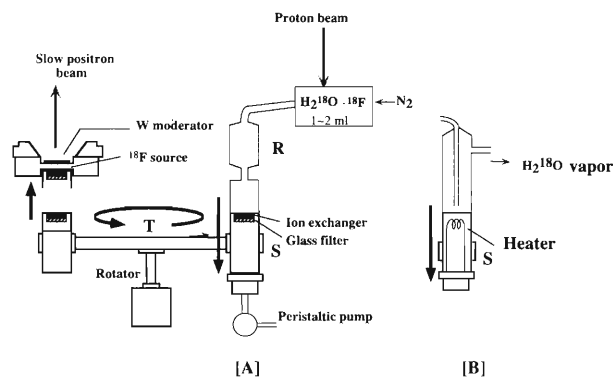


Fig. 1. Automated apparatus for preparing the  $^{18}\text{F}$  source.

As for the adsorption method, various adsorbent substances were tested for the  $^{18}\text{F}$ . The assembly consists of a turn table, T, source holder, S, and target-water receiver, R. The source holder can be moved up and down, and rotated at the down position. At the up position, it is either in water-tight contact with the receiver or placed very close to the moderator. The bombarded target water is once transferred into the receiver (R) by a nitrogen gas pressure. As the adsorbent material, a strongly basic anion exchange resin

(100–200 mesh, OH-form) was found to be suitable. The target water in the receiver is passed slowly through the resin bed with the aid of a peristaltic pump. In this method some thickness of the exchange resin was necessary to collect  $^{18}\text{F}$  efficiently by a one-through treatment. Since this causes low slow positron yield by self-absorption of the emitted positrons, the method has to be improved so that  $^{18}\text{F}$  is collected using a thin resin layer.

As for the evaporation method, a minute amount of  $\text{K}_2\text{CO}_3$  (0.1 mg) is first placed on the holder (S), and the target water is transferred on it and evaporated by heating from outside. The water vapor is carried by a nitrogen stream to be condensed and recovered, leaving the  $^{18}\text{F}$  on a small area (usually 3 to 4 mm diameter). It takes about 10 min for the collection and fixation of  $^{18}\text{F}$ . The evaporation method for  $^{18}\text{F}$  is thought to be superior to the other methods, giving  $10^6 \text{ s}^{-1}$  slow positrons. The use of gas and liquid targets possesses the following advantages over the on-site use of solid targets as a positron source: (1) the positron source can be placed in an ideal position close to the moderator foil; (2) long transport of slow positron beam is not necessary; (3) the source intensity can be monitored continuously, easily, and reliably; (4) the moderator is free from other radiations emitted from the target under bombardment; (5) a part of the product radionuclide can be used simultaneously for other purposes.

The polarized slow positrons are transferred to the detector guided with the magnetic field of the solenoid coils, the helmholtz coils and a deflector coil. Polarization of slow positron beam is measured by using magnetic quenching of positronium (Ps) due to Zeeman effect. High intensity polarized slow positron beam is used to derive information about the polarization of the new materials in which they annihilate.

### References

- 1) Y. Itoh et al.: Appl. Sur. Sci. **85**, 165 (1995) (SLOPOS-6).
- 2) Y. Itoh et al.: Appl. Sur. Sci. **116**, 68 (1997) (SLOPOS-7).
- 3) Y. Itoh et al.: Proc. Riken Symposium, "Basics and Application of Spin Polarized Positron Beam", p. 1 (1995).

\* Research and Development Dept., The Japan Steel Works Ltd.



## 4. Radiation Chemistry and Radiation Biology



Screening of Plants for Soil-Radionuclide Accumulators<sup>†</sup>

S. Gouthu, T. Arie, S. Ambe, and I. Yamaguchi

In case of radioactive fallout, persistence of long lived nuclides in soil and their subsequent transfer into food chain over a long period through plants is the key factor. The possibility of "phytoremediation" is suggested to reduce the radionuclides in soil. In order to exploit the natural potential of some plants in absorbing or accumulating certain radionuclides and thus in depleting the soil radioactivity, thirty-two plant species representing different vegetation types were tested

under laboratory conditions for their comparative ability in taking up radioactive Rb, Co, Sr and Cs. Each plant was supplied with an equal amount of "multi-tracer and cesium mixture" solution, and was grown for a period of 30 days before harvesting for measurements of the activity by Ge-detectors. Values of uptake percentage of <sup>58</sup>Co, <sup>83</sup>Rb, <sup>85</sup>Sr, and <sup>137</sup>Cs by 32 tested plant species in one month period are shown in Table 1.

As for the potential in absorbing the nuclides from

Table 1. Accumulation rates of <sup>60</sup>Co, <sup>83</sup>Rb, <sup>85</sup>Sr, and <sup>137</sup>Cs in different plant species.

Plant species	Common name	Plant dry wt. (in gm)	Uptake rate (in %/plant dry weight) <sup>a</sup>			
			<sup>60</sup> Co	<sup>83</sup> Rb	<sup>85</sup> Sr	<sup>137</sup> Cs
<i>Brassica campestris</i> L. (rapifera group)	Turnip (Hinona)	0.981	0.37 ± 0.17	8.50 ± 1.08	0.63 ± 0.18	0.18 ± 0.18
<i>B. campestris</i> L. (rapifera group)	Turnip (Komatsuna)	1.393	0.36 ± 0.08	13.93 ± 0.45	0.79 ± 0.06	0.29 ± 0.03
<i>B. campestris</i> L. (Pekinensis group)	Chinese cabbage	1.465	0.41 ± 0.09	13.77 ± 1.48	0.78 ± 0.04	0.09 ± 0.07
<i>B. campestris</i> L. (Japonica group)	Turnip (Kyona)	1.462	0.25 ± 0.03	9.78 ± 1.73	0.98 ± 0.15	0.16 ± 0.06
<i>B. oleracea</i> L. (Italica group)	Broccoli	1.218	1.22 ± 0.11	9.14 ± 1.53	0.65 ± 0.19	0.06 ± 0.01
<i>Glycine max</i> Merr.	Soybean	3.383	0.02 ± 0.03	6.13 ± 1.27	0.50 ± 0.07	0.17 ± 0.04
<i>Vigna radiata</i> R. Wilcz.	Mung bean	1.775	0.06 ± 0.01	6.04 ± 1.84	0.27 ± 0.23	0.08 ± 0.02
<i>Pisum sativum</i> L.	Pea	1.774	0.20 ± 0.18	9.67 ± 1.27	0.77 ± 0.09	0.51 ± 0.10
<i>Beta vulgaris</i> L. (cicla group)	Chard	1.555	0.12 ± 0.10	17.82 ± 3.17	0.40 ± 0.68	1.36 ± 0.27
<i>Salsola komarovii</i> Iljin	Okahijiki	0.932	0.20 ± 0.17	11.80 ± 3.72	0.18 ± 0.31	0.13 ± 0.09
<i>Amaranthus mangostanus</i> L.	Edible Amaranthus	0.278	0.22 ± 0.02	2.86 ± 0.39	0.27 ± 0.02	0.08 ± 0.01
<i>Apium graveolens</i> L.	Celery	0.362	0.01 ± 0.01	2.54 ± 0.64	0.27 ± 0.09	0.02 ± 0.01
<i>Daucus carota</i> L.	Carrot	0.368	0.03 ± 0.00	3.39 ± 0.36	0.43 ± 0.06	0.08 ± 0.02
<i>Lycopersicon esculentum</i> Mill.	Tomato	2.325	1.02 ± 0.01	25.60 ± 0.08	0.81 ± 0.01	1.42 ± 0.27
<i>Solanum melongena</i> L.	Eggplant	0.554	0.51 ± 0.22	6.57 ± 1.71	0.61 ± 0.25	0.07 ± 0.03
<i>Cucumis sativus</i> L.	Cucumber	1.637	0.17 ± 0.03	14.19 ± 2.12	2.12 ± 0.33	1.09 ± 0.29
<i>Abelmoschus esculentus</i> Moench.	Okra	0.614	0.09 ± 0.03	2.14 ± 0.42	0.74 ± 0.13	0.07 ± 0.01
<i>Eschscholzia californica</i> Cham.	California poppy	0.163	0.27 ± 0.07	3.89 ± 2.79	0.23 ± 0.06	0.04 ± 0.01
<i>Papaver nudicaule</i> L.	Iceland poppy	0.138	0.15 ± 0.06	2.17 ± 0.31	0.10 ± 0.01	0.03 ± 0.00
<i>Helianthus annuus</i> L.	Sun flower	1.696	0.28 ± 0.07	17.21 ± 4.19	1.36 ± 0.25	0.36 ± 0.27
<i>Matricaria</i> sp.	Matricaria	0.084	0.06 ± 0.06	1.36 ± 1.12	0.07 ± 0.07	0.02 ± 0.01
<i>Campanula medium</i> L.	Campanula bells	0.527	0.19 ± 0.03	6.51 ± 2.33	0.55 ± 0.11	0.08 ± 0.01
<i>Antirrhinum majus</i> L.	Snapdragon	0.097	0.01 ± 0.00	0.87 ± 0.12	0.08 ± 0.00	0.01 ± 0.00
<i>Dianthus caryophyllus</i> L.	Carnation	0.114	0.18 ± 0.06	1.58 ± 0.20	0.17 ± 0.02	0.03 ± 0.00
<i>Ipomoea batatas</i> Poir.	Sweet potato	0.039	0.01 ± 0.00	0.30 ± 0.02	0.02 ± 0.00	0.01 ± 0.00
<i>Pharbitis nil</i> Choisy.	Japanese morning glory	0.168	0.11 ± 0.02	1.27 ± 1.20	0.20 ± 0.10	0.03 ± 0.02
<i>Zea mays</i> L.	Maize	1.996	0.10 ± 0.01	13.97 ± 6.23	0.24 ± 0.10	0.38 ± 0.14
<i>Triticum vulgare</i> L. cv. chihoku	Wheat	0.378	0.00 ± 0.00	4.90 ± 4.52	0.22 ± 0.20	0.13 ± 0.11
<i>Oriza sativa</i> L. cv. koshikahari	Rice	0.236	0.03 ± 0.00	1.75 ± 0.18	0.09 ± 0.01	0.02 ± 0.01
<i>Pinnacle</i> sp.	Pinnacle grass	0.057	0.03 ± 0.00	0.41 ± 0.03	0.03 ± 0.00	0.01 ± 0.00
<i>Poa pratensis</i> L.	Kentucky bluegrass	0.115	0.03 ± 0.01	0.78 ± 0.04	0.10 ± 0.01	0.01 ± 0.00
<i>Allium tuberosum</i> Rottler	Chinese chive	0.153	0.00 ± 0.00	1.28 ± 0.40	0.07 ± 0.02	0.01 ± 0.00

a - The values indicate % uptake from the total supplied amount of nuclides and are the means of three replicates along with standard deviation.

soil, the ornamental plants like California poppy, Iceland poppy, carnation, Japanese morning glory, and matricaria showed high uptake rates per gram.<sup>1)</sup> Admitting that ornamental plants seemed to be better accumulators of the soil nuclides, they can not account for depleting soil radiation burden to any considerable level owing to their slow growth and little biomass. So, keeping in mind the importance of biomass and growing speed of the plants in phytoremediation, we considered the whole plant uptake values. From the results in Table 1, most crop plants like *Brassica* spp., tomato, and cucumber registered considerable uptake rates per plant because of more dry-weight per plant, though having less accumulating ability per gram compared with the plants like poppy, matricaria, and morning glory (data not shown). It is evident, from the comparison of per gram and total plant uptake values, that

the criteria for selection of plants should be not only the high uptake capability (per gram activity) of the plant species but the other factors like biomass, growing speed, and foliage spread should be taken into account.

In the present investigation we found some accumulator plants such as tomato, chard, and sunflower for Rb; broccoli and tomato for Co; cucumber, sunflower, turnip (Kyona), and tomato for Sr; and tomato, chard, and cucumber for Cs. This type of screening and selection of accumulators, followed by study of soil and other biological factors around rhizosphere will help in decreasing the soil nuclides and avoid them, to some extent, becoming equilibrated in the soil components.

## References

- 1) S. Gouthu et al.: J. Radioanal. Nucl. Chem. Lett. **222**, 247 (1997).

<sup>†</sup> Condensed from the article in J. Radioanal. Chem. **222**, 247 (1997).

## Possible Role of Soil-Microbes in Plant Uptake of Radionuclides

S. Gouthu, T. Arie, S. Ambe, and I. Yamaguchi

Root surface of plants supports active bacterial and fungal lives forming a symbiotic system in which the microbial symbiont is often known to enhance the plant capabilities in absorbing the soil mineral elements. In light of this, in phytoremediation of soils contaminated with radionuclides the use of specific combination of plant and microbe can maximize plant's uptake and accumulation. Towards this purpose, tomato and cucumber plants selected through screening for their ability to absorb soil radionuclides<sup>1)</sup> are tested for their uptake in association of some soil-microorganisms, known to be associated with these plant species. Fungal isolates of *Fusarium oxysporum* f.sp. *lycopersici* race 2 880621a-1 (Foly); *F. oxysporum* F-4 (NPF); *F. oxysporum* f.sp. *cucumerinum* Rfc1 (Focu); and also *Agrobacterium rhizogenes* SUPP 709 (Agr); were cultured on a liquid broth medium. Tomato (cv. Momotaro) and cucumber (cv. Suyo) plants were maintained in the green house conditions, and after 15 days of growth the Foly, NPF, and Agr were inoculated to tomato plants and the Focu and Agr were inoculated to cucumber plants by pouring liquid inocula. Multitracer containing the radionuclide elements of Mn, Co, Zn, Rb, Sr, and <sup>137</sup>Cs was supplied to the inoculated plants. The plants were grown for 30 days before harvesting for uptake measurements with Ge-detectors.

Figure 1 shows the uptake percentage of nuclides per gram dry weight of tomato plants and Fig. 2 that of cucumber plants. Inoculation of Agr was expected to increase the root growth by inducing adventitious roots, and thereby cause increased uptake. However, the production of adventitious root did not occur within the experimental period (data not shown). Tomato plants inoculated with Foly showed increased uptake of all the nuclides compared to the control plants. NPF inoculated tomato did not show any uptake difference. During the infection, Foly grows in to the tomato plants and establishes in the xylem vessels,<sup>2)</sup> whereas NPF only grows superficially on the root system. The degree of contact between the host root and the fungal species might be a reasons for this difference in uptakes. In the case of cucumber also the uptake of nuclides was more compared to control, but the increase in uptake was less pronounced. Increased accumulation of radionuclides from soil by plants inoculated with a specific mycorrhizal fungus was reported by Entry et al. (1994).<sup>3)</sup> However, the actual mechanism that was involved in the increased uptake of fungal infected plants remains to be investigated. The present result is an indication of the microbial-promoted plant uptake. Now we are trying to identify some non-pathogenic rhizosphere microbes that can be used for bioremediation with tomato and cucumber plants.

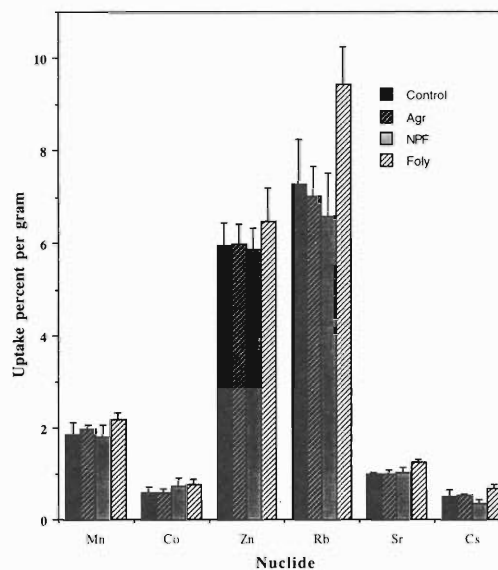


Fig. 1. Uptake of tomato inoculated with Agr, NPF, and Foly.

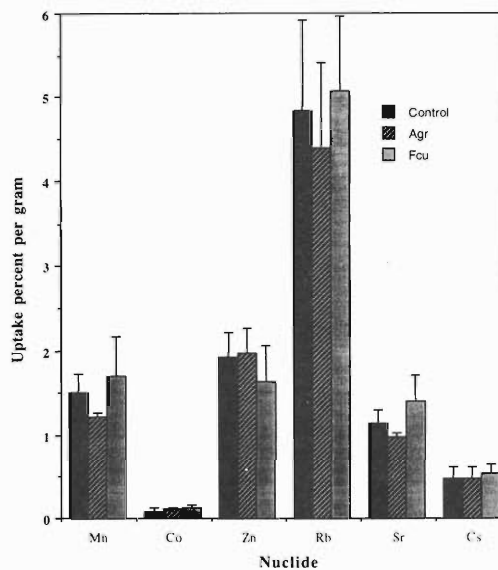


Fig. 2. Uptake of cucumber inoculated with Agr, and Focu.

## References

- 1) S. Gouthu et al.: J. Radioanal. Nucl. Chem. Lett. **222**, 247 (1997).
- 2) T. Arie et al.: Ann. Phytopathol. Soc. Jpn. **61**, 311 (1995).
- 3) J. A. Entry: Environ. Poll. **86**, 201 (1994).

## Effects of Heavy Ions on Survival of *Arabidopsis thaliana*

N. Shikazono, A. Tanaka, H. Watanabe,\* S. Tano,\* N. Fukunishi, and S. Kitayama

The biological effects of charged heavy particles, such as the relative biological effectiveness (RBE) on lethality as a function of linear energy transfer (LET), have been extensively studied in the bacteria, yeast and mammalian cells. In these unicellular systems, it was observed that RBE peaks on reproductive death were at around 100 keV/ $\mu\text{m}$ .<sup>1)</sup>

The effects of heavy ions on multicellular organisms are not yet fully understood. *Arabidopsis thaliana* (L.) Heynh. is a particularly suitable multicellular organism for studying the effects of heavy ions and of other kinds of radiation because its seeds and plants are small, it produces a large number of seeds, and because its life cycle is short.<sup>2)</sup> We have investigated the effects of heavy ions on the survival of *Arabidopsis* using various kinds of ions with LETs of 17–549 keV/ $\mu\text{m}$ , and found that the highest RBE value can be obtained by Ar ion irradiation (LET 252 keV/ $\mu\text{m}$ ).<sup>3)</sup> Using Ne ions at the RIKEN Ring Cyclotron, we have elucidated that the highest RBE appears at the LET of 352 keV/ $\mu\text{m}$ . To further investigate the dependence of RBE on LET in *Arabidopsis*, we used Ar ions of various LETs.

For irradiation, a single layer of the dry seeds of *Arabidopsis thaliana* ecotype Columbia was carefully sandwiched between kapton films (7.5  $\mu\text{m}$  thickness). Seeds were exposed to Ar ions from the RIKEN Ring Cyclotron. The LETs (252, 350, 396, 562, 656 keV/ $\mu\text{m}$ ) for Ar ions at RIKEN Ring Cyclotron were varied by placing absorbers in front of the irradiation site. The mean LETs were calculated by ELOSS code (modified OSCAR code). The plants were grown at 23 °C under continuous light (40  $\mu\text{E}/\text{m}^2/\text{s}$ ). One month after sowing, plants with expanded rosette leaves were scored as survivors. RBE value was estimated by comparing  $D_{37}$  for electrons with that for Ar ions.

The survival curves for Ar ions with LET 252, 350, 396, 562, and 656 keV/ $\mu\text{m}$  are shown in Fig. 1. Ar ions with LET of 396 keV/ $\mu\text{m}$  had the smallest shoulder. In Fig. 2, RBEs with Ne and Ar ions are plotted as a function of LET. RBE value of survival seems to have a peak at LET over 300 keV/ $\mu\text{m}$ .

The difference in the LET for the RBE peak in unicellular systems and in *Arabidopsis* might be explained by assuming that the endpoints compared in the two systems arose from different mechanisms. Recently, it was reported that the RBE peak on the interphase death compared to the reproductive death shifts to a higher LET (around 230 keV/ $\mu\text{m}$ ) in mammalian cells.<sup>4)</sup> The interphase death rather than the reproductive death may mainly contribute to the survival of

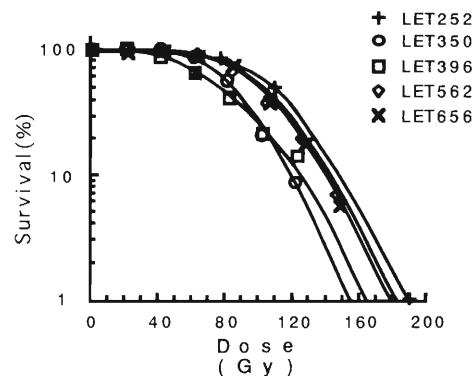


Fig. 1. Effects of Ar ion beams with different LETs on survival. +: LET 252 keV/ $\mu\text{m}$ ,  $\circ$ : LET 350 keV/ $\mu\text{m}$ ,  $\square$ : LET 396 keV/ $\mu\text{m}$ ,  $\diamond$ : LET 562 keV/ $\mu\text{m}$ ,  $\times$ : LET 656 keV/ $\mu\text{m}$ .

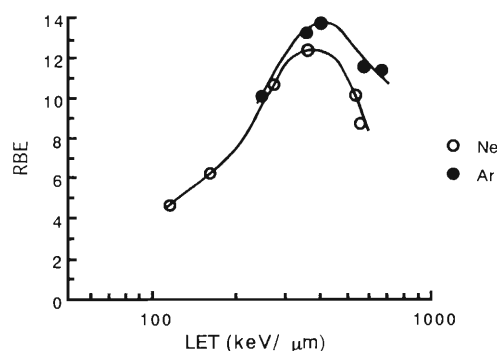


Fig. 2. RBE for lethality with Ne and Ar ions as a function of LET.

*Arabidopsis*. Alternatively, there is a possibility that different repair mechanism(s) may be the main cause of the different LETs for the RBE peak in unicellular systems and in *Arabidopsis* plants.

Isolation and characterization of radiation sensitive mutants of *Arabidopsis* may greatly facilitate the elucidation of underlying mechanisms of the occurrence of RBE peak.

### References

- 1) G. Kraft: Nucl. Sci. Appl. **3**, 1 (1987).
- 2) U. Bork et al.: Adv. Space Res. **9**(10), 117 (1989).
- 3) A. Tanaka et al.: Int. J. Radiat. Biol. **72**, 121 (1997).
- 4) H. Sasaki et al.: Radiat. Res. **148**, 449 (1997).

\* Advanced Science Research Center, JAERI

## Effective Plant-Mutation Method Using Heavy-Ion Beams (II)

T. Abe, C.-H. Bae, H. Takahashi, S. Kumata, and S. Yoshida

We found that accelerated heavy-ion beams are very effective tools for the mutagenesis of plants under a particular condition of the fertilization cycle. In the present paper we examine the effect of heavy-ion beams on various tissues of tobacco, and describe applicability of this new technique for screening the herbicide-resistant mutants.

Anthers from the tobacco (*Nicotiana tabacum* cv. BY-4 and Xanthi) flower-buds were cultured on so-called Nakata medium containing 2 mg/L IAA, 1 mg/L kinetin, 3% sucrose, and 0.6% agar. After 4 to 10 days of incubation, anthers were irradiated by the heavy-ion beams ( $^{14}\text{N}$  or  $^{20}\text{Ne}$  at 135 MeV/u) within a dose range of 5 to 100 Gy. The LET of the N and Ne ions were adjusted to be 28.5 and 63.0 KeV/ $\mu\text{m}$ , respectively. One month after the irradiation, the number of the pollen germination was counted. The high-dose irradiation caused a decrease of the germination where embryos developed from pollen grains (Fig. 1). Regenerated plants from the pollen grains which are androgenic haploids become homozygous dihaploids in a single generation, thus this technique can considerably shorten a breeding cycle and fixation of mutant line.

After 36 to 96 hours of pollination, *Nicotiana tabacum* cv. BY-4 intact embryos in the flowers of *Nico-*

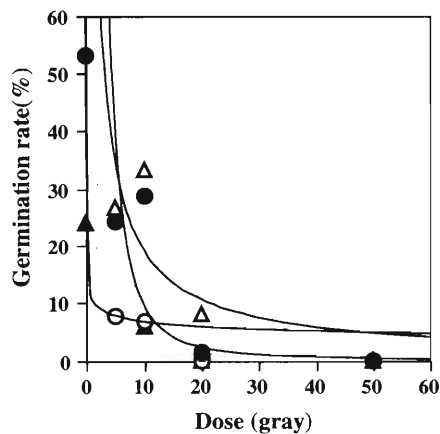


Fig. 1. Effects of the anther treatment with ion beams on the pollen germination. ●; N ion for BY-4, ○; Ne ion for BY-4, ▲; N ion for Xanthi, and △; Ne ion for Xanthi.

*tiana tabacum* cv. BY-4 were irradiated by heavy-ion beams ( $^{14}\text{N}$  at 135 MeV/u) for 36 to 96 hrs after pollination. The treated plants were cultivated in a green house and the resulting  $M_1$  seeds were harvested one month after the treatment. Two-months old  $M_1$  plants with dark green leaves were used in the resistance test against S-23142 (N-[4-chloro-2-fluoro-5-propargyloxy-phenyl]-3,4,5,6-tetrahydrophthalimide), a herbicide inhibiting Protox which is a key enzyme in the chlorophyll biosynthesis at chloroplasts. Young leaf tissues were treated with 0.5–1000  $\mu\text{M}$  S-23142 at 25 °C in the continuous light (approx. 78  $\mu\text{mol m}^{-2}\text{s}^{-1}$ ). After 2 days, the chlorophyll contents of each tissue were measured, and one tolerant plant was selected by this bioassay. Chlorophyll contents were decreased by 50% at 1.1  $\mu\text{M}$  of S-23142 in control (wild type) but at 1.1 mM of that in the tolerant plant (Fig. 2). The results obtained will open a new field of research on the mutation spectrum of herbicide targeting sites.

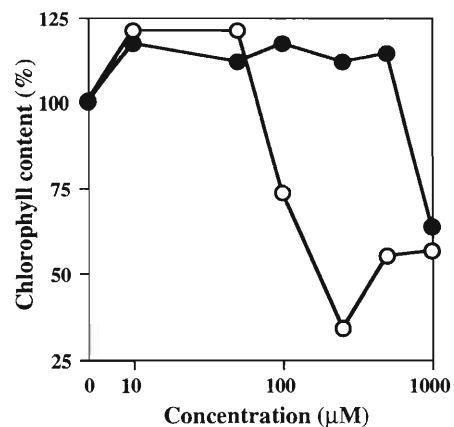


Fig. 2. Effects of S-23142 on chlorophyll contents of wild-type plant and the tolerant plant. ○; wild-type, and ●; tolerant plant.

### References

- 1) T. Abe et al.: in *Modification of gene expression and non-mendelian inheritance*, edited by Oono and Takaiwa (NIAR, Japan, 1995), p. 469.

## Cell Death and Mutation Induction on Cultured Cells by Irradiation of Heavy Ions and X-rays

T. Kawada,\* N. Shigematsu,\* H. Ito, S. Yamashita, A. Takeda,\* K. Toya,\*  
R. Ishibashi,\* A. Kubo,\* T. Kanai, Y. Furusawa, and F. Yatagai

In order to evaluate the biological effects of heavy-ion beams and X-rays on cultured cells, we have investigated the cell-killing effects and mutation induction at the *hprt* locus. Previously, we reported that heavy-ion beams showed much more powerful cell-killing effects than X-rays and that the higher frequency of mutation took place with heavy-ion beams compared with X-rays.<sup>1)</sup> In this report we have used one cell-line, MDA-MB231 (human breast cancer origin) to evaluate the biological effects of heavy-ion beams and X-rays and have studied the biological effect of fractionated irradiation against V79. The heavy-ion beams we employed were carbon (C) beams and neon (Ne) beams. Survival curves of MDA-MB231 against the dose of heavy-ion beams and X-rays were shown in Fig. 1(a). Carbon beams and neon beams had much more powerful cell-killing effects than X-rays. When the carbon and neon beams were used at the same LET level (80 keV/ $\mu$ m), carbon beam showed slightly stronger cell-killing effect. Fig. 1(b) shows that neon beams have a smaller mutation induction effect than that of carbon beams when the carbon beams and neon beams were employed at the same LET level (80 keV/ $\mu$ m). This tendency was similar to V79 and RMG1.<sup>1)</sup>

The effects of fractionated irradiation (3 hr interval) on cell survival and mutation frequency against V79 were also investigated. Comparison of biological

effects of V79 cells between single and fractionated irradiations, employing carbon beams and X-rays, is shown in Fig. 2(a) and Fig. 2(b). Carbon beams had no significantly different effects on cell-killing between single and fractionated irradiations, whereas X-rays had. When the carbon beam irradiation was fractionated, the mutation frequency was reduced although the survival curve was not affected. When cells were irradiated by X-rays, the cell survival was increased by fractionation, but the mutation frequency was not changed. On the other hand, when cells were irradiated by heavy-ion beams, survival curves were not affected, but the mutation frequency was reduced.

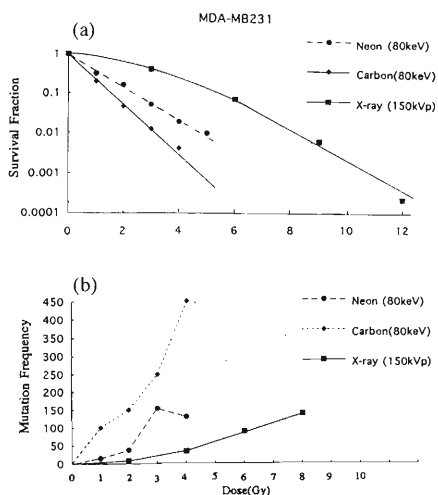


Fig. 1. (a) Survival curves of MDA-MB231 against X-rays and against carbon and neon beams, (b) Mutation frequencies against the X-ray, carbon beam and neon beam irradiation.

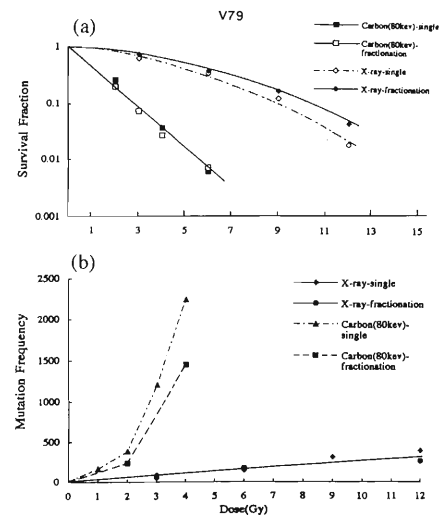


Fig. 2. Survival curves of V79 against X-rays and carbon beam by fractionation, (b) Mutation frequencies of the V79 per  $10^6$  cells after irradiated by X-rays and carbon beams by fractionation.

We have evaluated the mutation caused by carbon beams, neon beams, and X-rays. We conclude as follows. (1) The mutation frequency is higher for the cells which were irradiated with heavy-ion beams than with X-rays. (2) The mutation frequency of MDA-MB231 is less for the neon than carbon beams. This tendency is in accord with previous report. (3) When V79 was irradiated with heavy-ion beams, the fractionated treatment can reduce the mutation frequency without decreasing the cell-killing effects.

### References

- 1) N. Shigematsu et al: RIKEN Accel. Prog. Rep. **28**, 117 (1995).
- 2) K. Toya : Nippon Acta Radiol. **56**, 736 (1996).

\* Department of Radiology, Keio Univ. School of Medicine

## Cell Cycle Progression after Heavy-Ion Irradiation

K. Eguchi-Kasai, H. Itsukaichi, T. Kanai, and F. Yatagai

We have studied the cell cycle progression in cultured mammalian cells after irradiation with C-ion beams. Asynchronous V79 cells were irradiated by carbon ion beam ( $LET \approx 30 \sim 240 \text{ keV}/\mu\text{m}$ ) in monolayer using the cyclotron and HIMAC at NIRS and the RIKEN Ring Cyclotron. The cell population at  $G_2$  and M ( $G_2/M$ ) phase measured by flowcytometer (FCM) increased with incubation time after irradiation. Accumulation of cells at  $G_2/M$  phase was observed from 4 h after irradiation. Accumulation lasted for several hours, with a peak at around 6 h. Accumulation length depended on irradiation dose and LET. The maximum value and the width of the peak increased with irradiation dose for X-rays. For C ion with LET of 30 and 77  $\text{keV}/\mu\text{m}$ , the peak value increased with dose up to 3 Gy. Cells stayed at the  $G_2/M$  phase longer when they were irradiated by a higher dose or by the radiations with a higher LET. When cells were irradiated by the iso-survival dose, the profile of the  $G_2/M$  phase cells was similar each other for X-rays and C-ions with 3 LET values of 30, 77 and 240  $\text{keV}/\mu\text{m}$  (Fig. 1). However for C ion with LET of 240  $\text{keV}/\mu\text{m}$ , the ratio of  $G_2/M$  to total increased up to 8 h, later than the ion with lower LET. We have not analyzed longer incubation period for this LET C ion, because irradiation field at NIRS cyclotron is small and cell growth easily slow down. Further studies are needed at the higher LET region than 100  $\text{keV}/\mu\text{m}$ . In our first experiment

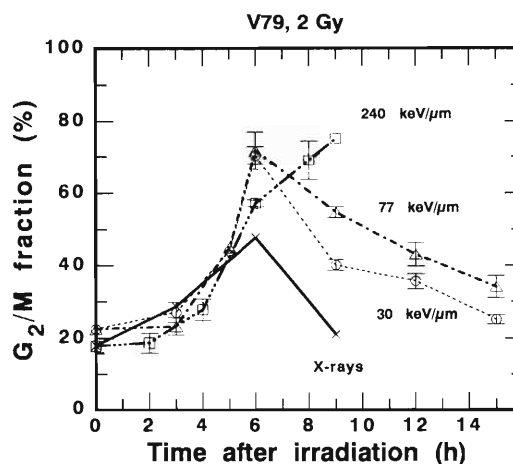


Fig. 1. Kinetics of the cell fraction at  $G_2/M$  phase after C-ion irradiation. Cells are irradiated by X-ray (X) or C ion. LET of C ion is indicated in figure in  $\text{keV}/\mu\text{m}$ .

of cell cycle analysis at the RIKEN Ring Cyclotron, little accumulation at  $G_2/M$  phase were observed for 8 h incubation after the C-ion irradiation with LET of 153  $\text{keV}/\mu\text{m}$ . Cells might be synchronized during the transportation from NIRS to RIKEN. We shall repeat similar experiments using the samples more carefully prepared.

## DNA Analysis of HPRT Mutations Induced by High-LET Carbon- and Neon-ion Beams

Y. Kagawa, T. Shimazu,\* N. Fukunishi, A. Fujie, M. Hirano,\* F. Hanaoka, and F. Yatagai

Analysis of the nature of mutations induced by high-LET heavy ions can contribute not only to basic research into biological effects but also to applications for radiation therapy and radiation risk estimation.

To obtain information about the mutations caused by exposure of cells to heavy-ion beams, we looked at that level of LET at which the particles lose most of their total energies and stop shortly after passing the cell. To achieve this exposure, the human lymphoblastoid TK6 cells were irradiated by the beams adjusted to LET 250, and 310 keV/ $\mu\text{m}$  for C- and Ne-ions, respectively. The hypoxanthine phosphoribosyltransferase (HPRT) mutant clones were selected by resistance to 6-thioguanine (5  $\mu\text{g}/\text{ml}$ ). As shown in Table 1, HPRT mutations were clearly induced by irradiation with each heavy-ion. We have analyzed precisely the obtained mutant clones by multiplex PCR, long PCR, and DNA sequencing of both genomic DNA and cDNA. The comparison of mutants by multiplex PCR analysis is shown in Table 2. Approximately 60% of the C-ion induced HPRT mutant clones showed point mutations. This result is consistent with our previous analysis of HPRT mutants from human embryo

cells after the exposure to a similar high LET C-ion irradiation.<sup>1,2)</sup> In contrast, about 85% of the mutants induced by Ne-ions were classified as deletion mutations. These events included unique mutations such as a complicated loss of multiple exon-regions, mutants with the presence or absence of the exon 6 region itself, and other unique events (data not shown). The exon 6 events were seen only after Ne-ion irradiation. We conclude that these C- and Ne-ion irradiations produce clearly different mutational specificities.

We are also exploring the use of long PCR methodology on genomic DNA to get more detailed information about the deletion mutants. Figure 1 shows some mutants that are grouped together by multiplex PCR analysis as exon 6 deletions. Clearly, long PCR shows each mutant to be distinct deletions of 3.4, 2.6, and 5.4 kb in size.

Table 1. The surviving fractions and mutation frequencies.

Heavy Ion	—	C	Ne
LET (keV/ $\mu\text{m}$ )	—	250	310
Dose (Gy)	0	3.0	3.0
Surviving fraction	1.0	0.23	0.20
Mutation frequency(X10 <sup>-6</sup> )	0.6	2.7	4.4

Table 2. Classification of mutational events by Multiplex PCR.

Ion (LET, keV/ $\mu\text{m}$ )	C (250)	Ne (310)
Whole region deletion	1	5
Partial region deletion	10	24
Point mutation	17	5
Total number of mutant clones	28	34

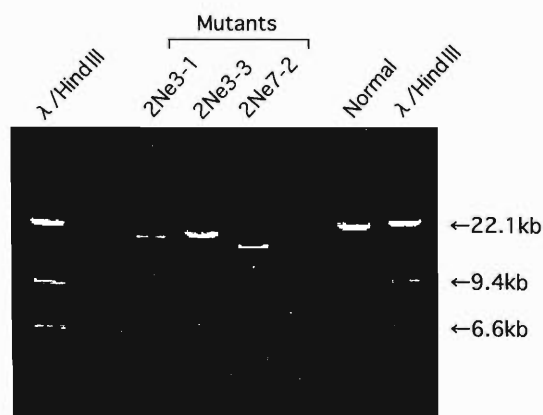


Fig. 1. Analysis by long PCR.

### References

- 1) M. Suzuki, M. Watanabe, M. Kanai, Y. Kase, F. Yatagai, T. Kato, and S. Matsubara: *Adv. Space Res.* **18**, 127 (1995).
- 2) Y. Kagawa, F. Yatagai, M. Suzuki, Y. Kase, A. Kobayashi, M. Hirano, T. Kato, M. Watanabe, and F. Hanaoka: *J. Radiat. Res.* **36**, 185 (1995).

\* Toray Research Center



## Luminescence Spectra and Decay Curves of Ion Irradiated Diamonds

J. Kaneko and K. Kimura

Recently, it has become possible to obtain high purity synthetic diamond crystals. These diamond crystals are used for development of electrical devices and radiation detectors.<sup>1)</sup> A cathode luminescence is a standard method for characterization of such diamond crystals, because it is possible to extract some information about band-gap energy, centers of impurities and vacancies. Such diamond crystals were irradiated by several kinds of ions at the RIKEN Linear Accelerator. Then the luminescence from diamond crystals was measured during this experiment. Moreover, a decay curve of free-exciton recombination luminescence was measured by using SISP (Single Ion hitting and Single Photon counting) system<sup>2)</sup> whose time resolution was better than 100 ps.

Synthetic high purity type IIa single diamond crystals were mainly used in this experiment. Luminescence spectra and decay curves were measured at room temperature and at 80 K. The band "A" which was reported in previous studies having used electron beams was dominant in the spectra at room temperature, and it had a very high luminescence efficiency. The wavelength for the center of the band "A" was previously reported as 427 nm (2.9 eV), but it was 483 nm (2.56 eV) on these synthetic type IIa diamonds. The decay time of the band "A" region of these diamond crystals was very slow and had a value of ms order.

Figure 1 shows a luminescence spectrum of synthetic type IIa diamond bombarded by He<sup>+</sup> ions at 80 K. The intensity of the band "A" decreased one tenth of that measured at room temperature. Moreover, the center of the band "A" shifted to the lower energy, i.e., 545 nm (2.27 eV). A peak regarded as free-exciton recombination luminescence was observed at 235 nm (5.27 eV). A free exciton recombination luminescence reflects a band gap energy of diamond, it is considered as an index of diamond crystal perfection. Figure 2 shows a decay curve of luminescence of the free exciton recombination luminescence. It consisted of two

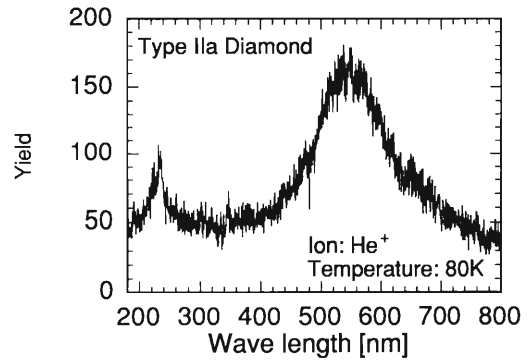


Fig. 1. Luminescence spectrum of IIa diamond irradiated by He<sup>+</sup> ions at 80 K.

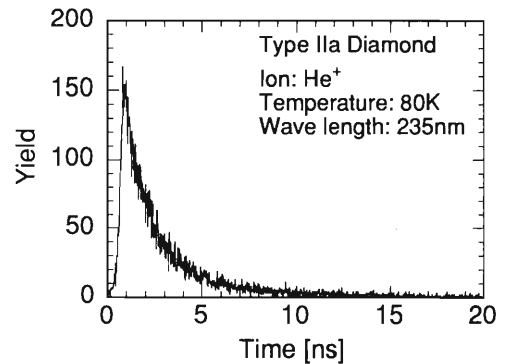


Fig. 2. Decay curve at 235 nm of IIa diamond irradiated by He<sup>+</sup> ions at 80 K.

components having decay times of 1.3 and 5.4 ns.

### References

- 1) J. Kaneko and M. Katagiri: Nucl. Instrum. Methods Phys. Res. A **383**, 547 (1996).
- 2) K. Kimura and J. Wada: Phys. Rev. B **48**, 15535 (1993).



## 5. Instrumentation



# Computing Environment Surrounding the Accelerator Research Facility

T. Ichihara, Y. Watanabe, and A. Yoshida

In this report, we describe a brief summary of the recent computing environment surrounding the RIKEN Accelerator Research Facility (RARF). General description of the data acquisition system at the RARF can be found elsewhere.<sup>1)</sup>

(1) Off-line data processing system

Figure 1 shows the main part of the computing environment of RARF. Open VMS/AXP clusters of 12 nodes are main components of the current data analysis processors. These nodes are connected by 100 Mbps FDDI and ethernet. Total 330 GB of hard disks are available for the storage of the experimental data.

Recently, the requirement to support the UNIX operating system at RARF has increased, and we have decided to install and support two UNIX systems at RARF. In the beginning of 1998, two Alpha CPUs

(Digital UNIX) at 600 MHz and two Ultra Sparc CPUs at 300 MHz (Solaris 2) have been installed for UNIX user's environment.

(2) On-line data acquisition system

Currently, seven VAX computers are used for CAMAC-based on-line experiments at the RARF. Independent measurements and detector tests can be performed without an interference. Gradual replacement of the data acquisition system from the VAX with Q22-bus interface (Kinetic 3922) to the Alpha workstation with PCI-bus interface (Kinetic 3915) is now in progress.<sup>2)</sup>

(3) Wide area computer network (WAN) connectivity

The WAN bandwidth between RIKEN and STA/IMnet internet has increased from 1.5 Mbps to 6.0 Mbps in April 1997. Since we need a much larger bandwidth (more than 10 Mbps) with BNL in USA for the RHIC Spin Project, we have submitted an application to the APAN (Asia-Pacific Advanced Network) project.<sup>3)</sup> The APAN project is expected to start operating in May 1998 and at that time the bandwidth of the APAN supported USA-Japan internet backbone is expected to become 45 Mbps.

(5) Address of the electronic-mail

The address of the electronic-mail for a general user of the RIKEN Accelerator Research Facility is described as follows, where the *userid* should be replaced by user's proper name.

(Internet)  
*userid@rikaxp.riken.go.jp*  
 (HEPnet/DECnet)  
*rikaxp::USERID (or 41823::userid)*

References

- 1) T. Ichihara et al.: IEEE. Transaction on Nuclear Science, **35-6**, 1628 (1989), see also <http://www.rarf.riken.go.jp/rarf/exp/comp/>
- 2) K. Yoshida et al.: to be published.
- 3) see for <http://www.apan.net/>

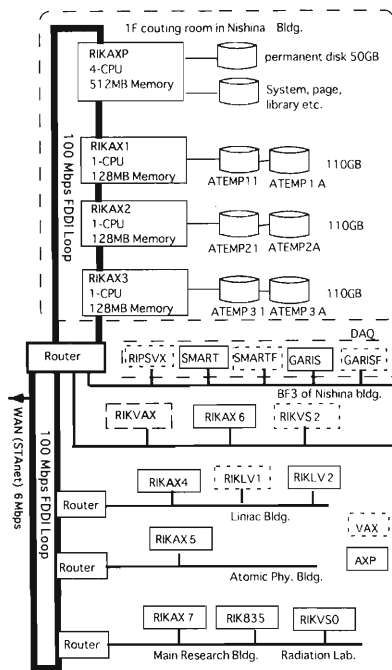


Fig. 1. Main part of the computing environment of RARF.

# Optimization of Hexapole Magnet for ECR Ion Source

T. Kurita, T. Nakagawa, and S. M. Lee

Usually the permanent hexapole magnet is used to impose the radial magnetic field for plasma confinement in ECR ion source.<sup>1)</sup> In the present paper, we investigate the magnetic field strengths with respect to the size of permanent magnet and to the number of magnet pieces in order to optimize the strength.

Figure 1 shows the cross sectional view of a typical hexapole magnet which consists of 24 pieces of permanent magnet. As a typical demagnetization curve  $B(H)$  of permanent magnet for calculation of magnet field, we adopted a straight line from  $(H=-130000 \text{ [A/m]}, B=0 \text{ [Gauss]})$  to  $(H=0 \text{ [A/m]}, B=130000 \text{ [Gauss]})$  as shown in Fig. 2. The dependence of the magnetic field strength on the size of permanent magnet is shown in Fig. 3. The horizontal axis is a ratio of the external radius to internal one. The vertical axis is a magnetic field strength at the half point of the internal radius. Each line is the case when number of pieces was 24. The dashed line indicates the case when internal radius was 4 cm. The solid line indicates the case when external radius was 2 cm.

As show in Fig. 3, when magnetic field made by magnets of different size is plotted as a function of the size of normalized with internal radius, the magnetic field does not depend on the internal radius of hexapole

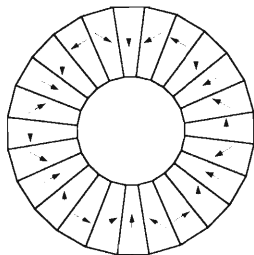


Fig. 1. The shape of Hexapole magnet consisting of 24 permanent magnet pieces. Arrows indicate the directions of the magnetization.

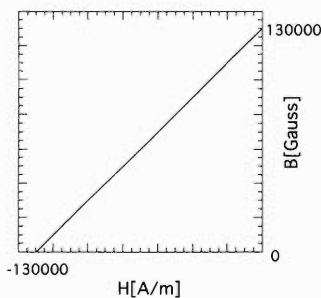


Fig. 2. Demagnetization curve  $B(H)$  of a typical permanent magnet.

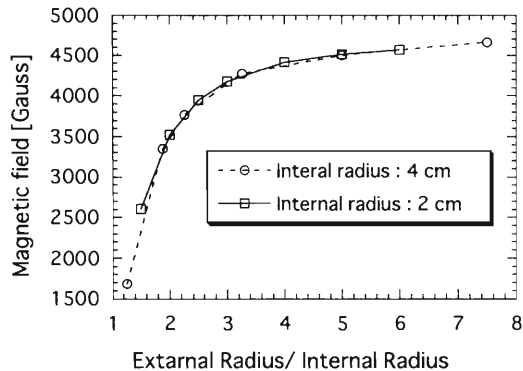


Fig. 3. Dependence of the magnetic field strength on the size of hexapole magnet.

magnet. The magnetic field strength increase with normalized radius up to  $\sim 3.5$  and then saturates almost.

Figure 4 shows the magnetic field strength as a function of the number of pieces. In this calculation, we used the one with internal radius of 4 cm and external radius of 9 cm. The magnet field strength at the half point of internal radius are plotted. Magnet field strength increases with the number of pieces as shown in Fig. 3. However the saturation appears from 24 or 30 pieces. It seems that a reasonable number of pieces is 24 or 30.

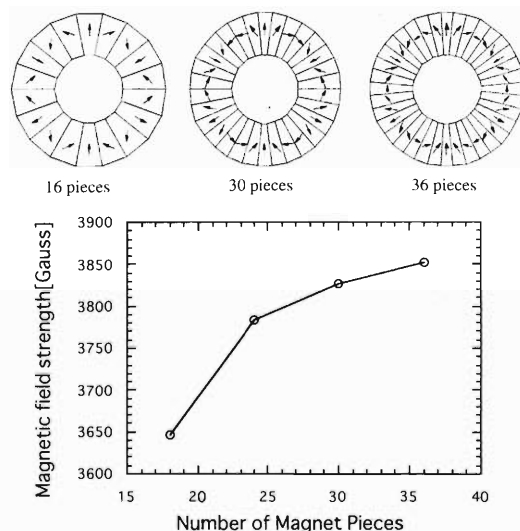


Fig. 4. The magnetic field strength as a function of the number of magnet pieces.

References

1) R. Geller: Ann. Rev. Nucl. Part. Sci. 40, 15 (1990).

## Development of the Slow Highly Charged Ion Beam below 100 eV/q from an ECR Ion Source for Ion-Atom Collision Experiments

M. Kitajima, Y. Nakai, Y. Kanai, Y. Yamazaki, Y. Awaya, and Y. Itoh

In order to study the charge transfer processes from highly charged ions to atoms and molecules in the collisional energy range of below 100 eV/u, a new experimental setup of producing a mono-energetic slow highly charged ion beam below 100 eV/q has been developed. The apparatus is set at the 30° beam line of the RIKEN 14.5 GHz Caprice ECR ion source.<sup>1)</sup> Schematic view of the apparatus is shown in Fig. 1. The apparatus consists of deceleration lens, beam collimator, and beam energy selector. Highly charged ions are extracted by the beam energy ranging 1–5 keV/q into the beam line. Since the final beam energy depends on the potential of the plasma chamber of the ion source, the beam line is floating from the ground potential, so that a sufficient extraction potential can be applied. The ion beam is decelerated down to the beam energy of 100 eV/q and focused by the deceleration lens and collimated by the collimator. The beam energy selector consists of entrance lenses, two sets of hemispherical electrostatic analyzer, and an exit lens. Typical currents of the energy selected N<sup>5+</sup> beam are 50 pA at the pass energy of 110 eV/q and 10 pA at the pass energy of 30 eV/q.

In order to obtain the resolving power of each of the

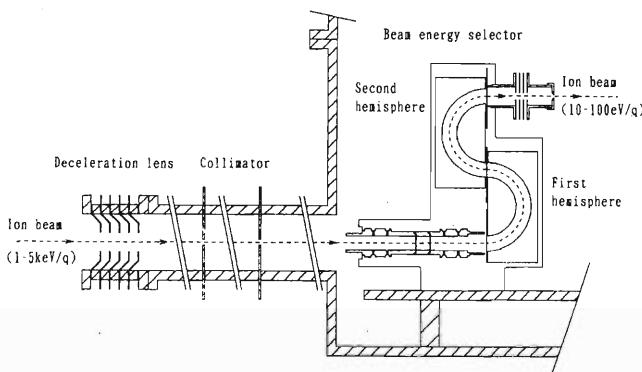


Fig. 1. Schematic view of the apparatus. Ion beam of 1–5 keV/q from the 14.5 GHz Caprice ion source is decelerated down to 10–100 eV/q and selected the energy.

hemispherical analyzer, energy broadening ( $\Delta E$ ) of ion beam passed through the first hemispherical analyzer has been measured by the second hemispherical analyzer. The resolving power has been determined by fitting the data with the next equation.

$$\Delta E = 2\sqrt{\frac{2(ax/2)^2 - (ax/2)^4}{(b/2)^2 + (ax/2)^2}}$$

Here,  $a$  is the resolving power of each hemispherical analyzer,  $b$  the energy broadening of the ion beam at the entrance slit of the first hemisphere,  $x$  the pass energy of the hemisphere, and  $\Delta E$  the measured energy broadening of ion beam passed through the first hemisphere. The results are shown in Fig. 2 as a function of the pass energy. The resolving power of each hemispherical analyzer has been determined from the above fitting and found to be 1/90.

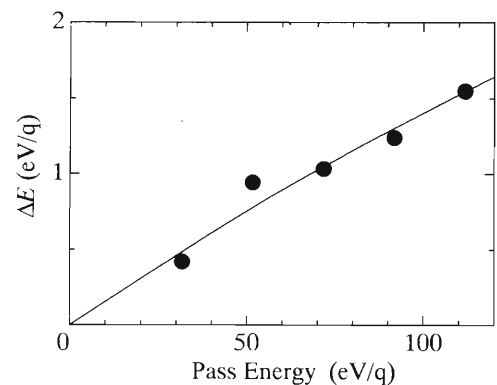


Fig. 2. The energy broadening  $\Delta E$  of ion beam passed through the first hemispherical analyzer as a function of the pass energy. Solid curve shows the results of the fitting with  $a = 1/90$  and  $b = 1.5$ .

### References

- 1) Y. Kanai et al.: RIKEN Accel. Prog. Rep. 30, 168 (1997).

## Precise Determination of Neutron Beam Polarization at 16 MeV

K. Sagara, T. Fujita, K. Shigenaga, H. Akiyoshi, K. Tsuruta, K. Ogata,  
T. Yagita, H. Okuda, H. Nakamura, and T. Nakashima\*

A 16 MeV  $\bar{n}$ -beam was produced by  ${}^2\text{H}(\vec{d}, \bar{n}){}^3\text{He}$  reaction at  $E_d = 13.15$  MeV, and the  $\bar{n}$ -beam polarization was determined using the  $\bar{n} + {}^4\text{He}$  scattering. Polarization of the  $\vec{d}$ -beam was measured using  ${}^3\text{He}(\vec{d}, \text{p})$  reaction. The production development of  $\bar{n}$ -beam has been made at Kyushu University, and a precise experiment on the analyzing power  $A_y(\theta)$  of  $\bar{n} + \text{d}$  scattering will be made using a high-intensity  $\vec{d}$ -beam available from RIKEN AVF Cyclotron.

The gas cell for  ${}^2\text{H}_2$  target was the same as was used to produce a 12 MeV  $\bar{n}$ -beam,<sup>1)</sup> except that the thickness of Ta window foils for the beam entrance and exit was increased from 3 to 5  $\mu\text{m}$  so as to increase the  ${}^2\text{H}_2$  gas pressure from 3 to 5 atm. The pressure of the  ${}^3\text{He}$  target gas was also raised from 1.5 to 2.5 atm. The  ${}^4\text{He}$  target was liquid, and worked also as a scintillator.

First, the analyzing powers  $A_y(\theta)$  and  $A_{yy}(\theta)$  of  ${}^3\text{He}(\vec{d}, \text{p})$  reaction were measured at  $E_d = 10\text{--}16$  MeV, and the maximum of  $A_y(\theta)$  was determined within an accuracy of about 0.7%.

Increase of the n-beam energy from 12 MeV to 16 MeV caused two problems. One problem was a large increase of the n- and  $\gamma$ -fluxes which were mainly produced at the window foils and at the beam stopper of Ta, and which hit the neutron counters of NE213 to yield large backgrounds. A shield of 30 cm thick lead attenuated the fluxes by about an order of magnitude. However, an additional lead could not reduce the flux. By surrounding the flux source with a 10 cm thick paraffin block, the n-flux was decreased by another order of magnitude. Although the  $\gamma$ -flux is still high, the  $\gamma$ -signals can be rejected using the n- $\gamma$  separation circuit.

Another problem was the absolute determination of the  $\bar{n}$ -beam polarization. From the  $\bar{n} + {}^4\text{He}$  experiment, we have obtained the data for  $K_y^y(0^\circ)A_y(\theta)$ . The polarization transfer coefficient  $K_y^y(0^\circ)$  of  ${}^2\text{H}(\vec{d}, \bar{n}){}^3\text{He}$  reaction can be determined with the knowledge of  $A_y(\theta)$ . Since  $A_y(\theta)$  of the  $\bar{n} + {}^4\text{He}$  scattering takes theoretically maximum value (=1) near 12 MeV, the maximum of  $A_y(\theta)$  at 12 MeV can be well approximated as 1.000. At 16 MeV, however, the approximation does not hold. Moreover, the existing several sets of the phase shifts for the n +  ${}^4\text{He}$  scattering predict different  $A_y(\theta)$ .

We therefore made a modified phase shift analysis. An existing set of the phase shifts was adopted as a starting point, and the cross section *data* were produced from the set. Then, the phase shifts and  $K_y^y(0^\circ)$  were so adjusted as to fit our  $K_y^y(0^\circ)A_y(\theta)$  data and the cross section *data*. Figure 1 shows the result. We

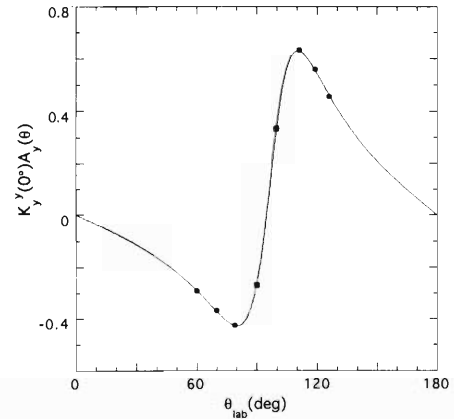


Fig. 1. Measured asymmetries for the  $\bar{n} + {}^4\text{He}$  scattering (filled circles) and the result of modified phase shift analysis curve.

have obtained almost the same values for  $K_y^y(0^\circ)$  and phase shifts from any set of the existing phase shifts. The  $K_y^y(0^\circ)$  value obtained at 16 MeV (preliminary) is shown in Fig. 2 together with our data at 12 MeV and TUNL data.<sup>2)</sup> A half of the difference between our data and TUNL data is due to the different  $A_y(\theta)$  values adopted.

The  $\bar{n}$ -beam polarizations  $p_y^n$  is expressed as

$$p_y^n = 3/2 K_y^y(0^\circ) p_y^d / [1 - 1/4 A_{zz}(0^\circ) p_{yy}^d]. \quad (1)$$

Since the analyzing power  $A_{zz}(0^\circ)$  of  ${}^2\text{H}(\vec{d}, \text{n}){}^3\text{He}$  reaction was also measured, we can determine  $p_y^n$  from the  $\vec{d}$ -beam polarization  $p_y^d$  and  $p_{yy}^d$ .

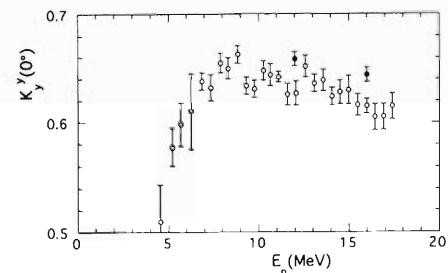


Fig. 2. Polarization transfer coefficient,  $K_y^y(0^\circ)$ , of the  ${}^2\text{H}(\vec{d}, \bar{n}){}^3\text{He}$  reaction. Filled and open circles are our data and TUNL data,<sup>2)</sup> respectively.

### References

- 1) K. Sagara et al.: RIKEN Accel. Prog. Rep. **28**, 121 (1995).
- 2) P. W. Lisowski et al.: Nucl. Phys. A **242**, 298 (1975).

\* Faculty of Science, Kyushu University

## Development and Characterization of the Self-TOF Neutron Detector

N. Nakao,<sup>\*1</sup> M. Nakao,<sup>\*2</sup> M. Sasaki,<sup>\*2</sup> T. Nakamura,<sup>\*2</sup> T. Shibata,<sup>\*1</sup> and Y. Uwamino

Since the facilities require more massive shields with increase of the accelerating beam current and energy, the shielding design at higher accuracy is essential to save the construction cost. Such shielding designs are performed according to the results of particle transport calculation using the variety of simulation codes. Although high neutron energy spectra are necessary in the shielding experiment for estimating the accuracy of such simulation codes, such data are very scarce above  $\sim 100$  MeV.

Now, spectrometries of high energy neutron are generally performed by measuring the neutrons attenuated by various kinds of moderators using various neutron detector devices such as  $^3\text{He}$  counter, TLD, and track detector. Then neutron energy spectra are obtained by an iteration type unfolding method using simulated spectra. This method, however, includes uncertainty of the simulated results and iteration processes, and has problems of not measuring the high energy neutrons. On the other hand, an unfolding method using a pulse-height distribution measured by an organic liquid scintillator gives much more accurate neutron energy spectra.<sup>1-3)</sup> This method, however, is limited by the scintillator size due to the leakage of the recoil protons generated in the scintillator, thus necessitating a huge scintillator to measure higher neutrons. Therefore, we have developed a new type neutron spectrometer system (called Self-TOF detector) which can measure energy spectra of such leaked protons in order to measure the neutrons of energy range 100 MeV  $\sim$  1 GeV.

This Self-TOF detector consists of an assembly of a 150-mm  $\times$  150-mm  $\times$  5-mm-thick scintillator as a veto counter (VET), 20 sets of 100-mm  $\times$  100-mm  $\times$  6-mm-thick radiator-scintillator (RAD), a 100-mm  $\times$  100-mm  $\times$  5-mm-thick scintillator as a start timing generator (STA), and 9 sets of 200-mm  $\times$  200-mm  $\times$  20-mm-thick scintillators as a stop timing generator (STO). The arrangement of the Self-TOF detector is shown in Fig. 1. All of the scintillators are NE102A plastic scintillators. The STO was set at 120 cm after the center of the STA. Thus, many of segments of RAD and of STO give a high detection efficiency. Particles emitted from RAD at angles of up to  $\sim 16$  degree can be measured, and the efficiency at 100 MeV neutrons is expected to be  $\sim 1\%$  according to the HETC-3STEP Monte Carlo code<sup>4)</sup> calculation.

Protons induced at a forward direction by incident neutrons in RAD pass through the rest of RAD and

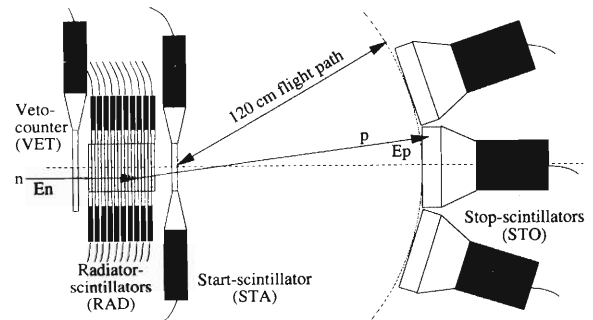


Fig. 1. The Self-TOF detector system.

STA, and are detected by one of the STO segments. The proton energy ( $E_p$ ) is estimated using the proton flight time (TOF-p) between STA and STO. Two photomultiplier tubes (PMT) are attached to STA to obtain a good time resolution; the mean time of two PMT outputs generates the start timing signal, which are independent of the scintillation position in STA. The initial energies of induced protons in RAD are obtained by adding the energy losses ( $\Delta E$ ) in RAD and STA to the  $E_p$  obtained by the TOF method. The radiator which generates protons can be easily found by observing all outputs of the RAD segments, and energy losses of the protons in RAD can be estimated.

In order to examine the detector performance and to estimate the accuracy of detector response calculation by the HETC-3STEP Monte Carlo code,<sup>4)</sup> a neutron irradiation experiment was performed using the quasi-monoenergetic neutrons produced by a 10-mm-thick  $^7\text{Li}$  target bombarded by 135 MeV/nucleon  $\text{H}_2^+$  ions at the E4 neutron beam course of the RIKEN Ring Cyclotron Facility. In this experiment, the response function of the detector system for a monoenergetic neutron was measured using only 6 sets of radiator-scintillators and 3 sets of stop-scintillators. The detector was placed behind the collimator at the position of 11 m from the Li target to STA in the neutron beam course as shown in Fig. 2. The coincidence events between STA and STO were selected, and all of the pulse heights from each photomultiplier and the proton flight times (TOF-p) were stored in the event-by-event mode. Incident neutron flight times (TOF-n) between the Li target and STA were also stored using chopper trigger signals of the cyclotron (repetition period:  $\sim 1\mu\text{sec}$ ), and the response of the detector for peak neutron energy ( $\sim 132$  MeV, FWHM:2.5 MeV) was obtained by an off-line analysis. Time resolution of the detector

<sup>\*1</sup> High Energy Accelerator Research Organization (KEK)

<sup>\*2</sup> Cyclotron and Radioisotope Center, Tohoku University

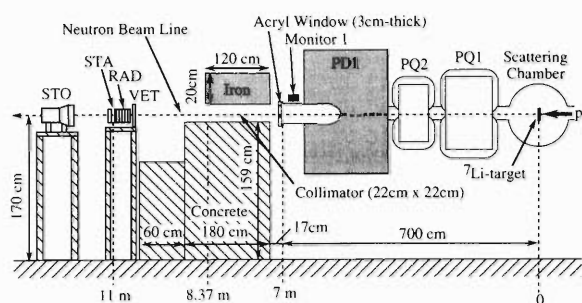


Fig. 2. Experimental setup at E4 neutron beam course in RIKEN.

system, which was estimated from the  $\gamma$ -ray events, is  $\sim 0.5$  nsec, and the energy resolution at 132 MeV is  $\sim 20$  MeV.

In a two dimensional plot of the TOF-p versus STO's light outputs, proton, deuteron, and  $\gamma$ -ray components can be seen in Fig. 3(a). The only proton events were selected as shown in Fig.3(b) by the help of energy loss difference in all radiators from their outputs. Then, the TOF-p distribution was converted into the proton energy spectrum. Figure 4(a) shows an energy spectrum of protons generated from six radiator-scintillators measured with the center stop-scintillator. In the distribution, knock-out protons are seen as the peak, which is little broad because of proton energy loss in the radiators. Figure 4(b) shows energy spectra of protons from one of the radiators measured with the center and side stop-scintillator, which were obtained by adding the sum of the proton energy losses in RAD and STA. These measured data are compared with that calculated by HETC code.<sup>4)</sup> The discrepancies are up to  $\sim 20\%$  between measured and calculated responses integrated in the peak region. On the other hand, low energy protons generated by carbon reactions are also seen in the low energy tail, and measured data is about twice as high as the calculated data. This can perhaps be considered that a part of deuteron components are included in the measured data at the low energy tail by this discrimination method.

In this work, the experimental detector response was obtained for 132 MeV monoenergetic neutrons, and it is concluded that the energy of neutrons higher than 100 MeV can be measured with this detector system. Neutron energy spectra can be obtained by an unfolding method using the response functions for various neutron energies. Since the actual neutron spectra are rather broad behind the shielding in the accelerator facility and since a high resolution of energy spectrum is

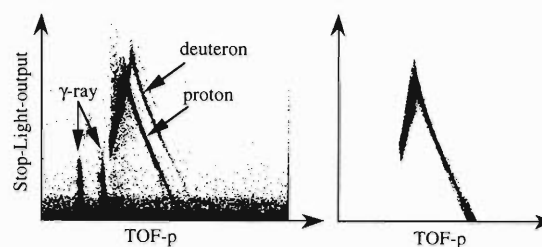


Fig. 3. Two dimensional plot of proton-TOF versus stop-counter-light-output : (a) raw data, and (b) the data after selecting only proton events.

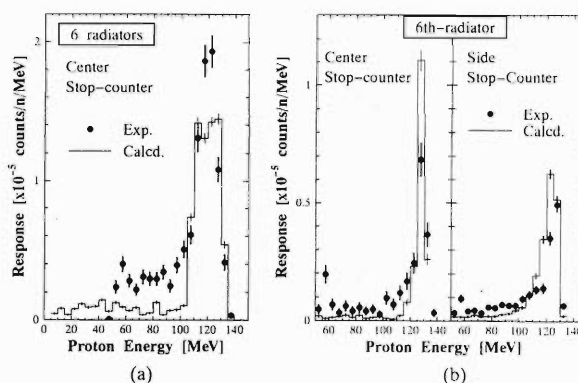


Fig. 4. Detector performance for 132 MeV neutrons, comparing with that calculated by the HETC code. (a) Proton energy spectrum measured with the center stop-counter by flight time of the protons generated from six radiators. (b) Energy spectrum of protons from the 6th-radiator measured with the center and side stop-counters after energy loss correction.

not required, this performance is enough for the neutron spectrometry and is expected to give more reliable and more accurate results than any other methods to our knowledge. We are now ready to measure the response functions of complete setup of the detector for higher energy neutrons, and to study the detector performance in order to obtain a much better energy resolution and discrimination of protons.

#### References

- 1) N. Nakao et al.: Nucl. Sci. Eng. **124**, 228 (1996).
- 2) H. Nakashima et al.: Nucl. Sci. Eng. **124**, 243 (1996).
- 3) N. Nakao et al.: J. Nucl. Sci. Technol. **34**, No. 4, p. 348 (1997).
- 4) N. Yoshizawa et al.: J. Nucl. Sci. Technol. **32**, No. 7, p. 601 (1995).

## Proton Induced Activation in GSO, BGO Scintillators

M. Kokubun,\*<sup>1</sup> E. Idesawa,\*<sup>1</sup> K. Matsuzaki,\*<sup>1</sup> T. Mizuno,\*<sup>1</sup>  
Y. Saito,\*<sup>2</sup> K. Takizawa,\*<sup>2</sup> and A. Yoshida

The Hard X-ray Detector(HXD) is one of the three experiments to be aboard ASTRO-E which is the fifth Japanese X-ray satellite scheduled to be launched in the year 2000.<sup>1)</sup> It covers the energy range from 50 to 600 keV by the GSO(Gd<sub>2</sub>SiO<sub>5</sub>;Ce) scintillators located at the bottom of a “well” made of the BGO(Bi<sub>4</sub>Ge<sub>3</sub>O<sub>12</sub>) scintillators.

In the orbit of the satellite, there are energetic ( $\sim 100$  MeV) protons which are trapped by the earth magnetic field and these particles will produce radioactive isotopes in the scintillators. Because these radioactivities are considered to become the dominant background for the HXD, it is important to study the characteristics of the effect of radioactivation on the ground.

We irradiated the GSO and BGO scintillators with the H<sub>2</sub><sup>+</sup> particles which were accelerated to 135 MeV/u at RIKEN Ring Cyclotron, and measured the induced radioactivities. The intensity of the beam was set to extremely low level ( $\sim 10^6$  counts/sec) in order to accurately count the number of H<sub>2</sub><sup>+</sup> particles which had penetrated the two plastic scintillators located vertically to the beam upstream of the target scintillator. Total  $\sim 10^9$  H<sub>2</sub><sup>+</sup>s were counted and this corresponds to the amount that one GSO is to be irradiated for about 100 days in the orbit.

Two radioactivated GSO scintillators were measured, one by a germanium detector to identify the radioactive isotopes produced and the other by a PMT to know the actual response against the radiations inside the GSO. Table 1 shows the identified radionuclides corresponding to their half lives.

Within a few days after irradiation, complicated and variable spectra from the radionuclides shown in the first row of Table 1 were obtained through the PMT. Though they might confuse the observational data in the orbit, it is expected that most events caused from these short-life nuclides can be rejected by the phoswich technic and anti-coincidence methods at the

Table 1. Identified radionuclides.

Half life ( $\tau$ )	identified nuclide
$\tau \leq 1day$	$^{152}_mTb, ^{150}_mTb, ^{149}_mTb$ $^{148}_mTb, ^{148}_mTb, ^{145}Gd, ^{158}Eu,$ $^{159}Gd, ^{154}Tb, ^{152}Tb,$ $^{151}Tb, ^{150}Tb, ^{149}Tb, ^{147}Tb$
$\tau \leq 30days$	$^{156}Tb, ^{155}Tb, ^{153}Tb, ^{149}Gd$ $^{147}Gd, ^{147}Eu, ^{146}Eu, ^{145}Eu$
$\tau \geq 30days$	$^{153}Gd, ^{151}Gd, ^{149}Eu, ^{146}Gd, ^{145}Sm$

BGO shield surrounding the GSO scintillators.

On the other hand, the spectra which were observed long time (more than 30 days) after the irradiation can be explained by the nuclear emissions radiated in the radioactive decays of only 5 or 6 radionuclides shown in the last row of Table 1. Though they can not be rejected from radioactivational backgrounds, because of their low energy ( $\sim \leq 200$  keV) gamma ray emissions which can be stopped within the GSO scintillator, we will again be able to subtract these long-term, stable backgrounds by using the off-source observational data. Furthermore, we have successfully obtained the Monte-Carlo simulated spectra which are expected from the radioactivated GSO scintillator read through a PMT, based on the nuclear data of the identified radionuclides. This simulation has reproduced more than 95% of the experimental data within the energy range from 50 to 500 keV. Therefore, the simulation can be another tool to understand the actual background of the HXD in the orbit.

### References

- 1) T. Kamae et al.: Proc. SPIE **2806**, 314 (1996).
- 2) K. Matsuzaki et al.: RIKEN Accel. Prog. Rep. **27**, 118 (1996).

\*<sup>1</sup> Department of Physics, University of Tokyo

\*<sup>2</sup> The Institute of Space and Astronautical Science

# In-Vacuum Plastic-Scintillator Hodoscope for Low-Background Measurements of Charged Particles

I. Hisanaga, T. Motobayashi, and Y. Ando

A vacuum chamber has been constructed, so that the plastic-scintillator hodoscope for Coulomb dissociation experiments<sup>1,2)</sup> can be mounted inside of it for reduction of background. In the last experiment the vacuum was sealed at 5 m downstream of the target just in front of the hodoscope, because the hodoscope was installed in the atmosphere. The window which sealed vacuum from air caused background reactions. The overall thickness of the window (mylar) and air was about  $10^{-2}$  g/cm<sup>2</sup>, which was comparable to the target thickness. Therefore, the yield from the background was comparable to that from the target. In the present setup, on the other hand, the relevant background was entirely eliminated.

The hodoscope system was set 5 m downstream of the secondary target position of the RIKEN Projectile-fragment Separator (RIPS), and measured the fragments, p and <sup>8</sup>B, produced from the <sup>9</sup>C + <sup>nat</sup>Pb interaction.<sup>†</sup>

Figure 1 shows a schematic view of the setup. The hodoscope consists of  $\Delta E$  and E walls with 5 and 60 mm thickness, respectively. The time of flight method was employed to measure the energies of the fragments. The  $\Delta E$  and E counters, which cover  $1 \times 1$  m<sup>2</sup> area, were divided vertically to 13 segments and horizontally to 16 segments for coincidence measurements of plural charged particles. The width of the  $\Delta E$  strips was 40 mm or 100 mm, while that of E strips was 30 mm or 75 mm. The central detectors have narrower width in order to stand for higher counting rates. Two Photomultiplier Tubes (PMTs) were coupled to both ends of each strips and measured the difference of arrival times to determine hitting positions.

We mounted the PMTs outside the vacuum chamber to avoid possible electric discharge in PMT bases. The mechanical construction around the PMT is shown in Fig. 2. A plastic light pipe per PMT sealed the vacuum chamber and also guided the light from the scintillator to the PMT outside the chamber. In vacuum, the scintillators and the light pipes were communicated across transparent rubber pads. Good optical contact was achieved due to the atmospheric pressure pushing the pads. Because the light pipes are allowed to move against the chamber wall, the corresponding motion of

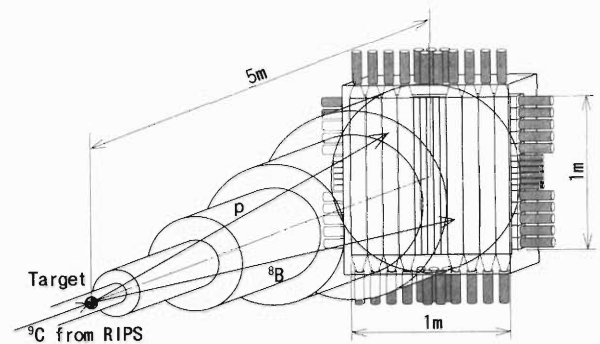


Fig. 1. The setup for  ${}^9\text{C} \rightarrow {}^8\text{B} + \text{p}$  Coulomb dissociation measurement.

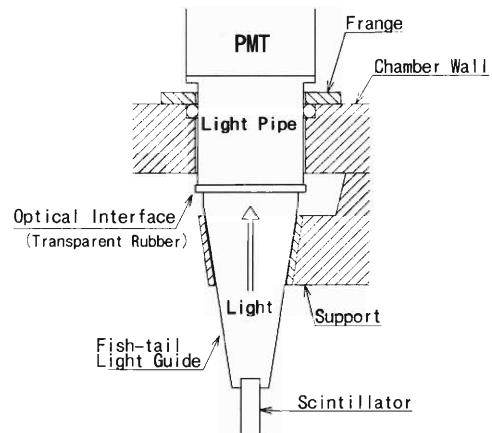


Fig. 2. Structure around the PMT.

flange does not give too large stress to the scintillators.

The pressure in the chamber achieved 7 Pa with a 2500 l/min oil-sealed rotary pump. This pressure is equivalent to the thickness of  $10^{-5}$  g/cm<sup>2</sup>, and was enough to realize the primary aim.

## References

- 1) T. Motobayashi et al.: Phys. Rev. Lett. **73**, 2680 (1994).
- 2) T. Kikuchi et al.: Phys. Lett. B **391**, 261 (1997).

<sup>†</sup> The aim of this experiment is to measure the  ${}^8\text{B}(p,\gamma){}^9\text{C}$  synthesis reaction cross section of astrophysical interest indirectly. The inverse process, Coulomb dissociation reaction  ${}^9\text{C} \rightarrow {}^8\text{B} + \text{p}$  corresponds to the  ${}^9\text{C}(\text{virtual } \gamma, \text{p}){}^8\text{B}$  reaction, where the virtual photon( $\gamma$ ) is produced during the collision between the projectile and the target.

## Beta-Ray Imaging Detector Using Scintillating Fibers

K. Morimoto and F. Tokanai

Genomic Linkage Map data<sup>1)</sup> are provided by means of autoradiographic films. This technique allows the detection over a large surface ( $35 \times 43 \text{ cm}^2$ ) area with excellent spatial resolution ( $\sim 50 \mu\text{m}$ ).  $^{32}\text{P}$  are currently used for landmarks. However they have two shortcomings: long exposure time (about two weeks) and lack of quantitative information.

To improve them, we are developing an imaging detector using scintillating fibers. This detector consists of two layers (X and Y layers) of scintillating fibers coupled to multianode photomultiplier tubes (MA-PMT). Each layer consists of 512 fibers with the cross section of 0.8 mm square (BICRON BCF-12 type). To reduce a dead space of fiber-belt the square type fiber was chosen.

Furthermore, to avoid using too many MA-PMT detectors and electronics, we used a matrix method as shown in Fig. 1. Each side of 256 fibers was arranged into a  $16 \times 16$  matrix. At the one end of fiber matrix is attached to a MA-PMT to read lateral 16 lines information and the other side is to read vertical 16 lines information. One of the MA-PMT gives the information package of 16 fibers (belt) and the other gives individual information of each package of 16 fibers (strip). Therefore, 256 fibers can be encoded by the two 16 ch MA-PMT. The signals from MA-PMT are sent to a discriminator whose threshold level is variable for each channel. Moreover, MA-PMT noise can be reduced by triggering the events which coincide between each side of fibers and each layer.

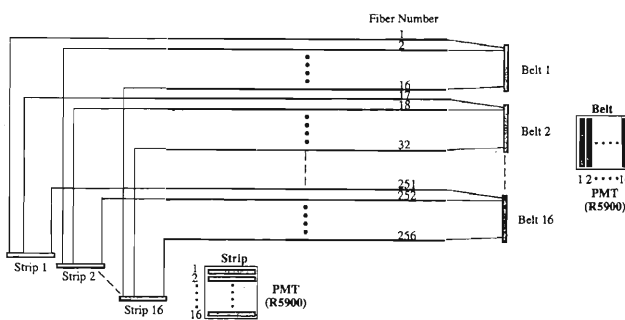


Fig. 1. Repartition of the 256 scintillating fiber unit extremities on the MA-PMTs.

These detectors include four identical sets of scintillation fiber in order to cover the genomic sheet, two of them give X-directional position the others give Y-directional position. These four detectors cover  $43 \times 43 \text{ cm}^2$  area.

The spatial resolution and cross talk of this detector were measured using the 1 MeV and 0.5 MeV internal-conversion electrons from a  $^{207}\text{Bi}$  source with a diameter of 3 mm. The position histograms for the X-axis

and Y-axis are shown in Fig. 2 and 3, respectively. These spatial resolutions for the 3 mm diameter beta-ray source are 4.8 mm (FWHM) for X-axis and 5.6 mm (FWHM) for Y-axis, respectively. The cross talk ratio is low, less than 5%.

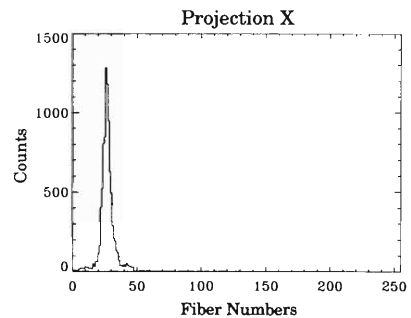


Fig. 2. Scintillation fiber projection on the X axis for the 3 mm diameter  $^{207}\text{Bi}$ .

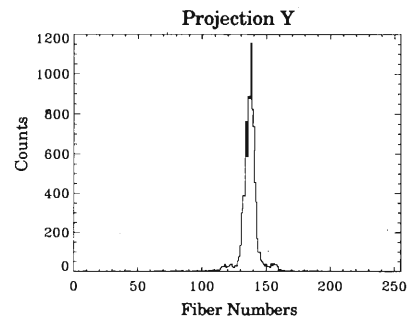


Fig. 3. Projection on the Y axis at the same event as X axis.

The problem still to be solved with this detector is its efficiency. It is about 0.5% which was estimated from the ratio of a detection rate to the source intensity. This relatively poor efficiency is explained by the low gain of the MA-PMT. To solve this problem we will try to put an amplifier between output signals of MA-PMT and discriminator.

A charged particle deposits the energy more than a beta-ray in the scintillation fibers at the same incident energy. Therefore, this type of detector can give a good S/N ratio and a good spatial resolution for charged particles. Therefore, this detector has the possibility of being a position sensitive charged particle detector for accelerator experiments. Currently we are making detectors using thinner fibers whose size is  $400 \mu\text{m}$  and  $250 \mu\text{m}$ .

### References

- 1) Y. Hayashizaki et al.: Genet. Soc. Am. **138**, 120 (1994).

## Development of a Fast Two-Dimensional PPAC

H. Kumagai and I. Tanihata

A two-dimensionally position-sensitive PPAC (Parallel Plate Avalanche Counter) for high counting-rate application has been developed for low-energy radioactive ion beams at the RIPS in RIKEN. A delay-line readout method has been used to pickup electron-induced signals from stripped cathodes. An electron-induced signal has a fast rise time and a fall time of about 4 ns, and is thus thousand times faster than the signals from ions, that are used in the previous model.

The previous model<sup>1)</sup> used the charge-division method for position determination and gave a good resolution and linearity. That model has been used for monitoring the position profiles of radioactive ion beams. However a pile up of signals becomes serious when the counting rate is higher than a few thousand per second. This is a natural limitation as long as one uses slow ion signals (rise time of 3  $\mu$ s). In contrast the present delay-line read-out model provides a good position information for a counting rate as high as  $10^6$ /s.

The delay-line readout was reported<sup>2)</sup> previously by several authors, but the position information was discretized on the strip position. In the present model, a position is read continuously without break. This condition was obtained after a adjustment of the rise time of the signal, electrode spacing, and delay line.

The cathode layout is shown in Fig. 1. The 2.40 mm wide strips with 0.15 mm inter-strip spacing are made by evaporation of Au with 30 nm in thickness. The base material is 1.5  $\mu$ m Mylar foil and is mounted onto a G10 frame of 2 mm thickness. The number of strips is 40 in both X and Y directions and thus provides the sensitive area of  $100 \times 100$  mm<sup>2</sup>. Each strip is connected to the delay-line taps described below.

The lumped-constant type delay line was used. The 110 mm long solenoid was wound by 0.3 mm $\phi$  Cu wire onto a 2 mm $\phi$  bakelite rod. The taps are made every 8 turns of coil. Then 39 pF capacitors are connected from the taps to the ground. The signals from the strip electrodes are also connected to these taps. This delay line had a 55  $\Omega$  impedance and a delay of 0.80 ns/mm. The attenuation measured by signals of 4 ns rise and fall times, signals from  $\alpha$  rays, was 15% in whole length. The rise time of 4.7 ns was observed after the transmission of the signal through the delay line. The combination of 4 ns rise time and 2 ns inter-strip delay time provided the best result for the linearity of

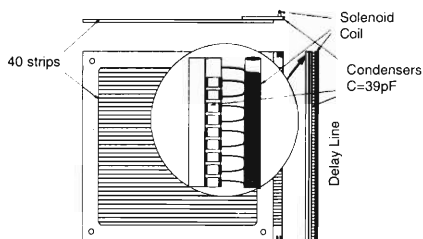


Fig. 1. The cathode structure of the delay-line PPAC.

the position information.

The anode was also made by Au evaporation onto the same Mylar foil on a same frame. The spacing between the anode and the cathode was 4 mm. The detector windows were made of 4  $\mu$ m Mylar foil with evaporated Al on the surface. The detector gas was 10 Torr C<sub>3</sub>F<sub>8</sub> and the operating bias was 880–900 Volts.

The integrated linearity obtained by an <sup>241</sup>Am alpha source is shown in Fig. 2. As seen in the figure, within  $\pm 45$  mm from the center of the detector, the errors are smaller than  $\pm 0.05$  mm for both X and Y directions. The error increases rapidly beyond 45 mm from the center. The position resolution within this  $\pm 45$  mm is  $\sigma = 0.3$  mm. The differential linearity for  $\Delta x = 2.5$  mm is better than  $\pm 1.5\%$ .

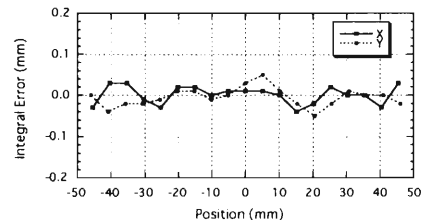


Fig. 2. Integral linearity of the PPAC.

The efficiency of the PPAC was tested by a 14.5A MeV <sup>7</sup>Be beam to be 83%. This efficiency is somewhat lower than the previous charge division type PPAC. It is considered to be due to the smaller induced signal from electrons. Therefore the present detector is effective only for low energies or for large Z particles at higher energies.

The total delay time of the delay line is 80 ns and it gives a resolving time of the detector. Positions of two or more particles coming into the detector within this time interval are not determined. However the sum of the TDC readout from the two ends of the delay line provides the hit multiplicity test. (The time difference is used for the position determination.) The time-sum from a single-particle hit does not depend on the position of the hit, but it shifts for a multiple-hit event. Therefore a shift of the time-sum indicates a multiple-hit event. This multiple-hit rate was only 9% of the total events even for an operation under the counting rate of  $10^6$ /s. The position resolution was  $\sigma = 0.4$  mm under this condition. A <sup>4</sup>He beam of 2A MeV was used for this test. It is recommended, however, to keep the counting rate below 250 kcps for long-term stable operation.

### References

- 1) H. Kumagai and K. Yoshida: RIKEN Accel. Prog. Rep. **28**, 127 (1995).
- 2) S. Beghini, L. Corradi, J. H. He, and A. Dal Bello: Nucl. Instrum. Methods Phys. Res. A **362**, 526 (1995).

## A Large Area PPAC/Ionization Chamber

K. Yoshida, M. Shimooka, R. Wada, T. Nakagawa, K. Nakagawa,  
I. Tanihata, Y. Aoki, and J. Kasagi

A large area parallel-plate avalanche counter (PPAC) and ionization chamber array has been constructed for the detection of fission fragments from a very heavy compound nucleus with mass  $A \geq 300$ . Recent theoretical calculation suggests a formation of such a heavy compound nucleus by the collision between heavy nuclei such as  $^{208}\text{Pb} + ^{208}\text{Pb}$ . A heavy compound nucleus, if it is formed, will decay to plural fragments by fission. The present detector is designed to detect such fragments to investigate formation of heavy compound nuclei. In order to distinguish the products from deep inelastic reaction, we focused on the detection of all the fragments from a ternary fission of heavy compound nucleus. The fragments from usual binary fission are less informative for the case, since they distribute in space similar to the reaction products of deep inelastic reaction.

The detector is designed to cover  $25\text{--}75^\circ$  in laboratory angle with respect to the beam axis. In order to obtain a high detection efficiency, it covers most of the region where the three fragments are expected. The forward angles in laboratory frame are excluded since a large number of elastically scattered beam particles are expected. As shown in Fig. 1, the detector is divided azimuthally to 12 identical units with a minimum dead space in between. Each unit is further divided into four sub-sections inside. Each sub-section consists of a PPAC and an ionization chamber (IC). The PPAC provides a position and a time-of-flight (TOF) informations. The IC gives energy of a fragment. In or-

der to obtain a reasonable mass resolution ( $\leq 10\%$  in FWHM), the flight path is set to be 50 cm.

The PPAC consists of one anode and two cathodes placed at the both sides of the anode in the distance of 2.5 mm. The position is obtained by the delay line method. The cathode strips of 4.7 mm in width are formed onto the  $1.5\ \mu\text{m}$  mylar foil by evaporating the  $60\ \mu\text{g}/\text{cm}^2$  gold with a 5 mm pitch. Each strip is connected with a 2 ns delay chip in between. The anode is made of the  $1.5\ \mu\text{m}$  mylar film coated with the  $60\ \mu\text{g}/\text{cm}^2$  gold in both sides. The timing signal is obtained from the anode.

The IC consists of an entrance window, a Frisch grid, and an anode. The entrance window is a  $4\ \mu\text{m}$  aluminized mylar attached to a stainless-steel honeycomb mesh with a 20 mm cell size and 0.15 mm in thickness. It sustains the pressure difference up to 150 torr. The window keeps the ground potential and electrically works as a cathode. The Frisch grid is made of a  $1.5 \times 1.5\ \text{mm}^2$  stainless-steel mesh with a line width of 0.1 mm. It is placed at 170 mm from the entrance

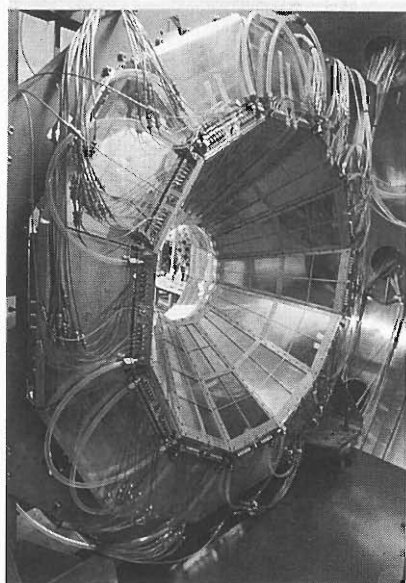


Fig. 1. Overview of the PPAC/ionization chamber.

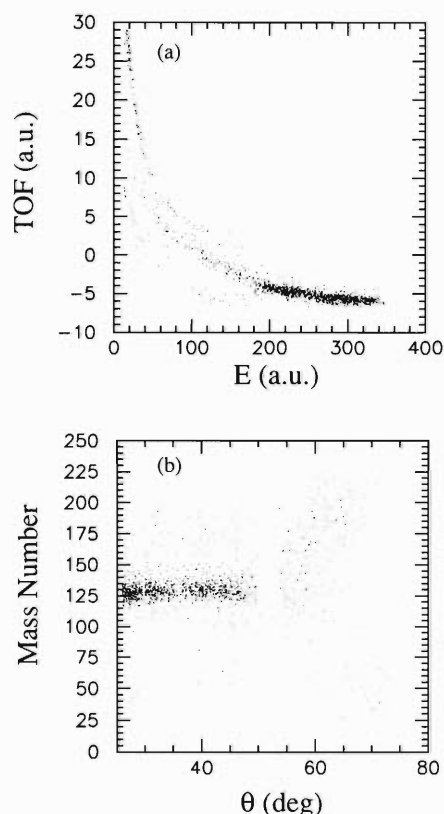


Fig. 2. TOF vs. E plot (a), and mass vs. theta plot (b), obtained from the  $^{129}\text{Xe} + ^{209}\text{Bi}$  reaction at 7 MeV/nucleon Xe beam.

window and the voltage 15–20% lower than the anode is applied. The anode is made of a printed circuit board and placed 10 mm apart from the grid. Field shaping grid is placed near the side wall of the chamber to form a homogeneous electric field between the entrance window and the Frisch grid.

The detector was tested with  $^{129}\text{Xe}$  beam at 7 MeV/nucleon delivered from the RIKEN Ring Cyclotron (RRC). The targets used were a self-supported  $^{209}\text{Bi}$  foil of 1 mg/cm<sup>2</sup> in thickness and a 1 mg/cm<sup>2</sup>  $^{232}\text{Th}$  foil backed with 16  $\mu\text{m}$  aluminum. The detector was irradiated by the elastically scattered  $^{129}\text{Xe}$  with energies from 6.2 MeV/nucleon (25°) to 2.5 MeV/nucleon (75°) for the case of  $^{209}\text{Bi}$  target and with energies from 4.7 MeV/nucleon to 2.1 MeV/nucleon for the case of  $^{232}\text{Th}$ . Both of the PPAC and the IC were operated with same isobutane gas but in different pressure; 5 torr for PPAC and 150 torr for IC. The applied anode-cathode voltages are 480 V for PPAC and 1500 V for IC.

A two-dimensional plot of TOF vs. energy deposit  $E$  in the IC obtained for  $^{129}\text{Xe} + ^{209}\text{Bi}$  reaction is shown in Fig. 2(a). TOF is obtained from the time difference between the PPAC signal and the RF signal of the RRC. The intensive locus at the large  $E$  and fast TOF is the elastically scattered  $^{129}\text{Xe}$ . Target-like products are also seen at the region of the small  $E$  and the slow TOF. The masses of detected particles were deduced from the TOF and  $E$  after correction of the energy loss of the particles in the PPAC and in the entrance window of the IC. The result is shown in Fig. 2(b) against the detection angles. The energy loss correction were 20% (25°, 6.2 MeV/nucleon) and 50% (80°, 2.5 MeV/nucleon) for  $^{129}\text{Xe}$ . The gap seen in Fig. 2(b) between 50° and 55° is due to the dead space of the detector. Elastically scattered  $^{129}\text{Xe}$  is clearly seen at 25–60°. In larger angles, elastic event was not observed since the grazing angle is 49° for the reaction. The mass resolution of 10% in FWHM is obtained for the  $^{129}\text{Xe}$ .

## A New Fluorescence Photon Detection System for Collinear Laser Spectroscopy

S. Ozawa, T. Ariga, K. Ikegami, N. Inabe, M. Kase, T. Katayama, T. Kubo, H. Okuno, I. Tanihata, M. Wakasugi, Y. Watanabe, Y. Yano, and A. Yoshida

In order to measure the atomic transition energy precisely in the high-energy and highly-charged ion beams, we have constructed an ultra-low background fluorescence detection system. We tested the system by measuring the D1 and D2 transitions in the Li-like  $^{11}\text{B}^{2+}$  ion (primary beam) accelerated up to 11.25 MeV/nucleon.

The experimental setup is shown in Fig. 1. The ion beam and the laser beam collide each other at the collision point. Excited ions emit fluorescence photons during the flight, and they are detected by the fluorescence detector. The fluorescence detector consists of a charcoal panel which can be cooled down to 18 K, optical filters, lenses, and photomultipliers. Since the cooled charcoal panel can make the vacuum of detector region two orders of magnitude higher than that at temperature of 298 K, the noise from the collisions between residual gas and ions was dramatically reduced. In fact, the noise signals from the second bunch of the ion beam completely disappeared at 18 K as shown in the timing spectra of Fig. 2. Since the laser beam collides with only the first bunch, the peak at the first bunch at 18 K contains fluorescence signals without noise. Dichroic filters and four movable collimators were placed to suppress the scattered light of laser beam. Small reflection rate of light of the charcoal panel was also effective to reduce the stray photons from laser beam.

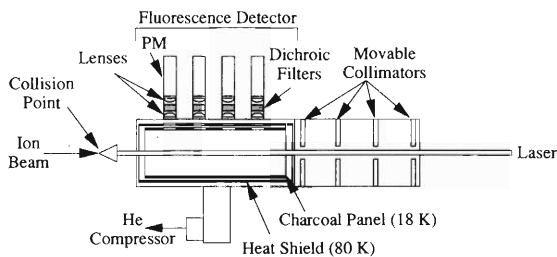


Fig. 1. The ultra-low background photon detection system.

The velocity of the ion beam was derived to be  $\beta = 0.15394(7)$  from the magnetic field strengths of RIPS. Taking a timing gate at the first bunch in Fig. 2, the fluorescence spectra due to the D1 and D2 transitions were obtained as shown in Fig. 3. The signal to noise ratio was about

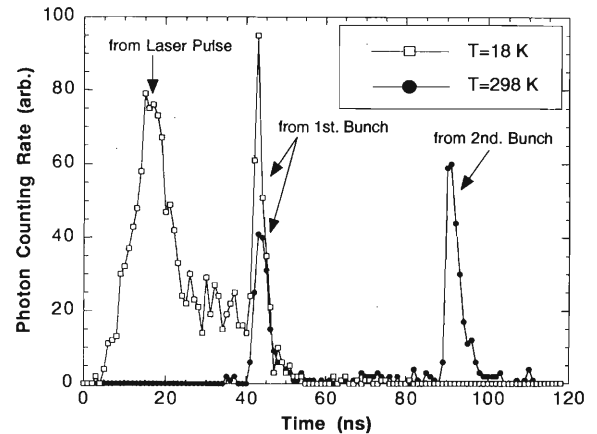


Fig. 2. The timing spectra measured with PM at the two different temperatures of the charcoal panel: 18 K with laser and 298 K without laser.

200. Transition energy of the D1 and D2 were estimated to be  $48346.8(33)$  and  $48380.0(33)$   $\text{cm}^{-1}$ , respectively. Both values are about  $12 \text{ cm}^{-1}$  smaller than the NBS values.<sup>1)</sup> Those differences are due to errors in the wavelength calibration. The counting rate of the fluorescence was found to be  $3.3 \times 10^{-6}$  counts/ion, which is more than forty-times better than the last experiment.<sup>2)</sup>

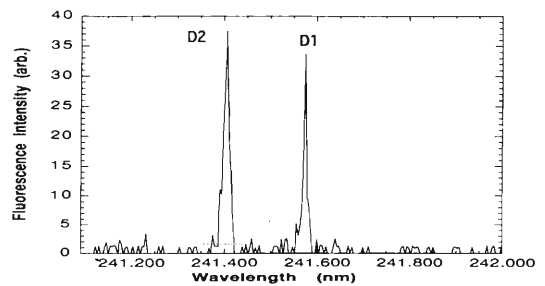


Fig. 3. The fluorescence spectra due to the D1 and D2 transitions.

### References

- 1) C. E. Moor: Atomic Energy Levels, NBS, Washington D.C. USA, (1949), p. 19.
- 2) M. Wakasugi: Phys. Scr. **73**, 70 (1997).

## Final Calibration of Cosmic Ray Heavy Ion Telescope for First Brazilian Scientific Satellite

T. Kohno, H. Kato, H. Miyasaka, and K. Nagata

An international collaboration of cosmic ray heavy ion observation with the first Brazilian scientific satellite<sup>1)</sup> is now being proceeded. It is planned to be launched around May 1998 by Chinese rocket, Long March. Our Japanese side is in charge of detector telescope including charge sensitive pre-amplifier and the detector bias voltage supply. The Naval Research Laboratory (NRL) of the United States is in charge of analogue circuit including ADC, and the Institute Nacional de Pesquisas Espaciais (INPE) of Brazilian side is in charge of digital circuit and interface for the satellite system. This instrument is named as ORCAS (Observações de Raios-Cósmicos Anômalos e Solares na Magnetosfera in Portuguese) that means observation of anomalous and solar cosmic rays in the magnetosphere.

We have two telescopes for ORCAS, one (named PRE) is for electron, proton and alphas with a small geometric factor; and another (named MAIN) for the heavy ions from He to Ne (high gain mode) and from C to Fe (low gain mode). But, we report here only the MAIN telescope due to small space of paper. The whole electronics for the flight model were gathered to RIKEN from Brazil and US this time. The three parts of telescope, analog circuit, and digital circuit were connected and tested. The cross sectional view of the MAIN telescope is shown in Fig. 1.

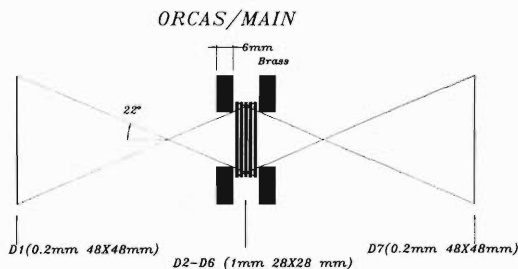


Fig. 1. Cross sectional view of the MAIN telescope.

We performed the final calibration test with  $\alpha$  and  $^{40}\text{Ar}$  beams. Using Al plates having various thicknesses in front of the telescope, we took data of ADC output in list mode for the beam with various energies. The beam energy was 45 MeV/nucleon and 95 MeV/nucleon for  $\alpha$  and Ar, respectively.

We show in Fig. 2 an example of pulse height distributions in each detector. The beam comes into D1 and stopped at D5. The detector thicknesses are shown in Fig. 1. We can see an increase of the pulse height after D1 due to decreasing particle energy.

Shown in Fig. 3 is the  $\Delta E$ -E scatter plots for Ar

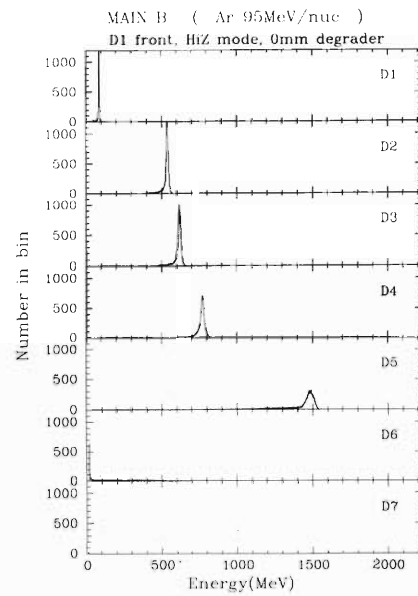


Fig. 2. Pulse height distributions in each detector. Ar-beam enter into D1 and stopped at D5. No Al plate in this case.

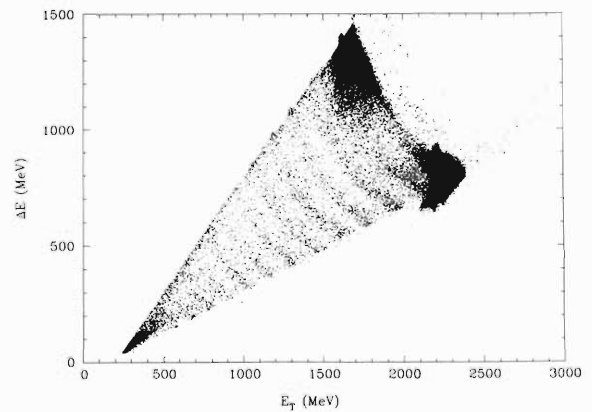


Fig. 3.  $\Delta E$ -E scatter plots for Ar-beam. Various Al thickness data are included.  $\Delta E$  (ordinate) means the energy deposition in a detector just before the stopped detector, and total E (abscissa) is sum of  $\Delta E$  plus energy deposition in the stopped detector.

beam. We can see tracks of the secondary elements produced by the nuclear fragmentation in the Al plate.

### References

- 1) A. Turtelli et al.: Proc. 24th Int. Cosmic Ray Conf., Vol. 4 (SH session), Rome, Sept., 1995, p. 1275.

## Performance Study of Radiation Detectors for Spacecraft

T. Goka, H. Matsumoto, T. Omoto, T. Kohno, Y. Muraki, K. Masuda, Y. Matsubara, I. Imaida, T. Sako, H. Tsuchiya, K. Taguchi, I. Tanaka, M. Fujii, and M. Nakazawa

The contribution of neutrons to the radiation exposure of astronauts has largely remained as an ignored problem. The problem of detecting neutron in space is difficult due to the intense charged particles (proton, etc.). In order to detect the solar neutron in the mixed field of neutrons and charged particles, we have developed a scintillation fiber detector. A proto-type of a scintillation fiber detector was tested with accelerator in 1996–1997. Signals from scintillation fibers are read by a system of multi-anode photomultipliers and CMOS LSI<sup>1)</sup> which consumes electric power very little.

**Experiment.** The purpose of this experiment was to confirm response of the scintillation fiber detector by proton. The energy of an incident neutron was able to determine by measuring the path lengths of the track of a recoiled proton and from the known incident direction. The test detector prepared for the experiment was a cubic arrangement of scintillation fibers with a volume of 1000 cm<sup>3</sup>. Each unit of scintillation fibers (16 × 16) have a width of 3 mm and a height of 3 mm as shown in Fig. 1. Two multi-anode photomultipliers (MAPMT, Hamamatu 4140-20) were used to read fiber's signal. Each MAPMT has 256 channels. Signals from outermost fibers facing toward the beam are used to veto charged particles in case neutrons are measured. E3 facility of Ring Cyclotron at RIKEN was used for the experiment in December 1996 and July 1997. The ion species of the beam were H<sub>2</sub><sup>+</sup> (H<sub>2</sub><sup>+</sup> → H<sup>+</sup> + H<sup>+</sup>). The energy of the beam was 135 MeV/n in 1996 and 110 MeV/n in 1997. One set of measurement was to measure the track lengths of protons in different energies. We changed the beam energy by using 20 to 70 mm thickness Aluminum (Al) degrader. A 135 MeV (110 MeV) proton dissipates all of its energy in the 70 mm (60 mm) thickness degrader, and the irradiation particles to reach detector are neu-

tron only. We had confirmed neutron track on above configuration. Another test was to detect images of neutrons and determine their energies

**Test Results.** There are two orthogonal planes on which tracks of particles are projected. In each measurement, an ADC value at each fiber is recorded. In order to determine the particle, the tracks of isolated pixels without any adjacent signals are removed. An example of neutron event after subtraction of such isolated pixels is shown in Fig. 2. The energy of incident proton was determined using their track lengths. The energies thus determined were compared with these expected as a function of the thickness of Al. In Fig. 3 preliminary results are plotted together with expected values. Based on the results of the test experiment at RIKEN in 1996 and 1997, improvement of the detector, data taking system, and analyses methods are in progress.

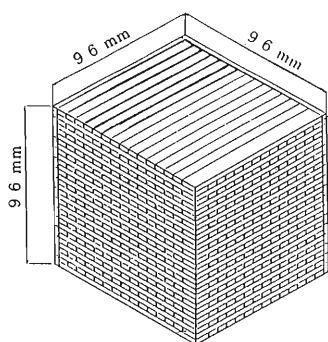


Fig. 1. Structure of scintillation fiber detector.

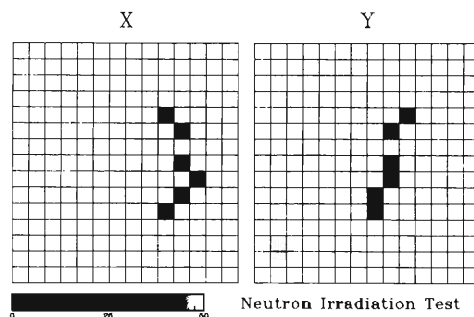


Fig. 2. An example of neutron event after subtraction of isolated pixels.

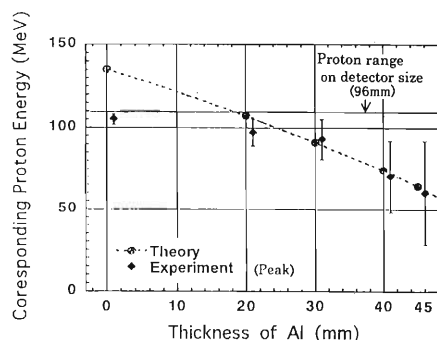


Fig. 3. Preliminary results of measurement of proton range distribution.

### References

- 1) H. Ikeda et al.: IEEE Trans. Nucl. Sci. 38, 135 (1991).

## Fabrication of the Muon Magnet for the RHIC SPIN Project

T. Ichihara, H. En'yo, Y. Goto, N. Hayashi, K. Imai, A. Masaïke, N. Saito,  
T.-A. Shibata, Y. Watanabe, and M. Ishihara

Muon magnet is one of the detector magnets to be installed in the PHENIX detector in order to analyze the momenta of muon and muon-pair with high resolution. RIKEN is taking a role of fabricating the Muon Magnet South (MMS). It is about 8 m tall and weighs approximately 200 metric tons.

The contract between RIKEN and Mitsubishi Electric Cooperation (Melco) was initiated in March 1996 for the MMS fabrication. In the previous report, we introduced the basic design concept of the MMS.<sup>1)</sup>

Preliminary design review (PDR) for the MMS was performed in May 1997 at the Lawrence Livermore National Laboratory (LLNL). Basic design concept was approved at the PDR. The detailed design work for the fabrication started after the PDR. Final design review (FDR) was carried out in July 1997 at the Brookhaven National Laboratory (BNL). At the FDR, a small modification was required to keep enough rooms for tracking detectors. This requirement was resolved by changing the configuration of the coil bus flags.

The construction of the MMS was completed in February 1997 at Melco Kobe Works.<sup>2)</sup> The inspection of the magnet was done on 26th and 27th in February 1997 with the attendances of RIKEN, Kyoto Univ., and LLNL. Figure 1 shows the photograph of the MMS during the inspection. Following items were inspected or tested at the Kobe Works.

### For Coils

- ① Pressure and leak tests
- ② Resistance check
- ③ Measurement of the insulation resistance
- ④ Inductance test
- ⑤ Impulse test
- ⑥ Dimensional check and assembly check
- ⑦ Measurement of the pressure drop
- ⑧ Dielectric test
- ⑨ Dimension check
- ⑩ Magnetic field measurement

### For Steels

- ① Lower plate level and back plate verticality
- ② Back plate flatness
- ③ Back plate center height
- ④ Piston head center height
- ⑤ Difference between piston head and back plate center
- ⑥ Difference between piston root and back plate center
- ⑦ Relative position of teacup to back plate
- ⑧ Relative position of lampshade panels to piston
- ⑨ Relative position of lampshade panels to back plate
- ⑩ Appearance
- ⑪ Inspection of parts

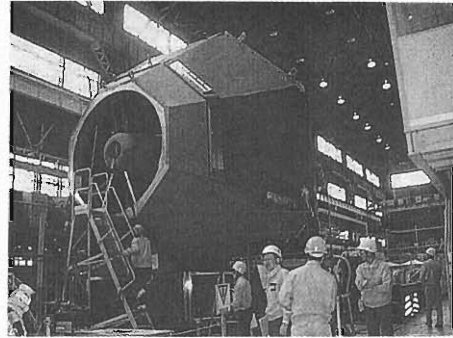


Fig. 1. Photograph of the MMS during the inspection at Melco Kobe Works. (Photo taken on 26th Feb., 1997).

No problem was found at the inspection. After the inspection, the whole magnet components were packed and transported to the BNL by ship. All the MMS components arrived at the BNL in April 1997 without damage. The assembly of the MMS has been started at the PHENIX experimental hall at the BNL in November 1997. Figure 2 shows the MMS during the assembly at the BNL. After the completion of the assembly, the mapping of the magnetic field is scheduled.

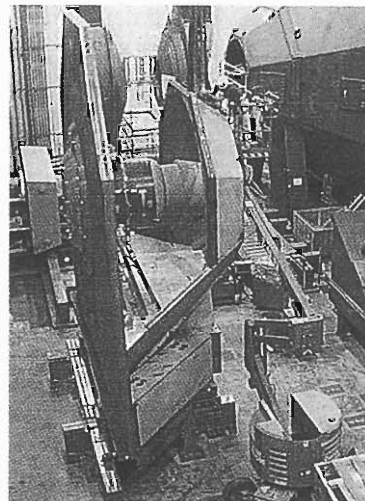


Fig. 2. Photograph of the MMS during the assembly at the PHENIX experimental hall at the BNL (Photo taken on 25th Dec., 1997).

### References

- 1) T. Ichihara et al.: RIKEN Accel. Prog. Rep. 30, 155 (1997).
- 2) see for <http://www.rarf.riken.go.jp/rarf/rhic/mms/>

## Plan of Computing Facility for RHIC Spin Project

Y. Watanabe, T. Ichihara, N. Saito, A. Taketani, and M. Ishihara

The RHIC<sup>1)</sup> (Relativistic Heavy Ion Collider) spin project<sup>2,3)</sup> is going now well into the latter half of its construction phase. One of the biggest remaining issues is the method and facility to cook data from the experimental setup.

PHENIX<sup>4)</sup> (a major detector of RHIC) is the most important detector to investigate the RHIC Spin physics, and is designed to produce 20 MBytes/s of data. The data will accumulate more than 200 TBytes in a year. It is not trivial issue to store and analyze such a big volume of data. On the other hand, the RHIC has other three experimental detectors (STAR,<sup>5)</sup> PHOBOS,<sup>6)</sup> BRAHMS<sup>7)</sup>); they have the same problem. The total amount of whole RHIC's data will reach more than 1,500 TBytes in a year. Therefore, a RHIC collaboration intends to assemble a big computing facility named RCF (RHIC Computing Facility)<sup>8)</sup> to be placed at BNL (Brookhaven National Laboratory).<sup>9)</sup>

Some important numbers which describe a planned capability of the RCF are following:

Total CPU Power	~ 20,000 SPECint95
Fixed disk	40 TBytes
Tape robots capacity	250 TBytes
Speed of data archive	200 MBytes/s
Total capacity of tapes	1,700 TBytes / year

These numbers indicate that the RCF will consist of more than 1,000 of recent fastest workstations, more than 1,000 of recent largest fixed disks, and a biggest tape storage system in the world. RCF will consume more than 30,000 tapes in a year. Such incredibly big numbers show that the RCF is one of the biggest computing facility in the world. However, the capability is expected not enough yet. For example, the tape robots can handle only 1/7 of the tapes produced in a year.

The RHIC Spin Project promoted by RIKEN, wishes earnestly to operate a computing facility (PHENIX-CC-J<sup>10)</sup>) which has similar capability of the

RCF, in order to make the physics outputs definite. The actual scale of the facility is currently under consideration. On the other hand, the capability will cover not only analyses of the data from detectors, but also simulations of physics modeling, detector responses, etc.

A key issue to operate such a big facility efficiently is to develop technologies which make many CPUs (~ 100) work coherently. Making the prototype for this purpose is an R&D work of the next Japanese fiscal year (JFY1998).

Another key issue that we should pay special attention is a method of data transfer between U.S and Japan. It is not trivial to transfer data more than 100 TBytes in a year. The network connection over the Pacific Ocean may be too expensive. Transporting of tapes by airplane is another possibility. However, it is not easy to put data which are distributed in the robots of the RCF into a set of sequential tapes. We need a special data duplicating facility to be attached to the RCF. We will start an R&D for such a facility, too in the early JFY1998.

We acknowledge Prof. Hideki Hamagaki, Prof. Jyunsei Chiba, and Prof. Ryugo Hayano for their close discussions with us.

### References

- 1) <http://www.rhic.bnl.gov/>
- 2) H. Akikawa et al.: RIKEN Accel. Prog. Rep. 31, 52 (1998).
- 3) <http://www.rarf.riken.go.jp/rarf/rhic/>
- 4) <http://www.rhic.bnl.gov/phenix/>
- 5) <http://www.rhic.bnl.gov/STAR/>
- 6) <http://phobos-srv.mit.edu/>
- 7) <http://www.rhic.bnl.gov/export1/brahms/WWW/brahms.html>.
- 8) <http://www.rhic.bnl.gov/html/RDG.html>
- 9) <http://www.bnl.gov/>
- 10) <http://www.rarf.riken.go.jp/rarf/rhic/rhic-cc-j>

## Factory Plan for PHENIX Muon Identifier

A. Taketani, K. Kurita, M. Ishihara, T. Ichihara, Y. Watanabe, N. Saito,  
N. Hayashi, H. En'yo, Y. Nakada, H. Sato, K. Imai, H. Torii,  
T.-A. Shibata, T. Sakuma, E. Taniguchi, and Y. Mao

A progress of the two PHENIX muon identification detector (MUID) in the fabrication factories is summarized in this paper.

The muon identification is quite important for RHIC spin project. For example, W boson may have a flavor-tagged spin information.<sup>1)</sup> The W boson can be identified easily with a high Pt muon. We will cover the forward and backward regions of PHENIX detector with so called MUID panels. The covered azimuthal angle is from 10 to 35 degree.

There are two differently size MUID panels to cover the MUID fiducial volumes. We need 20 small panels [2.9 m(H)  $\times$  4.4 m(V)] and 40 large panels [5.4 m(H)  $\times$  5.6 m(V)]. The small panels are assembled in KEK, and the large panels are assembled in Brookhaven National Laboratory. We will start the panel production in Dec. '97.

The two Iarocci tubes<sup>2)</sup> are staggered by half a cell interval to maximize the detection efficiency. These tubes are taped to the both sides of the Al mid-plane. The tubes are oriented horizontally in the front layers and vertically in the back layers. The Al frame supports the mid-plane. The tubes are protected from outside by Al cover plates. One end of the tube is connected to the readout electronics.

The tubes are produced at an Italian manufacture and shipped to our factories in Japan and USA. The received tubes are checked one by one, and only the ones which meet our criteria are installed on the panels.

At first the tubes are checked for their physical size. The resistance and capacitance between anode wire and ground wall are measured. Then, the gas flow system is connected to the tubes, and gas leakage is measured with manometer. The 5 kV high voltage (HV) is applied to the wire after replacing the gas volume with the working gas. After applying the HV for 5 days, the preamplifiers are connected to the wire and tested with cosmic rays. The pulse height and single count rate are measured. We designed the quality assurance (QA) setup to emulate the real MUID operation in experiment.

The frame of panel and mid-plane are assembled on a flipper table. A double-sided tape sticks first two tubes together with 5 mm staggering. Then the pair of tubes is stuck to the mid-plane. This procedure is

continued until the assembly side of the mid-plane is filled with tubes. Next, the Gas tubing, HV supply and readout electronics are connected. The copper sheet for shielding is placed on the top of the tubes covering the whole area. The Al cover-plates are anchored to the frame for screening. Once the front side of the panel is completed, the single count rate from cosmic ray is measured to check the integrity of the assembled layer.

The panel on the flipper table is set vertically with the tabletop that serves as a strong back of the panel. It is done so only when we can handle the panel by itself not worrying about the sagging of the mid-plane. The panel is detached from the table at this point and flipped sidewise. Now the completed side faces to the table. The panel is anchored to the table again and lay down flat. The backside of the panel is completed in the same manner described above.

The small panel can be transferred horizontally with another simple support structure to the storage place in the same factory. They are packed in well-sealed plastic bags, which protect the panels from humid air, and shipped by sea.

All of the small panels are shipped to the BNL MUID factory and they are tested with cosmic ray before the installation in the experimental hall.

All the small and large panels are transported from the BNL MUID factory with a removable strong back flat on a trailer to the experimental hall. Once a panel and the strong back arrive in the experimental hall, they are lifted by the main crane and set vertically. The strong back is set on a stand inside the hall. Then the crane is hooked to the panel again, and the panel is detached from the strong back. The panel is positioned by the crane and slid into a steel plate's gap from the side. 10 steel plates [13 m(H)  $\times$  10 (m)(V)] are already installed in the experimental hall 5 in the south and 5 in the north which consists 10 gaps in total. We plan to fill those gaps with 60 panels by the end of September 1998.

### References

- 1) H. En'yo et al.: RIKEN Accel. Prog. Rep. **30**, 34 (1997).
- 2) Y. Mao et al.: RIKEN Accel. Prog. Rep. **30**, 36 (1997).

## Design of Proton Polarimeter for AGS-E925

H. En'yo, Y. Goto, N. Hayashi, T. Ichihara, Y. Nakada, N. Saito,  
H. Sakai, H. Sato, H. Okamura, and T. Wakasa

The acceleration of the polarized proton beam up to 250 GeV/c is one of the important parts of the RIKEN RHIC/Spin project.<sup>1)</sup> For the operation of the accelerator and to extract the physics results an appropriate polarimeter is required. The currently designed polarimeter utilizes asymmetries for inclusive pion production in forward region in  $pp$  or  $p$ - $N$  collision.

The experiment AGS (Alternating Gradient Synchrotron) E925<sup>2)</sup> plans to measure those asymmetries of the charged pion production in  $p^\uparrow p$  or  $p^\uparrow$ -Carbon reaction at 23 GeV/c which is AGS-to-RHIC injection momentum, where  $p^\uparrow$  refers to transversely polarized proton. Its precise data will be a base for the future polarimeter. The experiment consists of the pion detection part and  $pp$  elastic collision part. This report will concentrate on the second part where we have contributed. The elastic arm provides an accurate measurement of the extracted beam polarization for the inclusive pion and a cross-check of the AGS internal polarimeter. It measures the left-right cross-section asymmetry of elastic reaction  $p^\uparrow p \rightarrow pp$  at momentum transfer squared  $-t = 0.1 - 0.2$  (GeV/c)<sup>2</sup>. Since the analyzing power in this region is known within 10% of error, the polarization of the beam can be obtained.

Figure 1 shows a double-arm telescope of the elastic arm set up. Each arm has four backward counters named as  $B1$ ,  $B2$ ,  $B3$  and  $B4$  from the target and corresponding forward counters  $F$ . ( $B1$  denotes  $BL1$  and/or  $BR1$ , and  $B2$ ,  $B3$  and  $B4$  denote similarly.  $F$  represents  $FLU \oplus FLD$  and/or  $FRU \oplus FRD$ ). The emission angle of recoil protons is around  $78 \pm 2$  degree. Their velocity is in the range of  $\beta \simeq 0.32 \sim 0.45$  and the momentum varies  $150 \sim 300$  MeV/c with its scattering angle. Time-of-flight ( $TOF$ ) between  $B1$  and  $B2$ , about 1 m in distance, is useful to separate recoil protons from  $\beta \simeq 1$  particles. The wedge shaped aluminum plate compensates the angle dependence of the energy, so that the recoil proton is stopped in the thick counter  $B3$ ; whereas the larger momentum particles, mostly pions, hit the veto counter  $B4$ .  $F$  counters de-

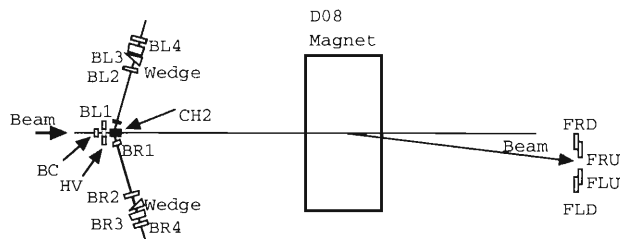


Fig. 1. A schematic drawing of the E925 elastic arm setup.  $F$  counters are about 11 m from the target. D08 is a spectrometer magnet for the pion arm.

tect the forward proton. Beam halo veto counter ( $HV$ ) and beam defined counter ( $BC$ ) were also shown in the figure.

The system had been installed and checked with the unpolarized proton beam during spring 1997.  $CH_2$  target was used for the elastic arm. Since our test was parasitic run, the beam condition was not optimized. The beam intensity was three orders of magnitude lower than requested. Even with this condition, we observed about 130 elastic events with the backward-forward coincidence. It was only about 15% of the estimated numbers, however the simulation studies were performed and it was shown that this discrepancy was explainable by the large beam divergence. The beam divergence should be less than 1 mrad to maintain reasonable acceptance. Without wedge set-up,  $B3$  ADC and  $TOF$  have very strong correlation and it was reproduced by the simulation (Fig. 2). This is a strong sign to show the validity of our system. Figure 3 shows the case with the wedge setup, which was also reproduced well by the simulation.

Overall, the performance of the system was satisfactory in the limited beam condition, and the system is ready for the polarized proton run.

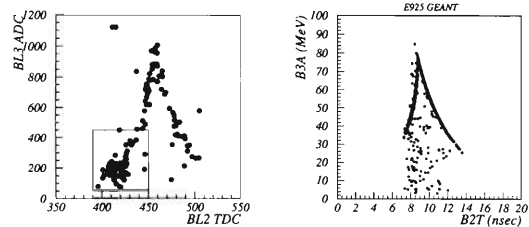


Fig. 2.  $B3ADC$ - $B2TDC$  scatter plots without the wedge ( $B1 \otimes B2 \otimes B3$  trigger). Left one is experimental data and right is a simulation result. The region indicated by a box on the left figure includes many background particles, which was not simulated.

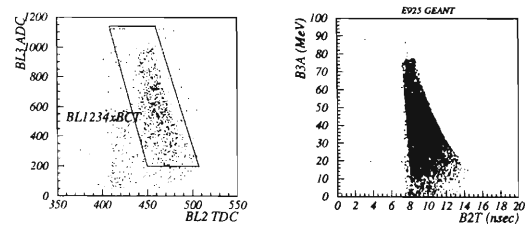


Fig. 3.  $B3ADC$  vs  $B2TDC$  scatter plot of data (left) and the simulation (right).

### References

- 1) H. En'yo et al.: RIKEN Accel. Prog. Rep. 30, 33 and 34 (1997).
- 2) K. Krueger et al.: ANL-HEP-TR-96-71 (1996).



## 6. Material Analysis



## RBS Study of Na Implanted Polystyrene

A. Nakao, Y. Suzuki, M. Iwaki, and E. Yagi

Polystyrene (PS) is one of the candidate materials for medical use, like cell culture materials. Cell adhesion control to polystyrene surface by ion implantation was observed.<sup>1)</sup> One of the most important factors for cell adhesion is considered to be wettability.

We have investigated the improvement in the wettability by ion implantation with various ion species, He, N, O, Ne, Na, Ar, Kr, etc, and observed that the Na-implantation was most effective. The contact angle of water for the surface of Na-implanted PS decreases to zero with increasing Na fluence, at low implantation energy.<sup>2)</sup> In contrast, the PS surface implanted with Ne, at the same implantation energy as in the case of Na, showed the contact angle of water higher than 70 degree, independently of implantation dose and irradiation energy.

For reduction of the contact angle of water by ion implantation, both irradiation defects by the implantation and implanted species themselves would contribute more or less. However, the result on the Ne implantation suggests that the former contribution is not large, because the implantation with Ne ions, having approximately the same mass as Na ions, should produce approximately the same irradiation damage. In addition, it was observed by the X-ray photoelectron spectroscopy (XPS) that the decrease of the contact angle of water in the Na-implanted PS is caused by the presence of the implanted Na atoms near or on the surface of PS.<sup>3)</sup> To understand the process for Na atoms to appear near or on the PS surface, as the first step, Na-implanted layers of PS have been investigated by Rutherford backscattering spectroscopy (RBS).

Na ions were implanted into PS at an energy of 50 keV with various fluences between  $1 \times 10^{16}$  to  $1 \times 10^{17}$  ions/cm<sup>2</sup> at room temperature. RBS spectra were measured at room temperature using a 1.5 MeV He<sup>+</sup> beam at a scattering angle of 168 degree. Figure 1 shows RBS spectra for fluences of  $1 \times 10^{16}$ ,  $3 \times 10^{16}$ ,  $5 \times 10^{16}$ , and  $1 \times 10^{17}$  ions/cm<sup>2</sup>. Carbon, oxygen, and sodium were observed in the PS surface layers. Calibration of energy was performed by measuring standard samples, gold and copper coated PS. The surface edges of C, O and Na are indicated by arrows in Fig. 1. For the fluence of  $1 \times 10^{16}$  ions/cm<sup>2</sup>, the depth profile of Na atoms in the PS shows a Gaussian-type distribution. With increasing fluence, the Na atoms become concentrated in the surface layer and the distribution starts deviating from the Gaussian distribution. Spec-

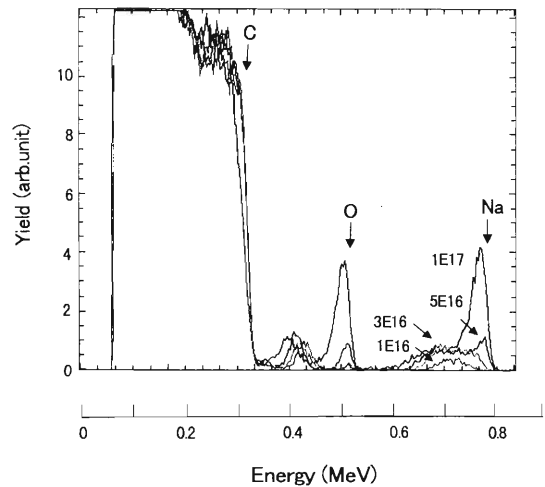


Fig. 1. RBS spectra of the PS samples implanted with various fluences of Na ions between  $1 \times 10^{16}$  to  $1 \times 10^{17}$  ions/cm<sup>2</sup> at the implantation energy of 50 keV at room temperature.

tra for oxygen are found to have two peaks. The peak in the deep layer is considered to have originated from the O atoms implanted accidentally during the Na implantation.

From these results, the process to give rise to a change in the depth distribution of Na and O atoms might be considered as follows: As the fluence increases, the concentration becomes so high that the Na atoms move out toward the surface to interact with oxygen in the residual gas and/or atmospheric oxygen. As a result, the Na atoms are accumulated in the surface region together with O atoms. Similar behavior was observed for the Li and K atoms implanted in glassy carbon, i.e., Li and K atoms were found to become concentrated near the surface of glassy carbon.<sup>4)</sup>

### References

- 1) Y. Suzuki, M. Kusakabe, J.-S. Lee, M. Kaiara, M. Iwaki, and H. Sasabe: Nucl. Instrum. Methods Phys. Res. B **65**, 142 (1992).
- 2) Y. Suzuki, M. Kusakabe, and M. Iwaki: Nucl. Instrum. Methods Phys. Res. B **80/81**, 1067 (1993).
- 3) A. Nakao, Y. Suzuki, and M. Iwaki: J. Colloid Interface Sci. (to be published in 1998).
- 4) K. Takahashi, K. Yoshida, and M. Iwaki: Electrochim. Acta. **35**, 1279 (1990).

## Chemical State Analysis of Third Period Elements in Atmospheric Air by High-Resolution PIXE

K. Maeda, K. Hasegawa,\*<sup>1</sup> A. Tonomura, M. Maeda,\*<sup>2</sup> and H. Hamanaka\*<sup>1</sup>

Fine structures of X-ray emission spectra reflect the chemical environments of atoms in target materials. Particle induced X-ray emission (PIXE) measurements in non-vacuum, especially in air, is quite suitable for biological, environmental and archaeological substances. We have developed a compact crystal spectrometer system for non-vacuum high-resolution PIXE analysis.<sup>1)</sup> The system has been designed to detect the low-energy X-rays of less than 3 keV effectively. This is because the third period elements (such as Na, Mg, Al, ...) with  $K$  X-ray energies of 1–3 keV play important roles in biological, environmental and archaeological substances. In the present report we demonstrate the ability of the system for *in situ* chemical state analysis of the third period elements, measuring  $K$  X-ray spectra of Al, Si, P and S in various compounds.<sup>2)</sup>

We adopted a multichannel-type crystal spectrometer combined with a position-sensitive proportional counter. A target sample was placed in the air and bombarded with a 2.1 MeV proton beam of 3 mm-diameter. Measured samples were an Al metal, a sintered alumina, a silicon crystal (c-Si), a fused quartz ( $\text{SiO}_2$ ), powders of chemicals of SiC,  $\text{Si}_3\text{N}_4$ , SiO, BP,  $\text{CaHPO}_4 \cdot 2\text{H}_2\text{O}$ ,  $\text{Na}_2\text{SO}_4$  and  $\text{Na}_2\text{SO}_3$ , soils of Flaming Mountains in China, powders of diatom frustules, a jewel of opal, and a fragment of a fossil wood. The sample was set on an aluminum target holder and the proton beam current was monitored from the Al holder. For insulator samples, a small bridge made from a carbon sheet was put between the Al holder and the target surface near ( $< 5$  mm) the beam spot.

Examples of measured spectra are shown in Figs. 1 and 2. There is some uncertainty in the channel number of each spectrum depending on the target positioning. The maximum value was estimated to amount to  $\pm 2$  channels corresponding to  $\pm 0.04^\circ$  in  $\theta$ . Chemical shifts of the main peak (denoted by  $K\beta_1$ ) of  $K\beta$  spectra are beyond this uncertainty.

The low-energy satellite  $K\beta'$  is caused by molecular orbital splittings due to formation of chemical bonds. The energy difference between the  $K\beta'$  and  $K\beta_1$  indicates the partner atom of the X-ray emitter. The Si  $K\beta_1$ -Si  $K\beta'$  energy differences are about 14, 11 and 9 eV for the Si-O compounds,  $\text{Si}_3\text{N}_4$  and SiC, respectively. In the spectrum of SiO the  $K\beta_1$  line consists of two peaks. The higher-energy peak is attributed to  $\text{Si}^0$  atoms and the lower-energy one is attributed to  $\text{Si}^{4+}$  atoms.

In analogy to the Si  $K\beta$  spectra of the Si-O compounds, the  $K\beta'$  satellite is again observed in the S  $K\beta$  spectra of  $\text{Na}_2\text{SO}_4$  and  $\text{Na}_2\text{SO}_3$  at the energy region 14 eV lower than the  $K\beta_1$  line. The high-energy

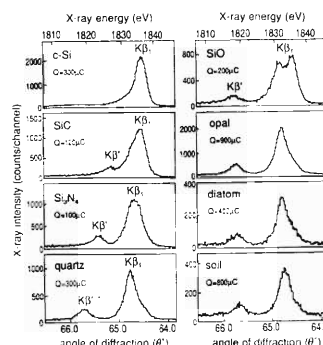


Fig. 1. Si  $K\beta$  spectra measured with an InSb (111) crystal. Q is the accumulated beam charge.

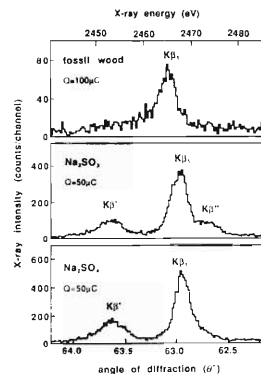


Fig. 2. S  $K\beta$  spectra measured with a NaCl (200) crystal. Q is the accumulated beam charge.

shoulder ( $K\beta''$ ) of the S  $K\beta_1$  line is useful to distinguish S in  $\text{SO}_3^{2-}$  from S in  $\text{SO}_4^{2-}$ . As an attempt of practical application of the system, we measured the S  $K$  X-ray spectra for a fossil wood of 400,000 years old,<sup>3)</sup> which contained 2–5% of S. As shown in Fig. 2, the  $K\beta'$  satellite of indicating the presence of oxygen compounds like  $\text{SO}_4^{2-}$  or  $\text{SO}_3^{2-}$  is not detected in the S  $K\beta$  spectrum of the fossil wood. The  $K\beta$  spectrum rather resembles that of sulfides ( $\text{S}^{2+}$ ). The S atoms in the fossil wood, at least in its surface layer, seem to be present as sulfide but not as sulfate nor sulfite. Thus, the chemical environment of the minor element, S, in a small area ( $\sim 10$  mm<sup>2</sup>) was successfully determined by using the newly developed in-air high-resolution PIXE system.

### References

- 1) K. Maeda et al.: Nucl. Instrum. Methods Phys. Res. B, in press.
- 2) K. Maeda, K. Hasegawa, H. Hamanaka, and M. Maeda: Nucl. Instrum. Methods Phys. Res. B, in press.
- 3) N. Kagemori: J. Geosci. Osaka City Univ. **16**, 11 (1973).

\*<sup>1</sup> College of Engineering, Hosei University

\*<sup>2</sup> Tokyo University of Fisheries

## Improvement in the Detection Limits of ERDA Using a Time-of-Flight Detection

W. Hong, S. Hayakawa,\* K. Maeda, S. Fukuda, K. Kimura, Y. Gohshi,\* and I. Tanihata

An advantage of the Time-Of-Flight Elastic Recoil Detection Analysis (TOF-ERDA) is the ability of detection of trace elements with extremely small background. If the large background peak of a heavy matrix in the energy spectrum was eliminated using a TOF-energy plot, the detection limit of light element is much lower than that obtained by the conventional ERDA.

A detection limit ( $L_D$ ) is defined by<sup>1)</sup>

$$L_D = 2.71 + 4.65\sqrt{Y_B} \quad (1)$$

at the 95% confidence level, where  $Y_B$  is the count of the background. To convert this detection limit in the unit of counts to the amount of element, or in this case the areal density, an additional consideration is necessary. The atomic density ( $N_D$ ) of the target element at the sample surface is calculated by

$$N_D = \frac{N[\varepsilon_0] \cos \alpha}{\sigma_0 \delta \eta \Omega Q} L_D, \quad (2)$$

where  $N$  is the number of the sample molecules per unit volume,  $[\varepsilon_0]$  the stopping cross section factor of the sample,  $\sigma_0$  the differential cross section of target atom at the sample surface,  $\delta$  the energy corresponding to one channel,  $\eta$  the detector efficiency,  $\Omega$  the solid angle,  $Q$  the number of the probe ions, and  $\alpha$  the incident angle of the beam measured with respect to the normal to the surface.

<sup>40</sup>Ar ions accelerated to 41.5 MeV by the RIKEN linac (RILAC) were used as probe ions. The beam size was 2 mm $\phi$ . The distance from the collimator to the sample was 30 cm. The incident and detector angles were 55° with respect to the beam direction. A SSB (Silicon Surface Barrier) detector was employed to measure the energy of recoil particles and to obtain a start signal. A time of flight detector was composed of two MCPs (Micro Channel Plate), and a 10  $\mu\text{g}/\text{cm}^2$  carbon film was used to obtain the stop signal. More details concerning the experimental setup are described in a previous publication.<sup>2)</sup> A SiO<sub>2</sub> film of 240 nm in thickness on a silicon wafer was used to evaluate the detection limits of the oxygen and silicon.

The energy spectrum of SiO<sub>2</sub> obtained by conventional ERDA is shown in Fig. 1(a). An oxygen peak appears on a silicon peak, which is the background of the oxygen peak. The separated peaks of oxygen and silicon by TOF-ERDA are shown in Fig. 1(b). There is no background from the heavy element under the oxygen peak any more.

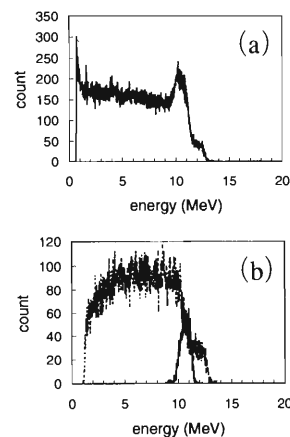


Fig. 1. Energy spectrum of a SiO<sub>2</sub> sample measured by (a) conventional ERDA and (b) TOF-ERDA. The dashed curve represents the Si peak, and the solid curve the O peak. The incident particle is Ar accelerated to 41.5 MeV.

The backgrounds at the surface of the oxygen and silicon peaks were evaluated from Fig. 1 by averaging the background values of 10 channels near to the surface channel. In Table 1, the results of a calculation using Eqs. 1 and 2 are summarized along with the experimental conditions. There are differences in the definitions of detection limit used by various authors. Therefore, the detection limit of the oxygen obtained by the TOF-ERDA in present work is reasonable compared to the reported value of 0.3 at% by D. K. Avasthi et al.,<sup>3)</sup> and are valid for most applications.

Table 1. The detection limits of the oxygen and silicon in a SiO<sub>2</sub> sample obtained by TOF-ERDA and ERDA.  $Y_B$  is the background count of the sample surface.  $L_D$  is the detection limit in count calculated by Eq. (1).  $N_D$  is the detection limit in the atoms/cm<sup>2</sup> calculated by Eq. (2). The confidence level is 95%.

Probe	$E_0$ (MeV)	Sample	$\eta\Omega Q$ (10 <sup>7</sup> )	Target	$\sigma$ (10 <sup>-24</sup> )	TOF-ERDA			Conventional ERDA		
						$Y_B$	$L_D$	$N_D$ (10 <sup>13</sup> )	$Y_B$	$L_D$	$N_D$ (10 <sup>13</sup> )
<sup>40</sup> Ar	41.5	SiO <sub>2</sub>	124	O	4.05	0.5	6.00	6.62	31	28.5	31.4
				Si	5.97	1.4	8.21	10.5	1.4	8.21	10.5

### References

- 1) L. A. Currie: Anal. Chem. **40**, 586 (1968).
- 2) W. Hong, S. Hayakawa, K. Maeda, S. Fukuda, M. Yanokura, M. Aratani, K. Kimura, Y. Gohshi, and I. Tanihata: Nucl. Instrum. Methods Phys. Res. B **124**, 95 (1997).
- 3) D. K. Avasthi, D. Kabiraj, A. Bhagwat, G. K. Mehta, V. D. Vankar, and S. B. Ogale: Nucl. Instrum. Methods Phys. Res. B **93**, 480 (1994).

\* Faculty of Engineering, University of Tokyo

# Determination of the Mass and Depth Resolutions of TOF-ERDA

W. Hong, S. Hayakawa,\* K. Maeda, S. Fukuda, K. Kimura, Y. Gohshi,\* and I. Tanihata

The most commonly used incident ions for Elastic Recoil Detection Analysis (ERDA) applications are low-energy He. However, the heavier projectile has many advantages. Combinations of various projectiles and various incident energies should be investigated in order to determine the optimum measurement conditions. Especially, optimization of the energy resolution of ERDA is a very important factor, because it is directly reflected to the mass resolution and to the depth resolution.

$^{20}\text{Ne}$ ,  $^{40}\text{Ar}$  and  $^{136}\text{Xe}$  ions accelerated by the RILAC were used as probes. The incident energies were 22.6 and 41.5 MeV for Ar, 20.0 MeV for Ne, and 138.1 MeV for Xe; all of them, except for 22.6 MeV  $^{40}\text{Ar}$ , were about 1 MeV/nucleon. The incident angle of the beam and angle of the detector were both set to be  $55^\circ$ , and the beam size was 2 mm in diameter.

A silicon surface barrier (SSB) detector and a time detector<sup>1)</sup> which is consisting of a  $10 \mu\text{g}/\text{cm}^2$  carbon foil and two micro channel plates (MCPs) were employed to measure the energy and the time of flight of a recoil particle. The details about experimental setup are in our previous publication.<sup>2)</sup> To determine the mass resolution and the depth resolution, a Si wafer was used as a sample.

The mass resolution of the measurement system was calculated according to

$$\left(\frac{\Delta M}{M}\right)^2 = \left(\frac{\Delta E}{E}\right)^2 + \left(\frac{2\Delta t}{t}\right)^2 + \left(\frac{2\Delta l}{l}\right)^2, \quad (1)$$

where  $M$  and  $E$  are the mass and the energy of a recoil particle, respectively;  $t$  and  $l$  are the time of flight and the length of flight path, respectively. The last term of Eq. (1) is negligible, since the path difference is very small.

The recoil energy  $E_2$  before reaching the telescope is

$$E_2 = K_R E_0 - \{S\}x, \quad (2)$$

where  $K_R$  is the recoil kinematic factor,  $E_0$  the incident energy,  $\{S\}$  the stopping cross section factor, and  $x$  the depth where the recoil occurred. The stopping cross section factor  $\{S\}$  can be calculated using Ziegler's tables.<sup>3)</sup> If the energy width of the particle recoiled from depth  $x$  by a mono-energetic incident beam is registered as  $\Delta E(x)$ , the depth resolution is defined as

$$r(x) = \Delta E(x) / \left(\frac{dE_m}{dx}\right) = \Delta E(x) / \{S\}. \quad (3)$$

The energy and time spectra of recoil particles from a Si wafer using the projectiles Ne, Ar and Xe are shown in Figs. 1 and 2, respectively.  $\Delta E(0)$  and  $\Delta t$  of Eq. (1) for each projectile were obtained from the leading edge of these spectra. The small peak in each spectrum is due to the contaminated carbon at the sample surface. The incident Ne peak scattered by the matrix element, Si, appears in Figs. 1(a) and 2(a).

The depth and mass resolutions at the surface of the sample, calculated by Eqs. (1) and (3), are summa-

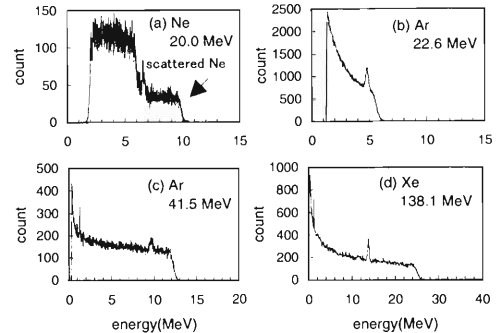


Fig. 1. Energy spectra obtained with the incident ions having different masses and energies.

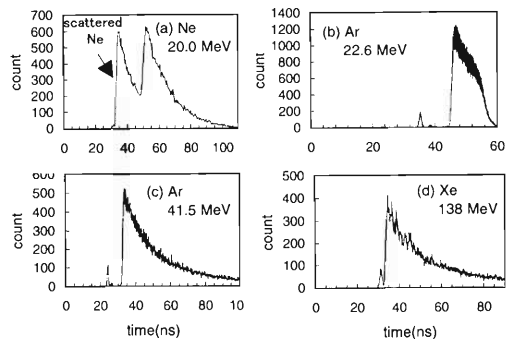


Fig. 2. Time spectra obtained with the incident ions having different masses and energies.

ri- zed along with the experiment conditions in Table 1. Though these mass and depth resolutions were overestimated, because of the surface contamination of the carbon, they are reasonable for most applications.

Table 1. Comparison of the near-surface mass resolutions  $\Delta M$  and the surface-depth resolutions  $r(0)$  between the incident energies and probes.  $\{S\}$  in  $\text{keV}/(10^{15} \text{ atoms}/\text{cm}^2)$  was calculated using Ziegler's table.  $\Delta M$  and  $r(0)$  in  $10^{15} \text{ atoms}/\text{cm}^2$  were calculated using Eqs. (1) and (3), respectively. The sample was a Si wafer.

Beam	Energy (MeV)	Recoiled atom	$\Delta t(0)$ (ns)	$\{S\}$	$\Delta E_m(0)$ (keV)	Surface depth resolution	Mass resolution $\Delta M$
$^{20}\text{Ne}$	20.0	Si	1.3	1.89	316	167	2.07
$^{40}\text{Ar}$	22.6	Si	1.1	2.18	470	216	2.32
	41.5	Si	0.9	2.43	530	218	1.90
$^{136}\text{Xe}$	138.1	Si	1.0	2.86	766	267	2.48

## References

- 1) K. Kimura and J. Wada: Phys. Rev. B **48**, 15535 (1993).
- 2) W. Hong et al.: Nucl. Instrum. Methods Phys. Res. B **124**, 95 (1997).
- 3) J. F. Ziegler et al.: *The Stopping and Range of Ions in Solids* (Pergamon Press, London, 1985).

\* Faculty of Engineering, University of Tokyo

## **IV. NUCLEAR DATA**



## Status Report of the Nuclear Data Group

Y. Tendow, A. Yoshida, A. Hashizume, and K. Kitao

The Nuclear Data Group has been carrying on three kinds of nuclear data activity described below since the previous year.<sup>1)</sup>

### (1) Nuclear reaction cross-section data (EXFOR)

Compilation of the charged particle nuclear reaction cross section coordinated by the IAEA Nuclear Data Section (NDS) has been continued. Following to our original objectives we have been collecting the reaction cross section data important to produce the following twenty typical radioisotopes for medical study: they are  $^{11}\text{C}$ ,  $^{13}\text{N}$ ,  $^{15}\text{O}$ ,  $^{18}\text{F}$ ,  $^{28}\text{Mg}$ ,  $^{52}\text{Fe}$ ,  $^{67}\text{Ga}$ ,  $^{68}\text{Ge}$ ,  $^{74}\text{As}$ ,  $^{77}\text{Br}$ ,  $^{82}\text{Br}$ ,  $^{77}\text{Kr}$ ,  $^{81}\text{Rb}$ ,  $^{82\text{m}}\text{Rb}$ ,  $^{111}\text{In}$ ,  $^{123}\text{Xe}$ ,  $^{127}\text{Xe}$ ,  $^{123}\text{I}$ ,  $^{124}\text{I}$ , and  $^{125}\text{I}$ . In order to maintain the completeness of the database, we also have been collecting reaction data which had not been included in the EXFOR master file up to the present.

In the previous year, we transmitted an EXFOR compilation file named 'TRANS R011'. That was our eleventh transmission to the NDS contained three entries 'R0051', 'R0052', 'R0053' with a total of 86 excitation curves. However, the data in the 'R0051' entry turned out to be already included in the EXFOR master and consequently it was not incorporated into it. The compilation of new entry 'R0054' and beyond as well as an alternative new entry 'R0051' is now in progress.

### (2) Evaluated Nuclear Structure Data File (ENSDF)

We have been participating in the ENSDF compilation network coordinated by the Brookhaven National Nuclear Data Center (NNDC). After the publication of  $A = 127, 129$  mass chain last year,<sup>2,3)</sup>  $A = 120$  mass-chain evaluation draft is now under the author's review prior to the printing. Because several new data on the high-spin states for  $A = 129$ , as well as for other neighboring masses, are coming out after that publication, we are planning to make some partial updatings for this mass data before long.

It is revealed that the current ENSDF coding format requires a proper upgrading in order to accommodate accumulating experimental data from recent advances in high-spin state physics using in-beam spectroscopy techniques.

### (3) Nuclear Science References (NSR)

We are engaged in collecting and compiling secondary references (unpublished works such as annual reports, conference proceedings, etc.) appeared in Japan since the previous year into the Nuclear Science

References (NSR) file format and transmitting them to the NNDC.

The compilation of 1996 annual reports has been completed and transmitted to the NNDC. Japanese secondary sources that were surveyed this year are as follows (shown in code name in NSR file):

RIKEN (RIKEN Accel. Prog. Rep.),  
 JAERI-TV (JAERI Tandem & V.D.G. Rep.),  
 JAERI-TIARA (JAERI Takasaki Ion Acc. Advanced Rad. Appl.),  
 INS (Inst. Nucl. Study, Univ. Tokyo),  
 UTTAC (Univ. Tsukuba Tandem Accel. Center),  
 RCNP (Res. Center Nucl. Phys., Osaka Univ.)  
 OULNS (Osaka Univ. Lab. Nucl. Study),  
 KUTL (Kyushu Univ. Tandem Acc. Lab.)  
 CYRIC (Cyclo. Radioisot. Center, Tohoku Univ.).

The long pending problem on the entry key-number of references to accommodate the publication year beyond 2000 has been settled finally. The previously used six-character key-number, e.g. 97Ab01 has been extended to eight characters as 1997Ab01. New data services are to be available in January, 1998 and onward from the NNDC after replacement of the processing programs and the NSR database rewritten incorporating the new key-numbers.

### (4) Others

The Technical NRDC (Nuclear Reaction Data Centers) Meeting was held at the IAEA NDS in Vienna on 26–28 of May 1997. The meeting is to be held every two years between the biennial plenary meeting named IAEA Advisory Group Meeting on the Coordination of NRDC. The Meeting mainly discussed technical aspects of construction, maintenance and dissemination of the EXFOR database. Major topics were the on-line data services through the WWW networks and the proper citation and reference guidelines for the electronic databases which are apt to be updated irregularly and/or frequently. These issues are to be discussed and fixed at the plenary NRDC meeting next year.

### References

- 1) Y. Tendow, A. Yoshida, A. Hashizume, and K. Kitao: RIKEN Accel. Prog. Rep. **30**, 165 (1997).
- 2) K. Kitao and M. Oshima: Nucl. Data Sheets **77**, 1 (1996).
- 3) Y. Tendow: Nucl. Data Sheets **77**, 631 (1996).



## **V. DEVELOPMENT OF ACCELERATOR FACILITIES**



## Progress of RI Beam Factory Project

Y. Yano, A. Goto, and T. Katayama

Within the on-going RI Beam Factory project, a cascade of a K930-MeV ring cyclotron (IRC) and a K2500-MeV superconducting ring cyclotron (SRC) will be constructed as an energy booster for the existing ring cyclotron (RRC). With this new cyclotron system the final energy will be increased up to more than 100 MeV/nucleon even for very heavy ions. By the projectile fragmentation these energetic heavy-ion beams are converted into the RI (radio-isotope) beams covering the whole range of atomic masses and the energies of several hundred MeV/nucleon. Moreover, this factory will include a next generation accelerator named the multi-use experimental storage rings (MUSES) consisting of an accumulator-cooler

ring (ACR), a booster synchrotron ring (BSR), and double storage rings (DSR). The MUSES will enable us to conduct various unique colliding experiments.

Bird's eye view of tentative layout of the new factory project is illustrated in Fig. 1. Optimization of these arrangements is under way.

During 1998 fiscal year, the three-year SRC construction budget for constructing six sets of superconducting sector magnets without their yokes has been approved.

The details of the R&D work to include the design work of each component are given in the following reports.

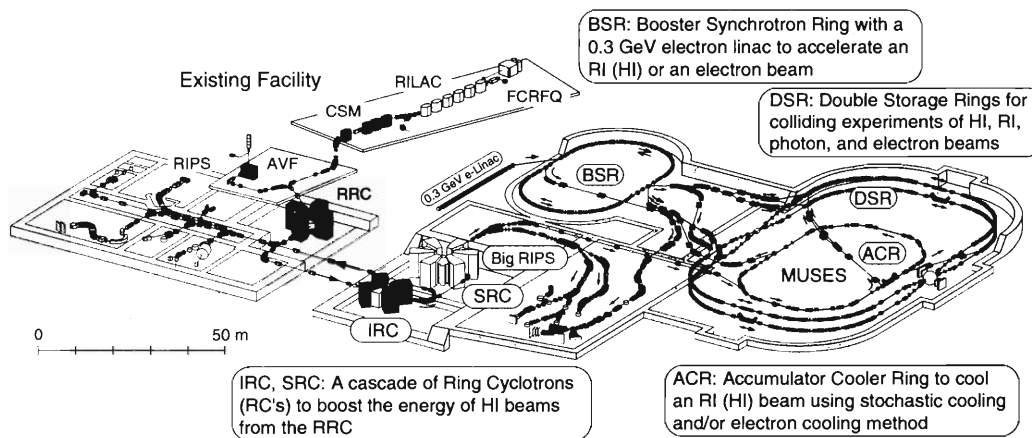


Fig. 1. Tentative layout of the designed RIKEN RI Beam Factory.

## Improvement of Sextupole Magnet for RIKEN 10 GHz ECRIS

M. Kidera, T. Kageyama, T. Nakagawa, J. Fujita, M. Kase, A. Goto, and Y. Yano

The 10 GHz ECRIS (Electron Cyclotron Resonance Ion Source) at RIKEN is used as the injector of AVF Cyclotron Accelerator.<sup>1)</sup> Various heavy ions of such as C, N, O, and Ar, are produced by the ion source, and are supplied for various experiments. For a long-time operation, a main problem at present is an instability in the beam intensity.

The supply of a stable beam is very important for better experiments. One of the main reasons of the beam instability could be a weak radial magnetic field generated by permanent sextupole magnet. The ECR surface is therefore too close to the wall of the plasma chamber. As a result, the ECR surfaces are disturbed by the collision of charged particles with the inner-surface of the chamber, implying that many ions and hot-electrons are reverted to the neutral particles and the low energy electrons, respectively. In order to improve the performance of the ECRIS we are designing a new sextupole magnet.

Cross-sectional view of the existing and new sextupole magnets are shown in Figs. 1(a) and (b), respectively. The new sextupole magnet is made from the N38H permanent magnets (Shin-etsu Kagaku Co.). Each of the magnet of 480 mm long consists of two pieces, and the direction of magnetic poles is at 36° relative to the chamber surface. As shown in Fig. 2, the magnetic lines of force of the sextupole magnet were calculated by a code POISSON using B/H function of the permanent magnet. In Fig. 3, the maxi-

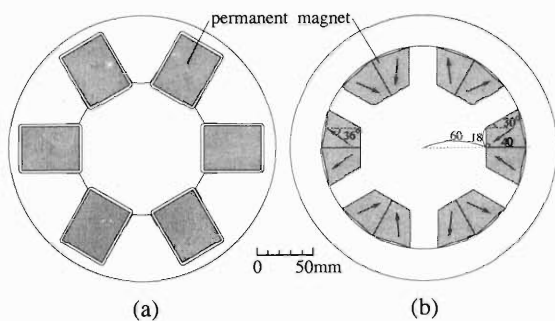


Fig. 1. Cross-sectional view of an existing sextupole magnet (a) and the new sextupole magnet (b).

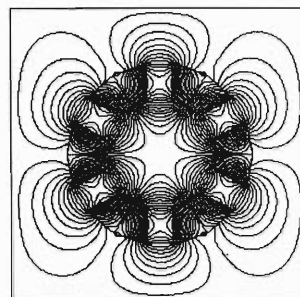


Fig. 2. The magnetic line of force of the new sextupole magnet. This result was calculated by the code POISSON.

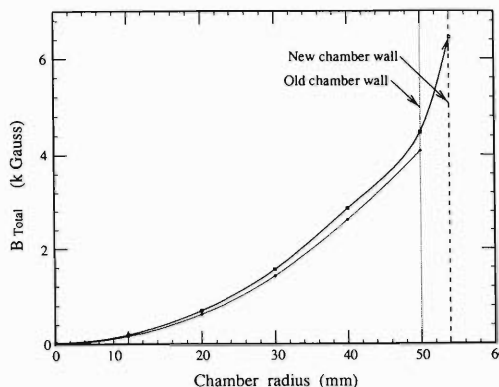


Fig. 3. The curve of the strength of the total magnetic field. The curve amount to maximum strength at the chamber surface.

imum strength of the total magnetic field at the new chamber surface is compared with that at the existing chamber well. The maximum strength of the new sextupole magnet is about 1.6 times that of the old one. By the new sextupole magnet, the confining magnetic field should be improved, and we expect that the stability of the plasma improves.

### References

- 1) T. Nakagawa, T. Kageyama, M. Kase, A. Goto, and Y. Yano: *Jpn. J. Appl. Phys.* **32**, 1335 (1993).

# Improvements of Low RF Power System in RIKEN 10 GHz ECRIS

J. Fujita, T. Kageyama, and T. Nakagawa

Some electric and mechanical troubles arose in 10 GHz ECRIS RF system frequently. They resulted mainly from poor mechanism of a mechanical rotary attenuator and from lack of the gain stability against temperature in a GaAs FET amplifier. These components, which had been used before the klystron amplifier, were replaced by new ones in April 1997. Block

diagrams of the previous and new systems are shown in Fig. 1. The RF inputs and outputs in the old system were all made through WRJ-10 type rectangular wave guides (shown by heavy lines in Fig. 1), but in the new one they were replaced by SMA type coaxial connectors so that arrangement and availability of the components are easy.

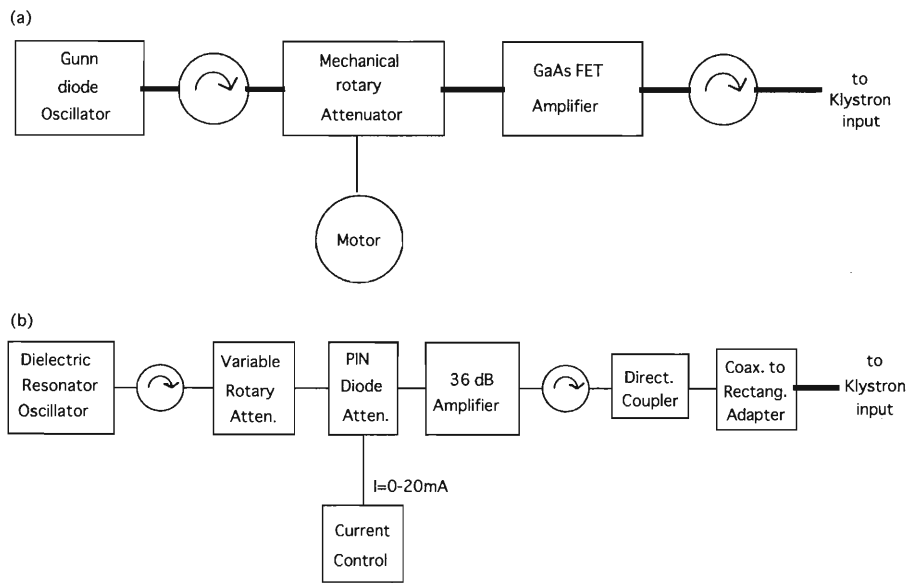


Fig. 1. Comparison between previous and new systems. (a) a previous system. (b) a new system.

The major changes are as follows.

(a) A Gunn Diode Oscillator (GDO) was replaced by a Dielectric Resonator Oscillator (DRO).

Oscillating frequency of the DRO has superior temperature stability (20 ppm per centigrade) to that of the GDO.

(b) A mechanical rotary attenuator was replaced by a PIN diode attenuator.

The PIN diode attenuator can vary the output power by changing an insertion loss from 3.25 dB to 30 dB. In addition to this PIN type, there is another attenuator which is a variable rotary attenuator and can protect

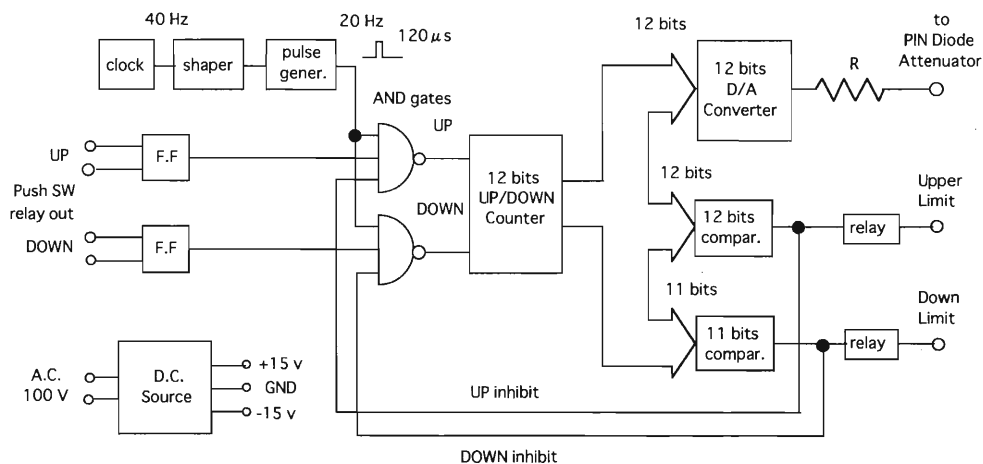


Fig. 2. A control circuit of a PIN diode attenuator.

input of the amplifier from being exposed to an excessive power due to troubles in the DRO or in the PIN diode attenuator.

(c) A GaAs FET amplifier was replaced by a solid state 36 dB amplifier.

A new amplifier is half in size, works with a single +15 volt-dc power supply, and keeps a stable operation up to 5 watts under a considerable temperature variation.

A directional coupler with coupling value of 20 dB and insertion loss less than 0.55 dB was newly placed after the amplifier in order to observe input power of the klystron. In the final stage, an adapter changing from the SMA coaxial connector to WRJ-10 rectangular wave guide was used to fit the input of the klystron.

The PIN diode attenuator is controlled by varying the conducting current from 0 to 20 mA which is fed, through a serial resistor, by a 12 bit DA converter. A block diagram of the current control circuit is shown in Fig. 2. The input of the DA converter is connected to the outputs of three 4-bit binary UP/DOWN counters. The three counters are put in series and count pulses with repetition rate of 20 Hz through AND gates opened by UP/DOWN switches on a control desk. Lower and upper limits of the attenuator are determined, not by analog levels of a voltage signal but by comparisons of the digital parallel 11 or 12 bit outputs of the counters.

So far the new system has not encountered a fatal trouble and is working well.

# Electron Beams Indeed Lower the Ion-Trapping Potential Barrier via Sheaths to Enhance the HCI Component in an ECRIS: Analytical Proof

M. Niimura, A. Goto, and Y. Yano

Based on theories of the collisionless sheath and mobility-limited diffusion, it was possible to prove analytically that the electron (e-) beams, prepared internally or externally and injected into an ECR ion source (ECRIS) plasma, can indeed lower the height of the ion-trapping potential barrier ( $\phi_i$ ) locally, thus prompting the highly charged ions (HCI) to cross over the  $\phi_i$  and contribute the extracted ion-beam current [See, inset of Fig. 1] The analytical results agree well with experimental<sup>1)</sup> results. Present paper has confirmed that it is the current, not the density<sup>2)</sup> nor the energy, of e-beam that can enhance the HCI component. No direct interaction is needed<sup>3)</sup> between the hot-to-warm electrons inside the ECRIS nucleus and the injected e-beam itself, as shown in the upper figure in Fig. 1. No conductive disk is needed: high work-function material<sup>4)</sup> as well as an insulator can fulfill the mission since the electric bias is created by the effect of sheath as shown in the lower figure of Fig. 1. These findings are vital for improvement of the ECRIS performance.

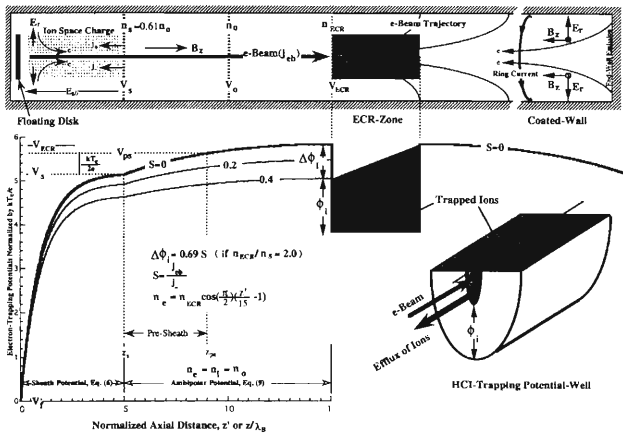


Fig. 1. Schematic diagram showing the internally closed-loop of e-beams (floating-disk and wall-coating schemes) whose  $j_{eb}$  can lower the height of  $\phi_i$ .

Consider that an end of the ECRIS plasma is terminated by an isolated plate, such as a disk and a piece of wall, orthogonally to the mirror magnetic field (MMF)  $B_z$ . Then, it is not difficult to explain that the ions will be uniformly distributed within the electron Debye length ( $\lambda_{eD}$ ), while the electrons are less distributed for the position closer to the plate ( $z = 0$ ). This means that a charge-separation electric field  $E_{s//}$  is created in the negative- $z$  direction (pointing the plate) within the domain  $0 \leq z \leq z_s \equiv \lambda_{eD}$  called sheath. Since  $-\int E_{s//} dz = V(z)$ , an increasing axial electrostatic potential is generated over the sheath. Assume such a wall (or ion) sheath filled

with the uniform ion density  $n_i = n_s$ , and a potential difference  $\phi \equiv V_s - V$  ( $\geq 0$ ) with which electrons are confined as  $n_e = n_s \exp(-e\phi/kT_e)$ ; where  $n_s$  ( $\equiv 0.61n_0$ ) and  $V_s$  are the particle density and potential at the sheath edge ( $z = z_s$ ). Then, the space charge density is  $\rho \equiv e(n_i - n_e) \cong \epsilon_0 \phi / \lambda_B$ , defining  $\lambda_B \equiv (\epsilon_0 kT_e / n_s e^2)^{1/2} \equiv 1.28 \lambda_{eD}$  with usual  $\lambda_{eD} \equiv (\epsilon_0 kT_e / n_0 e^2)^{1/2}$  expressed by the density at the pre-sheath ( $z = z_{ps}$ ) where  $n_e = \sum z_i n_i = n_0$ . Then, the Poisson equation  $\partial^2 V / \partial z^2 = -\rho / \epsilon_0$  is in the form:  $(\partial^2 / \partial z^2 - \lambda_B^{-2})V = -V_s / \lambda_B^2$ , which gives  $V(z) = -(V_s - V_f) \exp(-z / \lambda_B) + V_s$  under the boundary conditions  $V = V_f$  and  $V_s$  at  $z = 0$  and  $\infty$ , respectively. The self-consistent potential distribution is:

$$V(z) = \left[ 1 - \exp\left(\frac{-z}{\lambda_B}\right) \right] V_s \quad (\text{if } V_f = 0, \text{ in } 0 < z \leq z_s) \quad (1)$$

This  $V_s$  in Eq. (1) is lowered by the presence of an e-beam current ( $j_{eb}$ ), as will be seen later. On the other hand, in the next domain  $z_s \leq z \leq z_{ECR}$  the density obeys Boltzmann law. Therefore, the potential distribution is:

$$V(z) = V_{ECR} - \frac{kT_e}{c} \ln \frac{n_{ECR}}{n_e(z)} \quad (z_s \leq z \leq z_{ECR}) \quad (2)$$

This  $V_{ECR}$  too is lowered by  $j_{eb}$  as will be seen soon.

It is well known that ion saturation current density ( $j_+$ ) and the random electron current density ( $j_-$ ), both directing towards the plate, are given, respectively, by

$$j_+ \equiv cn_s v_B = 0.61 en_0 \sqrt{\frac{kT_e}{m_i}}, \quad (3)$$

$$j_- \equiv -cn_w \frac{\langle v_{eth} \rangle}{4} = -en_0 \frac{\langle v_{eth} \rangle}{4} \exp \frac{-e(V_s - V_f)}{kT_e} \quad (4)$$

where  $\langle v_{eth} \rangle \equiv (8kT_e / \pi m_e)^{1/2}$ . Now, if a portion of the above  $j_-$  is re-directed away from the plate, forming an e-beam with density  $j_{eb} \equiv -en_{eb} v_e$ . Then, the net current density arriving the wall is  $j_- - j_{eb} = (1 - S)j_-$ , where  $S \equiv j_{eb} / j_-$  ( $\leq 1$ ). Namely, when  $j_{eb} \neq 0$ , the right hand side of Eq. (4) should be divided by  $(1 - S)$  for the new  $j_-$ . Then, the isolated-plate condition:  $j_+ + j_- = 0$  gives  $V_s - V_f = (kT_e / 2e) [\ln(0.43 m_i / m_e) + 2 \ln(1 - S)]$ , or

$$V_s - V_f = \frac{kT_e}{e} [\ln 177 + \ln(1 - S)] \quad (\text{for argon}) \quad (5)$$

The term,  $\ln(1 - S)$ , is negative, thereby decreasing the value of  $V_s - V_f$  down to null if  $S = 1 - (m_c / 0.43 m_i)^{1/2} = 0.995$  for the case of argon. [See, Fig. 2]. When  $S \ll 1$ , we have  $\ln(1 - S) \cong -S$ , and therefore  $V_s - V_f$  decreases linearly with  $S$ . Substitution of  $V_s$  in Eq. (5) into Eq. (1) yields:

$$V(z) = \frac{kT_e}{e} \left[ 1 - \exp\left(\frac{-z}{\lambda_B}\right) \right] \cdot \ln[177(1 - S)] \quad (\text{if } V_f = 0) \quad (6)$$

This equation tells that indeed the potential is lowered as  $S$  or  $j_{eb}$  increases in the domain  $0 < z \leq z_s$ .

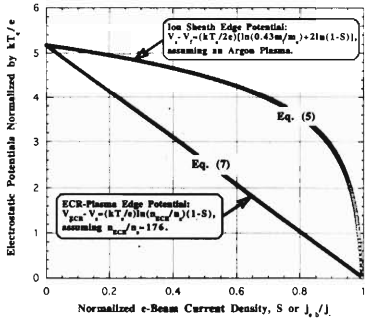


Fig. 2. Logarithmic and linear decays of the electron-trapping electrostatic potentials as a function of  $S$ .

Because the externally-fed rf-power is continually producing charged particles at the ECR-zone, there exists a positive density gradient ( $\nabla n$ ) towards the center. Consider that  $j_{eb}$  with density  $n_{cb}$  is injected into such a mobility limited domain. Since e-beams are spatially uniform,  $\nabla n_{cb} = 0$ . Then, we have  $\Gamma_c = -D_e \nabla n_c - \mu_e n_e E(1 - S)$ , where  $S \equiv \Gamma_{cb}/|\Gamma_e| = j_{eb}/|j_{eD}|$ . However,  $j_{eD} \equiv -eD_a \nabla n_c$  (from Fick's law), which ought to be  $j_-$  from the continuity of current at  $z_s$ . Hence,  $S \equiv j_{eb}/j_-$  as before. On the other hand  $\Gamma_i = -D_i \nabla n_i + \mu_i n_i E$ . Since  $\mu_e \gg \mu_i$ ,  $D_e \gg D_i$ , and  $n_e \approx n_i$  in  $z_s \leq z \leq z_{ECR}$ , the condition  $\Gamma_e = \Gamma_i$  at  $z = z_s$  determines the magnitude of ambipolar electric field ( $E_{amb}$ ). Integration of the  $E_{amb}$  from  $z = z_s$  to  $z_{ECR}$  yields:

$$V_{ECR} - V_s = (1 - S) \frac{kT_e}{e} \ln \frac{n_{ECR}}{n_s} \quad (7)$$

Figure 2 shows Eq. (7) for the case of  $n_{ECR}/n_s = 176$  for matching with Eq. (5) at  $S = 0$ . Substituting  $V_{ECR}$  of Eq. (7) into Eq. (2), we obtain

$$V(z) = (1 - S) \frac{kT_e}{e} \ln \frac{n_c(z)}{n_s} + V_s(z_s) \quad (8)$$

Since the ambipolar diffusion equation  $\partial n/\partial t = D_A \nabla^2 n$  has a trigonometric solution, Eq. (8) becomes, if  $n_{ECR}/n_c = 2$ :

$$V(z') = (1 - S) \frac{kT_e}{e} \ln \left[ 2 \cos \frac{\pi}{2} \left( \frac{z'}{15} - 1 \right) \right] + V_s(z'_s = 5) \quad (9)$$

where  $z' \equiv z/\lambda_B$ .  $V(z)$  is plotted in Fig. 1 with parameter  $S$ .

Change in the sheath potential with and without  $j_{eb}$  corresponds to a lowering of the ion-trapping potential barrier  $\phi_i$  by  $\Delta\phi$ . Namely,  $\Delta\phi_i = (V_s - V_f)_{S=0} - (V_s - V_f)_{S \neq 0}$ . Using Eq. (5), we have

$$\Delta\phi_i = -\frac{kT_e}{e} \ln(1 - S) \cong S \frac{kT_e}{e} (S \rightarrow 0) \quad (10)$$

Similarly, Eq. (7) gives

$$\Delta\phi_i = S \frac{kT_e}{e} \ln \frac{n_{ECR}}{n_s} \equiv S \cdot (V_{ECR} - V_s)_{S=0} \quad (11)$$

Now, the ECRIS extracted ion beam current ( $I_{ib}$ ) is given by  $I_{ib} \equiv Z_i e S_{end} \Gamma_{end} = Z_i e v_B n_z(0) \exp[-Z_i e \phi_i / kT_i]$ , where  $v_B = (kT_c/m_i)^{1/2}$ . As the  $\phi_i$  is lowered to  $\phi_i - \Delta\phi_i$ , the magnitude of  $I_{ib}$  enhances by the factor  $\eta \equiv I_{ib}(S)/I_{ib}(0) = \exp[Z_i e \Delta\phi_i / kT_i]$ . From Eqs. (10) or (11) we obtain:

$$\eta \equiv \frac{I_{ib}(S)}{I_{ib}(0)} = \exp \left[ Z_i S \frac{T_c}{T_i} \ln \frac{n_{ECR}}{n_s} \right] \quad \left( S = \frac{j_{eb}}{j_e} \right) \quad (12)$$

Since  $\Delta\phi_i \sim S \sim j_{eb} \sim V_{bias}^{3/2}$  when  $j_{eb}$  is the space-charge limited electron-beam current. Eq. (12) gives

$$I_{ib}(S) = I_{ib}(0) \exp[\text{Const} \cdot j_{eb}] = I_{ib}(0) \exp[\text{Const} \cdot V_{bias}^{3/2}] \quad (13)$$

Figure 3 shows a good agreement of experimental data by the expressions of the type of Eq. (13): for both  $I_{ib}$  and  $i_{ib}$ . The space-charge limited ion-beam current density, which represents the discharge current of e-gun circuit, is theoretically  $j_{ib} = 7.08$  and  $1.12$  mA/cm<sup>2</sup> for H<sup>+</sup> and Ar<sup>+</sup> ions, respectively, for the e-gun with  $d = 2$  mm and  $s = 0.57$  cm<sup>2</sup> at  $V_{bias} = 300$  V. This corresponds, the space-charge limited electron-beam current,  $j_{eb} = (m_i/m_e)^{1/2} j_{ib} = 303$  mA/cm<sup>2</sup>. Indeed,  $i_{ib}(\text{mA}) = 7.84 \times 10^{-4} V_{bias}^{3/2}$  in Fig. 3 can describe the experimental e-gun received ion-beam data quite well. As for the saturation current, Eq. (3) gives

$$j_+(A/m^2) = 1.51 \times 10^{-16} n_o (T_e)^{1/2} \quad (\text{for Ar}^{+11}) \quad (14)$$

in MKS units. In order to obtain  $T_e$ , we use Eq. (5) under  $S = 1$  or  $V_s - V_f = (T_e/2e) \ln(0.43m_i/m_e)$  to be compared with another experimental<sup>1)</sup> result:  $V_f = -14$  and  $-21$  V were observed at 400 and 800 W of rf power. This experiment was done with N<sup>+</sup> and V<sup>+</sup> was measured in reference to  $V_s = 0$ , so that  $V_f = -4.65T_e$  theoretically. This gives  $T_e = 3.0$  and  $4.5$  eV as the 1st stage  $T_e$ . Substitution of  $n_o = 1.61 \times 10^{11}$  cm<sup>-3</sup> (neutrals at  $p_o = 5$   $\mu$ Torr) and  $T_e = 4.5$  eV in to Eq. (14) gives  $I_+ = 2.9$  mA, which is in good agreement with the experimental saturation current ( $I_+ = 3.0$  mA) observable in Fig. 3.

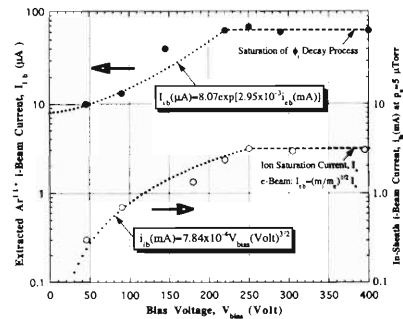


Fig. 3. ECRIS extracted ion-beam current ( $I_{ib}$ ) and e-gun received ion-beam current ( $i_{ib}$ ) as a function of  $V_{bias}$ , showing a good agreement of the present theory [dotted line] with experimental<sup>1)</sup> results [symbols].

This concludes that the  $I_{ib}$  in Fig. 3 is saturated prematurely, because the  $i_{ib}$  (proportional to  $j_{eb}$ ) has saturated; not because  $\Delta\phi_i \sim \phi_i$  has reached. There is thus room of improvement for the e-gun. As obvious from Eq. (14) we need to raise the  $T_e$  of cathode plasma in order to increase  $j_+$  or the magnitude of  $j_{eb}$ . Alternatively, a high-pressure light- $m_i$  gas (e.g., H<sub>2</sub>) is useful for the 1st stage by filling it independently from the 2nd stage.

## References

- 1) T. Nakagawa et al.: JJAP **32**, L1335 (1993).
- 2) M. Niimura et al.: RIKEN Accel. Prog. Rep. **28**, 150 (1995).
- 3) Z. Q. Xie: private communication.
- 4) S. Biri: private communication.

# RIKEN Duoplasmatron Ion Source: The Operating Principles Compared with ECRIS, and the Direction for Future

M. Niimura, T. Kageyama, K. Ikegami, M. Nagase, A. Goto, and Y. Yano

In order to identify the operating principles and to determine the future direction of the RIKEN duoplasmatron ion source (DPIS), the experimentally observed data were rationally analyzed. Present report introduces some of the analysis performed against the following two subjects. [i] Linear scaling of the extracted ion-beam current ( $I_{ib}$ ) with respect to the gas discharge current ( $I_d$ ). [ii] Solenoidal magnetic field ( $B_z$ ) dependence of the  $I_{ib}$  curve which depicts a peak at a specific field strength. This study has found the following principles actually operating in our DPIS. They are: formation of a double layer (DL) at the entrance of the intermediate electrode (IE); establishment of the sheath stability criterion (SSC) across the DL; acceleration and focusing of an electron ( $e^-$ ) beam by a potential jump of DL, free-fall ions determining the size of  $I_{ib}$ ; and ion-beam transport governed by the composite brightness ( $B_n$ ). As a result, we were successful to obtain: a correct scaling law of  $I_{ib}$  (the published formula was found to contain an error); a useful expression to predict the optimal field ( $B_{opt}$ ) to maximize  $B_n$  or  $I_{ib}$ ; and an advanced model the classical DPIS should evolve for future.

After its advent a quarter century ago, a variety of DPISs were extensively used, before ECRIS, as injectors for RFQs, linacs, cyclotrons, and synchrotrons. Recently, this device found new ways of use as a high-current e-gun,<sup>1)</sup> and as an intermittent substitute for ECRIS at the time for light ions.<sup>2)</sup> Further, DPIS seems quite hopeful as a Cs-free negative ion (e.g., 9 mA of  $H^-$ ) source,<sup>3)</sup> and even as a metal ion source.<sup>4)</sup>

As for [i], the typical data are already presented as Fig. 4 of Ref. 2. As the physics behind we suspect the SSC. As schematically illustrated in Fig. 1(a), an IE in the mid of a plasma diode causes a stagnation and subsequent depletion of electrons due to the change in its flow velocity (directing left to right in Fig. 1) at its entrance and subsequent canal, respectively. As a result, the electron and ion space charge layers are created. Such two sheaths are called double layer. [Fig. 1(c)–(e)]. These space charges induce an electrostatic potential  $\phi(z)$  via Poisson equation [Fig. 1(f)]. Electrons at the sheath edge (K) of cathode plasma and the ions at the sheath edge (A) of anode plasma fall into this potential-well,  $\phi(z)$ , gaining the same energy  $e\phi$ . We therefore have:<sup>5)</sup>

$$\frac{1}{2}mv_e^2 = \frac{1}{2}Mv_i^2 \equiv e\phi \quad (1)$$

Further, if  $\phi(z)$  satisfies  $\partial\phi/\partial z \equiv -E = 0$  at both K and A, the momentum-transfer equation of plasma,  $n_j m_j [(dv_j/dt + (v_j \cdot \nabla)v_j)] = n_j q_j (E + v_j \times B) - \nabla p_j$ , tells that both particles ( $j = e, i$ ) will have the same momentum flux:

$$n_{es}(K)m_e v_e \frac{dv_e}{dz} = n_{is}(A)m_i v_i \frac{dv_i}{dz} (\nabla p_e = \nabla p_i) \quad (2)$$

Equation (1) and integration of Eq. (2) by  $z$  yield the SSC:

$$n_{es}(K) = n_{is}(A) \quad (3)$$

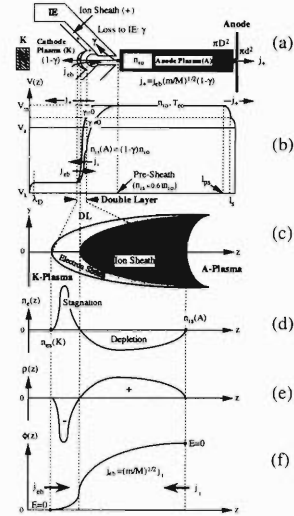


Fig. 1. Explanation of the DL and SSC, controlling DPIS.

This is a constraint for the densities at K and A.

Under the free-fall model of the ions at a positive potential edge, the extractable  $I_{ib}$  is given by the ion saturation current density  $j_+ \equiv en_{is}v_B \equiv 0.61en_{i0}(kT_{e0}/M)^{1/2}$ . Obviously,  $j_+$  is only a function of  $n_{i0}$  and  $T_{e0}$  at the center of anode plasma. [Fig. 1(b)]. Without a particle loss,  $n_{i0} = n_{is}(A)$  and  $j_+ = j_i = n_{i0}v_i$ . Under the SSC condition given by Eq. (3),

$$\frac{j_i}{j_{eb}} \equiv \frac{Z_i n_{is}(A)v_i}{n_{es}(K)v_e} = \sqrt{\frac{m}{M}} \quad (Z_i = 1) \quad (4)$$

This means  $j_+ = j_i = j_{eb}(m/M)^{1/2}$ , where  $j_{eb}$  is the e-beam current density crossing DL. However, some of ions are lost into IE by  $\gamma \equiv n_i(IE)/n_{i0} = 15 \sim 30\%$ .<sup>6)</sup> Then new values are:  $n'_{is}(A) = (1 - \gamma)n_{i0}$ , and  $j'_i \equiv n'_{is}(A)v_i = (1 - \gamma)n_{i0}v_i = (1 - \gamma)j_i$ . Therefore, under a loss,  $j_+ = j'_i = (1 - \gamma)j_{eb}(m/M)^{1/2}$ . This gives, since  $j_+ \equiv I_{ib}/\pi d^2$  and  $j_{eb} \equiv I_d/\pi D^2$ , the expected linear scaling law of  $I_{ib}$  against  $I_d$ :

$$I_{ib} = I_d \left(\frac{d}{D}\right)^2 \sqrt{\frac{m}{M}} (1 - \gamma) \quad (5)$$

This formula is more logical than the published one<sup>6)</sup> which gives an unrealistic infinite  $I_{ib}$  at  $\gamma = 0$  and an unrealistic finite  $I_{ib}$  even at  $\gamma = 1$ . If  $\gamma = 1$ ,  $I_{ib} = 0$  since  $j'_i = 0$ .

As for [ii], a typical data is shown by histograms in Fig. 2. These  $I_{ib}$  were measured downstream of the extraction electrodes with a Faraday cup (FC) by varying  $B_z$ . A beam current transported downstream and detected by a FC of aperture  $S$  is not given by  $I = j_+ S$ , but  $I = BS\Omega$ ; where  $B$  and  $\Omega$  are the brightness of ion source and the solid angle of detector seen from the ion source, respectively. Dimension of  $B$  ought to be the current density per unit solid angle, so that one can

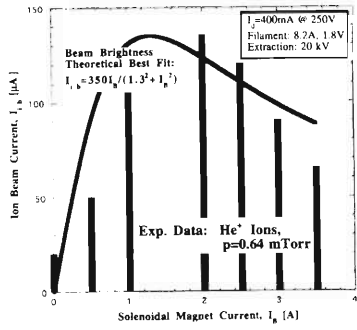


Fig. 2. Histogram of  $I_{ib}$  and its theoretical bestfit by Eq. (12).

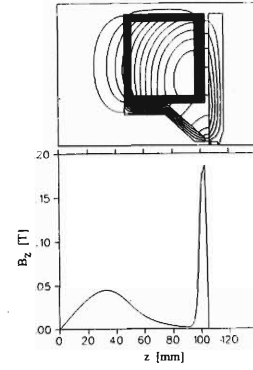


Fig. 3. Flux and  $B_z(z)$  of DPIS computed by Poisson code.

define  $B$  by a product of transverse emittances,  $\varepsilon_x \varepsilon_y$ :<sup>7)</sup>  
 $B(\text{A/m}^2 \text{ rad}^2) = I/\pi^2(\varepsilon_x \varepsilon_y)$ .

When the beam has its divergence angle  $\alpha$  at  $x$  on the horizontal plane, the definition of  $\varepsilon_x$  can write:

$$\varepsilon_x \equiv \frac{1}{\pi} \int \alpha(x) dx \equiv \frac{1}{\pi P} \int \int P_x dx \cong \frac{1}{\pi P_z} \int \int P_x dx \quad (6)$$

Since this emittance decreases as the momentum  $P_z$  ( $\sim P$ ) of particles increases by acceleration, Eq. (6) is normalized by multiplying the  $\gamma\beta \equiv \beta/(1-\beta^2)^{1/2}$  which is proportional to  $P_z$  ( $\equiv \gamma\beta m_{i0}c$ ) if  $m_{i0}$  is the ion rest mass. Then,

$$\varepsilon_{xn} \equiv \gamma\beta \varepsilon_x = \frac{\gamma\beta}{\pi P_z} \int \int dP_x dx = \frac{1}{\pi m_{i0}c} \int \int dP_x dx. \quad (7)$$

The rms emittance of  $\varepsilon_{xn}$  multiplied by  $\pi$  is given by

$$\pi \varepsilon_{xn}^{\text{rms}} \equiv \pi \sqrt{\langle \varepsilon_{xn}^2 \rangle} \equiv \frac{4}{m_{i0}c} \sqrt{\langle x^2 \rangle (P_x^2) - \langle x P_x \rangle^2} \quad (8)$$

Using the Lagrangian mechanics,  $P_x \equiv p_x - qA_x = p_x - (qB_y z/2)$  and  $\sqrt{\langle x^2 \rangle} = \sqrt{\langle y^2 \rangle} = R/2$ , Eq. (8) can be expressed as<sup>8)</sup>

$$\pi \varepsilon_{xn}^{\text{rms}} (\text{m rad}) \equiv 2R \sqrt{\frac{kT_i}{m_{i0}c^2} + \left(\frac{\omega_{ic}R}{4c}\right)^2} \quad (9)$$

where  $R$  is the beam radius and  $\omega_{ic} \equiv qB_y/m_{i0}$ . Equation (9) has a form of composite transverse energies of ions:

$$\pi \varepsilon_{xn}^{\text{rms}} = 2R \sqrt{\frac{kT_i + 0.5m_{i0}v^2}{m_{i0}c^2}} \quad (R = 2\sqrt{2}r_L) \quad (10)$$

Defining  $\mu \equiv m_{i0}/m_{p0}$ , Eq. (10) can be written numerically:

$$(\varepsilon_{xn}^{\text{rms}})^2 = 2.53 \times 10^{-10} \frac{R^2}{\mu} \left( 16.8T_i(\text{eV}) + \frac{Z_i^2 R^2 B_z^2 (\text{Gauss})}{\mu} \right)$$

When the beam's transverse motion is independent from the axial motion, the 4-D phase space volume is constant from Liouville theorem. Then,  $\int \int \int \int dP_x dP_y dx dy = (1/2)(\int \int dP_x dx)^2$ , and the normalized brightness can be written by using the relationship of Eq. (7) as

$$B_n \equiv \frac{I}{\frac{1}{2(m_{i0}c^2)^2} (\int \int dP_x dx)^2} = \frac{2I}{(\pi \varepsilon_{xn})^2} \quad (11)$$

Using the  $\varepsilon_{xn}^{\text{rms}}$  to count 86.5% of the beam current  $I = \pi R^2 q n_{is} u_B$ , we have the rms composite brightness:

$$B_n^{\text{rms}} \equiv \frac{2I}{(\pi \varepsilon_{xn}^{\text{rms}})^2} = \frac{0.5\pi q n_{is} u_B}{\left(\frac{kT_i}{m_{i0}c^2} + \left(\frac{\omega_{ic}R}{4c}\right)^2\right)^2} \equiv \frac{aB_z}{b + cB_z^2} \quad (12)$$

Here,  $n_{is} \sim B_z$  (since  $D \sim B_z^{-0.5}$  from adiabaticity) was assumed. Experimental data can be fitted well by Eq. (12) as shown by a solid curve in Fig. 2. Notice that  $I_{ib} \sim B_n$  and  $I_B \sim B_z$  in Fig. 2. Obviously, Eq. (12) gives a maximum at  $B_{\text{opt}} = (b/c)^{1/2} = 4(m_{i0}kT_i)^{1/2}/qR$ . Namely, one can predict  $B_{\text{opt}}$  by

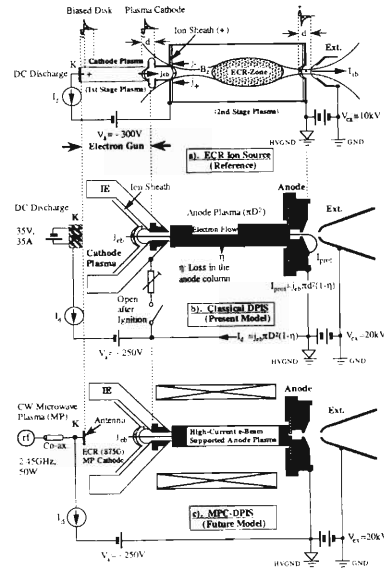


Fig. 4. ECRIS-DPIS comparison and a future DPIS with MPC.

$$B_{\text{opt}} = 4.10 \frac{\sqrt{\mu T_i (\text{eV})}}{Z_i R (\text{m})} \quad (\text{Gauss}) \quad (13)$$

For our case of  $\text{He}^{+1}$ , Eq. (13) gives  $B_{\text{opt}} = 1.6 \text{ kG}$  if  $T_i = 1 \text{ eV}$ . Figure 3 indicates that the  $B_z$  strength peaks at the anode plasma, and is widely adjustable by changing materials of the magnet pole pieces.

As Figs. 4(a) and 4(b) explain, the ECRIS plasma is generated, heated, and ionized by an rf source while assisted by an e-beam for extraction; whereas the DPIS plasma is generated, heated, and ionized all by an e-beam. Such comparative study has prompted us to the future DPIS: an advanced DPIS, operating with the CW e-beam produced by a microwave plasma cathode (MPC) e-gun<sup>1)</sup> as shown in Fig. 4(c). This will solve the unique problem of DPIS: longevity of cathode.

## References

- 1) Y. Matsubara et al.: Rev. Sci. Instrum. **61**, 541 (1990); M. E. Abdelaziz: Rev. Sci. Instrum. **61**, 457 (1990); B. H. Sun et al.: Rev. Sci. Instrum. **63**, 2598 (1992).
- 2) M. Niimura et al.: RIKEN Accel. Prog. Rep. **30**, 169 (1997).
- 3) Th. Sluyters: Nucl. Instrum. Methods **113**, 299 (1973).
- 4) K. Langbein: Rev. Sci. Instrum. **61**, 330 (1990).
- 5) J. E. Allen: Plasma Phys. Contr. Fusion **27**, 1343 (1985).
- 6) C. Lejeune: Nucl. Instrum. Methods **116**, 429 (1974).
- 7) P. Spadtke: Rev. Sci. Instrum. **63**, 2647 (1992).
- 8) Y. Batygin et al.: JAERI-Conf. **95-021**, 353 (1995).

# Warm-Electron Heating Mechanism in the Core of ECRIS Nucleus, and Relevant Diagnostic System

M. Niimura, A. Goto, and Y. Yano

The free-electron temperature ( $T_e$ ) in ECRIS plasmas is enigmatic: a “hot electron” temperature ( $T_{ch}$ ) to exceed 10 keV is routinely measured under the X-ray spectroscopy, but a “warm electron” temperature ( $T_{ew}$ ) is theoretically good enough to explain the charge state distribution (CSD) of extracted ion-beam currents. For an instance, Fig. 1(a) shows experimentally observed CSDs with typical ECRIS (LBNL 6.3 GHz and RIKEN 10 GHz) devices. The theoretical  $T_c$  agreeable with these data is  $T_{ew} = 500\text{--}1000$  eV, under a low RF power ( $\sim 100$  W) input, as envisaged from the theoretical CSD of Fig. 1(b) which are obtained by solving a set of 18-simultaneous rate equations under the condition  $n_c\tau_i = 10^{10}$  sec  $\text{cm}^{-3}$  with Maxwellian  $T_e$  as a parameter.<sup>1)</sup>

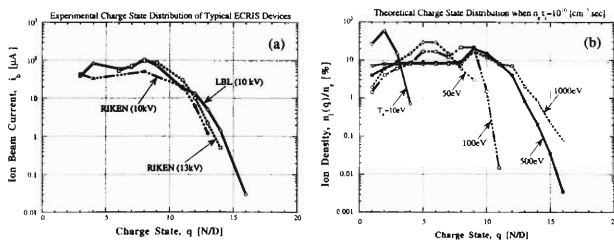


Fig. 1. Experimental (a) and theoretical (b) CSD of ECRIS.

There is an attempt to measure  $T_{ew}$ . However, the diagnostics based on the endloss electrons<sup>2)</sup> was obviously unable to measure  $T_{ew}$  of the confined electrons. Here, we propose a simple diagnostic method adequate to measure  $T_{ew}$  of the confined electrons, and present a new method to estimate the magnitude and time-history of  $T_{ew}$ .

The new method is based on the field annihilation heating (FAH). In order to understand the concept of FAH, consider a plasma cylinder with a hollow of radius  $R$  through which an external magnetic field  $B_z$  is applied. Case I: Time-varying  $B_z$  (or  $\partial B_z/\partial t \neq 0$ ) is externally given. Then, the Maxwell equation,  $-\partial B_z/\partial t = \nabla \times E$ , and Stokes' theorem can show that an azimuthal current ( $j_\theta$ ) is induced in the plasma of rectangular cross-section:

$$j_\theta = E_\perp/\eta = -\frac{R}{2\eta} \frac{\partial B_z}{\partial t}, \quad (1)$$

where  $\eta$  is the perpendicular resistivity of plasma. Because  $j_\theta$  of Eq. (1) is predominantly of electrons, the plasma electrons are Joule heated by the rate:

$$j_\theta^2 \eta = \frac{R^2}{4} \left( \frac{\partial B_z}{\partial t} \right)^2 [\text{W}/\text{m}^3] \quad (2)$$

This is the concept of Modified Betatron readily demonstrated in the thermo-nuclear fusion community.

FAH is an inverse process of this betatron plasma heating, as seen for the Case II: Steady  $B_{z0}$  (or  $\partial B_{z0}/\partial t = 0$ ) and  $j_\theta$  are externally given. Assume that the  $j_\theta$  is a diamagnetic current (in the negative  $\theta$ -direction) which will force to annihilate the  $B_{z0}$  of mirror magnetic field (MMF). Then, another Maxwell equation,  $\mu_0 j_\theta = (\nabla \times B)_\theta = -\partial B_z/\partial r$ , tells that new fields are generated both inside and outside of the current sheet as much as

$$B_z = -\mu_0 \int_0^{\pm \Delta R/2} j_\theta dr = \pm \mu_0 j_\theta \frac{\Delta R}{2} = \pm \frac{\mu_0 I_\theta}{2l}, \quad (3)$$

where  $\Delta R$  is the scale length of  $j_\theta$  or of  $B_z$ ,  $l$  is the height of hollow cylinder, and  $I_\theta = l \Delta R j_\theta$ . This  $B_z$  of Eq. (3) is in the negative- $z$  direction opposed to  $B_{z0}$ , thereby annihilating  $B_{z0}$  in the core plasma by the amount equal to  $|B_z|$ . Notice that the magnetic field decreases inside of the core plasma and increases outside of the mirror coil, but stays constant in-between. (Fig. 2). Therefore, a diamagnetic loop wound around the discharge chamber can induce the voltage  $V_\theta = -S(\partial|B_z|/\partial t)$ .

The axial field,  $B_z(0, t)$ , decreases from  $B_{z0}$  with time as the more  $|B_z(0, t)|$  arrives on the axis of the core plasma. With the Ohm's law,  $j_\theta \equiv E_\perp/\eta$ , two Maxwell equations yield the field diffusion equation:  $\partial B_z/\partial t = -(\eta/\mu_0) \nabla \times (\nabla \times B_z) = (\eta/\mu_0) \nabla_r^2 B_z$ . Technique of the separation of variables gives the so-

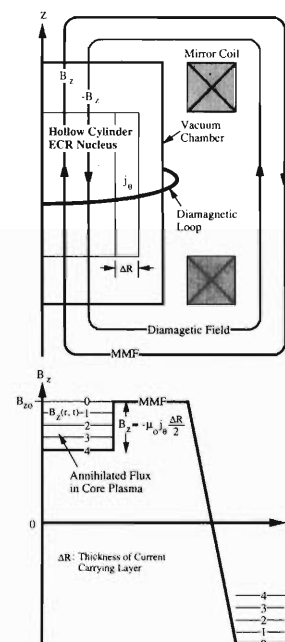


Fig. 2. Field annihilation and a diamagnetic loop.

lution for the diffusing field:

$$B_D(t) = B_z(0, t) - B_z(0, \infty) = |B_z(0, \infty)| \exp\left(-\frac{t}{\tau_D}\right) \cos \frac{\pi r}{2L}, \quad (4)$$

where

$$\tau_D = \frac{\mu_0}{\eta} \left(\frac{2L}{\pi}\right)^2, \quad \eta = 1.04 \times 10^{-4} Z \frac{\ln \Lambda}{T_e^{3/2}} \text{ [Ohm-m]}. \quad (5)$$

Note that  $L$  in Eq. (5) is the scale length of the  $B_z(r, t)$  inside the core (Fig. 3). The gradient of  $B_z(r, t)$  should be supported by the current density  $j_\theta \approx (\pi/2L) \cdot |B_z(0, t)|/\mu_0$ , and this  $j_\theta$  heats the local plasma. The thermal energy stored in the core plasma is given by

$$\begin{aligned} W_J &\equiv nkT_{ew} \equiv \int_0^t j_\theta^2 \eta \tau_D dt \frac{|B_z(0, \infty)|^2}{\mu_0} \exp\left(-\frac{2t}{\tau_D}\right) \\ &= 0.86 \frac{|B_z(0, \infty)|^2}{\mu_0} \quad (\text{at } t = \tau_D). \end{aligned} \quad (6)$$

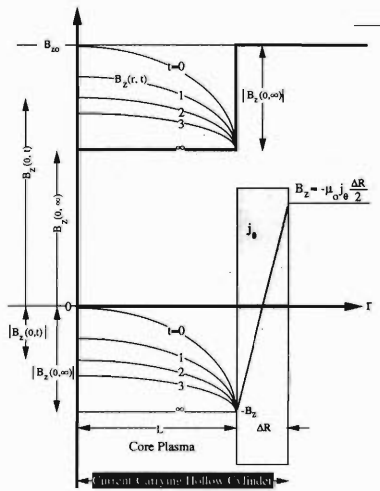


Fig. 3. Field diffusion and field annihilation heating (FAH) mechanisms.

The annihilating or diamagnetic field,  $B_d(t)$ , is given from Eq. (4) by

$$B_d(t) = B_D(0) - B_D(t) = |B_z(0, \infty)| \cdot \left[1 - \exp\left(-\frac{t}{\tau_D}\right)\right]. \quad (7)$$

This Eq. (7) is directly proportional to the integrated diamagnetic signal, because  $V_{int} \equiv \int V_\theta dt = -S|B_d(t)|$ . We found that the experimental diamagnetic signal<sup>3)</sup> indeed obeys the diffusion model of Eq. (7), and that  $\tau_D \approx 13$  ms as seen in Fig. 4. The scale length of the core-plasma was found semi-experimentally to be<sup>4)</sup>  $L \approx 0.04$  m. Then, Eq. (5) gives  $\eta = (\mu_0/\tau_D)(2L/\pi)^2 = 6.27 \times 10^{-8}$  [Ohm-m]. Since  $\ln \Lambda = 16$  for typical ECRIS plasmas, the  $\eta$  in Eq. (5) gives quite reasonable values:  $T_{ew} = 883$  eV if  $Z = 1$  and 1.40 keV if  $Z = 2$ . Here,  $Z = \langle Z_i \rangle = n_e/\Sigma n_i$ . These  $T_{ew}$  can be converted into  $W_J$  of Eq. (6), assuming  $n_e = 10^{12}$  cm<sup>3</sup>, from which one can estimate the dissipated fields to be  $|B_z(0, \infty)| = 132$  G and 167 G if  $Z = 1$  and 2, respectively. Since  $B_{ECR} = f_c(\text{Hz})/2.8 \times 10^{10} = 0.357$  T if  $f_c = 10$  GHz, those dissipated fields

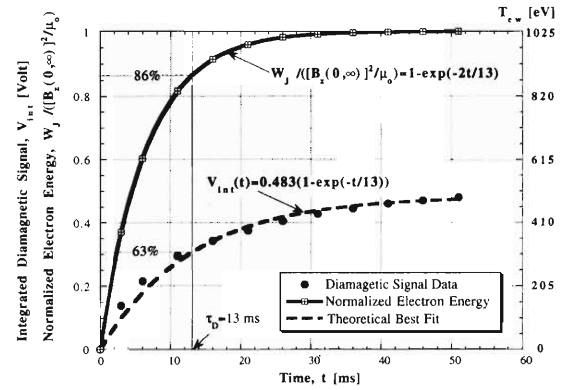


Fig. 4. Diamagnetic signal data and deduced  $T_{ew}$  time-history.

corresponds  $|B_z(0, \infty)|/B_{ECR} = 3.7\%$  and  $4.7\%$  for  $Z = 1$  and 2, respectively.

Suppose 100% of the ECR field 0.357T was annihilated, Eq. (6) gives  $W_J = 1.01 \times 10^5$  J/m<sup>3</sup> if  $n_e = 10^{12}$  cm<sup>3</sup>, yielding the theoretical maximum  $T_{ew} = 631$  keV. Of course, this  $T_{ew}$  is significantly over-estimating, partly because the uniform field ( $B_{z0}$ ) in the core is much smaller than  $B_{ECR}$  in practical devices.

Figure 5 shows a proposed experimental setup to measure  $T_{ew}$  via the HeI visible spectroscopy.  $T_{ew}$  can be determined from the singlet/triplet (443.7 nm/412.1 nm) line intensity ratio, which has readily been predicted as a function of  $T_e$  by the authors.<sup>5)</sup> This setup is equipped with a constant solid-angle ( $d\Omega$ ) collection optics, useful for scanning the diagnostic spots over the entire radius. This becomes important at the time to measure the absolute spectral intensity for determination of  $n_{ew}$  at different radii.

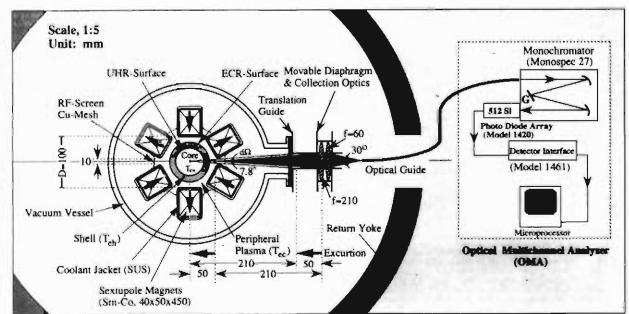


Fig. 5. Proposed diagnostics for  $T_{ew}$  of confined electrons.

## References

- 1) M. Niimura et al.: Proc. 12th Int'l Workshop on ECR Ion Source, Wako, 1995, p. 141.
- 2) K. Langbein: Rev. Sci. Instrum. **61**, 330 (1990).
- 3) C. Barue et al.: Rev. Sci. Instrum. **63**, 2844 (1992).
- 4) M. Niimura et al.: Proc. 13th Int'l Workshop on ECR Ion Sources, College Station-TX (1997), p. 52.
- 5) M. Niimura et al.: RIKEN Accel. Prog. Rep. **28**, 152 (1994).

## Production of Multicharged Os Ion Beams from Organic Metal Compounds Using RIKEN 18 GHz ECRIS

M. Kidera, T. Nakagawa, Y. Miyazawa, M. Hemmi, T. Chiba, N. Inabe, M. Kase, T. Kageyama, O. Kamigaito, A. Goto, and Y. Yano

For production of the metal ion beams by ECRIS (Electron Cyclotron Resonance Ion Source), several methods have been developed and utilized.<sup>1-3)</sup> One of these methods is called MIVOC (Metal Ions from Volatile Compounds) method.<sup>2,3)</sup>

Very recently, various kinds of ions were successfully produced using the MIVOC method from the RIKEN 18 GHz ECRIS.<sup>4)</sup> In order to produce intense beams of multicharged ions from these materials, we need a vapor pressure of  $10^{-4}$ – $10^{-3}$  Torr. In the case of Os, the temperature with which the vapor pressure becomes higher than  $10^{-4}$  Torr is 2800 °C. Thus, it is very difficult to produce Os ions from solid Os. The MIVOC method is a good method to produce such ions.

The experimental setup is the same as that described in Ref. 4. The chamber was connected by a gas-feeding tube via a large conductance, regulation valve to control the flow rate of the compound vapor. A few tens of milligrams of the compound powder was placed at the bottom of the MIVOC chamber. Air and moisture were evacuated until the vapor pressure of the compound became the dominant pressure in the MIVOC chamber. A gas-mixing method was not applied during the present experiment. In order to minimize contamination, the plasma chamber wall was covered with a thin aluminum tube which is easily removable, if necessary.<sup>5)</sup>

Figure 1 shows the charge state distribution of the Os ions produced from  $\text{Os}(\text{C}_5\text{H}_5)_2$ . The gas pressures in the plasma chamber and in the extraction stage were  $4.6 \times 10^{-7}$  and  $3.1 \times 10^{-7}$  Torr, respectively. Figure 2 shows the beam intensity of extracted Os ions as a function of RF power. In order to study the microwave

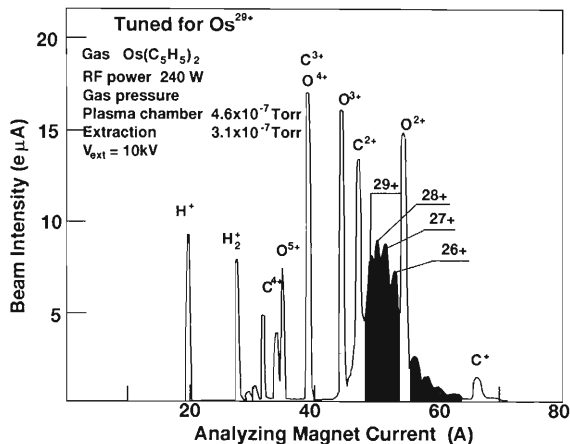


Fig. 1. The charge state distribution of Os ions. The ion source was tuned for the 29+.

power effects, the ion source was tuned for  $\text{Os}^{29+}$ . The ion current showed a maximum at the RF power of 240 W. Then, the power was reduced step by step down to 100 W. No other parameters were changed. Integrated Os (particle) currents stayed almost constant. Figure 3 shows the charge state distribution of the extracted Os ions. The ion source was tuned for producing the maximum intensity of each charge state.

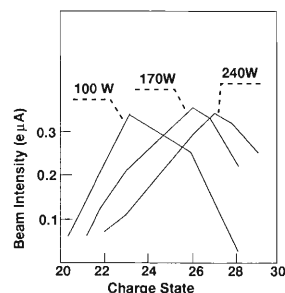


Fig. 2. The beam intensity of Os ions as a function of RF power. The ion source was tuned for producing the maximum intensity of 29+ ion.

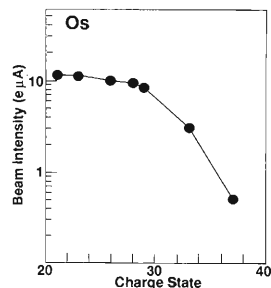


Fig. 3. The charge state distribution of extracted Os ions. The ion source was tuned for producing each charge state.

We have successfully produced multicharged Os ions from  $\text{Os}(\text{C}_5\text{H}_5)_2$  using the RIKEN 18 GHz ECRIS. The beam intensities of the  $\text{Os}^{28+}$  and  $\text{Os}^{33+}$  ions were 10 and 2.5  $\mu\text{A}$  at the RF power of 250 W, respectively.

### References

- 1) R. Geller: in *Electron Cyclotron Resonance Ion Sources and ECR plasma* (IOP, Bristol, 1996), p. 256 and references therein.
- 2) H. Koivisto et al.: Nucl. Instrum. Methods Phys. Res. B **94**, 291 (1994).
- 3) H. Waldmann and B. Martin: Nucl. Instrum. Methods Phys. Res. B **98**, 532 (1995).
- 4) T. Nakagawa et al.: Nucl. Instrum. Methods Phys. Res. A **396**, 9 (1997).
- 5) T. Nakagawa et al.: Jpn. J. Appl. Phys. **35**, 4077 (1996).

## Recent Development of the Variable-Frequency RFQ Linac for RILAC

O. Kamigaito, A. Goto, Y. Miyazawa, T. Chiba, M. Hemmi, M. Kase, S. Kohara,  
Y. Batygin, T. Nakagawa, E. Ikezawa, and Y. Yano

As already reported,<sup>1)</sup> the new injector for the RILAC, consisting of the 18-GHz ECR ion source and the variable-frequency RFQ, was installed in the RILAC beam line in August 1996. Figure 1 shows the layout of the injector RFQ along with the six tanks of the RILAC. Acceleration tests of the RILAC and RRC have been carried out continually using the beams from the new injector since the installation.

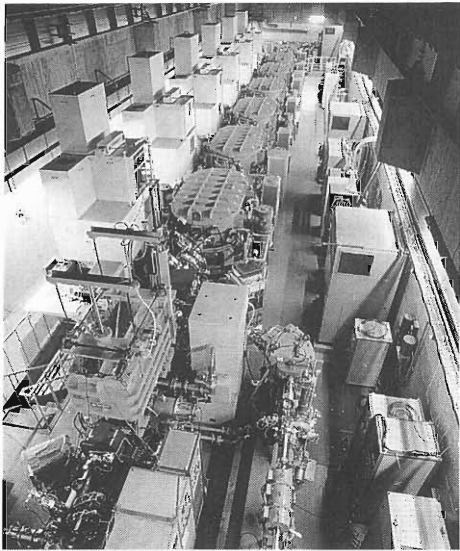


Fig. 1. Photograph of the RFQ along with the RILAC.

As the first step of the acceleration tests, we have tested the RILAC using various kinds of beams accelerated by the new injector. The accelerated ions were  $N^{2,3+}$ ,  $Ar^{2,4,5+}$ ,  $Fe^{7,8+}$ ,  $Ni^{8+}$ ,  $Kr^{5,11,18+}$ ,  $Te^{18+}$  and  $Xe^{7,17,19+}$ . They are indicated by the diamonds and open circles depending on the mode of acceleration in Fig. 2.

Due to the high performance of the new ion source,<sup>2)</sup> the beam intensity from the RILAC has remarkably increased. The maximum beam intensity achieved at the first step was  $13 \mu A$  for the  $N^{3+}$  beam at 2.5 MeV/nucleon, whose beam power was 450 W.

Another important result we have obtained is that the transmission efficiency of the RILAC has increased to 70%, as illustrated in Fig. 3, while it was 50% with the beam from the Cockcroft-Walton injector. In the tests, however, the transmission efficiency up to the entrance of the RILAC was about 70%. Considering that the efficiency through the RFQ was 88% in the preliminary test,<sup>3)</sup> this result was not good enough.

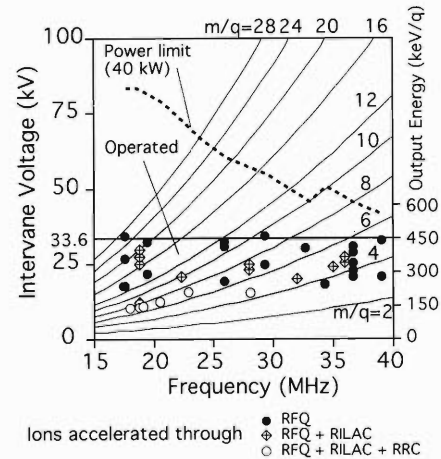


Fig. 2. Performance of the RFQ linac. The abscissa and the ordinate represent the resonant frequency and the intervane voltage, respectively. The output energy, which is proportional to the intervane voltage, is also indicated. The hatched area shows the region where the RFQ has ever been operated in the cw mode. The ions accelerated until July, 1997 are indicated by the closed circles, the diamonds, and the open circles. The solid curves represent the acceleration condition of ions, each of which is indicated by the  $m/q$ -value. The dashed curve shows the maximum attainable voltage with the present power source (40 kW).

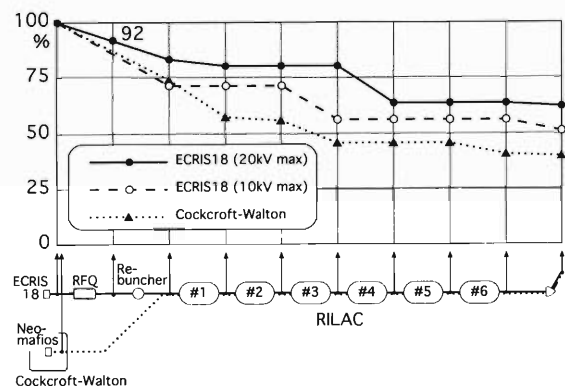


Fig. 3. Maximum transmission efficiency of the beam through the RILAC. The measurement was done with the Faraday cups indicated in the figure. The solid line represents the result of the beam from the new injector after the improvement in August, 1997. The dashed and the dotted lines are those of the beams from the new injector before the improvement and the Cockcroft-Walton injector, respectively.

Therefore, about one half of the extracted beam from the 18-GHz ECR ion source was accelerated with the RILAC.

As the second step, we started the acceleration tests of the RRC with the upgraded RILAC in December 1996. The accelerated ions were  $\text{Ar}^{5+}$ ,  $\text{Fe}^{7+}$ ,  $\text{Ni}^{8+}$ ,  $\text{Te}^{18+}$ ,  $\text{Kr}^{18+}$  and  $\text{Xe}^{17,19+}$  at the frequencies of 18.0, 18.8, 19.1, 20.5, 22.9 and 28.1 MHz. They are indicated by the open circles in Fig. 2.

In the first test using an  $^{36}\text{Ar}^{5+}$  beam, we achieved the beam current of 1 pμA, extracted from the RRC for the first time. In this test, about one fifth of the extracted beam from the ion source was accelerated to the final energy of 7.5 MeV/nucleon. The beam power was 300 W.

One of the advantages of the new injector is that highly charged ions are readily generated with the 18-GHz ECR ion source. Therefore, the charge stripper before the RRC has become unnecessary for the low-energy beams of the medium-heavy ions mentioned above, and consequently the stability of the beam has been improved.

On the other hand, the extraction voltage of the ECR ion source should be very low for the highly charged ions because the maximum extraction voltage was set to be 10 kV. For example, the extraction voltage was only 3 kV in the first test using the  $^{36}\text{Ar}^{5+}$  beam. This situation is not good for the beam intensity which is roughly proportional to the extraction voltage to the three half power.

Therefore, in August 1997, we raised the maximum extraction voltage to 20 kV in order to increase the beam intensity further. The vanes were replaced correspondingly, whose parameters are listed in Table 1.

After the improvement, the beam intensity has increased by a few times as expected. For example, the intensity of  $\text{Ar}^{5+}$  beam accelerated through the RILAC has increased to 25 eμA from 10 eμA at 0.7 MeV/nucleon. Moreover, the maximum transmission efficiency has been improved, as shown in Fig. 3. The maximum beam power ever achieved with the RILAC is 560 W for  $\text{O}^{5+}$  at 2.5 MeV/nucleon.

At the same time of replacement of the vanes, an additional Faraday cup was installed just after the RFQ in order to measure the transmission efficiency through the RFQ alone. According to the measured data, the

Table 1. Main Parameters of the RFQ.

	~ 07.1997	08.1997 ~
Frequency (MHz)	17.7 - 39.2	17.4 - 39.0
Mass-to-charge ratio (m/q)	6 - 26	6 - 26
Input energy (keV/q)	10	20
Output energy (keV/q)	450	450
Input emittance (mm·mrad)	145 π	145 π
Vane length (cm)	142	153
Intervane voltage (kV)	33.6	36.8
Mean aperture ( $r_o$ ;mm)	7.70	8.08
Min. aperture ( $a_{min}$ ;mm)	4.17	4.67
Max. modulation ( $m$ )	2.70	2.41
Focusing strength ( $B$ )	6.8	6.8
Max. defocusing strength	-0.30	-0.30
Final synchronous phase	-25°	-30°

efficiency was 92%, being slightly larger than that obtained in the preliminary test. The efficiency up to the entrance of the RILAC was, however, 80% at maximum as shown in Fig. 3. This means that some portion of the beam is lost in the matching section between the RFQ and the RILAC. In fact, it was recently found that the drift tube of the rebuncher has a smaller aperture than the actual beam size. New drift tubes are under fabrication to give a larger acceptance for the rebuncher.

In September 1997, we tested the RRC with the beam from the upgraded injector. In the first test, we extracted Argon beam of 1 pμA from the RRC. This intensity is the official limit allowed for our facility. If it were not for this limit, more intensive beam could have been extracted. In the second test using Xenon beam, the extracted beam current was 200 pA. The overall transmission efficiency was about 10% in these tests. In spite of this low efficiency, the beam intensity after the RILAC has increased by a few tenth of magnitude compared with those which had been available with the Cockcroft-Walton injector.

In summary, the development of the injector RFQ worked out satisfactorily. More efforts will be paid for the improvement of the transmission efficiency.

#### References

- 1) A. Goto et al.: RIKEN Accel. Prog. Rep. **30**, 186 (1997).
- 2) T. Nakagawa et al.: RIKEN Accel. Prog. Rep. **30**, 188 (1997).
- 3) O. Kamigaito et al.: RIKEN Accel. Prog. Rep. **30**, 189 (1997).

## Phase Stabilization of Injection Beam to RIKEN Ring Cyclotron

M. Kobayashi, A. Yoneda, M. Kase, M. Kidera, A. Goto, and Y. Yano

When the RIKEN Ring Cyclotron (RRC) is coupled with the one of its two injectors, RIKEN heavy-ion linac (RILAC), the beam transmission rate through the RRC is sometimes limited by the phase instabilities of the injection beam from the RILAC. Recently, it was tried to reduce the phase instabilities by a closed control loop system and to improve the efficiency of beam transmission through the RRC.

The beam phase is measured by capacitive pick-up probes in the beam transport line between the RILAC and the RRC. In the signals from the probe, an instability is sometimes observed in the beam phase, which

has a frequency range of 10–100 Hz. The instability is caused by the fluctuation of the rf voltages in some cavities of the RILAC. The average energy of a beam bunch at the exit of RILAC is affected by this fluctuation, and the effective beam phase is spread out after drifting along the long beam line down to the re-buncher which is installed on a half way between the RILAC and the RRC. The broadening sometimes becomes larger than the phase acceptance of the re-buncher, and therefore the beam transmission efficiency through the RRC becomes worse.

By using the phasemeter as shown in Fig. 1, a

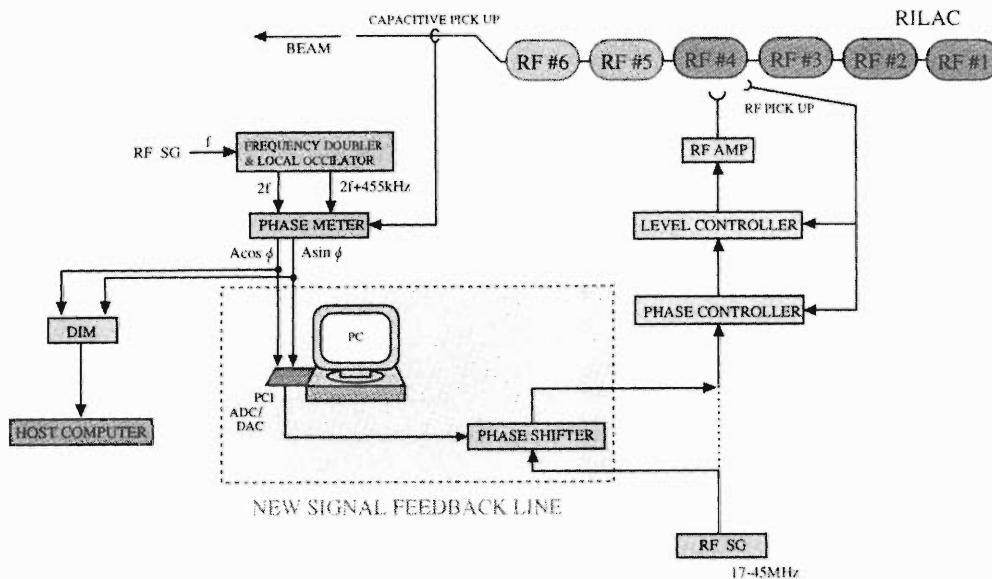


Fig. 1. Beam phase measurement and signal feedback system of the beam phase to the phase of rf cavity of the RILAC. The part surrounded by dotted line is a newly installed feedback line.

second-harmonic component of the beam signal is extracted and converted into two analog signals,  $A\cos\phi$  and  $A\sin\phi$ , where 'A' corresponds to a beam intensity and ' $\phi$ ' the beam phase relative to rf. The system has a response of 1 kHz and the data of these two signals are taken through an interface-board of DIM<sup>1)</sup> every 2 ms and stored in an 8 kB memory in it. And then, they are transferred to the host computer.

Figure 2(a) shows the data stored for a period of 4 s for 0.5 MeV/nucleon <sup>40</sup>Ar beam. In this case, the beam energy is 7.6 MeV/nucleon after the RRC. The harmonic number of the RRC is 11, and correspondingly only the first 4 cavities of the RILAC are used. Each point in the figure corresponds to one measurement. The distance between the 4th cavity (RF #4)

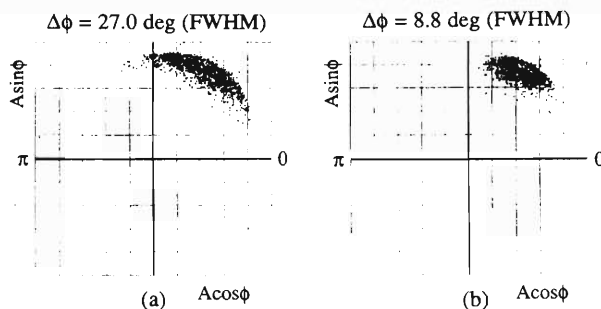


Fig. 2. Observed beam phase at the RILAC: (a) and (b) show the data without and with the feedback system, respectively. The  $\Delta\phi$  in FWHM is 27.0 deg for (a), and 8.8 deg for (b).

to the probe is about 24 m. From this figure, it is clear that the straggling width of the beam phase (azimuthal direction) is quite large, while the beam intensity (radial direction) seems relatively stable. The straggling value about the spread of the beam phase,  $\Delta\phi$ , is 27.0 deg in FWHM.

The phase and energy of the beam from RILAC are given as a function of the rf phase and amplitude of every cavity in use. Among them, the energy depends smoothly on the rf phase of the final cavity in use, while the output phase does not change so much. In other words, the energy of beam from the RILAC can be tuned intentionally by adjusting the rf phase of the final cavity<sup>2)</sup> without changing the beam output phase. The fluctuation of beam energy at the exit of RILAC, which is converted into the fluctuation of the beam phase at the phase probe location, can thus be suppressed by adjusting the rf phase of the final cavity.

According to this expectation, a new feedback system was developed as shown in the part surrounded by dotted line of Fig. 1. For the signal feedback system, a local personal computer (PC) with the ADC & DAC board is used. The two signals from the phasemeter

are fed into the ADC, and the PC calculates 'A',  $\phi$ , and the output signal  $V_{\text{out}}$ . The relationship for this output signal is given by  $V_{\text{out}} = V_o + (\phi - \phi_o)G$ , where  $G$  and  $V_o$  are the gain parameter and the offset voltage (+5 V constantly) of the system, respectively. The  $\phi_o$  is the center of the fluctuating phase and an input parameter. The  $V_{\text{out}}$  is set on the DAC when 'A' is within the available range. The circulation period is around 80  $\mu\text{s}$ . The output signal from the DAC is fed into the phase shifter which is inserted into the input line of the low-level circuit of the RF #4 system.  $G$  is selected by changing its value to minimize the phase spread.

Figure 2(b) shows the data obtained using the feedback system for the same beam as in Fig. 2(a). The  $\Delta\phi$  for a period of 4 s is reduced to 8.8 deg in FWHM, being one-third of the data without this feedback system. Further, by the use of this system, an improvement in the transmission rate of the RRC was observed.

#### References

- 1) T. Wada et al.: Sci. Papers I.P.C.R. **79**, 28 (1985).
- 2) M. Kase et al.: Sci. Papers I.P.C.R. **79**, 45 (1985).

## Beam Orbit Simulation in the Central Region of RIKEN AVF Cyclotron

D. Toprek, A. Goto, and Y. Yano

This paper describes a design modification of the central region at  $h = 2$  mode of acceleration in the RIKEN AVF cyclotron. We made a small modification to the electrode shape in the central region for optimization of the beam transmission. The central region is equipped with an axial injection system. The spiral type inflector is used for the axial injection. In Ref. 1 is shown the shape of the electrodes of the central region of former design. In the former design, the ion trajectory through the spiral inflector (with parameters:  $A = 2.6$  cm and  $k' = 0.0$  which are defined in Ref. 2) is analytically calculated, and the electric field distribution in the four acceleration gaps is described by a Gaussian function. In the present design, to treat more realistically both the spiral inflector and the central region, the electric field distributions in the inflector and in the four accelerating gaps have been numerically calculated from electric potential maps, produced by using the RELAX3D program.<sup>3,4)</sup> The optimized inflector has the following parameters:  $A = 2.2$  cm and  $k' = 0.3$ . For the simulation of the ion trajectories passing through the spiral inflector and the central region we used the CASINO<sup>5)</sup> and CYCLONE<sup>6)</sup> programs, respectively. As for the magnetic field distributions in the central region, we used the measured median plane map whose data were taken with an azimuthal step of 1.8 degree and a radial step of 2 cm.

Figure 1 shows the modified shape of the electrode in the central region of the RIKEN AVF cyclotron. The dotted area shows the area that has been cut off from the previously designed electrode, following to the new simulation result.

Figure 2 shows the simulated phase space diagrams in two transversal planes<sup>2)</sup>  $(u, p_u)$  and  $(h, p_h)$  at the exit of the inflector (solid line curves marked by the letters  $f_u$  and  $f_h$ , respectively), together with their initial phase space diagrams at its entrance (dashed and dotted lines, respectively). The emittance size in the initial phase space is  $\varepsilon_u = 140\pi$  mm mrad (dashed line) in the  $(u, p_u)$  plane and  $\varepsilon_h = 130\pi$  mm mrad (dotted line) in the  $(h, p_h)$  plane. By using the CASINO, we have made the simulation for seven particles whose initial positions in the phase space are indicated by open circles in Fig. 2. The simulation was made for the three cases with different longitudinal momentum values:  $\delta p_\nu \equiv \Delta p_\nu / p = -0.01, 0.0$ , and  $+0.01$ , where  $p$  is the total momentum of the ion. As seen in Fig. 2, the final phase space diagrams (solid lines) changes depending on the momentum values. This shows that the coupling effects are important. Figure 2 shows the case when the particle is inflected by decreasing the in-

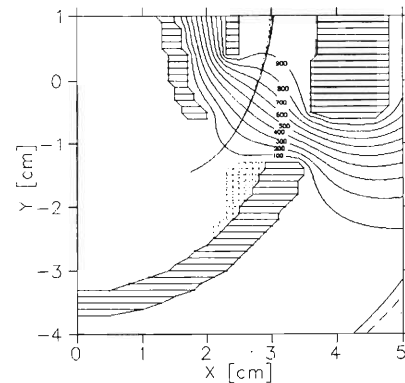


Fig. 1. The modified shape of the electrode in the central region of the RIKEN AVF cyclotron. The dotted area has been cut off from the previously designed electrode.

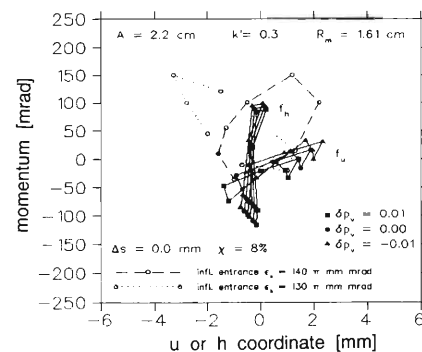


Fig. 2. Phase space diagram in two transversal planes  $(u, p_u)$  and  $(h, p_h)$  at the inflector entrance (dashed and dotted lines) and at its exit (solid line curves marked by letters  $f_u$  and  $f_h$ , respectively). The emittance at the inflector's entrance is  $\varepsilon_u = 140\pi$  mm mrad (dashed line) and  $\varepsilon_h = 130\pi$  mm mrad (dotted line), and the relative change of longitudinal component of the momentum of ions is  $\delta p_\nu = -0.01, 0.0$  and  $+0.01$ . The other marks are explained in the text.

flector voltage by 8% ( $\Delta s = 0$  mm,  $\chi = 8\%$ ) from the nominal (or analytical) value. This voltage of  $\chi = 8\%$  gives the best transmission.

The geometry of the central region has been tested with the orbit simulation carried out by means of the computer code CYCLONE. In Fig. 3, the simulated central trajectories of the reference ion are shown up to the second turns. The trajectories are shown for three cases with initial accelerating phases of  $-50, -55$  and  $-60$  degrees. For this simulation the dee voltage was assumed to be 50 kV. The initial radius  $r_0$  and radial

momentum  $p_{r0}$  were taken to be 2.26 cm and 0.67 cm, respectively, which were obtained from the CASINO calculations.

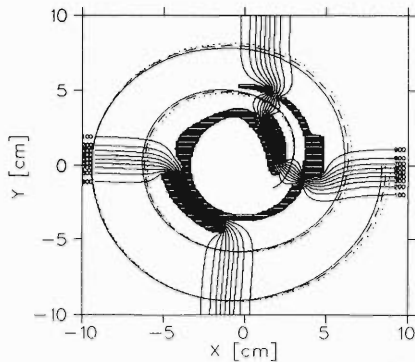


Fig. 3. The central trajectory of the reference ion ( $\eta = 0.357$ ,  $B_0 = 1.5T$ ,  $h = 2$ ) in the central region of the K70 AVF cyclotron for different values of the starting phase  $\phi_0$  with the equipotential contours of the numerically by calculated field.  $\phi_0 = -50^\circ$  (solid line),  $\phi_0 = -55^\circ$  (dashed line) and  $\phi_0 = -60^\circ$  (dotted line). The equipotential contours are plotted at each 10% of the full dee voltage  $U_0$ .

We next tested the phase acceptance of the central region of the machine by tracking the first two turns of the ions and by looking at the beam envelopes in both horizontal and vertical planes. The emittance of the beam was reconstructed from its emittance at the entrance of the inflector (see Fig. 2). The family of curves marked by letters of  $f_u$  and  $f_h$  (which correspond to the  $(u, p_u)$  and  $(h, p_h)$  planes at the inflector exit) now correspond to the  $(z, p_z)$  and  $(r, p_r)$  planes, respectively, at the entrance of the central region of the cyclotron. It was found that the phase acceptance was determined by the vertical beam spread. Figure 4 shows the vertical beam envelope simulated for the three different values of the initial phases  $\phi_0$ .

The same initial conditions as in Fig. 2 were used in the simulation. Only those starting phases which give vertical envelopes contained within the smallest vertical aperture of the central region are shown. From Fig. 4 we can see that the phase acceptance of the central region is about 10 degrees, which agrees with the result in the former design.

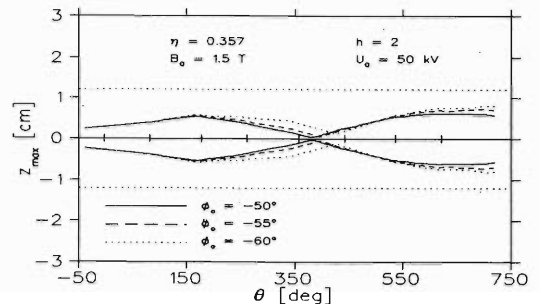


Fig. 4. The maximal vertical displacement of the beam in the first two turns for test ions in the K70 AVF cyclotron for different values of the starting phase  $\phi_0$ . The short lines crossing the abscissa show the electric gap positions, and the dotted lines parallel to abscissa indicate the minimal vertical aperture of the central region.

#### References

- 1) A. Goto et al.: Proc. 12th Int. Conf. on Cyclotrons and their Applications, Berlin, 1989, p. 439.
- 2) L. Root: M. Sc. Thesis, Univ. of British Columbia, 1972.
- 3) C. J. Kost and F. W. Jones: RELAX3D User's Guide and Reference Manual, TRI-CD-88-01, Vancouver, 1988.
- 4) Lj. M. Milinkovic: RELAX3D Spiral Injectors, TR30-DN-89-21, Vancouver, 1989.
- 5) F. B. Milton and J. B. Pearson: CASINO User's Guide and Reference Manual, TRI-DN-89-19, Vancouver, 1989.
- 6) B. F. Milton: CYCLONE VERS. 6.0, TRIUMF Internal Report, June 22, 1989.

## Design of a Resonator for a Flat-Top Acceleration System in RIKEN AVF Cyclotron

S. Kohara, Y. Miyazawa, O. Kamigaito, T. Chiba, and A. Goto

A resonator for a flat-top acceleration system in the RIKEN AVF Cyclotron is designed to improve the extraction efficiency and the energy spread of beam. In order to generate the flat-top accelerating voltage on the dee, an additional resonator or a transmission line is required, which is coupled to the fundamental-frequency resonator with a coupling capacitor.<sup>1)</sup> The flat-top accelerating voltage is obtained by the superimposition of the fundamental frequency and fifth-harmonic-frequency voltages. Structure and rf characteristics of the resonator designed for the flat-top acceleration system is described.<sup>2)</sup>

A layout of the AVF cyclotron is shown in Fig. 1. The AVF Cyclotron has two resonators, each of the coaxial quarter-wave-length type with a dee angle of  $83^\circ$ . The frequency range is from 12 to 23 MHz. The required maximum accelerating voltage is 50 kV. A movable shorting plate has been used for the coarse tuning and a capacitive tuner for the automatic fine tuning of the fundamental-frequency resonator. The stroke of the movable shorting plate is 2 m. The frequency-shift range of the capacitive tuner is about 500 kHz. A grounded-cathode tetrode (4CW50,000E) amplifier is capacitively coupled to the fundamental-frequency resonator with a fixed vacuum coupling capacitor (16 pF). Its maximum output power is 20 kW. In general, the required amplitude of the fifth-harmonic-frequency voltage is about  $1/25$  of the fundamental-frequency voltage, when the voltage distribution of the acceleration gap is assumed to be flat. Therefore, the frequency range and maximum voltage of the fifth-harmonic-frequency system are estimated to be from 60 to 115 MHz and 2 kV, respectively.

A cross-sectional view of the resonator designed for the flat-top acceleration system is shown in Fig. 2. It

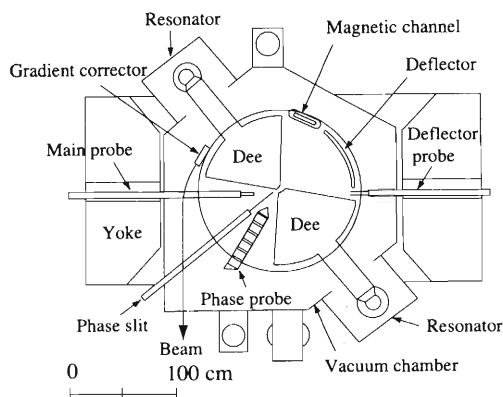


Fig. 1. Layout of the AVF cyclotron.

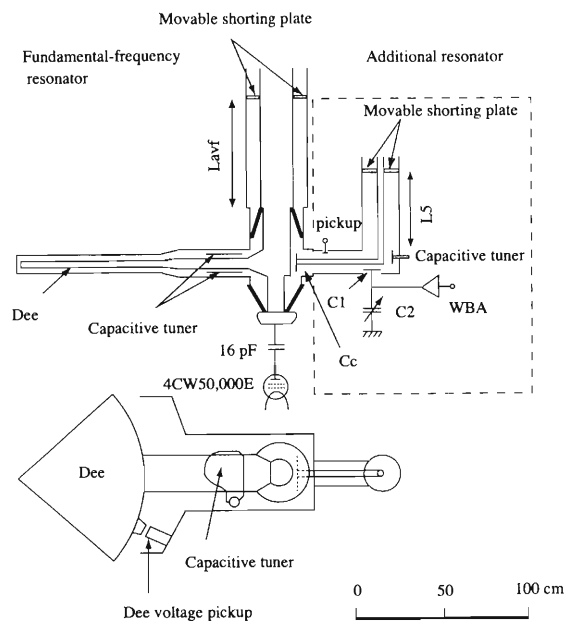


Fig. 2. Cross-sectional view of the resonator for the flat-top acceleration system.

consists of the fundamental-frequency and the additional resonators to generate the flat-top accelerating voltage on the dee. The additional resonator is employed to excite a higher harmonic resonance in the AVF resonator with the frequency five times of the fundamental frequency, but without a large shift in the fundamental frequency. The additional resonator consists of a transmission line and a coupling capacitor ( $C_c$ ). The fifth-harmonic resonant frequency is generated by adjusting both the position of the movable shorting plate ( $L_5$ ) and the coupling capacitance ( $C_c$ ) of the additional resonator after the fundamental frequency of the resonator is set by the movable shorting plate ( $L_{avf}$ ).

The rf characteristics of the resonator was calculated with the transmission-line approximation. Figure 3 shows the positions of the movable shorting plates of the additional and the fundamental-frequency resonators to obtain the fifth-harmonic resonant frequencies. The highest position of the movable shorting plate of the additional resonator is 50 cm when the coupling capacitance is 30 pF. Shunt impedances calculated as a function of the fifth-harmonic resonant frequency are shown in Fig. 4. The ratio of the voltage at the extraction position to that of the injection position of the AVF cyclotron is from 0.85 at 60 MHz to 0.49 at 115 MHz. Therefore, the required fifth-

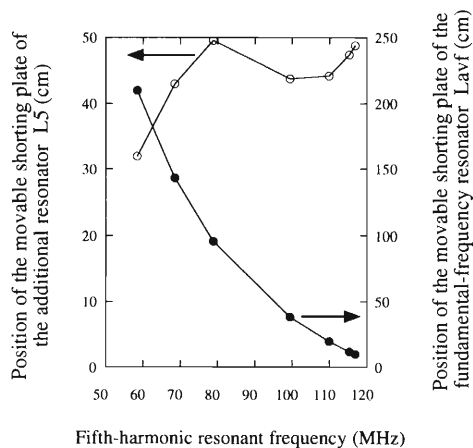


Fig. 3. Position of the movable shorting plates of the additional and the fundamental-frequency resonators calculated as a function of the fifth-harmonic resonant frequency. The coupling capacitance ( $C_c$ ) is 30 pF.

harmonic-frequency voltage at 115 MHz is estimated to be 1/17 of the fundamental-frequency voltage; its maximum voltage is to be 3 kV. Power losses are estimated to be 2,900 W at 58.5 MHz, 560 W at 80 MHz, and 690 W at 115 MHz when the voltage is 3 kV.

A power amplifier for the fifth-harmonic resonant frequency will be a solid-state wide-band amplifier (WBA) whose output impedance is 50  $\Omega$ . A capacitive divider is used to match the input impedance of the additional resonator to the output impedance of the wide-band amplifier. The capacitive divider con-

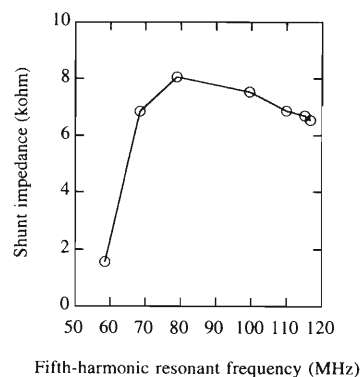


Fig. 4. Shunt impedance calculated as a function of the fifth-harmonic resonant frequency. The coupling capacitance ( $C_c$ ) is 30 pF.

sists of a coupling capacitor ( $C_1$ ) and a variable capacitor ( $C_2$ ). In order to obtain a good impedance matching, the capacitance of the variable capacitor is estimated to be from 90 to 120 pF when the coupling capacitance is 3 pF. Fabrication of a model resonator is in progress.

#### References

- 1) J. L. Conradie: National Accelerator Centre, South Africa, Dissertation presented for the degree of Doctor of Philosophy in Physics at the University of Stellenbosch (1992).
- 2) S. Kohara et al.: Proc. 11th Symp. on Accelerator Science and Technology, Harima, p. 194 (1997).

## New Emittance Measurement Using Two PPACs

A. Yoneda, H. Kumagai, M. Kobayashi, N. Fukunishi, M. Kase, A. Goto, and Y. Yano

A new emittance monitor has been developed, which is designed to measure precisely the emittance of a high-energy beam generated by the RIKEN Ring Cyclotron (RRC). This emittance monitor consists of two sets of two dimensional position sensitive gas counters (PPAC; parallel plate avalanche counter). Such PPAC itself can work as a beam image monitor for a low-intensity beam.<sup>1)</sup>

Figure 1 shows the principle of the emittance measurement using two PPACs. Suppose that two position-sensitive detectors are installed in a straight beam line with a distance of  $L$  (2.9 m in this case) in the interval, and that the sensitive areas are large enough to ensure all particles in the beam pass through the both detectors. When one particle passes through the detectors, two sets of two-dimensional position data,  $(X_a, Y_a)$  and  $(X_b, Y_b)$ , are obtained; where the suffix 'a' and 'b' are for the first (upstream) detector and the second (downstream) one, respectively. From the obtained data, a position and an angle of the particle are calculated easily as  $(X_a, X')$  and  $(Y_a, Y')$ , where  $X' = (X_b - X_a)/L$  and  $Y' = (Y_b - Y_a)/L$ . If the thickness of the detector is thin enough, the trajectory is not affected by the existence of the detector. The deflection of a beam due to the penetration of a counter (upstream) is estimated using by the Ziegler formula. Total thickness of the PPAC is estimated equivalent to 1.9 mg/cm<sup>2</sup> Mylar. As a result, the scattering angle of the beam after passing the PPAC in the beam line is about 0.2 mrad for the case of 70 MeV/nucleon <sup>12</sup>C beam. This means that the effect of angular scattering of the beam by the PPAC itself is negligible.

After accumulating these data  $(X_a, X')$  and  $(Y_a, Y')$  for a number of particles in the beam, the beam emittance can be determined.

The electrode assembly of the PPAC consists of an anode and two cathodes on both sides of the anode. These electrodes are parallel each other with 4.0 mm interval. The anode is a thin gold layer (60 μg/cm<sup>2</sup> in thickness) which is deposited on a 2.5 μm-thick Mylar film on its both sides. On the other hand, the cathode has 51 gold strips (60 μg/cm<sup>2</sup> in thickness) whose pitches are 1.0 mm on a 2.5 μm-thick Mylar film and hence, the sensitive area is 50\*50 mm<sup>2</sup>. The charge division method is employed for the signal readout. Two signals from both ends of the cathode are taken outside, and are used to get the position information. One cathode is used for the measurement of the X-position and the other one is used for the Y-position.

These electrodes are set inside of the aluminum box which has two windows (for the beam entrance and exit) of 50\*50 mm<sup>2</sup> in size, and the distance of the two windows is 32 mm. The window film is 2 μm-thick Mylar, on the surface of which aluminum (8 μg/cm<sup>2</sup>) is deposited. This counter box has a gas inlet and outlet and has four feedthroughs for the position signals from two cathodes and one feedthrough for the bias voltage to the anode. Two gas lines and five signal cables are introduced to the atmosphere through a counter support pipe. A gas of isobutane is supplied by a stable gas flow, keeping the pressure inside the counter around 8 torr.

The counter is set exactly on the beam axis remotely when in use, and removed out of the beam area other

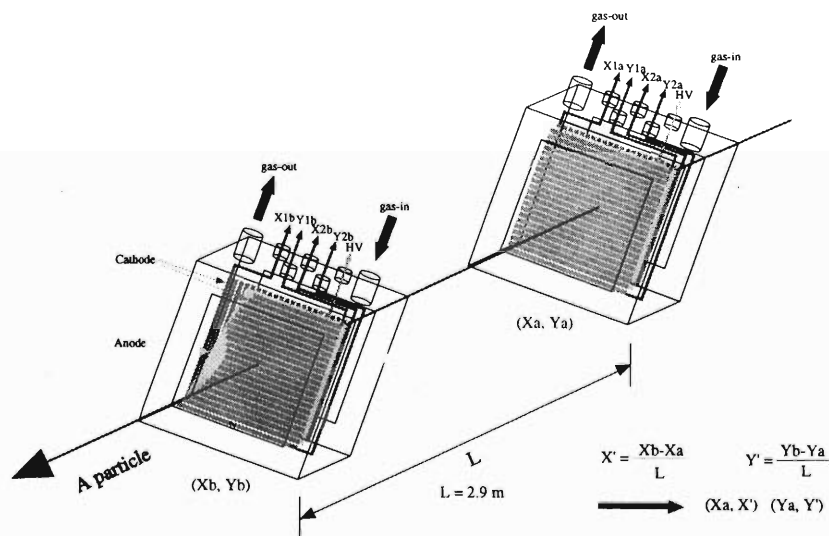


Fig. 1. Principle of the emittance measurement using two PPACs in series.

time. Two PPACs have been installed inside the beam diagnostic chambers separately, immediately after the extraction of RRC. There is no focusing element between the two chambers.

The PC takes eight signals, and only if the eight signals are all above the threshold, 10% of the maximum data range, it accumulates these data. If there is no threshold setting, accurate data cannot be obtained about the position information.

A test of the emittance measurement was performed with a beam of 110 MeV/nucleon  $^{22}\text{Ne}$ . The obtained data of the spatial distribution and emittance of the beam are shown in Figs. 2 and 3. The obtained emittances are  $15 \pi\text{mm}\cdot\text{mrad}$  for horizontal plane and  $4.6 \pi\text{mm}\cdot\text{mrad}$  for vertical one. The emittance in the horizontal plane might be enlarged due to a multi-turn-extraction and/or momentum dispersion effects. In Fig. 4, several spots due to the multi-turn extraction can be observed in the vertical plane.

From the result, it is clear that the PPAC system is very useful for the precise measurement of a low-intensity beam whose current not to exceed  $10^4$  particles/sec. By using these PPACs as beam emittance

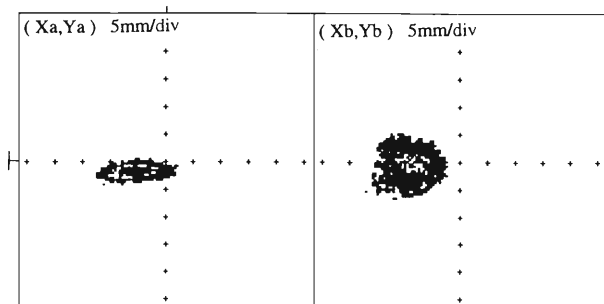


Fig. 2. The spatial distribution of a beam image measured by the PPAC.

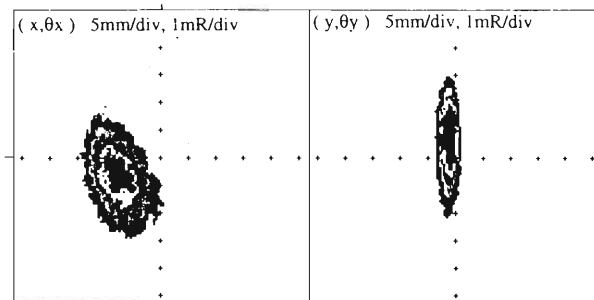


Fig. 3. Beam emittances measured by the PPAC. For a beam of 110 MeV/nucleon  $^{22}\text{Ne}$ , the obtained emittances are  $15 \pi\text{mm}\cdot\text{mrad}$  for horizontal plane and  $4.6 \pi\text{mm}\cdot\text{mrad}$  for vertical one.

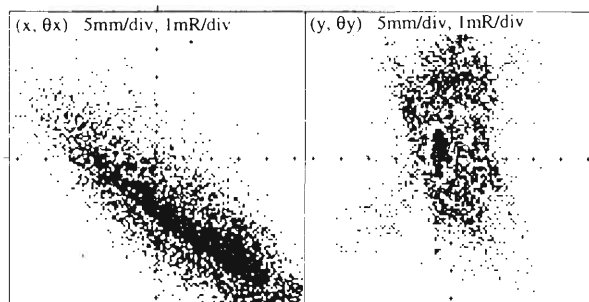


Fig. 4. Beam emittances measured by the PPAC. Several spots due to multi-turn extraction effect are shown by log scale in ordinate.

monitors, more accurate experiments may become possible.

#### References

- 1) H. Kumagai et al.: RIKEN Accel. Prog. Rep. **28**, 127 (1995).

## Heavy Ion Microbeam Project in RIKEN Accelerator Research Facility

N. Fukunishi, M. Kobayashi, A. Yoneda, M. Kidera, M. Kase, and Y. Yano

Recently, biologists have suggested a new type of experiments in which specified cells or organs are irradiated with heavy ions in order to elucidate complex communication mechanism between cells or between groups of cells. To promote this program, we are now planning to construct the new beam course which can provide microbeams.<sup>1)</sup> For producing a microbeam, we employ a beam collimation method because the beam intensity of the RIKEN Ring Cyclotron is sufficiently

high, and insertion of few devices into the present beam line is good enough to realize microbeams. We choose the aperture of  $50\ \mu\text{m}$  as a collimator for a first step of our project. The test bench of the collimator has been completed.<sup>2)</sup> The E5C course of the RIKEN Accelerator Research Facility was chosen as the microbeam course, and the beam transport was designed to make a parallel beam at the collimator in order to reduce undesired beam scattering. We show in Fig. 1 an example

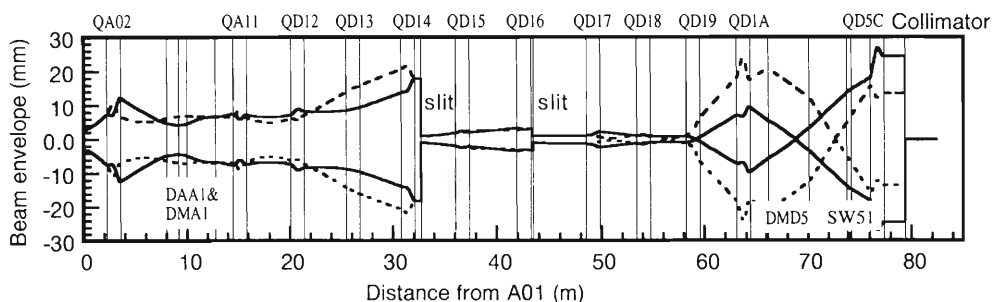


Fig. 1. Beam envelope in the E5C course. A solid (dashed) line is the horizontal (vertical) component. The A01 point is the object point of the beam optics. Vertical lines show positions of magnets, slits, and the collimator.

of calculated beam envelopes based on the first order theory of beam optics. The transmission efficiency is  $1.35 \times 10^{-9}$  in this case, and the resulting current of the microbeam is 840 ions/second for a 100 pA heavy-ion beam.

Figure 2 shows a conceptual design of the irradiation system. The thickness of the collimator is 10 mm even when a heavy metal is used, because the energy of heavy ions is quite high. In addition, we use a position-sensitive Si-detector (PSD) to resolve the beam axis. A microscope is installed to determine the target position. We fix the target on a movable stand and drive it using a stepping motor. We choose the minimum step as  $50\ \mu\text{m}$ . Utilizing these apparatuses, we set the target precisely on the beam axis. The scintillation counter placed above the target numerates the population of heavy ions. We also prepare a range shifter in order to vary the linear energy transfer. We set all devices on the same table which defend them from vibration. A beam profile monitor and a Faraday cup are prepared to assist the beam tuning, and we set them off from the beam axis during experiments. The first experiment with this system is scheduled in 1998.

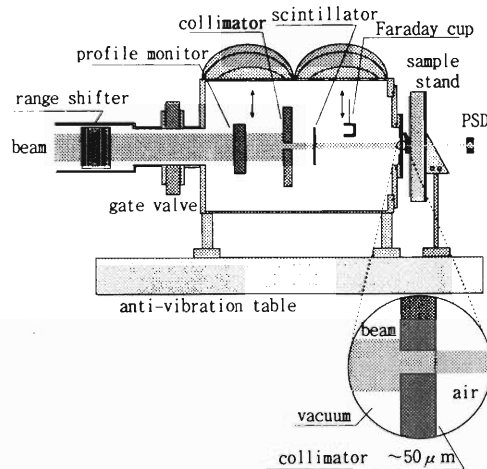


Fig. 2. Conceptual design of the irradiation system.

### References

- 1) N. Fukunishi et al.: Proc. 11th Symp. on Accelerator Science and Technology, Oct. (1997), to be published.
- 2) M. Anzai: Private communication.

## Initial Design of a Charge State Multiplier System for RIKEN RI Beam Factory

A. Bandyopadhyay, O. Kamigaito, A. Goto, and Y. Yano

The RI-beam factory project envisages to use a Charge State Multiplier<sup>1)</sup> (CSM) after the RILAC. The CSM consists of an accelerator - charge stripper - decelerator combination. A charge stripper placed after the accelerating section increases the  $q/A$  ratio of the beam and the decelerating section brings down the rigidity of the beam within the acceptable limit of the RRC.

The initial parameters for the CSM have been fixed by considering the acceleration of  $^{238}\text{U}$  ion at the frequency of 54.4 MHz. At present, the aim is to start with  $q = 22$  and optimize the production of  $q = 58$  from the stripper. Considering various aspects, the final energy for  $\text{U}^{22+}$  have been fixed around 3.84 MeV/u and the expected charge fraction of  $\text{U}^{58+}$  at this energy is 13.82%.<sup>2)</sup>

The focusing elements will not be placed within the drift tubes but in between the tanks in order to reduce the wall losses of tanks.<sup>1)</sup> As a consequence, the length of the individual tank should be moderate to confine the beam within reasonable transverse limits. It has been decided therefore to make four accelerating tanks and two decelerating tanks to reach this goal.

In order to find the dimensions of drift tube lengths and gap distances between the drift tubes, a program CELLGEN has been developed. The transit time factor has been calculated assuming a sharp edge approximation of the electric field between the drift tubes and assuming that the particle receives the total energy at the middle of each gap. In this design, the gap length in each tank has been kept same, equal to the half length of the first cell in each tank.

A beam dynamics code ARLIN1 has been developed for calculations of the transverse beam dynamics in the CSM. It is a first order matrix multiplication code capable of calculating the beam profile in the transverse plane starting with initial phase ellipse parameters. The defocusing effect of RF field in the drift-tube gap has been approximated to the action of a thin lens kept at the center of the gap. The change of the beam emittance due to the acceleration has been properly taken into account by adjusting the Twiss parameters at the center of each gap.

The optimization of quadrupole field strengths in between the tanks is yet to be implemented in the ARLIN1 program. Therefore, the code TRANSPORT<sup>3)</sup> has been additionally used for the initial optimization of the quadrupole fields for efficient transmission through the CSM. The arbitrary matrix option of the code has been used to describe the effect of RF defocusing in the tank. With these optimized fields the

code ARLIN1 has been used to find the beam profile.

Another code NEWCEL21 has been developed to study the longitudinal beam dynamics. Given the values of the synchronous phase and energy and of the half widths of their spread, the program generates a phase ellipse in the longitudinal phase space and tracks the motion of each particle up to the end of the tank. One can then draw the phase profile at any location within the tank.

The fixing of initial parameters of the drift tubes described above were performed assuming a flat voltage profile in each tank. In practice, however, the voltage profile is not exactly flat and it changes with frequency also. We have used the three dimensional RF structure analysis code MAFIA for the calculations of RF parameters and of the voltage distribution within the tanks.

We have opted for an IH type of structure (Fig. 1)

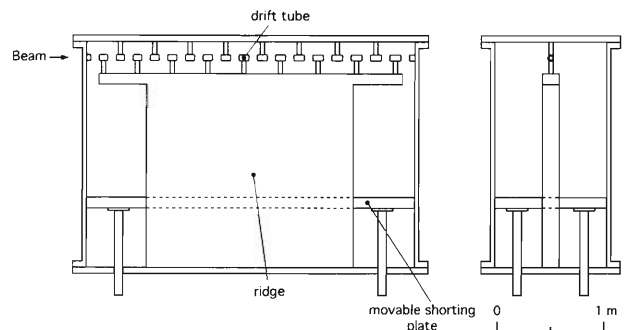


Fig. 1. Schematic diagram of a CSM tank.

for the CSM, as in the velocity range of operation this structure provides the highest shunt impedance. On top of this, the structure of the CSM should be of continuous frequency-variable type in the frequency range of 36 to 76 MHz, and it should have a maximum possible flat inter-gap voltage distribution in each tank. Further, the voltage distribution should not change much with the frequency. Figure 2 shows the optimized voltage distribution within the first tank for different frequencies. Identical results have been achieved for all the tanks. The dimensions of the ridge is found to be very critical in determining the voltage profile within the tank. The current through the RF contact between the ridge and the shorting plate is a matter of concern, especially at higher frequencies. Table 1 shows the important parameters for the CSM tanks.

The beam dynamics have been studied in the final

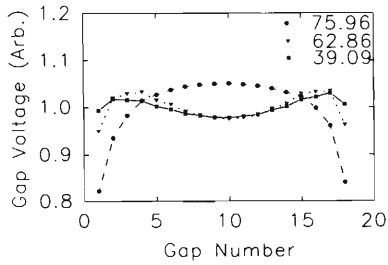


Fig. 2. Optimized voltage profile in the first CSM tank at three different frequencies in MHz.

Table 1. Tanks 1–4 are the acceleration section and tanks 5–6 are the deceleration section.  $\phi_s$  denotes the synchronous phase. The input ( $E_{in}$ ) and output ( $E_{out}$ ) energies correspond to the acceleration condition at 54.4 MHz, where the initial parameters were fixed. The effective shunt impedance ( $Z_s$ ), Q-value, the maximum current density on the sliding contact ( $J$ ), and the wall loss ( $P$ ) are estimated at the highest frequency of 76 MHz.

	Tank 1	Tank 2	Tank 3	Tank 4	Tank 5	Tank 6
Length (m)	3.051	3.525	3.940	4.313	3.663	2.914
Height (m)	1.750	1.750	1.750	1.750	1.750	1.750
Width (m)	1.050	1.050	1.050	1.050	1.050	1.050
No. of Gaps	18	18	18	18	16	16
$\phi_s$ (degree)	-25	-25	-25	-25	25	25
$E_{in}$ (MeV/u)	1.476	2.070	2.661	3.251	3.840	2.650
$E_{out}$ (MeV/u)	2.070	2.661	3.251	3.840	2.650	1.476
$Z_s$ (MW/m)	155.3	131.0	114.9	102.0	111.6	155.9
Q-value	29321	31144	31972	32767	32757	31063
$J$ (A/cm)	92	92	79	73	71	79
$P$ (kW)	126	130	132	136	77	81
Inter-gap Voltage (kV)	430	430	430	430	382	382

step with the optimized voltage profile, and the results of this study are shown in Figs. 3 and 4. The initial beam is assumed to have an emittance of  $30\pi$  mm-mrad in both transverse phase planes, and the longitudinal emittance being  $450\pi$  keV/u-degree. It has been found that the beam is fully transmitted through the CSM with the optimized quadrupole fields.

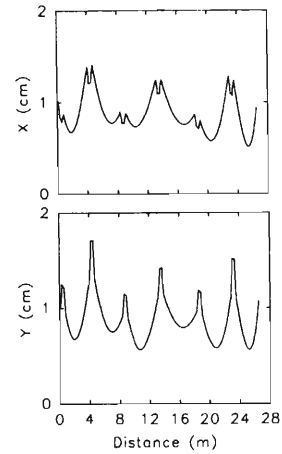


Fig. 3. Beam profile along the distance of the CSM in two transverse directions, where the inter-gap voltage distribution was calculated with the MAFIA code.

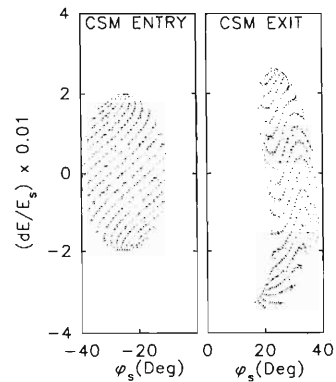


Fig. 4. Particle simulation in the longitudinal direction using the inter-gap voltage distribution calculated with the MAFIA code.

#### References

- 1) M. Tomizawa: RIKEN Accel. Prog. Rep. **29**, 228 (1995).
- 2) K. Shima et al.: Atomic Data & Nuclear Data Tables **51**, 173 (1992).
- 3) D. C. Carey, K. L. Brown et al.: SLAC-R-95-462.

## The Two Booster Ring Cyclotrons for RIKEN RI Beam Factory

A. Goto, T. Kubo, H. Okuno, T. Kawaguchi, T. Mitsumoto, T. Tominaka, S. Fujishima,  
J.-W. Kim, K. Ikegami, N. Sakamoto, S. Yokouchi, K. Sugii, T. Wada,  
J. Ohnishi, T. Morikawa, Y. Tanaka, and Y. Yano

In a previous design,<sup>1)</sup> the first one (4-sector ring cyclotron) of the two booster ring cyclotrons was planned to be superconducting one. After a further study, however, we found that it had better be a room-temperature (RT) one. The reasons why the RT cyclotron was considered advantageous compared with the original superconducting design are: the sector magnets of the RT booster in question can be designed to consume only 320 kW of power, no greater than that (480 kW) of our ring cyclotron currently in operation at RT (RRC); and the new booster can be easily designed after this RRC know-how (if it is chosen to be a RT one), because its structure and size are similar to those of familiar RRC.

Thus, we have renamed the 4-sector ring cyclotron as IRC (Intermediate Ring Cyclotron) from the former name SRC-4, and the 6-sector ring cyclotron as SRC (Superconducting Ring Cyclotron) from SRC-6.

Figure 1 shows a plan view of the designed IRC. Total power consumption of four pairs of main coils and twenty pairs of trim coils is 320 and 220 kW at the maximum magnetic field of 1.9 T, respectively. A flat-top rf resonator is used along with two main rf resonators. The main rf resonator is of a single-gap type with a rotatory plate; the flat-top resonator is of a single-gap type with a shorting plate.<sup>2)</sup> Details of all the components except for the rf resonators are being designed after the components of RRC.

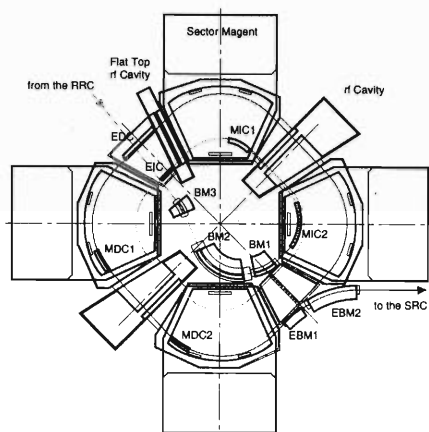


Fig. 1. Plan view of IRC.

Figure 2 shows a plan view of the designed SRC. Details of orbit analysis and design of the components such as the sector magnets, the rf resonators, and the injection system are reported elsewhere in this

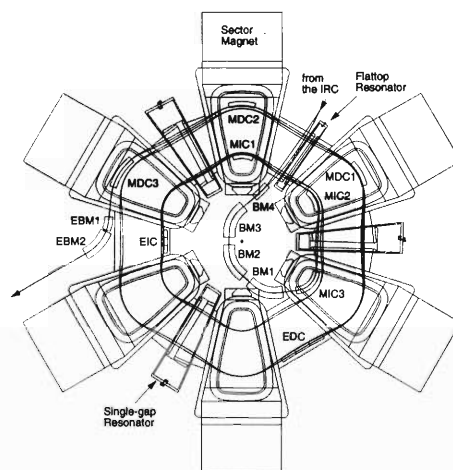


Fig. 2. Plan view of SRC.

Progress Report.

Fabrication of the prototype sector magnet of SRC has been continued: measurements of mechanical and electrical characteristics of the superconducting wires for the main and trim coils as well as detailed design of how to fix the coil vessel onto the cold pole were made. The items measured relating to the mechanical characteristics of the superconducting wires were: tensile strength, stress/strain hysteresis, fatigue, and stress/creep characteristics at room temperature and 77 K. The items measured on their cryogenic and electrical characteristics were: heat flux, Hall effect, and magnetic resistance at 4.2 K. Quench stability test was also made at 6 T for both the main and trim coils by making a small model of two-coil configurations. The results of these measurements were in good agreement with the design. Details of them and the design of the prototype sector magnet are reported elsewhere in this Progress Report.

The prototype sector magnet of SRC is scheduled to be completed in the summer of 1998 after a half-year delay from the first schedule. Until then planned to be made are: a model of superconducting magnetic channel and three units of sector magnet models with 1/6-scale in order to simulate the electromagnetic force exerted from the adjacent sector magnets.

### References

- 1) A. Goto et al.: RIKEN Accel. Prog. Rep. **30**, 196 (1997).
- 2) T. Saito et al.: Proc. 12th Int. Conf. on Cyclotrons and Their Applications, Berlin, p. 201 (1989).

# Orbit Analysis of RIKEN Superconducting Ring Cyclotron

T. Mitsumoto, A. Goto, T. Kawaguchi, J.-W. Kim, Y. Tanaka, T. Kubo,  
H. Okuno, T. Tominaka, S. Fujishima, and Y. Yano

The RIKEN superconducting ring cyclotron is one of the main accelerators for the “RI Beam Factory” which has started its construction as the next project of the RIKEN Accelerator Research Facility (RARF).<sup>1)</sup> The Superconducting Ring Cyclotron (SRC) is expected to boost the energy of ion beams up to 400 MeV/nucleon for light heavy ions like carbon, and up to 150 MeV/nucleon for very-heavy ions like uranium. Beam current is expected to be more than 100 pμA for light heavy ions and about 0.2 pμA for 150 MeV/nucleon for uranium ions. Figure 1 shows the region of expected ions from the SRC (grey area) and typical ions (white circles).

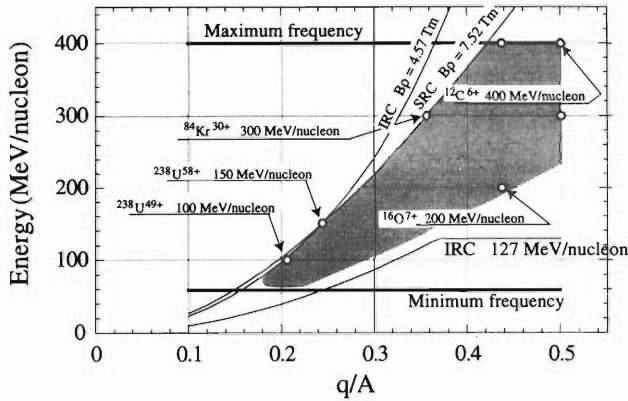


Fig. 1. The region of expected ions from the SRC is shown by grey area. White circles show the typical ions used for design calculation.

Main parameters of the SRC are listed in Table 1. Velocity gain factor is 1.51. Figure 2 shows a layout of the SRC. Six sector magnets, three main resonators, one flattop resonator, and injection and extraction devices, together with injection and extraction orbits, are shown.

Table 1. Main parameters of the SRC.

Number of sectors		6
Harmonics		6
Average radius:	Injection	3.56 m
	Extraction	5.36 m
Number of cavities	Main	3
	Flattop	1
Rotational frequency		3.0-6.36 MHz

In order to realize the high magnetic field and various magnetic inclinations, the sector magnet of the SRC has the followings: a set of superconducting main

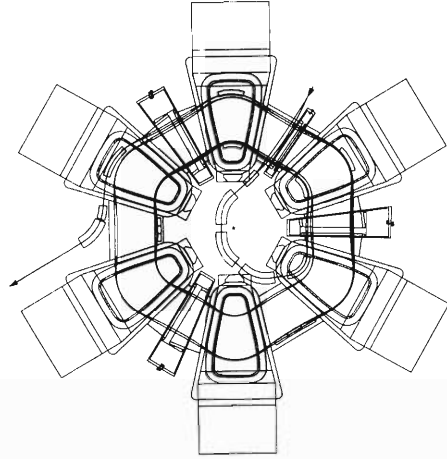


Fig. 2. Layout of the SRC.

coils for base field generation; five sets of superconducting trim coils for coarse adjustment to the isochronous field; and about 20 sets of normal conducting trim coils for fine adjustment to the isochronous field. Magnetic field distribution was calculated by a three dimensional code, TOSCA.<sup>2)</sup>

Size of the superconducting main coil is 284 mm (width) × 310 mm (height). The maximum excitation current is 6 MA per one sector magnet (two coils). The superconducting main coil is installed inside a He vessel made of stainless steel which is tightly fixed to the cold pole.

Five sets of the superconducting trim coils are placed on the inner surface of the cold pole. Two sets at the extraction side have current returns at the extraction side, which are not wound along beam orbits but are just straight in the beam region in order to avoid concave curvature of conductors. The rest three sets have current returns at the injection side. Schematic view of the superconducting trim coils is shown in Fig. 3. The

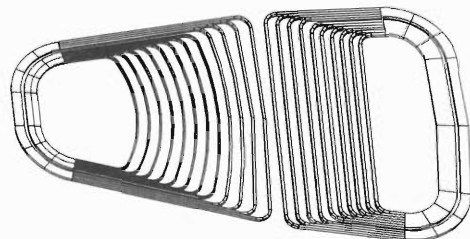


Fig. 3. Configuration of the superconducting trim coils is shown. Two of five sets have current returns at the extraction side and the others have them at the injection side.

first coil (of leftest in Fig. 3) on the injection orbit is wound along the beam orbit, then the curvature gradually becomes straight towards the extraction side.

The normal conducting trim coils are one-turn coils which are installed inside the cryostat chamber wall. We plan to use 20 coils at the acceleration region and one or two more coils at both injection and extraction regions. The maximum current of each coil is considered to be 500 Amps.

Shape of the yoke of sector magnet has been optimized in order to give an appropriate focusing force and to receive a tolerable shifting force of the cold mass. Figure 4 shows the upper half of the sector magnet.

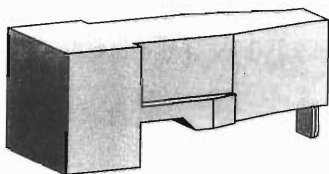


Fig. 4. Schematic view of the upper half of yoke is shown. Length, width and height of the yoke are 7.55 m, 3.3 m and 3.0 m, respectively.

By using the main coils and five sets of the superconducting trim coils, it is possible to adjust various distributions of isochronous fields within  $\pm 0.1\%$ . The normal conducting trim coils can improve the errors to the isochronous condition from  $\pm 0.1\%$  to  $\pm 0.01\%$ .

Influence of the resonances at  $\nu_z = 1$  and  $\nu_z = 1.5$  was studied. The minimum axial betatron frequency is set to be 1.05 in order to keep the axial shift of beam within  $\pm 5$  mm. The resonance at  $\nu_z = 1.5$  can be crossed. The amplitude increase by crossing the resonance is less than 10%, however. Figure 5 shows the working paths of typical ions.

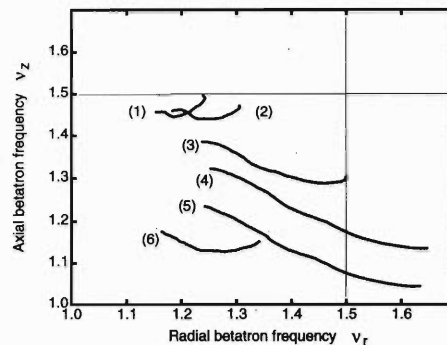


Fig. 5. Working paths of the radial and axial betatron frequencies of typical ions: (1)  $^{238}\text{U}^{49+}$  100 MeV/nucleon, (2)  $^{238}\text{U}^{58+}$  150 MeV/nucleon, (3)  $^{84}\text{Kr}^{30+}$  300 MeV/nucleon, (4)  $^{16}\text{O}^{7+}$  400 MeV/nucleon, (5)  $^{12}\text{C}^{6+}$  400 MeV/nucleon and, (6)  $^{16}\text{O}^{7+}$  200 MeV/nucleon.

#### References

- 1) Y. Yano et al.: RIKEN Accel. Prog. Rep. **31**, 181 (1998).
- 2) Vector Fields Limited, Oxford, England.

## Design of Sector Magnets for RIKEN Superconducting Ring Cyclotron

T. Kawaguchi, T. Mitsumoto, H. Okuno, T. Kubo, T. Tominaka, S. Fujishima, J.-W. Kim, K. Ikegami, N. Sakamoto, A. Goto, and Y. Yano

The RIKEN Superconducting Ring Cyclotron, SRC, will be one of the main accelerators for the "RIKEN RI-Beam Factory".<sup>1)</sup> Six superconducting sector magnets are to be used in the SRC.

Our progress made for the design of the sector magnets during 1997 is as follows: (1) A detailed design of the main and trim superconducting coils was finalized; (2) Mechanical stress and deformation of the main coil vessel caused by the coil's electromagnetic force were analyzed, and the dimensions of the coil vessel were

fixed; (3) Superconducting wires of 15.4 km and 4.6 km in length to be used for the main and trim coils were purchased for a prototype magnet;<sup>2)</sup> (4) Two small coils were made using the two kinds of superconducting wires mentioned above, and their stabilized currents against coil quench were measured. The results have verified the validity of our design;<sup>3)</sup> (5) Construction of the prototype magnet is in progress at respective manufactures.

The present design status is as follows. Figure 1

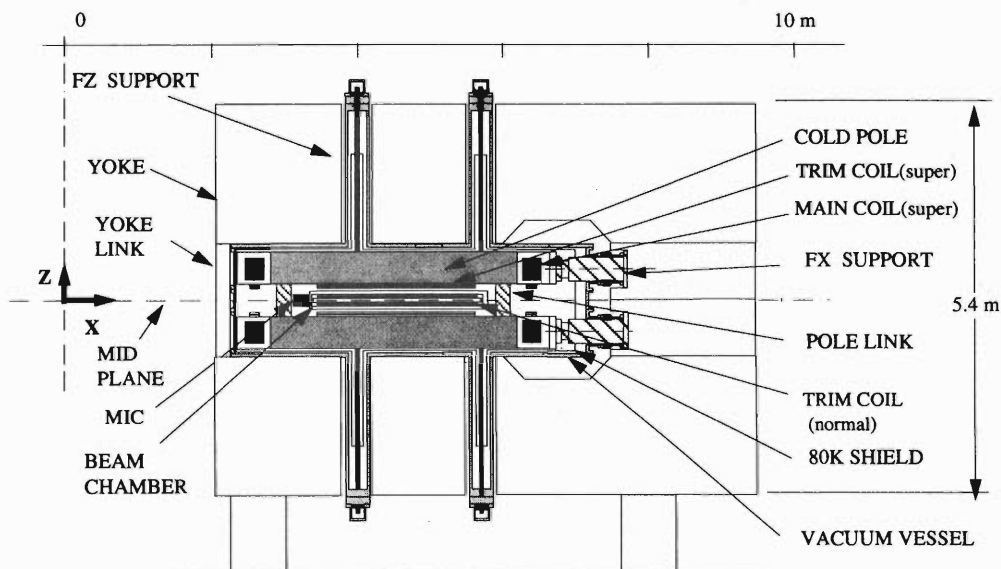


Fig. 1. Cross-sectional view of the SRC sector magnet.

shows the cross-sectional view of the SRC sector magnet. The basic parameters are shown on Table 1. Main components of the magnetic elements are superconducting and normal-conducting coils, cold poles, and a yoke. Two kinds of superconducting coils are used: i.e., a pair of main coils and one group of trim coils, and these superconducting coils are mechanically fixed to the cold-poles through their vessels. Another group of normal-conducting trim coils is arranged on the upper and lower surfaces of the beam chamber. Superconducting coils are all cooled by liquid helium and located in a cryostat to keep their temperature to be 4.5 K. The cryostat is like a big vacuum bottle, which consists of a vacuum vessel and an 80 K thermal shield.

One of the most serious points of design is how to control and how to support the huge electromagnetic force exerted on the superconducting coils. The

Table 1. Parameters of the sector magnet.

Average radii of beam injection	3.56 m
extraction	5.36 m
Sector angle of main coil	25 degree
Maximum magnetic field	
in the beam orbital area	4.5 T
in the main coil	5.5 T
in the trim coil	5.0 T
Main-coil's ampere turns per magnet	6.0 MA
Coil cooling method	LHe bath cooling
Stored magnetic energy for 6 magnets	390 MJ
( 75 % in air, 17 % in poles, 8 % in yokes)	
Maximum operation currents	
for main coil	5,000 A
for trim coil	500 A
Iron weight of 6 magnets	
poles	216 tons
yokes	3,630 tons

magnetic forces on the cold mass calculated with 3-D TOSCA/OPERA code are shown in Fig. 2. We have adopted a cold-pole arrangement which gives a mechanical support against the huge magnetic force of the main coil, and gives a reductions in the ampere-turns

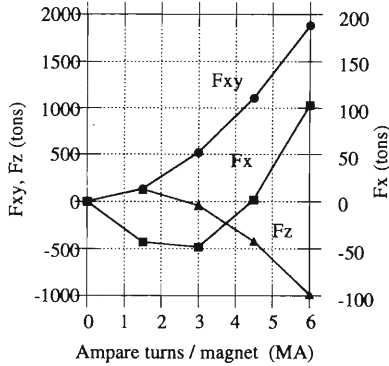


Fig. 2. Magnetic forces exerted on the cold mass.  $F_{xy}$  for half main coil (Expanding Force =  $\Sigma|F_{xy}|$ ).  $F_z$  for one coil and one cold pole.  $F_x$  for a magnet.

and the magnetic forces, compared with a warm-pole arrangement. The magnetic forces ( $F_{xy}$ ,  $F_z$ ) exerted on the main coils are all supported by the cold-poles through the coil vessels. The vertical magnetic force ( $F_z$ ) is supported with two pole links which are attached to the upper and lower cold poles. The shifting force ( $F_x$ ) in the radial direction is supported with four sets of the  $F_x$  supports which work at the same time as the thermal insulations between the room temperature and 4.5 K regions. This force ( $F_x$ ) is generated by both of the arrangement of six sector magnets and the asymmetric configuration of the coils and irons.

Another important point of design is how to prevent the coil quench. If a coil quench occurred in the main coil, the operation of the SRC has to be stopped at least for 2 weeks in order to re-cooldown of the coils. We have applied a cryogenic stabilization method on the main and trim superconducting coils to avoid coil quench. As the result of applying it, the average current density of the main and trim superconducting coils were designed to be 34 A/mm<sup>2</sup> and 39 A/mm<sup>2</sup>, respectively.

Figure 3 shows the cooling diagram. Two refrigera-

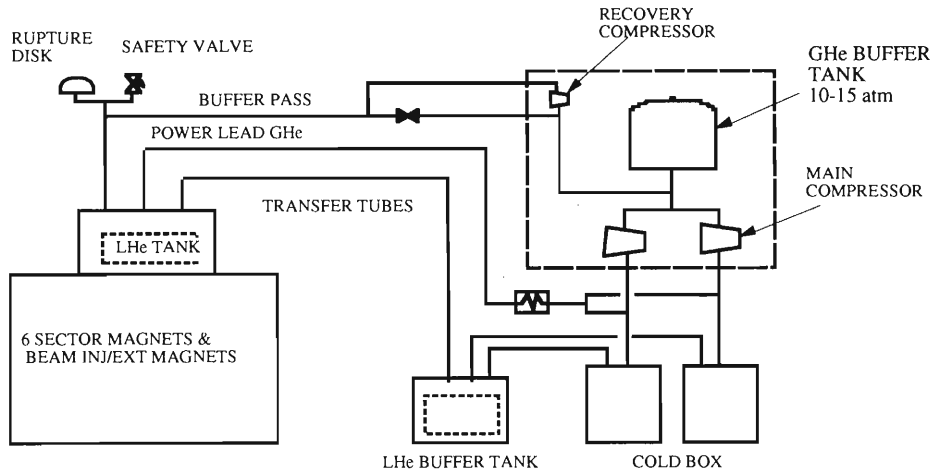


Fig. 3. Cooling system diagram.

tors having a capacity of 500 W each at 4.5 K will be used for cooling of the six sector magnets plus the beam injection/extraction magnets. The cold mass weight of the six sector magnets is 360 tons, and it will take one and a half months for the cooldown of the cold mass from room temperature to 4.5 K. We expect the SRC to operate more than 6000 hrs a year, so the cold mass should be kept in the low temperature as long as possible. When one refrigerator breaks down, the magnets can be kept at 5 to 6 K with another refrigerator. At the time of main power failure, a recovery compressor

driven by an emergency power source will recover the evaporated helium gas to the GHe buffer tank. We will use no liquid nitrogen in this cryogenic system for simplicity of the cooling system.

#### References

- 1) A. Goto et al.: RIKEN Accel. Prog. Rep. **31**, 205 (1998).
- 2) T. Kubo et al.: RIKEN Accel. Prog. Rep. **31**, 210 (1998).
- 3) T. Kawaguchi et al.: RIKEN Accel. Prog. Rep. **31**, 212 (1998).

## Design of a Prototype Sector Magnet for RIKEN Superconducting Ring Cyclotron

T. Kubo, T. Kawaguchi, H. Okuno, T. Mitsumoto, T. Tominaka, S. Fujishima, J.-W. Kim, Y. Tanaka, K. Ikegami, N. Sakamoto, S. Yokouchi, T. Morikawa, A. Goto, and Y. Yano

A superconducting ring cyclotron named SRC is to be built in the RIKEN RI-Beam Factory project as one of the post accelerators of the existing K540 Ring Cyclotron.<sup>1,2)</sup> The SRC is designed to have a K-value of 2500 MeV, consisting of six superconducting sector magnets. The design of SRC is described elsewhere in this progress report.<sup>3,4)</sup>

A full-scale model of the superconducting sector magnet is to be built as a prototype sector magnet, in order to make sure the design of sector magnet is valid under the condition as close to the real one as possible. If this prototype magnet is successful, we plan to use it as one of the sector magnets of SRC. The design of the magnet has been outlined in the last year's progress report.<sup>5)</sup> Here, we report on progress in the design as well as on status of fabrication.

Figure 1 shows a schematic drawing of the sector magnet. The huge electromagnetic force<sup>6)</sup> exerted on the main coils is supported by means of what we call cold-pole method. The pole pieces are separated from the iron return yoke and are cooled down together with the main coils in a cryostat. Two coil vessels accom-

modating the main coils are attached to the side of the upper and lower pole pieces, which are linked each other by pole links. This arrangement allows the pole pieces to work as mechanical supports against the electromagnetic force.

The cold mass, consisting of the cold poles, main coils and main-coil vessels, is supported by support links shown in Fig. 1. The eight vertical links (four links in each of the upper and lower side) support the weight of cold mass, while the four horizontal links (two links for each of the upper pole and lower pole) support the force that shifts the cold mass toward the side yoke.

Some details of the main coil vessel and cold pole are shown in Fig. 2. One of the important issues in the design of sector magnet is how to fix the coil vessel to the side of pole piece. Two kinds of schemes that we proposed are shown in Fig. 3. In the scheme shown by the upper figure, a sort of "hook" is used to fix the coil vessel to the pole. The coil vessel and the "hook" are assembled by welding. The second scheme shown by the lower figure in Fig. 3 uses screws to fix the coil vessel to the pole as well as to assemble the coil vessel. In the prototype magnet, we adopt the former scheme for the upper coil while the latter one for the lower coil, and plan to examine through the test operation of prototype magnet which scheme is better.

The design of main coil vessel was made estimating the stress caused by the electromagnetic force and thermal contraction. The material of coil vessel was chosen to be a stainless steel called SUS316L by considering its strength. The wall thickness of coil vessel was determined so that the estimated maximum stress does not exceed the allowable maximum stress of SUS316L.

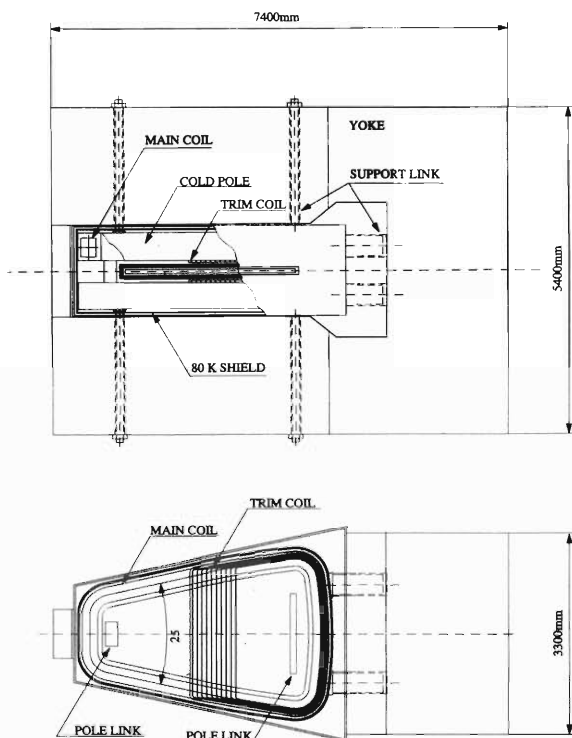


Fig. 1. Schematic drawing of the prototype sector magnet: a side view (upper figure); a top view (lower figure).

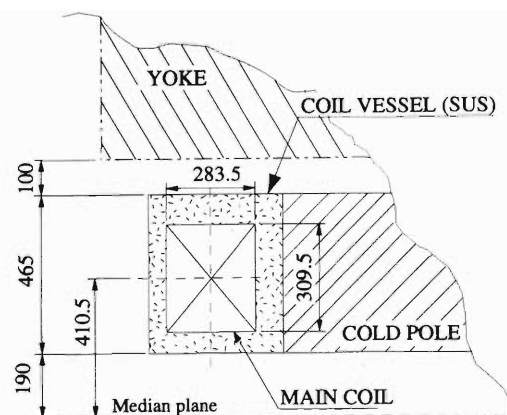


Fig. 2. Some details of the main coil and cold pole.

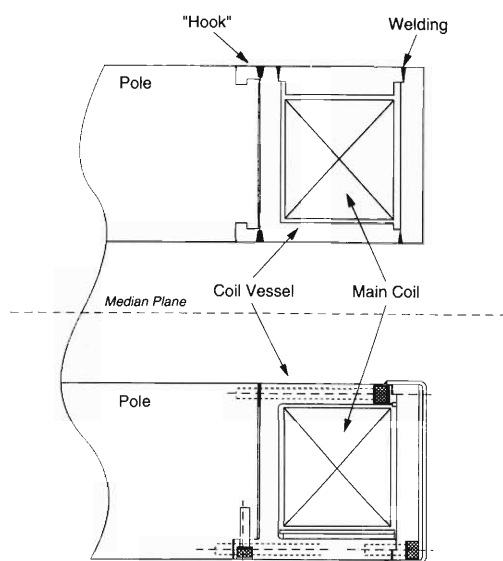


Fig. 3. Two kinds of schemes to fix the coil vessel to the cold pole.

The size and interval of screws were determined in the same way. The material of screws was chosen to be a stainless steel called A286. The displacement of the main-coil vessel due to the electromagnetic force was simulated to be about 1.1 mm in the horizontal direction and about 1.9 mm in the vertical direction at maximum. The fatigue limit was also checked for the coil vessel, welding spots of coil vessel, and screws. It is found that no breaks are expected for the assumed cycles of 10,000 (1 cycle/day for 30 years). Fabrication of the cold pole and coil vessel has started.

An aluminum-stabilized superconductor, designed based on Maddock's criterion, is used for the main coil. The details of the conductor are given in Ref. 5 along with those of the main-coil configuration. Fabrication of the conductor finished in the spring of 1997. The conductor specification was checked by testing several samples of conductor, and was found to be achieved.

Heat transfer from the Al stabilizer to liquid Helium was measured using a setup simulating the main-coil configuration. It was found that the measured heat transfer was large enough to achieve the design value of maximum stabilized current. The measurements of mechanical properties, such as stress-strain curve, fatigue, and creep, were also made using sample pieces of the conductor. It was found that the conductor was

strong enough against the electromagnetic force and thermal contraction.

Model trim coils, which correspond to a part of real trim coils, are to be fabricated and installed in the pole gap space as shown in Fig. 1. The conductor of trim coil has been designed to be cryogenically stable, based on Stekly's criterion. It is a rectangular conductor whose cross-sectional sizes are horizontally 2.9 mm and vertically 3.6 mm, consisting of a stabilizer housing of pure aluminum and a superconducting wire at the center of conductor. The superconducting wire is the same to the wire that constitutes the Rutherford-type cable used for the main-coil conductor.<sup>5)</sup> The cooling gaps of trim coil are taken to be 0.25 mm. The cooling efficiency is estimated to be 40% considering the spacers placed in the gaps. The trim coil is expected to be stable up to 550 A at 6 T. We plan to excite it with currents lower than 500 A for safety. The current density at 500 A is estimated to be about 41 A/mm<sup>2</sup>. The trim coil vessel is connected in series to the main coil vessel, so that the trim coil can be cooled by the liquid helium provided by a common refrigerator.

Fabrication of the trim-coil conductor finished also in the spring of 1997. Its specification was checked for several samples, and was found to be achieved. Heat transfer measurement of the Al stabilizer was made similarly to the main coil conductor, and a designed value of heat transfer was confirmed.

The maximum stabilized currents were measured in a realistic condition both for the main coil and trim coil conductors. A small test magnet was built for this purpose. The results are given elsewhere in this progress report.<sup>7)</sup>

The fabrication of prototype magnet is progressing. The coil winding starts in March 1998. The cold mass and cryostat will be completed in the summer of 1998.

#### References

- 1) Y. Yano: RIKEN Accel. Prog. Rep. **31**, 181 (1998).
- 2) A. Goto et al.: RIKEN Accel. Prog. Rep. **31**, 205 (1998).
- 3) T. Mitsumoto et al.: RIKEN Accel. Prog. Rep. **31**, 206 (1998).
- 4) T. Kawaguchi et al: RIKEN Accel. Prog. Rep. **31**, 208 (1998).
- 5) T. Kubo et al: RIKEN Accel. Prog. Rep. **30**, 201 (1997).
- 6) T. Kawaguchi et al: RIKEN Accel. Prog. Rep. **30**, 199 (1997).
- 7) T. Kawaguchi et al: RIKEN Accel. Prog. Rep. **31**, 212 (1998).

# Quench Stabilities of the Superconducting Wires for the Sector Magnets of RIKEN Superconducting Ring Cyclotron

T. Kawaguchi, H. Okuno, A. Goto, and Y. Yano

In this paper, results of numerical and experimental studies on the quench stabilities of the superconducting coils are described. The quench stabilizing currents of the main and trim superconducting coils were confirmed from this work. Hence, we have begun to wind the coil of the prototype magnet.

Sector magnets<sup>1)</sup> for the proposed superconducting ring cyclotron (SRC)<sup>2)</sup> of the RIKEN RI beam factory project require two kinds of superconducting coils: main and trim coils. Table 1 shows the parameters of the wire for these coils. The wires for the above-mentioned prototype magnet<sup>3)</sup> were already purchased. One of our basic design concepts for the sector magnets is to make quench-free superconducting coils to assure the reliable long-period operation of the SRC. For this purpose, we planned to use partial stabilization criteria (Maddock's stabilization<sup>4)</sup>) for the main coil, and full stabilization one (Stekly's stabilization<sup>5)</sup>) for the trim coil. The partial stabilization criterion is defined as follows: when a normal-conducting state happens in some part of coils due to the mechanical disturbance, the superconducting state can be recovered within a few seconds with the cooling by liquid helium (LHe). On the other hand, the full stabilization one is: even when the entire part of coils was turned into the normal-conducting state the superconducting state can be recovered immediately by LHe cooling. Although the full stabilization design is much safer than the partial one, it requires the lower current density coils. Therefore, we can not use this method to the main coils. However, for the trim coils it is hard to fix the coil windings in mechanically strong manner because of their configurations. We have thus decided to use the full stabilization criteria for the trim coils.

Table 1. Parameters of two superconducting wires.

Items	For main coil	For trim coil
Operation current (A)	5 0 0 0	5 0 0
Max. magnetic field (T)	6	6
Stabilizing criterion	Partial	Full
Stabilizing current (A) at 6 T, 4.5 K	≥ 6000	≥ 550
Critical current (A) at 6 T, 4.3K	≥ 11500	≥ 1150
Outer dimension (mm)	8.0 x 15.0	2.9x3.6
Materials	NbTi / Cu / Al	NbTi / Cu / Al
Section area ratio	1 / 1 / 17	1 / 1 / 15
RRR of Al	≥ 500	≥ 400
0.2 % yield strength of Al (kg/mm <sup>2</sup> )	≥ 5	≥ 4
Cooling surface ratio	5 0 %	4 0 %

Characteristics of the heat flux transport from the wires to LHe, and electric resistivities of the aluminum stabilizers of the wires, were measured in LHe at the wire manufacturer, Furukawa Electric Corporation. Using these measured data, the stabilization currents of the main and trim wires were calculated to be 6000 A and 750 A, respectively.

Next, we made a numerical calculation and an experimental study on the quench phenomena. The numerical calculation was done to understand the real transient phenomena and to obtain the suitable specifications (capacity and arrangement) of electric heaters and voltage taps for the experiment study. In Fig. 1, the calculated results of the voltage drop and the temperature of the main coil at 5500 A are given as a function of time. A pulsed heat loading of 60 W was applied to the wire over length of 0.4 m for 0.2 second. As seen in Fig. 1, the voltage drop becomes zero 0.3 sec after the heating. Then we can say that the main coil is stabilized against the quench at the excitation current of 5500 A. Figure 2 shows the another calculated result to find the fully stabilizing current of the trim coil. In this calculation, the normal-conducting length was increased to 4 m at 1000 A, and then the

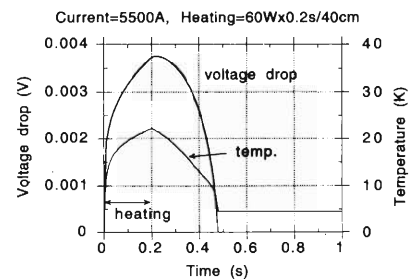


Fig. 1. Calculated voltage drop and maximum temperature of the test main coil.

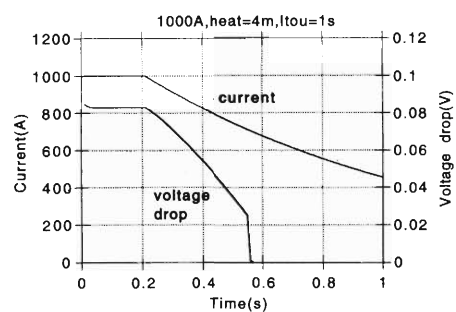


Fig. 2. Calculated voltage drop versus current of the test trim coil.

coil current was decreased with a time constant of 1 second. As seen in Fig. 2, the decreasing gradient of the calculated voltage drop suddenly changed toward zero at 730 A, which can conclude that the fully stabilizing current of the trim coil is 730 A.

Experimental study has been done at Mitsubishi Electric Corporation by using two small superconducting coils, a test main coil and a test trim coil, which use same superconducting wires and similar cooling configurations as the prototype magnet. In these coils, electric heaters were set on the wire surface to give a thermal disturbance instead of mechanical disturbance. The heating lengths are 0.4 m in the test main coil's wire of 115 m, and 0.1 m in the test trim coil's 55 m. Figures 3 and 4 show a drawing and a photograph of the three coils arrangement. The coils were cooled down to 4.5 K using LHe, and the stabilizing currents of the main and trim test-coils were measured under the total magnetic field of 6 T: 4.5 T from the bias coil and 1.5 T from the test main coil. Figures 5 and

6 show the measured results on the main and trim test-coils, which can be compared with Figs. 1 and 2. The stabilizing currents obtained from the experiment were 5700 A and 630 A for two coils, which are 1.14 and 1.26 times larger than the designed maximum operation currents of the main and trim coils. This has verified the validity of our design on quench stability. The difference between the calculated stabilizing current and measured one is thought due to the degradation of heat flux characteristics in real coils. It should be noted that the high current feeding up to 6500 A to the main superconducting wire was done for the first time in this experiment, because it was impossible to feed such a high current during the wire inspection test at the wire manufacturer due to their power supply limitation.

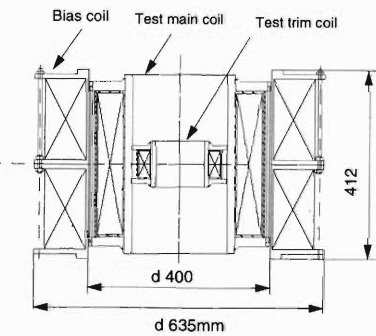


Fig. 3. A drawing of three coils configuration.

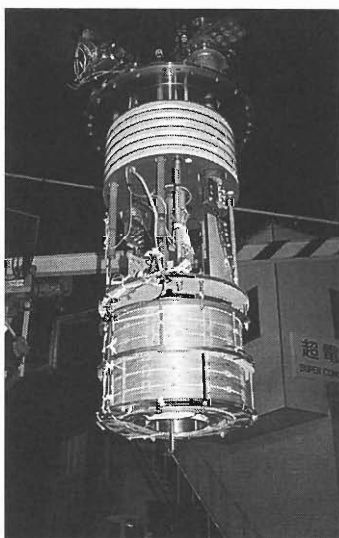


Fig. 4. An outward view photograph after three coils assembly.

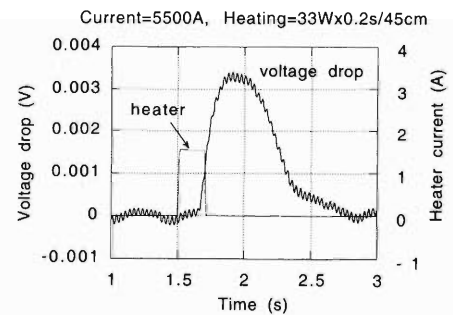


Fig. 5. Measured voltage drop of the test main coil.

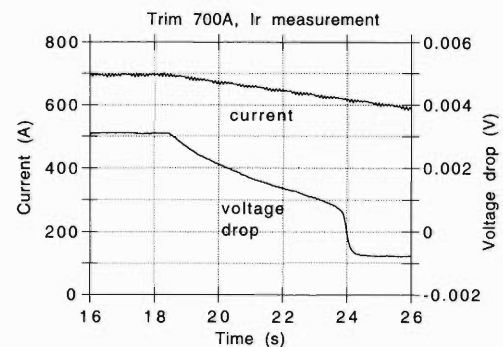


Fig. 6. Measured voltage drop versus current of the test trim coil.

#### References

- 1) T. Kawaguchi et al.: RIKEN Accel. Prog. Rep. **31**, 208 (1998).
- 2) A. Goto et al.: RIKEN Accel. Prog. Rep. **31**, 205 (1998).
- 3) T. Kubo et al.: RIKEN Accel. Prog. Rep. **31**, 210 (1998).
- 4) B. Maddock et al.: Cryogenics, Aug. 1969, pp. 261-273.
- 5) Z. Stekly et al.: IEEE Transaction NS-12, 1965, p. 367.

## Analysis of the Injection and Extraction Trajectories in RIKEN Superconducting Ring Cyclotron

S. Fujishima, H. Okuno, T. Tominaka, T. Mitsumoto, T. Kubo, T. Kawaguchi, J.-W. Kim, N. Sakamoto, A. Goto, and Y. Yano

In the RIKEN RI Beam Factory project, a six-sector Superconducting Ring Cyclotron (SRC) has almost been designed.<sup>1)</sup> The purpose of present analysis is to optimize the layouts and specifications of the injection and extraction elements in the SRC. For the optimization, the differences of trajectories in the elements and the required fields of the elements were minimized. Beam envelopes were also studied to adjust the beam width.

The SRC has strong stray field from the sector magnets,<sup>2)</sup> and this field strongly depends on the condition of acceleration. Thus, the trajectories of various beams differ considerably from each other. Besides, the injection and extraction elements should be installed in a small space limited with the sector magnets, RF-cavities, and vacuum chambers. These difficulties make the design of the injection and extraction systems challenging. The injection system consists of four bending magnets (BM1, BM2, BM3, and BM4), three magnetic inflection channels (MIC1, MIC2, and MIC3), and an electrostatic inflection channel (EIC). The extraction system consists of a bending magnet (EBM), three magnetic deflection channels (MDC1, MDC2, and MDC3), and an electrostatic deflection channel (EDC).<sup>3)</sup>

To analyze the injection and extraction trajectories in the SRC, an equation of motion was solved with Runge-Kutta-Gill method. Magnetic field of the sector magnets used in this analysis was calculated with a three-dimensional computer code, "TOSCA".

Table 1 shows energies and magnetic rigidities of typical two beams of  $^{16}\text{O}^{7+}$  and  $^{238}\text{U}^{58+}$ . Between these two beams, the difference of magnetic rigidities becomes the maximum, so that the difference of trajectories also becomes the maximum. To minimize the bore of the elements, the difference of trajectories must

be suppressed as small as possible. Length of each element was determined in consideration of the balance between the difference of trajectories in the element and the required field of the element.

Figure 1 shows schematic layout of the injection elements, and the injection trajectories of the typical two beams. Table 2 shows specifications of the injection

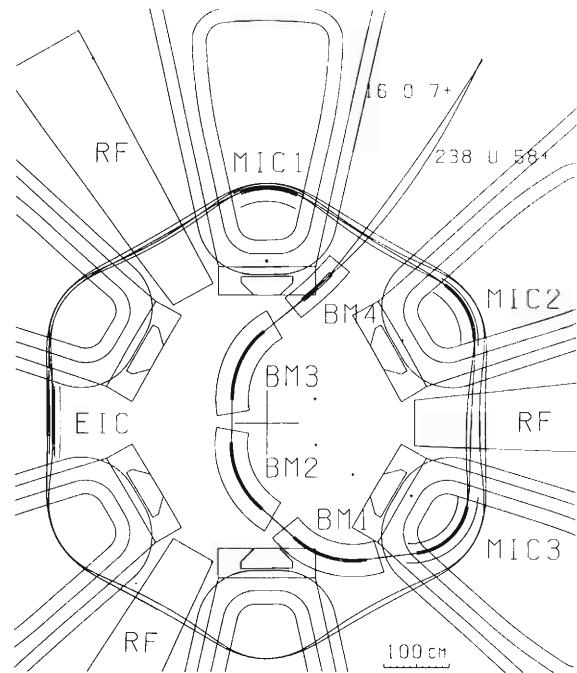


Fig. 1. Schematic layout of the injection elements, and the injection trajectories of the typical two beams.

Table 1. Energies and magnetic rigidities of typical two beams of  $^{16}\text{O}^{7+}$  and  $^{238}\text{U}^{58+}$ .

	Energy [MeV/u]		$B\rho$ [Tm]	
	Inj.	Ext.	Inj.	Ext.
$^{16}\text{O}^{7+}$	74.2	200	2.89	4.90
$^{238}\text{U}^{58+}$	58.0	150	4.57	7.52

Table 2. Specifications of the injection elements.

	Radius [cm]	Angle [deg.]	Length [cm]	B or E maximum
EIC	1000~	variable	100	95 kV/cm
MIC1	111	46.5	90	0.18 T
MIC2	110	52.5	101	0.27 T
MIC3	87	73.9	112	1.5 T
BM1	132	52.0	120	4.02 T
BM2	130.5	52.0	118	3.92 T
BM3	128	52.0	116	3.96 T
BM4	492.5	7.0	60	-0.8, +0.7 T

elements. The MIC3, BM1, BM2, BM3, and BM4 are superconducting.

Figure 2 shows difference of trajectories in the EIC. The EIC should be movable in the radial direction by 10 cm and its radius of curvature should be adjustable, because the gap between electrodes can be open 1 cm at most. Figure 3 shows difference of trajectories in the BM4. To minimize the difference of trajectories, the BM4 generates not only positive field but also negative one.

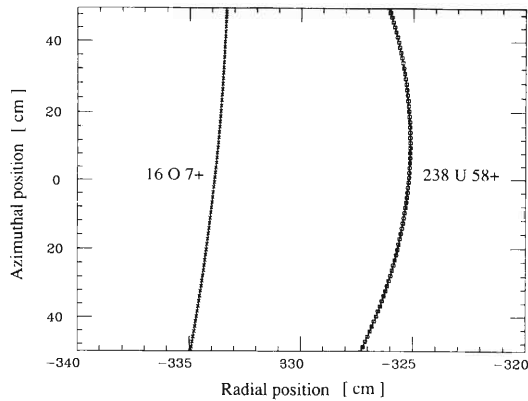


Fig. 2. Difference of trajectories in the EIC.

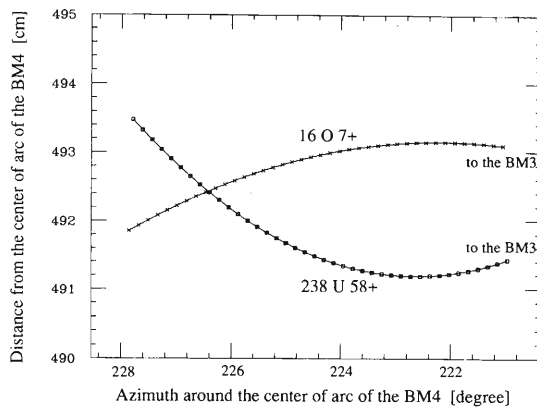


Fig. 3. Difference of trajectories in the BM4.

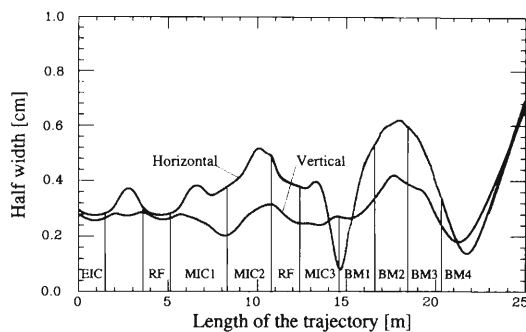


Fig. 4. Envelopes of the injected beam of  $^{238}\text{U}^{58+}$ , adjusted with gradient-field-coils.

Figure 4 shows envelopes of the injected beam of  $^{238}\text{U}^{58+}$ . Emittance was assumed to be 10 mm mrad. The envelopes can be adjusted with two gradient-field-coils built in the BM2 and BM3 additionally.

Figure 5 shows schematic layouts of the extraction elements, and the extraction trajectories of the typical two beams. Table 3 shows specifications of the extraction elements. The MDC3 and EBM are superconducting.

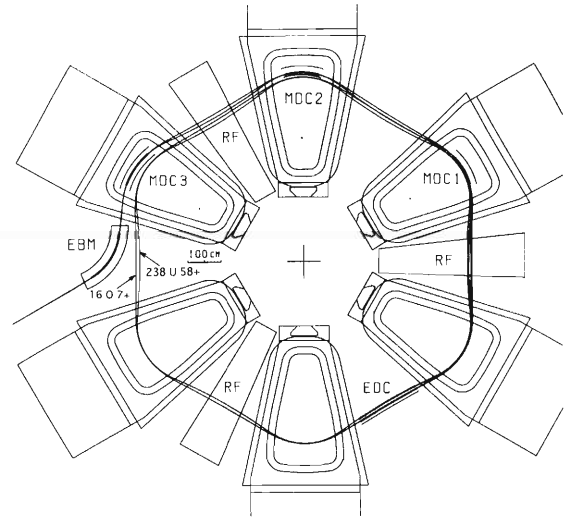


Fig. 5. Schematic layout of the extraction elements, and the extraction trajectories of the typical two beams.

Table 3. Specifications of the extraction elements.

	Radius [cm]	Angle [deg.]	Length [cm]	B or E maximum
EDC	2000~	variable	199	100 kV/cm
MDC1	185	32.0	103	0.2 T
MDC2	190	32.0	106	0.3 T
MDC3	230	30.0	120	1.12 T
EBM	175	52.0	159	3.9 T

Layouts and specifications of the injection and extraction elements in the SRC have almost been optimized. Further optimization is in progress.

#### References

- 1) A. Goto et al.: RIKEN Accel. Prog. Rep. **31**, 205 (1998).
- 2) T. Mitsumoto et al.: RIKEN Accel. Prog. Rep. **31**, 206 (1998).
- 3) H. Okuno et al.: RIKEN Accel. Prog. Rep. **31**, 216 (1998).

## Design Study of Injection System for RIKEN Superconducting Ring Cyclotron

H. Okuno, T. Tominaka, S. Fujishima, A. Goto, and Y. Yano

Superconducting magnets for the injection system of Superconducting Ring Cyclotron (SRC),<sup>1)</sup> are being designed. In this report, the characteristics and structure of those magnets are given.

The injection beam transport system consists of four bending magnets (BM1, BM2, BM3, and BM4), three magnetic inflection channels (MIC1, MIC2, and MIC3), and an electrostatic inflection channel (EIC), as shown in Fig. 1. Their specifications obtained from numerical analysis<sup>2)</sup> are shown in Table 1. All of BM's (BM1-4) and one of MIC's (MIC3) are required to be superconducting magnets in order to produce required strength of magnetic field. In the following section, we describe about design study of the BM1, which is anticipated to be the most difficult to construct with the superconducting elements.

There are three difficulties in designing the BM1. Firstly, we can not use iron yokes for magnetic shielding because the total flux of the stray field in the cen-

tral region of the SRC is so large that the ion yoke of BM1 (if used) would be saturated. We should therefore adopt active-shield type of magnets for the all BM's although the magnetic motive force is larger than that in the case of an iron-shield type of magnet. Secondly, the space available for the BM1 is very narrow: the BM1 has to be constructed in the space of about 20 cm in radial direction. In the coil-end region, both coil supports and cryostat walls have to be accommodated in the space of about 10 cm. Thirdly, the BM1 needs to be consisted of coils with negative curvature. This means that it is difficult to wind cables, because cables can not be wound with tension. Taking these three difficulties into account, we took cares of the following two points in the design of the BM1. Firstly, the coil structures should be simple. Secondly, its field generation should be as effective as possible: namely, the size of the constituent coils in radial and azimuthal directions should be as small as possible.

Here, we propose a new coil structure of the active-shield type. Figure 2 shows the cross section and the 3D-view of the coil structure. Eight current sheets located closer to the beam axis generate the magnetic field in the beam bore, and the rest four current sheets generate the field to cancel the fringe field from the eight current sheets. Such configurations of the current sheets can allow the structure of coils that does not require a "bent up" at the ends of the channel.

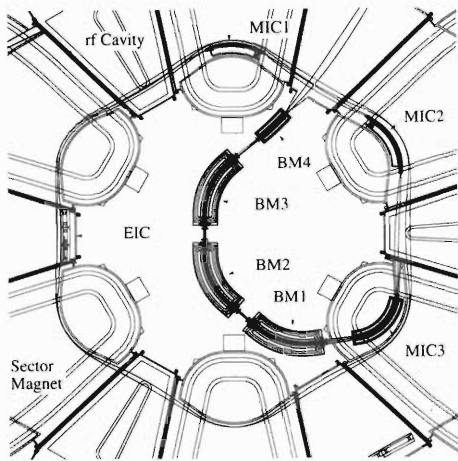


Fig. 1. Schematic layout of the injection elements for the SRC, and trajectories for injected beams.

Table 1. Parameters of the injection elements.

	Radius (cm)	Angle (deg.)	B or E (max.) (T) or (kV/cm)
EIC	—	—	95
MIC1	111	46.5	0.18
MIC2	110	52.5	0.27
MIC3	87	73.9	1.5
BM1	132	52.0	4.02
BM2	130	52.0	3.92
BM3	128	52.0	3.96
BM4	492.5	7.0	-0.8, +0.7

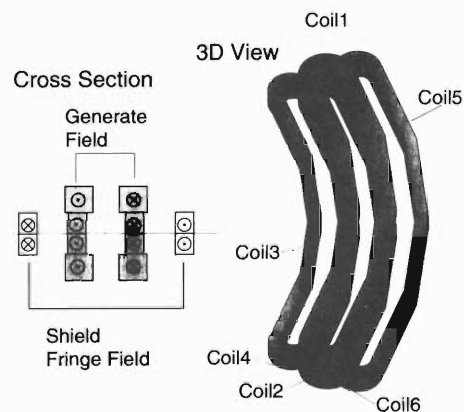


Fig. 2. Coil structure of the BM1.

The coil size and location were optimized by two-dimensional analysis of the magnetic field.<sup>3)</sup> Figure 3 shows a coil geometry and the performance which satisfies the specifications of the BM1.

Figure 4 shows the cross section of the coil support. The coils are mainly supported in the horizontal and

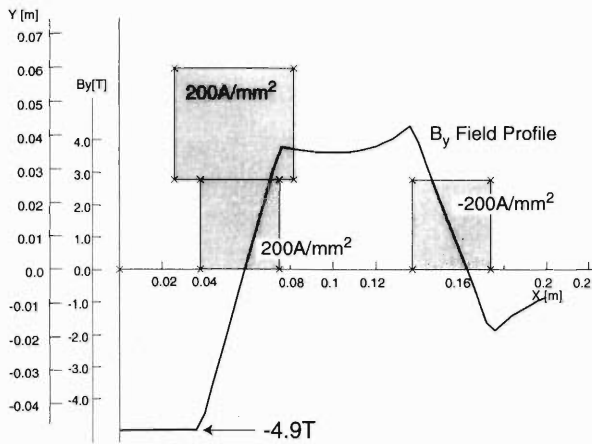


Fig. 3. Field distribution and coil geometry showing a quarter of the BM1.

the vertical directions by a pair of wall-to-wall clamps and bolts, respectively. In the design of the coil support, it is important to keep the coils compressive during the excitation phase, in order to avoid a coil movement which causes quench of the coil. For this purpose, a pre-stress is applied to the coil by Cotta, Bolt1 and Bolt2 seen in Fig. 4. Its strength should be large enough to compensate the shrink of the coils relative

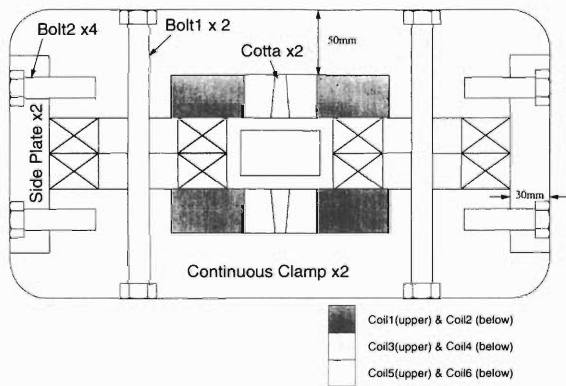


Fig. 4. Cross section of the coil support structure.

to the coil supports during the cool-down and excitation phases. In cool-down, the coils and their supports shrink with different rates. The shrink rates  $\alpha$  of the coils relative to the supports are shown in Table 2. In excitation, the magnetic forces deform the coils and the supports. The ratios  $\beta$  of the shrink of the coils and the deformation  $\gamma$  of the supports relative to the coil sizes are shown in Table 2. The pre-stress  $\sigma$  required during the assemble can be calculated by  $\sigma = E \times (\alpha + \beta - \gamma)$  where  $E$  represents the elastic modulus of the coil assumed to be 20 MPa. As shown in Table 2, the values of  $\sigma$  are less than their typical values of the yield strengths which are 70 MPa for the insulation of the coil. Further analysis and optimization of the support structure may decrease the maximum stress of the coil 3-6.

In summary, design study of the superconducting magnets for the injection system of RIKEN SRC was performed. It showed that difficulties of these magnets could be overcome using a simple coil structure which is easy to wind and support. Their full-scale models will be made in the near future.

Table 2. Summary of structural analysis on the cross section of the support structure. See the text about the definition of the symbols in the table.

	$\alpha$ [ $10^{-3}$ ]	$\beta$ [ $10^{-3}$ ]	$\gamma$ [ $10^{-3}$ ]	$\sigma_1$ [MPa]
Coil 1-2				
H	-0.75	-0.34	0.84	-38.6
V	-1.50	-0.25	0.58	-16.6
Coil 3-6				
H	-0.25	-0.36	1.73	-46.8
V	-1.50	-0.00	1.84	-66.8

#### References

- 1) A. Goto et al.: RIKEN Accel. Prog. Rep. **31**, 205 (1998).
- 2) S. Fujishima et al.: RIKEN Accel. Prog. Rep. **31**, 214 (1998).
- 3) T. Tominaka et al.: RIKEN Accel. Prog. Rep. **31**, 218 (1998).

# Optimization of the Superconducting Dipole Coils for Injection System of RIKEN Superconducting Ring Cyclotron

T. Tominaka, H. Okuno, S. Fujishima, A. Goto, and Y. Yano

The injection system for the RIKEN 6-sector superconducting ring cyclotron (SRC) consists of four bending magnets (BM1, BM2, BM3, BM4), three magnetic inflection channels (MIC1, MIC2, MIC3), and an electrostatic inflection channel (EIC). Four of the bending magnets and one of the three magnetic inflection channels are superconducting. An active-shield type magnet which is equipped with a pair of shield coils, as shown in Fig. 1, is adopted for these dipole magnets.<sup>1,2)</sup> In this report, optimization of the cross-sectional shape of an active-shield type dipole magnet is described.

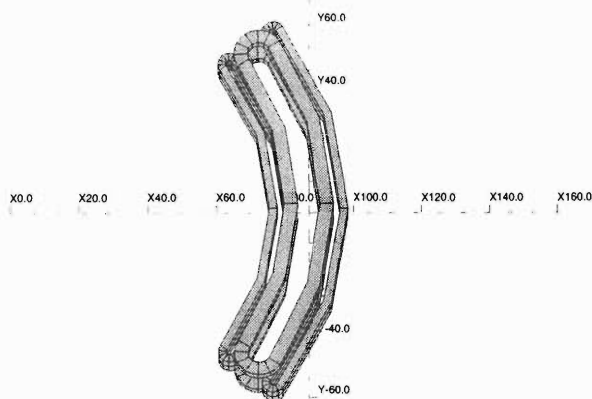


Fig. 1. Schematic view of the active-shield type dipole magnet.

The superconducting dipole magnets are planned to be composed of rectangular current-carrying blocks to ease the coil fabrication. A procedure to optimize the cross sectional shape is studied here with following two steps:<sup>3)</sup>

- (1) Rough optimization of the size and location of the current-carrying blocks.
- (2) Precise optimization of the locations of rectangular current blocks.

As the first step of optimization, a linear programming (LP) method can be used to acquire the initial cross sectional shapes for further optimization in the second step. In general, LP is effective to find the global minimum or maximum of any linear function subject to a set of constraints defined by linear inequalities. On the other hand, as the second step, an optimization method to find the local minima of arbitrary function is adopted. Then, the global minima of this optimization problem is found by the combination of these two steps.

A quarter of the cross-sectional geometry for opti-

mization is shown in Fig. 2. The region permitted as the location for current-carrying blocks is divided into small rectangular elements. The upper darker elements are reserved only for the main coil, while the lower elements are for both main and shield coils, constrained from the requirement of the final coil configuration. The current in each element is optimized by LP in such a way that the field homogeneity within the racetrack boundary (40 mm × 30 mm), shown by the gray line in Fig. 2, is better than 0.1%, and the fringe field at  $x > 0.25$  m, shown by a bullet in Fig. 2, is below 100 G. In this LP, the following objective function and various constraints are expressed by linear function and inequalities,

- objective function : total ampere turn,
- constraint (1) : minimum central field,
- constraint (2) : maximum current density,
- constraint (3) : lowest field homogeneity,
- constraint (4) : maximum fringe field,
- constraint (5) : maximum difference of currents between the lower main and shield blocks.

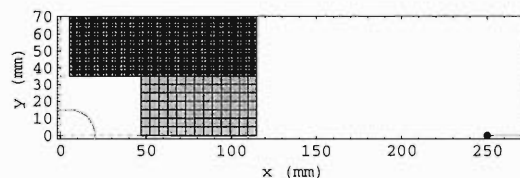


Fig. 2. Cross section of a magnetic inflection channel of the active shield type (MIC3), with the conductor (shaded) region for the linear programming.

As a result of LP, the current of each element is obtained, as shown with the darker element for the higher current in Fig. 3. Then, the optimized current distribution is approximated by two main rectangular current blocks and one shield current block, as shown in Fig. 4. However, this conversion to the rectangular shape of current blocks induces a deviation from the optimized arrangement in step 1.

As the second step which is a cross sectional position optimization step, the horizontal and vertical displacements of each current block shown as  $(x_1, y_1)$ ,  $(x_2, y_2)$ , and  $(x_3, y_3)$  in Fig. 4, corresponding to the coordinates in Figs. 5 and 6 are optimized. The procedure of the second step is as follows:<sup>4,5)</sup>

- (1) Calculation of the interior and exterior multipoles determined from the cross sectional configuration of coil.
- (2) Calculation of the field homogeneity from the interior multipoles and of the fringe field from the exterior

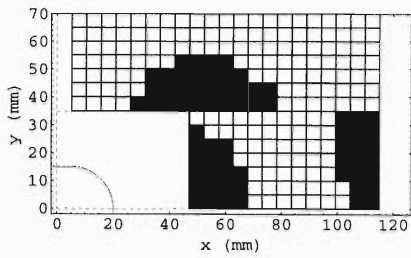


Fig. 3. Optimized cross section for obtaining  $B_0 = 1.5$  T, showing the darker element for the higher current, with the ampere turn,  $I_{total} = 5.28 \times 10^5$  A (at  $j_{max} = 150$  A/mm<sup>2</sup>).

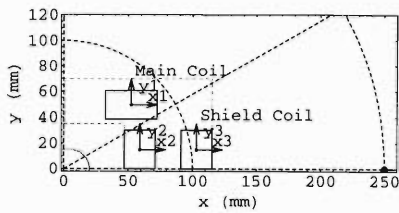


Fig. 4. Cross section of a magnetic inflection channel of active shield type (MIC3) explaining the second optimization.

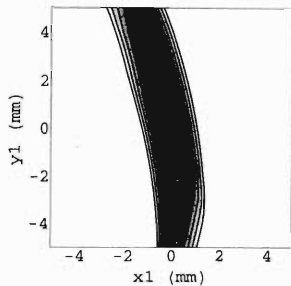


Fig. 5. Contour plot of  $(x_1, y_1)$  plane, satisfying  $|(B_y - B_{y0})/(B_{y0} + 4)| < 0.1\%$ , with  $x_2, y_2, x_3, y_3 = 0$ .

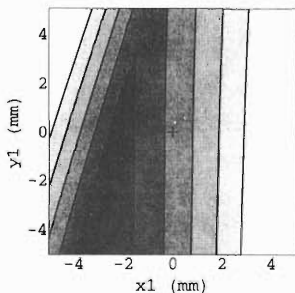


Fig. 6. Contour plot of  $(x_1, y_1)$  plane, satisfying  $|B_y(x > 0.25 \text{ m})| < 100$  G, with  $x_2, y_2, x_3, y_3 = 0$ .

multipoles.

(3) Search for the optimal locations of each current block corresponding to the minimum value of  $|(B_y - B_{y0})/(B_{y0} + 4)|$  to maximize the field homogeneity with the constraint for the fringe field.

The relation between the field homogeneity and the

multipoles of dipole coils, and that between the fringe field and the multipoles can be geometrically obtained for the specific homogeneous regions like the racetrack and for the requirement of the fringe field.<sup>5)</sup> Then, these relations are used for the calculation of the field homogeneity and of the fringe field.

The optimal locations of each current block corresponding to the minimum value of the fraction to maximize the field homogeneity and the allowable fringe field can be sought as the overlapped region of the two contour plots, as shown in Figs. 5 and 6. In these figures, the darker region corresponds to the favorable homogeneity (smaller value of the fraction) or the maximum fringe field, while the lighter region corresponds to the less favorable homogeneity (larger value of the fraction) than the prescribed one.

As a result, the optimal coil configuration producing the interior field distribution shown by Fig. 7, and the exterior field distribution shown by Fig. 8, can be obtained with the satisfaction of requirements by this optimization method.

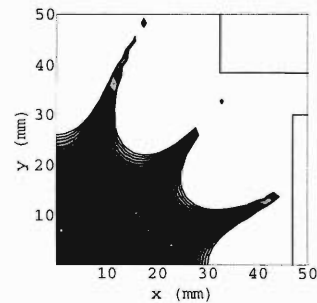


Fig. 7. Homogeneous field region, satisfying  $|(B_y - B_{y0})/(B_{y0} + 4)| < 0.1\%$ .

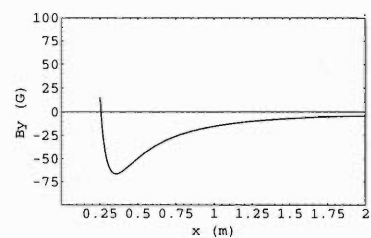


Fig. 8. Distribution of the fringe field,  $B_y$ , on the x axis ( $x > 0.25$  m).

#### References

- 1) C. R. Hoffmann et al.: Proc. 10th Int. Conf. on Cyclotron and their Applications, p. 222 (1984).
- 2) H. Okuno et al.: to be published in Proc. of 1997 Particle Accelerator Conf.
- 3) M. Kitamura et al.: IEEE Trans. Magn.-30, p. 2352 (1994).
- 4) T. Tominaka et al.: to be published in Proc. of 1997 Particle Accelerator Conf.
- 5) T. Tominaka et al.: Proc. 15th Magnet Technology Conf. (MT-15, 1997); to be published.

# Numerical Study of Single-Turn Extraction for RIKEN Superconducting Ring Cyclotron

J.-W. Kim, T. Mitsumoto, A. Goto, H. Okuno, T. Kubo,  
N. Sakamoto, and Y. Yano

The maximum beam power expected from the RIKEN superconducting ring cyclotron (SRC) is very high at the end of cyclotron acceleration. Hence, the beam extraction should be carried out with near 100% efficiency in order to minimize the heating and radiation problems by stray beams. Separation of the final turn needs to be sufficiently larger than the radial beam-width for a perfect single-turn extraction. However, the radial beam broadening due to resonance crossing, space charge, and the other imperfections in operation are not fully considered in the initial design calculations.

A main design particle is  $^{16}\text{O}^{7+}$  accelerating from 128 MeV/u to 400 MeV/u because of its largest number of turns. For such light nuclei accelerating to the highest design energy, the gain in orbital radius by the final acceleration is much smaller than the beam-width, so that other mechanism to enhance the turn separation needs to be employed. As empirically demonstrated on the RRC,<sup>1)</sup> an off-centered injection scheme could be effectively used. The precession induced by an orbital off-centeredness can increase the separation of the final turn. Figure 1 shows the motion of the radial phase ellipse during the last few turns of the  $^{16}\text{O}^{7+}$  beam with emittance of 10 mm-mrad. The pattern of precession is clearly visible. This is a case with the precession amplitude of about 1 cm. A larger turn separation by additional 2–3 mm seems to be obtainable by larger off-centeredness without notable distortion in the radial phase space, which may grant an extra operation margin in the presence of unexpected operational imperfections. The correct phase of precession at the time of extraction, on the other hand, can be controlled by the cavity voltage.

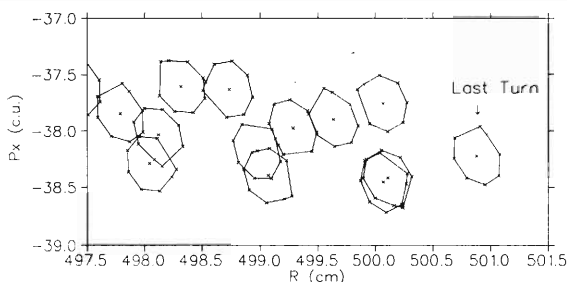


Fig. 1. Precession of radial phase ellipse for  $^{16}\text{O}^{7+}$  accelerating up to 400 MeV/u before extraction.  $P_x$  is the radial momentum in cyclotron units (c.u.). That is, the value of momentum is divided by  $m_0c$  (where  $m_0$  is the ion rest mass) and multiplied by a length unit  $a \equiv c/\omega_0$ .

The final turn is clearly separated at the entrance of the electrostatic deflector channel (EDC) as seen in Fig. 1. Interference was next checked against previous turns along the EDC, as shown in Fig. 2, because of its long length (2 m). The pattern of turn separation is well conserved along the EDC. The effect of EDC's electric field is not included in the calculation, however. Hence, the actual last-turn separation is much larger as the beam is deflected by the EDC whose gap is designed to be 10 mm.

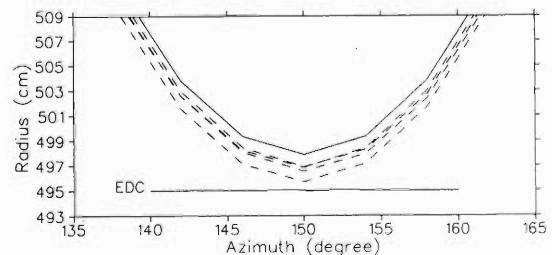


Fig. 2. Beam orbits near the EDC for the final turns. The last turn is plotted by the solid line, and the previous turns by the dashed lines.

For a single turn extraction the radial beam-width should be sharply defined. A flat-topping cavity which operates at the third harmonic of the main rf frequency will be used to flatten the top of sinusoidal rf waves. At present we consider to employ a flat-topping cavity which does not cover the inner few turns to save some space for other cyclotron elements, as have been adopted for the PSI proton ring cyclotron in Switzerland. That case is shown in Fig. 3 together with the case of a full radial coverage by the flat-topping cavity. Off-centered injection is not included in these calculations. Asymmetry in the phase acceptance can be seen when the radial coverage is not full. Additional distortion seems to occur under off-centering, but this result is not yet definite because of the uncertainty involved in describing rf electric fields at the inner radial end of the flat-topping cavity.

There are several mechanisms which can broaden the radial beam-width during acceleration. One serious process of such comes from the space charge effect. It is however not easy to implement this effect into the orbit tracking code. Instead, if using a simple analytic expression in Ref. 2, the limiting current for  $^{16}\text{O}^{7+}$  is found to be around 25  $\mu\text{A}$  for the phase width of  $20^\circ$ , 450 turns, and rf voltage of 550 keV on three single-gap cavities.

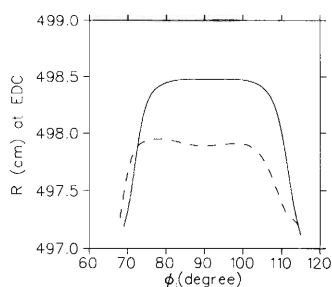


Fig. 3. The phase acceptance when employing a third harmonic flat-topping cavity. The plot is for the last turn prior to extraction. The solid line indicates the case of a full radial coverage by the flat-topping cavity, while the dashed line for the case of a partial radial coverage beyond  $r = 380$  cm.

A chief assumption on this limit in beam current is that the radial beam spread allowed is a half of the radial gain by acceleration. This limit, however, is not strictly applicable to the SRC since the final turn separation is mainly determined by precession. In addition, the space charge broadening could be partially compensated, for instance, by controlling the relative rf phase between the main and flat-topping cavities. In reality, an accurate evaluation of the limiting current is complicated as space charge and its correction schemes are involved. Since the beam-width increase may be inevitable in high current operation, its additional 1–2 mm increase needs to be acceptable in design.

Another serious condition is placed in reducing the

radial beam spread for ions which cross the  $\nu_r = 1.5$  ( $=3/2$ ) resonance. A small magnitude of the third harmonic gradient appears to deteriorate the radial phase space. Figure 4 shows a case when the gradient is 1 gauss/cm. The crossing of the resonance band is clearly displayed. The first harmonic component also affects the radial phase space when crossing the  $\nu_r = 1.5$  resonance, but its tolerance level is higher.

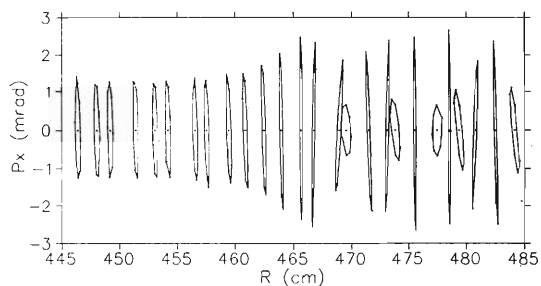


Fig. 4. The radial phase space motion when the  $^{16}\text{O}^{7+}$  beam crosses the  $\nu_r = 1.5$  resonance. The plot is made every five turn.  $P_x$  is the radial divergence, which is different from  $P_x$  defined in Fig. 1.

Further simulation of beam extraction is now under way, including the operational imperfections anticipated in the SRC.

#### References

- 1) Y. Yano: Proc. 8th Symp. on Accelerator Science and Technology, p. 10 (1991).
- 2) W. Joho: SIN Report, No. TM-11-4, Swiss (1968).

## Design of the RF Resonators for RIKEN Superconducting Ring Cyclotron

N. Sakamoto, O. Kamigaito, A. Goto, T. Mitsumoto, H. Okuno, and Y. Yano

For the RIKEN RI-Beam factory (RIBF) a new superconducting ring cyclotron (SRC)<sup>1)</sup> which consists of six superconducting sector magnets, three acceleration radio frequency (rf) resonators, and one flat-top resonator is planned to be constructed to provide heavy ion beams whose energy range is from 60 to 400 MeV/u. The SRC requires acceleration radio frequency resonators having a wide frequency range from 18 to 38 MHz with a harmonic number ( $h$ ) of 6 and having a high acceleration voltage of a few MV/turn. For example, in the case of  $^{16}\text{O}^{7+}$  acceleration up to the maximum energy of 400 MeV/u at the rf frequency of 38 MHz ( $h = 6$ ), an acceleration voltage of 2.4 MV/turn is needed to obtain a turn separation larger than 4 mm. Such a high voltage acceleration is also helpful to depress the longitudinal emittance growth of high intensity beams because the space charge effect can be depressed by a high voltage acceleration. Design study of the rf resonators for the SRC has been made by using a three dimensional RF calculation code, MAFIA.

The present design of the acceleration rf resonator for SRC is a single-gap type whose structure is basically same as that of RCNP Ring Cyclotron<sup>2)</sup> (RCNP-RC). The single-gap type resonator is suitable for the narrow valley section of the 6-sector ring cyclotron because its size is quite compact compared with the double-gap type resonator. The RCNP-RC type acceleration resonator<sup>2)</sup> has two main advantages. Firstly, the shunt impedance and Q-value are large. Secondly, the wall power loss is small because no electrical sliding-contact is used. These advantages are vital for high power resonators.

A schematic view of the RCNP-RC type resonator is shown in Fig. 1. The resonance is tuned by flapping the tuning panels. The resonances with the lowest

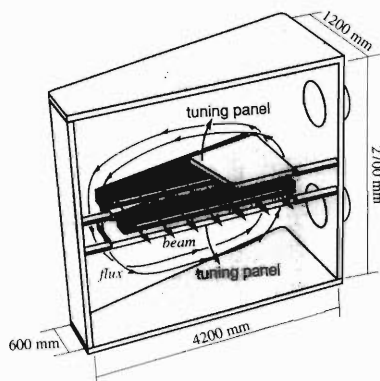


Fig. 1. Schematic view of the RCNP-RC type resonator.

and highest resonant frequencies are obtained when the panel angle is horizontal ( $0^\circ$ ) and vertical ( $90^\circ$ ), respectively. The lowest resonant frequency becomes lower by enlarging the width of the tuning panel. However, the resonant frequency of 18 MHz is hardly achieved because there remains small space in the valley section. Therefore, it is decided to adopt the double harmonic number 12 instead of 6 for the low energy operation so as to shift the frequency range from 18 to 23 MHz to the range from 36 to 46 MHz. Now the required frequency becomes from 23 to 46 MHz.

MAFIA calculation for the resonant frequency of the RCNP-RC resonator has been performed in order to know how large is the difference between the resonant frequency calculated and the one measured. The frequency range of the RCNP-RC rf resonator is from 30 to 52 MHz. It has turned out from the calculation that while the highest resonant frequency of 52 MHz is reproduced well, the calculated lowest frequency is smaller than the measured value by 8%.

A schematic drawing of the acceleration resonator is shown in Fig. 2. The frequency range obtained from MAFIA calculation is from 21.6 to 47.6 MHz. The shunt-impedance ( $R_s$ ) and the Q-value ( $Q$ ) for the tuning panel angles of  $0^\circ$  and  $90^\circ$  are shown in Table 1.

The values of  $R_s$  and  $Q$  at 38 MHz obtained by an interpolation\* are  $1.4 \text{ M}\Omega$  and  $3 \times 10^4$ , respectively, so that the net power required by the acceleration res-

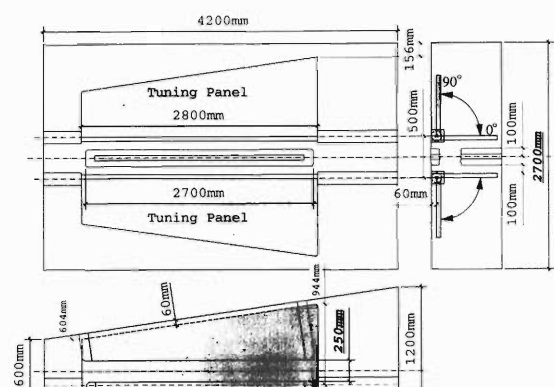


Fig. 2. Schematic drawing of the acceleration resonator. When the tuning panel angle is  $0^\circ$ , the open end of the tuning panel becomes very close to the wall in the opposite side, and a large electric field is produced between the tuning panel and the wall. The size of the gap has been set to be 60 mm which corresponds to 70% of the Kilpatrick factor with the Dee voltage of  $V_p = 300 \text{ kV}$ .

\* It is known from the RCNP data that  $R_s$  and  $Q$  are roughly proportional to the resonant frequency.

Table 1. Characteristics of the acceleration and flattop resonators for SRC.

parameters		acceleration	flattop
R <sub>s</sub> [MΩ]	21.6( 69) MHz	0.46	2.05
	47.6(138) MHz	1.90	0.59
Q	21.6( 69) MHz	25000	32000
	47.6(138) MHz	34000	27000

onator is roughly estimated to be 230 kW/resonator at 38 MHz.

Installation of a flattop system by the third harmonic deceleration method is planned. In the case of the double harmonic operation ( $h = 12$ ), the flattop acceleration is essential because the phase acceptance becomes 50% smaller than that of  $h = 6$  operation. The phase width  $\Delta\phi$ , which is defined by  $|V(\Delta\phi)|/V(\phi = 0) \leq 10^{-4}$ , for the non-flattop acceleration and flattop acceleration are  $\pm 0.81^\circ$  and  $\pm 7.3^\circ$ , respectively.

A schematic drawing of the present design of flattop resonator is shown in Fig. 3. The resonant frequency is changed by sliding the shorting plates. The frequency range is set to be from 69 to 138 MHz and the deceleration voltage is 11% of the acceleration voltage per turn.

The calculated electric field distribution along the gap center for the acceleration and flattop resonators are shown in Figs. 4(a) and 4(b), respectively. While the electric field of the acceleration resonator has a

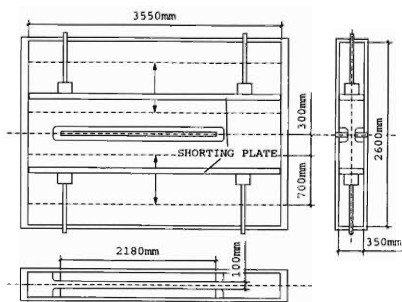


Fig. 3. Schematic drawing of the flattop resonator.

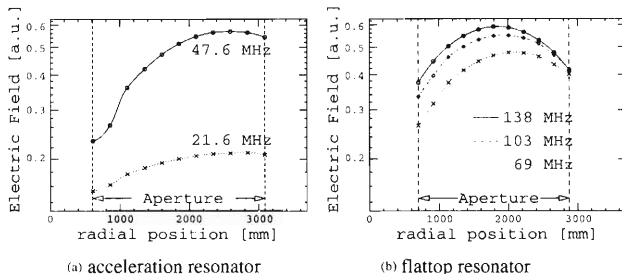


Fig. 4. Electric field distribution along the gap center of the acceleration and flattop resonators.

maximum at around the extraction region, the electric field of the flattop resonator has a maximum at around the middle of the Dee electrode. It is needed to see the effectiveness of the present design of the flattop system by calculating the acceleration orbits using the calculated electric field distribution.

Characteristics of the rf resonators of the present design are summarized in Table 2, and a proposed layout of the SRC is shown in Fig. 5. Three acceleration resonators and one flattop resonator are to be installed. Further investigation on the feasibility of our rf system is now in progress. A test with a 1/5 scaled model is planned to investigate the accuracy of the resonant frequency obtained from the model calculation by MAFIA.

Table 2. Calculated values of shunt-impedance and Q-value.

parameters	acceleration	flattop
number of unit	3	1
frequency [MHz]	23 ~ 46	69 ~ 138
length [cm]	420	355
height [cm]	270	260
width [cm]	60 <sub>(in)</sub> , 120 <sub>(out)</sub>	35
gap [mm]	250	100
aperture [mm×mm]	$\pm 30 \times 2480$	$\pm 30 \times 2180$
tuner	flapping panel	shorting panel
tuner stroke	0° ~ 90°	700 mm
feeder	inductive	inductive
Max. V <sub>p</sub> [MV/gap]	0.88	0.10
Max. Power [kW/resonator]	230	7

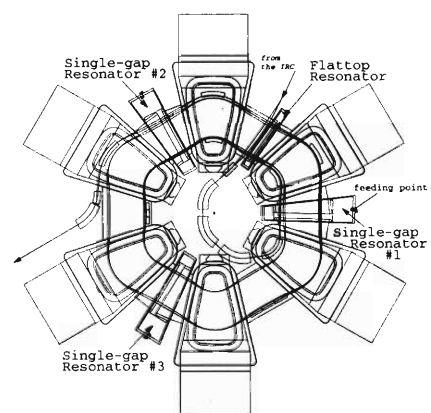


Fig. 5. Layout of the proposed SRC.

## References

- 1) A. Goto et al.: Proc. 11th Symp. on Accelerator Science and Technology (Harima, 1997), p. 53.
- 2) T. Saito et al.: Proc. 12th Int. Conf. on Cyclotrons and their Applications (Berlin 1989), p. 201.

# Estimation of Beam Chamber Pressure Required for RIKEN Superconducting Ring Cyclotron

K. Sugii, K. Ikegami, H. Okuno, S. Yokouchi, A. Goto, and Y. Yano

Beam transmissions are aimed to be above 99% for all ion beams available in the RIKEN Superconducting Ring Cyclotron (SRC).<sup>1)</sup> In a heavy-ion accelerator, beam losses are mainly caused by a change of charge state due to collisions of the beam against residual gas. Electron stripping is especially serious in such a higher-charge state heavy-ion accelerator like the SRC. Therefore, beam-chamber pressure is required to be as low as possible in order to reduce beam losses. In this report the beam-chamber pressure required for the SRC will be described.

A beam transmission ( $\eta$ ) is given by

$$\eta = \exp(-N_0 \sigma_T \beta c t P), \quad (1)$$

where  $N_0$  is the residual gas molecules per unit volume at 1 Pa and is  $2.5 \times 10^{14}$  molecules/cm<sup>3</sup>/Pa at 293 K,  $\sigma_T$  the charge-exchange cross section,  $\beta$  the ratio of ion velocity to light velocity ( $c$ ),  $t$  the accelerating time, and  $P$  the beam-chamber pressure. For a given cross section and accelerating time, the beam transmission can be obtained as a function of the beam-chamber pressure from Eq. (1).

Firstly, accelerating time of ion in a ring accelerator can be estimated by the following equation:

$$t = \{(\Delta E \cdot A)/(\Delta V \cdot q)\} \cdot (h/f), \quad (2)$$

where  $\Delta E$  is the beam energy difference between the injection and extraction,  $A$  the mass number,  $\Delta V$  the average of effective accelerating voltages per turn at the injection and extraction,  $q$  the charge number,  $h$  the harmonic number, and  $f$  the rf frequency. The accelerating time of  $^{238}\text{U}^{58+}$  should be evaluated, since the charge-exchange cross section of higher-charge state heavy ions such as  $^{238}\text{U}^{58+}$  is very large. Table 1 shows the typical parameters of rf cavities for  $^{238}\text{U}^{58+}$ . The accelerating time estimated from Eq. (2) using these parameters is  $1.343 \times 10^{-4}$  sec.

Secondly, it is necessary to estimate the electron-stripping cross section of fast heavy ions in collision

with residual gas molecules. In the case of the heavy ions accelerated to a very high energy range, there are few published data of the charge-exchange cross section. In the National Superconducting Cyclotron Laboratory (NSCL), the cross sections calculated from the Betz-Schmelzer approximation<sup>2)</sup> have been compared with published data.<sup>3)</sup> According to the comparison of the electron-stripping cross section, the approximation with a correction factor of 5 has been adopted in the high energy range of the K1200 cyclotron at the NSCL. When applying the above result to the SRC, we obtain the electron-stripping cross section of  $4 \times 10^{-18}$  cm<sup>2</sup> for  $^{238}\text{U}^{58+}$  at the injection energy 58.0 MeV/nucleon (see Table 1).

Finally, the beam transmission was calculated from Eq. (1) substituting  $1.343 \times 10^{-4}$  sec and  $4 \times 10^{-18}$  cm<sup>2</sup> for  $t$  and  $\sigma_T$  as a function of the beam-chamber pressure. Figure 1 shows the calculation results. As we can see from this figure, the beam-chamber pressure is necessary to be below  $5 \times 10^{-6}$  Pa in order to achieve the goal of 99% beam transmission.

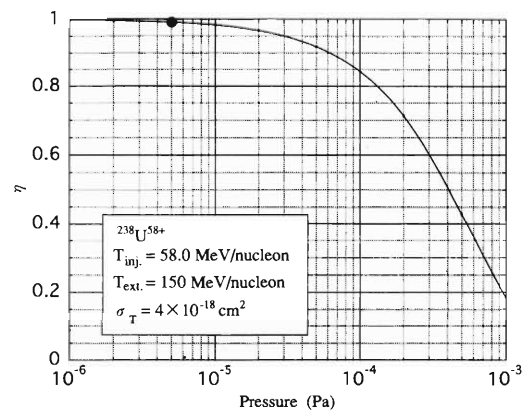


Fig. 1. Beam transmission of  $^{238}\text{U}^{58+}$  at the injection energy of 58.0 MeV/nucleon as a function of the beam-chamber pressure.

Table 1. Typical parameters of rf cavities for  $^{238}\text{U}^{58+}$ .

frequency (MHz)	27.2
harmonic number	6
$T_{\text{inj.}}$ (MeV/nucleon)	58.0
$T_{\text{ext.}}$ (MeV/nucleon)	150
$V_{\text{inj.}}$ (MV/turn)	0.38
$V_{\text{ext.}}$ (MV/turn)	0.86

## References

- 1) A. Goto et al.: RIKEN Accel. Prog. Rep. **31**, 205 (1998).
- 2) E. Baron, M. Bajard, and Ch. Ricaud: Nucl. Instrum. Methods Phys. Res. A **328**, 177 (1993).
- 3) *The K500⊗K1200 A Coupled Cyclotron Facility*: NSCL Rep., chap.4.4.3., p. 64 (July 1994).

## Design of Debuncher System in the Injection Line to Accumulator Cooler Ring of MUSES

K. Ohtomo and T. Katayama

The momentum spread ( $\Delta p/p$ ) of RI beams from the fragment separator (Big-RIPS) is relatively large. The required RF voltage to capture them into the RF buckets at Accumulator Cooler Ring (ACR) is proportional to the square of  $\Delta p/p$ . The value reaches 600 kV provided that  $\Delta p/p$  equals  $\pm 0.5\%$  and that the stacking efficiency is assured to be 80%.<sup>1)</sup> This voltage seems too high to realize with a ferrite-loaded RF cavity. Therefore, we are planning to install debuncher cavities in the injection line just prior to the injection kicker.

Simulations were performed in 6-dimensional phase spaces. The relations among distance, debuncher RF voltage required, phase, and momentum spread of beam are given by

$$\delta\phi = 2\pi \frac{L}{\beta\lambda} \frac{\Delta v}{v}, \quad (1)$$

$$\delta W = \frac{\Delta\phi}{\delta\phi} \Delta W, \quad (2)$$

$$e \frac{Q}{A} V \sin(h\delta\phi) = \Delta W \left( 1 - \frac{\Delta\phi\beta\lambda}{2\pi L\Delta v/v} \right) \cdots h\delta\phi < \frac{\pi}{2}, \quad (3)$$

$$e \frac{Q}{A} V = \Delta W \left( \frac{\pi/2}{h\delta\phi} - \frac{\Delta\phi\beta\lambda}{2\pi L\Delta v/v} \right) \cdots h\delta\phi > \frac{\pi}{2}. \quad (4)$$

Here,  $W$  is equal to the sum of kinetic energy  $T$  and rest-mass energy.  $\Delta\phi$  and  $\Delta W$  are the initial phase and energy spreads,  $\delta\phi$  is a maximum phase difference at debuncher,  $\delta W$  is an energy spread at debuncher,  $L$  is a distance between Big-RIPS and debuncher,  $\beta\lambda$  is an interval length between bunched beams,  $\Delta v/v$  is a velocity spread of beam,  $Q$  and  $A$  are charge and mass numbers,  $V$  is a voltage of debuncher, and  $h$  is a harmonic number of RF debuncher with respect to the RF of SRC.

In the above equations,  $\delta W$  is the minimum of energy spread after debunching. The phase spread at debuncher is  $h\delta\phi$ , and the most effective debunching is expected when  $h\delta\phi = 90$  degrees. In case  $h\delta\phi$  is larger than 90 degrees, over ranged particles can not receive sufficient acceleration or deceleration forces.

The voltages required for 4 typical nuclei are listed in Table 1. Here we assumed that the initial  $\Delta\phi$  and  $\Delta p/p$  are  $\pm 5$  degrees and  $\pm 0.5\%$ , respectively. The bunch interval  $\beta\lambda$  is 5.61 m.  $\delta p/p$  are momentum spreads after debunchers. The reason why the harmonic number is different for the uranium (U) from others is due to the difficulty to produce a long-range frequency-variable debuncher cavity.

Table 1. Beam parameters and debuncher RF voltage.

Nuclei:	C	Cu	Sn	U
$Q/A$	6/12	29/63	50/132	92/238
$T$ [MeV/u]	400	300	200	100
$\Delta p/p$ [%]	$\pm 0.5$	$\pm 0.5$	$\pm 0.5$	$\pm 0.5$
$\Delta v/v$ [%]	0.2447	0.2860	0.3388	0.4077
$\Delta W$ [MeV/u]	3.40	2.64	1.82	0.95
$freq$ [MHz]	38.17	34.94	30.32	22.94
$h$	6	6	6	7
$h freq$ [MHz]	229.02	209.63	181.93	160.59
$\Delta\phi$ [deg]	$\pm 5$	$\pm 5$	$\pm 5$	$\pm 5$
$h\Delta\phi$ [deg]	30	30	30	35
$h\delta\phi_{L=80m}$ [deg]	75.3	88.0	104.2	146.3
$h\delta\phi_{L=100m}$ [deg]	94.1	110.0	130.3	182.9
$\delta W_{L=80m}$ [MeV/u]	1.35	0.90	0.52	0.23
$\delta W_{L=100m}$ [MeV/u]	1.08	0.72	0.42	0.18
$(\delta p/p)_{L=80m}$ [%]	0.20	0.17	0.14	0.12
$(\delta p/p)_{L=100m}$ [%]	0.16	0.14	0.12	0.09
$V_{L=80m}$ [MV]	4.23	3.78	2.77	0.92
$V_{L=100m}$ [MV]	4.34	3.13	2.21	0.74

Numerical simulations have been performed by a 6-dimensional phase spaces beam tracking code, TRACEP.<sup>2)</sup> The result is shown in Fig. 1.

Though the carbon particles are almost debunched, the some of uranium particle spill out of the acceptable energy width of ACR cavity. The loss ratios are about 8 and 13% when the debuncher is located at  $L = 80$  and 100 m, respectively. This loss is inevitable when a same debuncher cavity is used for the particles with different energy spread. It is concluded that the distance  $L$  should be about 80 m and that the maximum RF voltage required for debunching is 4.2 MV.

The debuncher cavity has to have a wide tunable-frequency range. When the beam energy is between 80 to 120 MeV/u, the RF frequency of debuncher is 7-times higher than that of SRC. For much lower beam energy, the RF frequency of debuncher should be 8-times higher than that of SRC. The total frequency width ranges from 144 to 230 MHz.

As mentioned previously, the higher voltage is required for the higher frequency. It suggests that the resonant frequency should be changed by capacitance because shunt impedance is proportional to the capacitance to the minus one half power, and the larger the shunt impedance the smaller the dissipation power.

A type of debuncher cavities is a re-entrant  $\lambda/2$  push pull. The structure is cylindrical with a sliding nose for frequency tunability. Diameters of the inner duct and of the beam bore are assumed to be 180 and 60 mm, respectively. The nose surface to form gap is cut spher-

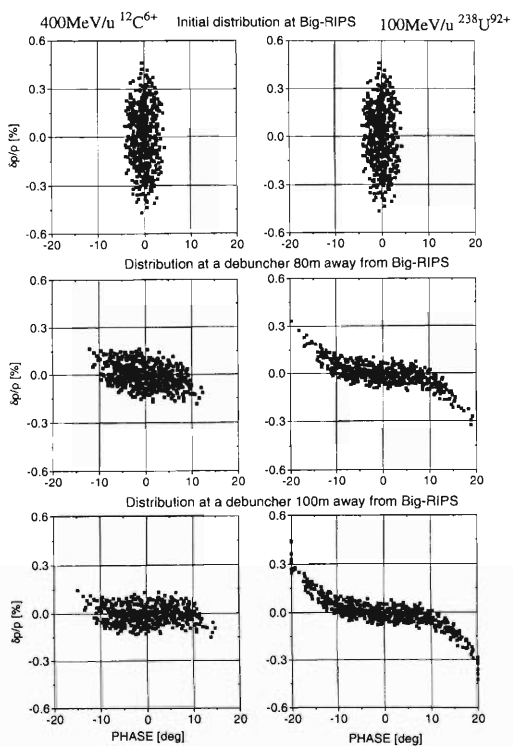


Fig. 1. Beam filamentation in  $\phi$ - $W$  plane. Left column displays carbon, while the right one displays uranium. Debuncher voltages are 4.2 and 0.9 MV, respectively. Top figures show particle distributions at Big-RIPS, middle figures show distributions after a debuncher located 80 m away from Big-RIPS, bottom figures show distributions after a debuncher located 100 m away from Big-RIPS.

ically so as to reduce electric field and chance of sparking. Low dissipation power and compactness of cavity are of great importance to the design. Calculations for optimizing the cavity diameter and length along the beam path were done by SUPERFISH at the maximum resonant frequency. The electric field is normalized in such a way that the gap voltage including transit time factor (TTF) is 1 MV.

The optimal length of cavity is turned to be 500 mm and the diameter of cavity is 800 mm. A quarter cross section of the optimized cavity computed by SUPERFISH is shown in Fig. 2. Parameters of the debuncher cavity for typical nuclei are listed in Table 2. Here, the number of cavity is assumed to be 5 so that the power dissipation should not exceed 80 kW per cavity. The reason of the power limit is due to the assumption to use a tetrode: RS2058 made by SIEMENS. This tetrode shows a good performance with the frequency range up to 230 MHz though the anode dissipation power is limited by 100 kW for pulse operation. The gap distance is 54 mm at the minimum resonant frequency of 144 MHz.

Each debuncher cavity has a series of RF amplifier system, which consists of tetrode power amplifier, solid

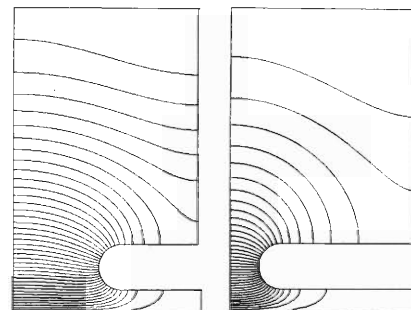


Fig. 2. Cross section of cavity and distribution of RF field by SUPERFISH numerical code. The left cavity is resonant at the maximum frequency (230 MHz) corresponding to 400 MeV/u of carbon, while the right one is resonant at 160 MHz, corresponding to 100 MeV/u of uranium. Both have coaxial symmetry line at each bottom boundary and have mirror symmetry line at each left boundary.

Table 2. Debuncher cavity parameters (for one cavity).

Nuclei	C	Cu	Sn	U
$T$ [MeV/u]	400	300	200	100
$d_{gap}$ [mm]	230	180	116	76
$freq$ [MHz]	229.02	209.63	181.93	160.59
$V_{eff}$ [MV]	1.0	0.8	0.6	0.2
TTF	0.869	0.913	0.954	0.961
Q-value	41400	37900	33900	31300
Power [kW]	79.3	54.1	35.5	4.7
$R_{shunt}$ [M $\Omega$ ]	17.0	14.5	11.4	9.3
Kilpatrick value	0.631	0.588	0.597	0.272

state pre-amplifier, and low level circuits. RF power is delivered with 1% duty cycle. The tetrode amplifier requires the anode, screen grid, control grid, and filament DC power supplies. The low level circuit includes modules of phase shifter, amplitude feedback loop, and fine tuning loop. Expected power consumption is 32 kVA for one debuncher and the total becomes up to 160 kVA.

In conclusion, the designed debuncher cavity has a wide tunable range of 144–230 MHz by moving the gap nose. The maximum voltage reaches to 1.15 MV per cavity when the resonant frequency is 230 MHz. The required total RF voltage for debunching is 4.3 MV. The five series of debuncher cavity system is required in order to reduce the momentum spread from  $\pm 0.5$  to  $\pm 0.15\%$  which is the acceptable level of capturing by RF bucket of ACR cavity.

#### References

- 1) Y. J. Yuan et al.: Proc. Eur. Part. Accel. Conf. p. 1338 (1996).
- 2) S. Yamada: 'Program manual; TRACEP', NIRS internal report (1990).

# Study of Stochastic Cooling at Accumulator Cooler Ring of MUSES

N. Inabe, K. Yoshida, M. Wakasugi, and T. Katayama

One of purposes for the accumulator cooler ring<sup>1)</sup> (ACR) at the MUSES project<sup>2)</sup> is cooling of ion beams including the radio-isotope (RI) beam produced by projectile-fragmentation in the Big-RIPS. Due to its production mechanism the RI beam has a large emittance ( $\varepsilon_x$ : horizontal,  $\varepsilon_y$ : vertical) and momentum spread ( $\Delta p/p$ ). Moreover, due to the multi-turn injection,  $\varepsilon_x$  of the beam injected into the ACR is very large. In the ACR the initial values of  $\varepsilon_x$ ,  $\varepsilon_y$  and  $\Delta p/p$  are  $125 \pi$  mm-mrad,  $10 \pi$  mm-mrad, and  $\pm 0.15\%$ , respectively. Requirement of cooling in the ACR is to have a very fast cooling time for the RI beam because the RI has an intrinsic life time.

Stochastic cooling<sup>3)</sup> is one of useful methods for cooling of ion beams. In particular, a fast cooling time is possible by the stochastic cooling in a region of large  $\varepsilon_x$ ,  $\varepsilon_y$  and  $\Delta p/p$ . On the other hand, in a region of small  $\varepsilon_x$ ,  $\varepsilon_y$  and  $\Delta p/p$ , the cooling time of the stochastic cooling is longer than that of electron cooling. Consequently the stochastic cooling will be used as pre-cooling that reduces the  $\varepsilon_x$ ,  $\varepsilon_y$  and  $\Delta p/p$  to about 10% of their initial values. After pre-cooling the electron cooling will be used to make the final values of  $\varepsilon_x$ ,  $\varepsilon_y$  and  $\Delta p/p$  small.

We have calculated the transverse and longitudinal cooling times of the stochastic cooling in several conditions. From these results availability of stochastic cooling was also investigated.

The transversal cooling time of the stochastic cooling is given by,<sup>4)</sup>

$$\frac{1}{\tau} = -\frac{W}{N} \left\{ -g_1 \sin \Delta\mu + \frac{1}{2} g_1^2 F \right\} \quad (1)$$

where

$W$  : band-width of a feed back system

$N$  : total number of particles

$\Delta\mu$  : phase advance between pickup and kicker

$g_1$  :  $= g \sqrt{\beta_p \beta_k}$ , where  $g$  is gain of a feed back system and  $\beta_p$  and  $\beta_k$  are  $\beta$  values of pick-up and kicker, respectively.

$F$  :  $= M + U$ ,  $M$  is the mixing factor and  $U$  is the noise factor given: (noise of system) divided by (beam noise per Schottky band).

Using Eq. (1), we calculated an optimum power of an amplifier to obtain the minimum cooling time. The obtained power is very large (more than 1 MW for  $N = 10^6$ ). Because this power is too large to realize, we have limited the power of the amplifier to be 10 kW.

We calculated the cooling times for  $^{11}\text{Be}^{4+}$  (400 MeV/u),  $^{39}\text{Ca}^{20+}$  (300 MeV/u),  $^{132}\text{Sn}^{50+}$  (200

MeV/u), and  $^{200}\text{Pb}^{80+}$  (100 MeV/u) with  $\Delta p/p = \pm 0.15\%$  and  $\varepsilon_x = 100 \pi$  mm-mrad. In the calculation we assumed that temperature of a pickup ( $T_n$ ) is 20 K, band width of an amplifier ( $W$ ) is 2 GHz and coupling impedance of pickup ( $Z_p$ ) is 100  $\Omega$ . The other parameters of the ACR are shown in Ref. 1.

In Fig. 1 the results are shown. The obtained cooling time is less than 0.1 s for the particle number  $10^3 \sim 10^7$  of RI beam. In particular for the beam with a high charge state the cooling time is very fast.

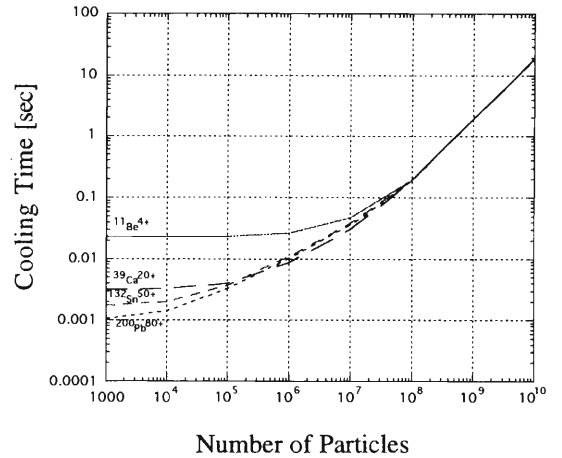


Fig. 1. Transversal cooling time.

We also studied longitudinal cooling time by a notch filter method<sup>5)</sup> which cooling is done in a region of dispersion free. Similar to the transversal cooling, the cooling time of the longitudinal cooling is limited by output power of the amplifier.

We calculated particle number dependence of the cooling time. Kinds of particles and conditions are the same as those used in the transversal cooling. In Fig. 2 results are shown. For number of particles  $\leq 10^7$  the obtained cooling times are less than 0.1 s. In particular the cooling time of the particle with high charge state is very fast. These tendencies are similar to the transversal cooling.

We have also calculated the cooling times for several values of the temperatures of a pickup system ( $T_n$ ) and of the coupling impedances ( $Z_p$ ). Figures 3 and 4 show  $T_n$  and  $Z_p$  dependences, respectively. In both calculations we assumed the number of particles  $10^5$ . For calculation of  $T_n$  dependence we assumed  $Z_p = 100 \Omega$  and for that of  $Z_p$  dependence,  $T_n = 20$  K. As shown in Fig. 3 the  $T_n$  dependence is weak. Cooling times of highly charged beams are shorter than 0.01 s even in 100 K. In the case of highly charged beams,

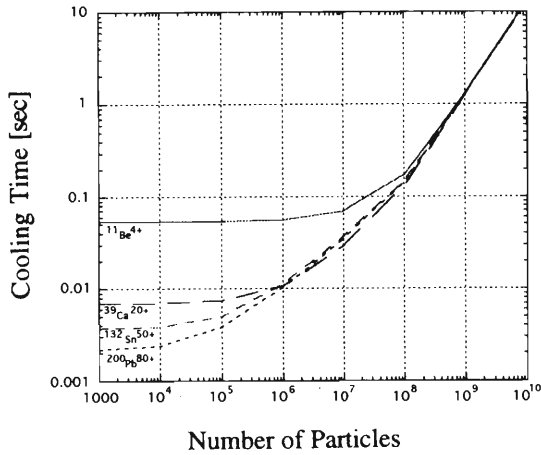


Fig. 2. Longitudinal cooling time.

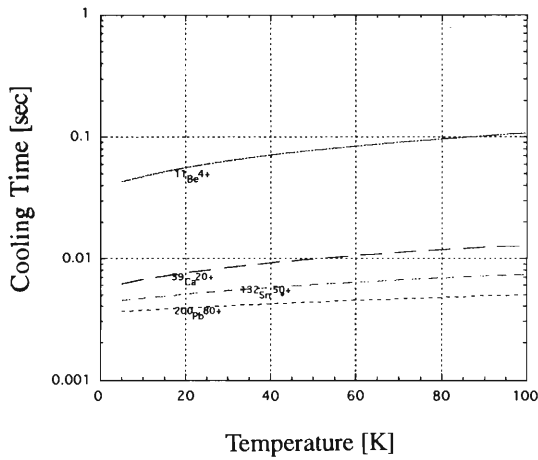


Fig. 3.  $T_n$  dependence of cooling time, where, number of particles is  $10^5$ .

signal-to-noise ratio is good because voltage induced at the pickup is much larger than that by noise. As shown in Fig. 4,  $Z_p$  dependence is strong, especially for the region below  $50 \Omega$ . To obtain  $\tau < 0.1$  s,  $Z_p$  is required to be  $Z_p > 50 \Omega$ .

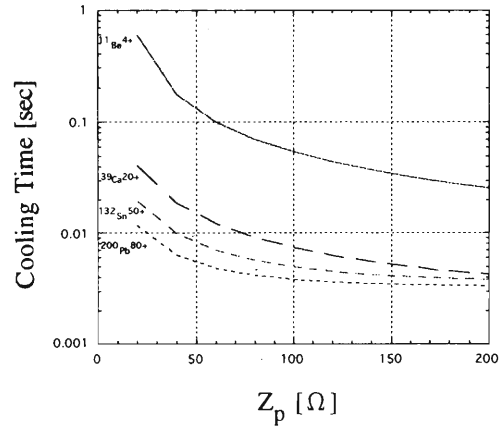


Fig. 4.  $Z_p$  dependence of cooling time, where, number of particles is  $10^5$ .

From calculations we found fast cooling times in almost whole region. This indicates that the stochastic cooling is advantage for the RI beam in ACR.

One of the important things to design a system of the stochastic cooling in ACR is to make a pickup system with a large coupling impedance. The large coupling impedance is also important to reduce a needed gain of the amplifier because the pickup voltage itself is large. On the other hand it is not necessary for the pickup system to have very low temperature. This makes construction of the system easy.

Based on the calculation we are designing a pickup system with high coupling impedance.

#### References

- 1) K. Ohtomo et al.: Proc. 17th PAC, Vancouver, May 1997; to be published.
- 2) T. Katayama et al.: Proc. STORI 96, September 1996, Bernkastel, Germany; to be published Nuclear Physics A.
- 3) S. van der Meer: CERN report, CERN/ISR-PO/72-31 (1978).
- 4) D. A. Goldberg et al.: LBL report, LBL-25924 (1989).
- 5) T. Katayama et al.: Particle Accelerators **21**, 99 (1987).

# Design of Booster Synchrotron for MUSES

T. Ohkawa and T. Katayama

The Booster Synchrotron Ring (BSR) is a part of Multi-Use Experimental Storage rings (MUSES). The BSR functions exclusively for the acceleration of ion and electron beams. The maximum accelerating energies are, for example: 3 GeV for proton; 1.45 GeV/nucleon for light ions of  $q/A = 1/2$ ; and 800 MeV/nucleon for heavy ions of  $q/A = 1/3$ . Electron beam is accelerated to 2.5 GeV from the injection energy 300 MeV.<sup>1)</sup> In this paper, results of lattice study of the BSR are presented.

As shown in Fig. 1, the BSR consists of two arc sections and two long straight sections. Each arc section is mirror symmetrical system against another, and contains two bending cells. Each bending cell is a dispersion suppressor arc, and consists of four FODO cells because this number of cells is specified to raise the transition  $\gamma$  ( $\gamma_t$ ) sufficiently large. The dispersion in the straight sections, other than the arc section, is zero. The length of a dipole magnet of 1.911 m is determined by the circumference specification. The maximum magnetic field of a dipole (1.5 T) is determined by the required maximum rigidity of 14.6 Tm. The lattice is specified by eight families of quadrupoles: QF1 and QD1; QF4 and QD4 in the arcs, QF2 and QD2, QF3 and QD3 in the long straight sections. The structure of one FODO cell and short straight section in the arc are given as follows.

$$\text{cel} = \text{QF1} \frac{d_1}{\text{B}} \frac{d_2}{\text{QD1}} \frac{d_1}{\text{B}} \frac{d_2}{\text{QD1}}$$

$$\text{str2} = \text{QF4} \frac{d_3}{\text{QD4}} \frac{d_s}{\text{QD4}} \frac{d_3}{\text{QF4}}$$

Then, the lattice of each arc section (60.365 m) is

$$\text{arc} = (\text{cel}, \text{cel}, \text{cel}, \text{cel}, \text{str2}, -\text{cel}, -\text{cel}, -\text{cel}, -\text{cel})$$

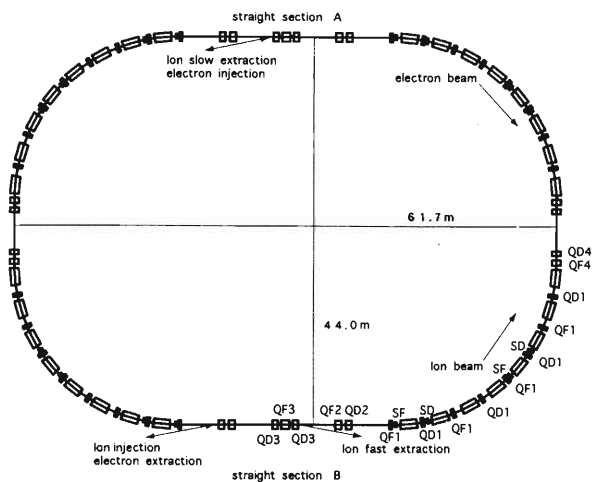


Fig. 1. A layout of BSR.

In this structure,  $d_1$  ( $d_2$ ) is 0.925 m (0.475 m) drift space which are reserved for sextupole magnets for the chromaticity correction and kicker magnets for the closed orbit correction.

The two long straight sections are mirror symmetry structure each other. The lattice of each section (23.876 m) is

$$\text{str1} = \frac{d_s}{\text{QF2}} \frac{d_3}{\text{QD2}} \frac{d_s}{\text{QD3}} \frac{d_3}{\text{QF3}}$$

$$\frac{d_3}{\text{QD3}} \frac{d_s}{\text{QD2}} \frac{d_3}{\text{QF2}} \frac{d_s}{\text{QF3}}$$

where  $d_s$  is a free space with a length of 4.276 m reserved for RF cavities, injection kickers or other devices.

Consequently, the whole lattice of BSR is described as follows:

$$\text{BSR} = (\text{arc}, \text{str1}, \text{arc}, \text{str1})$$

The parameters of the lattice are summarized in Table 1. The  $\beta$  and dispersion functions are shown in Fig. 2. The  $\gamma_t$  is 4.643 and the peak dispersion is 3.730 m. The peak  $\beta$  function are 14.010 m in horizontal direction and 16404 m in vertical direction.<sup>2)</sup> The calculation is performed using the MAD program.

Table 1. Lattice parameter of BSR.

Circumference	$C = 179.7159 \text{ m}$
Average radius	$R = 28.603 \text{ m}$
Max. magnetic rigidity	$B\rho = 14.6 \text{ Tm}$
Momentum compaction	$\alpha = 0.0458$
Transition gamma	$\gamma_t = 4.675$
Betatron tune values	$Q_x/Q_y = 6.691/6.212$
Natural chromaticity	$Q'_x/Q'_y = -8.670/-8.320$
Max. $\beta$ amplitude	$\beta_x/\beta_y = 14.010 \text{ m}/16.404 \text{ m}$
Max. dispersion	$D_x/D_y = 3.680 \text{ m}/0.0 \text{ m}$

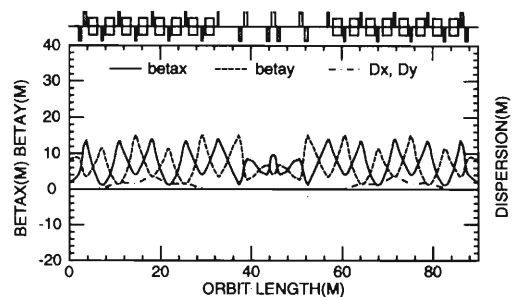


Fig. 2.  $\beta$  and dispersion functions along the lattice.

The dynamic aperture might be seriously reduced when chromaticity is corrected. This is because the average value of dispersion is lowered in a ring, corresponding to a high value of  $\gamma_t$ . In this lattice, the natural chromaticity values are  $-8.670$  (horizontal) and  $-8.320$  (vertical), and are corrected by two families of sextupoles SF and SD, (focusing and defocusing), associated with their respective quadrupoles as indicated in Fig. 1. The phase advance between two sextupoles belonging to one family is  $\pi$ . The normalized field strengths of sextupoles required to correct chromaticity are relatively large:  $9.236 \text{ m}^{-3}$  for the SF and  $-15.889 \text{ m}^{-3}$  for the SD. The tracking results using the beam with  $\pi\epsilon_x = 125\pi \text{ mm}\cdot\text{mrad}$ ,  $\pi\epsilon_y = 5\pi \text{ mm}\cdot\text{mrad}$ ,  $dp/p = 0$  and fully corrected chromaticity, are shown in Fig. 3. The largest initial betatron amplitude for which particles are still on a stable orbit is defined as a dynamic aperture. The above tracking results show that the dynamic aperture of BSR is larger than  $\pi\epsilon_x = 125\pi \text{ mm}\cdot\text{mrad}$  and  $\pi\epsilon_y = 5\pi \text{ mm}\cdot\text{mrad}$ .

We estimate the relation between position of particle at the central momentum and tune values when chromaticity is corrected. The results are shown in Table 2. It is found that the tune values of the particles with large initial betatron amplitude are changed.

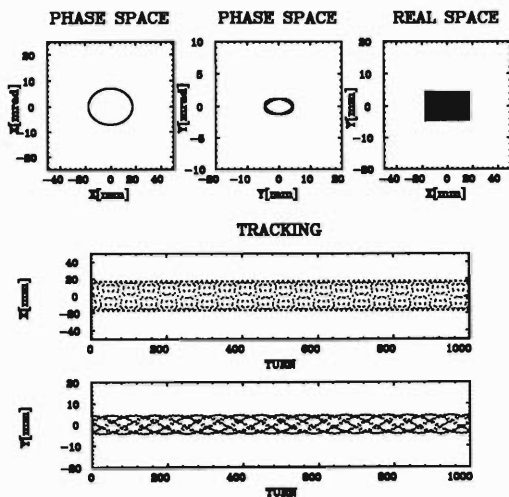


Fig. 3. Results of single-particle tracking ( $dp/p = 0$ ).

Table 2. Relation between position of particle and tune values (at  $dp/p = 0$ ).

No.	$\epsilon_x$	$\epsilon_y$	x	y	Qx	Qy
1	125	5	17.5	4.36	6.694	6.184
2	250	10	24.8	6.16	6.697	6.167
3	500	20	35.0	8.71	6.703	6.134
4	750	30	42.9	10.7	6.710	6.097
5	1000	40	49.5	12.3	6.718	6.052
6	1250	50	55.4	13.8	6.728	6.000
7	1500	60	60.7	15.1	6.738	5.948

Next, we have calculated the tracking for the seven particles as shown in the Table 2 with fully corrected chromaticity. In this case, all magnet elements are misaligned (misalignment is  $\pm 100 \mu\text{m}$  and rotational misalignment is  $\pm 0.1 \text{ mrad}$ ), and field error (sextupole component of dipole magnet is  $-0.1 \text{ m}^{-3}$ ) is introduced randomly. The above magnitudes of misalignment and field error are typical. Tracking results are shown in Fig. 4. It is found that the dynamic aperture of BSR is as large as  $\pi\epsilon_x = 1000\pi \text{ mm}\cdot\text{mrad}$  and  $\pi\epsilon_y = 40\pi \text{ mm}\cdot\text{mrad}$  within the limit of  $dp/p = \pm 10^{-3}$ . For example, results of seven-particle tracking with  $dp/p = 0$  are shown in Fig. 5.

We have found that the dynamic aperture of BSR is approximately eight times larger than the demanded acceptance of  $\pi\epsilon_x = 125\pi \text{ mm}\cdot\text{mrad}$  and  $\pi\epsilon_y = 5\pi \text{ mm}\cdot\text{mrad}$ .

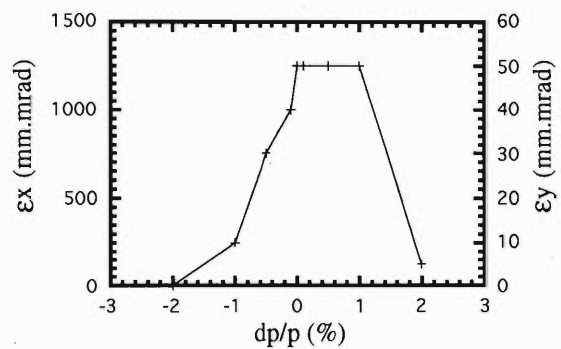


Fig. 4. dynamic aperture of BSR.

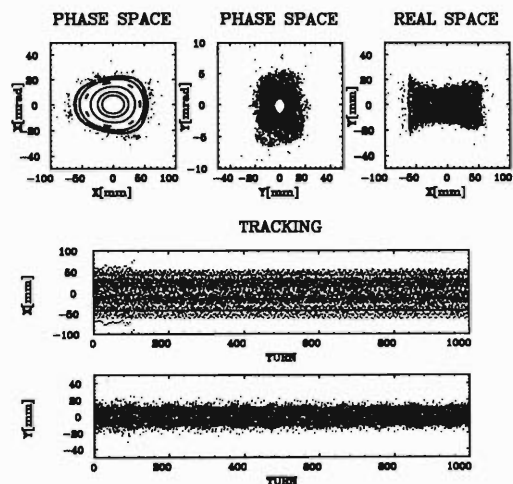


Fig. 5. Results of seven-particle tracking ( $dp/p = 0$ ).

#### References

- 1) T. Katayama et al.: Proc. 17th EPAC (Sitges, 1996), p. 563.
- 2) T. Ohkawa et al.: Proc. 17th PAC (Vancouver, 1997).

## Design of Slow Extraction System at Booster Synchrotron for MUSES

T. Ohkawa and T. Katayama

In booster synchrotron ring (BSR) the accelerated ion and electron beams will be fast extracted and subsequently injected into the Double Storage Rings (DSR) by one turn injection mode. As another operation mode, ion beams will be slowly extracted from BSR for the experiments. In this paper, injection and extraction (especially slow extraction) procedures of the BSR are presented.

Arrangements of the injection and extraction magnets are shown in Figs. 1 and 2. The BSR lattice is designed to be able to operate with two different extraction modes for ion beams: fast and slow extractions.

As seen in Fig. 1, an electrostatic septum (ES), four septum magnets (SM1, SM2, SM3, SM4) and three bump magnets (BM1) are used for the electron beam multi-turn injection. These magnets, except bump magnets, are used for the ion-beam slow extraction which is carried out by using a third order resonance ( $\nu_{res} = 20/3$ ).

As seen in Fig. 2, three septum magnets (SM2, SM3, SM5), four bump magnets (BM2, BM3) and ten kicker magnets (K1) are used for the ion-beam one turn injection. These magnets are also used for electron-beam fast extraction. The ion beam from the ACR is injected into BSR through the septum magnet SM5, SM3 and

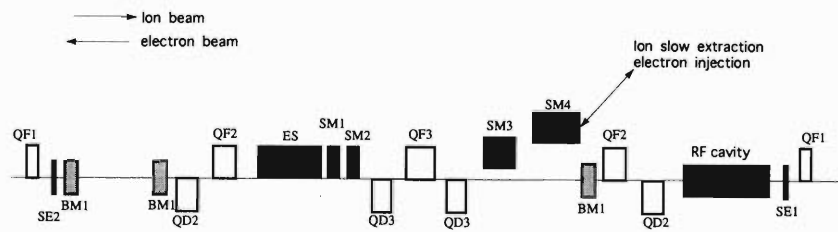


Fig. 1. An arrangement of straight section A.

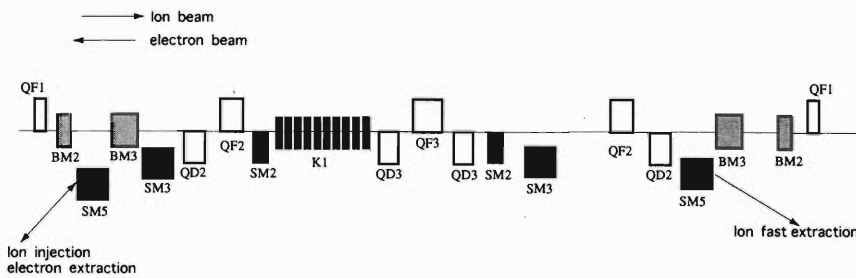


Fig. 2. An arrangement of straight section B.

SM2 located at the straight section of BSR. The ion-beam is eventually kicked and placed in the reference orbit by the kicker magnets. These kicker magnets are used for the ion-beam fast extraction. Therefore, kicker magnets must be risen and fallen less than 50 ns.<sup>1)</sup>

On slow extraction process, at first, the sextupole magnets (SE) as a resonance exciter are excited. Secondly, the horizontal tune is moved from the operating value 6.691 to a value near the third order resonance (20/3) by changing the excitation currents of quadrupole magnets. Beams which have deviated inside by the distance more than 25 mm from the central

orbit at the entrance of the ES are deflected inward as large as 3 mrad by the static high voltage of ES.

The betatron oscillation can be expressed by the following relation:

$$\begin{pmatrix} X \\ Y \end{pmatrix} = \begin{pmatrix} 1 - \alpha\epsilon & \sqrt{1 + \alpha^2}\epsilon \\ -\sqrt{1 + \alpha^2}\epsilon & 1 + \alpha\epsilon \end{pmatrix} \begin{pmatrix} X_0 \\ Y_0 \end{pmatrix},$$

where

$$X = \frac{1}{\sqrt{2}} \left[ \sqrt{1 + \alpha^2} + \alpha \right] \frac{1}{2} (x - y)$$

$$Y = \frac{1}{\sqrt{2}} \left[ \sqrt{1 + \alpha^2} - \alpha \right] \frac{1}{2} (x + y)$$

$$y = \frac{\beta}{\sqrt{1+\alpha^2}} x'.$$

Let  $\Psi_i$  be the deflection due to the  $i$ -th sextupole magnet ( $SE_i$ ). Then,

$$\Psi_i = g_i x_i^2, \quad g_i = \frac{B_i''}{2B\rho},$$

where  $x_i$  is the displacement of the orbit from the equilibrium orbit at  $SE_i$  and  $g_i$  is the strength of the  $SE_i$ . Here we assume that the transfer matrix  $\Gamma_i$  from electric septum to sextupole magnet is

$$\Gamma_i = \begin{pmatrix} a_i & b_i \\ c_i & d_i \end{pmatrix}.$$

In the third resonance, particles pass each sextupole magnets three times per period. Therefore, taking a summation of the contributions from each magnet over one period, we have a Hamiltonian:

$$H = -\frac{\varepsilon}{2}(X^2 + Y^2) + \frac{\beta}{3\sqrt{1+\alpha^2}} \Sigma \{ (X^3 - 3XY^2)g_i' A_i + (Y^3 - 3YX^2)g_i' B_i \},$$

where  $\Sigma$  means the summation over one revolution. Defining the angle of rotation of the coordinates  $\Psi$  as given by  $\tan 3\Psi = -\Sigma g_i B_i / \Sigma g_i A_i$ , the coordinates are transformed as

$$\begin{pmatrix} X' \\ Y' \end{pmatrix} = \begin{pmatrix} \cos \Psi & \sin \Psi \\ -\sin \Psi & \cos \Psi \end{pmatrix} \begin{pmatrix} X \\ Y \end{pmatrix}.$$

Then, we can rewrite the above Hamiltonian as

$$H = -\frac{\varepsilon}{2}(X'^2 + Y'^2) + \frac{\beta g \sqrt{A^2 + B^2}}{3\sqrt{a + \alpha^2}} (X'^3 - 3X'Y'^2),$$

from which we can obtain the following three unstable fixed points:

$$A : (X'_1, Y'_1) = \left( \frac{\sqrt{1+\alpha^2}}{\beta g \sqrt{A^2 + B^2}}, 0 \right),$$

$$B : (X'_2, Y'_2) = \left( -\frac{1}{2}X'_1, -\frac{\sqrt{3}}{2}X'_1 \right),$$

$$C : (X'_3, Y'_3) = \left( -\frac{1}{2}X'_1, \frac{\sqrt{3}}{2}X'_1 \right).$$

Transforming back to the  $(x, x')$  plane, we obtain the following unstable fixed point:<sup>2)</sup>

$$A : (x_1, x'_1) = \left( G \cos(\Psi - \chi), -\frac{\sqrt{1+\alpha^2}}{\beta} G \cos(\Psi + \chi) \right)$$

$$B : (x_2, x'_2) = \left( G \cos \left( \Psi - \chi + \frac{2}{3}\pi \right), -\frac{\sqrt{1+\alpha^2}}{\beta} G \cos \left( \Psi + \chi + \frac{2}{3}\pi \right) \right)$$

$$C : (x_3, x'_3) = \left( G \cos \left( \Psi - \chi - \frac{2}{3}\pi \right), -\frac{\sqrt{1+\alpha^2}}{\beta} G \cos \left( \Psi + \chi - \frac{2}{3}\pi \right) \right)$$

where

$$\tan \chi = \sqrt{1+\alpha^2} + \alpha,$$

and

$$G = \frac{\varepsilon(1+\alpha^2)^{\frac{3}{4}}}{\beta g \sqrt{A^2 + B^2}}.$$

The area of the triangular separatrix in the  $(x, x')$  plane is given by

$$S = \frac{3\sqrt{3}}{4} |\sin 2\chi| \frac{\sqrt{1+\alpha^2}}{\beta} G^2.$$

Here,  $S$  is assumed to be  $10\pi$  mm·mrad. The momentum spread is  $dp/p = \pm 0.1\%$ . Hence, a beam is extracted from that with  $dp/p = 0.1\%$  to that with  $dp/p = -0.1\%$  by turns. When a beam with  $dp/p = 0$  has horizontal tune value  $Q_0$ , a beam with  $dp/p = 0.1\%$  has  $Q_0 + \xi dp/p$ . If the value of  $\varepsilon$  is same, the extracted direction of the beam is same. Result of the simulation  $\varepsilon$  is shown in Fig. 3. As shown in Fig. 3, at the entrance of ES the outgoing trajectories are overlapped each other.<sup>3)</sup> Thus, we have found that the ion-beam slow extraction can successfully be carried out by using the third order resonance.

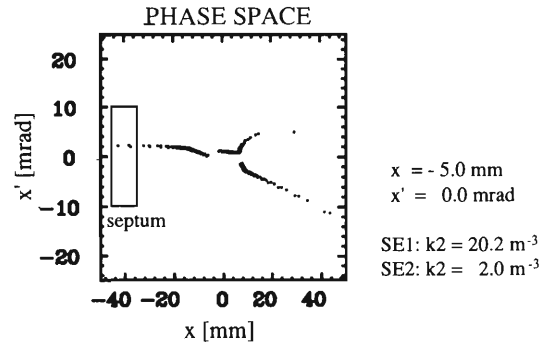


Fig. 3. The separatrices and outgoing trajectories of beams with  $dp/p = -0.1, 0, 0.1\%$ , respectively, at ES.

#### References

- 1) T. Ohkawa et al.: Proc. 17th PAC (Vancouver, 1997).
- 2) Y. Kobayashi: Nucl. Instrum. Methods **83**, 77 (1970).
- 3) T. Ohkawa et al.: Proc. 11th SAST, Harima Science Garden City, Japan, 1997, p. 285 (1997).

## Simulation Study of Ion Beam Bunching with Electron Cooler at Double Storage Ring of MUSES

M. Takanaka and T. Katayama

Collision experiments with ion-ion beams and ion-electron beams are planned in the double storage rings (DSR) of RI-beam factory project. Bunched ion beams will be formed to obtain a high luminosity by controlling the momentum spread with an RF system, while the beams are cooled by an electron cooler. The longitudinal and transverse space-charge forces are dominant over the inductive or resistive force induced through the coupling impedances between beams and vacuum chamber in the region of DSR energy below 1.5 GeV/u. Both space-charge forces become large with the bunch shortening.

The bunch shortening is known to be disturbed by the longitudinal space-charge force below the transition energy. Beams are trapped into more resonances, when incoherent or coherent betatron-tune shift is made larger by the monopole or dipole component of the transverse space-charge force, respectively. These phenomena are not good for obtaining the high luminosity. Simulations of the beam bunching can predict whether there is any obstacle to obtaining a high luminosity.

In the simulation where coupled-bunch phenomena are not dealt, the following forces have been taken into account as forces acting on ions:

- the RF force,
- the longitudinal and the transverse electron cooling forces,<sup>1)</sup>
- the linear and the nonlinear forces coming from the ring lattice,
- the longitudinal space-charge force,
- the monopole and dipole components of the transverse space-charge force.

The longitudinal space-charge force has been estimated by using a following equation for the space-charge impedance of a round beam having a Gaussian radial charge distribution:

$$\left[ \frac{Z_{\parallel}}{n} \right]_{sp} = i \frac{g(r)}{2\beta\gamma^2} Z_0,$$

$$g(r) \approx - \int_{x=\frac{r^2}{2\sigma^2}}^{\infty} \frac{e^{-x}}{x} dx + 2 \log \left( \frac{b}{r} \right),$$

$$g(0) \approx 0.577 + 2 \log \left( \frac{b}{\sqrt{2}\sigma} \right),$$

where  $\sigma$  is the standard deviation of the distribution,  $r$  the radial position from the center of the beam,  $Z_0$  the free space impedance, and  $b$  the inner radius of the vacuum chamber assumed to be cylindrical and perfectly conducting. As actual beams are not round, the following expression has been used for the  $\sigma$ :

$$\sigma = \sqrt{\frac{\sigma_h^2 + \sigma_v^2}{2}},$$

where  $\sigma_h$  and  $\sigma_v$  stand for the horizontal and the vertical rms beam sizes, respectively. The dipole component of the transverse space-charge force has been estimated by using the following equation for a ring type of space-charge impedance:

$$Z_{\perp} = i \frac{Z_0 R}{\beta^2 \gamma^2} \left( \frac{1}{9\sigma_h \sigma_v} - \frac{1}{b^2} \right),$$

where  $R$  is the mean radius of the DSR.

If a beam is electron-cooled under a constant RF voltage, the momentum spread of the beam decreases until the longitudinal microwave instability occurs. Therefore, for the sake to avoid such an instability the momentum-spread control is necessary in a way that increase of RF voltage can cancel the decrement of the momentum spread due to the electron cooling.

As an example, simulated results are shown below for an  $U_{238}^{92+}$ -ion beam of 150 MeV/u. The parameters of the coasting beam to be bunched, of the ring, and of the electron cooler as input data for the simulation have been listed in a previous report.<sup>2)</sup> The initial charge distribution of the coasting beam was assumed to be flat along the RF phase axis, while it was assumed to be Gaussian along the momentum axis. The transverse phase-space distribution was assumed to be Gaussian, too. The average beam current used in the simulation was 3.4 mA. The peak current reaches 59 mA, when the beam with 6-rms momentum spread of  $10^{-3}$  and rms transverse emittance of  $10^{-6}\pi$  m-rad is bunched to the 6-rms length of 0.4 m. The peak current is the threshold one estimated with Keil-Schnell criterion for the longitudinal microwave instability.<sup>3)</sup>

A sextupole element located at the cooling section has been introduced in the simulation as a source of nonlinear force. The field strength expressed by  $B''l\beta_{ec}/B\rho$  was assumed to be  $0.3 m^{-1}$ , where  $\beta_{ec}$  is the  $\beta$  function at the section. The strength is equal to about 1/10–1/30 of the effective strength of the sextupole magnets used for slow beam extractions. The sextupole field induces the following major resonances near and below the working point:

$$3\nu_h = 22,$$

$$-\nu_h + 2\nu_v = 4, \text{ and}$$

$$\nu_h = 7.$$

The stop bandwidths of the above three resonances are estimated at about 0.0001, 0.0002, and 0.0004 for a beam of the rms emittance of  $10^{-6}\pi$  m-rad,

respectively.<sup>4)</sup> The simulation has shown that there is no remarkable enhancement in the transverse emittance due to the nonlinearity even when the incoherent betatron-tune spread is over 0.5 owing to the improvement of the bunch shortening, as shown in Fig. 1.<sup>2)</sup> This means that the incoherent tune spread does not cause any problem in the beam bunching when the working point under no space-charge effect is chosen to be far from the minor-resonance lines as well as the major-resonance lines.

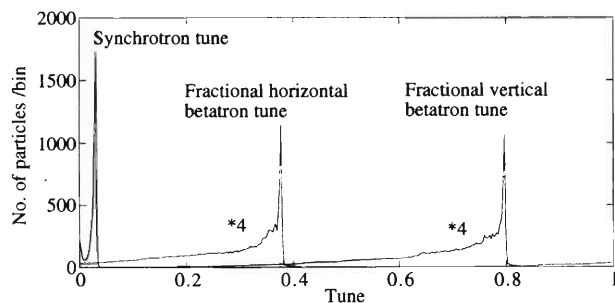


Fig. 1. Tune distribution for 5000 particles when the beam bunches in the 6-rms bunch length of 1 m. The distributions of the betatron tune are magnified vertically by four times.

The simulation has shown an effect of the dipole component of the transverse space-charge force on the bunch shortening, as shown in Fig. 2. The beam reaches a quasi-equilibrium state after 40 ms of bunching, when the dipole component is neglected. The final 6-rms bunch length is 1 m. When the dipole component is taken into account in the horizontal direction, however, the bunch length becomes 0.5 m only after 30 ms of bunching. The RF voltage of 300 kV is required for the short bunch. The rms transverse emittance does not decrease largely from  $10^{-6}\pi$  m-rad.

The bunched beam has a shape as shown in Fig. 3 at 35 ms of bunching. The shape is approximately represented by a summation of a Gaussian and a parabolic curve. The parabolic curve corresponds to the distribution of the cooled ions that hardly do synchrotron oscillation around the bunch center.

The instantaneous beam current of 60 mA, which has been simulated here, reaches the threshold current of the longitudinal microwave instability as mentioned above. Further simulations in which the resistive-wall impedance and other broad-band impedances are taken into account will predict the effect of the single-bunch instability on the bunched and space-charge

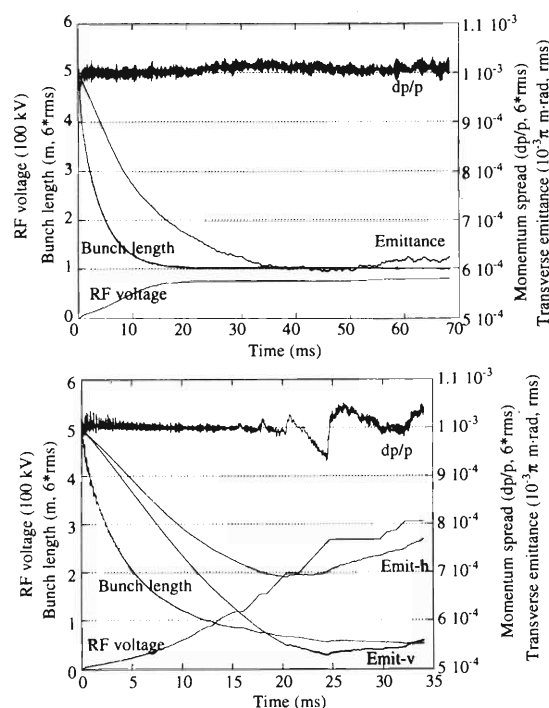


Fig. 2. Transition of the beam bunching. Upper Figure: the dipole component is not taken into account. Lower Figure: the dipole component is taken into account in the horizontal direction.

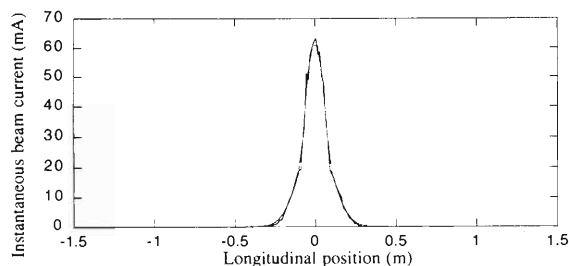


Fig. 3. Bunch shape with a summation of a Gaussian and a parabolic curve at 35 ms of bunching when the dipole component is taken into account.

dominated beams.

#### References

- 1) I. N. Meshkov: Phys. Part. Nucl. **25**, 631 (1994).
- 2) M. Takanaka and T. Katayama: Proc. PAC'97 (1998), to be published.
- 3) A. Hofmann: CERN **77-13**, 139 (1977).
- 4) L. R. Evans: CERN **84-15**, 319 (1984).

## Diffusion Beam-Beam Instability in the Presence of Beam Cooling

Y. Batygin and T. Katayama

One of the serious reasons for limited performance of a circular collider is the instability due to beam-beam interaction. Let us consider head-on collisions of strong electron beam against counteracted beam of heavy ion particles with the charge to mass ratio  $Z/A$ . Luminosity of an electron-ion collider is given by

$$L = \frac{fN_i N_e}{4\pi\sigma^2} N_{\text{bunch}}, \quad (1)$$

where  $f$  is the particle revolution frequency in a ring,  $N_i$  and  $N_e$  the numbers of ions and electrons per bunch, respectively,  $N_{\text{bunch}}$  the number of bunches per beam, and  $\sigma$  is the rms (root-mean-square) size of electron beam.

Significance of the beam-beam phenomena is characterized by the value of beam-beam parameter  $\xi$ , which has a meaning of the linear part of betatron tune shift due to beam-beam collisions:

$$\xi = \frac{r_p \beta^* \frac{Z}{A} N_e}{4\pi\gamma_i \sigma^2}, \quad (2)$$

where  $r_p = e^2/4\pi\epsilon_0 mc^2$  is the value of classical radius of proton,  $\beta^*$  the value of a beta-function of the collider, and  $\gamma_i$  the ion beam energy. In existing ion colliders the maximum value of  $\xi$  does not exceed the magnitude of  $\xi = 0.004$ .<sup>1)</sup> Limitation in  $\xi$  results in constraints of the luminosity  $L$ , which follows from Eqs. (1) and (2):

$$L < \frac{fN_i N_{\text{bunch}} \gamma_i}{\beta^* r_p} \frac{A}{Z} \xi_{\text{max}}. \quad (3)$$

Previous study<sup>2)</sup> indicated an importance of factor of the noise in beam-beam interaction. Noise diffusion instability can be easily detected via numerical calculations as well as in analytical study under a fluctuation in the opposite beam size  $\sigma_n = \sigma_o \left(1 \pm \frac{u \cdot u_n}{2}\right)$ , where  $u$  is a noise amplitude and  $u_n$  a uniform random function with unit amplitude. Beam emittance growth after  $n$  turns under noise regime is given by

$$\frac{\epsilon_n}{\epsilon_o} = \sqrt{1 + Dn}, \quad (4)$$

where the diffusion coefficient  $D$  is a function of the beam-beam parameter, noise amplitude, and ratio of ion beam size,  $a$ , to electron beam size  $2\sigma$ :

$$D = \pi^2 (\xi u)^2 \left(\frac{a}{2\sigma}\right)^4. \quad (5)$$

As it follows from Eq. (5), a noise beam-beam instability can exist under any value of the beam-beam parameter  $\xi$ . This can be one of the reasons why a

small value of  $\xi$  was achieved in existing colliders. Two conditions are essential to initiate a noisy beam-beam instability: beam-beam kick has to be a nonlinear function of coordinate and the parameter of the kick (rms beam size  $\sigma$ ) has to be subject to noise. In contrast to the stochastic particle motion due to overlapping of nonlinear beam-beam resonance islands, a noise beam-beam instability appears in much more simple conditions without excitation of resonances.

Actual value of the noise amplitude in beam size has not been measured so far. It can be estimated from indirect data. Let us assume, that the maximum number of turns in existing colliders for one-day operation is  $n_{\text{max}} = 3 \cdot 10^8$ . To prevent doubling of beam emittance, product of diffusion coefficient with the maximum number of turns has to be  $Dn_{\text{max}} < 3$ . Therefore, estimated value of diffusion coefficient is  $D = 10^{-8}$  and expected value of noise amplitude is:

$$u = \frac{1}{\xi} \sqrt{\frac{D}{\pi^2}} = 6 \cdot 10^{-3}. \quad (6)$$

Electron and stochastic cooling techniques are effective methods to decrease the phase space volume of the beam. Let us consider a numerical model, combining betatron particle motion in the presence of beam-beam collisions with particle cooling:

$$\begin{aligned} \begin{pmatrix} x_{n+1} \\ p_{n+1}^x \end{pmatrix} &= \exp\left(-\frac{1}{N_{\text{damp}}}\right) \begin{pmatrix} \cos \theta & \sin \theta \\ -\sin \theta & \cos \theta \end{pmatrix} \\ &\cdot \begin{pmatrix} x_n \\ p_n^x + \Delta p_n^x \end{pmatrix} + M_x, \\ \begin{pmatrix} y_{n+1} \\ p_{n+1}^y \end{pmatrix} &= \exp\left(-\frac{1}{N_{\text{damp}}}\right) \begin{pmatrix} \cos \theta & \sin \theta \\ -\sin \theta & \cos \theta \end{pmatrix} \\ &\cdot \begin{pmatrix} y_n \\ p_n^y + \Delta p_n^y \end{pmatrix} + M_y, \end{aligned} \quad (7)$$

where  $N_{\text{damp}}$  is the number of turns required to cool the beam,  $\theta$  a betatron angle, and  $\Delta p_n^x$  a beam-beam kick given by

$$\Delta p_n^x = -4\pi\xi \times \frac{1 - \exp(-r^2/2\sigma_n^2)}{(r^2/2\sigma_n^2)}, \quad (8)$$

analogously for  $\Delta p_n^y$ . Matrices  $M_x$ , and  $M_y$  describe the ion beam excitation due to scattering:<sup>3)</sup>

$$\begin{aligned} x &\rightarrow x + \lambda_1 \hat{r}_1, & p_x &\rightarrow p_x + \lambda_2 \hat{r}_2, \\ y &\rightarrow y + \lambda_3 \hat{r}_3, & p_y &\rightarrow p_y + \lambda_4 \hat{r}_4, \end{aligned} \quad (9)$$

where  $\lambda_i$  ( $i = 1, \dots, 4$ ) are parameters defining the final equilibrium phase space volume of the beam,  $\hat{r}_i$  the Gaussian random numbers with average value  $\langle \hat{r} \rangle = 0$  and rms value  $\langle \hat{r}^2 \rangle = 1$ .

Figure 1 presents results of the numerical simulation of combined effect of beam-beam interaction and beam cooling. As can be seen, without cooling, the beam emittance monotonously increases due to beam-beam collisions, while with a cooling, an equilibrium in the beam size is achieved if cooling rate is equal to the increment of beam-beam instability.

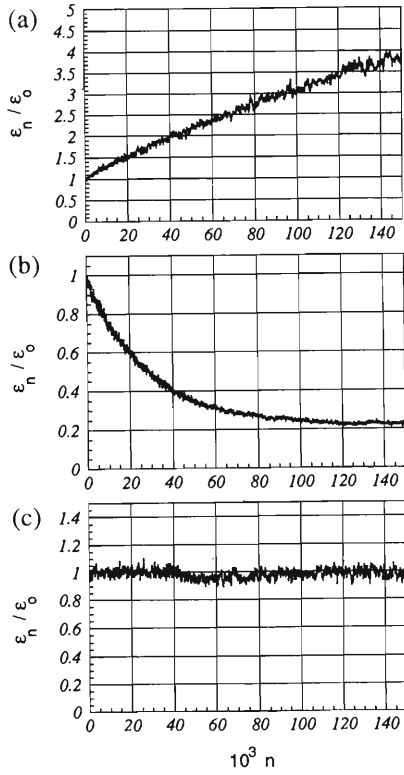


Fig. 1. Beam emittance growth under (a) noise beam-beam instability, (b) beam cooling without beam-beam collisions, (c) combined effect of beam cooling and beam-beam interaction: equilibrium.

Let us define the effect of cooling on the beam-beam instability. Decrease in the beam emittance due to cooling at the initial stage can be described by

$$\frac{\varepsilon_n}{\varepsilon_0} = \exp\left(-\frac{n}{N_{\text{damp}}}\right) \approx 1 - \frac{n}{N_{\text{damp}}}. \quad (10)$$

On the other hand, beam emittance growth due to noisy beam-beam instability is described by

$$\frac{\varepsilon_n}{\varepsilon_0} \approx 1 + \frac{D_n}{2}. \quad (11)$$

Therefore, the required cooling rate to prevent beam-beam instability, expressed in cooling number of turns, is:

$$N_{\text{damp}} = \frac{2}{D}. \quad (12)$$

Cooling rate is a function of collider regime parameters. Taking the expected number of  $N_{\text{damp}} = 2 \cdot 10^7$ , which corresponds to cooling time of 20 sec in the Double Storage Ring (DSR), and the noise amplitude  $u = 6 \cdot 10^{-3}$ , the maximum value of beam-beam tune shift achieved is

$$\xi_{\text{max}} = \frac{1}{\pi u} \sqrt{\frac{2}{N_{\text{damp}}}} = 0.017. \quad (13)$$

Luminosity is proportional to the maximum value of beam-beam parameter (see Eq. 3). Therefore, utilizing the beam cooling can result in increasing of luminosity at least by a factor of 4.

#### References

- 1) F. Willeke: Particle Accelerators **59**, 27 (1995).
- 2) Y. Batygin and T. Katayama: Noise instability in non-linear beam-beam interaction, RIKEN-AF-AC-3, Mar. (1997), to be published in NIM - A.
- 3) K. Hirata, H. Moshammer, and F. Ruggiero: Particle Accelerators **40**, 205 (1993).

## Stationary Particle Distribution of Intense Bunched Beam in RF Accelerating Field

Y. Batygin

Emittance conservation of a high brightness particle beam is an issue for existing and future high intensity accelerator projects. If the beam is matched with external focusing field, its distribution function as well as beam emittance are conserved. Finding matched conditions for the beam requires solutions of the self-consistent problem for beam distribution function in phase space. Self consistent particle distribution creates a potential in which particle motion maintains this distribution.

The problem of stationary self-consistent particle distribution in RF field was considered in several books and papers. In Ref. 1 solution of one-dimensional problem for longitudinal phase space was found. Space charge density of cylindrical bunch was found to be constant in every cross section of the bunch, but dependent on longitudinal coordinate. In Ref. 2 spatial particle distribution in 3-dimensional configuration space was calculated numerically. In this paper an analytical approximate solution for 3-D self-consistent particle equilibrium is found.

Consider an intense bunched beam of particles with charge  $q$  and mass  $m$ , propagating in an uniform focusing channel with an applied accelerating RF field. Single-particle Hamiltonian of particle motion is given by:<sup>1)</sup>

$$H = \frac{p_x^2 + p_y^2}{2m\gamma} + \frac{p_z^2}{2m\gamma^3} + U_{\text{ext}} + q\frac{U_b}{\gamma^2}, \quad (1)$$

$$U_{\text{ext}} = \frac{qv_s E}{\omega} \left[ I_0 \left( \frac{\omega r}{\gamma v_s} \right) \sin \left( \varphi_s - \frac{\omega}{v_s} z \right) - \sin \varphi_s + \frac{\omega}{v_s} z \cos \varphi_s \right] + \frac{m\gamma}{2} \Omega_r^2 r^2, \quad (2)$$

where  $U_{\text{ext}}$  is a potential of external field,  $U_b$  is a potential of space charge field of the beam,  $\gamma$  is a particle energy,  $E$  is an amplitude of accelerating field,  $v_s$  is a velocity of synchronous particle,  $\varphi_s$  is a synchronous phase,  $\omega$  is an RF frequency,  $\Omega_r$  is a transverse frequency of particle oscillation,  $r$  is a particle radius, and  $z$  is a longitudinal deviation from synchronous particle. General approach to find a self-consistent beam distribution function is to represent it as a function of Hamiltonian  $f = f(H)$ . Convenient way is to use an exponential function  $f = f_0 \exp(-H/H_0)$ . Unknown constant  $H_0$  can be expressed as a function of beam parameters:

$$16 \cdot H_0 = \frac{mc^2}{\gamma} \frac{\varepsilon_t^2}{\langle x_{\text{rms}}^2 \rangle} = \frac{mc^2}{\gamma} \frac{\varepsilon_l^2}{\langle y_{\text{rms}}^2 \rangle} = \frac{mc^2}{\gamma^3} \frac{\varepsilon_l^2}{\langle z_{\text{rms}}^2 \rangle}, \quad (3)$$

where  $\varepsilon_t$  and  $\varepsilon_l$  are the rms (root-mean-square) transverse and longitudinal beam emittances, respectively,

$\langle x_{\text{rms}}^2 \rangle = \langle y_{\text{rms}}^2 \rangle = R/2$  and  $\langle z_{\text{rms}}^2 \rangle$  are the rms beam sizes, and  $R$  is the beam radius. Equation (3) expresses the equipartitioning condition<sup>3,4)</sup> of stationary distribution function.

To find a self-consistent particle distribution, one has to solve a nonlinear Poisson's equation for unknown space charge potential of the beam. Introducing dimensionless variables:

$$V_{\text{ext}} = \frac{qU_{\text{ext}}}{H_0}, \quad V_b = \frac{qU_b}{H_0}, \quad \xi = \frac{r}{a}, \quad \eta = \frac{z}{a}, \quad (4)$$

where  $a$  is a channel radius, Poisson's equation in cylindrical polar coordinates can be expressed as

$$\frac{1}{\xi} \frac{\partial V_b}{\partial \xi} + \frac{\partial^2 V_b}{\partial \xi^2} + \frac{\partial^2 V_b}{\partial \eta^2 \gamma^2} = -\frac{8kb}{\delta\varphi} \left( \gamma \frac{a}{R} \right)^2 \exp(-(V_{\text{ext}} + V_b \gamma^{-2}). \quad (5)$$

Here,  $\delta\varphi \equiv \Delta\varphi/(2\pi)$  is a reduced phase bunch length,  $b \equiv 2IR^2/(\beta\gamma I_c \varepsilon_t^2)$  is a dimensionless value of beam brightness,  $I$  is a beam current, and  $I_c \equiv 4\pi\varepsilon_0 mc^3/q$  is a characteristic value of beam current. To solve the nonlinear equation (5), let us follow the method suggested in Ref. 5.

Represent unknown space charge potential of the beam by Fourier-Bessel series:

$$V_b = V_0 + \sum_{n=0}^{\infty} \sum_{m=1}^{\infty} J_0(\nu_{om}\xi) [A_{nm} \cos(k_z n\eta) + B_{nm} \sin(k_z n\eta)], \quad (6)$$

where  $J_0(\zeta)$  is a Bessel function,  $\nu_{om}$  is a  $m$ -th root of the equation  $J_0(\zeta) = 0$ , and  $k_z \equiv \omega a/v_s$  is a wave number. Expansion (6) obeys Dirichlet boundary condition  $V_b(a) = V_0$  at the surface of the channel. Constant  $V_0$  is defined in such a way that the total potential of the structure vanishes at the bunch center:

$$V_{\text{ext}}(0,0) + V_b(0,0)\gamma^{-2} = 0.$$

To find an approximate solution of Poisson's equation, let us take only the first term in the near-center expansion of exponential function as  $\exp(-V_{\text{ext}} - V_b \gamma^{-2}) \approx 1 - V_{\text{ext}} - V_b \gamma^{-2}$ . Poisson's equation then becomes:

$$\sum_{n=0}^{\infty} \sum_{m=1}^{\infty} \left[ 1 + \frac{\nu_{om}^2 + (k_z n)^2 \gamma^{-2}}{8kb} (\delta\varphi) \left( \frac{R}{a} \right)^2 \right] J_0(\nu_{om}\xi) [A_{nm} \cos(k_z n\eta) + B_{nm} \sin(k_z n\eta)] = (1 - V_{\text{ext}})\gamma^2 - V_0. \quad (7)$$

Space charge dominated beam transport is achieved, if  $b \gg 1$ . It gives a possibility to simplify the Poisson's

equation (7). Expression in square brackets in Eq. (7) can be taken as a constant close to unity:

$$1 + \frac{\nu_{om}^2 + (k_z n)^2 \gamma^{-2}}{8kb} (\delta \varphi) \left( \frac{R}{a} \right)^2 \approx 1 + \delta, \quad \delta \ll 1. \quad (8)$$

With this approximation, self-consistent space charge dominated beam potential is:

$$V_b = -\frac{\gamma^2}{1 + \delta} V_{ext}. \quad (9)$$

Second approximation to the self-consistent potential is given by holding one more term in the expansion of exponential function as  $\exp(-V_{ext} - V_b \gamma^{-2}) \approx 1 - V_{ext} - V_b \gamma^{-2} + 0.5(V_{ext} + V_b \gamma^{-2})^2$ , so that we have

$$V_b = \gamma^2 [1 + \delta - V_{ext} - \sqrt{(1 + \delta - V_{ext})^2 - V_{ext}(V_{ext} - 2)}]. \quad (10)$$

With increasing of beam brightness ( $\delta \rightarrow 0$ ), solution of Eq. (10) becomes close to that of Eq. (9).

Taking the first approximation (9), the Hamiltonian corresponding to the self-consistent bunch distribution is as follows:

$$H = \frac{p_x^2 + p_y^2}{2m\gamma} + \frac{p_z^2}{2m\gamma^3} + \left( \frac{\delta}{1 + \delta} \right) U_{ext}. \quad (11)$$

Equation (11) indicates that in the presence of intense, bright bunched beam ( $\delta \ll 1$ ) the stationary

longitudinal phase space of the beam becomes narrow in momentum spread, remaining, in the first approximation, the same in coordinate. This is in a qualitative agreement with the study of Ref. 1.

Self consistent space charge distribution of matched beam in the channel is given from Poisson's equation by

$$\rho_b = -\varepsilon_o \Delta U_b. \quad (12)$$

Substitution of Eq. (10) into Eq. (12) gives the stationary particle density distribution inside the bunch:

$$\rho(r, z) = \rho_o \left\{ 1 - \frac{\delta}{\sqrt{(1 + \delta)^2 - 2\delta V_{ext}}} - \frac{\delta^2}{32\gamma^2 \langle x_{rms}^2 \rangle} \left( \frac{c}{a\Omega_r} \right)^2 \left( \frac{\partial V_{ext}}{\partial \xi} \right)^2 + \left( \frac{\partial V_{ext}}{\gamma \partial \eta} \right)^2 \right\} \quad (13)$$

#### References

- 1) I. M. Kapchinsky: Theory of Resonance Linear Accelerators (Harwood, 1985).
- 2) M. Reiser: Theory and Design of Charged Particle Beams (Wiley, New York, 1994).
- 3) R. Jameson: IEEE Trans. Nucl. Sci. NS-28, 2408 (1981).
- 4) I. Hofmann: IEEE Trans. Nucl. Sci. NS-28, 2399 (1981).
- 5) Y. Batygin: to be published in Phys. Rev. E.

## High Brightness Beam Transport in a Quadrupole Focusing Channel with Octupole Field Component

Y. Batygin

Prevention of emittance growth and halo formation in a high-intensity beams are a key problem for the next generation of particle accelerators. Importance of the problem is connected with the efforts of development of the particle accelerators for heavy ion fusion, spallation neutron sources, and radioactive waste transmutation. Beam with a nonuniform profile is mismatched within a linear focusing channel. It results in a beam emittance growth and halo formation. Matching of a realistic nonuniform beam with a focusing channel can be obtained, if the focusing field is not a linear function of radius any more.<sup>1)</sup> Ideal way to create a required nonlinear potential distribution is a plasma lens with specific distribution of opposite charged particles. Another possibility is connected with utilization of an alternating-gradient focusing channel with higher order multipole components.<sup>2)</sup> In this paper the effect of octupole field component on the beam matching in a quadrupole focusing channel is examined.

Consider an uniform four-vanes quadrupole focusing structure with octupole field component. Electrostatic potential of such structure is given by

$$U(r, \varphi, t) = \left( \frac{G_2}{2} r^2 \cos 2\varphi + \frac{G_4}{4} r^4 \cos 4\varphi \right) \sin \omega_o t, \quad (1)$$

where  $G_2$  is a quadrupole field gradient,  $G_4$  is an octupole field gradient, and  $\omega_o$  is an operating frequency. Oscillating field (1) creates an effective scalar potential

$$U_{\text{ext}}(r, \varphi) = \frac{qE^2(r, \varphi)}{4m\omega_o^2} = \frac{mc^2}{q} \frac{\mu_o^2}{\lambda^2} \left[ \frac{1}{2} r^2 + \eta r^4 \cos 2\varphi + \frac{\eta^2}{2} r^6 \right], \quad (2)$$

where  $\mu_o \equiv qG_2\lambda^2/(\sqrt{8}\pi mc^2)$  is a smoothed transverse oscillation frequency,  $\lambda = 2\pi c/\omega_o$  is a wavelength, and  $\eta = G_4/G_2$  is a ratio of the two field components. Fig. 1 illustrates equipotential lines of the effective potential (2). As seen, for a small radius ( $r$ ) the equipotential lines are close to circles because the quadratic term  $\sim r^2$  is dominant in Eq. (2). With a larger  $r$ , on the other hand, they are close to a distorted ellipse.

In Ref. 3 it was found that the self-consistent stationary particle distribution of a matched high-brightness beam has such a shape that the space charge beam potential  $U_b$  is opposite to an arbitrary external focusing potential  $U_{\text{ext}}$ :

$$U_b = -\gamma^2 \frac{kb}{1+kb} U_{\text{ext}}, \quad (3)$$

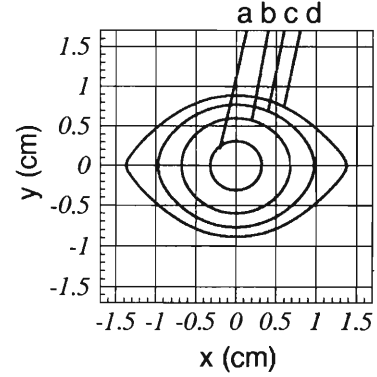


Fig. 1. Lines of equal values of the potential function  $C = \frac{1}{2}r^2 + \eta r^4 \cos 2\varphi + \frac{\eta^2}{2}r^6$  for  $\eta = -0.148$ : (a)  $C = 0.05$ , (b)  $C = 0.2$ , (c)  $C = 0.35$ , and (d)  $C = 0.49$ .

where  $b \equiv 2IR^2/(\beta\gamma I_c \varepsilon^2)$  is a dimensionless value of beam brightness,  $I$  is a beam current,  $I_c \equiv 4\pi\varepsilon_o mc^3/q$  is a characteristic value of beam current,  $\beta$  and  $\gamma$  are particle velocity and energy, respectively,  $R$  is a beam radius,  $\varepsilon$  is a normalized beam emittance, and  $k$  is a beam profile parameter ( $k = 1$  for uniform beam and  $k = 2$  for Gaussian beam). Space charge density of the matched high-brightness beam is determined by Poisson's equation:

$$\rho_b(r, \varphi) = -\varepsilon_o \Delta U_b = \rho_o [1 + 6\eta r^2 \cos 2\varphi + 9\eta^2 r^4]. \quad (4)$$

Beam with distribution of (4) is maintained in the channel with effective potential (2). Due to the term  $\cos 2\varphi$ , space charge density of (4) is a decreasing function with  $x$ -coordinate, but increasing function with  $y$ -coordinate, being  $r^2 = x^2 + y^2$  (see Fig. 2a).

Realistic beam distribution has monotonically decreasing density function with radius. Good approximation to realistic beams is a distribution of the form:

$$\rho_b = \rho_o \left[ 1 - \left( \frac{r}{R} \right)^2 \right]^2, \quad (5)$$

which is close to the truncated Gaussian distribution (see Fig. 2b). Therefore, realistic beam with distribution of (5) is expected to be matched in  $x$ -coordinate, but mismatched in  $y$ -coordinate.

In Fig. 3 some results of particle-in-cell simulations for the beam with distribution (5) in a quadrupole channel with octupole component are presented. Initial beam distribution given by Eq. (5) was truncated along equipotential lines to make beam close to the matched beam given by Eq. (4). As seen, after 100 cm

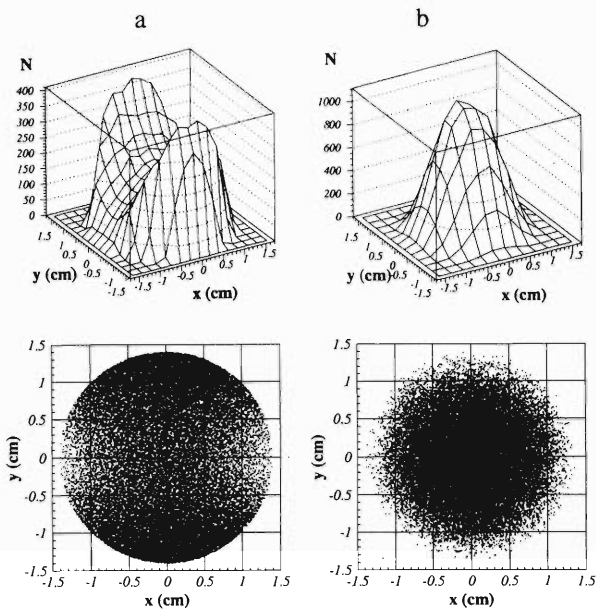


Fig. 2. a: Matched beam with the density profile  $\rho_b = \rho_o (1 + 6\eta r^2 \cos 2\varphi + 9\eta^2 r^4)$  in quadrupole-octupole channel with parameter  $\eta = -0.1$  and b: beam with the particle distribution  $\rho_b = \rho_o \left[1 - \left(\frac{r}{R}\right)^2\right]^2$ .

of beam transport, which corresponds to one betatron particle oscillation, emittance of the beam is slightly distorted at  $x$ - $p_x$  phase plane, but seriously distorted at  $y$ - $p_y$  phase plane. Therefore, utilizing octupole component in a quadrupole channel is not sufficient to provide beam matching. Better results were observed in computer simulation of the beam in a quadrupole structure with duo-decapole field component.<sup>3)</sup> In that

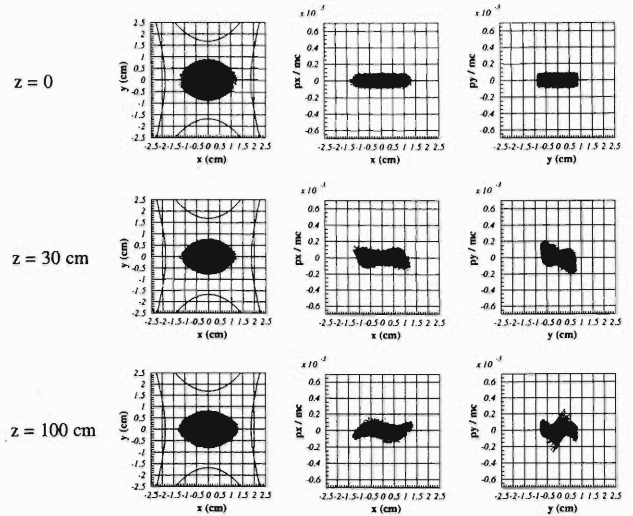


Fig. 3. Dynamics of the 150 keV, 100 mA and 0.06  $\pi$  cm mrad proton beam with distribution of Eq. (5) in a four vane quadrupole structure with the field gradient  $G_2 = 50$  kV/cm<sup>2</sup> and the octupole component  $G_4 = -3.5$  kV/cm<sup>4</sup>.

case the effective potential and matched beam profile are symmetric functions with  $y$  as well as  $x$  coordinates, and realistic beam is much better matched with quadrupole focusing structure.

#### References

- 1) Y. Batygin: Phys. Rev. E **53**, 5358 (1996).
- 2) Y. Batygin: Phys. Rev. E **54**, 5673 (1996).
- 3) Y. Batygin: Proc. 1997 Particle Accelerator Conference, Vancouver, Canada (to be published).

## Design of 300 MeV Electron Linac at MUSES

M. Wakasugi, Y. Kamino,\* and T. Katayama

We have designed an electron linac to be used as an injector of the booster synchrotron (BSR) at MUSES project. Electron beam accelerated up to a required energy by the BSR is injected into the double storage rings (DSR), and it is used for electron-RI collision<sup>1)</sup> or for high brilliant X ray production.<sup>2)</sup> Depending on the experiment, two kinds of specifications are required for the electron beam at the linac. When we make electron-RI collision experiments, electrons should be in a specified RF bucket in the DSR because of synchronous collision. This means that the BSR has to be operated with the single-bunch operation mode. So, the electron beam after the linac has to have a short

pulse length and high peak current. On the other hand, every RF bucket should be filled with electrons at the DSR, for X ray production, and the BSR be operated with the multi-bunch operation mode. In this case the electron beam from the linac has to have a long pulse length. The electron linac, therefore, is required to have the specifications summarized in Table 1.

From the requirement of both experiments, the minimum electron beam energy is decided to be 300 MeV. The linac consists of three parts: an electron gun, an injection part, and a regular part. They are shown in Fig. 1.

The electron gun includes a cathode-grid assembly

Table 1. Specifications of electron beam after the linac.

		Long pulse mode	Short pulse mode
RF frequency	(MHz)	2856	
Energy	(MeV)	>300	
Repetition rate	(Hz)	50	
Energy spread	(%)	±0.25	
Normalized emittance	( $\pi$ mm mrad)	100	
Pulse width	(nsec)	5000	1
Peak current	(A)	0.1	1

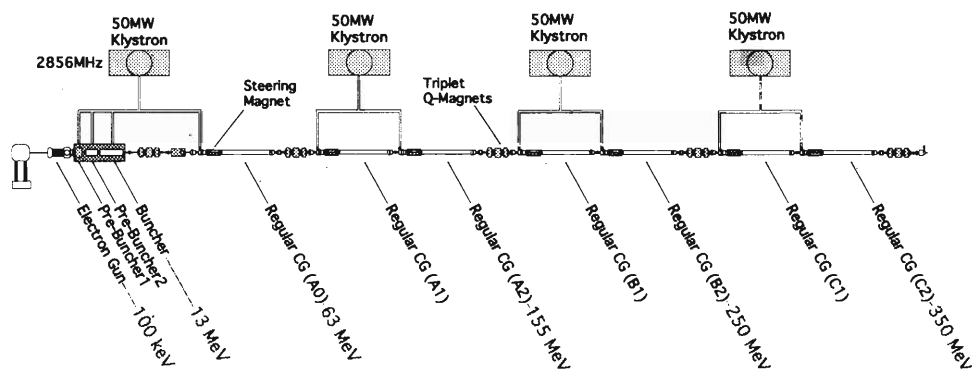


Fig. 1. A conceptual 300 MeV electron linac system at MUSES.

which has a cathode area of 0.5 cm<sup>2</sup> and allows the maximum current of 1.6 A. These parameters have been decided from the beam quality point of view. The electron beam is extracted with an acceleration voltage of 100 kV from the gun. Pulsing for both modes are made by pulsing grid voltage. The simulated beam trajectory in the gun, obtained using computer code EGUN2, is shown in Fig. 2.

The injection part consists of a pre-buncher 1, pre-buncher 2, and buncher. The pre-buncher 1 is a

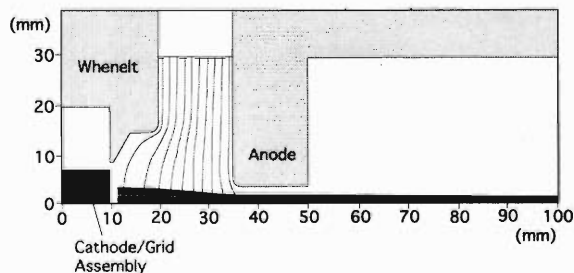


Fig. 2. Ray trace of the electron beam at electron gun.

\* Mitsubishi Heavy Industries, Ltd.

standing-wave type single cavity, and its gap voltage is 10 kV. The required RF power is estimated to be 1 kW. The pre-buncher 2 is a traveling-wave type and consisting of the four cavities made from disks and spacers. The phase velocity ( $v_{ph}/c$ ) is 0.77 which is matched with the beam velocity. Acceleration gain is 2.0 MeV/m and RF power of 170 kW is required. The buncher is a constant gradient (CG) tube including 30 cavities. Acceleration gain is 11 MeV/m and input RF power is 15 MW. All bunching devices are in a solenoid coil for focusing in low energy region. Finally, expected electron beam energy at the end of the injection part is 13 MeV, and the phase spread and the energy spread are expected to be within 4 deg and 200 keV, respectively, as shown in Fig. 3.

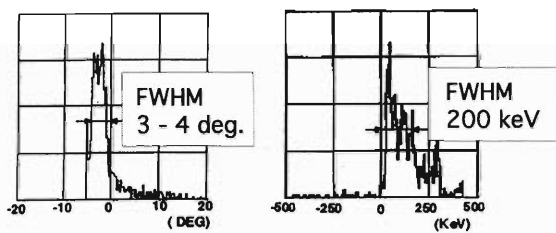


Fig. 3. Phase and energy distributions at exit of injection part for short pulse mode.

The regular part consists of seven CG tubes. We provide three groups of CG tubes: three tubes for group A, two tubes for group B, and two tubes for group C. The CG tubes in groups A, B, and C have attenuation constants of 0.5, 0.6, and 0.7 [Neper], respectively, and different aperture sizes to avoid the cumulative beam break up (C-BBU). One CG tube has 80 cavities, with total length of 3 m and acceleration gain of about 16 MeV/m taking a beam loading effect into account. Five triplet-quadrupole magnets work as a focusing element during the beam transport, and the beam size at the exit of the linac is expected to be about 1 mm in diameter.

All cavities and tubes are driven by four klystrons having each peak power of more than 50 MW and fre-

quency of 2856 MHz as shown in Fig. 1. RF power of the first klystron is divided into bunching devices and the A0 regular tube. Each of the other klystrons supplies two CG tubes the RF power.

We have estimated energy resolution of the beam by taking the following points into account: (1) fluctuation of RF voltage due to instability of klystron, (2) fluctuation of phase due to instability of klystron, (3) beam distribution in E- $\theta$  phase space, (4) deviation of acceleration phase due to error of phasing process, (5) reactive phase distortion, and (6) initial beam loading effect. For (1) and (2), we have estimated to be less than  $\pm 0.09\%$ , and phase spread for (3) is less than  $\pm 2$  deg as shown in Fig. 3. The phase shift for (4) is expected to be less than  $\pm 1$  deg. We further expected that the initial beam loading effect can be suppressed with the modulation of RF power before beam loading. If we supply the RF voltage as shown in Fig. 4, every bunches feel the same field in the CG tube. The field is the same with the equilibrium state after beam loading for the case of normal RF power filling method. Finally, we were able to estimate the energy resolution to be about  $\pm 0.2\%$  which is better than the requirement.

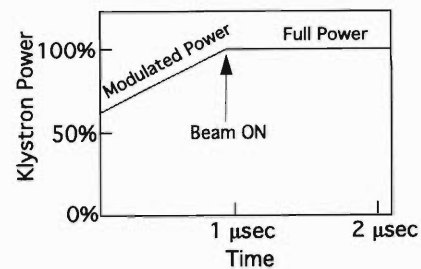


Fig. 4. RF power modulation sequence at beam loading.

#### References

- 1) T. Katayama et al.: Proc. 5th Eur. Part. Accel. Conf. p. 563 (1996).
- 2) M. Wakasugi et al.: Proc. 5th Eur. Part. Accel. Conf. p. 611 (1996).

## Design of Apple-II Type Undulator for MUSES

M. Wakasugi and T. Katayama

We have designed an Apple-II type undulator, which will be installed into the double storage ring (DSR) in MUSES project. According to requirements from physics experiments, we have to continuously change the X ray energy from 30 to 800 eV and its polarization as well. That is why we are to chose Apple-II type.

Apple-II type undulator has two pairs of magnetic arrays as shown in Fig. 1. X ray energy can be changed continuously by driving vertically the gap-width as shown by white arrow in Fig. 1. The polarization can be changed by shifting the phase (D) between pairs of the magnetic arrays shown by black arrows in Fig. 1. In one period, total 16 permanent-magnet chips are used, and the length of one period is 30 mm. The minimum gap-width has been decided to be 20 mm by considering size of the vacuum tube which is put inbetween magnetic arrays. The gap driving range is 6.7 mm with a step of less than 5  $\mu\text{m}$ . The minimum gap-driving step corresponds to the X ray energy-scanning step of 0.1 eV at X ray energy of 100 eV.

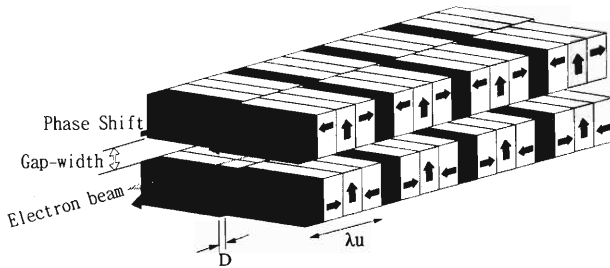


Fig. 1. Magnetic structure of Apple-II type undulator.

Phase-driving changes mainly the X ray polarization from linear polarization to circular polarization. It also changes slightly the X ray energy, because the bending factors  $K_x$  and  $K_y$  in horizontal and vertical directions, respectively, are change by the phase driving. Therefore, if we want to scan the energy without changing the polarization, we have to drive both the gap and phase simultaneously. Relations between the gap-width, the phase-shift and K values are summarized in Table 1.

The phase shifts of 0 mm and 15 mm give linearly polarized X ray in the horizontal and vertical directions, respectively. The shift of about 11.25 mm, which corresponds to the 3/8 length of one period, gives the circularly polarized X ray. For these cases, magnetic field strengths on beam axis are shown in Fig. 2

We have calculated the photon spectrum with the undulator described above. Parameters of electron beam used here are shown in our previous paper.<sup>1)</sup> Figure 3 shows typical examples for the cases of lin-

Table 1.  $K_x$  and  $K_y$  values vs. gap-width and phase-shift.

Phase (mm)	Gap width (mm)					
	20		23		26.7	
	$K_x$	$K_y$	$K_x$	$K_y$	$K_x$	$K_y$
0	0	0.712	0	0.521	0	0.356
3.75	0.143	0.658	0.098	0.482	0.062	0.328
7.5	0.261	0.504	0.179	0.370	0.115	0.252
11.25	0.342	0.272	0.235	0.199	0.151	0.137
15	0.370	0	0.255	0	0.163	0

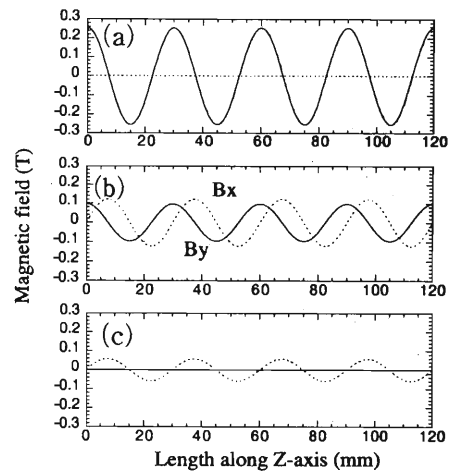


Fig. 2. Magnetic field strength at the phase shifts of 0 mm (a), 11.25 mm (b), and 15 mm (c). It is assumed that the magnetic field is 1.3 T at the pole tip.

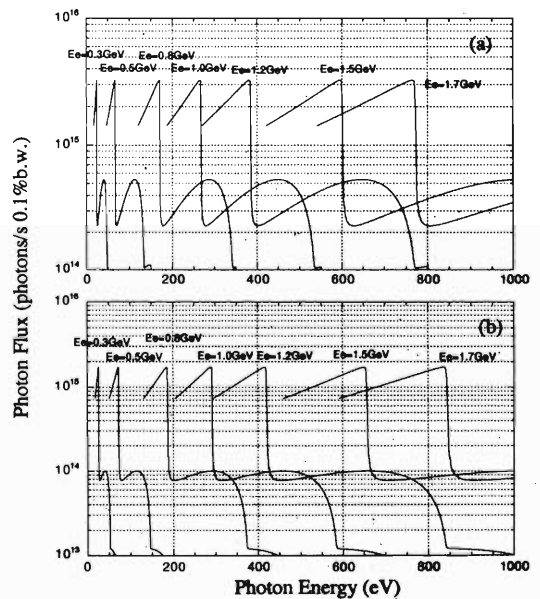


Fig. 3. Calculated X-ray photon flux for the cases of linear polarization (a) and circular polarization (b).

ear polarization and circular polarization. To cover required X ray energy range, we have to change not only the gap-width but also the electron beam-energy. Electron beam energy will be changed from 0.3 GeV to 1.7 GeV. Intensity of the X ray is expected to be more than  $10^{15}$  photons/s/0.1%b.w. in both polarizations, which exceeds requirement to the good.

We have made mechanical design of the undulator, and a realistic drawing is shown in Fig. 4. We provide a 6.7 m space to install the undulator in the DSR. Actually, it is not so easy to make 6-m long undulator because it is too long to keep high precision for the

gap-width and phase-shift drivings. So, we will separate it into two units. Figure 4 shows one unit of the undulator. Each unit contains: 80 periods of magnetic array, a correction magnet, gate valves, servo motor for both gap-width and phase-shift drivings, vacuum tube and some monitors, so on. Two units are connected in tandem and are put at the undulator section of the DSR. The size of the unit is 3.1 m long, 2.8 m wide and 2.4 m long, and the weight is expected to be 7.5 t per unit. Accuracy of the gap-width driving can be achieved better than  $5 \mu\text{m}$  using linear guides and position sensors. That of phase driving is expected to be

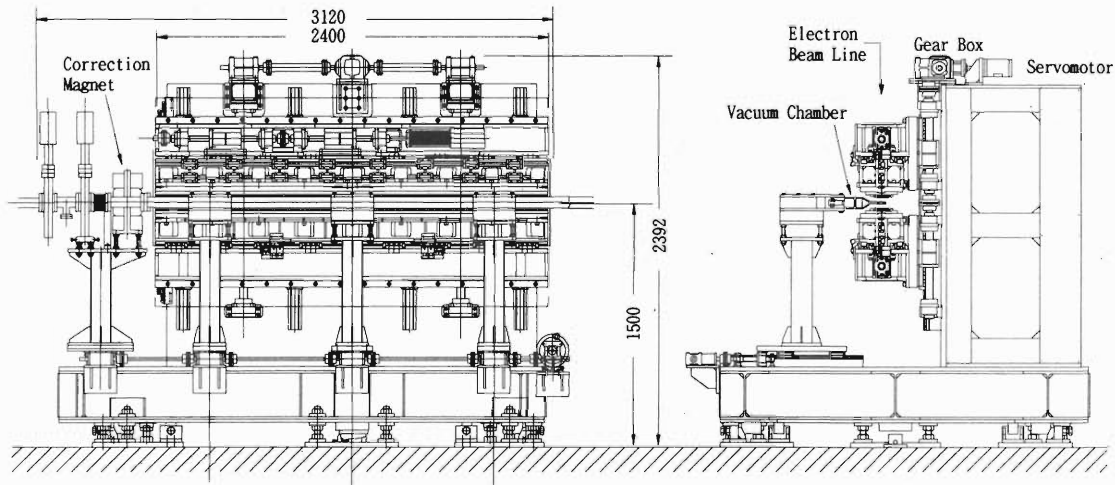


Fig. 4. Mechanical construction of one unit of the undulator, designed here.

$25 \mu\text{m}$ . Magnetic force which acts on a magnetic array is estimated to be 1.07 t in horizontal direction, 0.17 t in vertical direction, and 0.78 t in direction of beam.

Vacuum tube has three rooms as shown in Fig. 5. One is for the low emittance electron beam and it is put inbetween magnetic arrays when we use the DSR as a synchrotron radiation light source. The second room is for the ion beam or for the large emittance electron beam. When this room is used, the gap-width of the undulator is expanded to 300 mm so that the magnetic field dose not affect the beams. The third room is for NEG pump. When we want to use ion beams or large emittance electron beams, the chamber will be moved horizontally without breaking vacuum.

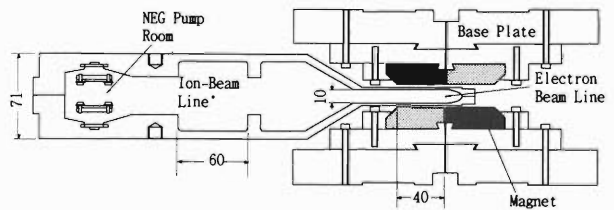


Fig. 5. Vacuum tube put inbetween magnetic arrays.

#### References

- 1) M. Wakasugi et al.: Proc. Part. Accel. Conf. (1997).

## Safety Design of RIKEN RI Beam Factory

N. Fukunishi, S. Ito, Y. Uwamino, and T. Kurosawa

We estimate here the shielding thickness required for the RIKEN RI Beam Factory (RIBF). The RIBF plans to provide high-intensity heavy-ion beams for fundamental research. Hence, we need a precise estimation of shielding thickness to assure radiation safety. We employ here two different methods in estimating the shielding thickness. For a 400 MeV/nucleon heavy-ion beam, we use the experimental data of double differential neutron yields with thick targets<sup>1)</sup> as source terms of shielding calculation. Deep penetration of neutrons into the absorber is calculated by using the ANISN code which is widely used for the calculation of neutron transport. The cross section data used here is based on the HILO86R data sheet. On the other hand, we do not have experimental data useful for the radiation protection estimation against a 1.5 GeV/nucleon heavy-ion beam. Hence, we employed the Moyer model which is widely used for the radiation shielding computation against high-energy proton accelerators. In our case, fast neutrons mainly contribute to the dose equivalent, and the neutron production strongly depends on the energy and mass number of accelerated ions. We assumed here that the neutron production is proportional to the square of the beam energy below 800 MeV/nucleon, and is proportional to the beam energy above 800 MeV/nucleon. We also assumed that the neutron production is proportional to the mass number of the ion. For the details of calculations, see Ref. 2.

We summarize in Table 1 the shielding thickness required for a <sup>40</sup>Ca beam. The shielding material chosen here is ordinary concrete. We may have to use other shielding material, for example iron absorber, in case that the shielding thickness given in Table 1 exceeds the distance from the source. As shown in Table 1,

Table 1. Shielding thickness required for the RIBF.

Accelerator	Energy (MeV/u)	Beam Loss <sup>3)</sup> (pps)	Place	Direction	Shielding thickness (m) required to satisfy the condition that the dose equivalent < D (μSv/hour) at the distance L (m) from the source					
					D=6	D=20	D=6	D=20		
					L=10	L=10	L=20	L=20		
SRC	400	6*10 <sup>10</sup>	extraction	forward	9.54	8.84	8.73	8.03		
				lateral	4.43	3.79	3.69	3.05		
		6*10 <sup>12</sup>	dump	forward	12.22	11.52	11.41	10.71		
				lateral	6.89	6.24	6.15	5.51		
ACR	400	1.62*10 <sup>11</sup>	injection	forward	10.92	10.22	10.12	9.41		
				lateral	5.70	5.06	4.96	4.32		
		1.8*10 <sup>10</sup>	ring	lateral	3.76	3.10	3.38	2.74		
				6*10 <sup>9</sup>	extraction	forward	9.00	8.30	8.20	7.49
		lateral	3.94			3.30	3.20	2.56		
		BSR	400	1.74*10 <sup>9</sup>	injection	forward	8.28	7.58	7.47	6.77
						lateral	3.28	2.64	2.54	1.90
				8.7*10 <sup>9</sup>	ring	lateral	4.05	3.39	3.67	3.02
						8.7*10 <sup>9</sup>	extraction	forward	8.50	7.76
				lateral	6.11			5.37	5.26	4.53
				DSR	1500	3*10 <sup>6</sup>	injection	forward	3.64	2.91
		lateral	1.26					0.52	0.41	0.0
3*10 <sup>8</sup>	ring	lateral	2.05			1.46	1.70	1.15		

we need shielding thickness more than 10 meters for a couple of high radiation areas in the RI beam factory.

### References

- 1) T. Kurosawa: Master Thesis (Tohoku University, 1997) and private communication.
- 2) Details of calculation are in "MUSES Conceptual Design Report", RIKEN-Cyclotron (1997).
- 3) Present values for the beam loss are suggested by the RIKEN accelerator group who design these accelerators for the RIBF project.

# Spin Depolarization Due to Beam-Beam Instability

Y. Batygin and T. Katayama

In our previous study<sup>1)</sup> we found the following matrix of spin advance in a collider ring with one beam-

beam interaction point and two Siberian Snakes installed:

$$\begin{pmatrix} S_x \\ S_y \\ S_z \end{pmatrix} = \begin{pmatrix} (-1)^{n+1} \left\{ 1 - \frac{\varphi^2}{2} \left[ \sum_{i=0}^n \cos(i\theta + \Psi) \right]^2 \right\} & \frac{\varphi^2}{4} \left[ \sum_{i=0}^n (-1)^{i+n} \sin 2(i\theta + \Psi) + \dots \right] & (-1)^{n+1} \varphi \sum_{i=0}^n \cos(i\theta + \Psi) \\ \frac{\varphi^2}{4} \left[ \sum_{i=0}^n (-1)^{i+1} \sin 2(i\theta + \Psi) + \dots \right] & 1 - \frac{\varphi^2}{2} \left\{ \sum_{i=0}^n (-1)^i \sin(i\theta + \Psi) \right\}^2 & \varphi \sum_{i=0}^n (-1)^i \sin(i\theta + \Psi) \\ (-1)^n \varphi \sum_{i=0}^n \cos(i\theta + \Psi) & \varphi \sum_{i=0}^n (-1)^{i+n} \sin(i\theta + \Psi) & (-1)^{n+1} \left[ 1 - \frac{n+1}{2} \varphi^2 + \dots \right] \end{pmatrix} \begin{pmatrix} S_{x,0} \\ S_{y,0} \\ S_{z,0} \end{pmatrix}, \quad (1)$$

where  $n$  is a turn number,  $\Psi$  is an initial phase of betatron particle oscillations,  $\theta$  is a betatron angle,  $\varphi$  is a small parameter as

$$\varphi = \frac{I r G}{I_c \sigma^2} \ll 2\pi, \quad (2)$$

$I$  is a beam current,  $I_c = 4\pi\epsilon_0 m_0 c^3 / q = (A/Z) \cdot 3.13 \cdot 10^7$  Amp is a characteristic value of the beam current,  $l$  is a bunch length  $r$  is a radius of particle trajectory,  $G = 1.7928$  is the anomalous magnetic moment of proton, and  $\sigma$  is an rms (root-mean-square) beam size. From attained matrix, it follows that spin depolarization is not taking place or suppressed if betatron tune values are chosen far away from low-order resonances, and that beam-beam collisions are stable. Actually, suppose that the initial spin has only one transverse component, i.e.,  $S_x = 0$ ,  $S_y = 1$  and  $S_z = 0$ . After  $n$  turns, the average and rms values of spin components are as follows:<sup>1)</sup>

$$\bar{S}_x = 0, \quad \bar{S}_z = 0, \quad \bar{S}_y = 1 - \frac{1}{8} \left( \frac{\tilde{\varphi}}{\cos(\tilde{\theta}/2)} \right)^2, \quad (3)$$

$$\overline{\langle S_x^2 \rangle} = \left[ \frac{\tilde{\varphi}^2}{8(\cos \tilde{\theta})} \right]^2, \quad \overline{\langle S_y^2 \rangle} = \frac{3}{256} \left[ \frac{\tilde{\varphi}}{\cos(\tilde{\theta}/2)} \right]^4,$$

$$\overline{\langle S_z^2 \rangle} = \left[ \frac{\tilde{\varphi}}{2 \cos(\tilde{\theta}/2)} \right]^2, \quad (4)$$

where  $\tilde{\varphi}$  and  $\tilde{\theta}$  are the average values of parameters  $\varphi$ ,  $\theta$  among all particles. In Fig. 1 results of particle motion and suppressed spin depolarization in the presence of stable beam-beam interaction are presented.

There are several mechanisms which lead to particle instability under beam-beam collisions. Excitation of nonlinear resonances and unstable stochastic particle motion due to overlapping of resonance islands are the fundamental phenomena in beam-beam interaction.<sup>2)</sup> Another mechanism of unstable particle motion is a diffusion created by random fluctuations in distribution of the opposite beam. In Ref. 3 the noise beam-beam instability was studied for the case of random fluctuations in the opposite beam size

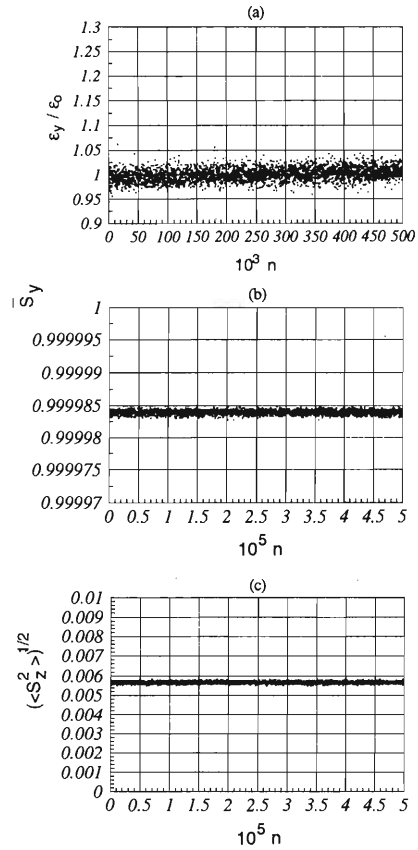


Fig. 1. (a) Beam emittance, (b) average value of  $\bar{S}_y$ , (c) rms value of  $\left(\overline{\langle S_z^2 \rangle}\right)^{1/2}$  as a function of the turn number for stable beam-beam interaction.

$$\sigma_n = \sigma_o \left( 1 \pm \frac{u \cdot u_n}{2} \right), \quad (5)$$

where  $u$  is a noise amplitude and  $u_n$  is an uniform random function with unit amplitude. It was shown that in the presence of noise, beam emittance increases with the turn number  $n$  as

$$\frac{\varepsilon_n}{\varepsilon_0} = \sqrt{1 + Dn}. \quad (6)$$

Here, diffusion coefficient  $D$  is the functions of beam-

beam parameter  $\xi$ , noise amplitude  $u$ , and ratio of beam size  $a$  with respect to opposite beam size  $2\sigma_0$ :

$$D = \pi^2(\xi u)^2 \left( \frac{a}{2\sigma_0} \right)^4. \quad (7)$$

Noise in the beam-beam collision always induces instability if beam-beam kick is a nonlinear function of the coordinate. Due to diffusion character, noise beam-beam instability does not have a threshold character and can exist at any value of beam-beam tune shift. Increase of beam emittance is accompanied with increase of beam size.

In Fig. 2 the results of beam dynamics and spin depolarization in the presence of noisy beam-beam instability are presented. Parameters of the process were chosen the same as for the stable beam-beam interaction without noise as presented in Fig. 1. The value of noise amplitude  $u = 0.025$  was chosen arbitrarily, to demonstrate the main features of diffusion beam-beam instability. As is seen, increase of beam sizes due to beam-beam collisions results in spin depolarization. It is also expected from analytical formulas (3)–(4), where the average and rms beam parameters are proportional to the powers of the small parameter  $\varphi$ , which, is proportional to beam size according to Eq. (2). Therefore, if beam is subjected to beam-beam instability, it causes spin depolarization.

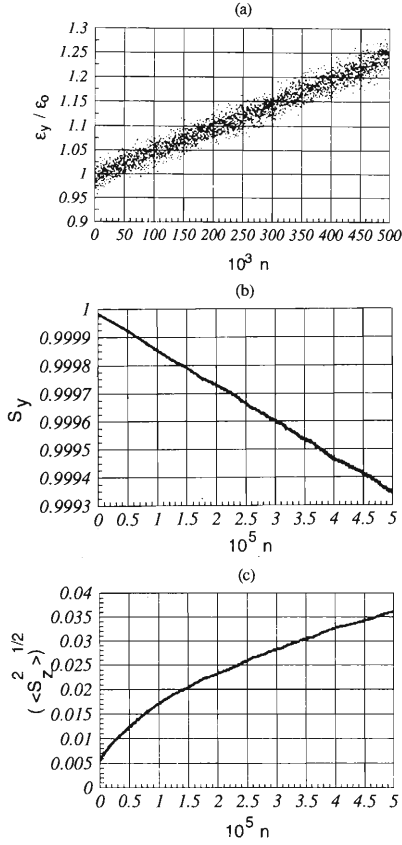


Fig. 2. (a) Beam emittance, (b) average value of  $\bar{S}_y$ , (c) rms value of  $(\langle S_x^2 \rangle)^{1/2}$  as a function of the turn number for unstable beam-beam interaction.

#### References

- 1) Y. Batygin and T. Katayama: Proc. 11th Symp. on Accelerator Science and Technology, 21–23 Oct. 1997, SPring-8, Harima Science Garden City, p. 822 (1997).
- 2) L. R. Evans: CERN 84-15, p. 319 (1984).
- 3) Y. Batygin and T. Katayama: “Noise instability in nonlinear beam-beam interaction”, RIKEN-AF-AC-3, March 1997, NIM-A, Vol. 404, p. 1 (1998)

# Study of Spin and Orbital Motion in Siberian Snake Based on Calculated Three Dimensional Magnetic Field

M. Xiao and T. Katayama

The study on orbital motion and spin precession of polarized protons in Siberian Snakes in RHIC is one of the subjects of particular interest in RHIC Spin Project.<sup>1,2)</sup> For a better representation, the simulation based on three dimensional (3D) magnetic field map (calculated or measured) is of importance. The work has been initiated by Luccio,<sup>3)</sup> but two main problems on the optimization of the numerical spin matrix and orbit matrix for Siberian Snakes still remain. The two problems are: (1) numerical spin matrices should be unitary, and (2) numerical orbit matrices should be symplectic, that is to say, the determinant of them should be exactly unity (1).

Each Siberian Snake consists of four right-handed helical dipole magnets. The results of magnetic field measurement for the prototype of a helical magnet agreed well with the 3D numerical calculation by TOSCA.<sup>4)</sup> It was therefore encouraged to work further based on the calculated magnetic field map for a modified magnet configuration, and to look for suitable methods to solve the problems mentioned above.

Bicubic spline function method was introduced first to interpolate  $B_w(x, y, s_k)$  ( $w = x, y$  or  $s$ ) ( $k = 1, 2, \dots, L_k$ ) and their derivatives in Cartesian coordinates for the calculated magnetic field map given on the  $(x, y)$  plane ( $s = s_k$ ),

$$B_w(x, y, s_k) = \sum_{K,L=1}^4 A_{wijKL}(x, y)(x - x_i)^{K-1}(y - y_j)^{L-1}$$

$$x_i \leq x \leq x_{i+1}, y_j \leq y \leq y_{j+1}$$

$$(i = 1, 2, \dots, m - 1; j = 1, 2, \dots, n - 1)$$

where the coefficients  $A_{wijKL}(x, y)$  can be determined by one-dimensional cubic spline function, and the corresponding boundary conditions were calculated by two-dimensional 3-points Lagrangian function. The interpolation in  $s$ -direction was done again by one-dimensional spline function,

$$B_w(x, y, s) = \sum_{N=1}^4 A_{wkN}(s)(s - s_k)^{N-1}$$

$$s_k \leq s \leq s_{k+1}, (k = 1, 2, \dots, L_k - 1).$$

The equations of orbital motion in natural coordinates are

$$\frac{du}{ds} = w \cdot [uvB_x - (1 + u^2)B_y + vB_s]$$

$$\frac{dv}{ds} = w \cdot [(1 + v^2)B_x - uvB_y - vB_s]$$

where  $u = x' = \frac{dx}{ds}$ ,  $v = y' = \frac{dy}{ds}$ ,  $w = e \cdot \frac{\sqrt{u^2 + v^2 + 1}}{m_0 \gamma V}$ , and  $V$  is the velocity of a charged particle.  $B_x$ ,  $B_y$  and  $B_s$  are the components of magnetic field in  $x$ ,  $y$  and  $s$  directions respectively. The equations of spin precession are

$$\frac{dS_x}{ds} = S_s P_y - S_y P_s$$

$$\frac{dS_y}{ds} = S_x P_s - S_s P_x$$

$$\frac{dS_s}{ds} = S_y P_x - S_x P_y$$

where

$$P_x = \Gamma_1 \cdot [-uB_s + (1 + v^2)B_x - uvB_y] + u \cdot \Gamma_2$$

$$P_y = \Gamma_1 \cdot [-vB_s + (1 + u^2)B_x - uvB_y] + v \cdot \Gamma_2$$

$$P_s = \Gamma_1 \cdot [-uB_x - vB_y + (u^2 + v^2)B_s] + \Gamma_2$$

where

$$\Gamma_1 = \frac{h}{B\rho} \cdot (1 + G\gamma),$$

$$\Gamma_2 = \frac{h}{B\rho} \cdot (1 + G)(uB_x + vB_y + B_s),$$

$$h = \frac{1}{\sqrt{u^2 + v^2 + 1}}, B\rho = m_0 \gamma V, G = 1.7928456.$$

Fourth-order Runge-Kutta method in Cartesian coordinates was used to integrate the above equations in the simulation. The axis of spin precession was calculated from the results of the integration of two groups of spin precession. The related program SSTRAN was written in FORTRAN based on the calculation methods discussed above.

Three components of the magnetic field distribution on the axis ( $x = 0, y = 0$ ) for full Snakes are shown in Fig. 1. Based on the field strength of the first helical magnet, the field strength of the second helical magnet was optimized so as to obtain the orbital angles

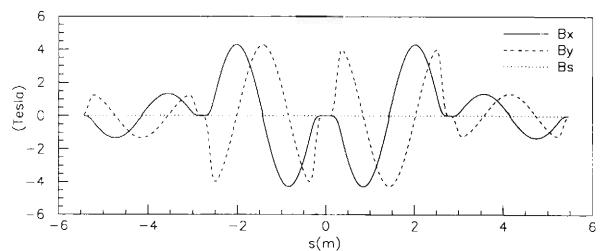


Fig. 1. Magnetic field distributions of the full Siberian Snakes on axis ( $x = 0, y = 0$ ).

$x'_e, y'_e$  at the exit of the Snakes as small as possible and  $S_{ye}$  as closed to  $-1$  as possible for the ray with initial conditions of  $(x_o, x'_o, y_o, y'_o) = (0., 0., 0., 0.)$  and  $(S_{xo}, S_{yo}, S_{so}) = (0, 1, 0)$ . The amplitude of the first magnetic field strength is 1.33626T, the finally optimized amplitude of the second magnetic field strength is 4.13649T, and the final results of orbital motion and spin precession are as follows:

$$\begin{aligned} (x_e, x'_e, y_e, y'_e) &= (0.24, 0.01111, -0.46, -0.08429) \\ (S_{xe}, S_{ye}, S_{se}) &= (0.015536 - 0.999734 - 0.017042) \end{aligned}$$

where the units are mm for  $x_e, y_e$ , and mrad for  $x'_e, y'_e$ . The spin axis obtained is  $51.4737^\circ$  (plane angle with s axis) and  $-0.0441^\circ$  (space angle with y-s plane). The trajectory and spin precession in full Snakes are shown in Fig. 2(a) and (b).

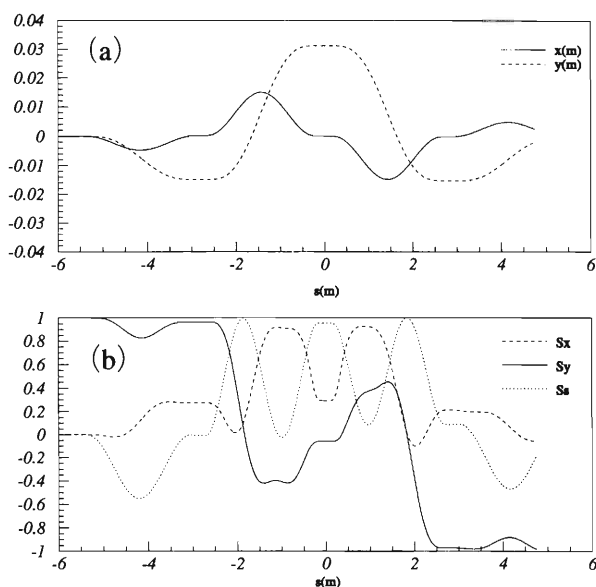


Fig. 2. Orbital motion and the spin precession of the ray with  $(x_o, x'_o, y_o, y'_o) = (0., 0., 0., 0.)$ , and  $(S_{xo}, S_{yo}, S_{so}) = (0, 1, 0)$ : (a) orbital motion, and (b) spin precession.

With the same initial orbit condition of  $(x_o, x'_o, y_o, y'_o) = (0., 0., 0., 0.)$ , three representative rays with initial spins  $(S_{xo}, S_{yo}, S_{so}) = (1, 0, 0), (0, 1, 0)$  and  $(0, 0, 1)$  were traced respectively, and then the spin matrix was obtained directly by the final precessed spin. That is

$$M_s = \begin{bmatrix} 0.2242 & -0.0131 & 0.9745 \\ 0.0155 & -0.9997 & -0.0170 \\ 0.9744 & 0.0190 & -0.2239 \end{bmatrix},$$

The determinant of  $M_s$  is  $1 + 1.4777 \times 10^{-7}$ . The dependence of the matrix elements on the particle position and angle was also investigated. The calculation was repeated for different values of  $(x_o, x'_o, y_o, y'_o)$ . The spin precession of some of the rays with large  $r$  ( $r > 3.0\text{cm}$ ) rotated unregularly, but most of them turned out to be very close to each other, and the determinant of their matrices had the same order of deviation ( $10^{-7}$ ) from unity.

To calculate the orbit matrix  $M_T$ , a certain number of rays, whose initial conditions were generated at random with Gaussian distribution in emittance, were traced. By solving a system of algebraic equations between the final and initial coordinates of the same ray, the 0th order  $4 \times 4$  matrix was obtained. The following numerical orbit matrix was calculated from the results of 16 rays traced,

$$M_T = \begin{bmatrix} 0.9939 & 10.8281 & -0.0170 & -0.0336 \\ -0.0043 & 0.9657 & 0.0060 & -0.0074 \\ 0.0006 & 0.1631 & 0.9844 & 10.6717 \\ 0.0006 & 0.0626 & -0.0049 & 0.9485 \end{bmatrix},$$

The determinant of  $M_T$  is  $1 - 4.9183 \times 10^{-3}$ .

To check the Maxwellian properties for a given magnetic field map, first derivatives were directly calculated by the coefficients of spline function  $A_{wijKL}$ . The results showed that  $\nabla \cdot \vec{B} = 0$  was well satisfied ( $10^{-6}$ ) in the region around the axis, and the error of  $\nabla \times \vec{B} = 0$  was mainly originated from  $(\nabla \times \vec{B})_x$ , which may be due to the small value of  $B_s$  and its rapid change with  $y$ .

Further work will be done for adjusting the magnetic field map to satisfy Maxwell equations, and a symplectic integration method will be taken to integrate the equations of orbital motion and of spin precession.

#### References

- 1) K. Brown (BNL) et al.: Spin Note AGS/RHIC/SN No. 001, January 19, 1996.
- 2) T. Katayama: Spin Dynamics in Synchrotron and Storage Ring, November, 1995.
- 3) A. U. Luccio: Spin Note AGS/RHIC/SN No. 041, November 5, 1996.
- 4) M. Okamura: Spin Note AGS/RHIC/SN No. 060, August 20, 1997.

# Calculation and Measurement of Magnetic Field in Half-Length Helical Snake Magnet for RHIC

M. Okamura, T. Tominaka, T. Kawaguchi, and T. Katayama

We have studied on acceleration of polarized proton beams in RHIC as a part of the RHIC-Spin project. Development of the superconducting helical dipole magnets<sup>1)</sup> which are to be used as the Siberian Snakes is one of the key to the success of this project. In order to confirm the performance of the magnet, a half-length model magnet was fabricated by the end of 1996. Three dimensional field analysis has been performed for it using the code TOSCA.<sup>2)</sup>

The coils of the model magnet are divided into sixteen current carrying blocks. The separation between the coils and the yoke is only 5.5 mm, and the yoke enhances the field strength about 50%. The current blocks were designed to be used with two sizes of currents in the ratio of 9 to 11. In order to increase the quench limit, the coils in the stronger field area have a lower current. In the latest design of the helical magnet, an uniform current over the cross-section will be used in stead of the 9 to 11 ratio, to simplify the operation.

The measurements were performed on the model magnet in February and June of 1997 in a vertical dewar at BNL. The operating current in the "low-current" blocks is expected to be 280 A for 4.0 T. The model magnet quenched at 139% of the operating current, and the field strength at the center of the magnet reached 5.0 T. Using TOSCA, field strengths of peaks, which are found at the inner edge of the coils nearest to the poles in the body, were estimated. According to 3D analysis, the coil is expected to quench at 395 A in the "low-current" blocks corresponding to a dipole field strength of 5.3 T near the beam axis. The experimental result almost reached the calculated quench current. The comparison is summarized in Table 1.

Table 1. Quench performance.

	Experiment	Calculation
Max. current at lower current blocks (A)	388	395
Max. current at higher current blocks (A)	474	483
Max. field at the center of the model (T)	5.0	5.3

To measure the field distribution in the model magnet, Hall probes connected to a cylinder were used. Rotating coils are usually used to measure magnetic fields for synchrotron magnets. However, this method only measures the average field over the length of the coil. On the other hand, Hall probes have a small sensing area, a few mm<sup>2</sup>, and can measure local magnetic fields. The cylinder was passed through to a long aluminum shaft and rotated by a stepping motor. The field was sampled at 64 points per revolution. This cylinder was also moved axially by another stepping motor to measure the field distribution along the beam axis. The reference radius of the multipole components was 31 mm in analysis. The model magnet was excited by an uniform current. In the case of dipole component, agreement in both the field strength and phase

angle is very good. In the case of sextupole component, as shown in Fig. 1, agreement in the end regions, where relatively strong multipole fields are distributed, is excellent. However, some discrepancies are observed in the body section. It is a possibility that some spurious multipole components were observed due to the planar Hall effect.

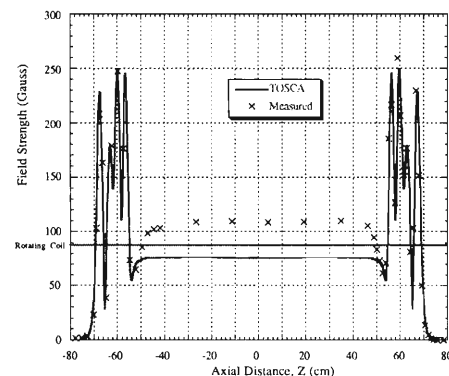


Fig. 1. Amplitude of the sextupole component (105A/cable for all current-carrying blocks).

To specify the field quality at the center of the model magnet, we used a tangential rotating coil which has been used for other RHIC magnets. The length and opening angle of this rotating coil are 230 mm and 15 degrees respectively. In the case of the helical dipole magnets, there is some reduction in signal due to a rotation of the field over the length of the measuring coil. For example, the sensitivity of the rotating coil for the decapole component decreases by 67% of the sensitivity for a normal straight magnet. The measured harmonics were corrected for this reduction in sensitivity. The results measured by using this rotating coil are shown by a dotted line in Fig. 1. The calculated ratio of the sextupole components to the dipole component are smaller than the measured value by about  $1 \times 10^{-3}$ . The current dependence of the sextupole component (due to the saturation if iron material) agrees with the 3D calculation. In this measurement, again, an uniform operating current was applied for all current blocks, and the multipole components are larger than the design values which assume the use of two currents.

The fabricated model magnet showed a good performance. The measured results of the model agree quite well with the 3D calculations. Thus, we can rely on the field calculations and have validated our mechanical design and fabrication method.

## References

- 1) Vector Fields Limited, Oxford, UK.
- 2) M. Okamura et al.: Proc. Particle Accel. Conf. (1997).

# Optimization of Full-Length Helical Snake Magnet for RHIC

M. Okamura, T. Tominaka, and T. Katayama

A half-length model of the helical magnet for RHIC has been built and tested successfully. Now we are finalizing a design for the full-length helical dipole magnet.

From the cryogenic point of view, it is necessary to minimize the heat leak from the independently powered helical dipole magnets for RHIC. Therefore, a thin round cable of 1 mm diameter comprised of seven wires will be used instead of the Rutherford-type cable used in the regular arc magnets. The Kapton-wrapped cables are wound in the precisely machined helical slots on an aluminum cylinder. Thin fiberglass sheets containing b-stage epoxy are inserted between layers. Finally, the wound cables are locked in the slots by heating, while applying radial pressure. All techniques mentioned above were applied in the half-length model fabrication and the built model showed a good quench performance. Only a remained problem is the coil winding method. The coils for the model magnet were wound by hand, and considerable skill and time were required. An automatic winding process is currently being developed.

Multipole components of the model magnet are shown in Table 1. In the original design of this magnet, it had been assumed to use two currents, 9 to 11 ratio of the current in cables. However, to simplify the system, it is decided to use uniform current instead of the two currents. Accordingly, in the cross-sectional magnet design, number of layers at the most inside slots, closest to each poles, of both inner and outer coils was reduced from 9 to 8 layers. The re-optimized values are also indicated in Table 1. The calculated values were computed using 3D magnetic calculation by TOSCA.

According to the basic idea, if helical dipole magnets are employed for the Siberian Snake, deflections of beam orbits will be canceled due to 360 degree rotation of magnetic field. However, in actual magnets, there are fringing fields and therefore 360 degree rota-

Table 1. The multipole component at the center region of the magnet.

	Experiment	Calculation
Fabricated half-length model		
Sextupole (300A/cable)	$-5.7 \times 10^{-3}$	$-5.1 \times 10^{-3}$
Decapole (300A/cable)	$6.4 \times 10^{-4}$	$3.4 \times 10^{-4}$
Sextupole (100A/cable)	$-6.2 \times 10^{-3}$	$-5.3 \times 10^{-3}$
Decapole (100A/cable)	$7.6 \times 10^{-4}$	$6.2 \times 10^{-4}$
Re-optimized design		
Sextupole (300A/cable)	-	$3.7 \times 10^{-3}$
Decapole (300A/cable)	-	$-2.6 \times 10^{-4}$
Sextupole (83A/cable)	-	$6.0 \times 10^{-3}$
Decapole (83A/cable)	-	$4.2 \times 10^{-4}$

The above values are derived from the expansion of the azimuthal field component. The reference radius is set to 31 mm.

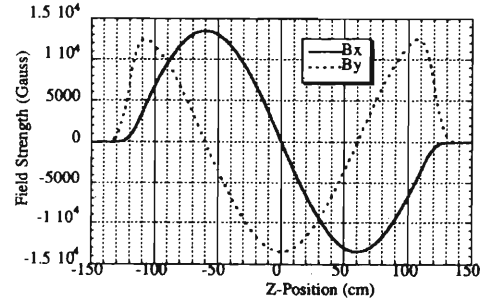


Fig. 1. Vertical and horizontal components in a helical dipole magnet.

tion does not always cancel the deflection of orbits. In Fig. 1, a typical magnetic field of the full-length helical snake magnet is shown by vertical,  $B_y$ , and horizontal,  $B_x$ , components. Applying the coordinates which are used by this figure, a symmetry condition makes an integral of  $B_x$  component along the beam axis automatically zero. Therefore, we have to pay attention only to the  $B_y$  component, and have to optimize the integral of this component to become zero in designing helical magnets. When this condition is achieved, we may say that this magnet has effectively 360 degree of rotation angle. Table 2 shows the measured and predicted transverse fields. The measured integrated field was constructed based on the Hall probe scan over the half-length magnet. The body portion, which shows a constant change of the phase angle of the dipole component, was extended to fit the full-length magnet. The predicted values were calculated using the TOSCA, where the re-optimized cross-section and slightly modified coil end design were taken into account. The modification of the coil ends is to match with the automatic winding. All these values are well within the requirements from beam optics considerations. Furthermore, we can adjust the rotation angle modifying the iron yoke length after the first measurement of the full-length helical dipole magnet.

The design of the full length helical dipole magnet has been completed. The automatic winding method, which is a single remained issue of the magnet fabrication, is now in progress. The first full-length magnet will be constructed and tested in this spring.

Table 2. The integrated transverse field.

	Integral of Bx	Integral of By (Tm)
Measured (220A/cable)	$1.5 \times 10^{-3}$	$5.8 \times 10^{-4}$
Re-optimized (300A/cable)	-	$-6.9 \times 10^{-4}$
Re-optimized (83A/cable)	-	$2.0 \times 10^{-4}$



## **VI. RADIATION MONITORING**



## Routine Works for Radiation Safety in the Ring Cyclotron Facility

S. Fujita, S. Ito, S. Nakajima, H. Uehara,\*<sup>1</sup> T. Arakawa,\*<sup>2</sup>  
Y. Uwamino, and N. Nakanishi

The radiation safety control system has worked well steadily during this year (1997) so as to enable us to execute radiation monitoring service continuously and automatically.

From the accumulated data of leakage neutrons, the radiation level in the controlled area was found much less than the safety limit (0.3 mSv/week). Leakage of neutrons at the boundary of the accelerator facility has been recorded with the monitor installed in the ground-floor computer room just above a bending magnet that guides the beams from the Ring Cyclotron vault to the distribution corridor. We found that the radiation level is much less than the safety limit (1 mSv/year). Leakage of  $\gamma$  rays and neutrons were not possible to detect with environmental monitors set outside the building during this reporting period.

A film badge (FB) with an Optical Character Reader (OCR)-code had been used to open the gate at the entrance of the controlled area, while a card with a bar-code had been used to check a user and to open the gate of experimental vaults. It sometimes caused for users to forget or lose the card. In the last winter, the FB system was replaced by a new type with a bar-code. With this change, all of the OCR and bar-code-card readers<sup>1)</sup> were exchanged with new FB-readers of no contact type. So, there is no need for users to carry the card, and the procedure to open the gate became simple. Moreover, the mechanical troubles have much decreased in the new FB-reader system, and the user registration has also become easy. Figure 1 is the photograph showing a new FB-reader system at the entrance gate for the controlled area, and Fig. 2 is the photograph of showing new FB-readers on top of the gate-bar at the entrance of experimental vault.

In this winter-98, we are going to install a new hand-foot-cloth monitor system at the entrance room for controlled area, which is able to detect  $\beta(\gamma)$  and  $\alpha$  rays.

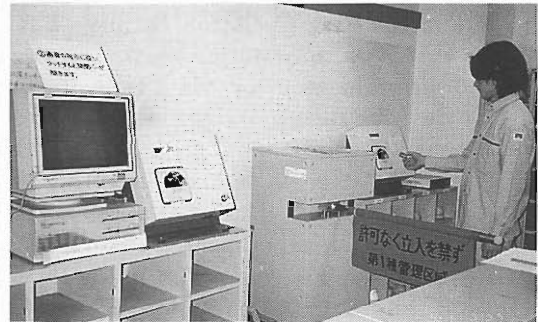


Fig. 1. Photograph of a new FB-reader system at the entrance gate for the controlled area.

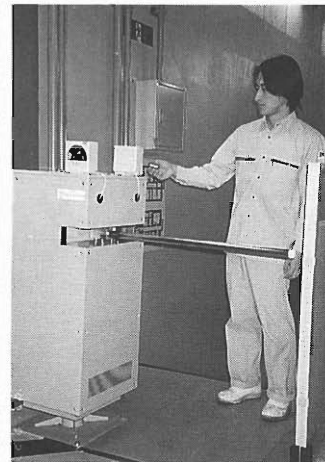


Fig. 2. Photograph of new FB-readers on top of the gate-bar at the entrance of experimental vault.

### References

- 1) S. Fujita and N. Nakanishi: RIKEN Accel. Prog. Rep. **28**, 186 (1995).

\*<sup>1</sup> Faculty of Science and Technology, Chuo University

\*<sup>2</sup> Faculty of Science, Science University of Tokyo

## Dose Rates Due to Residual Radioactivity in the Ring Cyclotron Facility

S. Fujita, H. Uehara,\*<sup>1</sup> T. Arakawa,\*<sup>2</sup> S. Ito, S. Nakajima, Y. Uwamino, and N. Nakanishi

Residual radioactivities were measured on the surface at various points by using ionization-chamber survey meters in the Ring Cyclotron Facility. The measurements were performed during the routine overhaul period and after almost every beam time. In the following, we describe the significant dose rates observed through measurements.

Just after the last beam time of the spring term, a routine overhaul started. During the last beam time of the spring term, an experiment with an <sup>22</sup>Ne beam of 110 MeV/nucleon was carried out in the E6 experimental vault from August 1 to 8, 1997. The dose rates in the Ring Cyclotron and the injector AVF cyclotron were measured on Aug. 27 and 28, 1997 during the overhaul period. The results are shown in Fig. 1 for the Ring Cyclotron.

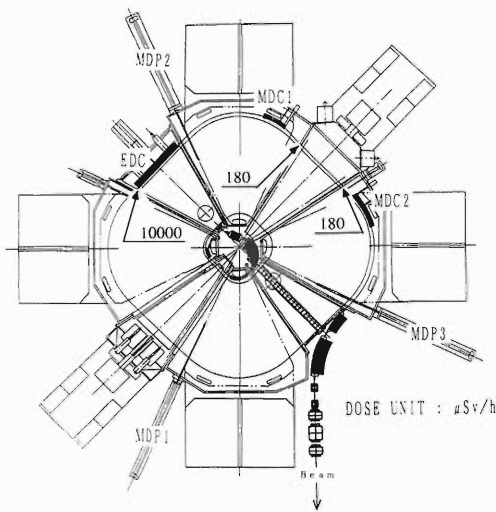


Fig. 1. Detection points around the RIKEN Ring Cyclotron: EDC, the electrostatic deflection channel; MDC1, the magnetic deflection channel 1; MDC2, the magnetic deflection channel 2; MDP1, the main differential probe 1; MDP2, the main differential probe 2; MDP3, the main differential probe 3. Indicated numbers are dose rates in units of  $\mu\text{Sv/h}$ .

Besides the above routine measurement, dose rates inside the AVF cyclotron were measured when its acceleration chamber was opened on December 25, '96 because of a trouble of insulation of the deflector in vacuum. The results are shown in Fig. 2 for the injector AVF cyclotron.

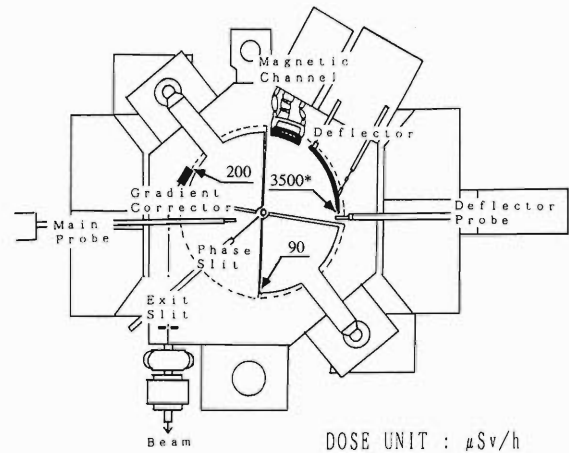


Fig. 2. Dose rates measured inside the injector AVF cyclotron. They are given in units of  $\mu\text{Sv/h}$ , and \* indicates an extra measurement on December 25.

Table 1. Summary of the dose rates measured along the beam lines with ionization-chamber survey meters. The points a-z indicate the detection points shown in Fig. 3.

Detection point	Measured dose rate ( $\mu\text{Sv/h}$ )	Date	The experiment preceded			
			particle	energy (MeV/n)	intensity (enA)	period (days)
a	100	Mar 7, '97	C-13	115	1350	3
b	600	Jun 17, '97	d	135	140	4
c	800	Jun 17, '97	d	135	140	4
d	80	Jun 17, '97	d	135	140	4
e	1000	Jun 17, '97	d	135	140	4
f	350	Mar 7, '97	C-13	115	1350	3
g	130	Oct 18, '96	C-13	100	1600	4
h	350	Apr 25, '97	Fe-56	90	200	3
i	70	Oct 18, '96	C-13	100	1600	4
j	550	Nov 13, '96	p	113	600	3
k	130	Aug 11, '97	Ne-22	110	1900	8
l	120	Dec 18, '96	Ne-22	110	1200	8
m	160	Sep 18, '97	O-18	100	1800	8
n	200	Apr 28, '97	Ne-22	110	1800	6
o	1000	Aug 11, '97	Ne-22	110	1900	8
p	120	Dec 18, '96	Ne-22	110	1200	8
q	600	Feb 5, '97	p	113	1360	2
r	300	Nov 13, '96	p	113	600	3
s	60	Nov 13, '96	p	113	600	3
t	500	Nov 13, '96	p	113	600	3
u	60000	Nov 13, '96	p	113	600	3
v	50	Nov 27, '96	N-14	135	2000	4
w	1500	Nov 27, '96	N-14	135	2000	4
x	1200	Nov 27, '96	N-14	135	2000	4
y	50	Feb 27, '97	d	135	240	8
z	180	Feb 27, '97	d	135	240	8

\*<sup>1</sup> Faculty of Science and Technology, Chuo University

\*<sup>2</sup> Faculty of Science, Science University of Tokyo

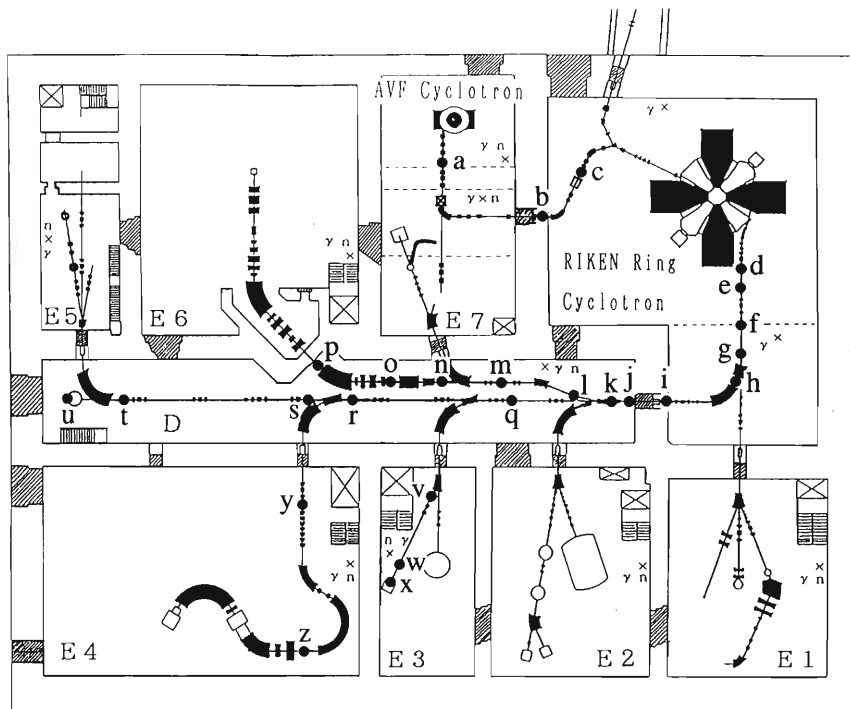


Fig. 3. Layout of the RIKEN Ring Cyclotron Facility as of 1997. Detection points of residual activities along the beam lines are denoted by a-z.

In the period from Oct. 1, 1996 to Sep. 30, 1997, dose rates were measured along the beam lines. The bulletted points a-z in Fig. 3 denote the places where the dose rates exceeded  $50 \mu\text{Sv/h}$ . Table 1 summarizes

the observed dose rates with the dates on which the measurements were performed. The maximum dose rate was found to be  $60 \text{ mSv/h}$  ( $60,000 \mu\text{Sv/h}$ ) at the target chamber, denoted by the point u in Fig. 3.

## Residual Induced-Radioactivity at the Old 160 cm Cyclotron

Y. Uwamino, S. Ito, S. Shinohara, and K. Harasawa

Construction of the RI Beam Factory requires the removal of some of the old radiation facilities located adjacent to the existing ring cyclotron. They possess an unsealed radioactivity-handling facility, small electrostatic accelerators, and an old 160-cm cyclotron. Only the last one has been already shutdown though, it is the most massive item and it still contains induced radioactivity.

The 160-cm cyclotron was built in 1966, operated for 23 years with beams of proton to  $^{20}\text{Ne}$ , and was shutdown in April 1990. The maximum energy was 17 MeV for protons and 160 MeV for  $^{20}\text{Ne}$ . The maximum beam intensity was  $30\ \mu\text{A}$  for protons and  $0.3\ \mu\text{A}$  for  $^{20}\text{Ne}$ . The total weight of the magnet is 330 tons including the coil.<sup>1)</sup>

For estimating the amount of radioactive waste from the 160-cm cyclotron, we took several samples from it, and measured them with a Ge detector for a gamma-ray spectrometry. The preliminary results of the measurement are shown in Table 1.

The measured radioactivity is only  $^{60}\text{Co}$  for the most samples. However, the  $^{55}\text{Fe}$  and  $^{63}\text{Ni}$  radionuclides, which cannot be detected by the Ge detector, are also expected in the iron and copper material, respectively, as speculated from the decommissioning experience<sup>2)</sup> of the FM cyclotron at the Institute for Nuclear Study, University of Tokyo. The amount of  $^{63}\text{Ni}$  can be estimated to be about 10 times higher than that of  $^{60}\text{Co}$  in copper, but the radiation toxicity is  $1/40$  of  $^{60}\text{Co}$ .<sup>3)</sup> Since the half life of  $^{55}\text{Fe}$  is shorter than  $^{60}\text{Co}$  and the radiation toxicity is  $1/60$  of  $^{60}\text{Co}$ , the effect of  $^{55}\text{Fe}$  can be neglected.

There is no statement on the exemption limit against the solid waste in the Japanese law. So, we cannot consider any substances as non-radioactive waste if it contains non-negligible amount of radioactivity. Considering the amount of radioactivity in the natural rock or soil, the concentration of  $0.2\ \text{Bq/g}$  of  $^{60}\text{Co}$  can be considered as non-radioactive, and the radioactivity of this concentration can be detected by a handy scintillation survey meter. Compared with the exemption limit of  $1\ \text{Bq/g}$  for  $^{60}\text{Co}$  in the Swiss legislation which is adopted at CERN, our criterion may be too much less than the reasonable value.

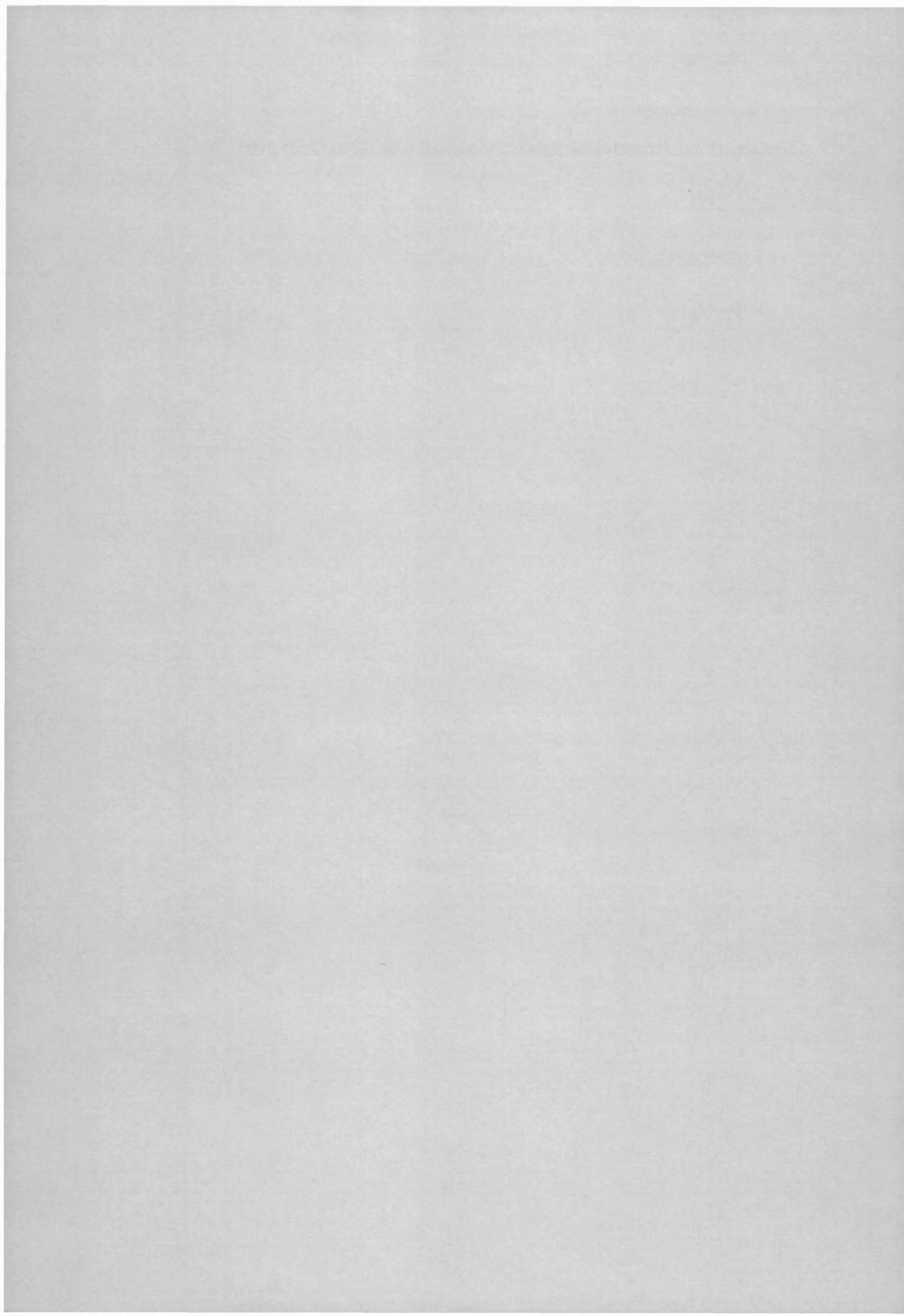
Table 1. Residual radioactivity measured in the old 160 cm cyclotron.

position	material	nuclide	activity
earth plate	Cu	$^{60}\text{Co}$	0.10 Bq/g
earth plate	Cu	$^{60}\text{Co}$	0.12
deflector	Cu	$^{207}\text{Bi}$	5.23
		$^{65}\text{Zn}$	2.10
		$^{22}\text{Na}$	1.14
		$^{60}\text{Co}$	22.24
deflector	brass	$^{60}\text{Co}$	1.01
deflector	SS	$^{60}\text{Co}$	10.53
extraction duct	SS	$^{60}\text{Co}$	3.53
extraction duct	brass	$^{60}\text{Co}$	1.22
extraction duct	Fe	$^{60}\text{Co}$	0.37
extraction duct	Fe	$^{60}\text{Co}$	0.15
diffusion pump	Fe	$^{60}\text{Co}$	0.09
		Dec	SS $^{60}\text{Co}$ 15.67
Dec	SS	$^{60}\text{Co}$	5.81
resonator	Fe	$^{60}\text{Co}$	0.06
resonator	SS?	$^{60}\text{Co}$	0.04
resonator meter	ferrite	$^{60}\text{Co}$	9.62
yoke	Fe	$^{60}\text{Co}$	0.41
yoke	Fe	$^{60}\text{Co}$	0.83
pole tip	Fe	$^{60}\text{Co}$	2.52

On our criterion, the substances excepting the earth plate, the diffusion pump, and the iron at resonator are all treated as radioactive. In general, iron and copper parts placed far from the beam orbit are non-radioactive, while almost all parts of the stainless-steel are radioactive.

### References

- 1) Y. Awaya et al., Ed.: RIKEN Accel. Prog. Rep. Suppl. (1990).
- 2) "Production of induced radioactivity and its safe handling at accelerator facilities", Report of the committee for "Problems on induced radioactivity at accelerator facilities", Japan Radioisotope Association (1994). (in Japanese)
- 3) Swiss Legislation on Radiological Protection, 814.501 Ordinance of 22 June 1994.





## VII. LIST OF PUBLICATIONS

### 1. Accelerator development and accelerator physics

Y. Yano and I. Tanihata: "New application of radioisotopes at big accelerators", *Radioisotopes*, pp. 36–49 (1995).

O. Kamigaito, A. Goto, Y. Miyazawa, T. Chiba, M. Hemmi, M. Kase, S. Kohara, Y. Batygin, and Y. Yano: "Development of a folded-coaxial RFQ linac for the RILAC", *Proc. 18th Int. Linear Accelerator Conf.*, Geneva, Switzerland, Aug., edited by C. Hill and M. Vretenar, CERN, pp. 863–865 (1996).

Y. Yano: "RIKEN Ring Cyclotron: 10 years of progress, future development", *Genshiryoku Kougyou*, pp. 42–53 (1997).

Y. Yano, A. Goto, and T. Katayama: "RIKEN RI-Beam Factory Project", *JARA J.*, **6**, 1–9 (1997).

A. Goto, T. Kubo, H. Okuno, T. Kawaguchi, T. Mitsumoto, T. Tominaka, S. Fujishima, J. W. Kim, K. Ikegami, N. Sakamoto, S. Yokouchi, T. Morikawa, K. Sugii, and Y. Yano: "The Booster Ring Cyclotrons for the RIKEN RI Beam Factory", *Proc. 11th Symp. on Accelerator Science and Technology*, Harima, 1997-10, edited by Y. Miyahara, JASRI, pp. 53–55 (1997).

O. Kamigaito, A. Goto, Y. Miyazawa, T. Chiba, M. Hemmi, M. Kase, S. Kohara, T. Nakagawa, E. Ikezawa, Y. Batygin, and Y. Yano: "Acceleration tests of the folded-coaxial RFQ linac for the RILAC", *Proc. 11th Symp. on Accelerator Science and Technology*, Harima, 1997-10, edited by Y. Miyahara, JASRI, pp. 92–94 (1997).

Y. Yano, A. Goto, and T. Katayama: "RIKEN RI-Beam Factory Project", *Proc. 11th Symp. on Accelerator Science and Technology*, Harima, 1997-10, edited by Y. Miyahara, JASRI, pp. 136–138 (1997).

Y. Batygin and T. Katayama: "Spin depolarization in presence of beam-beam interaction", *Proc. 11th Symp. on Accelerator Science and Technology*, Harima, 1997-10, edited by Y. Miyahara, JASRI, pp. 282–284 (1997).

M. Takanaka and T. Katayama: "Simulation of beam bunching using electron cooling for the ion storage ring of RIKEN RI-Beam Factory Project", *Proc. 11th Symp. on Accelerator Science and Technology*, Harima, 1997-10, edited by Y. Miyahara, JASRI, pp. 291–293 (1997).

D. Toprek, A. Goto, and Y. Yano: "Beam orbit simulation in the central region of the RIKEN AVF Cyclotron", *Proc. 11th Symp. on Accelerator Science and Technology*, Harima, 1997-10, edited by Y. Miyahara, JASRI, pp. 537–539 (1997).

O. Kamigaito, A. Goto, Y. Miyazawa, T. Chiba, M. Hemmi, S. Kohara, M. Kase, T. Nakagawa, Y. Batygin, Y. Yano, E. Ikezawa, T. Aihara, T. Ohki, H. Hasebe, and H. Yamauchi: "Acceleration tests of

the folded-coaxial RFQ for the RILAC", *Proc. 22nd Linear Accelerator Meet. in Japan*, Sendai, 1997-09, edited by Tohoku Univ., pp. 47–49 (1997).

A. Goto, T. Kubo, H. Okuno, T. Kawaguchi, T. Mitsumoto, T. Tominaka, S. Fujishima, J. W. Kim, K. Ikegami, N. Sakamoto, S. Yokouchi, T. Morikawa, Y. Tanaka, and Y. Yano: "The Superconducting Ring Cyclotrons for RIKEN RI Beam Factory", *16th RCNP Osaka Int. Symp. on Multi-GeV High-Performance Accelerators and Related Technology*, pp. 87–88 (1997).

Y. Yano: "RIKEN Ring Cyclotron: 10 years of progress, future development", *Science & Technology in Japan*, **1**, 2–5 (1997).

Y. Batygin: "Dynamics of beam-beam interaction", *SPring-8 Proc. Workshop on Beam Physics*, Hyogo, 1996-11, SPring-8, pp. 161–188 (1997).

### 2. Nuclear physics and nuclear instrumentation

N. Hasebe, Y. Mishima, T. Doke, J. Kikuchi, T. Hayashi, T. Takashima, M. Kobayashi, N. Takehana, H. Shirai, T. Yanagimachi, A. Nakamoto, H. Murakami, K. Nagata, T. Kohno, K. Munakata, C. Kato, S. Yanagita, Y. Yamada, M. Ehara, T. Kashiwagi, T. Koi, J. Sequeiros, J. Medina, and B. Wilken: "Composition and energy spectra of anomalous cosmic rays observed by the GEOTAIL satellite", *Adv. Space Res.*, **19**, 813–816 (1997).

H. Kurasawa and T. Suzuki: "Nuclear medium effects to be observed and not to be observed", *Genshikaku Kenkyu* **42**, 41–48 (1997).

T. Takashima, T. Doke, T. Hayashi, J. Kikuchi, K. Itsumi, M. Kobayashi, H. Shirai, N. Takehana, N. Hasebe, K. Kondoh, T. Kohno, K. Munakata, C. Kato, S. Yanagita, Y. Yamada, D. Reames, and T. von Rosenvinge: "The first observation of sulfur in anomalous cosmic rays by the GEOTAIL and the WIND spacecrafts", *25th Int. Cosmic Ray Conf. Contributed Papers*, Vol. 2: Sessions SH4-6, Durban, South Africa, 1997-07, edited by Potgieter M. S., Raubenheimer B. C., and van der Walt D. J., Potchefstroom Univ., pp. 285–288 (1997).

T. Kohno, I. Yamagiwa, H. Miyasaka, T. Goka, and H. Matsumoto: "Observation of heavy ions with ADEOS satellite", *25th Int. Cosmic Ray Conf. Contributed Papers*, Vol. 2: Sessions SH4-6, Durban, South Africa, 1997-07, edited by Potgieter M. S., Raubenheimer B. C., and van der Walt D. J., Potchefstroom University, pp. 317–320 (1997).

G. I. Pugacheva, A. A. Gusev, T. Kohno, I. M. Martin, W. Spjeldvik, and T. Almand: "The 1-9 MeV/nucleon HE flux dynamics in the inner magnetosphere during 1984-1986", *25th Int. Cosmic Ray Conf. Contributed Papers*, Vol. 2: Sessions SH4-6,

- Durban, South Africa, 1997-07, edited by Potgieter M. S., Raubenheimer B. C., and van der Walt D. J., Potchefstroom University, pp. 353-356 (1997).
- Y. Muraki, K. Masuda, Y. Matsubara, T. Sako, I. Imaida, H. Tsuchiya, T. Kohno, T. Goka, H. Matsumoto, T. Omoto, Y. Fujiwara, K. Taguchi, M. Nakazawa, I. Tanaka, M. Fujii, and H. Ikeda: "Scintillation fiber telescope for detecting neutrons in a satellite experiment", 25th Int. Cosmic Ray Conf. Contributed Papers, Vol. 5: Sessions OG 10 & 11, Durban, South Africa, 1997-07, edited by Potgieter M. S., Raubenheimer B. C., and van der Walt D. J., Potchefstroom University, pp. 41-44 (1997).
- M. Iwasaki, S. N. Nakamura, and T. Ito: "Precise measurement of X-rays in K-mesic hydrogen atom", *Nihon Butsuri Gakkaishi* **52**, 272-275 (1997).
- Y. Uwamino, T. Soewarsono, H. Sugita, Y. Uno, T. Nakamura, T. Shibata, M. Imamura, and S. Shibata: "High-energy p-Li neutron field for activation experiment", *Nucl. Instrum. Methods Phys. Res. A* **389**, 463-473 (1997).
- T. Ikeda, M. Chapman, Y. Igarashi, J. Imazato, J. Lee, M. Khabibullin, O. Mineev, H. M. Shimizu, S. Shimizu, A. Suzuki, A. Watanabe, and T. Yokoi: "High-precision magnetic field mapping with a three-dimensional hall probe for a T-violation experiment in  $K_{\mu 3}$  decay", *Nucl. Instrum. Methods Phys. Res. A* **401**, 243-262 (1997).
- S. Yamaji, F. A. Ivanyuk, and H. Hofmann: "Variation of transport coefficients for average fission dynamics with temperature and shape", *Nucl. Phys. A* **612**, 1-25 (1997).
- D. Hirata, K. Sumiyoshi, I. Tanihata, Y. Sugahara, T. Tachibana, and H. Toki: "A systematic study of even-even nuclei up to the drip lines within the relativistic mean field framework", *Nucl. Phys. A* **616**, 438-445 (1997).
- S. Frauendorf and J. Meng: "Tilted axis cranking in triaxial deformed nuclei", *Nucl. Phys. A* **617**, 131-147 (1997).
- K. Sugawara-Tanabe and A. Arima: "New dynamical  $SU(3)$  symmetry in deformed nuclei", *Nucl. Phys. A* **619**, 88-96 (1997).
- N. Dinh Dang, A. Arima, T. Suzuki, and S. Yamaji: "Study of Gamow-Teller resonance in  $^{90}\text{Nb}$  and  $^{208}\text{Bi}$ ", *Nucl. Phys. A* **621**, 719-735 (1997).
- H. Akiyoshi: "Analyzing powers of proton-deuteron radiative capture reaction at 17.5 MeV", *Nuclear Study* **42**, 53-62 (1997).
- K. Sakai, Y. Masuda, T. Adachi, K. Asahi, M. Doi, M. Harada, S. Ishimoto, M. Inuma, J. Kura, A. Masaike, Y. Matsuda, K. Morimoto, S. Muto, K. Okumura, H. Sato, H. M. Shimizu, A. Yoshimi, and Z. Zheng: "Observation of parity-violating neutron spin rotation in the  $n$ - $^{139}\text{La}$  p-wave resonance", *Phys. Lett. B* **391**, 11-14 (1997).
- T. Nakamura, T. Motobayashi, Y. Ando, A. Mengoni, T. Nishio, H. Sakurai, S. Shimoura, T. Teranishi, Y. Yanagisawa, and M. Ishihara: "Coulomb excitation of  $^{11}\text{Be}$ ", *Phys. Lett. B* **394**, 11-15 (1997).
- H. Kurasawa, K. Yabana, and T. Suzuki: "Damping width of the Mie Plasmon", *Phys. Rev. B* **56**, R10063-R10066 (1997).
- F. A. Ivanyuk, H. Hofmann, V. V. Pashkevich, and S. Yamaji: "Transport coefficients for shape degrees in terms of Cassini ovaloids", *Phys. Rev. C* **55**, 1730-1746 (1997).
- N. Dinh Dang and F. Sakata: "Thermal damping width of the giant dipole resonance in hot nuclei", *Phys. Rev. C* **55**, 2872-2884 (1997).
- V. G. Soloviev, A. Arima, and N. Dinh Dang: "Possible enhancement of the  $E1$  decay rates of double giant dipole states", *Phys. Rev. C* **56**, R603-R605 (1997).
- N. Dinh Dang, A. Arima, V. G. Soloviev, and S. Yamaji: "Possible deviation of the sum of strengths for the double giant dipole resonance from the harmonic oscillator limit", *Phys. Rev. C* **56**, 1350-1356 (1997).
- J. Meng and P. Ring: "A giant halo at the neutron drip line", *Phys. Rev. Lett.* **79**, 1234-1238 (1997).
- N. Dinh Dang, A. Arima, T. Suzuki, and S. Yamaji: "Spreading of Gamow-Teller resonance in  $^{90}\text{Nb}$  and  $^{208}\text{Bi}$ ", *Phys. Rev. Lett.* **79**, 1638-1641 (1997).
- K. Kondoh, N. Hasebe, M. Kobayashi, J. Hamada, Y. Mishima, T. Doke, J. Kikuchi, T. Hayashi, T. Takashima, N. Takehana, T. Yanagimachi, S. Yanagita, Y. Yamada, K. Munakata, C. Kato, H. Yanaizumi, K. Nagata, T. Koi, T. Kohno, and K. Fujiki: "Interplanetary particle event related to cosmic ray modulation", *Proc. 5th and 6th Symp. of Solar Terrestrial Energy Program (STEP)*, Sendai, 1997, edited by H. Ohya, pp. 270-278 (1997).
- A. Arima, N. Dinh Dang, T. Suzuki, and S. Yamaji: "Study of Gamow-Teller resonance in  $^{208}\text{Bi}$  taking  $1p1h$ - $2p2h$  configuration mixing and ground-state correlations beyond RPA into account", *Proc. Int. Symp. on Non-Nucleonic Degrees of Freedom Detected in Nuclei (NNDF '96)*, Osaka, 1996-09, edited by T. Minamisono, Y. Nojiri, T. Sato, and K. Matsuta, World Scientific, pp. 361-364 (1997).
- H. Toki, K. Sumiyoshi, D. Hirata, Y. Sugahara, and I. Tanihata: "Relativistic many body theory for unstable nuclei and neutron stars", *Proc. Int. Symp. on Origin of Matter and Evolution of Galaxies in the Universe*, Atami, 1996, edited by T. Kajino, Y. Yoshii, and S. Kubono, World Scientific, pp. 367-374 (1997).
- N. Dinh Dang, A. Arima, T. Suzuki, and S. Yamaji: "Spreading of Gamow-Teller resonance in  $^{90}\text{Nb}$  and  $^{208}\text{Bi}$ ", *Proc. RIKEN Symp. on Giant Resonances*, Wako, 1997-01, edited by N. Dinh Dang and S. Yamaji, pp. 30-38 (1997).
- H. Kurasawa and T. Suzuki: "Double giant resonance states", *Proc. RIKEN Symp. on Giant Resonances*, Wako, 1997-01, edited by N. Dinh Dang and S.

- Yamaji, pp. 157–163 (1997).
- H. Kurasawa and T. Suzuki: “Landau damping of the Mie Plasmon”, *Soryushiron Kenkyu* **95**, B35–B38 (1997).
- J. Meng and P. Ring: “Relativistic Hartree-Bogoliubov description of lithium isotopes”, *Z. Phys. A* **358**, 123–124 (1997).
- K. Sugawara-Tanabe: “Magnetic dipole transitions in the superdeformed bands of  $^{193}\text{Tl}$ ”, *Z. Phys. A* **359**, 9–10 (1997).
- ### 3. Atomic and solid-state physics
- G. Tatara, M. Matsuda, K. Katsumata, T. Kambara, Y. Awaya, T. Mitamura, M. Terasawa, Y. Endoh, K. Yamada, and S. Hosoya: “Bose-glass transition in heavy-ion irradiated  $\text{La}_{1.85}\text{Sr}_{0.15}\text{CuO}_4$  single crystal”, *Czech. J. Phys.* **46**, s1555–s1556 (1996).
- Y. Kino, M. R. Harston, I. Shimamura, E. A. G. Armour, and M. Kamimura: “Asymptotic form of three-body  $(\text{dt}\mu)^+$  and  $(\text{dd}\mu)^+$  wave functions”, *Hyperfine Interact.* **101/102**, 325–328 (1996).
- Y. Yamazaki: “Multiply charged ions, hollow atoms, potential sputtering”, *Hyomen Kagaku* **18**, 752–758 (1997).
- R. Kadono, I. Watanabe, and K. Nagamine: “Quantum diffusion of positive muon in pure tantalum”, *Hyperfine Interact.* **105**, 233–237 (1997).
- R. Kadono, R. M. Macrae, K. Nagamine, and K. Nishiyama: “Mu centers in crystalline Ge under illumination”, *Hyperfine Interact.* **105**, 303–308 (1997).
- R. Kadono, R. M. Macrae, and K. Nagamine: “Muonium centers in heavily n-doped Si under illumination: Evidence for Mu-hole interaction”, *Hyperfine Interact.* **105**, 327–331 (1997).
- T. Kambara, A. Igarashi, N. Watanabe, Y. Nakai, T. M. Kojima, and Y. Awaya: “Recoil-ion momentum distribution of single-electron capture to the ground and excited states in 0.5–1 MeV/u  $\text{B}^{4+,5+}$ -He collisions”, *J. Phys. B: At. Mol. Opt. Phys.* **30**, 1251–1260 (1997).
- Y. Nakai, A. Itoh, T. Kambara, Y. Bitoh, and Y. Awaya: “The fragment ion distribution of  $\text{C}_{60}$  in close collision with fast carbon ions”, *J. Phys. B: At. Mol. Opt. Phys.* **30**, 3049–3058 (1997).
- R. Kadono: “Muon spin relaxation in disordered spinpeierls system: Evidence for modulated antiferromagnetic ordering in  $\text{Cu}_{1-\delta}\text{Zn}_\delta\text{GeO}_3$ ”, *J. Phys. Soc. Jpn.* **66**, 505–506 (1997).
- K. Kawatsura, M. Sataka, M. Imai, K. Komaki, Y. Yamazaki, K. Kuroki, Y. Kanai, S. Arai, and N. Stolterfoht: “Low-energy Rydberg electron spectra from 64 MeV  $\text{S}^{q+} + \text{He}$  and C-foil collisions using zero-degree electron spectroscopy”, *Nucl. Instrum. Methods Phys. Res. B* **124**, 381–385 (1997).
- H. Tawara, T. Azuma, T. Ito, K. Komaki, Y. Yamazaki, T. Matsuo, T. Tonuma, K. Shima, A. Kitagawa, and E. Takada: “X rays from radiative electron capture into continuum states in relativistic heavy-ion collisions”, *Phys. Rev. A* **55**, 808–811 (1997).
- I. Kink, R. Hutton, B. Nyström, I. Martinson, K. Ishii, K. Ando, T. Kambara, Y. Nakai, T. M. Kojima, and Y. Awaya: “Lifetime of the  $3p\ ^2P_{3/2}$  level in Na-like  $\text{Kr}^{25+}$ ”, *Phys. Rev. A* **55**, 3229–3232 (1997).
- M. R. Harston, S. Hara, Y. Kino, I. Shimamura, H. Sato, and M. Kamimura: “Effects of the finite size of the ion  $(\text{dd}\mu)^+$  on the energy levels of the molecules  $(\text{dd}\mu)\text{e}$  and  $(\text{dd}\mu)\text{dee}$ ”, *Phys. Rev. A* **56**, 2685–2691 (1997).
- V. I. Korobov and I. Shimamura: “Auger transition rates for metastable states of antiprotonic helium  $\text{He}^+\bar{p}$ ”, *Phys. Rev. A* **56**, 4587–4594 (1997).
- A. Igarashi and I. Shimamura: “S-wave resonances in positron scattering by  $\text{He}^+$ ”, *Phys. Rev. A* **56**, 4733–4736 (1997).
- R. Kadono, R. M. Macrae, K. Nishiyama, and K. Nagamine: “Evidence for muonium passivation in n-doped Ge”, *Phys. Rev. B* **55**, 4035–4038 (1997).
- A. Yamashita, K. Ishii, T. Yokoo, J. Akimitsu, M. Hedo, Y. Inada, Y. Onuki, E. Yamamoto, Y. Haga, and R. Kadono: “Anomalous field dependence of magnetic penetration depth in the vortex state of  $\text{CeRu}_2$ ”, *Phys. Rev. Lett.* **79**, 3771–3774 (1997).
- R. Hutton, I. Martinson, B. Nyström, K. Ando, Y. Awaya, P. K. Bengtsson, T. Kambara, Y. Kanai, T. M. Kojima, Y. Nakai, K. Ishii, and M. Jäger: “Intercombination transitions in beryllium-like and boron-like iron”, *Phys. Scr.* **55**, 431–433 (1997).
- K. Ishii, T. Nishida, Y. Kimura, M. Fujiwara, T. Nakano, S. Kawae, K. Ando, and T. Kambara: “Beam-foil spectra of highly-charged neon ions in visible region”, *Phys. Scr., Omiya*, 1996-09, edited by Y. Awaya and T. Kambara, Royal Swedish Academy of Sciences, **T73**, 73–74 (1997).
- K. Ishii, T. Nishida, Y. Kimura, S. Kawae, T. Nakano, K. Ando, and Y. Awaya: “Beam-foil spectra of highly-charged argon ions in visible region”, *Phys. Scr., Omiya*, 1996-09, edited by Y. Awaya and T. Kambara, Royal Swedish Academy of Sciences, **T73**, 75–76 (1997).
- P. K. Bengtsson, K. Ando, T. Kambara, Y. Awaya, and R. Hutton: “Intercombination lines in highly charged Al- and Si-like ions”, *Phys. Scr., Omiya*, 1996-09, edited by Y. Awaya and T. Kambara, Royal Swedish Academy of Sciences, **T73**, 81–82 (1997).
- T. Kambara: “Recoil-ion momentum spectroscopy of fast collisions with HCT”, *Phys. Scr., Omiya*, 1996-09, edited by Y. Awaya and T. Kambara, Royal Swedish Academy of Sciences, **T73**, 162–166 (1997).
- T. Mitamura, M. Terasawa, X. J. Fan, T. Kohara, K. Ueda, T. Kambara, Y. Awaya, M. Matsuda, G. Tatara, N. Takezawa, and K. Fukushima: “Swift heavy-ion irradiation effects on the superconducting material  $\text{La}_{1.85}\text{Sr}_{0.15}\text{CuO}_4$ ”, *Phys. Scr., Omiya*, 1996-09, edited by Y. Awaya and T. Kambara, Royal

- Swedish Academy of Sciences, **T73**, 337–339 (1997).
- M. Matsuda, G. Tatara, K. Katsumata, T. Kambara, Y. Awaya, T. Mitamura, M. Terasawa, K. Yamada, Y. Endoh, and S. Hosoya: “Swift heavy-ion irradiation effects on the single crystal  $\text{La}_{1.85}\text{Sr}_{0.15}\text{CuO}_4$ ”, Phys. Scr., Omiya, 1996-09, edited by Y. Awaya and T. Kambara, Royal Swedish Academy of Sciences, **T73**, 340–342 (1997).
- X. J. Fan, M. Terasawa, T. Mitamura, T. Kohara, K. Ueda, H. Tsubakino, T. Kambara, Y. Awaya, M. Matsuda, G. Tatara, K. Fukushima, and N. Takezawa: “Suppression of vortex motion in  $\text{La}_{1.85}\text{Sr}_{0.15}\text{CuO}_4$  with the splayed configuration of columnar defects”, Physica C **282/287**, 2105–2106 (1997).
- K. Kawatsura, H. Kageyama, R. Takahashi, D. Hamaguchi, S. Arai, Y. Aoki, S. Yamamoto, H. Takeshita, H. Naramoto, T. Kambara, M. Oura, Y. Kanai, and Y. Awaya: “Copper L X-ray spectra measured by a high resolution ion-induced X-ray spectrometer”, Radiat. Phys. Chem. **49**, 617–622 (1997).
4. Radiochemistry, radiation chemistry, and radiation biology
- R. Amano, S. Oishi, S. Enomoto, and F. Ambe: “Unique behavior of rubidium in mice under low oxygen atmosphere”, Ann. Clin. Lab. Sci. **27**, 358–364 (1997).
- R. Hirunuma, K. Endo, M. Yanaga, S. Enomoto, S. Ambe, A. Tanaka, M. Tozawa, and F. Ambe: “The use of a multitracer technique for studies of the uptake and retention trace elements in rats”, Appl. Radiat. Isot. **48**, 727–733 (1997).
- Y. Itoh, Z. Peng, K. Lee, M. Ishii, A. Goto, N. Nakanishi, M. Kase, and Y. Ito: “Slow positron beam production by irradiation of  $\text{p}^+$ ,  $\text{d}^+$ , and  $\text{He}^{2+}$  on various targets”, Appl. Surf. Sci. **116**, 68–72 (1997).
- M. Suzuki, Y. Kase, T. Kanai, F. Yatagai, and M. Watanabe: “LET dependence of cell death and chromatin-break induction in normal human cells irradiated by neon-ion beams”, Int. J. Radiat. Biol. **72**, 497–503 (1997).
- R. Hirunuma, N. Sotogaku, K. Endo, S. Enomoto, S. Ambe, and F. Ambe: “Application of the multitracer technique: Metabolic study of trace elements in Se-deficient rats”, J. Inorg. Biochem. **67**, 22 (1997).
- N. Sotogaku, R. Hirunuma, K. Endo, S. Enomoto, S. Ambe, and F. Ambe: “Study of the binding of various trace elements to blood components and serum proteins by mean of the multitracer technique”, J. Inorg. Biochem. **67**, 23 (1997).
- S. Enomoto, R. G. Weginwar, R. Hirunuma, S. Ambe, and F. Ambe: “Metabolic study of trace elements in acute alcoholic mice”, J. Inorg. Biochem. **67**, 27 (1997).
- S. Enomoto, B. Liu, S. Ambe, R. Amano, and F. Ambe: “Accumulation of inorganic elements in ddY mice implanted with *Ehrlich sarcoma*”, J. Inorg. Biochem. **67**, 28 (1997).
- N. Hayakawa, S. Enomoto, R. Hirunuma, K. Endo, S. Ambe, and F. Ambe: “Metabolic study of trace elements in liver cancer bearing rats”, J. Inorg. Biochem. **67**, 29 (1997).
- T. Ozaki, S. Enomoto, Y. Minai, S. Ambe, F. Ambe, and T. Tominaga: “Determination of lanthanides and other trace elements in ferns by instrumental neutron activation analysis”, J. Radioanal. Nucl. Chem. **217**, 117–124 (1997).
- B. Liu, S. Ambe, S. Enomoto, R. G. Weginwar, and F. Ambe: “Preparation of carrier-free group tracers from a gold target irradiated by high-energy heavy ions”, J. Radioanal. Nucl. Chem. **223**, 3–7 (1997).
- K. Eguchi-Kasai and H. Ohara: “Effect of particle irradiation on cell cycle progression”, Jpn. J. Cancer Clin. **43**, 201–204 (1997).
- T. Nozaki, Y. Itoh, Z. Peng, Y. Ito, N. Nakanishi, H. Yoshida, and A. Goto: “Preparation of positron source for slow positron beam by ion bombardment on liquid and gas targets”, Mater. Sci. Forum, **255/257**, 799–801 (1997).
- H. Wang, S. Ambe, N. Takematsu, and F. Ambe: “Model study of influence of acid rain on adsorptive behavior of trace elements on soil by the multitracer technique”, Proc. Int. Congr. of Acid Snow and Rain 1997, Niigata, 1997-10, edited by K. Aoyama, K. Katoh, T. Murano, T. Paces, and Y. Taguchi, pp. 363–368 (1997).
- H. Sasaki, F. Yatagai, T. Kanai, Y. Furusawa, F. Hanaoka, W. Zhu, and P. Mehnati: “Dependence of induction of interphase death of Chinese hamster ovary cells exposed to accelerated heavy ions on linear energy transfer”, Radiat. Res. **148**, 449–454 (1997).
- Y. Takahashi, Y. Minai, S. Ambe, Y. Makide, F. Ambe, and T. Tominaga: “Simultaneous determination of stability constants of humate complexes with various metal ions using multitracer technique”, Sci. Total Environ. **198**, 61–71 (1997).
- S. Enomoto, B. Liu, R. G. Weginwar, S. Ambe, and F. Ambe: “Distribution and pathological studies on rare-earth elements in non-insulin dependent diabetes mellitus mice”, Trace Elem. Man Anim. (Proc. Int. Symp. on Trace Elements in Man and Animals, 9th) **9**, 347–348 (1997).
- S. Enomoto, B. Liu, R. G. Weginwar, S. Ambe, and F. Ambe: “Multitracer study on the uptake of inorganic ions by tumor”, Trace Elem. Man Anim. (Proc. Int. Symp. on Trace Elements in Man and Animals, 9th) **9**, 363–364 (1997).
- S. Enomoto, R. G. Weginwar, B. Liu, S. Ambe, and F. Ambe: “Biodistribution of gold complexes in mice”, Trace Elem. Man Anim. (Proc. Int. Symp. on

Trace Elements in Man and Animals, 9th) **9**, 568–569 (1997).

## 5. Material analysis

Z. Peng, Y. Itoh, S. Q. Li, and S. Wang: “Study of ionic transport in polymer electrolyte using positron lifetime distribution method”, *Appl. Phys. A* **63**, 267–270 (1996).

Y. Itoh, H. Murakami, and A. Kinoshita: “Positron/positronium annihilation in low dimensional silicon materials”, *Appl. Surf. Sci.* **102**, 423–426 (1996).

K. Maeda, H. Hamanaka, and K. Hasegawa: “High resolution PIXE using crystal spectrometer combined with position sensitive detectors”, *Int. J. PIXE*, **6**, 97–116 (1996).

J. Kawai, H. Adachi, Y. Kitajima, K. Maeda, S. Hayakawa, and Y. Gohshi: “Inelastic mean free path of photoelectrons in Ag determined by total reflection X-ray photoelectron spectroscopy”, *Anal. Sci.* **13**, 797–801 (1997).

K. Maeda and K. Hasegawa: “High-resolution PIXE analysis using a position-sensitive crystal spectrometer”, *Ioniz. Radiat. (Tokyo)* **23**, 9–19 (1997).

W. Hong, S. Hayakawa, K. Maeda, S. Fukuda, M. Yanokura, M. Aratani, K. Kimura, Y. Gohshi, and I. Tanihata: “Improvement in the detection limits

of elastic recoil detection analysis (ERDA) using a time-of-flight detection”, *Jpn. J. Appl. Phys.* **36**, L952–L954 (1997).

W. Hong, S. Hayakawa, K. Maeda, S. Fukuda, M. Yanokura, M. Aratani, K. Kimura, Y. Gohshi, and I. Tanihata: “Determination of the mass resolution and the depth resolution of time of flight elastic recoil detection analysis using heavy ion beams”, *Jpn. J. Appl. Phys.* **36**, 5737–5740 (1997).

Y. Itoh, H. Murakami, H. Takeno, S. Ushio, and T. Takenaka: “Positron lifetime in floating-zone-grown silicon water”, *Mater. Sci. Forum*, **255/257**, 545–547 (1997).

W. Hong, S. Hayakawa, K. Maeda, S. Fukuda, M. Yanokura, M. Aratani, K. Kimura, Y. Gohshi, and I. Tanihata: “Development of a high mass-resolution TOF-ERDA system for a wide mass range”, *Nucl. Instrum. Methods Phys. Res. B* **124**, 95–99 (1997).

K. Maeda: “Water analysis by PIXE”, *Proc. 34th Seminar on Science and Technology, Small Accelerators & Their Application, Tokyo, 1997-02, Interchange Association*, pp. 171–178 (1997).

H. Hamanaka, K. Hasegawa, and K. Maeda: “Application of a position-sensitive X-ray detector to high-resolution PIXE measurements”, *Proc. 34th Seminar on Science and Technology, Small Accelerators & Their Application, Tokyo, 1997-02, Interchange Association*, pp. 295–300 (1997).

## VIII. LIST OF PREPRINTS

1997

RIKEN-AF-NP

- 249 N. Hayashi, Y. Goto, and N. Saito: “Possible measurements of the gluon polarization in the nucleon with PHENIX detector system”
- 250 Y. Mochizuki, K. Oyamatsu, and T. Izuyama: “Exotic nuclear rod formation induced by superfluid vortices in neutron star crusts”
- 251 N. Saito: “Spin physics at RHIC”
- 252 V. G. Soloviev, A. Arima, and N. Dinh Dang: “On a possible enhancement of the E1 decay rates of double giant dipole states”
- 253 K. K. Korshennikov, E. A. Kuzmin, E. Yu. Nikolskii, O. V. Bochkarev, S. Fukuda, S. A. Goncharov, S. Ito, T. Kobayashi, S. Momota, B. G. Novatskii, A. A. Ogloblin, A. Ozawa, V. Privora, I. Tanihata, and K. Yoshida: “The  $L = 1$  excitation in the halo nucleus  $^{11}\text{Li}$ ”
- 254 T. Suzuki and T. Otsuka: “Gamow-Teller transitions from  $^{11}\text{Li}$  and  $^{12}\text{Be}$ ”
- 255 N. Dang, A. Arima, V. G. Soloviev, and S. Yamaji: “Possible deviation of the sum of strengths for double giant dipole resonance from harmonic oscillators’s limit”
- 256 T. Teranishi, S. Shimoura, Y. Ando, M. Hirai, N. Iwasa, T. Kikuchi, S. Moriya, T. Motobayashi, H. Murakami, T. Nakamura, T. Nishio, H. Sakurai, T. Uchibori, Y. Watanabe, Y. Yanagisawa, and M. Ishihara: “Isobaric analog state of  $^{11}\text{Li}$ ”
- 257 K. Varga and Y. Suzuki: “Solution of few-body problems with the stochastic variational method: I. Central forces”
- 258 L. Ya. Glozman, W. Plessas, K. Varga, and R. F. Wagenbrunn: “Unified description of light- and strange-baryon spectra”
- 259 J. Meng, I. Tanihata, and S. Yamaji: “The proton and neutron distribution in Na isotopes: The development of halo and shell structure”
- 260 H. Kurasawa and T. Suzuki: “Nuclear response to electromagnetic field”
- 261 H. Kurasawa: “Double giant resonance states”
- 262 H. Kurasawa and T. Suzuki: “Nuclear medium effects to be observed and not to be observed”
- 263 H. Kurasawa and T. Suzuki: “The continuity equation of RPA”
- 264 H. Kurasawa, K. Yabana, and T. Suzuki: “Damping width of the Mie Plasmon”
- 265 M. R. Ahmady, E. Kou, and A. Sugamoto: “Intermediate pseudoscalar resonance contributions to  $B \rightarrow Xs, \gamma, \gamma$ ”
- 266 Y. S. Mochizuki, T. Izuyama, and I. Tanihata: “Dynamics of exotic nuclear rod formation for neutron star glitches”
- 267 K. Oyamatsu, I. Tanihata, Y. Sugahara, K. Sumiyoshi, and H. Toki: “Can the equation of state of asymmetric nuclear matter be studied using unstable nuclei?”

- 268 D. Hirata, K. Sumiyoshi, I. Tanihata, Y. Sugahara, and H. Toki: “Systematic study of even-even nuclei up to the drip lines in terms of relativistic many body framework”
- 269 N. D. Dang and A. Arima: “Quantal and thermal dampings of giant dipole resonance in  $^{90}\text{Zr}$ ,  $^{120}\text{Sn}$  and  $^{208}\text{Pb}$ ”
- 270 N. D. Dang and A. Arima: “Temperature dependence of quantal and thermal dampings of the hot giant dipole resonance”
- 271 M. Oi, N. Onishi, N. Tajima, and T. Horibata: “Signature and angular momentum in 3d-creaked HFB states”
- 272 J. Meng, K. Sugawara-Tanabe, S. Yamaji, P. Ring, and A. Arima: “The pseudo-spin symmetry in realistic nuclei”
- 273 N. D. Dang and F. Sakata: “Relation between the damping hot giant dipole resonance and the complex admittance of an irreversible process”
- 274 M. R. Ahmady, E. Kou, and A. Sugamoto: “Non-spectator contribution: A mechanism for inclusive  $B \rightarrow Xsn'$  and exclusive  $B \rightarrow K(*)n'$  decays”
- 275 H. Okamura, S. Ishihara, N. Sakamoto, H. Otsu, T. Uesaka, T. Wakasa, Y. Satou, H. Sakai, T. Niizeki, H. Ohmura, and T. Ichihara: “Detector system of the first focal-plane of the spectrometer SMART at RIKEN”
- 276 A. Arima: “Dynamical symmetries and nuclear structure”
- 277 S. Nagataki, M. Hashimoto, K. Sato, S. Yamada, and Y. S. Mochizuki: “High ratio of  $^{44}\text{Ti}/^{56}\text{Ni}$  in Cas A and axiaymmetric collapse-driven supernova explosion”

#### RIKEN-AF-NC

- 1 T. Katayama, Y. Batygin, N. Inabe, K. Ohtomo, T. Ohkawa, M. Takanaka, M. Wakasugi, S. Watanabe, Y. Yano, K. Yoshida, J. Xia, Y. Rao, and Y. Yuan: “Muses project at RIKEN RI Beam Factory”
- 2 I. Meshkov: “Physics and technique of electron cooling”
- 3 Y. K. Batygin and T. Katayama: “Noise instability in nonlinear beam-beam interaction”

## IX. PAPERS PRESENTED AT MEETINGS

### 1. Accelerator development and accelerator physics

- Y. Yano: "RI Beam Factory and its expected pioneering work", 22nd Japan Conf. on Radiation and Radioisotopes, Yokohama, Dec. (1996).
- A. Goto, T. Kubo, H. Okuno, T. Kawaguchi, T. Mitsumoto, T. Tominaka, S. Fujishima, J. W. Kim, K. Ikegami, N. Sakamoto, S. Yokouchi, T. Morikawa, Y. Tanaka, and Y. Yano: "The Superconducting Ring Cyclotrons for RIKEN RI Beam Factory", 16th RCNP Osaka Int. Symp. on Multi-GeV High-Performance Accelerators and Related Technology, (RCNP, Osaka Univ.), Osaka, Mar. (1997).
- J. W. Kim: "Accelerator technology at RIKEN", Symp. on Accelerator Transmutation Technology '97, (Electrical Engineering and Science Research Institute), Seoul, Korea, Apr. (1997).
- M. Takanaka and T. Katayama: "Simulation of beam bunching with electron cooling for the ion storage ring of RIKEN RI-Beam Factory Project", 1997 Particle Accelerator Conf. (PAC '97), (TRIUMF), Vancouver, Canada, May (1997).
- T. Kawaguchi, T. Kubo, T. Mitsumoto, H. Okuno, T. Tominaka, J. W. Kim, S. Fujishima, K. Ikegami, N. Sakamoto, S. Yokouchi, T. Morikawa, Y. Tanaka, A. Goto, and Y. Yano: "Design of the sector magnets for the RIKEN Superconducting Ring Cyclotron", 1997 Particle Accelerator Conf. (PAC '97), (TRIUMF), Vancouver, Canada, May (1997).
- Y. Yano, A. Goto, and T. Katayama: "RIKEN RI-Beam Factory Project", 1997 Particle Accelerator Conf. (PAC '97), (TRIUMF), Vancouver, Canada, May (1997).
- T. Tominaka, M. Okamura, and T. Katayama: "Analytical field calculation of helical dipole magnets for RHIC", 1997 Particle Accelerator Conf. (PAC '97), (TRIUMF), Vancouver, Canada, May (1997).
- T. Tominaka, K. Hatanaka, and T. Katayama: "Multiple expansion for a single helical current conductor", 1997 Particle Accelerator Conf. (PAC '97), (TRIUMF), Vancouver, Canada, May (1997).
- T. Tominaka, H. Okuno, S. Fujishima, T. Mitsumoto, T. Kubo, T. Kawaguchi, Y. Tanaka, J. W. Kim, K. Ikegami, N. Sakamoto, S. Yokouchi, T. Morikawa, A. Goto, and Y. Yano: "Design study of the injection and extraction elements for the RIKEN Superconducting Ring Cyclotron", 1997 Particle Accelerator Conf. (PAC '97), (TRIUMF), Vancouver, Canada, May (1997).
- T. Mitsumoto, A. Goto, T. Kawaguchi, J. W. Kim, Y. Tanaka, T. Kubo, H. Okuno, T. Tominaka, S. Fujishima, K. Ikegami, N. Sakamoto, T. Morikawa, S. Yokouchi, and Y. Yano: "Orbit analysis for the RIKEN Superconducting Ring Cyclotron", 1997 Particle Accelerator Conf. (PAC '97), (TRIUMF), Vancouver, Canada, May (1997).
- S. Fujishima, H. Okuno, T. Tominaka, T. Mitsumoto, T. Kubo, T. Kawaguchi, J. W. Kim, K. Ikegami, N. Sakamoto, S. Yokouchi, T. Morikawa, Y. Tanaka, A. Goto, and Y. Yano: "Numerical analyses of the injection and extraction trajectories for the RIKEN Superconducting Ring Cyclotron", 1997 Particle Accelerator Conf. (PAC '97), (TRIUMF), Vancouver, Canada, May (1997).
- O. Kamigaito, A. Goto, Y. Miyazawa, T. Chiba, M. Hemmi, M. Kase, S. Kohara, Y. Batygin, and Y. Yano: "Acceleration test of the folded-coaxial RFQ linac for the RILAC", 1997 Particle Accelerator Conf. (PAC '97), (TRIUMF), Vancouver, Canada, May (1997).
- O. Kamigaito, A. Goto, Y. Miyazawa, T. Chiba, M. Hemmi, S. Kohara, M. Kase, T. Nakagawa, Y. Batygin, Y. Yano, E. Ikezawa, T. Aihara, T. Ohki, H. Hasebe, and H. Yamauchi: "Acceleration tests of the folded-coaxial RFQ for the RILAC", 22nd Linear Accelerator Meet. in Japan, (Tohoku Univ.), Sendai, Sept. (1997).
- Y. Mizutani, K. Hori, T. Yamamoto, M. Miki, Y. Izumi, S. Seki, T. Kozawa, K. Ushida, Y. Yoshida, and S. Tagawa: "Development of a pulse radiolysis system by using picosecond electron pulses and femtosecond laser pulses", 22nd Linear Accelerator Meet. in Japan, (Tohoku Univ.), Sendai, Sept. (1997).
- M. Kase, M. Kobayashi, A. Yoneda, and I. Yokoyama: "Beam diagnostic instruments for RIKEN Ring Cyclotron", 3rd European Workshop on Beam Diagnostics and Instrumentation for Particle Accelerators, (LNF-INFN Frascati), Frascati, Italy, Oct. (1997).
- T. Kawaguchi, J. W. Kim, T. Kubo, Y. Imai, and T. Minato: "A 6T He-free superconducting solenoid for RI beam production", 15th Int. Conf. on Magnet Technology (MT15), (Institute of Electrical Engineering), Beijing, China, Oct. (1997).
- T. Kawaguchi, T. Kubo, T. Mitsumoto, H. Okuno, T. Tominaka, J. W. Kim, S. Fujishima, K. Ikegami, N. Sakamoto, S. Yokouchi, T. Morikawa, Y. Tanaka, A. Goto, and Y. Yano: "Design of the sector magnets for the RIKEN Superconducting Ring Cyclotron", 15th Int. Conf. on Magnet Technology (MT15), (Institute of Electrical Engineering), Beijing, China, Oct. (1997).
- T. Tominaka, H. Okuno, S. Fujishima, A. Goto, and Y. Yano: "Relation between field homogeneity and multipole coefficients for dipole coils", 15th Int. Conf. on Magnet Technology (MT15), (The Institute of Electrical Engineering), Beijing, China, Oct. (1997).
- M. Takanaka and T. Katayama: "Simulation of beam bunching using electron cooling for the ion storage ring of RIKEN RI-Beam Factory Project",

- 11th Symp. on Accelerator Science and Technology, (JASRI), Harima, Oct. (1997).
- Y. Yano, A. Goto, and T. Katayama: "RIKEN RI-Beam Factory Project", 11th Symp. on Accelerator Science and Technology, (JASRI), Harima, Oct. (1997).
- O. Kamigaito, A. Goto, Y. Miyazawa, T. Chiba, M. Hemmi, M. Kase, S. Kohara, T. Nakagawa, E. Ikezawa, Y. Batygin, and Y. Yano: "Acceleration tests of the folded-coaxial RFQ linac for the RILAC", 11th Symp. on Accelerator Science and Technology, (JASRI), Harima, Oct. (1997).
- N. Fukunishi, M. Kobayashi, A. Yoneda, M. Kidera, M. Kase, and Y. Yano: "Heavy ion microbeam project in RIKEN Ring Cyclotron", 11th Symp. on Accelerator Science and Technology, (JASRI), Harima, Oct. (1997).
- A. Yoneda, H. Kumagai, M. Kobayashi, M. Kidera, M. Kase, A. Goto, and Y. Yano: "New emittance measurement using two PPACs", 11th Symp. on Accelerator Science and Technology, (JASRI), Harima, Oct. (1997).
- M. Kase, A. Goto, T. Kageyama, I. Yokoyama, M. Nagase, S. Kohara, T. Nakagawa, N. Inabe, K. Ikegami, O. Kamigaito, M. Kidera, J. Fujita, and Y. Yano: "Status report on RIKEN Ring Cyclotron", 11th Symp. on Accelerator Science and Technology, (JASRI), Harima, Oct. (1997).
- M. Kobayashi, A. Yoneda, M. Kase, M. Kidera, A. Goto, and Y. Yano: "Phase stabilization of injection beam to RIKEN Ring Cyclotron", 11th Symp. on Accelerator Science and Technology, (JASRI), Harima, Oct. (1997).
- T. Mitsumoto, A. Goto, T. Kawaguchi, J. W. Kim, Y. Tanaka, T. Kubo, H. Okuno, T. Tominaka, S. Fujishima, K. Ikegami, N. Sakamoto, T. Morikawa, S. Yokouchi, K. Sugii, and Y. Yano: "Orbit analysis for the RIKEN Superconducting Ring Cyclotron", 11th Symp. on Accelerator Science and Technology, (JASRI), Harima, Oct. (1997).
- S. Fujishima, H. Okuno, T. Tominaka, T. Mitsumoto, T. Kubo, T. Kawaguchi, J. W. Kim, K. Ikegami, N. Sakamoto, K. Sugii, T. Morikawa, Y. Tanaka, T. Wada, A. Goto, and Y. Yano: "Analysis of the injection and extraction trajectories in the RIKEN Superconducting Ring Cyclotron", 11th Symp. on Accelerator Science and Technology, (JASRI), Harima, Oct. (1997).
- S. Kohara, Y. Miyazawa, O. Kamigaito, and A. Goto: "Design of a resonator for a flat-top acceleration system in the RIKEN AVF Cyclotron", 11th Symp. on Accelerator Science and Technology, (JASRI), Harima, Oct. (1997).
- Y. Mizutani, K. Hori, T. Yamamoto, M. Miki, Y. Izumi, S. Seki, T. Kozawa, K. Ushida, Y. Yoshida, and S. Tagawa: "Development of a pulse radiolysis system by using picosecond electron pulses and femtosecond laser pulses", 11th Symp. on Accelerator Science and Technology, (JASRI), Harima, Oct. (1997).
- Y. Mizutani, K. Hori, T. Yamamoto, M. Miki, Y. Izumi, S. Seki, T. Kozawa, K. Ushida, Y. Yoshida, and S. Tagawa: "Development of a pulse radiolysis system by using picosecond electron pulses and femtosecond laser pulses", 40th Symp. on Radiation Chemistry, (Radiation Chemical Society of Japan), Tokaimura, Oct. (1997).
- T. Kawaguchi, H. Okuno, A. Goto, Y. Yano, and B. Ikeda: "Quench stabilities of Al stabilized superconducting wires for a superconducting ring cyclotron", 57th Meet. on Cryogenics and Superconductivity, (Cryogenics and Superconductivity Engineering Conference of Japan), Takamatsu, Nov. (1997).
- T. Tominaka, T. Kawaguchi, M. Okamura, and T. Katayama: "Magnetic measurement of a helical dipole magnet", 57th Meet. on Cryogenics and Superconductivity, (Cryogenics and Superconductivity Engineering Conference of Japan), Takamatsu, Nov. (1997).
- T. Tominaka, H. Okuno, S. Fujishima, A. Goto, and Y. Yano: "Relation between field uniformity and multipole coefficients", 57th Meet. on Cryogenics and Superconductivity, (Cryogenics and Superconductivity Engineering Conference of Japan), Takamatsu, Nov. (1997).

## 2. Nuclear physics and nuclear instrumentation

- H. Kurasawa and T. Suzuki: "Double giant resonance states", RIKEN Symp. on Giant Resonances, Wako, Jan. (1997).
- M. Kobayashi, T. Doke, J. Kikuchi, T. Hayashi, T. Takashima, N. Takehana, H. Shirai, N. Hasebe, K. Kondoh, T. Kashiwagi, T. Yanagimachi, A. Nakamoto, H. Murakami, T. Kohno, K. Munakata, C. Kato, S. Yanagita, Y. Yamada, and M. Ehara: "A relation between solar wind and CIR particles observed by GEOTAIL satellite", 52nd Ann. Meet. of Physical Society of Japan, Nagoya, Mar. (1997).
- R. Susukita: "Observation by means of arrival times of Cherenkov protons using the CANGAROO telescope", 52nd Ann. Meet. of Physical Society of Japan, Nagoya, Mar. (1997).
- I. Imaida, Y. Muraki, Y. Matsubara, K. Masuda, T. Sako, T. Goka, H. Matsumoto, T. Omoto, Y. Fujiwara, K. Taguchi, M. Nakazawa, I. Tanaka, M. Fujii, T. Kohno, and H. Ikeda: "Accelerator beam experiment of multi-anode neutron sensor", 52nd Ann. Meet. of Physical Society of Japan, Nagoya, Mar. (1997).
- T. Takashima, T. Doke, J. Kikuchi, T. Hayashi, M. Kobayashi, N. Takehana, H. Shirai, S. Miyatani, N. Hasebe, K. Kondoh, T. Kashiwagi, T. Yanagimachi, A. Nakamoto, H. Murakami, T. Kohno, K. Munakata, C. Kato, S. Yanagita, Y. Yamada, and M.

- Ehara: "Time variation of particle (10-30 MeV/n) intensity observed by GEOTAIL-HEP", 52nd Ann. Meet. of Physical Society of Japan, Nagoya, Mar. (1997).
- H. Kurasawa and T. Suzuki: "Nuclear medium effects to be observed and not to be observed", Int. Workshop on Nuclear Medium Effect via Nucleon Induced Reaction, (RCNP, Osaka Univ.), Kyoto, Mar. (1997).
- H. Kurasawa, K. Yabana, and T. Suzuki: "The width of the Mie Plasmon", Structure of Atomic Clusters, (Kyoto Univ.), Kyoto, Mar. (1997).
- Y. Watanabe: "Survey of DVD as a large scale data storage system", Computing Research Center Seminar, (KEK), Tsukuba, May (1997).
- E. Kim, T. Nakamura, Y. Uwamino, M. Imamura, N. Nakao, and S. Tanaka: "Neutron activation cross sections of  $^{12}\text{C}$ ,  $^{27}\text{Al}$ ,  $^{59}\text{Co}$ ,  $^{\text{nat}}\text{Cu}$  and  $^{209}\text{Bi}$  nuclides in the energy range of 20 MeV to 200 MeV", Int. Conf. on Nuclear Data for Science and Technology, (Nuclear Data Centre, ENEA ICTP), Trieste, Italy, May (1997).
- N. Nishimori, K. Sagara, T. Fujita, H. Akiyoshi, H. Nakamura, and T. Nakashima: "Precise experiment on  $\bar{n}+d$  scattering at 12 MeV", 15th Int. Conf. on Few-Body Problems in Physics, (KVI), Groningen, The Netherlands, July (1997).
- T. Kohno, I. Yamagiwa, H. Miyasaka, T. Goka, and H. Matsumoto: "Observation of heavy ions with ADEOS satellite", 25th Int. Cosmic Ray Conf., (International Union of Pure and Applied Physics), Durban, South Africa, July (1997).
- T. Takashima, T. Doke, T. Hayashi, J. Kikuchi, K. Isumi, M. Kobayashi, H. Shirai, N. Takehana, N. Hasebe, K. Kondoh, T. Kohno, K. Munakata, C. Kato, S. Yanagita, Y. Yamada, D. Reames, and T. von Rosenvinge: "The first observation of sulfur in anomalous cosmic rays by the GEOTAIL and the WIND spacecrafts", 25th Int. Cosmic Ray Conf., (International Union of Pure and Applied Physics), Durban, South Africa, July (1997).
- G. I. Pugacheva, A. A. Gusev, T. Kohno, I. M. Martin, W. Spjeldvik, and T. Almand: "The 1-9 MeV/nucleon He flux dynamics in the inner magnetosphere during 1984-1986", 25th Int. Cosmic Ray Conf., (International Union of Pure and Applied Physics), Durban, South Africa, July (1997).
- Y. Muraki, K. Masuda, Y. Matsubara, T. Sako, I. Imaida, H. Tsuchiya, T. Kohno, T. Goka, H. Matsumoto, T. Omoto, Y. Fujiwara, K. Taguchi, M. Nakazawa, I. Tanaka, M. Fujii, and H. Ikeda: "Scintillation fiber telescope for detecting neutrons in a satellite experiment", 25th Int. Cosmic Ray Conf., (International Union of Pure and Applied Physics), Durban, South Africa, July (1997).
- T. Uesaka, H. Okamura, T. Ohnishi, Y. Satou, S. Ishida, N. Sakamoto, H. Otsu, T. Wakasa, T. Nonaka, G. Yokoyama, K. Sekiguchi, K. Ito, T. Wakui, M. Wakasugi, Y. Yano, S. Haruyama, T. Ikeda, and H. Sakai: "Measurement of polarization correlation coefficient for the  $^3\text{He}(\vec{d}, p)^4\text{He}$  reaction", 4th Int. Symp. Deuteron '97, (Joint Institute for Nuclear Research), Dubna, Russia, July (1997).
- K. Sugawara-Tanabe and K. Tanabe: "Doubly periodic motion in superdeformed states and  $\Delta I = 2$  staggering", Int. Symp. on Symmetries in Science X, (Technische Univ. Clausthal and Technische Univ. Graz), Bregenz, Austria, July (1997).
- K. Yoneda, N. Aoi, H. Iwasaki, H. Sakurai, H. Ogawa, T. Nakamura, W.-D. Schmidt-Ott, M. Shaefer, M. Notani, N. Fukuda, E. Ideguchi, T. Kishida, S. S. Yamamoto, and M. Ishihara: "Measurement of half-lives and delayed neutron emission probabilities of light nuclei near the drip line ( $Z = 5 \sim 7$ )", 1997 Fall Meet. of Physical Society of Japan, Hachioji, Sept. (1997).
- K. Sugawara-Tanabe, N. Yoshida, and A. Arima: "Deformation effect on the pairing interaction", 1997 Fall Meet. of Physical Society of Japan, Hachioji, Sept. (1997).
- T. Horibata, M. Oi, and N. Onishi: "Constrained GCM Calculation based on 3D-CHFB", 1997 Fall Meet. of Physical Society of Japan, Hachioji, Sept. (1997).
- T. Horibata, M. Oi, and N. Onishi: "GCM calculation in which the expectation values of angular momentum and particle number are conserved", 1997 Fall Meet. of Physical Society of Japan, Hachioji, Sept. (1997).
- M. Oi, N. Onishi, N. Tajima, and T. Horibata: "Tilted axis rotating states of Osmium182", 1997 Fall Meet. of Physical Society of Japan, Hachioji, Sept. (1997).
- J. Meng, K. Sugawara-Tanabe, S. Yamaji, P. Ring, and A. Arima: "Pseudo-spin symmetry in realistic nuclei", 1997 Fall Meet. of Physical Society of Japan, Hachioji, Sept. (1997).
- S. Ishida, Y. Satou, H. Sakai, H. Okamura, H. Otsu, N. Sakamoto, T. Uesaka, T. Wakasa, T. Ohnishi, T. Nonaka, G. Yokoyama, T. Niizeki, T. Ichihara, K. Hatanaka, and N. Nishimori: "Measurement of the spin transfer observables via the  $^{12}\text{C}(d, d')$  reaction", 1997 Fall Meet. of Physical Society of Japan, Hachioji, Sept. (1997).
- N. Kawamura, K. Nagamine, T. Matsuzaki, K. Ishida, S. N. Nakamura, S. Sakamoto, M. Tanase, M. Kato, K. Kurosawa, K. Kudoh, N. Takeda, and G. H. Eaton: "Muon catalyzed fusion experiment for D-T system at RIKEN-RAL Muon Facility (6) Fusion neutron measurement", 1997 Fall Meet. of Physical Society of Japan, Hachioji, Sept. (1997).
- K. Ishida, K. Nagamine, T. Matsuzaki, S. N. Nakamura, N. Kawamura, S. Sakamoto, M. Tanase, M. Kato, K. Kurosawa, K. Kudoh, N. Takeda, and G. H. Eaton: "Muon catalyzed fusion experiment for DT system at RIKEN-RAL Muon Facility (7) Alpha sticking X-ray measurement", 1997 Fall Meet.

- of Physical Society of Japan, Hachioji, Sept. (1997).
- K. Sumiyoshi, S. Yamada, H. Suzuki, and W. Hillebrandt: "Explosion of neutron star with minimum mass and r-process", 1997 Fall Meet. of Physical Society of Japan, Hachioji, Sept. (1997).
- H. Kurasawa and T. Suzuki: "Double giant resonance states", Tours Symp. on Nuclear Physics III, (University of Tours), Tours, France, Sept. (1997).
- T. Horibata, M. Oi, and N. Onishi: "Constraint GCM + 3-dimensional cranked HFB", 3rd Workshop for Physics of RI Beam Factory: Mean Field in Unstable Nuclei, Wako, Nov. (1997).
- K. Sumiyoshi: "Mean-field frameworks for astrophysics", 3rd Workshop for Physics of RI Beam Factory: Mean Field in Unstable Nuclei, Wako, Nov. (1997).
- T. Nakamura: "Radioactive ion beam research at RIKEN", Int. Conf. on Fission and Properties of Neutron-rich Nuclei, (Vanderbilt University), Sanibel Island, U.S.A., Nov. (1997).
- K. Sumiyoshi, B. Carlson, I. Tanihata, Y. Sugahara, S. Sugimoto, H. Toki, and D. Hirata: "Ground state properties of unstable nuclei in the relativistic mean field framework", Int. Symp. on Innovative Computational Methods in Nuclear Many-Body Problems, (RCNP, Osaka Univ.), Osaka, Nov. (1997).
- H. Kurasawa and T. Suzuki: "Spin dipole states of deformed nuclei", Int. Symp. on New Facet of Spin Giant Resonances in Nuclei, (Univ. Tokyo), Tokyo, Nov. (1997).
- S. Ishida, Y. Satou, H. Sakai, H. Okamura, H. Otsu, N. Sakamoto, T. Uesaka, T. Wakasa, T. Ohnishi, T. Nonaka, G. Yokoyama, T. Niizeki, T. Ichihara, K. Hatanaka, and N. Nishimori: "Study of isoscalar spin strength via the  $^{12}\text{C}(\vec{d}, \vec{d}')$  reaction", Int. Symp. on New Facet of Spin Giant Resonances in Nuclei, (Univ. Tokyo), Tokyo, Nov. (1997).
- Y. Mizoi, T. Fukuda, Y. Matsuyama, T. Miyachi, H. Miyatake, N. Aoi, N. Fukuda, M. Notani, Y. Watanabe, K. Yoneda, H. Sakurai, Y. Watanabe, A. Yoshida, and M. Ishihara: "Measurement of cross sections of the  $^8\text{Li}(\alpha, n)^{11}\text{B}$  reaction and the  $^8\text{Li}(\alpha, \alpha n)^7\text{Li}$  reaction with the new MUSIC detector", Int. Symp. on Origin of Matter and Evolution of Galaxies '97, (CNS, Univ. Tokyo), Atami, Nov. (1997).
- K. Sumiyoshi, S. Yamada, H. Suzuki, and W. Hillebrandt: "Explosion of a neutron star just below the minimum mass", Int. Symp. on Origin of Matter and Evolution of Galaxies '97, (CNS, Univ. Tokyo), Atami, Nov. (1997).
- K. Sumiyoshi, H. Suzuki, S. Yamada, and W. Hillebrandt: "The fate of a neutron star just below the minimum mass", Neutron Stars and Pulsars: Thirty Years after the Discovery, (Rikkyo Univ.), Tokyo, Nov. (1997).
- ### 3. Atomic and solid-state physics
- T. Kambara: "Three dimensional recoil-ion momentum spectroscopy for atomic collision studies", RIKEN Symp. on Studies on Condensed Matter Physics, Atomic Physics, Nuclear Chemistry, and Biology and Medicine Using RIKEN Accelerators, Wako, Feb. (1997).
- N. Ishikawa, Y. Chimi, A. Iwase, K. Tsuru, O. Michikami, T. Kambara, T. Mitamura, Y. Awaya, and M. Terasawa: "Velocity effects on defect production in ion-irradiated high-Tc superconductors", 52nd Ann. Meet. of Physical Society of Japan, Nagoya, Mar. (1997).
- D. Chiba, T. Takayanagi, K. Wakiya, Y. Kanai, T. Kambara, and Y. Awaya: "Measurement of angular distribution for emitted electrons with toroidal spectrometer (II)", 52nd Ann. Meet. of Physical Society of Japan, Nagoya, Mar. (1997).
- M. Kokubu, E. Idesawa, T. Kamae, A. Kubota, Y. Saito, M. Tashiro, Y. Fukazawa, K. Makishima, K. Matsuzaki, T. Mizuno, J. Kataoka, T. Takahashi, K. Takizawa, A. Yoshida, and HXD Team: "An activation testing of GSO, BGO scintillators for cosmic hard X-ray detectors", 52nd Ann. Meet. of Physical Society of Japan, Nagoya, Mar. (1997).
- E. Yagi: "Application of accelerators in materials researches", Center for Advanced Research of Energy Technology Symp., Hokkaido University, Sapporo, Mar. (1997).
- E. Yagi: "Materials researches with accelerators", Hasiguti Memorial Symp., Tokyo, Mar. (1997).
- E. Yagi: "Solid krypton formation in aluminium and state of hydrogen dissolved in metals investigated by the channelling method", 1st TESLA Workshop on Modification of Materials by Ion Beams, (TESLA Scientific Center), Beograd, Yugoslavia, Apr. (1997).
- E. Yagi: "Formation of heavy inert gas bubbles in metals", 13th Int. Conf. on Ion Beam Analysis (IBA-13), Lisbon, Portugal, July (1997).
- A. Igarashi and I. Shimamura: "S-wave resonances in  $e^+ + \text{He}^+$  scattering", 22nd Ann. Meet. of Society for Atomic Collision Research, Kyoto, Aug. (1997).
- T. Ichioka, Y. Yamazaki, K. Komaki, T. Azuma, and K. Kuroki: "Atomic physics with ultra slow antiprotons", 22nd Ann. Meet. of Society for Atomic Collision Research, Kyoto, Aug. (1997).
- M. Kitajima, Y. Nakai, Y. Kanai, Y. Yamazaki, Y. Awaya, and Y. Itoh: "Present status of the low energy multi-charged ion-atom collision experiment using the RIKEN ECRIS", 22nd Ann. Meet. of Society for Atomic Collision Research, Kyoto, Aug. (1997).
- S. Ninomiya, Y. Yamazaki, K. Komaki, T. Azuma, H. Masuda, F. Koike, K. Kuroki, and M. Sekiguchi: "Interaction of slow highly charged ions with a microcapillary Ni foil", 22nd Ann. Meet. of Society for Atomic Collision Research, Kyoto, Aug. (1997).
- T. Kambara, Y. Nakai, T. M. Kojima, Y. Awaya, I.

- Shimamura, V. Mergel, H. Schmidt-Böcking, B. D. DePaola, and M. Kimura: "Differential cross section of single electron capture in 10 MeV Ar<sup>8+</sup>+He collisions", 22nd Ann. Meet. of Society for Atomic Collision Research, Kyoto, Aug. (1997).
- T. Miyabe, H. Tsuchida, M. Imai, A. Itoh, N. Imanishi, Y. Nakai, and T. Kambara: "Fragment Process of C<sub>60</sub> by fast charged particles II", 22nd Ann. Meet. of Society for Atomic Collision Research, Kyoto, Aug. (1997).
- S. Koike, E. Yagi, and H. Kojima: "The terminal solubility curves of hydrogen in Nb-Mo (3 at%) alloys", 1997 Fall Meet. of Japan Institute of Metals, Sendai, Sept. (1997).
- T. Kambara: "Atomic physics at the planned new RIKEN Facility", 3rd Euroconference on Atomic Physics with Stored Highly Charged Ions, Ferrara, Italy, Sept. (1997).
- Y. Kobayashi, Y. Yoshida, K. Hayakawa, K. Yukihiro, J. Nakamura, H. Haesslein, R. Sielemann, S. Nasu, N. Inabe, Y. Watanabe, A. Yoshida, M. Kase, A. Goto, Y. Yano, E. Yagi, and F. Ambe: "In-beam Mössbauer spectrometers for materials science at RIKEN Accelerator Research Facility", Int. Conf. on the Applications of the Mössbauer Effect, Rio de Janeiro, Brazil, Sept. (1997).
- Y. Yoshida, Y. Kobayashi, K. Hayakawa, K. Yukihiro, J. Nakamura, E. Yagi, F. Ambe, and S. Nasu: "Jump processes of <sup>57</sup>Fe atoms in solid Ar and solid Xe", 1997 Fall Meet. of Physical Society of Japan, Kobe, Oct. (1997).
- A. Yamashita, K. Ishii, T. Yokoo, J. Akimitsu, M. Hedo, Y. Inada, Y. Onuki, E. Yamamoto, Y. Haga, and R. Kadono: "Anomalous field dependence of magnetic penetration depth in the vortex state of CeRu<sub>2</sub>", 1997 Fall Meet. of Physical Society of Japan, Kobe, Oct. (1997).
- K. Ishii, S. Kawae, T. Nakano, K. Ando, H. Oyama, and T. Kambara: "Rydberg transitions of highly charged neon ion in beam-foil collision", 1997 Fall Meet. of Physical Society of Japan, Kobe, Oct. (1997).
- K. Ando, T. Nakano, K. Ishii, S. Kawae, T. Kambara, and H. Oyama: "Rydberg transition of highly charged krypton ion in beam-foil collision", 1997 Fall Meet. of Physical Society of Japan, Kobe, Oct. (1997).
- H. Tsuchida, T. Miyabe, M. Imai, A. Itoh, N. Imanishi, Y. Nakai, and T. Kambara: "Study of C<sub>60</sub>-mutifragmentation in heavy-ion collisions C: Mass correlation", 1997 Fall Meet. of Physical Society of Japan, Kobe, Oct. (1997).
- S. Uramoto, H. Sato, and I. Shimamura: "Doubly excited states of the hydrogen molecule", 1997 Fall Meet. of Physical Society of Japan, Kobe, Oct. (1997).
- N. Kuroda, N. Ishikawa, S. Okayasu, A. Iwase, H. Ikeda, R. Yoshizaki, and T. Kambara: "Pinning in Bi-based superconductors irradiated with 3.5 GeV Xe ion", 1997 Fall Meet. of Physical Society of Japan, Kobe, Oct. (1997).
- H. Sakairi, E. Yagi, and A. Koyama: "Annealing of Cu<sub>3</sub>Au irradiated with protons,  $\alpha$ -particles or C ions at liquid nitrogen temperature", 8th Int. Conf. on Fusion Reactor Materials, Sendai, Oct. (1997).
- E. Yagi: "Formation of heavy inert gas bubbles in materials", 8th Int. Conf. on Fusion Reactor Materials, Sendai, Oct. (1997).
- I. Shimamura: "Physics of electron collision processes manifest in their cross sections", 1997 Fall Meet. of Physical Society of Japan, Kobe, Nov. (1997).
- T. Ichioka: "Production of slow antihydrogen beam", 14th RIKEN Symp. on Atomic Physics Using Accelerators, Wako, Dec. (1997).
- Y. Yamazaki: "Interaction of ions with matter", RIKEN Symp. on Materials Science in RIKEN RI Beam Factory, Wako, Dec. (1997).
- T. Nishimura: "Vibrationally elastic scattering of positrons from methane molecules", Uchu-Kagaku Kenkyuusyo Uchu Kuukan Genshi Bunshi Katei Kenkyuukai, Sagamihara, Dec. (1997).
- S. Uramoto, H. Sato, and I. Shimamura: "Superexcited states of the hydrogen molecule", Uchu-Kagaku Kenkyuusyo Uchu Kuukan Genshi Bunshi Katei Kenkyuukai, Sagamihara, Dec. (1997).

#### 4. Radiochemistry, radiation chemistry, and radiation biology

- S. Enomoto: "Study on bio-trace elements by using the multitracer technique", RIKEN Symp. on Studies on Condensed Matter Physics, Atomic Physics, Nuclear Chemistry, and Biology and Medicine Using RIKEN Accelerators, Wako, Feb. (1997).
- R. Hirunuma, N. Sotogaku, K. Endo, S. Enomoto, S. Ambe, and F. Ambe: "Study of the uptake of trace elements in Se-deficient rats", 117th Ann. Meet. of Pharmaceutical Society of Japan, Tokyo, Mar. (1997).
- S. Enomoto: "Dynamics of bio-trace elements by using the multitraces technique", 40th Ann. Symp. of Japan Society of Plasma Spectroscopic Analysis, Nagoya, Mar. (1997).
- R. Hirunuma, N. Sotogaku, K. Endo, S. Enomoto, S. Ambe, and F. Ambe: "The uptakes of various trace elements in Se deficient rats", RIKEN Symp. on Bio-Trace Elements '97, Wako, Mar. (1997).
- N. Sotogaku, R. Hirunuma, K. Endo, S. Enomoto, S. Ambe, and F. Ambe: "Study on binding of blood serum and various trace elements", RIKEN Symp. on Bio-Trace Elements '97, Wako, Mar. (1997).
- S. Enomoto: "Dynamics of various trace elements in liver diseases", RIKEN Symp. on Bio-Trace Elements '97, Wako, Mar. (1997).
- T. Ozaki, S. Enomoto, Y. Minai, S. Ambe, F. Ambe, and Y. Makide: "Influence of aluminum on the up-

- take of various cations from a solution into carrots", 4th Int. Conf. on Methods and Applications of Radioanalytical Chemistry, (American Nuclear Society), Hawaii, U.S.A., Apr. (1997).
- T. Shinonaga, S. Ambe, and I. Yamaguchi: "Uptake rate of trace elements by soybean plant", 4th Int. Conf. on Methods and Applications of Radioanalytical Chemistry, (American Nuclear Society), Hawaii, U.S.A., Apr. (1997).
- T. Nozaki, Y. Itoh, Z. Peng, Y. Ito, N. Nakanishi, H. Yoshida, and A. Goto: "Preparation of positron source for slow positron beam by ion bombardment on liquid and gas targets", 11th Int. Conf. on Positron Annihilation (ICPA-11), Kansas, U.S.A., May (1997).
- R. Hirunuma, S. Enomoto, S. Ambe, F. Ambe, N. Sotogaku, and K. Endo: "Study of the uptake of trace elements in Se-deficient rats using the multitracer technique", 8th Ann. Meet. of Japan Society for Biomedical Research on Trace Elements, Tokyo, July (1997).
- N. Sotogaku, K. Endo, R. Hirunuma, S. Enomoto, S. Ambe, and F. Ambe: "Binding properties of various metals to blood components and serum proteins", 8th Ann. Meet. of Japan Society for Biomedical Research on Trace Elements, Tokyo, July (1997).
- S. Enomoto, R. Hirunuma, S. Ambe, and F. Ambe: "Biobehavior of various trace elements in hepatopathy animals", 8th Ann. Meet. of Japan Society for Biomedical Research on Trace Elements, Tokyo, July (1997).
- R. Hirunuma, N. Sotogaku, K. Endo, S. Enomoto, S. Ambe, and F. Ambe: "Application of the multitracer technique: Metabolic study of trace elements in selenium-deficient rats", 8th Int. Conf. on Bioinorganic Chemistry, (Science Council of Japan, Chemical Society of Japan), Yokohama, July (1997).
- N. Sotogaku, R. Hirunuma, K. Endo, S. Enomoto, S. Ambe, and F. Ambe: "Studies of the binding of various trace elements to blood components and serum proteins by means of the multitracer technique", 8th Int. Conf. on Bioinorganic Chemistry, (Science Council of Japan, Chemical Society of Japan), Yokohama, July (1997).
- N. Hayakawa, S. Enomoto, R. Hirunuma, K. Endo, S. Ambe, and F. Ambe: "Metabolic study of trace elements in liver cancer bearing rats", 8th Int. Conf. on Bioinorganic Chemistry, (Science Council of Japan, Chemical Society of Japan), Yokohama, July (1997).
- S. Enomoto, R. G. Weginwar, R. Hirunuma, S. Ambe, and F. Ambe: "Metabolic study of trace elements in acute alcoholic mice", 8th Int. Conf. on Bioinorganic Chemistry, (Science Council of Japan, Chemical Society of Japan), Yokohama, July (1997).
- S. Enomoto, B. Liu, S. Ambe, and F. Ambe: "Accumulation of inorganic elements in ddY mice implanted with *Ehrlich sarcoma*", 8th Int. Conf. on Bioinorganic Chemistry, (Science Council of Japan, Chemical Society of Japan), Yokohama, July (1997).
- T. Abe, C. H. Bae, T. Matsuyama, and S. Yoshida: "Hormone mutants obtained by heavy-ion beam irradiation", Plant Biology '97, (American Society of Plant Physiologists), Vancouver, Canada, Aug. (1997).
- F. Ambe and S. Enomoto: "The multitracer technique in bio-trace element research", RIKEN Int. Symp. on Bio-Trace Elements '97 (BITREL '97), Hachioji, Aug. (1997).
- R. Hirunuma, N. Sotogaku, K. Endo, S. Enomoto, S. Ambe, and F. Ambe: "Comparison of behavior of trace elements between selenium-deficient and normal rats using the multitracer technique", RIKEN Int. Symp. on Bio-Trace Elements '97 (BITREL '97), Hachioji, Aug. (1997).
- J. Chou, S. Enomoto, S. Ambe, and F. Ambe: "Multitracer study on binding activity of various trace elements to metallothionein", RIKEN Int. Symp. on Bio-Trace Elements '97 (BITREL '97), Hachioji, Aug. (1997).
- R. G. Weginwar, M. Katayama, S. Enomoto, S. Ambe, T. Ozaki, and F. Ambe: "Metabolism of trace elements in marine euglena: A study using the multitracer", RIKEN Int. Symp. on Bio-Trace Elements '97 (BITREL '97), Hachioji, Aug. (1997).
- T. Ozaki, S. Enomoto, Y. Minai, S. Ambe, and F. Ambe: "Influence of aluminium on the uptake of various cations from a solution into carrots", RIKEN Int. Symp. on Bio-Trace Elements '97 (BITREL '97), Hachioji, Aug. (1997).
- R. Amano, S. Oishi, S. Enomoto, and F. Ambe: "Simultaneous tracing of 14 elements in mice and rats using the radioactive multitracer technique", RIKEN Int. Symp. on Bio-Trace Elements '97 (BITREL '97), Hachioji, Aug. (1997).
- N. Sotogaku, K. Matsumoto, K. Endo, R. Hirunuma, S. Enomoto, S. Ambe, and F. Ambe: "Metal binding properties of various trace elements to serum proteins by means of the multitracer technique", RIKEN Int. Symp. on Bio-Trace Elements '97 (BITREL '97), Hachioji, Aug. (1997).
- S. Enomoto: "Trends in bio-trace elements research on ICBIC8 and BITREL'97", 16th Symp. of Bio Trace Elements Research, Gifu, Aug. (1997).
- F. Yatagai, Y. Kagawa, N. Fukunishi, N. Inabe, T. Shimazu, M. Hirano, K. Eguchi-Kasai, Y. Furusawa, K. Tatsumi, M. Watanabe, T. Kato, and F. Hanaoka: "Analysis of mutations in the human HPRT gene induced by heavy-ion irradiation", 7th Int. Conf. on Environmental Mutagens, Toulouse, France, Sept. (1997).
- F. Yatagai, Y. Kagawa, N. Fukunishi, N. Inabe, T. Shimazu, S. Kanai, M. Hirano, M. Suzuki, K. Eguchi-Kasai, Y. Furusawa, K. Tatsumi, M. Watanabe, T. Kato, and F. Hanaoka: "Analysis of mutations in the human HPRT gene induced by heavy-ion irradiation", 6th Workshop on Heavy-Charged Par-

- titles in Biology and Medicine, (GSI), Baveno, Italy, Sept. (1997).
- C. H. Bae, T. Abe, T. Matsuyama, T. Nakano, and S. Yoshida: "Effect of heavy-ion beam irradiation on mutation induction in plants at pollination stage II", 92nd Meet. of Japanese Society of Breeding, Tottori, Oct. (1997).
- T. Nozaki, Y. Itoh, Z. Peng, Y. Ito, N. Nakanishi, H. Yoshida, and A. Goto: "Preparation of  $^{18}\text{F}$  source for slow positron beam by proton bombardment of  $^{18}\text{O}$ -water", Asia-Pacific Symp. on Radiochemistry '97, (Kumamoto University), Kumamoto, Oct. (1997).
- S. Ambe, T. Ozaki, R. G. Weginwar, S. Enomoto, and F. Ambe: "Production of carrier-free multitracers containing Mg-28 and Ca-47 by high-energy heavy-ion irradiation", Asia-Pacific Symp. on Radiochemistry '97, (Kumamoto University), Kumamoto, Oct. (1997).
- R. Hirunuma, N. Sotogaku, K. Endo, S. Enomoto, S. Ambe, and F. Ambe: "Application of the multitracer technique: Time dependence of distribution of trace elements in Se-deficient rats", Asia-Pacific Symp. on Radiochemistry '97, (Kumamoto University), Kumamoto, Oct. (1997).
- S. Enomoto, R. Hirunuma, S. Ambe, and F. Ambe: "Dynamics of trace elements in liver disease rat and mice", Asia-Pacific Symp. on Radiochemistry '97, (Kumamoto University), Kumamoto, Oct. (1997).
- J. Chou, S. Enomoto, S. Ambe, and F. Ambe: "Multitracer study on coordinating of the rare-earth element with metallothionein", Asia-Pacific Symp. on Radiochemistry '97, (Kumamoto University), Kumamoto, Oct. (1997).
- S. Oishi, R. Amano, A. Ando, S. Enomoto, and F. Ambe: "Simultaneous biobehavior of Sc, Mn, Fe, Co, Zn, Se, Rb, and Zr trace elements in C57BL/6N mice", Asia-Pacific Symp. on Radiochemistry '97, (Kumamoto University), Kumamoto, Oct. (1997).
- R. G. Weginwar, M. Katayama, S. Ambe, S. Enomoto, T. Ozaki, and F. Ambe: "Metabolism of trace elements in marine Euglena: A study using the multitracer", Asia-Pacific Symp. on Radiochemistry '97, (Kumamoto University), Kumamoto, Oct. (1997).
- H. Wang, S. Ambe, N. Takematsu, and F. Ambe: "Model study of influence of acid rain on adsorptive behavior of trace elements on soil by the multitracer technique", Int. Congr. of Acid Snow and Rain 1997, (Research Association of Acid Snow and Rain), Niigata, Oct. (1997).
- T. Shinonaga, S. Ambe, and I. Yamaguchi: "Uptake and translocation of Sr, Tc, and Cs in soybean plants", Int. Meet. on Influence of Climatic Characteristics upon Behavior of Radioactive Elements, (Institute for Environmental Sciences), Rokkashomura, Oct. (1997).
- S. Ambe, T. Shinonaga, T. Ozaki, S. Enomoto, H. Yasuda, and S. Uchida: "Multitracer study on uptake of elements by komatsuna", Int. Meet. on Influence of Climatic Characteristics upon Behavior of Radioactive Elements, (Institute for Environmental Sciences), Rokkashomura, Oct. (1997).
- N. Shigematsu, T. Kawada, R. Ishibashi, T. Nakayama, A. Takeda, A. Kubo, and H. Ito: "Analysis of mutation induction by X-rays and heavy ion beams", Meet. of Japanese Society for Therapeutic Radiology and Oncology, Kagawa, Oct. (1997).
- K. Inoue, M. Kitoh, T. Oka, A. Samura, and Y. Hama: "The study of change of chemical structure and surface topology in polyethylenes irradiated by C and Ar ion-beams under air and vacuum", 40th Symp. on Radiation Chemistry, Tokaimura, Oct. (1997).
- M. Miki, Y. Mizutani, K. Okamoto, Y. Izumi, Y. Furusawa, K. Ushida, Y. Yoshida, and S. Tagawa: "Study on the behavior of geminate ion pair in alkane by using picosecond pulse radiolysis", 40th Symp. on Radiation Chemistry, (Radiation Chemical Society of Japan), Tokaimura, Oct. (1997).
- N. Sotogaku, K. Endo, R. Hirunuma, S. Enomoto, S. Ambe, and F. Ambe: "Biochemical studies of blood components and transport protein with various trace elements", 41st Symp. on Radiochemistry, (Kumamoto University), Kumamoto, Oct. (1997).
- H. Araki, J. Sanada, S. Morimoto, A. Yokoyama, T. Saito, H. Baba, Y. Ohkubo, and Y. Kobayashi: "Heavy-ion induced fission in the medium energy region", 41st Symp. on Radiochemistry and Asia-Pacific Symp. on Radiochemistry '97, (Kumamoto University), Kumamoto, Oct. (1997).
- Y. Furusawa, M. Saitou, T. Kanai, and F. Yatagai: "REB and OER for a lethal effect of super high-LET  $^{56}\text{Fe}$  and  $^{40}\text{Ar}$  ion beam on V79 cell", 40th Ann. Meet. of Japan Radiation Research Society, Kyoto, Nov. (1997).
- H. Sasaki, M. Parinaz, F. Yatagai, Y. Furusawa, and F. Hanaoka: "Mechanisms of interphase-death induction for CHO cells exposed to accelerated heavy-ions", 40th Ann. Meet. of Japan Radiation Research Society, Kyoto, Nov. (1997).
- F. Yatagai, Y. Kagawa, M. Hirano, N. Fukunishi, N. Inabe, S. Kanai, T. Shimazu, K. Eguchi-Kasai, Y. Furusawa, M. Suzuki, M. Watanabe, T. Kato, K. Tatsumi, and F. Hanaoka: "Analysis of mutations in the human HPRT gene induced by high LET heavy-ion irradiation", 40th Ann. Meet. of Japan Radiation Research Society, Kyoto, Nov. (1997).
- Y. Itoh, T. Nozaki, A. Goto, N. Nakanishi, Y. Ito, and H. Yoshida: "Development of spin polarized positron beam", Tohoku Daigaku Kinzoku Kenkyusho Kyodoriyo Kenkyukai Yodenshi niyoru Zairyo Nano Kozokaiseki, Sendai, Nov. (1997).
- F. Yatagai, Y. Kagawa, M. Hirano, N. Fukunishi, N. Inabe, S. Kanai, K. Eguchi-Kasai, Y. Furusawa, M. Suzuki, M. Watanabe, T. Kato, K. Tatsumi, and F. Hanaoka: "Analysis of mutation in the human HPRT gene induced by high-let heavy-ion", 26th Ann. Meet. of Japan Environmental Mutagen Re-

- search Society, Kanagawa, Dec. (1997).
- M. Yoshimasu, T. Abe, S. Yoshida, T. Inoue, F. Ling, and T. Shibata: "Using heavy-ion beam for isolation of yeast mitochondrial DNA ricombination deficient mutants", 20th Ann. Meet. of Japanese Society of Molecular Biology, Kyoto, Dec. (1997).
- K. Inoue, M. Kitou, T. Oka, A. Samura, Y. Hama, and F. Yatagai: "The study of change of chemical structure in polyethylenes irradiated by C and Ar ion-beams under air and vacuum", Meet. on Dielectric and Electrical Insulating Materials of IEEEJ, Tokyo, Dec. (1997).
- Y. Itoh, T. Nozaki, A. Goto, N. Nakanishi, Y. Ito, and H. Yoshida: "The development of positron source for spin polarized positron beam", PF Slow-Positron Facility Workshop, (KEK), Tsukuba, Dec. (1997).
- S. Ambe: "Influence of acid rain and organic matters on the adsorption of trace elements on soil", Symp. on the Behavior of Trace Substances in the Environment, (Kyoto Univ.), Kumatori, Dec. (1997).
- ### 5. Material analysis
- W. Hong, S. Hayakawa, K. Maeda, S. Fukuda, M. Yanokura, M. Aratani, K. Kimura, Y. Gohshi, and I. Tanihata: "Measurements of mass resolution and depth resolution of TOF-ERDA on a Si wafer", 44th Spring Meet. of Japan Society of Applied Physics Related Society, (Nihon Univ.), Tokyo, Mar. (1997).
- W. Hong, S. Hayakawa, K. Maeda, S. Fukuda, M. Yanokura, M. Aratani, K. Kimura, Y. Gohshi, and I. Tanihata: "Development of a high mass-resolution TOF-ERDA system for a wide mass range from hydrogen to middle heavy elements", Asianalysis IV, (Kyushu Univ.), Fukuoka, May (1997).
- Y. Itoh, H. Murakami, H. Takeno, S. Ushio, and T. Takenaka: "Positron lifetime in floating-zone grown silicon wafer", 11th Int. Conf. on Positron Annihilation (ICPA-11), Kansas City, U.S.A., May (1997).
- W. Hong, S. Hayakawa, K. Maeda, S. Fukuda, M. Yanokura, M. Aratani, K. Kimura, Y. Gohshi, and I. Tanihata: "Light-element measurements in a metallic material using heavy-ion TOF-ERDA", 13th Conf. of Ion Beam Analysis, (Instituto Tecnológico e Nuclear), Lisbon, Portugal, July (1997).
- K. Maeda, K. Hasegawa, H. Hamanaka, and M. Maeda: "Chemical state analysis in atmospheric air by high resolution PIXE", 13th Int. Conf. on Ion Beam Analysis, (Instituto Tecnológico e Nuclear), Lisbon, Portugal, July (1997).
- H. Murakami, Y. Itoh, and A. Kinoshita: "Surface of porous silicon studied by positron annihilation spectroscopy-lifetime, doppler broadning and age-momentum correlation", Silicon Heterostructures: From Physics to Devices, (Conference Chain Thomas Pearsall, Univ. Washington), Tuscany, Italy, Sept. (1997).
- K. Hasegawa, S. Nakayama, H. Hamanaka, and K. Maeda: "Crystal spectrometer PIXE system using multi-anode PSPC", 15th PIXE Symp. Japan, Takasaki, Nov. (1997).
- H. Yoshiki, K. Maeda, T. T. Inamura, A. Tonomura, and T. Tsuruda: "Trace element analysis of feathers", 15th PIXE Symp. Japan, Takasaki, Nov. (1997).
- H. Murakami, N. Onizuka, J. Sasaki, and Y. Itoh: "Positron annihilation in amorphous fine powder", Tohoku Daigaku Kinzoku Kenkyusho Kyodoriyo Kenkyukai Yodenshi niyoru Zairyo Nano Kozokaiseki, Sendai, Nov. (1997).
- H. Murakami and Y. Itoh: "Positronium age-momentum correlation for material characterization", PF Slow-Positron Facility Workshop, (KEK), Tsukuba, Dec. (1997).
- H. Hamanaka, A. Tonomura, N. Izkura, K. Hasegawa, K. Maeda, and S. Yumoto: "Chemical state analysis of Al compounds crystal spectrometer PIXE", 16th Symp. on Materials Science and Engineering Research Center of Ion Beam Technology, Housei University, Koganei, Dec. (1997).

## X. LIST OF SYMPOSIA

(Jan.–Dec. 1997)

- 1) Symp. on Giant Resonances  
27–28 Jan., Wako, RIKEN, Cyclotron Lab.
- 2) Symp. on Studies on Condensed Matter Physics, Atomic Physics, Nuclear Chemistry,  
and Biology and Medicine Using RIKEN Accelerators  
14 Feb., Wako, RIKEN, Atomic Physics Lab.
- 3) Symp. on Accelerator Techniques in RI Beam Factory Project  
19 Mar., Wako, RIKEN, Cyclotron Lab.
- 4) RIKEN Symp. on Bio-Trace Elements '97  
25 Mar., Wako, RIKEN, Nuclear Chemistry Lab.
- 5) Symp. on RI Beam Factory and Astrophysics  
24–25 Apr., Wako, RIKEN, Computational Science Lab. and Linear Accelerator Lab.
- 6) Workshop on Open Standards for Cascade Models at RHIC  
23–27 June, New York, BNL, Radiation Lab.
- 7) Workshop on Perturbative QCD as a Probe of Hadron Structure  
14–25 July, New York, BNL, Radiation Lab.
- 8) Workshop on Nuclear Reactions in Unstable Nuclei  
17–18 July, Wako, RIKEN, Linear Accelerator Lab.
- 9) Workshop on Hadron Helicity-Flip at RHIC Energies  
21 July–30 Aug., New York, BNL, Radiation Lab.
- 10) RIKEN Int. Symp. on Bio-Trace Elements '97 (BITREL'97)  
2–4 Aug., Hachioji, RIKEN, Nuclear Chemistry Lab.
- 11) Workshop on Cluster Physics in Unstable Nuclei  
5–6 Aug., Wako, RIKEN, Linear Accelerator Lab.
- 12) Workshop on Non-Equilibrium Many Body Physics  
23–25 Sept., New York, BNL, Radiation Lab.
- 13) 3rd INFN-RIKEN Meet. on Perspectives in Heavy Ions Physics  
13–15 Oct., Padova, Univ. of Padova & LNL, Radiation Lab.
- 14) Informal Meet. on the Nuclear Equation of State  
23 Nov., Wako, RIKEN, Linear Accelerator Lab.
- 15) Workshop on Mean Field in Unstable Nuclei  
25–26 Nov., Wako, RIKEN, Linear Accelerator Lab.
- 16) Symp. on Quarks and Gluons in Nucleon  
28–29 Nov., Wako, RIKEN, Radiation Lab.
- 17) 14th Symp. on Atomic Physics Using Accelerators  
16 Dec., Wako, RIKEN, Atomic Physics Lab.
- 18) RIKEN Symp. on Materials Science in RIKEN RI Beam Factory  
22–23 Dec., Wako, RIKEN, Nuclear Chemistry Lab.

## XI. LIST OF SEMINARS

(Jan.–Dec. 1997)

Radiation Lab., Cyclotron Lab., and  
Linear Accelerator Lab.

- 1) G. P. Berg, Indiana Univ. (U.S.A.), 14 Jan.  
“Experiments at 0 degree and accelerator projects at IUCF”
- 2) W. Benenson, Michigan State Univ. (U.S.A.), 16 Jan.  
“NSCL upgrade project”
- 3) N. Christ, Columbia Univ. (U.S.A.), 29 Jan.  
“The QCDSF project and computational quantum field theory”
- 4) J. Meng, Technische Universität München/-RIKEN (Germany/Saitama), 10 Feb.  
“Halo and giant halo for nuclei near the drip-line”
- 5) V. G. Soloviev, Joint Inst. for Nuclear Research (Dubna), 13 Feb.  
“On vibrational excitations in nuclei”
- 6) T. Marumori, Tsukuba Univ. (Ibaraki), 13 Feb.  
“On band termination of nuclear collective rotation”
- 7) K. Amos, Univ. Melbourne (Australia), 17 Mar.  
“Fully microscopic model analysis of proton-nucleus scattering: Elastic and discrete state inelastic events”
- 8) N. Cindro, Ruder Bošković Institute (Zagreb), 17 Mar.  
“The Hanbury-Brown/Twiss effects in nuclear and subnuclear physics: Measuring nuclear dimensions by astrophysical method”
- 9) G. C. Hillhouse, Stellenbosch Univ. (South Africa), 1 Apr.  
“Nuclear medium effects via quasielastic ( $\vec{p}, \vec{p}'$ ) and ( $\vec{p}, \vec{n}$ ) scattering”
- 10) A. Gelberg, Univ. Köln (Germany), 11 Apr.  
“The interacting boson model and mixed symmetry status in the  $A = 130$  mass region”
- 11) Y. Utsuno, Univ. Tokyo (Tokyo), 21 Apr.  
“Nuclear structure of  $A \sim 80$  calculated by quantum Monte Carlo diagonalization method”
- 12) C. Samanta, Saha Institute of Nuclear Physics (India), 6 May  
“Elastic scattering of  $^{11}\text{Li}$ ”
- 13) S. Kuyucak, Australian National Univ. (Australia), 12 May  
“Vibron model: An algebraic approach to molecular spectroscopy”
- 14) W. T. H. van Oers, University of Manitoba (Canada), 16 May  
“Studies of fundamental symmetries in nuclear reactions”
- 15) L. Ya. Glozmann, Univ. of Graz (Austria), 26 May  
“Baryons and chiral symmetry in QCD”
- 16) D. Bucurescu, Institute of Atomic Physics (Romania), 27 May  
“Spectroscopy of the  $N = Z$  nuclei  $^{52}\text{Fe}$  and  $^{84}\text{Mo}$ ”
- 17) K. Sumiyoshi, Computational Science lab., RIKEN (Saitama), 2 June  
“Explosion of a neutron star just below the minimum mass: A possible site for r-process”
- 18) I. T. Cheon, Yonsei Univ. (South Korea), 4 July  
“Induced pseudoscalar coupling constant”
- 19) A. B. Kurepin, Institute for Nuclear Research, Russian Academy of Science (Russia), 17 July  
“Narrow nuclear resonance of high excitation energies”
- 20) W. Q. Shen, Shanghai Institute of Nuclear Research (China), 8 Aug.  
“Azimuthal distribution and azimuthal correlation and Smolukuski calculation about fission delay for  $10.6 \text{ MeV/u } ^{84}\text{Kr} + ^{27}\text{Al}$ ”
- 21) H. Wollnik, Univ. Giessen (Germany), 12 Aug.  
“Mass measurements of exotic nuclei at ESR of the GSI”
- 22) S. Nakamura, Muon Science Lab., RIKEN (Saitama), 26 Sept.  
“A new data acquisition system for RIKEN-RAL  $\mu\text{-CF}$  experiment”
- 23) B. Gruber, Southern Illinois University (U.S.A.), 29 Oct.  
“Algebraic shells and the interacting boson model of the nucleus”

- 24) J. Lattimer, State Univ. of New York, Stony Brook (U.S.A.), 21 Nov.  
“Observational constraints of the equation of state: Recent developments”
- 25) P. Descouvemont, Free University of Bruxelles (Belgium), 25 Nov.  
“Light nuclear systems in a microscopic cluster description”
- 26) E. Sthephenson, Indiana Univ. Cyclotron Facility (U.S.A.), 27 Nov.  
“Physics with the IUCF K600 spectrometer”
- 27) I. Katayama, Univ. Tokyo (Tokyo), 4 Dec.  
“Proposals of a new cyclotron ion guide”
- 28) M. Sambataro, Catania section of the National Institute of Nuclear Physics (Italy), 9 Dec.  
“Boson and fermion mappings of fermion systems”
- 29) Ian. S. Towner, Queen’s University (Canada), 12 Dec.  
“Isospin-symmetry breaking in Fermi beta decay and the determination of  $V_{ud}$ ”

#### Atomic Physics Lab.

- 1) T. Kambara, ISAS (Sagamihara), 17 Apr.  
“Atomic collisions studied by recoil ion momentum analyses”
- 2) K. Yoshino, Harvard-Smithsonian Center for Astrophysics (U.S.A.), 17 Apr.  
“The combination of a VUV Fourier-transform spectrometer and synchrotron radiation for molecular absorption”
- 3) T. M. Kojima, ISAS (Saitama), 26 June  
“4d Photoionization of lanthanide ions”
- 4) M. Inokuti, Argonne National Laboratory (U.S.A.), 14 Nov.  
“Review of scientific research programs and organizations”
- 5) S. Uramoto, ISAS (Saitama), 20 Nov.  
“Superexcited states of the hydrogen molecule”

#### RI Beam Factory

- 1) Y. Lin, Tsinghua Univ. (China), 18 Feb.  
“Electron linear accelerators’ R&D at Tsinghua University”
- 2) J. Vamos, Institute of Nuclear Research ATOMKI (Hungary), 8 Apr.  
“Status of the new Hungarian 14.5 GHz ECR ion source”
- 3) I. Miura, RCNP (Japan), 21 Apr.  
“AVF Cyclotron and Ring Cyclotron in RCNP”
- 4) T. T. Inamura, RIKEN (Japan), 23 Apr.  
“SPECTROSCOPY by Hantaro NAGAOKA: Pioneer Nuclear-Structure Study made at RIKEN”
- 5) A. Bandyopadhyay, VECC (India), 23 June  
“Design of Variable-frequency IH-Linac for CSM”
- 6) S. Biri (Institute of Nuclear Research/Hungary), 14 Nov.  
“Recent Improvements on the ATOMKI 14.5 and on the RIKEN 18 GHz ECRIS”

## XII. LIST OF PERSONNEL

### RIKEN Accelerator Research Facility

ISHIHARA Masayasu 石原正泰 (Facility Director)  
AMBE Fumitoshi 安部文敏 (Vice Facility Director)  
YANO Yasushige 矢野安重 (Vice Facility Director)

### Linac Division

CHIBA Toshiya 千葉利哉  
IKEZAWA Eiji 池沢英二  
KOHARA Shigeo 小原重夫

HEMMI Masatake 逸見政武  
KASE Masayuki 加瀬昌之  
MIYAZAWA Yoshitoshi 宮沢佳敏\*<sup>1</sup>

### Ring Cyclotron Division

FUJITA Jiro 藤田二郎  
IKEGAMI Kumio 池上九三男  
KAGEYAMA Tadashi 影山正  
KASE Masayuki 加瀬昌之  
KUBO Toshiyuki 久保敏幸  
NAKAGAWA Takahide 中川孝秀  
OKUNO Hiroki 奥野広樹  
YOKOYAMA Ichiro 横山一郎

GOTO Akira 後藤彰\*<sup>1</sup>  
INABE Naohito 稲辺尚人  
KAMIGAITO Osamu 上垣外修一  
KOHARA Shigeo 小原重夫  
NAGASE Makoto 長瀬誠  
OGIWARA Kiyoshi 荻原清  
SAKAMOTO Naruhiko 坂本成彦

### Experimental Support Division

ICHIHARA Takashi 市原卓  
KANAI Yasuyuki 金井保之  
KUMAGAI Hidekazu 熊谷秀和  
MORITA Kosuke 森田浩介  
YATAGAI Fumio 谷田貝文夫

KAMBARA Tadashi 神原正\*<sup>1</sup>  
KOBAYASHI Toshio 小林俊雄  
MATSUZAKI Teiichiro 松崎禎一郎  
WATANABE Yasushi 渡邊康

### Radioisotope Facilities Division

AMBE Fumitoshi 安部文敏\*<sup>1</sup>

KOBAYASHI Yoshio 小林義男

### Radiation Protection Group

FUJITA Shin 藤田新\*<sup>1</sup>  
NAKAJIMA Shunji 中島諄二

ITO Sachiko 伊藤祥子  
UWAMINO Yoshitomo 上菘義朋

### Administration Division

NAKAMURA Toshiko 中村とし子  
NUMATA Shigeo 沼田茂男

NISHIGUCHI Fumiyoshi 西口文彬\*<sup>2</sup>

### Steering Committee

AMBE Fumitoshi 安部文敏  
GOTO Akira 後藤彰  
ISHIHARA Masayasu 石原正泰  
KATSUMATA Koichi 勝又紘一  
MATSUOKA Masaru 松岡勝  
MIYAZAWA Yoshitoshi 宮沢佳敏  
NAKANISHI Noriyoshi 中西紀喜  
TAKAMI Michio 高見道生  
YAGI Eiichi 八木栄一  
YANO Yasushige 矢野安重  
YOSHIDA Shigeo 吉田茂男

AONO Masakazu 青野正和  
HANAOKA Fumio 花岡文雄  
KAMBARA Tadashi 神原正  
KOBAYASHI Toshio 小林俊雄  
MATSUZAKI Teiichiro 松崎禎一郎  
NAGAMINE Kanetada 永嶺謙忠  
NISHIGUCHI Fumiyoshi 西口文彬  
TANIHATA Isao 谷畑勇夫\*<sup>3</sup>  
YAMAZAKI Yasunori 山崎泰規  
YATAGAI Fumio 谷田貝文夫

\*<sup>1</sup> Group Leader, \*<sup>2</sup> Manager, \*<sup>3</sup> Chairperson

## Scientific and Engineering Personnel

### RI Beam Factory Project Office

ENOMOTO Shuichi 榎本秀一\*1  
INABE Naohito 稲辺尚人  
KIM Jong Won 金鍾元\*1  
OHNISHI Jun-ichi 大西純一  
SAKAMOTO Naruhiko 坂本成彦  
WAKASUGI Masanori 若杉昌徳

IKEGAMI Kumio 池上九三男  
KAMIGAITO Osamu 上垣外修一  
KUBO Toshiyuki 久保敏幸  
OKUNO Hiroki 奥野広樹  
TANABE Toshiya 田辺敏也  
YANO Yasushige 矢野安重\*2

\*1 Contract Researcher, \*2 Head

### Cosmic Radiation Laboratory

KATO Hiroshi 加藤博  
YOSHIDA Atsumasa 吉田篤正

KOHNO Tsuyoshi 河野毅

(Visitors)

GOKA Tateo 五家建夫 (NASDA)  
HASEBE Nobuyuki 長谷部信行 (Fac. Gen. Educ., Ehime Univ.)  
KASHIWAGI Toshisuke 柏木利介 (Fac. Eng., Kanagawa Univ.)  
KATO Chihiro 加藤千尋 (Fac. Sci., Shinshu Univ.)  
MATSUMOTO Haruhisa 松本晴久 (NASDA)  
MUNAKATA Kazuoki 宗像一起 (Fac. Sci., Shinshu Univ.)  
MURAKAMI Hiroyuki 村上浩之 (Fac. Sci., Rikkyo Univ.)  
NAGATA Katsuaki 永田勝明 (Fac. Eng., Tamagawa Univ.)  
NAKAMOTO Atsushi 中本淳 (Fac. Sci., Rikkyo Univ.)  
TAKASHIMA Takeshi 高島健 (Fac. Sci. Eng., Waseda Univ.)  
YAMAGIWA Iwao 山極巖 (Tobu High School)  
YANAGIMACHI Tomoki 柳町朋樹 (Fac. Sci., Rikkyo Univ.)

(Students)

HOSHIDA Takashi 星田貴志 (Grad. Sch. Fac. Sci., Nagoya Univ.)  
MIYASAKA Hiromasa 宮坂浩正 (Grad. Sch. Sci. Eng., Saitama Univ.)

### Cyclotron Laboratory

AKIYOSHI Hiromichi 秋吉啓充\*1  
FUJITA Jiro 藤田二郎  
FUKUNISHI Nobuhisa 福西暢尚\*3  
HIRUNUMA Rieko 蛭沼利江子\*5  
ITO Sachiko 伊藤祥子  
KAGEYAMA Tadashi 影山正  
KATAYAMA Takeshi 片山武司\*6  
KOHARA Shigeo 小原重夫  
MORITA Kosuke 森田浩介  
NAKAGAWA Keiko 中川恵子\*1  
NAKAJIMA Shunji 中島諄二  
OHNISHI Tetsuya 大西哲哉\*2  
SUZUKI Toshio 鈴木敏男\*6  
TAKANAKA Masao 高仲政雄\*3  
UESAKA Tomohiro 上坂友洋\*1  
WADA Takeshi 和田雄\*4  
YANO Yasushige 矢野安重\*7

ARIGA Takehiro 有賀健博\*2  
FUJITA Shin 藤田新  
GOTO Akira 後藤彰\*4  
ISHIDA Satoru 石田悟\*1  
IWASA Naohito 岩佐直仁\*1  
KASE Masayuki 加瀬昌之  
KIDERA Masanori 木寺正憲\*5  
KUROKAWA Meiko 黒川明子\*1  
NAGASE Makoto 長瀬誠  
NAKAGAWA Takahide 中川孝秀  
OGIWARA Kiyoshi 荻原清  
OTSUKA Takaharu 大塚孝治\*6  
TAGAYA Yu 多加谷祐\*2  
UCHIYAMA Koji 内山浩志\*2  
UTSUNO Yutaka 宇都野譲\*2  
YAMAJI Shuhei 山路修平\*4  
YOKAYAMA Ichiro 横山一郎

\*1 Special Postdoctoral Researcher, \*2 Junior Research Associate, \*3 Contract Researcher,

\*4 Senior Scientist, \*5 Postdoctoral Researcher, \*6 Senior Visiting Scientist, \*7 Chief Scientist

(Visitors)

ABE Yasuhisa 阿部恭久 (Yukawa Inst. Theor. Phys., Kyoto Univ.)  
ABURAYA Takashi 油谷崇志 (NASDA)  
ARAKAWA Kazuo 荒川和夫 (JAERI, Takasaki Rad. Chem. Res. Estab.)  
BABA Shinji 馬場信次 (NASDA)  
BANDYOPADHYAY Arup (Variable Energy Cycl. Cent., India)  
BANDYOPADHYAY Tapas (Variable Energy Cycl. Cent., India)  
BANERJEE Vaishali (Variable Energy Cycl. Cent., India)  
BATYGIN Yuri (Elect. Phys. Dept., Moscow Eng. Phys. Inst., Russia)  
BHATTACHAYA Sankar (Variable Energy Cycl. Cent., India)  
BIRI Sandor (ATOMKI, Hungary)  
CHAKRABARTI Alok (Variable Energy Cycl. Cent., India)  
CHATTOPADHYAY Subrata (Univ. Texas, Arlington, U.S.A.)  
DATÉ Schin 伊達伸 (JASRI)  
DINH DANG Nguen 廷燈阮 (Inst. Nucl. Sci. Tech., Vietnam Atom Ener. Com., Vietnam)  
EJIRI Hiroyasu 江尻宏泰 (Fac. Sci., Osaka Univ.)  
EN'YO Hideto 延与秀人 (Fac. Sci., Kyoto Univ.)  
FUJIOKA Manabu 藤岡学 (Cycl. Radioisot. Cent., Tohoku Univ.)  
FUJISAWA Takashi 藤沢高志 (Denki Kogyo Co., Ltd.)  
FUJISHIMA Shiro 藤島史郎 (I.H.I.)  
FUJITA Yoshitaka 藤田佳孝 (Fac. Sci., Osaka Univ.)  
FUJIWARA Ichiro 藤原一郎 (Dept. Economy, Otemon Gakuin)  
FUJIWARA Mamoru 藤原守 (RCNP, Osaka Univ.)  
FUKUDA Mitsuhiro 福田光宏 (JAERI, Takasaki Rad. Chem. Res. Estab.)  
FURUNO Kohe 古野興平 (Tandem Accel. Cent., Univ. Tsukuba)  
FURUSE Kaoru 古瀬馨 (NASDA)  
FUTAMI Yasuyuki 二見康之 (N.I.R.S.)  
GOKA Tateo 五家建夫 (NASDA)  
GRUBER Bruno (Tech. Univ. Clausthal, Germany)  
GU Wei (Inst. Modern Phys., Academia Sinica, China)  
HAMA Hiroyuki 浜広幸 (I.M.S.)  
HARADA Toru 原田融 (Sapporo Gakuin Univ.)  
HASHIMOTO Miwa 橋本美和 (NASDA)  
HASHIMOTO Osamu 橋本治 (Fac. Sci., Tohoku Univ.)  
HATANAKA Kichiji 畑中吉治 (RCNP, Osaka Univ.)  
HATSUKAWA Yuichi 初川雄一 (JAERI, Tokai Res. Estab.)  
HATTORI Toshiyuki 服部俊幸 (Res. Lab. Nucl. React., Tokyo Inst. Technol.)  
HAYANO Ryugo 早野龍五 (Fac. Sci., Univ. Tokyo)  
HIRAO Yasuo 平尾泰男 (N.I.R.S.)  
HIROSE Takayuki 広瀬孝幸 (NASDA)  
HONMA Michio 本間道雄 (Aizu Univ.)  
HONMA Toshihiro 本間寿広 (Cycl. Radioisot. Cent., Tohoku Univ.)  
HORIBATA Takatoshi 堀端孝俊 (Fac. Eng., Aomori Univ.)  
HORIGUCHI Takayoshi 堀口隆良 (Fac. Sci., Hiroshima Univ.)  
HORIUCHI Hisashi 堀内昶 (Fac. Sci., Kyoto Univ.)  
HOSONO Kazuhiko 細野和彦 (Dept. Eng. Sci., Himeji Inst. Tech.)  
IGARASHI Toshio 五十嵐敏雄 (NASDA)  
IKEDA Akitsu 池田秋津 (Shizuoka Inst. Sci. & Tech.)  
IKEDA Kiyomi 池田清美 (Fac. Sci., Niigata Univ.)  
IKEDA Nobuo 池田伸夫 (Fac. Sci., Kyushu Univ.)  
IKEZOE Hiroshi 池添博 (JAERI, Tokai Res. Estab.)  
IMAI Kenichi 今井憲一 (Fac. Sci., Kyoto Univ.)  
INAMURA Takashi T. 稲村卓 (Former Staff of RIKEN)  
INOUE Makoto 井上信 (Inst. Chem. Res., Kyoto Univ.)  
ISHIZUKA Takeo 石塚武男 (Fac. Sci., Saitama Univ.)  
ITO Yasuo 伊藤泰男 (Atomic Energy Res. Cent., Univ. Tokyo)  
ITO Yoshiko 伊東芳子 (Adv. Res. Inst. Sci. & Eng., Waseda Univ.)  
IWAMOTO Akira 岩本昭 (JAERI, Tokai Res. Estab.)

IWASHITA Yoshihisa 岩下芳久 (Inst. Chem. Res., Kyoto Univ.)  
 IZUMOTO Toshiaki 泉本利章 (Coll. Sci., Rikkyo Univ.)  
 JEONG S. C. (High Energy Accel. Res. Organization)  
 JIN Weigou 金衛国 (Fac. Sci., Toho Univ.)  
 KAMIMURA Masayasu 上村正康 (Fac. Sci., Kyushu Univ.)  
 KANAZAWA Mitsutaka 金沢光隆 (N.I.R.S.)  
 KATAYAMA Ichiro 片山一郎 (High Energy Accel. Res. Organization)  
 KATO Kiyoshi 加藤幾芳 (Fac. Sci., Hokkaido Univ.)  
 KATO Shohei 加藤昌平 (Fac. Sci., Osaka Univ.)  
 KATORI Kenji 鹿取謙二 (Fac. Sci., Osaka Univ.)  
 KATSURAGAWA Hidetsugu 桂川秀嗣 (Fac. Sci., Toho Univ.)  
 KAWAGUCHI Takeo 川口武男 (Mitsubishi Electric Co., Ltd.)  
 KITAGAWA Hisashi 北川尚 (Inst. Phys., Univ. Tsukuba)  
 KOBAYASHI Misaki 小林美咲 (Science Service Co., Ltd.)  
 KOHAMA Akihisa 小濱洋央 (Fac. Sci., Univ. Tokyo)  
 KONDO Michiya 近藤道也 (RCNP, Osaka Univ.)  
 KOTAJIMA Kyuya 古田島久哉 (Fac. Eng., Tohoku Univ.)  
 KOYEN Ali R. (Univ. Texas, Arlington, U.S.A.)  
 KUDO Hisaaki 工藤久昭 (Fac. Sci., Niigata Univ.)  
 KUMATA Masayuki 熊田雅之 (N.I.R.S.)  
 LEE Kong Ok 李康玉 (Rika Women's Coll., Korea)  
 LEE Sang Mu 李相茂 (Inst. Phys., Univ. Tsukuba)  
 LI Hongling 李洪玲 (RCAST, Univ. Tokyo)  
 LIU Sheng Li (Inst. Modern Phys., Academia Sinica, China)  
 MAEDA Kazuhide 前田和秀 (Fac. Sci., Kyushu Univ.)  
 MATSUDA Sumio 松田純夫 (NASDA)  
 MATSUI Yoshiko 松井芳子 (Fac. Tech., Agri. Tech., Univ. Tokyo)  
 MATSUKI Seishi 松木征史 (Inst. Chem. Res., Kyoto Univ.)  
 MATSUMOTO Akihiro 松本暁洋 (NASDA)  
 MATSUSE Takehiro 松瀬丈浩 (Fac. Textile Sci. Tech., Shinshu Univ.)  
 MATSUYANAGI Kenichi 松柳研一 (Fac. Sci., Kyoto Univ.)  
 MATUZAKI Masayuki 松崎昌之 (Fukuoka Univ. Ed.)  
 MENG Jie  
 MINAMISONO Tadanori 南園忠則 (Fac. Sci., Osaka Univ.)  
 MITSUMOTO Toshinori 蜜本俊典 (Sumitomo Heavy Industries, Ltd.)  
 MIURA Iwao 三浦岩 (RCNP, Osaka Univ.)  
 MIYATAKE Hiroari 宮武宇也 (KEK)  
 MIZUNO Yoshiyuki 水野義之 (RCNP, Osaka Univ.)  
 MIZUSAKI Takahiro 水崎高浩 (Fac. Sci., Univ. Tokyo)  
 MORI Yoshiharu 森義治 (KEK)  
 MORIKAWA Tetsuya 森川鐵也  
 MOTONAGA Shoushichi 元永昭七 (Former Staff of RIKEN)  
 MUKHOPADHTAY M. (Variable Energy Cycl. Cent., India)  
 MURAKAMI Hideoki 村上英興 (Tokyo Gakugei Univ.)  
 MURAKAMI Tetsuya 村上哲也 (Fac. Sci., Kyoto Univ.)  
 MURAYAMA Toshiyuki 村山利幸 (Univ. Tokyo, Mercantile Marine)  
 MUTO Kazuo 武藤一雄 (Fac. Sci., Tokyo Inst. Technol.)  
 NAGAFUCHI Teruyasu 永渕照康 (Toshiba Corp.)  
 NAGAI Yasuki 永井泰樹 (Fac. Sci., Tokyo Inst. Technol.)  
 NAGAI Yuki 永井由紀 (NASDA)  
 NAKADA Hitoshi 中田仁 (Coll. Art & Sci., Chiba Univ.)  
 NAKAHARA Hiromichi 中原弘道 (Fac. Sci., Tokyo Metrop. Univ.)  
 NAKAI Ko-zi 中井浩二 (Fac. Sci. Tech., Sci. Univ. Tokyo)  
 NAKAMURA Hiroyuki 中村裕之 (Fac. Sci., Kyushu Univ.)  
 NAKAMURA Ichiro 中村市郎 (Fac. Sci., Saitama Univ.)  
 NAKAMURA Takashi 中村尚司 (Cycl. Radioisot. Cent., Tohoku Univ.)  
 NAKAO Noriaki 中尾徳晶 (KEK)  
 NAKASHIMA Hiroshi 中島宏 (JAERI, Tokai Res. Estab.)

NODA Akira 野田 章 (Inst. Chem. Res., Kyoto Univ.)  
 NODA Kouji 野田耕司 (N.I.R.S.)  
 NOMURA Toru 野村 亨 (KEK)  
 NOZAKI Tadashi 野崎 正 (Kagami Memorial Lab., Materials & Sci., Waseda Univ.)  
 OGAWA Kengo 小川健吾 (Dept. Eng., Sci., Himeji Inst. Tech.)  
 OHIRA Hideharu 大平秀春 (NASDA)  
 OHKAWA Tomohiro 大川智宏 (Mitsubishi Heavy Industries, Ltd.)  
 OHNISHI Naoki 大西直毅 (Coll. Art Sci., Univ. Tokyo)  
 OHTOMO Kiyotaka 大友清隆 (Sumitomo Heavy Industries, Ltd.)  
 OHTSUKI Tsutomu 大槻 勤 (Lab. Nucl. Sci., Tohoku Univ.)  
 OHYA Jiro 大矢次郎 (NASDA)  
 OKAMOTO Hiromi 岡本宏巳 (Inst. Chem. Res., Kyoto Univ.)  
 OKAMURA Hiroyuki 岡村弘之 (Fac. Sci., Univ. Tokyo)  
 OKUMURA Susumu 奥村 進 (JAERI, Takasaki Rad. Chem. Res. Estab.)  
 OOTOMO Hiromitsu 大友洋光 (NASDA)  
 OTA Kiyoshi 太田 清 (Fac. Sci., Saitama Univ.)  
 PERSSON Jonas  
 SAGARA Kenshi 相良建至 (Fac. Sci., Kyushu Univ.)  
 SAITO Motozo 齐藤始三 (Former Staff of RIKEN)  
 SAKAI Hideyuki 酒井英行 (Fac. Sci., Univ. Tokyo)  
 SAMBATARO Michelangelo (I.N.F.N., Catania)  
 SATO Ken-ichi 佐藤憲一 (Dept. Phys., Tohoku Coll. Pharm.)  
 SATO Kenji 佐藤健次 (RCNP, Osaka Univ.)  
 SATO Yukio 佐藤幸夫 (N.I.R.S.)  
 SEKINE Toshiaki 関根俊明 (JAERI, Tokai Res. Estab.)  
 SHIBATA Tokushi 柴田德思 (KEK)  
 SHIKAZONO Naomoto 鹿園直基 (JAERI, Tokai Res. Estab.)  
 SHIMIZU Akira 清水 昭 (RCNP, Osaka Univ.)  
 SHIMOMURA Kouichiro 下村浩一郎 (Meson Sci. Lab., KEK Brunch, Univ. Tokyo)  
 SHIN Kazuo 秦 和夫 (Fac. Eng., Kyoto Univ.)  
 SHIN Seung Ai 辛 承愛 (Rika Women's College, Korea)  
 SHINDO Hiroyuki 新藤浩之 (NASDA)  
 SHINOZUKA Tsutomu 篠塚 勉 (Cycl. Radioisot. Cent., Tohoku Univ.)  
 SHIRAI Toshiyuki 白井敏之 (Nucl. Sci. Res. Fac., Inst. Chem. Res., Kyoto Univ.)  
 SHIROV Grigori (J.I.N.R., Dubna)  
 SHUGYO Shin-ichi 修行新一 (NASDA)  
 SIDORIN Anatoly (J.I.N.R., Dubna)  
 SUEKI Keisuke 末木啓介 (Fac. Sci., Tokyo Metrop. Univ.)  
 SUGAI Isao 菅井 勲 (KEK)  
 SUGII Kazuo 杉井一生 (Osaka Vacuum, Ltd.)  
 SUGIMOTO Kenji 杉本憲治 (NASDA)  
 SUGIYAMA Hiroki 杉山大樹 (NASDA)  
 SUMIYOSHI Hiroyuki 住吉広行 (Matsusho-Gakuen Junior Coll.)  
 SUZUKI Toshio 鈴木俊夫 (Coll. Sci. Tech., Nihon Univ.)  
 SUZUKI Takahiro 鈴木隆博 (NASDA)  
 SYRESSINE Evgucni (J.I.N.R., Dubna, Russia)  
 TAGISHI Yoshihiro 田岸義宏 (Tandem Accel. Cent., Univ. Tsukuba)  
 TAJIMA Naoki 田嶋直樹 (Coll. Art Sci., Univ. Tokyo)  
 TAKADA Masashi 高田真志 (N.I.R.S.)  
 TAKEMASA Tadashi 武政尹士 (Kyoto Univ. Edu.)  
 TAKEUCHI Suehiro 竹内末広 (JAERI, Tokai Res. Estab.)  
 TAKIGAWA Noboru 滝川 昇 (Fac. Sci., Tohoku Univ.)  
 TAMAGAKI Ryoza 玉垣良三 (Fac. Sci., Kyoto Univ.)  
 TANABE Kazuko 田辺和子 (Otsuna Women's Coll.)  
 TANABE Kousai 田辺孝哉 (Fac. Sci., Saitama Univ.)  
 TANAKA Jinichi 田中仁市 (KEK)  
 TANAKA Kazuhiro 田中和廣 (Medical Dept., Jyuntendo Univ.)  
 TANAKA Yasushi 田中保志 (Kyokuto Boeki Kaisha, Ltd.)

TANIKAWA Masashi 谷川勝至 (Fac. Sci., Univ. Tokyo)  
 TOHYAMA Mitsuru 遠山 満 (Kyorin Univ.)  
 TOMIMASU Takio 富增多喜夫 (Free Electr. Laser Res. Inst. Inc.)  
 TOMINAKA Toshiharu 富中利治 (Hitachi, Ltd.)  
 TOMITANI Takehiro 富谷武浩 (N.I.R.S.)  
 TOMIZAWA Masahito 富澤正人 (KEK)  
 TOMODA Toshiaki 友田敏章 (Fac. Eng., Aomori Univ.)  
 TOPREK Dragan (VINCA, Inst. Nucl. Sci., Yugoslavia)  
 TORIYAMA Tamotsu 鳥山 保 (Dept. Phys., Musashi Inst. Technol.)  
 TSUBAKI Noriyuki 椿 則幸 (NASDA)  
 TSUKINO Akihisa 月野晃久 (NASDA)  
 UTSUNOMIYA Hiroaki 宇都宮弘章 (Fac. Sci., Konan Univ.)  
 WADA Michiharu 和田道治 (KEK)  
 WADA Ryoichi 和田良一 (Texas A & M Univ., U.S.A.)  
 WADA Takahiro 和田隆宏 (Fac. Sci., Konan Univ.)  
 WAKAI Masamichi 若井正道 (Fac. Sci., Osaka Univ.)  
 WAKUTA Yoshihisa 和久田義久 (Fac. Eng., Kyushu Univ.)  
 WATANABE Ikuo 渡辺郁男 (Toshiba Corp.)  
 WATANABE Shin-ichi 渡辺伸一 (Cent. Nucl. Study, Grad. Sch. Sci., Univ. Tokyo)  
 WU Dezhong (Inst. Modern Phys., Academia Sinica, China)  
 YABANA Kazuhiro 矢花一浩 (Fac. Sci., Niigata Univ.)  
 YAMANOUCI Mikio 山内幹雄 (Inst. Phys., Univ. Tsukuba)  
 YAMAZAKI Hirohito 山崎寛仁 (Lab. Nucl. Sci., Tohoku Univ.)  
 YAMAZAKI Takashi 山崎 魏 (RCNP, Osaka Univ.)  
 YOKOUCHI Shigeru 横内 茂 (Osaka Vacuum, Ltd.)  
 YONEDA Akira 米田 晃  
 YONEMARU Mitsunori 米丸充規 (NASDA)  
 YOSHIDA Nobuaki 吉田宣章 (Fac. Sci., Univ. Tokyo)  
 YOSHINAGA Naotaka 吉永尚孝 (Fac. Sci., Saitama Univ.)  
 YOSHIOKA Yasuhiro 吉岡康弘 (NASDA)  
 YOSHIZAWA Yasukazu 吉沢康和 (Fac. Eng., Kyushu Univ.)  
 YUAN Ping (Inst. Modern Phys., Academia Sinica, China)  
 ZHANG Wenzhi (Inst. Modern Phys., Academia Sinica, China)

(Students)

AOKI Yuka 青木由香 (Grad. Sch. Sci., Tohoku Univ.)  
 ARIGA Takehiro 有賀健博 (Fac. Sci., Saitama Univ.)  
 FUJITA Tatsuru 藤田 建 (Interdisciplinary Grad. Sch. Eng. Sci., Kyushu Univ.)  
 HASHIMOTO Satoshi 橋本 賢 (Dept. Phys., Grad. Sch. Sci., Univ. Tokyo)  
 KIM Eun Joo (Grad. Sch. Sci., Tohoku Univ.)  
 KINOSHITA Tadashi 木下 忠 (Grad. Sch. Sci., Tohoku Univ.)  
 KURITA Tetsuro 栗田哲郎 (Inst. Phys., Univ. Tsukuba)  
 KUROSAWA Tadahiro 黒澤忠弘 (Grad. Sch. Sci., Tohoku Univ.)  
 NAKAO Makoto 中尾 誠 (Grad. Sch. Sci., Tohoku Univ.)  
 OGATA Kentaro 緒方研太郎 (Fac. Sci., Kyushu Univ.)  
 OI Makito 大井万紀人 (Grad. Sch. Arts Sci., Univ. Tokyo)  
 OKUDA Hikaru 奥田 光 (Fac. Sci., Kyushu Univ.)  
 OSHIMA Nagayasu 大島永康 (Grad. Univ. Adv. Stud.)  
 OZAWA Shuichi 小澤修一 (Coll. Sci., Rikkyo Univ.)  
 SASAKI Michiya 佐々木道也 (Grad. Sch. Sci., Tohoku Univ.)  
 SHIGENAGA Kouichi 重永晃一 (Fac. Sci., Kyushu Univ.)  
 SONE Hayato 曾根逸人 (Fac. Sci. Tech., Sci. Univ. Tokyo)  
 TANIGUCHI Shingo 谷口真吾 (Grad. Sch. Sci., Tohoku Univ.)  
 TSURUTA Kaoru 鶴田 薫 (Interdisciplinary Grad. Sch. Eng. Sci., Kyushu Univ.)  
 WAKUI Takashi 湧井崇志 (Fac. Sci., Toho Univ.)  
 YAGITA Takanori 八木田貴典 (Fac. Sci., Kyushu Univ.)

## Linear Accelerator Laboratory

CHIBA Toshiya 千葉利哉	FUJIMAKI Masaki 藤巻正樹
FUKUDA Shigekazu 福田茂一 <sup>*1</sup>	HEMMI Masatake 逸見政武
IKEZAWA Eiji 池沢英二	KASE Masayuki 加瀬昌之
KOBAYASHI Toshio 小林俊雄 <sup>*2</sup>	KORSHENINNIKOV Alexei
KUMAGAI Hidekazu 熊谷秀和	KUSAKA Kensuke 日下健祐
MIYAZAWA Yoshitoshi 宮沢佳敏	MOCHIZUKI Yuko S. 望月優子 <sup>*1</sup>
MOMOTA Sadao 百田佐多生 <sup>*1</sup>	OGAWA Yoko 小川洋子 <sup>*1</sup>
OHTSU Hideaki 大津秀暁 <sup>*1</sup>	OZAWA Akira 小沢顕
SUZUKI Takeshi 鈴木健	TANIHATA Isao 谷畑勇夫 <sup>*4</sup>
TONUMA Masao 戸沼正雄	YOSHIDA Koichi 吉田光一

<sup>\*1</sup> Special Postdoctoral Researcher, <sup>\*2</sup> Senior Scientist, <sup>\*3</sup> Postdoctoral Researcher,  
<sup>\*4</sup> Chief Scientist

### (Visitors)

ADACHI Shizuko 安達静子 (ICFD)  
AHMADY Mohammad (Western Ontario Univ., Canada)  
ARATANI Michi 荒谷美智 (Inst. Environmental Sci.)  
BOLBOT Michael (Notre Dame Univ., U.S.A.)  
BOYD Richard (Ohio Univ., U.S.A.)  
BROCKMANN Roff (Inst. Phys., Univ. Mainz, Germany)  
DAVID Dean J. (CALTEC, U.S.A.)  
DEMYANOVA Alla S. (Kurchatov Inst. Atomic Energy, Russia)  
FUJIWARA Mamoru 藤原守 (RCNP, Osaka Univ.)  
FÜLÖP Zsolt (ATOMKI, Hungary)  
GOLOVKOV Mkhel S. (Kurchatov Inst., Russia)  
GONCHAROV Sergei A. (Kurchatov Inst., Russia)  
HIRENZAKI Satoru 日連崎悟 (Fac. Sci., Nara Women's Univ.)  
HORIUCHI Hisashi 堀内昶 (Fac. Sci., Kyoto Univ.)  
IWAMOTO Akira 岩本昭 (JAERI, Tokai Res. Estab.)  
IZUYAMA Takeo 伊豆山健夫 (Fac. Sci., Toho Univ.)  
KATORI Kenji 鹿取謙二 (Fac. Sci., Osaka Univ.)  
KIKUCHI Jun 菊地順 (Sci. Eng. Res. Lab., Waseda Univ.)  
KIMURA Kikuo 木村喜久雄 (Fac. Eng., Nagasaki Inst. Appl. Sci.)  
KOLATA James (Notre Dame Univ., U.S.A.)  
MARUYAMA Tomoyuki 丸山智之 (Fac. Sci., Kyoto Univ.)  
MATSUTA Kensaku 松多健策 (Fac. Sci., Osaka Univ.)  
MATSUYAMA Yoshitaka 松山芳孝 (Inst. Nucl. Study, Univ. Tokyo)  
MATUOKA Nobuyuki 松岡伸行 (Res. Cent. Nucl. Phys., Osaka Univ.)  
MITTING M. (GANIL, France)  
MIYAKE Yasuo 三明康郎 (Fac. Sci., Univ. Tsukuba)  
MIYAMURA Osamu 宮村修 (Fac. Sci., Hiroshima Univ.)  
MOCHIZUKI Keiko 望月圭子 (Fac. Sci., Osaka Univ.)  
MORIMOTO Koji 森本幸司 (JST)  
MURAOKA Mitsuo 村岡光男 (Fac. Eng., Aomori Univ.)  
NOJIRI Yoichi 野尻洋一 (Kochi Univ. Technol.)  
OGAWA Kengo 小川健吾 (Coll. Arts. Sci., Chiba Univ.)  
OGLOBLIN Alexei A. (Kurchatov. Inst., Russia)  
OHNISHI Akira 大西明 (Fac. Sci., Hokkaido Univ.)  
OHTSUBO Takashi 大坪隆 (Fac. Sci., Niigata Univ.)  
OJIMA Minoru 小嶋稔 (Fac. Sci., Osaka Univ.)  
OMATA Kazuo 小俣和夫 (Inst. Nucl. Study, Univ. Tokyo)  
ORYU Shinsho 尾立晋祥 (Fac. Sci. and Tech., Sci. Univ. Tokyo)  
OYAMATSU Kazuhiro 親松和浩 (Dept. Energy Eng. Sci., Nagoya Univ.)  
PETRASCU Horia (Inst. Phys. Nucl. Eng., Romania)  
PETRASCU Marius (Inst. Phys. Nucl. Eng., Romania)  
RAIMANN Gerhard (Ohio State Univ., U.S.A.)

SAGAWA Hiroyuki 佐川弘幸 (Cent. Mathematical Sci., Aizu Univ.)  
 SAKAI Hideyuki 酒井英行 (Fac. Sci., Univ. Tokyo)  
 SATO Kazuhiro 佐藤和広 (Tokyo Fire Dept.)  
 SEKI Ryoichi 関 亮一 (California Univ., U.S.A.)  
 SHERRIL B. (Michigan State Univ., U.S.A.)  
 SUDA Toshimi 須田利美 (Fac. Sci., Tohoku Univ.)  
 SUGANUMA Hideo 菅沼秀夫 (RCNP, Osaka Univ.)  
 SUGAWARA Masahiko 菅原昌彦 (Fundam. Sci., Chiba Inst. Technol.)  
 SUZUKI Hideyuki 鈴木英之 (KEK)  
 SUZUKI Tsuneo 鈴木恒雄 (Fac. Sci., Kanazawa Univ.)  
 SUZUKI Yasuyuki 鈴木宣之 (Fac. Sci., Niigata Univ.)  
 TACHIBANA Takahiro 橋 孝博 (Senior High School of Waseda Univ.)  
 TAKAHASHI Yoshiyuki 高橋義幸 (Alabama Univ., U.S.A.)  
 TAKAHASHI Yutaka 高橋 豊 (Fac. Sci., Osaka Univ.)  
 TOKANAI Fuyuki 門叶冬樹 (JST)  
 TOKI Hiroshi 土岐 博 (RCNP, Osaka Univ.)  
 TORBJOEN Baeck (Stochholm Univ., Sweden)  
 VARGA Kalman (Inst. Nucl. Res., Hungarian Acad. Sci., Hungary)  
 WADA Takahiro 和田隆宏 (Fac. Sci., Konan Univ.)  
 YAGI Hirosuke 八木浩輔 (Fac. Sci., Univ. Tsukuba)  
 YORANN Alhassid (Yale Univ., U.S.A.)  
 ZAHAR Mohamed (Dept. Phys., Notre Dame Univ., U.S.A.)

(Students)

BOKU Yudan 朴 勇男 (Fac. Sci. Eng., Waseda Univ.)  
 FUKUDA Naoki 福田直樹 (Fac. Sci. Eng., Waseda Univ.)  
 HIBINO Masaru 日比野 優 (Fac. Sci. Eng., Waseda Univ.)  
 HIYAMA Emiko 肥山詠美子 (Fac. Sci., Kyushu Univ.)  
 HONG Wang 洪 完 (Fac. Eng., Univ. Tokyo)  
 IKEDA Takayuki 池田隆之 (Grad. Sch., Osaka Univ.)  
 ISHIGA Kenichi 石賀健一 (Grad. Sch., Osaka Univ.)  
 KABURAGI Akira 柚木 彰 (Grad. Sch., Waseda Univ.)  
 KANO Kenji 叶 健治 (Fac. Sci., Univ. Tsukuba)  
 KATO Toshiyuki 加藤俊幸 (Fac. Sci. Eng., Waseda Univ.)  
 KIUCHI Hiroshi 木内 宏 (Fac. Sci., Saitama Univ.)  
 KONO Sachiko 甲野祥子 (Fac. Sci. Eng., Waseda Univ.)  
 KOZU Tomotake 神津友武 (Fac. Sci. Eng., Waseda Univ.)  
 MARUYAMA Yukiko 丸山由紀子 (Fac. Sci., Osaka Univ.)  
 MATSUMOTO Akiko 松本晶子 (Fac. Sci. Eng., Waseda Univ.)  
 MIKI Keitaro 三木敬太郎 (Fac. Sci., Konan Univ.)  
 OZAKI Kiminori 尾崎公教 (Fac. Sci. Eng., Waseda Univ.)  
 SAITO Masanori 斎藤正憲 (Fac. Sci., Osaka Univ.)  
 SAKAGUCHI Takao 坂口貴男 (Fac. Sci. Eng., Waseda Univ.)  
 SHIMOOKA Masaaki 下岡正明 (Fac. Sci., Kyoto Univ.)  
 TAKAHASHI Yoshiyuki 高橋義幸 (Fac. Sci. Eng., Waseda Univ.)  
 TAKAHASHI Kenichi 高橋賢一 (Grad. Sch., Waseda Univ.)  
 TAKEHANA Naohiro 竹花直弘 (Fac. Sci. Eng., Waseda Univ.)  
 TAKENAKA Sunao 竹中 直 (Fac. Sci. Eng., Waseda Univ.)  
 TERUHI Shigeru 照日 繁 (Fac. Sci. Eng., Waseda Univ.)  
 WANG Haiming 王 海鳴 (Fac. Sci., Univ. Tokyo)  
 YAMASHITA Akira 山下 顕 (Fac. Sci., Univ. Tokyo)

#### Radiation Laboratory

BEUMEL Didier* <sup>1</sup>	DEVI Yelamanchili Durga* <sup>1</sup>
GOTO Yuji 後藤雄二* <sup>2</sup>	HAHN Kevin I.* <sup>2</sup>
HAYASHI Naoki 林 直樹* <sup>2</sup>	HIRAI Masaaki 平井正明* <sup>3</sup>
ICHIHARA Takashi 市原 卓* <sup>4</sup>	IDEUCHI Eiji 井手口榮治* <sup>2</sup>

ISHIHARA Masayasu 石原正泰*5	KISHIDA Takashi 岸田 隆
KURITA Kazuyoshi 栗田和好*2	MATSUKI Tsuneki 松木常樹*3
MIZOI Yutaka 溝井 浩*2	NOTANI Masahiro 野谷将広*2
OHTA Shigemi 太田滋生*6	OKAMURA Masahiro 岡村昌宏*2
OOYAMA Ken 大山 健*3	SAITO Naohito 齊藤直人
SAKURAI Hiroyoshi 櫻井博儀	TERANISHI Takashi 寺西 高*2
WATANABE Yasushi 渡邊 康	WATANABE Yutaka 渡辺 裕*3
YANAGISAWA Yoshiyuki 柳沢善行*3	YOSHIDA Atsushi 吉田 敦

\*1 STA Fellow, \*2 Special Postdoctoral Researcher, \*3 Junior Research Associate,  
\*4 Senior Scientist, \*5 Chief Scientist, \*6 Visiting Researcher

(Visitors)

ABE Yasuhisa 阿部恭久 (Yukawa Inst. Theor. Phys., Kyoto Univ.)  
 ADACHI Minoru 足立 實 (Fac. Sci., Tokyo Inst. Technol.)  
 ANDO Yoshiaki 安藤嘉章 (Coll. Sci., Rikkyo Univ.)  
 ASAHИ Koichiro 旭 耕一郎 (Fac. Sci., Tokyo Inst. Technol.)  
 AWAYA Yoko 栗屋容子 (Musashino Art Univ.)  
 BECK F. A. (CRN, France)  
 BROGLIA R. (Dept. Phys., Univ. Milano, Italy)  
 CASTEN Rick (Dept. Phys., Brookhaven Natl. Lab., U.S.A.)  
 CHRIST Norman H. (Dept. Phys., Columbia Univ., U.S.A.)  
 DOOI Makoto 堂井 真 (Inst. Phys., Univ. Tsukuba)  
 EN'YO Hideto 延与秀人 (Fac. Sci., Kyoto Univ.)  
 FLOCARD Hubert (Div. Phys. Theor., IPN, France)  
 FUCHI Yoshihide 渕 好秀 (Inst. Nucl. Study, Univ. Tokyo)  
 FUKUDA Mitsunori 福田光順 (Grad. Sch. Sci., Osaka Univ.)  
 FUKUDA Tomokazu 福田共和 (Inst. Nucl. Study, Univ. Tokyo)  
 FURUTAKA Kazuyoshi 古高和禎 (JAERI, Adv. Sci. Res. Cent.)  
 HAMAGAKI Hideki 浜垣秀樹 (Cent. Nucl. Study, Univ. Tokyo)  
 HAMAMOTO Ikuko 浜本育子 (Dept. Theor. Phys., Lund Univ., Sweden)  
 HASEGAWA Takeo 長谷川武夫 (Fac. Eng., Miyazaki Univ.)  
 HATSUDA Tetsuo 初田哲男 (Inst. Phys., Univ. Tsukuba)  
 ICHIMURA Munetake 市村宗武 (Grad. Sch. Arts & Sci., Univ. Tokyo)  
 IEKI Kazuo 家城和夫 (Coll. Sci., Rikkyo Univ.)  
 IWASA Naohito 岩佐直仁 (Lab. Nucl. Studies, Fac. Sci., Osaka Univ.)  
 IZUMI Hideaki 出水秀明 (Fac. Sci., Grad. Sch. Sci., Osaka Univ.)  
 KAMAE Tsuneyoshi 釜江常好 (Dept. Phys., Grad. Sch. Sci., Univ. Tokyo)  
 KASAGI Jirota 笠木治郎太 (Lab. Nucl. Sci., Tohoku Univ.)  
 KATAYAMA Ichiro 片山一郎 (Cent. Nucl. Study, Univ. Tokyo)  
 KATO Seigo 加藤静吾 (Fac. Edu., Yamagata Univ.)  
 KATORI Kenji 鹿取謙二 (Lab. Nucl. Studies, Fac. Sci., Osaka Univ.)  
 KIM Jong Chan 金 鐘贊 (Dept. Phys., Seoul Natl. Univ., Korea)  
 KITAO Kensuke 喜多尾憲助 (Data Eng. Inc.)  
 KODAIRA Jirou 小平治郎 (Fac. Sci., Hiroshima Univ.)  
 KOIKE Yuji 小池裕司 (Fac. Sci., Niigata Univ.)  
 KOSOWER David A. (Dept. Phys., Univ. Milano)  
 KUBONO Shigeru 久保野 茂 (Cent. Nucl. Study, Univ. Tokyo)  
 KUMANO Shunzo 熊野俊三 (Fac. Sci. and Eng., Saga Univ.)  
 KUSAKARI Hideshige 草刈英榮 (Fac. Edu., Chiba Univ.)  
 LEE Sang Mu 李 相茂 (Inst. Phys., Univ. Tsukuba)  
 LIU Xin (Cent. Nucl. Study, Univ. Tokyo)  
 LIU Zhong (Inst. Mod. Phys., Acad. Sinica, China)  
 LOUKIANOV Serguei (Flerov Lab. Nucl. Reactions, JINR, Russia)  
 MAEDA Kazushige 前田和茂 (Grad. Sch. Sci., Tohoku Univ.)  
 MAO Yajun (Dept. Nucl. Phys., China Inst. Atom. Energy, China)  
 MATSUDA Satoshi 松田 哲 (Dept. Fundamental Sci., Fac. Integrated Human Studies, Kyoto Univ.)  
 MATSUI Tetsuo 松井哲男 (Yukawa Inst. Theor. Phys., Kyoto Univ.)

MATSUYANAGI Kenichi 松柳研一 (Fac. Sci., Kyoto Univ.)  
 MENGONI Alberto  
 MITARAI Shiro 御手洗志郎 (Fac. Sci., Kyushu Univ.)  
 MITSUOKA Shinichi 光岡真一 (JAERI)  
 MIYACHI Takashi 宮地孝 (Cent. Nucl. Study, Univ. Tokyo)  
 MIYATAKE Hiroari 宮武宇也 (Inst. Particle Nucl. Phys., KEK)  
 MORII Toshiyuki 森井俊行 (Fac. Human Develop., Kobe Univ.)  
 MORIKAWA Tsuneyasu 森川恒安 (Dept. Phys., Fac. Sci., Kyushu Univ.)  
 MORINOBU Shunpei 森信俊平 (Dept. Phys., Fac. Sci., Kyushu Univ.)  
 MOTOBAYASHI Toru 本林透 (Dept. Phys., Coll. Sci., Rikkyo Univ.)  
 MOTTELSON Ben R. (NORDITA, Nordisk Inst. Teoretisk Fysik, Denmark)  
 MUELLER Ludwig (Phys. Dept., Univ. Padova, Italy)  
 MURAKAMI Takeshi 村上健 (Natl. Inst. Radiol. Sci.)  
 NAGAI Yasuki 永井泰樹 (Fac. Sci., Tokyo Inst. Technol.)  
 NAGASHIMA Yasuo 長島泰夫 (Inst. Phys., Univ. Tsukuba)  
 NAKAMURA Takashi 中村隆司 (Dept. Phys., Grad. Sch. Sci., Univ. Tokyo)  
 NAKAMURA Msanobu 中村正信 (Fac. Sci., Kyoto Univ.)  
 NAKAYAMA Shintaro 中山信太郎 (Fac. Integrated Arts and Sci., Tokushima Univ.)  
 NIIZEKI Takashi 新関隆 (Fac. Sci., Tokyo Inst. Technol.)  
 NORO Tetsuo 野呂哲夫 (Res. Cent. Nucl. Phys., Osaka Univ.)  
 ODAHARA Atsuko 小田原厚子 (Nishinippon Inst. Tech.)  
 OGAWA Masao 小川雅生 (Interdisciplinary Grad. Sch. Sci. Eng., Tokyo Inst. Technol.)  
 OKAMURA Hiroyuki 岡村弘之 (Dept. Phys., Grad. Sch. Sci., Univ. Tokyo)  
 ORIHARA Hikonojyo 織原彦之丞 (Cycl. Radioisot. Cent., Tohoku Univ.)  
 OSHIMA Masumi 大島真澄 (JAERI, Adv. Sci. Res. Cent.)  
 OTSUKA Takaharu 大塚孝治 (Dept. Phys., Grad. Sch. Sci., Univ. Tokyo)  
 PENIONJKEVITCH Yuri (Flerov Lab. Nucl. Reactions, JINR, Russia)  
 SAGAWA Hiroyuki 佐川弘幸 (Cent. Mathematical Sci., Aizu Univ.)  
 SAKAGUCHI Harutaka 坂口治隆 (Fac. Sci., Kyoto Univ.)  
 SAKAI Mitsuo 坂井光夫 (Univ. Tokyo)  
 SAKURAGI Hiroyuki 櫻木弘之 (Fac. Sci., Osaka City Univ.)  
 SATO Hiroshi 佐藤竝 (Seikei Univ.)  
 SATO Hikaru 佐藤皓 (KEK)  
 SCHAEFER Markus (Physicalisches Inst., Goettingen Univ., Germany)  
 SCHMIDT-OTT Wolf-Dieter (Physicalisches Inst., Goettingen Univ., Germany)  
 SHIBATA Toshiaki 柴田利明 (Fac. Sci., Tokyo Inst. Technol.)  
 SHIMIZU Hajime 清水肇 (Fac. Sci., Yamagata Univ.)  
 SHIMIZU Yoshifumi 清水良文 (Fac. Sci., Kyushu Univ.)  
 SHIMODA Tadashi 下田正 (Grad. Sch. Sci., Osaka Univ.)  
 SHIMOURA Susumu 下浦享 (Coll. Sci., Rikkyo Univ.)  
 SIGNORINI Cosimo (Phys. Dept., Univ. Padova, Italy)  
 SUGAWARA Masahiko 菅原昌彦 (Chiba Inst. Technol.)  
 SUZUKI Masayo 鈴木昌世 (JASRI)  
 SUZUKI Yasuyuki 鈴木宜之 (Fac. Sci., Niigata Univ.)  
 TAJIMA Yasuhisa 田島靖久 (Cycl. Radioisot. Cent., Tohoku Univ.)  
 TAKADA Eiichi 高田栄一 (Natl. Inst. Radiol. Sci.)  
 TAKAHASHI Noriaki 高橋憲明 (Grad. Sch. Sci., Osaka Univ.)  
 TAKAHASHI Tadayuki 高橋忠幸 (Inst. Space and Astronautical Sci.)  
 TAKIGAWA Noboru 滝川昇 (Grad. Sch. Sci., Tohoku Univ.)  
 TANAKA Masahiko 田中雅彦 (Inst. Nucl. Study, Univ. Tokyo)  
 TANOKURA Atsushi 田野倉敦 (Fac. Sci. Technol., Sophia Univ.)  
 TERAOKA Atsuki 寺川貴樹 (Cycl. Radioisot. Cent., Tohoku Univ.)  
 THOMPSON Ian Joseph (Phys. Dept., Univ. Surrey, U.K.)  
 TOKI Hiroshi 土岐博 (Res. Cent. Nucl. Phys., Osaka Univ.)  
 TOYOKAWA Hidenori 豊川秀訓 (JASRI)  
 UENO Hideki 上野秀樹 (Lab. Nucl. Studies, Fac. Sci., Osaka Univ.)  
 UNO Masahiro 宇野正宏 (Ministry Edu., Sci. Culture)  
 WAKAMATSU Masashi 若松正志 (Lab. Nucl. Studies, Fac. Sci., Osaka Univ.)

WU Heyu 吳 和宇 (Inst. Mod. Phys., Acad. Sinica, China)  
YAMAMOTO Sukeyasu 山本祐靖 (Fac. Sci. Technol., Sophia Univ.)  
YAMANISHI Teruya 山西輝也 (Fac. Eng., Fukui Univ. Technol.)  
YOSHINAGA Naotaka 吉永尚孝 (Fac. Sci., Saitama Univ.)  
YOSOI Masaru 與曾井 優 (Fac. Sci., Kyoto Univ.)  
ZHOU Xiao Hong 周 小紅 (Inst. Mod. Phys., Acad. Sinica, China)

(Students)

AOI Nori 青井 考 (Dept. Phys., Grad. Sch. Sci., Univ. Tokyo)  
FUJIOKA Hiroyuki 藤岡博幸 (Dept. Phys., Grad. Sch. Sci., Univ. Tokyo)  
FUKAI Atsushi 深井 篤 (Coll. Sci., Rikkyo Univ.)  
FUKUDA Naoki 福田直樹 (Dept. Phys., Grad. Sch. Sci., Univ. Tokyo)  
FUKUSAKA Shoichi 福坂将一 (Dept. Phys., Grad. Sch. Sci., Univ. Tokyo)  
GOMI Tomoko 五味朋子 (Coll. Sci., Rikkyo Univ.)  
HAYASHIGAKI Arata 林垣 新 (Fac. Sci., Niigata Univ.)  
HIGURASHI Yoshihide 日暮祥英 (Coll. Sci., Rikkyo Univ.)  
HIRAI Masanori 平井正紀 (Fac. Sci., Saga Univ.)  
HIROSHIMA Tomotsugu 廣嶋友継 (Coll. Sci., Rikkyo Univ.)  
HISANAGA Isamu 久永 勇 (Coll. Sci., Rikkyo Univ.)  
HORIKAWA Hirotsugu 堀川博嗣 (Fac. Human Development, Kobe Univ.)  
IMAI Nobuaki 今井伸明 (Dept. Phys., Grad. Sch. Sci., Univ. Tokyo)  
ITO Kazuya 伊藤和也 (Grad. Sch. Sci., Tohoku Univ.)  
IWASAKI Hanako 岩崎華子 (Coll. Sci., Rikkyo Univ.)  
IWASAKI Hironori 岩崎弘典 (Dept. Phys., Grad. Sch. Sci., Univ. Tokyo)  
IWATA Yoshiyuki 岩田佳之 (Coll. Sci., Rikkyo Univ.)  
KIJIMA Takeshi 鬼島 丈 (Coll. Sci., Rikkyo Univ.)  
KOBAYASHI Hiroshi 小林 寛 (Coll. Sci., Rikkyo Univ.)  
KOREKI Taku 是木 卓 (Coll. Sci., Rikkyo Univ.)  
MATSUZAKI Keiichi 松崎恵一 (Dept. Phys., Grad. Sch. Sci., Univ. Tokyo)  
MINEMURA Toshiyuki 峯村俊行 (Coll. Sci., Rikkyo Univ.)  
MIYAKE Mami 三宅麻美 (Fac. Sci., Kyushu Univ.)  
MIYAMA Masanori 深山正紀 (Fac. Sci., Saga Univ.)  
MIZUMURA Yuuki 水村裕記 (Fac. Sci., Tokyo Inst. Technol.)  
MOTOMURA Shinji 本村信治 (Fac. Sci., Kyushu Univ.)  
NAGAKURA Masaki 長倉正樹 (Fac. Sci., Tokyo Inst. Technol.)  
NAGAOKA Satoshi 長岡悟史 (Dept. Phys., Grad. Sch. Sci., Univ. Tokyo)  
NAKADA Yoko 中田陽子 (Fac. Sci., Kyoto Univ.)  
NAKAMURA Shinichirou 中村真一朗 (Coll. Sci., Rikkyo Univ.)  
NAKANO Joe 中野 譲 (Cent. Nucl. Study, Univ. Tokyo)  
NISHIKAWA Miyuki 西川美幸 (Dept. Phys., Grad. Sch. Sci., Univ. Tokyo)  
NISHIO Teiji 西尾禎治 (Coll. Sci., Rikkyo Univ.)  
NISHIYAMA Naoki 西山直樹 (Fac. Sci., Niigata Univ.)  
NONAKA Takamasa 野中敬正 (Dept. Phys., Grad. Sch. Sci., Univ. Tokyo)  
NOZAWA Takeo 野澤豪生 (Fac. Sci., Tokyo Inst. Technol.)  
OGAWA Hiroshi 小川博嗣 (Fac. Sci., Tokyo Inst. Technol.)  
ONISHI Kazuaki 大西一聡 (Dept. Phys., Grad. Sch. Sci., Univ. Tokyo)  
OONISHI Tetsuya 大西哲哉 (Dept. Phys., Grad. Sch. Sci., Univ. Tokyo)  
SAISHU Souichi 最首壮一 (Fac. Sci., Tokyo Inst. Technol.)  
SAITO Yoshitaka 齋藤芳隆 (Dept. Phys., Grad. Sch. Sci., Univ. Tokyo)  
SAKAI Hiroshi 酒井 洋 (Coll. Sci., Rikkyo Univ.)  
SAKUMA Tai 佐久間 泰 (Fac. Sci., Tokyo Inst. Technol.)  
SATO Yoshiteru 佐藤義輝 (Dept. Phys., Grad. Sch. Sci., Univ. Tokyo)  
SATO Hiroki 佐藤博紀 (Fac. Sci., Kyoto Univ.)  
SEKIGICHI Kimiko 関口仁子 (Dept. Phys., Grad. Sch. Sci., Univ. Tokyo)  
SERATA Masaki 世良田真来 (Coll. Sci., Rikkyo Univ.)  
SHIBATA Masataka 柴田雅隆 (Fac. Sci., Kyushu Univ.)  
SUZUKI Mitsuharu 鈴木光晴 (Coll. Sci., Rikkyo Univ.)  
SUZUKI Ken 鈴木 謙 (Fac. Sci., Tokyo Inst. Technol.)

SUZUKI Takayuki 鈴木孝幸 (Fac. Sci., Tokyo Inst. Technol.)  
 TAKAHASHI Makoto 高橋誠 (Coll. Sci., Rikkyo Univ.)  
 TAKEUCHI Satoshi 武内聡 (Coll. Sci., Rikkyo Univ.)  
 TANAKA Fuyuhiko 田中冬彦 (Dept. Phys., Grad. Sch. Sci., Univ. Tokyo)  
 TANIGUCHI Etsuji 谷口悦史 (Fac. Sci., Tokyo Inst. Technol.)  
 TANIMOTO Sayaka 谷本明佳 (Fac. Sci., Grad. Sch. Sci., Osaka Univ.)  
 TATSUKI Masayuki 田附昌幸 (Coll. Sci., Rikkyo Univ.)  
 TSUDA Masaki 津田理樹 (Fac. Sci., Tokyo Inst. Technol.)  
 TSUTSUMI Takeshi 堤剛志 (Fac. Sci., Kyushu Univ.)  
 TUCHIDA Hideo 土田英夫 (Fac. Sci., Kyushu Univ.)  
 UCHIYAMA Yasuhito 内山靖仁 (Fac. Sci., Tokyo Inst. Technol.)  
 WATANABE Hiroshi 渡邊寛 (Fac. Sci., Kyushu Univ.)  
 XIAO Mei Gin 肖美琴 (Grad. Sch. Sci., Univ. Tokyo)  
 YAKO Kentaro 矢向謙太郎 (Dept. Phys., Grad. Sch. Sci., Univ. Tokyo)  
 YAMANE Tomoki 山根知樹 (Fac. Sci., Tokyo Inst. Technol.)  
 YOKOYAMA Go 横山剛 (Dept. Phys., Grad. Sch. Sci., Univ. Tokyo)  
 YONEDA Kenichiro 米田健一郎 (Dept. Phys., Grad. Sch. Sci., Univ. Tokyo)  
 YOSHIDA Takufumi 吉田琢史 (Dept. Phys., Grad. Sch. Sci., Univ. Tokyo)  
 YOSHIMI Akihiro 吉見彰洋 (Fac. Sci., Tokyo Inst. Technol.)  
 ZHANG Lin Feng 張林峰 (Fac. Sci., Tokyo Inst. Technol.)

#### Atomic Physics Laboratory

ANDO Kozo 安藤剛三	AWAYA Yohko 粟屋容子* <sup>1</sup>
IGARASHI Akinori 五十嵐明則	KAMBARA Tadashi 神原正* <sup>2</sup>
KANAI Yasuyuki 金井保之	KITAJIMA Masashi 北島昌史
KOJIMA Takao M. 小島隆夫	MARTINSON Indrek* <sup>3</sup>
NAKAI Yoichi 中井陽一	NISHIDA Masami 西田雅美
NISHIMURA Tamio 西村民男	NYSTRÖM Bosse* <sup>4</sup>
OURA Masaki 大浦正樹	OYAMA Hitoshi 大山等
SCHMIDT-BÖCKING Horst* <sup>3</sup>	SHIMAMURA Isao 島村勲* <sup>2</sup>
THURIEZ Sebastien* <sup>4</sup>	URAMOTO Seiichi 浦本聖一
YAMAZAKI Yasunori 山崎泰規* <sup>1</sup>	

---

\*<sup>1</sup> Chief Scientist, \*<sup>2</sup> Senior Scientist, \*<sup>3</sup> Eminent Scientist, \*<sup>4</sup> Visiting Researcher

(Visitors)

ACHLER Matthias (Inst. Kernphysik, Univ. Frankfurt, Germany)  
 AMUSIA Miron Ya (A. F. Ioffe Phys. Chem. Inst., Russia)  
 AZUMA Toshiyuki 東俊行 (Grad. Sch. Arts & Sci., Univ. Tokyo)  
 CHIMI Yasuhiro 知見康弘 (JAERI, Tokai Res. Estab.)  
 DePAOLA Brett D. (Kansas State Univ., U.S.A.)  
 FENG Xin (Dept. Phys., Univ. Ottawa, Canada)  
 FUJIMA Kazumi 藤間一美 (Fac. Eng., Yamanashi Univ.)  
 FUKUDA Hiroshi 福田宏 (Sch. Administration and Informatics, Univ. Shizuoka)  
 HARA Shunsuke 原俊介 (Dept. Gen. Educ., Tsukuba Coll. Technol.)  
 HINO Ken-ichi 日野健一 (Dept. Appl. Phys. Chem., Univ. Electro-Commun.)  
 HIRAYAMA Takato 平山孝人 (Dept. Phys., Gakushuin Univ.)  
 HULDT Sven (Lund Inst. Technol., Lund Univ., Sweden)  
 HUTTON Roger (Lund Inst. Technol., Lund Univ., Sweden)  
 ICHIMURA Atsushi 市村淳 (Inst. Space and Astr. Sci.)  
 ISHII Keishi 石井慶之 (Dept. Eng. Sci., Kyoto Univ.)  
 ISHIKAWA Norito 石川法人 (JAERI, Tokai Res. Estab.)  
 ITOH Akio 伊藤秋男 (Fac. Eng., Kyoto Univ.)  
 ITOH Yoh 伊藤陽 (Fac. Sci., Josai Univ.)  
 IWASE Akihiro 岩瀬彰宏 (JAERI, Tokai Res. Estab.)  
 KANEKO Shinichi 金子真一 (Fac. Sci., Tokyo Inst. Technol.)  
 KAWATSURA Kiyoshi 川面澄 (Fac. Eng. Design, Kyoto Inst. Technol.)

KIMURA Masahiro 木村正廣 (Kochi Univ. Technol.)  
 KIMURA Mineo 季村峯生 (The Sch. Allied Health Sciences, Yamaguchi Univ.)  
 KNUDSEN Helge (Univ. Aarhus, Denmark)  
 KOBAYASHI Nobuo 小林信夫 (Dept. Phys., Tokyo Metrop. Univ.)  
 KOHARA Takao 小原孝夫 (Fac. Sci., Himeji Inst. Technol.)  
 KOIKE Fumihiko 小池文博 (Sch. Med., Kitasato Univ.)  
 KOIZUMI Tetsuo 小泉哲夫 (Dept. Phys., Rikkyo Univ.)  
 KOMAKI Ken-ichiro 小牧研一郎 (Grad. Sch. Arts & Sci., Univ. Tokyo)  
 KOWARI Kenichi 小割健一 (Dept. Appl. Phys. Chem., Univ. Electro-Commun.)  
 KUROKI Kenro 黒木健郎 (Natl. Res. Inst. Police Sci.)  
 KUROTA Naoshi 黒田直志 (JAERI, Tokai Res. Estab.)  
 MATSUO Takashi 松尾崇 (Dept. Pathol., Tokyo Med. Dent. Univ.)  
 MATSUZAWA Michio 松澤通生 (Dept. Appl. Phys. Chem., Univ. Electro-Commun.)  
 MITAMURA Tohru 三田村徹 (Fac. Eng., Himeji Inst. Technol.)  
 MIZOGAWA Tatsumi 溝川辰巳 (Nagaoka Coll. Technol.)  
 MOHRI Akihiro 毛利明博 (Fac. Integrated Human Studies, Kyoto Univ.)  
 MUKOYAMA Takeshi 向山毅 (Inst. Chem. Res., Kyoto Univ.)  
 NAKAMURA Masato 中村正人 (Coll. Sci. Technol., Nihon Univ.)  
 NISHIDA Nobuhiko 西田信彦 (Fac. Sci., Tokyo Inst. Technol.)  
 OHTANI Shunsuke 大谷俊介 (Inst. Laser Sci., Univ. Electro-Commun.)  
 OKAYASU Satoru 岡安悟 (JAERI, Tokai Res. Estab.)  
 OKUNO Kazuhiko 奥野和彦 (Dept. Phys., Tokyo Metrop. Univ.)  
 SAKATA Hideaki 坂田英明 (Fac. Sci., Tokyo Inst. Technol.)  
 SAKURAI Makoto 桜井誠 (Fac. Sci., Kobe Univ.)  
 SATO Hiroshi 佐藤浩史 (Fac. Sci., Ochanomizu Univ.)  
 SATOH Kazuhiko 佐藤一彦 (Fac. Sci., Tokyo Inst. Technol.)  
 SATOH Yukinori 佐藤幸紀 (Res. Inst. Sci. Meas., Tohoku Univ.)  
 SEKIOKA Tsuguhisa 関岡嗣久 (Fac. Eng., Himeji Inst. Technol.)  
 SHIBATA Hiromi 柴田裕実 (Res. Cent. Nucl. Sci., Univ. Tokyo)  
 SHIMA Kunihiko 島邦博 (Tandem Accel. Cent., Univ. Tsukuba)  
 SHIMAKURA Noriyuki 島倉紀之 (Fac. Sci., Niigata Univ.)  
 SOEJIMA Kouichi 副島浩一 (Fac. Sci., Niigata Univ.)  
 SUZUKI Isao 鈴木功 (Electrotech. Lab.)  
 TAKAYANAGI Toshinobu 高柳俊暢 (Dept. Phys., Sophia Univ.)  
 TAWARA Hiroyuki 俵博之 (Natl. Inst. Fusion Sci.)  
 TERASAWA Mititaka 寺澤倫孝 (Fac. Eng., Himeji Inst. Technol.)  
 TOSHIMA Nobuyuki 戸嶋信幸 (Inst. Appl. Phys., Univ. Tsukuba)  
 WAKIYA Kazuyoshi 脇谷一義 (Dept. Phys., Sophia Univ.)  
 WATANABE Shinichi 渡辺信一 (Dept. Appl. Phys. Chem., Univ. Electro-Commun.)  
 YAGISHITA Akira 柳下明 (KEK)  
 YODA Jun 依田潤 (Natl. Res. Lab. Metrol.)  
 YOSHINO Masuhiro 吉野益弘 (Lab. Phys., Shibaura Inst. Technol.)  
 ZOU Yaming 邹亚明 (Shanghai Jiao Tong Univ., China)

(Students)

CHIBA Daisuke 千羽大介 (Dept. Phys., Sophia Univ.)  
 FAN Xiao Jun 樊晓骏 (Fac. Eng., Himeji Inst. Technol.)  
 FUJINO Atsushi 藤野敦 (Dept. Phys., Rikkyo Univ.)  
 HORI Masaki 堀正樹 (Dept. Phys., Grad. Sch. Sci., Univ. Tokyo)  
 ICHIOKA Toshiyasu 市岡利康 (Grad. Sch. Arts & Sci., Univ. Tokyo)  
 ITO Akira 伊藤聡 (Dept. Phys., Rikkyo Univ.)  
 IWAI Yoshio 岩井良夫 (Grad. Sch. Arts & Sci., Univ. Tokyo)  
 KAMEI Takehito 亀井武仁 (Dept. Phys., Sophia Univ.)  
 KAWAE Sotaro 川江宗太郎 (Dept. Eng. Sci., Kyoto Univ.)  
 KIMURA Yasuyuki 木村恭之 (Dept. Eng. Sci., Kyoto Univ.)  
 MATSUSHIMA Hiroshi 松島広 (Grad. Sch. Arts & Sci., Univ. Tokyo)  
 NAKANO Tomohide 仲野友秀 (Dept. Eng. Sci., Kyoto Univ.)  
 ONO Yasuhiro 小野泰弘 (Fac. Sci. Tokyo Inst. Technol.)

SUGIYAMA Yukiko 杉山幸子 (Dept. Phys., Sophia Univ.)  
TAGUCHI Yoshio 田口義雄 (Fac. Sci., Tokyo Inst. Technol.)  
TSUCHIDA Hidetsugu 土田秀次 (Fac. Eng., Kyoto Univ.)  
YAMASHITA Kenya 山下賢哉 (Dept. Phys., Grad. Sch. Sci, Univ. Tokyo)

### Muon Science Laboratory

FUJITA Ayumi 藤田あゆみ*1	FUKAYA Atsuko 深谷敦子*1
HIGEMOTO Wataru 髭本 亘*1	ISHIDA Katsuhiko 石田勝彦
KADONO Ryosuke 門野良典	KOYAMA Akio 小山昭雄
KRISHNAMURTHY Vemuru*2	MACRAE Roderick M.*3
MATSUZAKI Teiichiro 松崎禎市郎*4	NAGAMINE Kanetada 永嶺謙忠*5
NAKAMURA Satoshi N. 中村 哲	PRATT Francis L.*2
STRASSER Patrick*1	WATANABE Isao 渡邊功雄
WIDMAN Eberhard*6	YAGI Eiichi 八木栄一*4

\*1 Special Postdoctoral Researcher, \*2 Visiting Researcher, \*3 Riken Fellow,  
\*4 Senior Scientist, \*5 Chief Scientist, \*6 STA Fellow

(Visitors)

AKIMITSU Jun 秋光 純 (Coll. Sci. Eng., Aoyama Gakuin Univ.)  
ASAI Kichizo 浅井吉蔵 (Univ. Electro-Commun.)  
DAS Prasad Tara (Dept. Phys., State Univ. New York, Albany, U.S.A.)  
HASHIMOTO Masashi 橋本雅史 (JAERI, Tokai Res. Estab.)  
KATO Mineo 加藤峯生 (JAERI, Tokai Res. Estab.)  
KINO Yasushi 木野康志 (Fac. Sci., Tohoku Univ.)  
KUROSAWA Kiyoyuki 黒沢清行 (JAERI, Tokai Res. Estab.)  
MATSUSHITA Akira 松下 明 (Contract Researcher)  
MIYAKE Yasuhiro 三宅康博 (KEK)  
NISHIDA Nobuhiko 西田信彦 (Fac. Sci., Tokyo Inst. Univ.)  
NISHIYAMA Kusuo 西山樟生 (KEK)  
PRATT Francis Laurence (Dept. Phys., Univ. Oxford, U.K.)  
SHIMOMURA Koichiro 下村浩一郎 (KEK)  
SAKAMOTO Shinichi 坂元眞一 (KEK)  
TANASE Masakazu 棚瀬正和 (JAERI, Tokai Res. Estab.)  
TORIKAI Eiko 鳥養映子 (Fac. Eng., Yamanashi Univ.)

(Students)

KAWAMURA Naritoshi 河村成肇 (Fac. Sci., Univ. Tokyo)  
OOHIRA Seiko 大平聖子 (JKA)  
SASAHARA Takafumi 笹原孝文 (Fac. Sci. Eng., Chuo Univ.)  
TOYODA Akihisa 豊田晃久 (Fac. Sci., Univ. Tokyo)

### Magnetic Materials Laboratory

KATSUMATA Koichi 勝又紘一*1	MATSUDA Masaaki 松田雅晶
OKADA Takuya 岡田卓也*2	TATARA Gen 多々良 源*3

\*1 Chief Scientist, \*2 Senior Scientist, \*3 Visiting Researcher

### Computational Science Laboratory

EBISUZAKI Toshikazu 戎崎俊一*1	MIURA Hitoshi 三浦 均*2
SHIMIZU Tetsuya 清水鉄也*2	SUMIYOSHI Kousuke 住吉光介

\*1 Chief Scientist, \*2 Special Postdoctoral Researcher

(Visitor)  
HONG Shen 申 虹 (RCNP, Osaka Univ.)

(Student)  
SUGIMOTO Satoru 杉本 聡 (RCNP, Osaka Univ.)

### Inorganic Chemical Physics Laboratory

AMBE Shizuko 安部 静子  
MAEDA Kunuko 前田 邦子  
TAKAMI Michio 高見 道生\*2  
HUI Qin 惠 秦\*1  
MATSUO Yukari 松尾由賀利

---

\*1 Visiting Researcher, \*2 Chief Scientist

(Visitors)  
ARAI Nobuaki 荒井 修亮 (Dept. Fisheries, Kyoto Univ.)  
KAWAI Jun 河合 潤 (Dept. Metallurgy, Kyoto Univ.)

(Students)  
NAKAYAMA Satoshi 中山 哲史 (Coll. Eng., Hosei Univ.)  
TONOMURA Atsuro 殿村 淳朗 (Coll. Eng., Hosei Univ.)

### Nuclear Chemistry Laboratory

AMBE Fumitoshi 安部 文敏\*1  
KOBAYASHI Yoshio 小林 義男  
ENOMOTO Shuichi 榎本 秀一\*2  
TAKEMATSU Noburu 竹松 伸

---

\*1 Chief Scientist, \*2 Special Postdoctoral Researcher

(Visitors)  
AMANO Ryohei 天野 良平 (Sch. Health Sci., Kanazawa Univ.)  
BABA Hiroshi 馬場 宏 (Fac. Sci., Osaka Univ.)  
CHANG Zheng 常 征  
CHOU Ju (Changchun Inst. Appl. Chem., China)  
ENDO Kazutoyo 遠藤 和豊 (Showa Coll. Pharm. Sci.)  
FURUKAWA Michiaki 古川 路明 (Fac. Sci., Nagoya Univ.)  
FURUSATO Naohisa 古里 直久 (Coll. Sci. Eng., Aoyama Gakuin Univ.)  
HIRUNUMA Rieko 蛭沼利江子 (Showa Coll. Pharm. Sci.)  
ITO Nobuhiko 伊藤 伸彦 (Sch. Veter. Med. Animal Sci., Kitasato Univ.)  
KATAYAMA Masayuki 片山 眞之 (Fac. Agr., Univ. Osaka Pref.)  
KATAYAMA-SUGAWARA Yohko 片山 洋子 (Fac. Sci. Living, Osaka City Univ.)  
KIMURA Kan 木村 幹 (Coll. Sci. Eng., Aoyama Gakuin Univ.)  
KOJIMA Sadao 小島 貞男 (Nucl. Med. Cent., Aichi Medical Univ.)  
MATSUMOTO Ken-ichiro 松本 謙一郎 (Showa Coll. Pharmaceutic. Sci.)  
MINAI Yoshitaka 葉袋 佳孝 (Fac. Human, Musashi Univ.)  
NASU Saburo 那須 三郎 (Fac. Eng. Sci., Osaka Univ.)  
OHKUBO Yoshitaka 大久保 嘉高 (Res. Reactor Inst., Kyoto Univ.)  
OISHI Shigeo 大石 茂雄 (Sch. Health Sci., Kanazawa Univ.)  
OKAMOTO Yayoi 岡本 弥生 (Showa Coll. Pharmaceutic. Sci.)  
OKAMOTO Yoichi 岡本 洋一 (Showa Coll. Pharm. Sci.)  
OZAKI Takuo 尾崎 卓郎 (Fac. Sci., Univ. Tokyo)  
SAITO Tadashi 斎藤 直 (Fac. Sci., Osaka Univ.)  
SHIBATA Seiichi 柴田 誠一 (Res. Reactor Inst., Kyoto Univ.)  
SHINOHARA Atsushi 篠原 厚 (Fac. Sci., Nagoya Univ.)  
WANG Haifang (Peking Univ., China)  
WEGINWAR Rajiv G. (Chandrapur Coll. Engineer., India)  
YOKOTA Yuko 横田 裕子 (Coll. Sci. Eng., Aoyama Gakuin Univ.)  
YOKOYAMA Akihiko 横山 明彦 (Fac. Sci., Osaka Univ.)

YOSHIDA Yutaka 吉田 豊 (Shizuoka Inst. Sci. Technol.)

(Students)

ABE Daisuke 阿部大輔 (Fac. Sci., Toho Univ.)  
ARAKI Hirokazu 荒木宏一 (Fac. Sci., Osaka Univ.)  
DAIRAKU Tomohisa 大樂知久 (Fac. Sci., Nagoya Univ.)  
HAYAKAWA Nobutaka 早川信隆 (Showa Coll. Pharm. Sci.)  
IRIGUCHI Yuko 入口優子 (Fac. Sci. Living, Osaka City Univ.)  
ITOH Masahiro 伊藤昌宏 (Shizuoka Inst. Sci. Technol.)  
ITOH Naoya 伊藤直弥 (Coll. Sci. Eng., Aoyama Gakuin Univ.)  
ITOU Mayu 伊藤麻由 (Sch. Veter. Med. Animal Sci., Kitasato Univ.)  
MORIMOTO Shinya 森本真哉 (Fac. Sci., Osaka Univ.)  
MUKAI Kazuhiko 向和彦 (Fac. Sci., Osaka Univ.)  
MURASE Nobuyuki 村瀬伸幸 (Shizuoka Inst. Sci. Technol.)  
MURATA Chihiro 村田千裕 (Fac. Sci., Nagoya Univ.)  
MUROYAMA Toshiharu 室山俊浩 (Fac. Sci., Nagoya Univ.)  
NAKANISHI Kouichi 中西孝市 (Shizuoka Inst. Sci. Technol.)  
NISHIZAWA Satoshi 西沢諭 (Sch. Hygien. Sci., Kitasato Univ.)  
ODA Hirotaka 小田寛貴 (Fac. Sci., Nagoya Univ.)  
OIKAWA Shinji 及川真司 (Fac. Sci., Kanazawa Univ.)  
SANADA Jun 真田潤 (Fac. Sci., Osaka Univ.)  
SEKIGUCHI Akiko 関口明子 (Coll. Sci. Eng., Aoyama Gakuin Univ.)  
SOGA Kyoko 曾我恭子 (Fac. Sci., Nagoya Univ.)  
SOTOGAKU Naoki 外角直樹 (Showa Coll. Pharm. Sci.)  
TAKAHASHI Yoshio 高橋嘉夫 (Fac. Sci., Univ. Tokyo)  
YASHIKI Kazuhiro 屋鋪一尋 (Fac. Sci., Toho Univ.)

#### Chemical Dynamics Laboratory

KIMURA Kazuie 木村一宇

USHIDA Kiminori 丑田公規

(Visitor)

KAZAMA Shigeo 風間重雄 (Dept. Phys., Chuo Univ.)

(Students)

HONG Wan 洪完 (Dept. Chem., Univ. Tokyo)  
ITOH Noriaki 伊藤憲昭 (Osaka Inst. Technol.)  
KANEKO Junichi 金子純一 (JAERI, Tohkai)

#### Cellular Physiology Laboratory

HANAOKA Fumio 花岡文雄\*<sup>1</sup>

KITAYAMA Shigeru 北山滋

YATAGAI Fumio 谷田貝文夫\*<sup>2</sup>

---

\*<sup>1</sup> Chief Scientist, \*<sup>2</sup> Senior Scientist

(Visitors)

ANDO Koichi 安藤興一 (Natl. Inst. Radiol. Sci.)  
FUKUMURA Akifumi 福村明史 (Natl. Inst. Radiol. Sci.)  
FURUSAWA Yoshiya 古澤佳也 (Natl. Inst. Radiol. Sci.)  
HAMA Yoshimasa 浜義昌 (Sci. Eng. Res. Lab., Waseda Univ.)  
HOSHINO Kazuo 星野一雄 (Natl. Inst. Radiol. Sci.)  
IIZUKA Masayuki 飯塚正之 (Natl. Inst. Radiol. Sci.)  
ITO Hisao 伊東久夫 (Sch. Med., Chiba Univ.)  
ITOH Hiroko 伊藤浩子 (Natl. Inst. Radiol. Sci.)  
ITSUKAICHI Hiromi 五日市ひろみ (Natl. Inst. Radiol. Sci.)  
KANAI Tatsuaki 金井達明 (Natl. Inst. Radiol. Sci.)  
KASAI Kiyomi 笠井清美 (Natl. Inst. Radiol. Sci.)

KAWACHI Kiyomitsu 河内清光 (Natl. Inst. Radiol. Sci.)  
 KIMOTO Masafumi 木元正史 (Natl. Inst. Radiol. Sci.)  
 KOBAYASHI Yasuhiko 小林泰彦 (JAERI, Takasaki Rad. Chem. Res. Estab.)  
 KOHNO Toshiyuki 河野俊之 (Natl. Inst. Radiol. Sci.)  
 KOIKE Sachiko 小池幸子 (Natl. Inst. Radiol. Sci.)  
 KOJIMA Eiichi 小島栄一 (Natl. Inst. Radiol. Sci.)  
 KUBOTA Nobuo 窪田宜夫 (Fac. Med., Yokohama City Univ.)  
 LI Ryonpha 李玲華 (Natl. Inst. Radiol. Sci.)  
 MATSUFUJI Naruhiro 松藤成弘 (Natl. Inst. Radiol. Sci.)  
 MINOHARA Shinichi 箕原伸一 (Natl. Inst. Radiol. Sci.)  
 MIYAHARA Nobuyuki 宮原信幸 (Natl. Inst. Radiol. Sci.)  
 MURAIISO Chidori 村磯知採 (Natl. Inst. Radiol. Sci.)  
 MURAKAMI Masahiro 村上正弘 (Natl. Inst. Radiol. Sci.)  
 OHARA Hiroshi 大原弘 (Dept. Gen. Cult., Okayama Univ.)  
 OKUMURA Toshiyuki 奥村敏之 (Fac. Med., Univ. Tsukuba)  
 SAITO Mizuho 斉藤瑞穂 (Natl. Inst. Radiol. Sci.)  
 SASAKI Hiroshi 佐々木弘 (Fac. Med., Kyushu Univ.)  
 SHIKAZONO Naoya 鹿園直哉 (JAERI, Takasaki Rad. Chem. Res. Estab.)  
 SOGA Fuminori 曾我文宣 (Inst. Nucl. Study, Univ. Tokyo)  
 SUDO Michio 須藤美智雄 (Natl. Inst. Radiol. Sci.)  
 TAGUCHI Yasuko 田口泰子 (Natl. Inst. Radiol. Sci.)  
 TAKATUJI Toshihiro 高辻俊宏 (RI Cent., Nagasaki Univ.)  
 TANAKA Atsushi 田中淳 (JAERI, Takasaki Rad. Chem. Res. Estab.)  
 TANAKA Kaoru 田中薫 (Natl. Inst. Radiol. Sci.)  
 TATSUZAKI Hideo 立崎英夫 (Fac. Med., Univ. Tsukuba)  
 TOMURA Hiromi 外村浩美 (Natl. Inst. Radiol. Sci.)  
 TSUBOI Atsushi 坪井篤 (Natl. Inst. Radiol. Sci.)  
 TSUBOUCHI Susumu 坪内進 (Suzuka Med. Technol. Univ.)  
 WATANABE Masami 渡辺正己 (Fac. Pharm., Nagasaki Univ.)  
 YAMASHITA Shoji 山下昌次 (Natl. Saitama Hospital)

#### Plant Functions Laboratory

ABE Tomoko 阿部知子 BAE Chang-Hyu 裴昌休\*<sup>1</sup>  
 MATSUYAMA Tomoki 松山知樹\*<sup>2</sup> TAKAHASHI Yoshiko 高橋佳子  
 YOSHIDA Shigeo 吉田茂男\*<sup>3</sup>

\*<sup>1</sup> Postdoctoral Researcher, \*<sup>2</sup> Special Postdoctoral Researcher, \*<sup>3</sup> Chief Scientist

(Visitors)

HASHIMOTO Takashi 橋本隆 (Dep. Biosci., NAIST)  
 SATO Fumihiko 佐藤文彦 (Dep. Agr. Chem., Kyoto Univ.)  
 SATO Shinobu 佐藤忍 (Inst. Bio. Sci., Tsukuba Univ.)  
 SUZUKI Kenichi 鈴木賢一 (Suntory Ltd.)

(Students)

IWAI Hiroaki 岩井宏暁 (Inst. Bio. Sci., Tsukuba Univ.)  
 KUMATA Shuji 熊田秀治 (Weed Sci. Cent., Utsunomiya Univ.)  
 TAKAHASHI Hideki 高橋英樹 (Coll. Agr. & Vet. Med., Nihon Univ.)

#### Microbial Toxicology Laboratory

ARIE Tsutomu 有江力 YAMAGUCHI Isamu 山口勇\*

\* Chief Scientist

(Visitors)

GOUTHU Satyanarayana

NOSE Yasuhiro 能勢泰寛  
SHINONAGA Taeko 篠永妙子  
WATANABE Tadakazu 渡部忠一 (Agro-Kanesho Co., Ltd.)

#### Safety Center

HARASAWA Kaoru 原沢 薫	KAGAYA Satoru 加賀屋 悟
MATSUZAWA Yasuhide 松沢安秀	MIYAGAWA Makoto 宮川真言
NAKANISHI Noriyoshi 中西紀喜*	SHINOHARA Shigemi 篠原茂己
UWAMINO Yoshitomo 上蓑義朋	YAMANAKA Akira 山仲 暁
YOSHIKI Hajime 吉識 肇	

---

\* Head

#### Surface Characterization Center

IWAKI Masaya 岩木正哉*	NAKAO Aiko 中尾愛子
--------------------	-----------------

---

\* Head

#### Radioisotope Technology Division

GORDON Alasdair* <sup>1</sup>	SUZUKI Makoto 鈴木 任* <sup>2</sup>
YATAGAI Fumio 谷田貝文夫* <sup>3</sup>	

---

\*<sup>1</sup> STA Fellow, \*<sup>2</sup> Special Postdoctoral Researcher, \*<sup>3</sup> Head

(Visitors)

FUJIE Akio 藤江章雄 (Furuuchi Chemicals)  
KAGAWA Yasuhiro 香川康浩 (Toray Res. Cent. Inc.)  
KASE Youko 加瀬陽子 (Natl. Inst. Radiol. Sci.)  
MAEZAWA Hiroshi 前澤 博 (Fac. Med., Tokai Univ.)  
OGURA Koichi 小倉紘一 (Coll. Ind. Technol., Nihon Univ.)  
SUZUKI Masao 鈴木雅雄 (Fac. Pharm., Nagasaki Univ.)

(Student)

SAITO Tomohiro 斎藤智廣 (Fac. Life Sci., Tokyo Univ. Pharmacy & Life Sci.)

## AUTHOR INDEX

- ABE Ryo 阿部 亮 5  
 ABE Tomoko 阿部知子 148  
 ADACHI Minoru 足立 實 72, 77  
 AIHARA Toshimitsu 藍原利光 3  
 AKAGI Hiroyasu 赤木宏安 5  
 AKIKAWA Hisashi 秋川藤志 52, 53  
 AKIYOSHI Hiromichi 秋吉哲充 67, 158  
 ALONSO Jose R. 70  
 AMANO Ryohei 天野良平 126, 127  
 AMBE Fumitoshi 安部文敏 119, 120, 121, 122, 123,  
 124, 125, 126, 127, 128,  
 129, 130, 131, 132, 133,  
 134, 135, 138, 139, 140,  
 141  
 AMBE Shizuko 安部静子 123, 124, 125, 128, 129, 130,  
 131, 132, 133, 134, 135, 136,  
 137, 138, 139, 140, 141, 145,  
 146  
 ANDO Atsushi 安東 醇 127  
 ANDO Kozo 安藤剛三 91, 92, 93, 94  
 ANDO Yoshiaki 安藤嘉章 10, 64, 67, 68, 69, 75, 162  
 AOI Nori 青井 考 64, 65, 69, 71, 72, 73, 74, 76, 121  
 AOKI Yuka 青木由香 165  
 ARAKAWA Takesi 荒川 猛 253, 254  
 ARAKI Hirokazu 荒木宏一 142  
 ARIE Tsutomu 有江 力 145, 146  
 ARIGA Takehiro 有賀健博 167  
 ARIMA Akito 有馬朗人 17, 19, 20, 26, 29  
 ASAHI Koichiro 旭 耕一郎 72, 77  
 ASAMITSU Atsushi 朝光 敦 106  
 AWAGA Kunio 阿波賀邦男 111  
 AWAYA Yohko 粟屋容子 94, 157  
 BABA Hiroshi 馬場 宏 142  
 BAE Chang-Hyu 裴 昌然 148  
 BAKALOVA K. 89  
 BAKALOV Dimitre 89  
 BANDYOPADHYAY Arup 203  
 BATYGIN Yuri 52, 192, 235, 237, 239, 246  
 BAUMANN Thomas 78  
 BLANK Bertrum 78  
 BLUNDELL Stephen J. 113  
 BOCHKAREV Oleg 79  
 BOUÉ Frederic 78  
 BUENKER Robert J. 81  
 CEDERWALL Bo 56  
 CHIBA Daisuke 千羽大介 95  
 CHIBA Toshiya 千葉利哉 3, 191, 192, 198  
 CHIMI Yasuhiro 知見康弘 97  
 CHOU Ju 劉 菊 133, 134, 135  
 CHULKOV Leonid 79  
 CORTINA Dolores 79  
 CZAJKOWSKI Serge 78  
 DELBAR Therry 10  
 DINH DANG Nguyen 廷燈 阮 19, 20, 27, 28, 29  
 EATON Gordon H. 49, 50, 51  
 EGUCHI-KASAI Kiyomi 江口(笠井)清美 150  
 ENDO Kazutoyo 遠藤和豊 130, 131, 132  
 ENOMOTO Shuichi 榎本秀一 123, 126, 127, 128, 129,  
 130, 131, 132, 133, 134,  
 135, 137, 138, 139, 140,  
 141  
 EN'YO Hideto 延与秀人 52, 53, 170, 172, 173  
 FAN Xiao-Jun 樊 曉駿 99  
 FEINAUER Adolf 119  
 FÖRSTER Andreas 78  
 FRANCE III Ralph 10  
 FUJIE Akio 藤江章雄 151  
 FUJII Masayuki 藤井雅之 169  
 FUJISAWA Eiji 藤澤栄二 52, 53  
 FUJISHIMA Shiro 藤島史朗 205, 206, 208, 210, 214,  
 216, 218  
 FUJITA Jiro 藤田二郎 5, 182, 183  
 FUJITA Shin 藤田 新 253, 254  
 FUJITA Tatsuru 藤田 建 158  
 FUJIWARA Hideki 藤原秀樹 64, 67, 69, 75  
 FUKAO Tetsuhiro 深尾哲宏 66, 70  
 FUKUDA Mitsunori 福田光順 66, 70  
 FUKUDA Naoki 福田直樹 65, 67, 71, 72, 73, 74, 76  
 FUKUDA Shigekazu 福田茂一 66, 70, 72, 77, 177, 178  
 FUKUDA Tomokazu 福田共和 65  
 FUKUNISHI Nobuhisa 福西暢尚 15, 147, 151, 200,  
 202, 245  
 FUKUSAKA Shoichi 福坂将一 62, 63  
 FÜLÖP Zsolt 67  
 FURUSAWA Yoshiya 古澤佳也 149  
 GAI Moshe 10, 64, 78  
 GEIBEL Christoph 108  
 GEISSEL Hans 78, 79  
 GOHSHI Yoichi 合志陽一 177, 178  
 GOKA Tateo 五家建夫 169  
 GONO Yasuyuki 郷農靖之 56, 57, 58  
 GOTO Akira 後藤 彰 5, 143, 181, 182, 185, 187,  
 189, 191, 192, 194, 196, 198,  
 200, 203, 205, 206, 208, 210,

- 212, 214, 216, 218, 220, 222,  
224
- GOTO Yuji 後藤雄二 44, 52, 53, 54, 55, 170, 173
- GOUTHU Satyanarayana 145, 146
- GROSSE Eckart 78
- GU Jian-Ping 81
- HAHN Kevin Inskik 10, 64, 67, 69
- HAMANAKA Hiromi 浜中廣見 176
- HANAOKA Fumio 花岡文雄 151
- HARASAWA Kaoru 原沢 薫 256
- HASEBE Hiroo 長谷部裕雄 3
- HASEGAWA Ken-ichi 長谷川賢一 176
- HASHIMOTO Masa-aki 橋本正章 40
- HASHIMOTO Masashi 橋本雅史 49, 50, 51
- HASHIZUME Akira 橋爪 朗 179
- HATANAKA Kichiji 畑中吉治 52, 61, 62
- HAYAKAWA Kazuo 早川一生 120, 121
- HAYAKAWA Shinjiro 早川慎二郎 177, 178
- HAYASHIGAKI Arata 林垣 新 46
- HAYASHI Naoki 林 直樹 44, 52, 53, 54, 55, 170, 172,  
173
- HAYES William 113
- HELLSTRÖM Margareta 78, 79
- HEMMI Masatake 逸見政武 3, 191, 192
- HIGEMOTO Wataru 髭本 亘 105, 106, 110
- HIGURASHI Yoshihide 日暮祥英 67
- HILLEBRANDT Wolfgang 35
- HINO Ken-ichi 日野健一 82
- HIRAI Masaaki 平井正明 10, 64, 67, 69
- HIRAI Masanori 平井正紀 44, 45
- HIRANO Masahiko 平野昌彦 151
- HIRATA Daisy 25
- HIROSE Takayuki 広瀬孝幸 101
- HIRSCH Gerhard 81
- HIRUNUMA Rieko 蛭沼利江子 128, 129, 130, 131, 135
- HISANAGA Isamu 久永 勇 67, 75, 162
- HOFMANN Helmut 31, 32
- HOMMA Takayuki 本間隆之 5
- HONG Wan 洪 完 152, 177, 178
- HONMA Michio 本間道雄 15, 16
- HORIBATA Takatoshi 堀端孝俊 21, 22, 23
- HORIKAWA Hirotsugu 堀川博嗣 44
- HSIA Yuanfu 夏 元復 122
- HUI Qin 惠 秦 104
- HULDST Sven 93, 94
- HUTTON Roger 93, 94
- ICHIHARA Takashi 市原 卓 52, 61, 62, 63, 155, 170,  
171, 172, 173
- ICHIKAWA Ryuji 市川龍二 5
- IDEUCHI Eiji 井出口栄治 56, 57, 58, 73, 74, 76
- IDESAWA Eriko 出沢恵理子 161
- IEKI Kazuo 家城和夫 64
- IGARASHI Akinori 五十嵐明則 87
- IKEDA Hiroshi 池田 博 98
- IKEGAMI Kumio 池上九三男 5, 167, 187, 205, 208,  
210, 224
- IKEZAWA Eiji 池沢英二 3, 192
- IMAI Ken'ichi 今井憲一 52, 53, 170, 172
- IMAIDA Isamu 今井田伊佐宗 169
- IMAMURA Mineo 今村峯雄 59
- INABE Naohito 稲辺尚人 5, 167, 191, 227
- ISHIBASHI Ryochi 石橋了知 149
- ISHIDA Katsuhiko 石田勝彦 49, 50, 51, 113
- ISHIDA Satoru 石田 悟 60, 61, 62, 63
- ISHIDA Takayuki 石田尚行 112
- ISHIE Masami 石江真砂美 126
- ISHIHARA Masayasu 石原正泰 10, 52, 53, 56, 57, 58,  
64, 65, 66, 67, 68, 69,  
71, 72, 73, 74, 75, 76,  
77, 170, 171, 172
- ISHII Keishi 石井慶之 91, 92
- ISHIKAWA Norito 石川法人 97, 98
- ISSHIKI Hiroshi 一色 博 5
- ITO Hisao 伊東久夫 149
- ITO Sachiko 伊藤祥子 66, 245, 253, 254, 256
- ITO Yasuo 伊藤泰男 143
- ITOH Kazuya 伊藤和也 60, 62, 63
- ITOH Noriaki 伊藤憲昭 152
- ITOH Yoh 伊藤 陽 157
- ITOH Yoshiko 伊東芳子 143
- ITSUKAICHI Hiromi 五日市ひろみ 150
- IVANOV Marian 79
- IVANYUK Fedor A. 31, 32
- IWAKI Masaya 岩木正哉 175
- IWAMA Tetsu 岩間 哲 42
- IWASA Naohito 岩佐直仁 10, 67, 78
- IWASAKI Hironori 岩崎弘典 67, 71, 72, 73, 74, 75, 76
- IWASE Akihiro 岩瀬彰宏 97, 98
- IWATA Yoshiyuki 岩田佳之 64, 69, 75
- IZUMI Hideaki 出水秀明 72, 77
- IZUYAMA Takeo 伊豆山健夫 38, 39
- JANIK Rudolf 79
- KADONO Ryosuke 門野良典 109, 114, 115
- KAGAWA Yasuhiro 香川康浩 151
- KAGEYAMA Tadashi 影山 正 5, 182, 183, 187, 191
- KALVIUS Georg Michael 109
- KAMBARA Tadashi 神原 正 90, 91, 92, 93, 94, 96,  
97, 98, 99, 100

- KAMEI Takehito 亀井武仁 95
- KAMIGAITO Osamu 上垣外修一 5, 191, 192, 198, 203, 222
- KAMINO Yuichiro 神納祐一郎 241
- KANAI Tatsuaki 金井達明 149, 150
- KANAI Yasuyuki 金井保之 95, 96, 157
- KANAZAWA Yasunobu 金澤康信 46
- KANEKO Junichi 金子純一 152, 153
- KANEKO Shin-ichi 金子真一 100
- KASAGI Jirohta 笠木治郎太 165
- KASE Masayuki 加瀬昌之 5, 101, 167, 182, 191, 192, 194, 200, 202
- KATAYAMA Masayuki 片山眞之 138
- KATAYAMA Takeshi 片山武司 52, 167, 181, 225, 227, 229, 231, 233, 235, 241, 243, 246, 248, 250, 251
- KATO Hiroshi 加藤 博 168
- KATO Mineo 加藤岑生 49, 50, 51
- KAWABATA Yoshiyuki 川端好之 82
- KAWADA Tetsuya 川田哲也 149
- KAWAE Sotaro 川江宗太郎 91, 92
- KAWAGUCHI Takeo 川口武男 205, 206, 208, 210, 212, 214, 250
- KAWAGUCHI Takeshi 川口武司 52
- KAWAMURA Naritoshi 河村成肇 49, 50, 51
- KIDERA Masanori 木寺正憲 5, 182, 191, 194, 202
- KIJIMA Takeshi 鬼島 文 67
- KIKUCHI Tadashi 菊地 正 10, 64, 69
- KIM Eunjoo 金 琅珠 59
- KIM Jong-Won 金 鐘元 205, 206, 208, 210, 214, 220
- KIMURA Kazuie 木村一宇 152, 153, 177, 178
- KIMURA Kikuo 木村喜久雄 79
- KIMURA Mineo 季村峯生 81, 85, 90
- KIMURA Motoe 木村元江 126
- KISHIDA Takashi 岸田 隆 56, 57, 58, 73
- KITAGAWA Hisashi 北川 尚 11, 43
- KITAJIMA Masashi 北島昌史 157
- KITAO Kensuke 喜多尾憲助 179
- KITAYAMA Shigeru 北山 滋 147
- KOBAYASHI Kiyoshi 小林清志 5
- KOBAYASHI Misaki 小林美咲 5, 194, 200, 202
- KOBAYASHI Toshio 小林俊雄 66, 70, 71, 79
- KOBAYASHI Yoshio 小林義男 119, 120, 121, 122, 142
- KOCZON Piotr 78
- KOHAMA Akihisa 小濱洋央 42
- KOHARA Shigeo 小原重夫 3, 5, 192, 198
- KOHARA Takao 小原孝夫 99
- KOHLMEYER Bernd 78
- KOHNO Tsuyoshi 河野 毅 101, 168, 169
- KOIKE Shigetoshi 小池茂年 102
- KOIKE Yuji 小池裕司 46
- KOJIMA Takao M. 小島隆夫 90
- KOKUBUN Motohide 国分紀秀 161
- KOROBV Vladimir I. 88, 89
- KORSHENINNIKOV Alexei 79
- KOWARI Ken-ichi 小割健一 86
- KOYAMA Akio 小山昭雄 103
- KRATZER Andreas 109
- KREBS Gary F. 70
- KRISHNAMURTHY V. V. 107, 108
- KUBO Atsushi 久保敦司 149
- KUBO Toshiyuki 久保敏幸 10, 71, 72, 74, 76, 77, 167, 205, 206, 208, 210, 214, 220
- KUBONO Shigeru 久保野 茂 10, 64
- KUBOYAMA Satoshi 久保山智司 101
- KUDO Katsuhisa 工藤勝久 49, 50, 51
- KULESSA Reinhard 78
- KUMAGAI Hidekazu 熊谷秀和 164, 200
- KUMANO Shunzo 熊野俊三 44, 45
- KUMATA Shuji 熊田秀治 148
- KURASAWA Haruki 倉沢治樹 12, 18, 34
- KURITA Kazuyoshi 栗田和好 52, 54, 172
- KURITA Tetsuro 栗田哲郎 156
- KURODA Naoshi 黒田直志 98
- KURODA Shinji 黒田眞司 110
- KUROKAWA Meiko 黒川明子 10
- KUROKAWA Nobuo 黒河暢雄 72
- KUROSAWA Kiyoyuki 黒沢清行 49, 50, 51
- KUROSAWA Tadahiro 黒沢忠弘 245
- KUWAHARA Hideki 桑原英樹 106, 107
- LAUE Frank 78
- LEE Sang Moo 李 相茂 156
- LEUNG Ki 86
- LIPNIK Peter 10
- LUKYANOV Sergei M. 74
- MACRAE Roderik M. 114
- MAEDA Kuniko 前田邦子 176, 177, 178
- MAEDA Masaru 前田 勝 176
- MAIE Takeshi 真家武士 5
- MAKIDE Yoshihiro 巻出義紘 125, 139, 140
- MAO Yajun 冒 亜軍 52, 53, 172
- MARCHAND Claire 78
- MARTINSON Indrek 93, 94
- MASAI Taku 政井 琢 85
- MASAIKE Akira 政池 明 52, 170
- MASUDA Kimiaki 増田公明 169

- MATSUBARA Yutaka 松原 豊 169
- MATSUDA Sumio 松田純夫 101
- MATSUKI Tuneki 松木常樹 41
- MATSUMOTO Haruhisa 松本晴久 169
- MATSUMOTO Ken-ichiro 松本謙一郎 131, 132
- MATSUMOTO Yasuhiro 松本康寛 70
- MATSUTA Kensaku 松多健策 66, 70
- MATSUYAMA Yoshitaka 松山芳孝 65
- MATSUZAKI Keiichi 松崎恵一 161
- MATSUZAKI Teiichiro 松崎禎市郎 49, 50, 51
- MATSUZAWA Michio 松澤通生 82
- MENG Jie 孟 杰 13, 14, 17
- MENGGONI Alberto 71
- MERGEL Volker 90
- MICHIKAMI Osamu 道上 修 97
- MICHOTTE Carrine 10
- MIHARA Mototsugu 三原基嗣 66, 70
- MIKI Keitaro 三木敬太郎 64, 69
- MINAI Yoshitaka 葉袋佳孝 125, 139, 140
- MINAMISONO Kei 南園 啓 70
- MINAMISONO Tadanori 南園忠則 66, 70
- MINEMURA Toshiyuki 峯村俊行 64, 67, 69, 75
- MITAMURA Tohru 三田村 徹 99
- MITARAI Shiro 御手洗志郎 56, 57, 58
- MITSUMOTO Toshinori 密本俊典 205, 206, 208, 210, 214, 220, 222
- MIYACHI Takahiko 宮地岳彦 65
- MIYAKE Mami 三宅麻美 56, 57, 58
- MIYAKE Toru 三宅 徹 70
- MIYAMA Masanori 深山正紀 44, 45
- MIYASAKA Hiromasa 宮坂浩正 168
- MIYASHITA Naoyuki 宮下尚之 82
- MIYATAKE Hiroari 宮武宇也 65, 72
- MIYAZAWA Yoshitoshi 宮沢佳敏 3, 191, 192, 198
- MIZOI Yutaka 溝井 浩 65
- MIZUMURA Yuki 水村裕記 77
- MIZUNO Tsunefumi 水野恒史 161
- MIZUSAKI Takahiro 水崎高浩 15, 16
- MOCHIZUKI Yuko S. 望月優子 38, 39, 40
- MOMOTA Sadao 百田佐多生 66, 70
- MONKHORST H. J. 89
- MONKMAN Andrew P. 113
- MORII Toshiyuki 森井俊行 44, 47, 48
- MORIKAWA Tetsuya 森川鐵也 205, 210
- MORIKAWA Tsuneyasu 森川恒安 56, 57, 58
- MORIMOTO Kouji 森本幸司 163
- MORIMOTO Shinya 森本真哉 142
- MORISHITA Akio 森下暁夫 70
- MORIYA Shingo 守屋真吾 10
- MOTOBAYASHI Tohru 本林 透 10, 64, 67, 68, 69, 75, 78, 162
- MOTOMURA Shinji 本村信治 56, 57, 58
- MUENZENBERG Gottfried 79
- MURAKAMI Hiroyuki 村上浩之 10, 64, 69, 75
- MURAKAMI Takeshi 村上 健 56
- MURAKI Yasushi 村木 綏 169
- NAGAMINE Kanetada 永嶺謙忠 49, 50, 51, 105, 106, 107, 108, 110, 111, 112, 113, 114, 115, 116
- NAGASE Makoto 長瀬 誠 5, 187
- NAGATA Katsuaki 永田勝明 168
- NAGATAKI Shigehiro 長滝重博 40
- NAKADA Yoko 中田陽子 52, 53, 172, 173
- NAKAGAWA Keiko 中川恵子 165
- NAKAGAWA Takahide 中川孝秀 5, 156, 165, 182, 183, 191, 192
- NAKAI Yoichi 中井陽一 90, 95, 96, 157
- NAKAJIMA Shunji 中島諄二 253, 254
- NAKAMURA Hiroyuki 中村裕之 158
- NAKAMURA Satoshi N. 中村 哲 49, 50, 51
- NAKAMURA Takashi 中村隆司 10, 59, 64, 66, 67, 68, 69, 71, 73, 74, 75, 76, 159
- NAKANISHI Noriyoshi 中西紀喜 143, 253, 254
- NAKANO Tomohide 仲野友英 91, 92
- NAKAO Aiko 中尾愛子 175
- NAKAO Makoto 中尾 誠 159
- NAKAO Noriaki 中尾徳晶 59, 159
- NAKASHIMA Takao 中島孝夫 158
- NAKAZAWA Michio 中澤道夫 169
- NASU Saburo 那須三郎 120, 121
- NICKEL Frank 79
- NIIMURA Masanobu 新村正信 185, 187, 189
- NIIZEKI Takashi 新関 隆 61, 62, 63
- NISHIDA Maki 西田真樹 127
- NISHIDA Nobuhiko 西田信彦 100
- NISHIMORI Nobuyuki 西森信行 61
- NISHIMURA Tamio 西村民男 84, 85
- NISHIO Teiji 西尾禎二 10, 64, 68, 69, 75
- NISHIYAMA Kusuo 西山樟生 106, 111
- NOGAMI Takashi 野上 隆 112
- NOJIRI Yoichi 野尻洋一 66, 70
- NONAKA Takamasa 野中敬正 60, 61, 62
- NOSE Yasuhiro 能勢泰寛 141
- NOTANI Masahiro 野谷将広 65, 67, 71, 72, 73, 74, 75, 76, 77
- NOZAKI Tadashi 野崎 正 143

- NYSTRÖM Bo 93, 94, 96  
 ODAHARA Atsuko 小田原厚子 56, 58  
 OESCHLER Helmut 78  
 OGATA Kentaro 緒方研太郎 158  
 OGAWA Hiroshi 小川博嗣 72, 73, 74, 76, 77  
 OGAWA Yoko 小川洋子 9  
 OGIWARA Kiyoshi 荻原 清 7  
 OGLOBLIN Alexei 79  
 OHIRA Hideharu 大平秀春 101  
 OHIRA Seiko 大平聖子 111, 112  
 OHKAWA Tomohiro 大川智宏 229, 231  
 OHKI Tomonori 大木智則 3  
 OHKUBO Yoshitaka 大久保嘉高 142  
OHNISHI Jun-ichi 大西純一 205  
 OHNISHI Tetsuya 大西哲哉 60, 61, 62, 63  
 OHNUMA Hajime 大沼 甫 63  
 OHTOMO Kiyotaka 大友清隆 225  
 OHTSUBO Takashi 大坪 隆 66, 70  
 OI Makito 大井万紀人 21, 23  
 OISHI Shigeo 大石茂雄 126, 127  
 OKAMURA Hiroyuki 岡村弘之 52, 60, 61, 62, 63, 173  
 OKAMURA Masahiro 岡村昌宏 52, 250, 251  
 OKAYASU Satoru 岡安 悟 98  
 OKUDA Hikaru 奥田 光 158  
OKUNO Hiroki 奥野広樹 72, 77, 167, 205, 206, 208,  
 210, 212, 214, 216, 218,  
 220, 222, 224  
 OMOTO Takanobu 尾本敬信 169  
 ONISHI Naoki 大西直毅 21, 22, 23  
 ONISHI Takashi 大西 崇 66  
 ONO Yasuhiro 小野泰弘 100  
 ORIHARA Hikonojyo 織原彦之丞 63  
 OTSU Hideaki 大津秀暁 60, 61, 62, 71  
 OTSUKA Takaharu 大塚孝治 15, 16  
 OYAMA Hitoshi 大山 等 91, 92, 93  
 OYAMATSU Kazuhiro 親松和浩 36, 37, 38  
 OZAKI Takuo 尾崎卓郎 123, 137, 138, 139, 140  
 OZAWA Akira 小沢 顕 66, 70, 78, 79  
 OZAWA Shuichi 小澤修一 67, 167  
 PASHKEVICH Vital V. 32  
 PENIONZHKEVICH Yuri E. 74  
 PFUTZNER Marek 79  
 PRATT Francis L. 113, 115  
 PRAVIKOFF Michel S. 78  
 PRIBORA Vacili 79  
 RING Peter 13, 17  
 ROY Dayeeta 47  
 RUAN Jian-Zhi 阮 健治 10  
 SAGARA Kenshi 相良建至 158  
 SAGAWA Hiroyuki 佐川弘幸 11  
 SAITO Naohito 齋藤直人 44, 52, 53, 54, 55, 170, 171,  
 172, 173  
 SAITO Tadashi 齋藤 直 142  
 SAITO Yoshitaka 齋藤芳隆 161  
 SAKAI Hideyuki 酒井英行 52, 60, 61, 62, 63, 173  
 SAKAI Kenji 酒井健二 72, 77  
 SAKAIRI Hideo 坂入英雄 103  
 SAKAMOTO Naruhiko 坂本成彦 60, 61, 62, 63, 205,  
 208, 210, 214, 220,  
 222  
 SAKAMOTO Shinichi 坂元眞一 49, 50, 51  
 SAKATA Fumihiko 坂田文彦 27, 28  
 SAKATA Hideaki 坂田英明 100  
 SAKEMI Yasuhiro 酒見泰寛 43, 52  
 SAKO Takashi 塔 隆志 169  
 SAKUMA Tai 佐久間 泰 52, 172  
 SAKURAI Hiroyoshi 櫻井博儀 10, 64, 65, 67, 68, 69,  
 71, 73, 74, 75, 76  
 SANADA Jun 真田 潤 142  
 SASAKI Michiya 佐々木道也 159  
 SATO Hikaru 佐藤 皓 52  
 SATO Hiroki 佐藤博紀 52, 53, 172, 173  
 SATO Hiromi 佐藤広海 72, 77  
 SATO Hiroshi 佐藤 雄 33, 81, 83  
 SATO Katsuhiko 佐藤勝彦 40  
 SATO Kazunori 佐藤和則 70  
 SATOU Yoshiteru 佐藤義輝 60, 61, 62, 63  
 SCHÄFER Markus 72, 73  
 SCHEIDENBERGER Christoph 79  
 SCHMIDT-BÖCKING Horst 90  
 SCHMIDT-OTT Wolf-Dieter 72, 73  
 SCHWAB Erwin 78  
 SCHWAB Wolfgang 78  
 SEEGER Alfred 119  
 SEKIGUCHI Kimiko 関口仁子 60, 62, 63  
 SENGER Peter 78  
 SHEN Hong 申 虹 36  
 SHIBATA Masataka 柴田雅隆 56, 57, 58  
 SHIBATA Seiichi 柴田誠一 59  
 SHIBATA Tokushi 柴田徳思 159  
 SHIBATA Toshi-aki 柴田利明 44, 52, 53, 55, 170, 172  
 SHIGEMATSU Naoyuki 茂末直之 149  
 SHIGENAGA Koichi 重永晃一 158  
 SHIKAZONO Naoya 鹿園直哉 147  
 SHIMAMURA Isao 島村 勲 81, 83, 85, 87, 88, 89  
 SHIMAZU Tsuneo 島津恒夫 151  
 SHIMIZU Noritaka 清水則孝 16  
 SHIMODA Tadashi 下田 正 72

- SHIMOOKA Masaaki 下岡正明 165
- SHIMOURA Susumu 下浦 享 10, 64, 67, 68, 69, 71, 75
- SHINOHARA Shigemi 篠原茂巳 256
- SHINONAGA Taeko 篠永妙子 136, 137
- SHIRATO Shoji 白土鈔二 10
- SHIZGAL Bernie D. 86
- SHUGYO Shinichi 修行新一 101
- SIELEMANN Rainer 119
- SIMON Haik 79
- SITAR Brano 79
- SOLOVIEV Vadim G. 19, 20
- SOTOGAKU Naoki 外角直樹 130, 131, 132
- SPARN G. 108
- SPEER Jürgen 78
- STEGLICH F. 108
- STRMEN Peter 79
- STURM Christian 78
- SUDOH Kazutaka 須藤和敬 47
- SUEMMERER Klaus 79
- SUGAHARA Yuichi 菅原雄一 37
- SUGAWARA-TANABE Kazuko 田辺和子 17, 24, 26, 30
- SUGII Kazuo 杉井一生 205, 224
- SUGIMOTO Kenji 杉本憲治 101
- SUGIMOTO Satoru 杉本 聡 25
- SUMIYOSHI Kohsuke 住吉光介 25, 35, 36, 37
- SÜMMERER Klaus 78
- SUN Zuxun 47, 52
- SUROWIEC Alicja 78
- SUROWKA Grzegorz 78
- SUZUKI Hideyuki 鈴木英之 35
- SUZUKI Ken 鈴木 謙 72, 77
- SUZUKI Masataka 鈴木正恭 64, 69
- SUZUKI Takahiro 鈴木隆博 101
- SUZUKI Takayuki 鈴木孝幸 72, 77
- SUZUKI Takeshi 鈴木 健 66, 79
- SUZUKI Toshio 鈴木俊夫 11, 12, 18, 34
- SUZUKI Yoshiaki 鈴木嘉昭 175
- SYMONS T. James M. 70
- TAGUCHI Kouji 田口孝治 169
- TAGUCHI Yoshio 田口義雄 100
- TAJIMA Naoki 田嶋直樹 23
- TAJIMA Yasuhisa 田島靖久 63
- TAKABATAKE Toshiro 高島俊郎 109
- TAKAHASHI Hideki 高橋英樹 148
- TAKAHASHI Katsuhiko 高橋克彦 5
- TAKAHASHI Noriaki 高橋憲明 72
- TAKAHASHI Yoshio 高橋嘉夫 125
- TAKAMI Michio 高見道生 104
- TAKANAKA Masao 高仲政雄 233
- TAKAYANAGI Toshinobu 高柳俊暢 95
- TAKEDA Atsuya 武田篤也 149
- TAKEDA Naoto 武田直人 49, 50, 51
- TAKEDA Sadamu 武田 定 70
- TAKEMATSU Noburu 竹松 伸 124
- TAKETANI Atsushi 竹谷 篤 52, 171, 172
- TAKEUCHI Satoshi 武内 聡 67, 75
- TAKITA Kohki 滝田宏樹 110
- TAKIZAWA Kyoko 滝沢京子 161
- TANABE Kazuko see SUGAWARA-TANABE
- TANABE Kosai 田辺孝哉 24, 30
- TANAKA Atsushi 田中 淳 147
- TANAKA Hidekazu 田中秀数 105
- TANAKA Hiroshi 田中 大 85
- TANAKA Isamu 田中 勲 169
- TANAKA Shun'ichi 田中俊一 47
- TANAKA Susumu 田中 進 59
- TANAKA Yasushi 田中保志 205, 206, 210
- TANASE Masakazu 棚瀬正和 49, 50, 51
- TANIGAKI Minoru 谷垣 実 11, 66, 70
- TANIGUCHI Etsuji 谷口悦史 44, 52, 55, 172
- TANIHATA Isao 谷畑勇夫 9, 14, 37, 39, 66, 70, 79, 164, 165, 167, 177, 178
- TANIMOTO Sayaka 谷本明佳 72
- TANO Shigemitsu 田野茂光 147
- TENDOW Yoshihiko 天道芳彦 179
- TERANISHI Takashi 寺西 高 10, 64, 67, 68, 69, 71, 74, 75, 76, 78
- TERASAWA Mititaka 寺澤倫孝 99
- TOKANAI Fuyuki 門叶冬樹 163
- TOKI Hiroshi 土岐 博 25, 36, 37
- TOKURA Yoshinori 十倉好紀 106, 107
- TOMINAGA Takeshi 富永 健 125
- TOMINAKA Toshiharu 富中利治 52, 205, 206, 208, 210, 214, 216, 218, 250, 251
- TONOMURA Atsuro 殿村敦朗 176
- TOPREK Dragan 196
- TORII Hisayuki 鳥井久行 52, 53, 172
- TOYA Kazuhito 戸矢和仁 149
- TSUCHIDA Hideo 土田英夫 56, 57, 58
- TSUCHIYA Harufumi 土屋晴文 169
- TSUDA Masaki 津田理樹 72, 77
- TSUKIORI Noritoshi 月居憲俊 5
- TSURU Koji 霧 浩二 97
- TSURUTA Kaoru 鶴田 薫 158
- TSUTSUMI Takeshi 堤 剛志 56, 57, 58

- UCHIBORI Takeshi 内堀武司 10, 64, 69  
 UCHIDA Shigeo 内田滋夫 137  
 UCHIYAMA Yasuhito 内山靖仁 72, 77  
 UEDA Koh-ichi 上田光一 99  
 UEHARA Hideki 上原秀樹 253, 254  
 UENO Hideki 上野秀樹 72  
 UESAKA Tomohiro 上坂友洋 60, 61, 62, 63  
 UHLIG Florian 78  
 UMEO Kazunori 梅尾和則 109  
 URAI Teruo 浦井輝夫 7  
 URAMOTO Seiichi 浦本聖一 83  
 UTSUNO Yutaka 宇都野 穰 15  
 UTSUNOMIYA Hiroaki 宇都宮弘章 64, 69  
 UWAMINO Yoshitomo 上菘義朋 59, 159, 245, 253,  
 254, 256  
 VON SCHÜTZ J. U. 114  
 WADA Nobuo 和田信雄 111  
 WADA Ryoichi 和田良一 165  
 WADA Takeshi 和田 雄 205  
 WAGNER Andreas 78  
 WAKASA Tomotsugu 若狭智嗣 52, 60, 61, 62, 173  
 WAKASUGI Masanori 若杉昌徳 167, 227, 241, 243  
 WAKIYA Kazuyoshi 脇谷一義 95  
 WAKUI Takashi 涌井崇志 60  
 WALUS Wladyslaw 78  
 WANG Haifang 王 海芳 124  
 WATANABE Hiroshi 渡辺 宏 56, 57, 58, 147  
 WATANABE Isao 渡邊功雄 105, 106, 107, 108, 109,  
 111, 112, 115, 116  
 WATANABE Shinichi 渡辺信一 82  
 WATANABE Tsutomu 渡部 力 81  
 WATANABE Yasushi 渡邊 康 10, 52, 53, 64, 65, 69,  
 76, 121, 155, 167, 170,  
 171, 172  
 WATANABE Yutaka X. 渡辺 裕 65, 71, 74, 75, 76  
 WEGINWAR Rajiv G. 128, 129, 138  
 WILDS Edward L. 64  
 WINKLER Martin 79  
 WU Heyu 吳 和宇 52  
 XIAO Meiqin 肖 美琴 52, 248  
 YABANA Kazuhiro 矢花一浩 34  
 YAGI Eiichi 八木栄一 7, 102, 103, 119, 175  
 YAGITA Takanori 八木田貴典 158  
 YAKOU Kentaro 矢向謙太郎 62, 63  
 YAMADA Shoichi 山田章一 35, 40  
 YAMAGUCHI Akira 山口 明 111  
 YAMAGUCHI Isamu 山口 勇 136, 145, 146  
 YAMAJI Shuhei 山路修平 14, 17, 20, 31, 32  
 YAMAMOTO Sukeyasu Steven 山本裕靖 73  
 YAMANISHI Teruya 山西輝也 44, 47  
 YAMASHITA Shoji 山下昌次 149  
 YAMAUCHI Hiromoto 山内啓資 3  
 YAMAZAKI Yasunori 山崎泰規 157  
 YANAGISAWA Yoshiyuki 柳澤善行 10, 64, 67, 68, 69,  
 75  
 YANO Hideo 矢野英雄 111  
 YANO Yasushige 矢野安重 5, 167, 181, 182, 185, 187,  
 189, 191, 192, 194, 196,  
 200, 202, 203, 205, 206,  
 208, 210, 212, 214, 216,  
 218, 220, 222, 224  
 YASUDA Hiroshi 保田浩志 137  
 YATAGAI Fumio 谷田貝文夫 149, 150, 151  
 YAZAKI Koichi 矢崎絃一 42  
 YOKOUCHI Shigeru 横内 茂 205, 210, 224  
 YOKOYAMA Akihiko 横山明彦 142  
 YOKOYAMA Go 横山 剛 60, 61, 62, 63  
 YOKOYAMA Ichiro 横山一郎 5  
 YONEBAYASHI Tomoko 米林朋子 127  
 YONEDA Akira 米田 晃 5, 194, 200, 202  
 YONEDA Ken-ichiro 米田健一郎 65, 71, 72, 73, 74, 76,  
 77  
 YONEYAMA Shigenobu 米山茂信 52, 53  
 YOSHIDA Atsumasa 吉田篤正 161  
 YOSHIDA Atsushi 吉田 敦 65, 72, 74, 77, 121, 155,  
 167, 179  
 YOSHIDA Hyogo 吉田兵吾 143  
 YOSHIDA Koichi 吉田光一 66, 70, 79, 165, 227  
 YOSHIDA Nobuaki 吉田宣章 26  
 YOSHIDA Shigeo 吉田茂男 148  
 YOSHIDA Yutaka 吉田 豊 119, 120, 121  
 YOSHIMI Akihiro 吉見彰洋 72, 77  
 YOSHIZAKI Ryozo 吉崎亮造 98  
 YOSOI Masaru 与曾井 優 52  
 YUKIHIRA Ken-ichi 行平憲一 120, 121  
 ZHOU Xiao Hong 周 小紅 56, 57, 58  
 ZOU Yaming 邹 亚明 93, 94



## **RIKEN Accelerator Progress Report Vol. 31**

理化学研究所加速器年次報告 第31巻 (1998)

印刷 平成 10 年 (1998) 3 月 20 日  
発行 平成 10 年 (1998) 3 月 31 日

発行者 理化学研究所  
代表者 有馬朗人  
〒351-0198 埼玉県和光市広沢 2 番 1 号  
電話 (048) 462-1111

編集者 理化学研究所加速器研究施設  
運営委員会

印刷所 株式会社ユニバーサル・アカデミー・プレス  
〒113-0033 東京都文京区本郷 6 丁目 16 番 2 号 BR本郷 5 ビル

定価 5,000 円  
(消費税別)



理化学研究所

埼玉県 和光市 広沢